UCLouvain

epl

École polytechnique de Louvain

Micro Energy Harvesting using Reverse Electrodialysis with Porous Silicon Membranes

Author: Romain HANUS

Academic year 2025–2026
Doctoral thesis

Dissertation committee

Prof. Laurent A. Francis (UCLouvain, advisor)
Prof. Denis Flandre (UCLouvain, secretary)
Prof. Tristan Gilet (ULiège)
Prof. Abel Santos (University of Adelaide, Australia)
Prof. Christophe Craeye (UCLouvain, chair)

Acknowledgements

First and foremost, I would like to express my deepest gratitude to Professor Laurent A. Francis, the promotor of this work. From the day we first met in 2018, during my master's thesis, a collaboration began that ultimately led to this doctoral journey. Encouraged by the results we obtained during my master's research, the idea of continuing toward a PhD naturally emerged.

He placed his trust in me and supported my application for a teaching assistant position, which marked the true beginning of this path. Since then, he has consistently been present through meetings, detailed feedback, conferences, and even informal discussions over lunch. While never imposing unnecessary pressure, he has always been available to answer questions, sometimes late in the evening or during weekends. Over the years, our relationship evolved from student–professor to colleague–mentor, and I am sincerely grateful for that.

Next, I would like to express my gratitude to Prof. Denis Flandre, Prof. Tristan Gilet, Prof. Abel Santos, and Prof. Christophe Craeye for accepting to serve as members of my PhD jury. Their careful reading and valuable feedback during my private defense helped improve this thesis substantially. In particular, I would like to thank Prof. Tristan Gilet and Prof. Denis Flandre for their advice as members of my support committee, and Prof. Christophe Craeye for accepting to chair my defense. My deepest thanks also go to Prof. Abel Santos for the opportunity to collaborate on research related to osmotic energy generation using nanoporous anodic alumina and ionic rectification properties.

I would also like to thank my family and friends. My parents, Sophie and Didier, never hesitated to support me when I decided to pursue a second master's degree, which eventually led me to begin this PhD. They always trusted the path I chose throughout my academic career. Beginning this doctorate also coincided with the start of my independent life: buying a house, purchasing a car, and taking on new responsibilities. Managing these commitments alongside research was challenging at times, but I never felt overwhelmed nor unsupported, because they were always there to guide me and help me when needed.

While parents share wisdom and unconditional support, the struggles and passions of everyday life are often best shared with friends. To my friends: your presence throughout this journey was just as important as that of my family and supervisor. Sharing laughter, beers, holidays, and simple moments of joy helped balance the inevitable frustrations of research, especially during those long days in the lab when experiments refused to work.

I would also like to express my sincere gratitude to my colleagues, many of whom have become close friends. Sharing a workspace with someone who does not always speak much is not necessarily easy, but you showed patience, offered advice, shared laughter, and made everyday work enjoyable. Roselien Vercauteren was the first to guide me into the research field and helped me learn how to work in the cleanroom.

Margot, Ramy, Nicolas, Justine, and Grégoire made the office a vibrant and enjoyable place to work. Our discussions, whether about research, health, or future projects, were always stimulating. A special note to Grégoire: sharing our passion for future technologies and for sport, especially cycling and running, as well as facing similar challenges in the lab, made this journey lighter and far more enjoyable. I will always be grateful for those shared moments.

I also wish to thank all the members of the ELEN and ICTEAM departments. In particular, I would like to thank the WINFAB staff, namely Christian Renaux, Sébastien Faniel, Miloud Sitout, and Nicolas André, as well as my many WINFAB colleagues: Romain Tuyaerts, Gilles Scheen, Michaël Coulombier, and many others. Their advice, our many discussions, and the good times we shared transformed the cleanroom into a very pleasant and welcoming environment.

I would also like to thank the members of the Welcome Platform. I am also grateful to the administrative and technical staff of ICTEAM for their support throughout these years and for the many friendly discussions in the corridor or during lunch breaks: Viviane Sauvage, Anne Gillet, Isabelle Dargent, Brigitte Dupont, François Hubin, Cristel Derzelle, Jean Deschuyter, and Nathalie Ponet.

Lastly, and most importantly, I want to thank my beloved wife, Dima. We met almost at the same time we both began our PhD journeys at UCLouvain. We shared everything together: the confinement during COVID, struggles at work, difficult collaborations, failed experiments, and moments of doubt. Your support meant everything to me. Without you, this work might not have seen the light of day. You were my lighthouse in the storm. Seeing you succeed in your own path motivated me to succeed as well. Your strength and resilience inspired me to push through my own difficulties.

Marrying you also gave me a new family. Their support, even from afar in Lebanon, strengthened me further. Knowing that they believed in us and in our future projects kept me motivated and confident throughout this journey.Our journey continues, and I will stand by you just as you have always stood by me.

Abstract

This thesis investigates porous silicon (pSi) as a CMOS-compatible nanoporous ion-exchange membrane for nanofluidic reverse electrodialysis (nRED), with the long-term objective of enabling miniaturized salinity-gradient energy harvesters for autonomous microsystems and low-power IoT platforms. While conventional reverse electrodialysis relies on dense polymer ion-exchange membranes optimized for large-scale stacks, nanofluidic approaches exploit surface-charge-governed ion transport in nanoscale pores and offer a possible route toward microfabricated energy conversion devices. However, despite promising results at the single-pore level, the translation of such concepts into integrable membrane technologies remains limited, and porous silicon had not previously been investigated as an active membrane material for nRED.

To address this gap, the thesis combines theoretical analysis, numerical modeling, membrane fabrication, and experimental benchmarking. A physics-based model of ionic transport in charged nanopores under salinity gradients was first developed to determine how pore radius, porosity, and surface charge density affect permselectivity, ionic resistance, and output power. The simulations revealed a fundamental trade-off between selectivity and conductance and identified a fabrication window in which pores below about 20 nm are expected to be favorable at the membrane scale.

Based on these insights, porous silicon membranes were fabricated and tested in a custom reverse electrodialysis platform. Two fabrication routes were explored. A self-supported approach proved unsuitable because the final DRIE step altered pore opening and induced unstable, rectifying electrical behavior. A second route based on electropolishing lift-off enabled the fabrication of free-standing membranes with preserved porous structure and stable I–V characteristics suitable for RED characterization. Their experimental response followed the qualitative trends predicted by the numerical model, confirming that ionic transport is governed by surface-charge-dominated nanofluidic effects.

Most importantly, this work demonstrates for the first time that porous silicon can function as an ion-selective membrane for nanofluidic reverse electrodialysis. Under the tested conditions, the best free-standing membrane achieved a maximum

power density of about 1.33 mW/m^2. To further improve performance, hybrid membranes combining a thin selective active layer with a thicker support layer were fabricated, and an adaptive surface-charge regulation model was introduced to better capture the coupling between surface chemistry and ion transport. Although these developments improved physical understanding and highlighted viable optimization routes, they also showed that substantial limitations remain, especially regarding surface-charge modeling, membrane resistance, and practical upscaling.

Overall, the thesis establishes porous silicon as a new platform for selective ion transport in nRED and provides the first integrated framework linking pore design, fabrication, electrochemical benchmarking, and numerical interpretation. Beyond salinity-gradient energy harvesting, the results open perspectives for porous silicon in iontronic, sensing, and lab-on-chip applications where CMOS compatibility and nanoscale control are decisive advantages.

Contents

List of Abbreviations **11**

1 Introduction to nRED **13**
1.1 Energy challenges with the internet of things 13
1.1.1 The need for alternative energy resources 14
1.1.2 Self-Powered sensors and energy management architectures . 15
1.2 Salinity gradient power and Reverse electrodialysis technology . . . 17
1.2.1 Salinity gradient power 17
1.2.2 Reverse electrodialysis 18
1.3 Nano Reverse electrodialysis 24
1.3.1 Full scale Anodic Aluminum Oxide membrane 25
1.4 Objectives of the thesis 27
1.5 Thesis outline 28

2 Reverse electrodialysis: Fundamendals **30**
2.1 Basic theory for RED 30
2.1.1 RED equivalent circuit 30
2.1.2 Output power analysis 33
2.2 Measurement methods 35
2.2.1 Permselectivity, membrane potential and transport number . 36
2.2.2 Membrane ionic resistance 38

3 Ion exchange membrane for RED **45**
3.1 Donnan exclusion, membrane potential and permselectivity: thermodynamics considerations 46
3.1.1 Donnan potential 46
3.1.2 Transport number 52
3.1.3 Membrane potential 53
3.1.4 Permselectivity 60
3.2 Ionic/electrical characteristic 61
3.2.1 Linear Regime 62

3.2.2 Limiting regime and overlimiting region . . . 64
3.3 Polymer based IEM . . . 66
3.3.1 Physical structure . . . 67
3.3.2 Characterization of polymer IEM . . . 68
3.3.3 Requirement for IEM for larger scale RED . . . 69
3.3.4 RED at reduced Scale: implications for membrane design . . 70
3.4 State of the art for polymer IEM for RED . . . 71
3.4.1 Conventional Polymer IEM . . . 71
3.4.2 Fabrication strategies for newly designed IEMs for RED . . 73

4 Nanoporous IEM and nRED 78
4.1 Electrical double layer . . . 78
4.1.1 Planar description . . . 80
4.1.2 Influence of parameters . . . 85
4.1.3 Confined geometry . . . 88
4.1.4 Breakdown of key assumptions with confinement . . . 91
4.2 Inorganic porous IEM . . . 97
4.2.1 Track-etched membranes (TEMs) . . . 98
4.2.2 Anodic Aluminum Oxide (AAO) membranes . . . 100
4.2.3 Block Copolymer Membranes . . . 103
4.2.4 Other nanostructured ion-exchange materials: structures and fabrication . . . 104
4.3 Techniques for improving ion selectivity and membrane resistance . 107
4.3.1 Surface Modification . . . 108
4.3.2 Geometry modification . . . 109
4.4 State of the art for nanoporous and nanochannel systems for RED 112
4.5 Discussion and outlook . . . 117

5 Porous Silicon membranes 119
5.1 Porous silicon: fundamentals and membrane . . . 119
5.1.1 PSi fabrication . . . 121
5.1.2 PSi characterisation . . . 127
5.2 Porous silicon membranes . . . 131
5.2.1 Porous membranes fabrication techniques . . . 131
5.2.2 Properties . . . 145
5.2.3 Applications . . . 147
5.2.4 Discussion and outlook . . . 154

6 Porous silicon characteristics for nRED 156
6.1 Motivation . . . 156
6.2 Materials and methods . . . 156

6.2.1 Porous silicon study and characterisation . . . 156
6.2.2 Modelling of a single Si pore ionic I–V characteristic . . . 157
6.3 Results . . . 163
6.3.1 Porous layer properties . . . 163
6.3.2 Simulation of ionic I–V characteristics . . . 170
6.4 Discussion . . . 187
6.5 Conclusion . . . 189

7 Process for porous silicon membrane fabrication and analysis as membrane for nRED 191
7.1 Introduction and motivation . . . 191
7.2 Materials and experimental set-up . . . 192
7.2.1 Materials: pSi membrane . . . 192
7.2.2 Materials: set-up for characterisation . . . 192
7.3 Self-supported porous silicon membranes: fabrication and characterisation . . . 196
7.3.1 Self-supported porous silicon membranes: fabrication . . . 196
7.3.2 Self-supported porous silicon membranes: I–V results . . . 207
7.3.3 Discussion . . . 214
7.4 Free-standing porous silicon membranes: fabrication and characterisation . . . 215
7.4.1 Free-standing porous silicon membranes: fabrication . . . 215
7.4.2 Free-standing porous silicon membranes: I–V results . . . 226
7.5 Performances comparison with other membranes and discussion . . . 235
7.5.1 Performances comparison . . . 235
7.5.2 Model analysis and roads for improvement . . . 237
7.6 Conclusion . . . 237

8 Routes for improved pSi membrane for nRED 240
8.1 Introduction and motivation . . . 240
8.2 Fs-pSi step membrane: numerical analysis, fabrication and I–V results 241
8.2.1 Fs-pSi step membrane: numerical analysis . . . 241
8.2.2 FS-pSi step membrane: fabrication and I–V results . . . 244
8.2.3 Discussion . . . 248
8.3 Surface charge regulation as an improvement over the fixed-charge model for numerical analysis . . . 250
8.3.1 COMSOL model for adaptive surface charge density . . . 251
8.3.2 Numerical results . . . 251
8.3.3 Discussion . . . 255
8.4 Conclusion . . . 257

9 Complementary studies and perspectives 259
9.1 Complementary work . . . 259
9.1.1 Surface charge density determination from electroosmotic flow 259
9.1.2 Paper-based reverse electrodialysis systems . . . 260
9.1.3 Upscaling of free-standing porous silicon membranes . . . 260
9.1.4 General perspectives . . . 261
9.2 Perspectives for improving the characterisation and performances of pSi as an IEM . . . 261
9.3 Is pSi for nRED application worth it ? . . . 262
9.3.1 Hydrodynamic feasibility model for small-scale NRED operation 263
9.3.2 Proposed theoretical strategy for feasibility assessment . . . 266

10 Conclusions 270

A Image processing 275

B Determination of the surface charge density of a nanoporous silicon membrane during electroosmotic pumping 278
B.1 Abstract . . . 278
B.2 Electro-osmotic pumping . . . 279
B.3 Existing PSi electroosmotic pumps . . . 281
B.4 Objectives of this master's thesis . . . 282
B.5 Materials and methods . . . 283
B.5.1 Materials . . . 283
B.5.2 Methods . . . 283
B.5.3 Analytical model determining pump flow performance . . . 286
B.6 Experimental results . . . 288
B.6.1 Variation of material and pore size . . . 288
B.6.2 Surface modification . . . 289
B.6.3 Determination of zeta potential and surface charge density . 290
B.7 Conclusion . . . 293

C Paper-based stacked reverse electrodialysis cells for energy generation from salinity gradient 294
C.1 Abstract . . . 294
C.2 Properties of paper . . . 295
C.3 Fabrication of paper based microfluidic . . . 296
C.4 Paper based microfluidic . . . 297
C.5 Paper-based RED . . . 299
C.6 Objectives of this master's thesis . . . 300
C.7 Materials and methods . . . 301

C.8 Experimental results . . . 302
C.8.1 Fan-shaped for controlled flow rate . . . 302
C.8.2 stacked paper-based RED devices . . . 304
C.8.3 Power density depending on the flow rate . . . 307
C.9 Paper-based RED with porous silicon membranes . . . 308
C.10 Conclusion . . . 311

D Porous silicon flake fabrication from a full Si wafer for membrane use in RED applications 313
D.1 Objective . . . 313
D.2 Material and methods . . . 314
D.3 Results . . . 315
D.3.1 Single masked die membrane study . . . 315
D.3.2 Full masked wafer . . . 320
D.4 Perspectives and conclusion . . . 321

List of Abbreviations

Table 1: List of abbreviations

Abbreviation	**Meaning**
AAO	Anodic Aluminum Oxide
AEM	Anion exchange membrane
AFM	Atomic force microscopy
ALD	Atomic layer deposition
AR	Area resistance
BCP	Block Copolymer
CAPMIX	Capacitive mixing
CEM	Cation exchange membrane
COF	Covalent Organic Framework
CP	Concentration polarisation
CVD	Chemical vapour deposition
DBL	Diffusion boundary layer
DRIE	Deep reactive ion etching
EDL	Electric double layer
EDX	Energy Dispersive X-ray
EIS	Electrochemical impedance spectroscopy
fs-pSi	Free-standing porous silicon
IEC	Ion exchange capacity
IEM	Ion exchange membrane
IOT	Internet of things
LPCVD	Low-pressure chemical vapour deposition
MCU	Micro-controller unit
MEB	Mixing entropy batteries
MOF	Metal-organic framework
nRED	Nano-reverse electrodialysis
OCV	Open circuit voltage
PB	Poisson-Boltzmann
PECVD	Plasma enhanced chemical vapour deposition

Abbreviation	Meaning
PNP	Poisson-Nernst-Planck
PRO	Pressure retarded osmosis
PSi	Porous silicon
PSiM	Porous silicon membrane
PZC	Point of zero charge
RED	Reverse electrodialysis
RIE	Reactive ion etching
SEM	Scanning electron microscopy
SERS	Surface-Enhanced Raman Scattering
SGP	Salinity gradient power
SLIM	Spectroscopic Liquid Infiltration Method
SMU	Source/monitor units
TEM	Transmission electron microscopy
UCL	Université catholique de Louvain
VPD	Vapour pressure difference utilization

Chapter 1

Introduction to nRED

1.1 Energy challenges with the internet of things

The Internet of Things (IoT) refers to the interconnection of physical devices through the internet using embedded sensors, electronics, and software. The term was first introduced by Kevin Ashton in 1999 to describe systems in which physical objects interact with digital networks [1]. Since then, IoT has evolved beyond basic machine-to-machine (M2M) communication and now enables large-scale automation across numerous sectors, including healthcare, industry, transportation, and smart homes.

IoT devices communicate over wired or wireless networks and are often remotely controlled or monitored. Current projections estimate that more than 32 billion IoT devices will be deployed worldwide by 2030 [2]. These devices typically operate as part of wireless sensor networks (WSNs), in which distributed nodes collect data and transmit it to a central gateway or base station for processing and storage.

Energy consumption is a critical constraint in IoT systems. For most sensor nodes, wireless data transmission is significantly more energy-intensive than local data processing or sensing. In addition, IoT devices often experience long idle periods between short activity phases, making ultra-low-power operation essential for extending battery lifetime. Table 1.1 summarizes the typical power consumption ranges of commonly used IoT sensors, highlighting the wide variation in energy demand depending on sensing modality.

Sensor Type	Power Consumption
Low-power GPS	5 W[a]
Motion detection	4 W[a]
Gas	500–800 mW[a]
Acoustic	500 mW[a]
Pressure	10–15 mW[b]
Humidity	3–15 mW[b]
Acceleration	10 mW[b]
Temperature	0.5–10 mW[b]

Table 1.1: Typical power consumption of IoT sensors. [a]Active (peak) power consumption. [b]Typical operating power under continuous or low-frequency sampling conditions [3–7].

To maximize system efficiency, significant research efforts have focused on so-called "zero-power" or ultra-low-power designs, aiming to minimize energy consumption through optimized sensor operation, duty cycling, and wireless communication protocols.

More recently, the emergence of the Artificial Intelligence of Things (AIoT) has further amplified energy challenges in digital infrastructures. Artificial intelligence training and deployment currently take place predominantly in data centres, where servers account for approximately 60% of electricity consumption, while cooling systems can represent up to 30% depending on efficiency [8]. According to the International Energy Agency, global data centre electricity consumption reached approximately 415 TWh in 2024 and is projected to nearly double by 2030, driven largely by the rapid adoption of AI-accelerated servers [8].

This growing energy demand exposes the limitations of centralized, cloud-based intelligence and strengthens the case for AIoT architectures that shift computation closer to the sensor or edge level. While edge intelligence can significantly reduce communication-related energy costs, embedding intelligence locally increases the power requirements of individual nodes. As AIoT devices are often deployed in large numbers and in remote or inaccessible environments, this reinforces the need for sustainable energy sources capable of supplying continuous power in the μW–mW range. Consequently, passive energy-harvesting approaches are increasingly being explored to enable long-term, maintenance-free operation of IoT and AIoT systems.

1.1.1 The need for alternative energy resources

The main challenge for pervasive smart spaces is energy sustainability. Wireless Sensor Networks (WSNs), essential for IoT, rely on non-rechargeable batteries, which have limited lifetimes and high maintenance costs. To overcome this, micro-

scale energy harvesting offers a promising alternative by extracting energy from the environment to partially or fully power devices.

Unlike macro-scale energy harvesting (e.g., solar or wind farms), micro-scale energy harvesters are small, low-power systems that use sources such as solar light, radio frequency, thermal, vibration, airflow, and acoustic noise. These systems offer low maintenance costs, environmental friendliness, and energy scalability, but their efficiency depends on the stability of energy sources and the power demands of IoT sensors. Different energy sources provide varying power levels, as shown in Table 1.2.

Energy source	**Type**	**Typical power**
Outdoor solar light	Natural	100 mW/cm^2 (outdoor)
Indoor solar light	Artificial/natural	100 μW/cm^2 (artificial light) 10 mW/cm^2 (filtered solar light)
Ambient radio frequency	Artificial	0.001 μW/cm^2 (Wifi) 0.1 μW/cm^2 (GSM)
Thermoelectric	Artificial	60 μW/cm^2
Vibration	Artificial	4 μW/cm^3 (human motion) 800 μW/cm^3 (machines)
Ambient airflow	Natural/artificial	1 mW/cm^2
Acoustic noise	Natural/artificial	960 nW/cm^3

Table 1.2: Energy harvesting sources. Reproduced from [3].

In addition to the extensively investigated renewable energy sources such as solar radiation, thermal gradients, and biomechanical inputs, fluidic energy systems, specifically those utilizing hydrodynamic forces (mechanical energy) and salinity differentials (chemical potential), represent pervasive and underexploited resources in natural environments. Among these, salinity gradient energy, which originates from the Gibbs free energy difference between solutions of varying salinity, offers a theoretically clean and sustainable means of energy conversion.

1.1.2 Self-Powered sensors and energy management architectures

While micro-scale energy harvesting provides access to ambient energy sources, the electrical output of such harvesters is typically low-voltage, intermittent, and highly variable. Consequently, harvested energy cannot be directly supplied to electronic loads without intermediate conditioning and storage stages. This has led to the development of self-powered sensing systems, in which energy harvesting,

storage, and power management are integrated to enable autonomous operation [9, 10].

Self-powered systems are particularly relevant in the context of large-scale IoT deployment, where battery replacement becomes economically and environmentally unsustainable. Alagumalai *et al.* highlight that the projected scale of distributed sensor nodes renders conventional battery-powered approaches impractical, thereby motivating architectures capable of long-term, maintenance-free operation [10]. Rather than eliminating energy storage entirely, modern self-powered systems combine ambient energy harvesting with intelligent energy management strategies.

The fundamental architecture of a self-powered sensor node is illustrated in Figure 1.1, adapted from Kokert *et al.* [11]. It consists of three primary components: (i) an energy harvester, (ii) an energy storage element, and (iii) electrical consumers such as microcontrollers, sensors, and wireless communication modules. To interconnect these components, two power converters are typically employed: one between the harvester and the storage element, and another between the storage unit and the load.

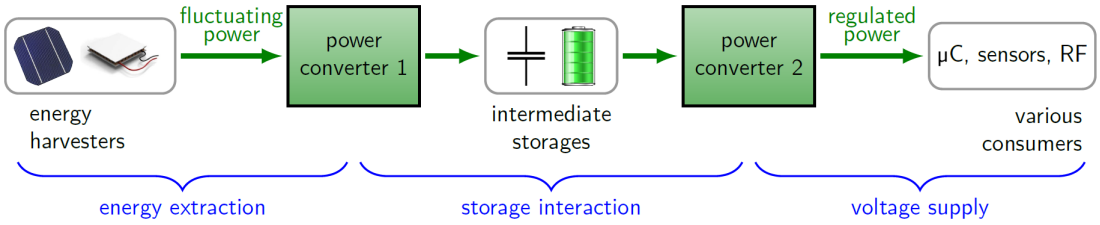


Figure 1.1: Power converters supply power to consumers from energy-harvesting sources. Taken from [11].

The first converter conditions the raw harvested energy, often performing voltage boosting and maximum power point tracking (MPPT) to maximize energy extraction. The second converter regulates the voltage supplied to the load, ensuring stable operation despite fluctuations in harvested power or storage voltage. As described by Kokert *et al.*, power management fulfills three major functions: energy extraction optimization, controlled energy storage, and regulated energy delivery to the load [11]. Behavioral modeling of these DC/DC converters is essential to evaluate system-level efficiency under ultra-low-power conditions.

Energy storage elements, commonly supercapacitors or rechargeable micro-batteries, buffer harvested energy and enable duty-cycled operation. This allows short high-power transmission bursts to be supported by a relatively low average harvested power in the μW–mW range [9]. Such buffering decouples instantaneous energy generation from load demand, significantly enhancing system robustness.

Recent commercial developments further demonstrate the technological maturity of this approach. Ultra-low-power energy management integrated circuits, such as those evaluated by Jirgl *et al.*, integrate cold-start capability, voltage regulation, and energy storage control within compact platforms suitable for embedded systems [12]. These devices can operate from millivolt-level inputs and efficiently manage harvested energy from weak sources.

1.2 Salinity gradient power and Reverse electrodialysis technology

1.2.1 Salinity gradient power

Salinity Gradient Power (SGP) or Salinity gradient energy, also referred to as 'Blue Energy', is generated by converting the chemical potential between a diluted and a concentrated salt solutions into useful energy such as electrical and mechanical energy [13]. It is a clean, sustainable energy source and the process itself does not produce any toxic gas emissions.

The maximum theoretical work that can be extracted from the mixing of solutions, excluding expansion work, is described by the Gibbs free energy of mixing, $\Delta_{mix}G$ [14]. In the case of ideal-dilute solutions, where the enthalpy of mixing ($\Delta_{mix}H = 0$) is zero, the Gibbs free energy of mixing can be expressed as:

$$\Delta_{mix}G = \Delta G_b - (\Delta G_c + \Delta G_d), \tag{1.1}$$

$$\Delta_{mix}G = -(n_c + n_d)T\Delta_{mix}s_b - (-n_cT\Delta_{mix}s_c - n_dT\Delta_{mix}s_d) \tag{1.2}$$

with the subscript c referring to the concentrated salt solution (such as seawater), d to the dilute salt solution (such as freshwater), b to the resulting brackish mixture, n the number of moles and T the temperature;

$\Delta_{mix}s$ represents the contribution of the molar entropy of mixing (J/mol.K) to the total molar entropy of the corresponding electrolyte solution, according to:

$$\Delta_{mix}s = -R\sum_i x_i \ln x_i \tag{1.3}$$

Theoretically, 2.3 MJ of Gibbs free energy can be generated by mixing 1 m^3 of freshwater with a large volume of seawater [15]. Consequently, compared to other electrical energy storage, the power density of salinity gradient energy is rather small as shown in Table 1.3. This makes salinity gradient power based battery applications hardly feasible. However, one of the advantages of salinity gradient power is the quantity of salted and fresh water around the world.

Systems	Specific energy (Wh/kg)	Energy density (Wh/L)
Pumped hydroelectric storage	0.5-1.5	0.5-1.5
Salinity gradient energy	0.6	0.6
Battery		
Lead acid	30-50	50-80
Li-ion	75-200	200-500
Fuel cell	800-10000	500-30000
Solar fuels	800-100 000	500-10 000

Table 1.3: Specific energies and energy densities of electrical energy storage systems [15]. More data in [15].

1.2.2 Reverse electrodialysis

Reverse electrodialysis (RED) is a well-established and widely studied method for extracting salinity gradient power (SGP) [16, 17]. The simplest configuration for converting salinity-gradient power (SGP) (Eq. (1.2)) into electrical power via reverse electrodialysis (RED) is shown in Fig. 1.2. Two compartments containing electrolyte solutions of different salinities are separated by an ion-exchange membrane (IEM), in this case, a cation-exchange membrane (CEM). The movement of ions across the membrane generates an ionic current, which is converted into electrical current at the working electrodes and delivered to an external load.

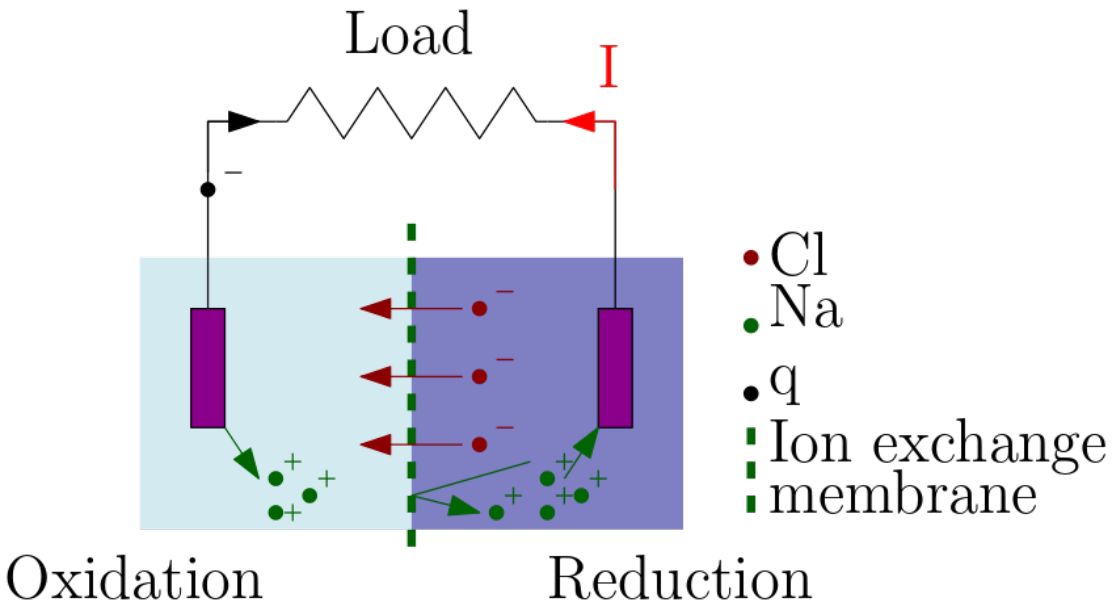


Figure 1.2: Schematic representation of the simplest reverse electrodialysis (RED) cell. Two electrolyte compartments of different salinities are separated by a cation-exchange membrane (CEM), generating a potential difference converted into electrical power at the electrodes.

1.2.2.1 RED equivalent circuit

Across the membrane, an electrochemical potential difference $\Delta\varphi_m$ or E_m, called the membrane potential, is established, which depends on the saline concentration gradient and the cationic selectivity of the membrane, T_+, as given by [18]:

$$E_m = \Delta\varphi_m = -\frac{RT}{F}(2T_+ - 1)\log\left(\frac{\gamma_{C_H}C_H}{\gamma_{C_L}C_L}\right), \tag{1.4}$$

where C_i and γ_{C_i} denote, respectively, the ionic concentration and activity coefficient in compartment i, R is the universal gas constant, T the absolute temperature, and F the Faraday constant. The cationic transport number T_+ reflects the membrane's ability to exclude anions; it ranges from 1 for a perfectly cation-selective membrane to 0 for a perfectly anion-selective one. More details about the origin and derivation are given in Chapter 3.

In the absence of an external electrical connection, ionic transport across the membrane is blocked by charge build-up, which generates an opposing electric field. This field prevents further ion migration and maintains the concentration difference. When the two compartments are connected through external electrodes, the circuit is closed, allowing the excess charge (anions in this case) to be balanced

through redox reactions at the electrodes. The resulting electron flow constitutes an electrical current that can be used to power an external load, thereby converting electrochemical potential energy into electrical energy.

An electrical equivalent circuit for the RED cell can be established once the electrical behaviour of the membrane under a concentration gradient is known. In 3.2.1 Chapter 3, it is explained why the electrical response of an ion-exchange membrane varies linearly with the concentration gradient. Accordingly, the membrane and the adjacent solutions are typically modelled as a non-ideal voltage source with an open-circuit voltage $\Delta V = E_m$ and an internal resistance R_{cell}. The presence of redox electrodes introduces additional overpotentials; however, for the sake of clarity in this introductory discussion, these contributions are neglected but are detailed in Chapter 2. The equivalent electrical circuit for the closed-circuit configuration shown in Figure 1.2 is presented in Figure 1.3.

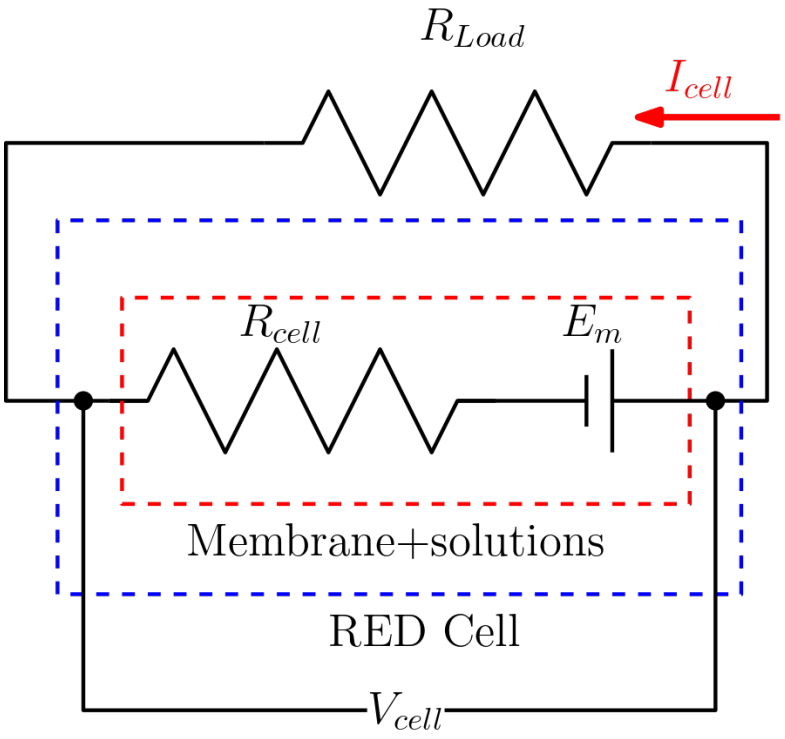


Figure 1.3: Equivalent electrical circuit for a RED cell composed of a membrane and the adjacent solutions, represented as a voltage source E_m in series with an internal resistor R_{cell}. The membrane and solutions are connected to an external load resistor R_{load}. The voltage drop associated to the working/counter electrodes is neglected. V_{cell} represents the output voltage of the cell.

The current in the circuit is computed using Ohm's law,

$$I_{cell} = \frac{E_m}{R_{cell} + R_{Load}}. \tag{1.5}$$

The output voltage of the RED as a function of the resistance load is

$$V_{cell} = R_{Load} I_{cell}. \tag{1.6}$$

Combining both equations to eliminate R_{Load} gives

$$I_{cell} = \frac{E_m - V_{cell}}{R_{cell}}. \tag{1.7}$$

Figure 1.4 shows I_{cell} as a function of V_{cell}. Any point on the curve represents a different load resistance value. When there is no load, the circuit is opened and the $I_{cell} = 0$. The measured V_{cell} is then equal to E_m, the membrane potential. On the opposite, if the load resistance is replaced by a short-circuit, $V_{cell} = 0$ and the short circuit current $I_{sc} = I_{cell,V_{cell}=0} = \frac{E_m}{R_{cell}}$.

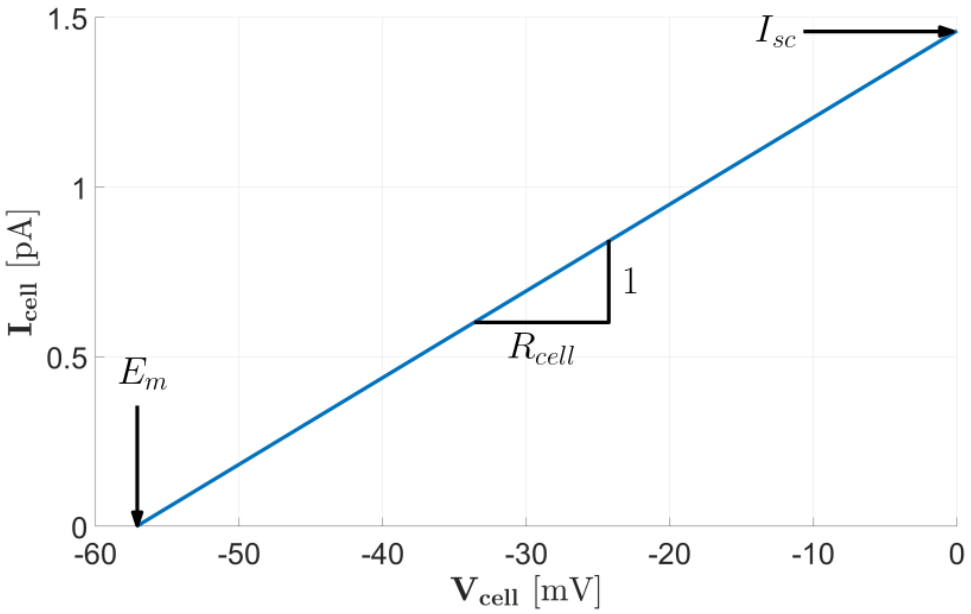


Figure 1.4: Typical linear I-V curve for a RED cell. Any point on the curve represents a different connected load to the cell. When the circuit is opened, $V_{cell} = E_m$. When the circuit is short-circuited, $I_{cell} = I_{sc}$.

The maximum output power is achieved when the load resistance is matching the cell resistance, which gives

$$P_{Load,max} = \frac{E_m^2}{4R_{cell}}. \tag{1.8}$$

1.2.2.2 RED in practice

In practice, a standard RED system usually consists of a series of alternating cation exchange membranes (CEMs) and anion exchange membranes (AEMs), which together form repeating units of flow channels for high-salinity (HS) and low-salinity (LS) feed streams (see Fig. 1.5). In this configuration, each membrane potential adds up, increasing the maximum output circuit voltage. Driven by the concentration gradients, cations from the HS compartment migrate through CEMs toward the LS side, while anions move in the opposite direction across AEMs. This flow of ions is converted in electricity by redox reaction on the electrodes, converting the electrochemical potential energy into electrical energy

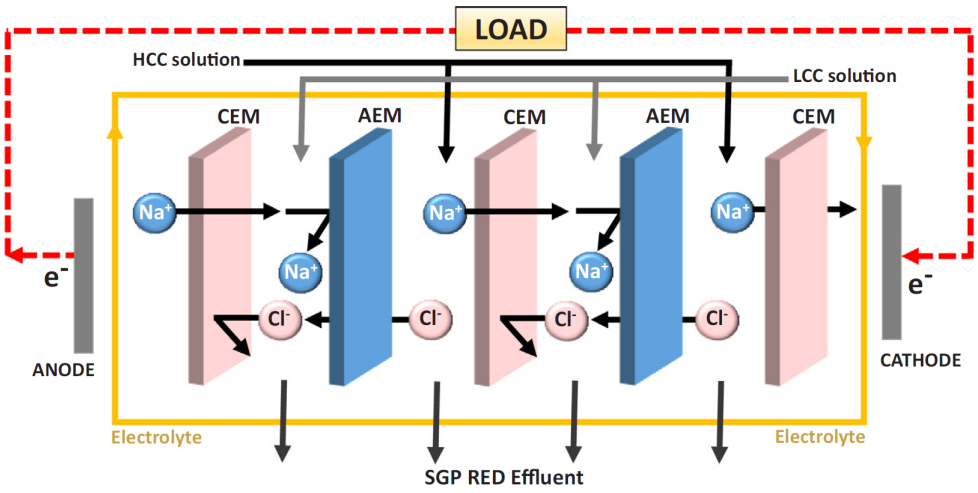


Figure 1.5: Schematic representation of a reverse electrodialysis (RED) stack. Alternating cation-exchange (CEM) and anion-exchange (AEM) membranes define successive high-concentration (HCC) and low-concentration (LCC) compartments. The salinity gradient across each membrane generates an electrochemical potential that drives ion-selective transport, while redox reactions at the terminal electrodes close the circuit and enable continuous electrical power generation. Taken from [19].

Various other technologies have been developed to extract energy from salinity gradient power. Among Reverse Electrodialysis (RED), Pressure Retarded Osmosis PRO is another prominent membrane-based approaches [17]. In contrast to RED using the flow of ions, PRO operates by exploiting the osmotic pressure difference that arises from water flux across a semi-permeable membrane, which drives a turbine in an external hydraulic loop.

A modification of conventional RED is Microbial Reverse Electrodialysis (MRED), which addresses the limitations associated with traditional electrode reactions [20].

In classical RED systems, redox reactions at the electrodes close the electrical circuit; however, these reactions often suffer from high overpotentials due to thermodynamic constraints, leading to considerable energy losses. As a result, large stacks of membrane cells are typically required to achieve viable energy recovery. In MRED, these inefficiencies are mitigated by employing exoelectrogenic microorganisms at the anode to oxidize organic substrates and facilitate oxygen reduction at the cathode, thereby enhancing system performance and reducing overpotentials [21].

While the aforementioned technologies depend on membranes to separate solutions of varying salinity, there also exist non-membrane-based alternatives for harnessing SGP. These include mixing entropy batteries (MEB) [22], capacitive mixing (CAPMIX) [16, 23], and vapor pressure-driven systems (VPD) [24]. Among all current developments, RED and PRO remain the most technologically mature and promising. However, because both rely on membranes for operation, their viability is closely tied to membrane-related factors, including cost, operational lifespan, and energy conversion efficiency.

1.2.2.3 Historical development of RED

The foundational concept of salinity gradient power was first introduced by Pattle in 1954 [25]. In his bench-scale experiment, he constructed a 'hydroelectric pile' composed of 47 alternating pairs of acidic and basic membranes, each with an area of 8 cm^2. By mixing freshwater and seawater at 39 °C, the setup generated an electromotive force of 3.1 V and achieved a power density of approximately 0.2 W/ m^2.

It was not until the 1970s that theoretical frameworks for RED began to emerge. Fair and Osterle (1971) proposed a model based on ion transport through charged capillary membranes [26], while Weinstein and Leitz (1976) developed a theoretical model for RED stacks incorporating ion exchange membranes [27]. Early analyses suggested that RED could become a viable competitor among alternative energy technologies [28, 29].

Nevertheless, initial experimental implementations often resulted in suboptimal performance, characterized by very low power densities,for instance, just 0.4 W/m^2 using hypersaline (250 g/L NaCl) and dilute (1 g/L NaCl) streams [30], and limited energy conversion efficiencies, ranging between 1.8% and 11.7% [31]. During this early development phase, significant milestones were reached, including the first documented case of membrane fouling in RED systems by Ratkje et al. in 1986 [32], as well as the introduction of a hybrid RED-electrolysis setup capable of concurrently generating electricity and producing acidic and basic solutions in the electrode chambers [33].

Extensive research on RED emerged in the early 2000s , which coincides with

the spike in the cost of fossil fuel energy [34]. During this period, systematic studies on the role of ion exchange membranes (IEMs) [35, 36], stack configuration [35, 37–39], and operating conditions [39–43] in RED power generation were performed. With the availability of commercial IEMs and improved stack design, significant improvements in power density were realized (e.g., a maximum value of 0.93 W/m^2 was obtained using NaCl solutions of 0.5 M and 0.017 M as feed solutions [36, 42]). Meanwhile, hybrid processes involving RED, desalination facilities, and solar power were proposed by Brauns to enable simultaneous energy production and water purification [41, 44].

Tremendous advances in RED performance have been achieved over last decade with the exciting progresses in IEMs and spacer designs. In 2012, the first tailor-made IEM specifically designed for RED showed a power density of 1.27 W/m^2 [45]. This has been followed by a wave of RED membrane development work [46–49]. The majority of these tailor-made RED membranes are polymer based; most of them have much thinner membrane thickness (26–91 μm) compared to conventional polymer IEMs used for electrodialysis in order to achieve lower electric resistance (0.28–2.26 $\Omega \cdot cm^2$).

1.3 Nano Reverse electrodialysis

Traditionally, reverse electrodialysis (RED) systems have employed dense polymer ion exchange membranes (IEMs) for harvesting salinity gradient power (SGP). These membranes were primarily developed for large-scale energy recovery, targeting estuarine or industrial brine mixing processes where significant volumetric flow rates are available. The main objective of classical RED research has therefore been the optimization of membrane resistance, permselectivity, and mechanical robustness for modular stacks operating at the meter scale.

Recently, however, ion-selective porous membranes have emerged as a promising alternative platform due to their potential to significantly enhance power density [50]. Unlike dense polymer membranes, nanoporous structures exploit surface-charge-driven ion transport within confined geometries, enabling enhanced electrokinetic effects and potentially higher volumetric power densities.

Initial studies in this field focused on single-pore systems to elucidate the fundamental mechanisms of ion transport under salinity gradients and to estimate upper bounds of power output. For instance, a single boron nitride nanotube exposed to a 1000-fold KCl concentration gradient generated a power output of approximately 20 pW [51]. Similarly, Guo *et al.* (2010) reported a nanofluidic SGP device employing a single ion-selective track-etched nanopore in a polyimide membrane that yielded a power output of 26 pW [52]. Projected to a porous membrane with a pore density of 10^8–10^{10} cm^{-2}, the estimated power density ranges

from 20 to 2600 W/m^2, up to three orders of magnitude higher than conventional RED systems [52–56]. These projections have catalyzed a surge of research into nanoporous membrane technologies for osmotic energy harvesting, giving rise to a distinct subfield commonly referred to as nanofluidic RED (nRED) or nanopore-based power generation (NPG) [57–61].

Beyond the pursuit of high power densities, nanofluidic RED introduces an important conceptual shift in scale. Whereas conventional RED systems are designed for centralized, large-area installations, nanoporous membranes open the possibility of miniaturized and integrable osmotic energy harvesters. At the micro- and mesoscale, continuous chemical potential gradients, such as those encountered in environmental waters, biological fluids, or industrial effluents, may serve as localized energy sources. In this context, nanofluidic RED becomes particularly relevant for low-power applications, including autonomous sensing platforms and distributed IoT devices, where μW–mW power levels are sufficient when combined with appropriate energy management architectures.

Ion transport in these porous membranes is governed by nanofluidic principles, where electrostatic and surface-charge effects dominate over bulk diffusion. When the pore size approaches the Debye length, electrical double layers overlap, enabling charge-selective transport and the maintenance of concentration gradients across nanoscale channels. Despite the conceptual promise, significant challenges remain in translating single-pore performance to macroscopic membranes. Fabricating large-area membranes with sufficiently high and uniform pore densities remains non-trivial, and achieving stable surface functionalization under realistic operating conditions is still an active area of research.

1.3.1 Full scale Anodic Aluminum Oxide membrane

In order to overcome the difficulty in fabricating membranes with high pore density at a large scale, anodic porous alumina was also explored [54]. It features packed nanopores with a uniform pore radius in the range of 4–200 nm. Also adding a dense silica layer to the surface of this porous alumina substrate substantially increases the anti-fouling ability [62].

However, it is now well established that power density does not scale linearly with pore density. Above a critical pore density (typically around $10^4\,cm^{-2}$), performance degradation is observed due to concentration polarization, which reduces both ion selectivity and conductivity [59, 63, 64]. It has also that because of concentration polarization effects, the power density achieved in practical nRED experiments using small membrane samples is often several orders of magnitude lower than the values reported in bench-scale studies from the literature [60].

Performance can be further enhanced through optimization of nanopore geometry, surface chemistry, and electrolyte composition [65–67]. Numerous theoretical

studies using Poisson–Nernst–Planck (PNP) modeling have examined how nanochannel geometry influences performance [68, 69]. Specifically, incorporating asymmetry into the nanochannel design has been shown to enhance power output, either by improving ionic selectivity and/or by reducing the overall channel resistance. In this regard, full-scale membrane with such asymmetric pore geometry have been fabricated, usually consisting of a support layer with an added thin active layer on one side [65, 70–72]. In [65], it has been demonstrated that the addition of the active layer to AAO increased the power density to 7.2 times what could be achieved in symmetric AAO pores.

Anodic aluminum oxide (AAO) is widely employed for laboratory-scale fabrication of nanoporous membranes because of its low cost, chemical stability, and ability to produce uniform, high-aspect-ratio nanopores over large areas. However, AAO fabrication typically relies on a two-step anodization process requiring aluminum substrates, specific electrolytes, and tightly controlled voltages, which complicates direct integration into CMOS-compatible microsystems [73]. Further processing, such as pre-patterning, membrane detachment, or transfer, is often necessary for incorporation into microfluidic or energy-harvesting devices like reverse electrodialysis (RED) systems. Additional limitations reported in the literature include delamination from the underlying substrate due to mechanical stress [74], non-uniform film thickness and pore ordering over large areas [74], the persistence of a barrier oxide layer that hinders pore connectivity [75], and difficulties in achieving reliable adhesion and maintaining pore uniformity when AAO is transferred onto silicon supports [76]. A notable exception was demonstrated by Osmanbeyoglu et al. [77], who fabricated thin ($\simeq$1 µm) AAO membranes directly on silicon using Al films with a Ti adhesion layer, proving CMOS-compatible integration is possible, though still requiring multiple processing and etching steps. These challenges highlight why, although AAO remains attractive for fundamental studies, its integration into scalable nanofluidic and CMOS processes is still problematic.

On one hand, the addition of a thin active layer, such as ion-selective coatings or charged polymers, onto AAO membranes has been shown to enhance ion selectivity and improve power output in reverse electrodialysis (RED) systems [65, 70–72]. This approach can make AAO more competitive for energy harvesting. On the other hand, the introduction of such layers adds complexity to the fabrication process, requiring additional deposition, alignment, and bonding steps, which may limit scalability and reproducibility, especially for microdevice integration.

An alternative strategy to enhance performance without adding an active layer is to directly modulate the pore geometry of the AAO membrane during the anodization process. While voltage modulation, stepwise anodization, and post-processing treatments (such as pore widening or chemical etching) can yield non-uniform or hierarchical pore structures, these methods remain comparatively

limited in precision and require careful optimization [78]. Achieving fine control over constrictions or complex internal geometries within AAO remains challenging, particularly when uniformity across large areas is required.

1.4 Objectives of the thesis

While nanofluidic reverse electrodialysis (nRED) has demonstrated remarkable theoretical power densities at the single-pore level, the translation of these concepts to full-scale, integrable membranes remains largely unexplored. Most experimental studies have relied on track-etched membranes, AAO templates, or single nanopores, which, although useful for mechanistic understanding, are not readily compatible with standard silicon microfabrication processes. In particular, anodic aluminium oxide (AAO) membranes, despite their well-defined pore geometry, suffer from limited CMOS compatibility and complex integration within MEMS platforms.

Porous silicon (PSi), in contrast, offers intrinsic compatibility with silicon-based microfabrication, precise control of nanoscale pore geometry, and the possibility of dynamic tuning during electrochemical etching [79, 80]. Parameters such as pore diameter, length, porosity, and morphology can be adjusted in real time, enabling the fabrication of tailored nanostructures including graded porosity layers, constrictions, and asymmetric pore geometries. These features make PSi a promising candidate for engineered ion-selective membranes suitable for nanofluidic RED.

However, at the time of this work, no systematic study had investigated porous silicon membranes specifically for nanofluidic reverse electrodialysis. In particular, the relationship between pore geometry, surface charge density, ionic transport mechanisms, and achievable power density in PSi membranes remains unexplored.

The central hypothesis of this thesis is that porous silicon membranes, when appropriately engineered at the nanoscale, can operate as effective ion-selective membranes for miniaturized reverse electrodialysis systems.

To test this hypothesis, the work is structured around three main objectives:

1. **Understanding ionic transport in nanoporous ion-exchange membranes.** Develop a combined theoretical and numerical framework describing ion transport in charged nanoporous structures under salinity gradients, with particular emphasis on surface-charge-dominated regimes and Debye-length-scale confinement. This objective aims to identify the key physical parameters governing permselectivity, ionic conductance, and power generation in nanoscale channels, and to establish performance limits relevant to porous silicon geometries.

2. **Establishing a benchmarking platform for porous silicon membranes in nRED.** Design and implement a laboratory-scale reverse electrodialysis

setup suitable for the systematic characterization of porous silicon membranes. This includes the development of a reproducible experimental protocol for measuring open-circuit voltage, internal resistance, ionic selectivity, and output power density under controlled salinity gradients. The objective is to provide a standardized framework enabling quantitative comparison between porous silicon membranes and conventional ion-exchange materials.

3. **Coupling experiments with numerical modeling to guide membrane optimization.** Integrate experimental measurements with numerical simulations in order to correlate pore geometry, surface charge density, and membrane thickness with the resulting electrochemical performance. This combined approach aims to identify optimization pathways toward maximizing output power density while maintaining structural stability and CMOS compatibility.

Reverse electrodialysis was selected as the base technology for this investigation due to its relative simplicity at the laboratory scale and its suitability for controlled characterization of ion-selective membranes. Unlike single-pore measurements, RED provides a macroscopic framework in which membrane permselectivity and transport resistance can be evaluated under realistic operating conditions.

Ultimately, this thesis seeks to bridge the gap between nanofluidic transport theory and microfabricated membrane technology by demonstrating, for the first time, the feasibility of porous silicon as a functional ion-exchange membrane for nanofluidic reverse electrodialysis. By combining modeling, benchmarking, and experimental validation, the work establishes a foundation for the development of CMOS-compatible osmotic energy harvesters targeting micro-scale and distributed energy applications.

1.5 Thesis outline

The thesis is divided into two main parts. The first part provides the theoretical framework necessary to understand ion-transport phenomena in both polymer-based and nanoporous ion-exchange membranes (IEMs).

Chapter 2 describes the fundamentals of reverse electrodialysis (RED) together with its mathematical formulation, and provides a state-of-the-art comparison between polymer and nanoporous membranes for RED applications. Chapter 3 introduces the working principles of conventional polymer IEMs. Chapter 4 then explains how ionic selectivity emerges in nanoporous systems and presents the different types of nanoporous membrane structures reported in the literature. Chapter 5 introduces the fabrication principles and physicochemical properties of

porous silicon membranes, followed by a review of their use in various technological applications.

The second part of the manuscript presents the original research conducted in this work and is organized as follows:

- Chapter 6 investigates how fabrication parameters influence the structural properties of porous silicon layers. A numerical model for charged nanopores is introduced, assuming that surface complexation of SiO_2 results in a net negative surface charge density. The I–V characteristics of single nanopores are studied as a function of pore size and concentration ratio. Based on these numerical results, a target pore size and porosity range are selected.

- Chapter 7 details the fabrication processes developed to produce porous silicon membranes. A first route yields self-supported membranes, whose I–V characteristics are measured in a custom RED test cell. Due to limitations observed with this approach, a second route leading to free-standing membranes is developed. Their performance is analysed using insights from Chapter 6 and benchmarked against commercial polymer IEMs.

- Chapter 8 explores two possible improvements: one related to fs-pSi membranes for RED, and the other concerning the numerical modelling strategy. Leveraging the versatility of the anodisation process, hybrid membranes combining a thin selective active layer with a thicker support layer are fabricated and tested. In parallel, an adaptive surface-charge regulation model based on surface complexation is implemented numerically and compared with experimental trends.

The thesis then presents a summary of the contributions from Master theses conducted under our supervision in the context of this work, followed by a discussion of the perspectives for porous silicon as an ion-exchange membrane for nRED in the context of energy harvesting for PMIC applications. Finally, the manuscript concludes with a summary of the main contributions and an outlook for future research.

Chapter 2

Reverse electrodialysis: fundamendals

2.1 Basic theory for RED

The configuration analysed in this chapter is the one presented in Figure 1.2. The theoretical framework and developments presented in the following sections are based on the assumptions that the ionic species are K^+ and Cl^- and that the working electrodes are Ag/AgCl. Potassium chloride (KCl) is commonly employed in the literature, as seen in Table 4.1, because K^+ and Cl^- exhibit nearly identical ionic diffusion coefficients, minimizing parasitic potentials such as the Henderson potential that can distort measurements of membrane selectivity. Ag/AgCl electrodes are likewise widely used owing to their ease of fabrication, chemical stability, and gas-free redox behavior, as well as their compatibility with KCl and NaCl electrolytes.

2.1.1 RED equivalent circuit

The open-circuit diffusion potential of a RED cell pair, given by eq. (1.4), is typically of the order of 50–100 mV, this voltage remains small enough for the system to behave linearly. The reason is that the local potential variation across each transport region (membrane phase and adjacent boundary layers) is only a fraction of this total value, and thus remains comparable to or smaller than the thermal voltage $RT/F \simeq 25$ mV. Consequently, the local ionic distributions remain close to their equilibrium values, and the Nernst–Planck equations can be linearized locally (see 3.2.1 in Chapter 3). Thus, the membrane and the adjacent solutions are usually modelled as a non-ideal voltage source with voltage output $\Delta V = E_m$ and internal resistance R_{cell}. The equivalent electrical circuit for the closed-circuit

in Figure 1.2 is shown in Figure 2.1.

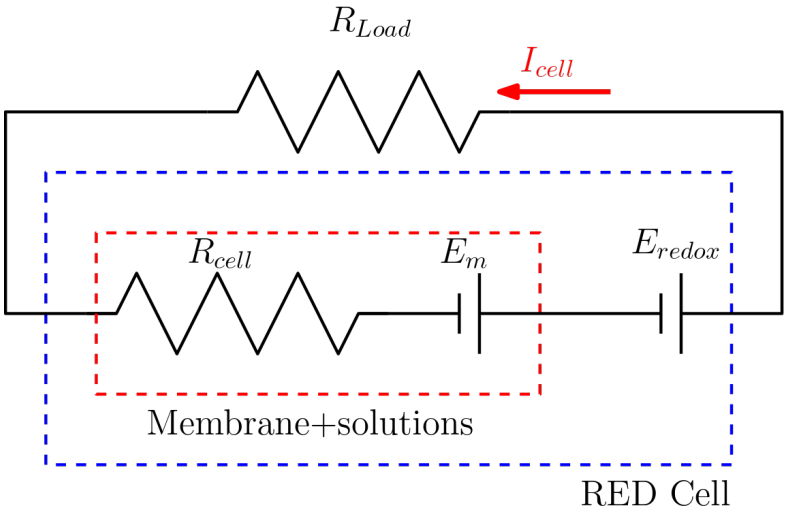


Figure 2.1: Equivalent electrical circuit for a RED cell composed of a membrane and the adjacent solutions, represented as a voltage source E_m in series with an internal resistor R_{cell}, and working/counter electrodes with redox potential E_{redox}, connected to an external load resistor R_{load}.

2.1.1.1 Electrode potential and overpotential (E_{redox} and η_{el}).

In the equivalent circuit representation of a reverse electrodialysis (RED) cell, E_{redox} denotes the potential established at the electrode–electrolyte interface. Its role is to enable the conversion between ionic current inside the electrolyte and electronic current in the external circuit. When an electrode is in contact with an electrolyte, an interfacial equilibrium is established through an electrochemical reaction of the general form:

$$\text{Ox} + ne^- \leftrightarrow \text{Red}, \tag{2.1}$$

where Ox and Red denote the oxidized and reduced species, respectively, and n is the number of electrons transferred. At equilibrium, the electrode potential is determined by the Nernst equation [81, 82]:

$$E_{\text{redox}} = E^{\circ}_{\text{redox}} + \frac{RT}{nF} \ln\left(\frac{a_{\text{Ox}}}{a_{\text{Red}}}\right), \tag{2.2}$$

where E°_{redox} is the standard potential of the redox couple, R the universal gas constant, T the temperature, F the Faraday constant, and a_i the activities of the species involved.

In most of the studies using a single ion-exchange membrane separating two electrolyte compartments, silver/silver chloride (Ag/AgCl) electrodes are usually used. These electrodes act as the working and counter electrodes of the electrochemical cell, enabling charge transfer between the electronic circuit and the ionic phases. The interfacial equilibrium is described by:

$$\mathrm{AgCl(s)} + e^- \leftrightarrow \mathrm{Ag(s)} + \mathrm{Cl^-(aq)}, \tag{2.3}$$

and the corresponding equilibrium potential follows [83, 84]:

$$E_{\mathrm{Ag/AgCl}} = E^{\circ}_{\mathrm{Ag/AgCl}} - \frac{RT}{F} \ln(a_{\mathrm{Cl^-}}), \tag{2.4}$$

with $E^{\circ}_{\mathrm{Ag/AgCl}} = +0.222$ V versus SHE at 25 ℃ for a 1 M KCl solution. The potential difference between the two electrodes is then given by:

$$\Delta E_{\mathrm{redox}} = -\frac{RT}{F} \ln\left(\frac{a_{\mathrm{Cl^-},H}}{a_{\mathrm{Cl^-},L}}\right), \tag{2.5}$$

which directly reflects the difference in chloride activity between the concentrated and dilute compartments.

During current flow, the electrode potential deviates slightly from its equilibrium value due to kinetic and mass–transport limitations, producing a small additional voltage loss known as the *electrode overpotential* [81, 82]:

$$\eta_{\mathrm{el}} = E_{\mathrm{actual}} - E_{\mathrm{redox}}. \tag{2.6}$$

For reversible electrode systems such as Ag/AgCl in chloride electrolytes, the interfacial reaction exhibits rapid electron-transfer kinetics and a high exchange current density, leading to activation losses typically below a few millivolts [83, 84]. As a result, η_{el} can generally be neglected in working RED-type cells, particularly under low to moderate current densities.

In the broader context of RED stacks, electrode overpotentials and electrode potentials are also commonly dismissed [17, 38, 85]. This simplification is justified by the use of reversible redox systems (e.g., Fe^{2+}/Fe^{3+} or hexacyanoferrate couples) located in electrode rinse solutions of similar concentration, where both electrodes operate under nearly identical conditions, as shown in Figure 2.2.

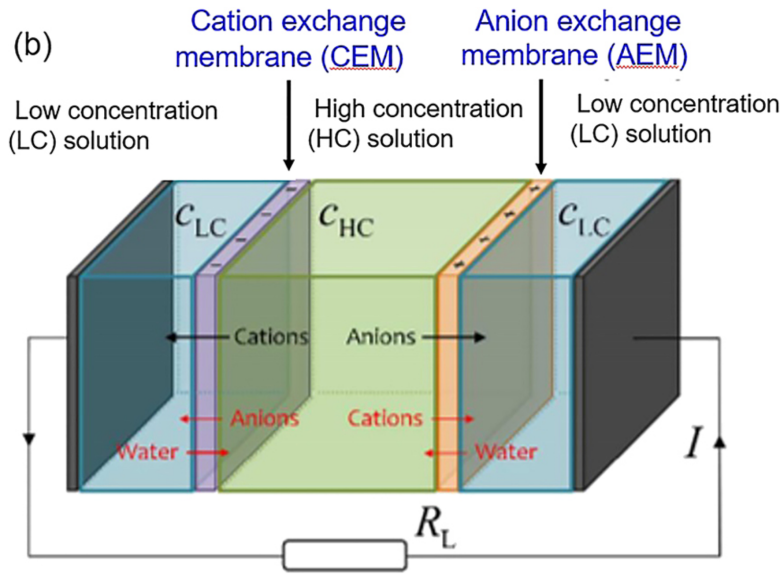


Figure 2.2: Reverse electrodialysis cell configuration where the working and counter electrodes operates in similar conditions. Taken from [86].

Under such circumstances, the potential difference between electrodes remains close to zero and the associated polarization losses are small compared to the overall electromotive force generated by the stack. Therefore, E_{redox} andη_{el} are usually omitted in equivalent electrical circuit representations or implicitly included within the total cell resistance R_{cell}.

2.1.2 Output power analysis

For the sake of the present analysis, focused on the transport properties of the membrane and its performance rather than the cell performance with the electrode included, the electrode potential term E_{redox} will be omitted. This assumption is consistent with most studies on ion-exchange membranes and reverse electrodialysis systems, where electrode contributions are also omitted (see studies in Table 4.1). The simplified circuit to analysed is shown in Figure 1.3.

The power delivered to the load is given by

$$P_{Load} = I_{cell} V_{cell}, \tag{2.7}$$

Combining (1.5) and (1.6) into the last equation gives the power delivered to the load as a function of the load and cell resistance, and the membrane potential:

$$P_{Load} = \frac{R_{Load} E_m^2}{(R_{cell} + R_{Load})^2}. \tag{2.8}$$

Figure 2.3 shows the typical curve for P_{Load} as a function of R_{Load}. The maximum output power is achieved when the load resistance is matching the cell resistance, which gives

$$P_{Load,max} = \frac{E_m^2}{4R_{cell}}. \tag{2.9}$$

Finally, the energy conversion efficiency is defined as the ratio of the output energy (electrical energy) to the input energy [26] (Gibbs free energy of mixing).

$$\eta = \frac{V_{cell} I_{cell}}{RT \log\left(\frac{\gamma_{C_H} C_H}{\gamma_{C_L} C_L}\right) \int (\bar{J}_+ + \bar{J}_-) d\bar{A}} \tag{2.10}$$

Here $\int (\bar{J}_+ + \bar{J}_-) d\bar{A}$ is the number of ions transported through the membrane. The total current crossing the membrane is computed as

$$I = \int (\bar{J}_+ - \bar{J}_-) d\bar{A}. \tag{2.11}$$

Using the following simplification, $\int \bar{J}_+ d\bar{A} / \int \bar{J}_- d\bar{A} \simeq T_+/(1 - T_+)$, the efficiency is given as

$$\eta = \frac{V_{cell}(1 - 2T_+)}{\frac{RT}{zF} \log\left(\frac{\gamma_{C_H} C_H}{\gamma_{C_L} C_L}\right)} \tag{2.12}$$

Because the power generation is maximized when $V_{cell} = E_{diff}/2$, the efficiency corresponding to the maximum power generation is given as

$$\eta_{max} = \frac{(1 - 2T_+)^2}{2} \tag{2.13}$$

Therefore, the efficiency of a perfectly ion-selective nanopore at the maximum power output is 50%.

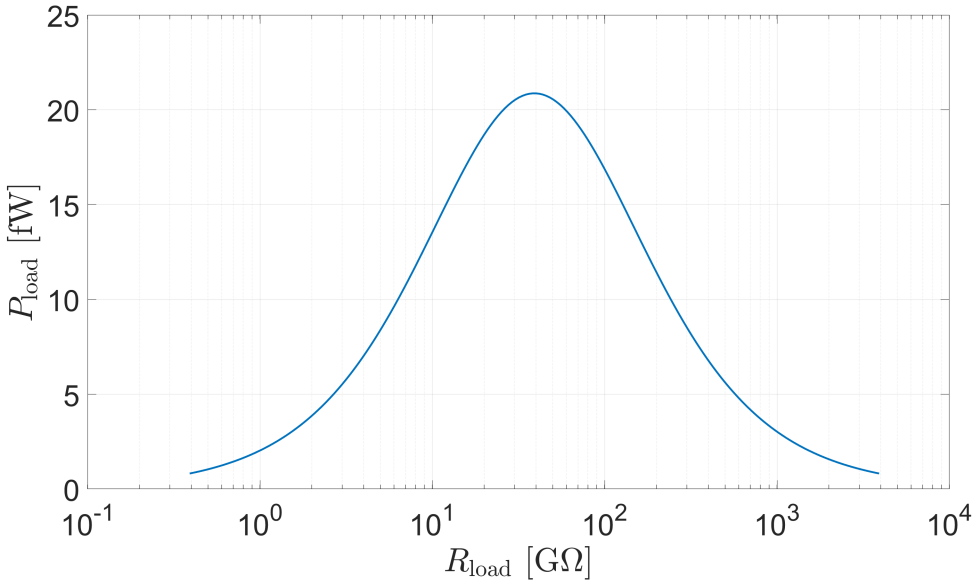


Figure 2.3: Typical curve for the power delivered by the RED cell as a function of the load resistance R_{Load}. The power delivered is maximum when the load resistance matches the internal cell resistance R_{cell}.

2.2 Measurement methods

When characterizing a membrane, several key metrics must be determined. Among them, the ionic resistance and permselectivity are the most critical, as they define the theoretically attainable power output. For practical applications, chemical and mechanical stability over time are also essential. As discussed in Section 3.3.2, parameters such as water content and ion-exchange capacity are important for polymer membranes, as they influence both performance and long-term stability.

Polymer membranes are known to undergo various types of degradation over time, including biofouling and chemical degradation [87]. Conducting a parallel analysis of these aspects would be highly relevant. However, within the time frame of this thesis, only the membrane ionic resistance and permselectivity are investigated.

2.2.1 Permselectivity, membrane potential and transport number

To determine the permselectivity (defined in3.1.4) of a membrane under given conditions (temperature, concentration gradient, ionic species, etc.), the membrane potential must first be measured, after which eq. (3.36) can be evaluated. The most common approach consists of a direct potential measurement using a high-impedance voltmeter connected across the membrane through two reference electrodes in an open-circuit configuration, as illustrated in Figure 2.4. This configuration allows the potential difference arising from ion transport and concentration gradients across the ion-exchange membrane (IEM) to be measured without significant current flow.

During membrane potential measurements, both solution compartments are gently stirred to minimize concentration polarization and maintain uniform ionic composition near the membrane surfaces. Stirring is performed symmetrically on both sides to avoid hydrodynamic pressure differences. Under these conditions, the measured potential corresponds closely to the true membrane potential at steady state [18].

According to Strathmann [18], the measured membrane potential corresponds to the apparent permselectivity, which is systematically higher than the real value because water transport by osmosis and electroosmosis is not accounted for. As expressed in Eq. (2.182) in [18], the total potential difference across a membrane generally includes a contribution from the electrochemical potential of the solvent, in addition to the ionic term. In the simplified TMS form that is given here by (3.25), this water-related term is neglected, leading to a measured potential $\Delta\varphi_m$ that slightly exceeds the true electrochemical potential difference. Consequently, the calculated permselectivity is slightly overestimated. Nevertheless, Strathmann notes that this deviation is generally small, and the direct potential measurement remains a reliable method for comparative characterization.

Once the membrane potential is known, it is possible to evaluate the transport number of a membrane. Transforming eq. (1.4),

$$T_+ = \frac{-E_m F}{2RT \log\left(\frac{\gamma_{C_H} C_H}{\gamma_{C_L} C_L}\right)} + \frac{1}{2}, \tag{2.14}$$

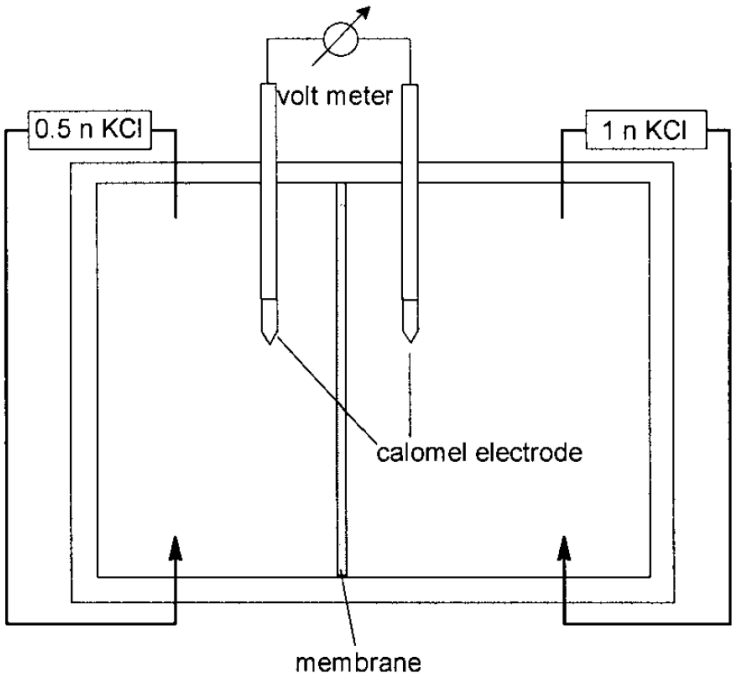


Figure 2.4: Schematic drawing of a test cell used to determine the membrane potential. Two reference electrodes, placed as close as possible to the membrane, measure the voltage drop across it. Stirring of the solution, represented here by recirculation, helps to minimize concentration polarization effects and maintain a uniform ionic composition near the membrane surface. Adapted from [18].

2.2.1.1 Reference electrode

A reference electrode is an electrochemical electrode that maintains a stable and well-defined potential, independent of the composition of the external solution. It provides a fixed potential against which other potentials in the electrochemical system can be measured. In IEM studies, two identical reference electrodes are placed on opposite sides of the membrane to determine the membrane potential.

The stability of a reference electrode originates from a reversible redox couple with a constant activity ratio of its ionic species, ensuring that its potential, given by the Nernst equation, remains constant as long as the temperature and internal composition are maintained. Common examples include the silver/silver chloride (Ag/AgCl) electrode:

$$\mathrm{AgCl(s)} + e^- \leftrightharpoons \mathrm{Ag(s)} + \mathrm{Cl^-}, \tag{2.15}$$

whose potential depends solely on the chloride ion activity, and the saturated calomel electrode (SCE), based on the equilibrium between mercury and mercurous

chloride. Because the internal ionic activity is fixed and the redox reaction is reversible, the potential is stable, reproducible, and insensitive to small current flows, provided that no significant current passes through the electrode.

When two identical reference electrodes are used, the potential difference recorded by the voltmeter corresponds to the membrane potential:

$$E_{\text{mem}} = E_{\text{ref},1} - E_{\text{ref},2} + \Delta\varphi_m, \tag{2.16}$$

where $\Delta\varphi_m$ is the electric potential difference across the membrane. Since both electrodes share the same internal potential, any measured voltage originates exclusively from the electrochemical processes occurring across the membrane.

2.2.2 Membrane ionic resistance

2.2.2.1 Determination of ionic resistance in RED cells

The ionic resistance of an ion-exchange membrane depends on the electrolyte composition, temperature, and measurement configuration, and must therefore always be reported together with the experimental conditions. In principle, the intrinsic membrane resistance can be determined under symmetric conditions, that is, using identical electrolyte concentrations on both sides of the membrane. As described by Strathmann [18], two measurements are performed: one with the membrane inserted and one without it, and their difference yields the intrinsic membrane resistance:

$$R_{\text{membrane}} = R_{\text{cell,mem}} - R_{\text{cell,empty}}.$$

However, this ideal method is not applicable to reverse electrodialysis (RED), which inherently operates under asymmetric conditions, with high- and low-concentration solutions on each side of the membrane. Because the membrane resistance strongly depends on the local ionic concentration, symmetric measurements do not reflect the actual operating environment. Moreover, removing the membrane would cause the two solutions to mix, making a reference measurement physically impossible.

For RED systems, the membrane resistance must therefore be evaluated directly under asymmetric conditions using the experimental current–voltage (I–V) response. In this configuration, the measured resistance always includes contributions from both the membrane and the adjacent solution layers:

$$R_{\text{cell}} = R_{\text{membrane}} + R_{\text{solution}}.$$

The cell resistance is obtained from the slope of the I–V curve in the ohmic (linear) region, between the open-circuit potential and the short-circuit condition.

The relationship between cell voltage, current, and resistance is

$$E_{\text{cell}} = E_{\text{m}} - I\,R_{\text{cell}}, \tag{2.17}$$

where E_{m} is the membrane (open-circuit) potential. By fitting the linear portion of the experimental I–V curve,

$$\frac{dE_{\text{cell}}}{dI} = -R_{\text{cell}}, \tag{2.18}$$

the absolute value of the slope provides the total cell resistance:

$$R_{\text{cell}} = \left|\frac{dE_{\text{cell}}}{dI}\right|. \tag{2.19}$$

Although this method does not isolate the membrane resistance alone, it is the most relevant and widely used approach for RED applications, since the resistance of the solution layers is always present and directly affects the overall cell performance and power output.

2.2.2.2 Electrochemical impedance spectroscopy (EIS).

An alternative and more accurate method for determining membrane resistance is electrochemical impedance spectroscopy (EIS), which evaluates the frequency-dependent complex impedance of the cell [18]. As introduced in 3.2.2, because ions contribute differently to charge transport in the bulk compared to inside the membrane, concentration gradients develop near the membrane surfaces, giving rise to diffusion boundary layers and concentration polarization layer. EIS allows to distinguish between these different layer based on their different frequency responses as shown in Figure 2.5.

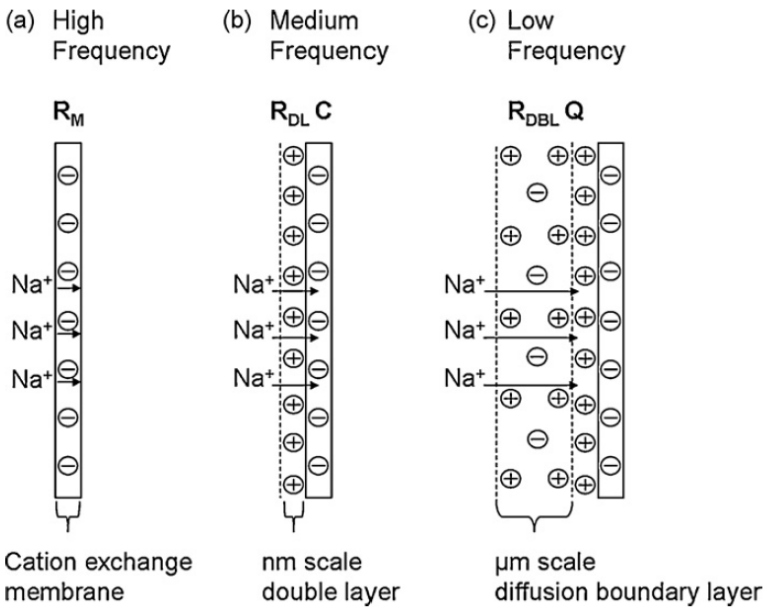


Figure 2.5: Phenomena occurring in the cation exchange membrane and in the layer adjacent to the membrane. The transition of the different phenomena into equivalent electrical elements is also shown. RM is the membrane resistance, RDL is the resistance of the interfacial ionic transfer from the solution through the double layer into the membrane, C is the capacitance of the interfacial ionic charge at the membrane surface (double layer), RDBL is the diffusion boundary layer resistance and Q is the constant phase element representing a non-ideal capacitor of the diffusion boundary layer. Taken from [88].

In this approach, the entire system, comprising the membrane, the electrolyte solution, and the electrodes, is treated as a single black-box. A schematic of the set-up is shown in Figure 2.6.

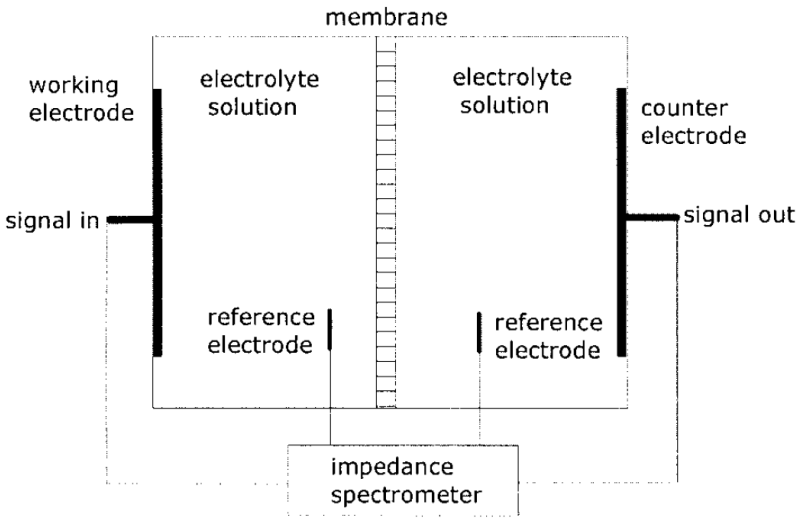


Figure 2.6: Schematic representation of the electrochemical impedance spectroscopy (EIS) configuration used for membrane resistance measurements. An AC voltage of defined amplitude and frequency is applied between the two working electrodes (WE), while the resulting current is collected at the counter electrodes (CE). Two reference electrodes (RE) are positioned close to the membrane surfaces to monitor the local potential drop across the membrane and to minimise contributions from electrode reactions. This configuration enables accurate determination of the membrane impedance by isolating the resistive and capacitive elements associated with the membrane from those of the electrolyte and electrodes. Taken from [18].

A sinusoidal voltage of defined amplitude and frequency is applied through the working electrodes, and the response is collected at the counter electrodes. The signal is usually a superposition of a DC signal and a small AC perturbation as shown in Figure 2.7. In some cases, reference electrodes may be introduced to minimise the influence of electrode reactions and improve the accuracy of the membrane resistance determination. The resulting current response is measured. From this response, both the impedance magnitude and the phase shift relative to the input signal are obtained. Repeating this procedure over a wide frequency range makes it possible to distinguish the different resistive and capacitive contributions that are fitted to an equivalent electrical circuit as presented in Figure 2.8.

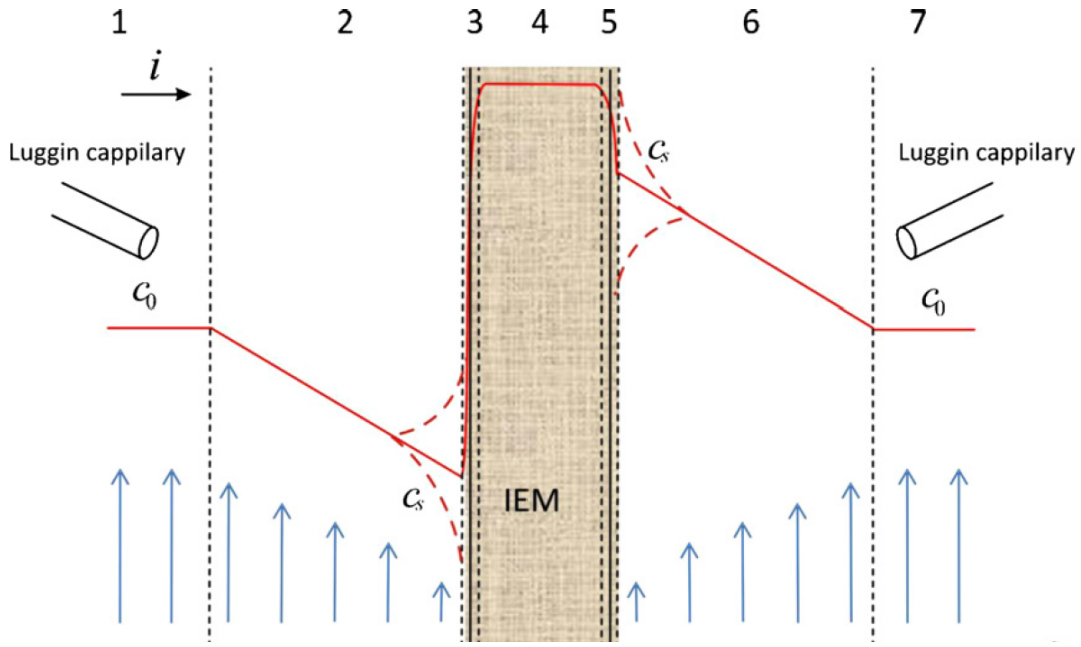


Figure 2.7: Three-layer system consisted of a cation-exchange membrane and two adjoining solution diffusion layers. Zones 1 and 7 are the bulk solution; 2 and 6, the diffusion layers; 3 and 5, interfacial layers; 4, the membrane bulk. Solid lines show stationary concentration profile under a DC bias; dashed lines, the deviations due to a small AC signal. Reprinted from [89].

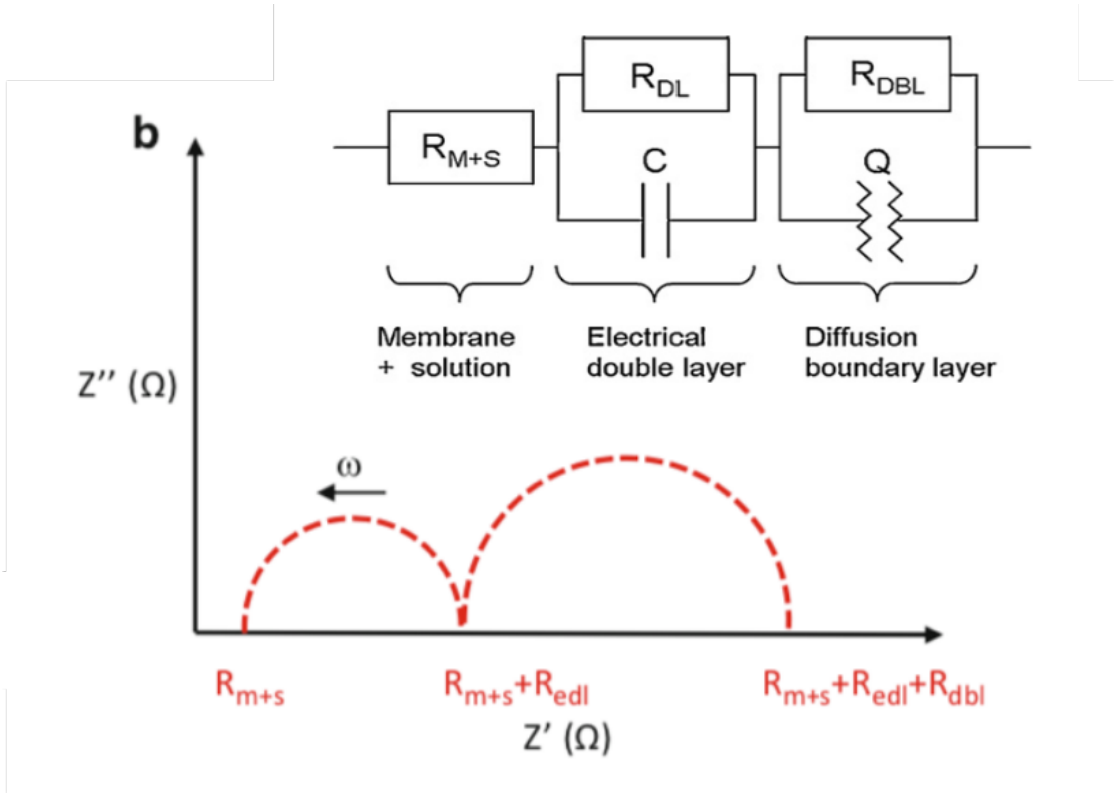


Figure 2.8: Nyquist plot and corresponding equivalent circuit model typically used for ion-exchange membranes, including the membrane and solution resistance ($R_{\mathrm{m+s}}$), the resistance and capacitance of the electrical double layer (R_{edl}, C_{edl}), and the resistance and constant-phase element of the diffusion boundary layer (R_{dbl}, CPE_{dbl}). Reproduced from [88].

In a Nyquist representation (Z'' versus Z'), the high-frequency intercept corresponds to the combined membrane and solution resistance ($R_{\mathrm{m+s}}$), while the subsequent semicircles represent the interfacial and diffusion-related processes. However, to accurately extract the intrinsic membrane resistance from the impedance spectrum, the measurement is ideally performed under symmetric conditions, i.e., with identical electrolyte concentrations on both sides of the membrane. Under these conditions, the spectra can be more reliably modelled and the solution and interfacial resistances effectively separated [18]. In reverse electrodialysis (RED) configurations, however, asymmetric salt concentrations are intrinsic to operation, and the establishment of truly symmetric reference conditions is therefore not representative of the real system.

Nevertheless, several studies have shown that EIS can be successfully adapted to RED systems operating under realistic salinity gradients. Choi *et al.* [90] first

demonstrated the feasibility of EIS on a small-scale RED stack, investigating the influence of flow rate and salt concentration on the different resistive components. Later, Pintossi *et al.* [91] performed in-situ impedance spectroscopy on a one-cell-pair RED stack operating with 0.017 M and 0.508 M NaCl solutions (simulating river and seawater), and were able to distinguish the ohmic, interfacial, and diffusion-related resistances of the individual membranes during fouling and cleaning. These studies illustrate that, although technically demanding, EIS can provide valuable insights into RED systems when the cell geometry, flow conditions, and frequency range are carefully controlled.

Therefore, while EIS offers a more rigorous frequency-resolved separation of the different resistive contributions, DC methods remain the most straightforward and practical choice for evaluating the total ohmic losses under typical RED operating conditions.

Chapter 3

Ion exchange membrane for RED: Physical interpretation

Conventional polymer ion-exchange membranes are specialized semi-permeable membranes that selectively allow only certain ions to pass (either cations or anions), depending on its fixed charge [18]. They are used in various processes that differ in purpose but share a common principle: they control the selective transport of ions through under an electric potential. These processes fall into three main categories [92]:

- Mass separation (e.g., electrodialysis, Donnan dialysis, diffusion dialysis).
- Chemical synthesis (e.g., chlorine-alkali electrolysis, water electrolysis for hydrogen and oxygen).
- Energy conversion and storage (e.g., fuel cells, batteries).

Their technological maturity varies: electrodialysis and chlorine-alkali electrolysis are well-established, while fuel cells are still developing but hold high potential for future energy applications.

This chapter aims at explaining the physical origin of the selective property of polymer IEMs and their physical structure. First, at the membrane level, the Donnan potential is developed mathematically starting from thermodynamics principle. From this, the membrane potential $\Delta\varphi_m$ of an IEM separating two solutions of different saline concentrations c^{s2} and c^{s1} is expressed in term of the membrane property. Finally, the physical structure of the polymer membrane is detailed.

3.1 Donnan exclusion, membrane potential and permselectivity: thermodynamics considerations

When an ion-exchange membrane (IEM) is placed in contact with an electrolyte solution, a complex electrostatic structure arises due to the presence of fixed charges within the membrane. These charges may originate from ionizable chemical groups covalently bound to the polymer matrix, or from ion adsorption onto internal surfaces, as commonly observed in porous or nanostructured membranes. Once charged, the membrane attracts counter-ions from the surrounding electrolyte while repelling co-ions, leading to a rearrangement of ionic concentrations both at the membrane–solution interface and within the internal structure of the membrane. This selective partitioning of ions leads to:

- An unequal concentration of ions on both sides of the membrane.
- The development of an electric potential difference across the membrane–solution interface, known as the Donnan potential.

In the following part of the section, the origins of the Donnan exclusion are explained in term of thermodynamics starting from the definition of the electrochemical potential $\bar{\mu_i}$:

$$\bar{\mu_i}^j = \mu_i^j + |z_i| F \varphi^j, \tag{3.1}$$

with μ_i^j the chemical potential of component i in the phase j, z_i the valence charge of the component i, F the Faraday's constant and φ^j the electrical potential of phase j. This will help to understand the different parameters influencing the permselectivity. The developments are based on [18].

3.1.1 Donnan potential

First, consider an ion-exchange membrane put into contact with an electrolyte solution. Initially, this membrane is electrically neutral but the contact with the water induces the membrane to release mobile ions which are mainly of one type (either cations or anions). The membrane is then charged compared to its dry state as shown in Figure 3.1.

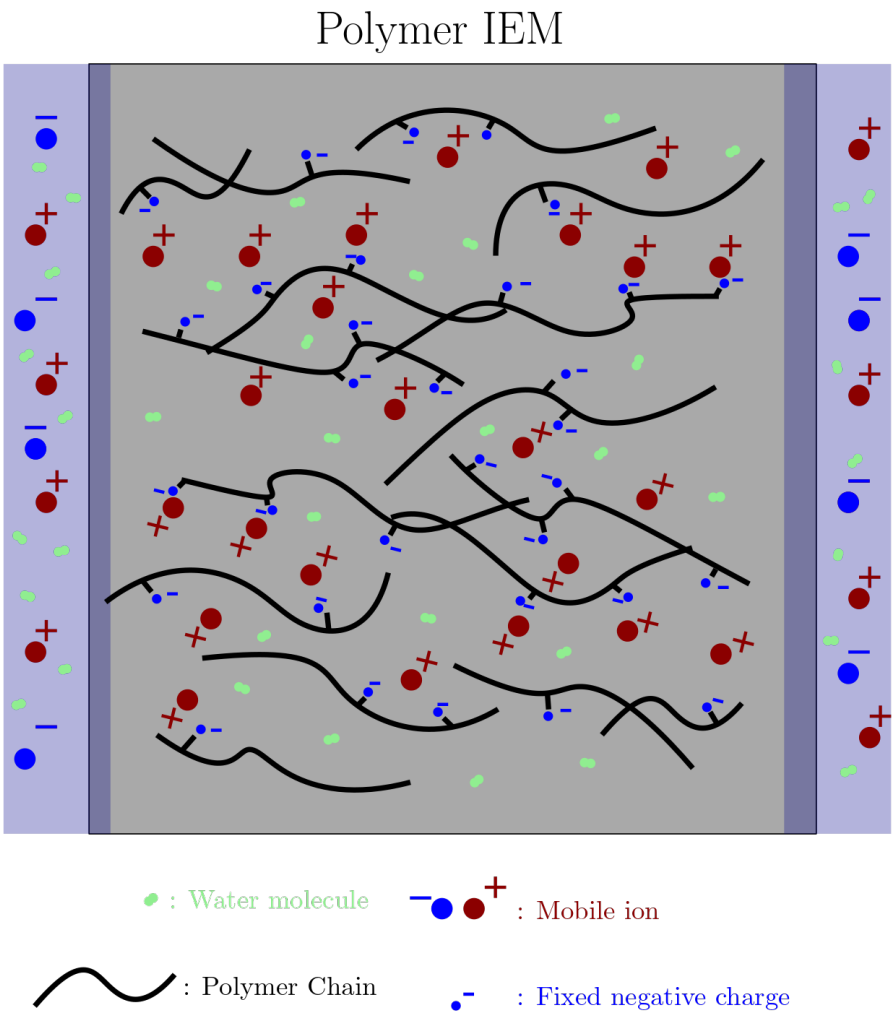


Figure 3.1: Structure of a polymer ion-exchange membrane in contact with water. The membrane consists of polymer chains bearing ionizable groups. Upon hydration, these groups release mobile ions (e.g., cations, shown in red), leaving behind fixed countercharges on the polymer backbone (negative charges shown in blue).

When a hydrated ion-exchange membrane is brought into contact with an adjacent electrolyte solution, the internal environment of the membrane differs from that of the bulk solution. As a result, an ion experiences different interactions depending on whether it resides inside the membrane (phase m) or in the external solution (phase s).

At equilibrium, the electrochemical potentials of each ionic species must be

equal in the two phases. Thus, for ion i:

$$\begin{aligned} & \bar{\mu}_i^m = \bar{\mu}_i^s \\ \Leftrightarrow \quad & \mu_i^m + z_i F \varphi^m = \mu_i^s + z_i F \varphi^s, \end{aligned} \tag{3.2}$$

where μ_i is the chemical potential, z_i the ionic valence, and φ the electrical potential in each phase.

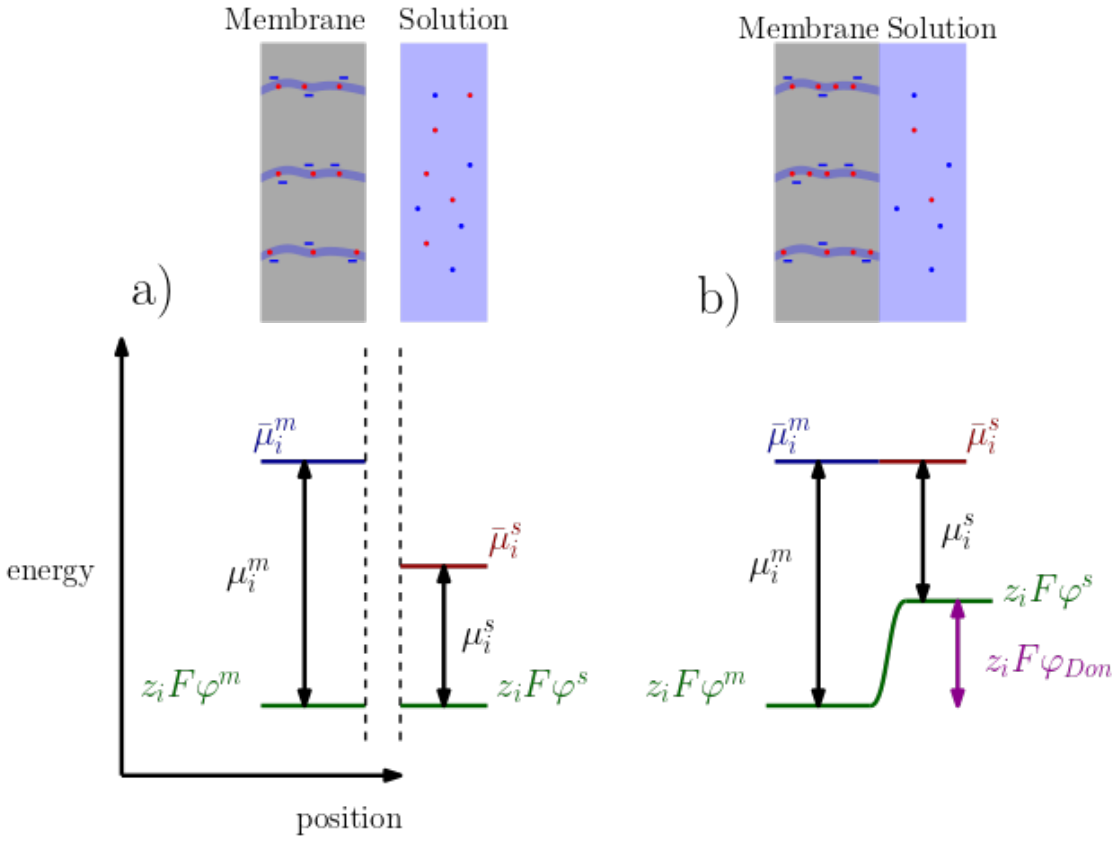


Figure 3.2: Establishing electrochemical equilibrium across an ion exchange membrane and a solution. a) The two adjacent phase have different concentration in mobile ions before coming into contact .b) Upon contact, the ions try to migrate to equilibrate their electrochemical potential, but only counter mobile ions are allowed to enter the membrane, leaving a net charge imbalance and an electric potential difference between the two phase, called the Donnan potential.

The electrical potential difference between the membrane and the adjacent solution is then

$$\varphi^m - \varphi^s = \frac{1}{|z_i|\,\mathrm{F}} \left(\mu_i^s - \mu_i^m\right) = \varphi_{Don}, \tag{3.3}$$

where φ_{Don} is called the Donnan potential. The chemical potential μ_i is also a function of temperature, pressure, and composition, and its change can be expressed by:

$$d\mu_i = \bar{S}_i dT + \bar{V}_i dp + \sum_j \left(\frac{\partial \mu_i}{\partial n_j}\right)_{T,p,n_{k\neq j}} dn_j, \tag{3.4}$$

with $\bar{S}_i$ and $\bar{V}_i$ are the partial molar entropy and volume respectively, T the absolute temperature and p the pressure. At constant pressure and temperature the chemical potential of a component i is given by:

$$(\mu_i)_{p,T} = \mu_i^0 + RT \ln a_i, \tag{3.5}$$

with R the gas constant, μ_i^0 is the chemical potential of the pure component i under standard conditions of temperature and pressure and a_i the activity given by

$$a_i = \gamma_i X_i, \tag{3.6}$$

where γ_i is the activity coefficient and $X_i = n_i/(n_i + \sum_j n_j)$ is the mole fraction of the component i in a mixture. In practice however, the mole fraction is irrelevant (in term of order of magnitude) to be used and it is often replaced by a more convenient concentration ratio to a standard state c_0 such that

$$a_i = \gamma_i c_i / c_0. \tag{3.7}$$

The activity coefficient describes the deviation of a real mixture from an ideal solution and its value is in between 0 and 1. The activity approaches 1 when the solution concentration is low.

Any change in chemical potential of a component i in a real mixture at isothermal conditions is obtained by injecting eq. (3.5) in eq. (3.4):

$$(\mathrm{d}\mu_i)_T = \bar{V}_i \mathrm{d}p + \mathrm{RTd} \ln a_i. \tag{3.8}$$

The last equation is important for describing mass transport between two systems separated by a membrane since most ion exchange membrane are working at constant temperature. Assuming perfect equilibrium within each mixture, the total change for a component i in one mixture to another is given by:

$$(\Delta\mu_i)_T = (\mu_i' - \mu_i'')_T = \bar{V}_i \Delta p + \mathrm{RT} \ln \frac{a_i'}{a_i''}, \tag{3.9}$$

where $(')$ and $('')$ refer to the two mixtures separated by the wall, with Δp the pressure difference between the two mixtures. Now going back to the case with the

membrane in contact a solution, we rename mixture $'$ as the solution s and $''$ as the membrane m. Introducing eq. (3.9) into eq. (3.3), this gives

$$(\varphi_{Don})_T = \varphi^m - \varphi^s = \frac{1}{|z_i|\,F}\left[\mathrm{RT}\ln\frac{a_i^s}{a_i^m} + \bar{V}_i(p^s - p^m)\right]. \tag{3.10}$$

Note that $p^m - p^s = \Delta\pi$ is also referred to as swelling pressure. The swelling pressure can be considered as the osmotic pressure difference between the solution and the membrane phase. The osmotic pressure difference $\Delta\pi$ can be calculated from the water activity (a_w) in the membrane and in the solution. In this work, isothermal condition and constant pressure will always be assumed such that

$$(d\bar{\mu}_i)_{T,p} = RT\,(d\ln a_i)_{T,p} + |z_i|Fd\varphi \tag{3.11}$$

and

$$(\varphi_{Don})_{T,p} = \frac{1}{|z_i|\,F}\mathrm{RT}\ln\frac{a_i^s}{a_i^m}. \tag{3.12}$$

The Donnan potential is usually denoted as φ_{Don} rather than $\Delta\varphi_{\mathrm{Don}}$, since it implicitly refers to a potential difference between an ion-exchange membrane and an adjacent electrolyte solution. The Donnan potentials formed between a cation-exchange membrane (CEM) or an anion-exchange membrane (AEM) and a bulk solution are illustrated in Figure 3.3. The corresponding distributions of fixed and mobile ions are also shown.

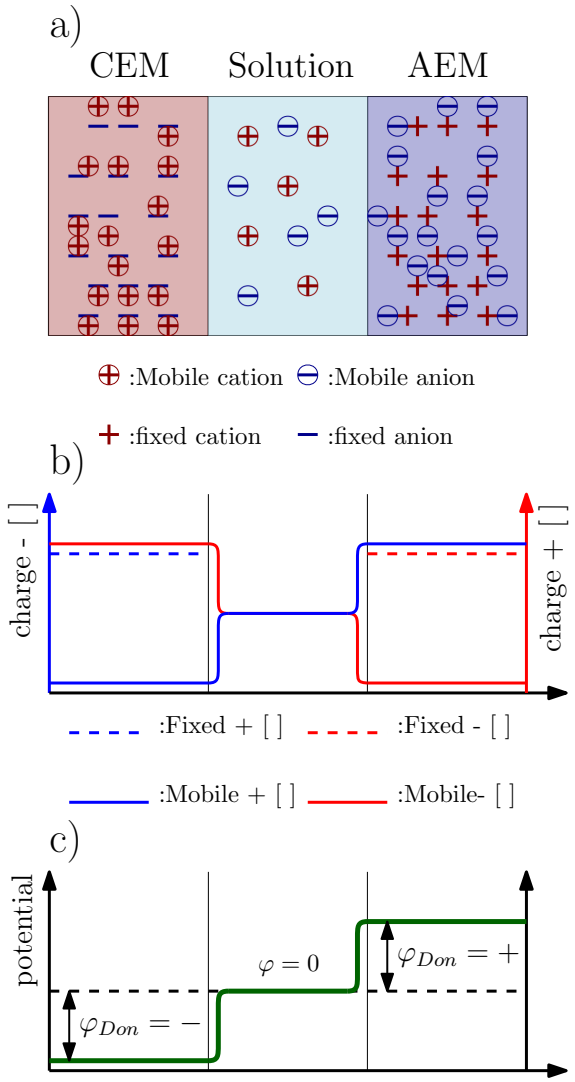


Figure 3.3: Schematic illustration of (a) the distribution of ions between a bulk solution and a cation- and anion-exchange membrane, (b) the concentration profiles of fixed and mobile ions, and (c) the electrical potential profile across the membrane–solution interfaces. The Donnan potentials at the membrane–solution interfaces are indicated. Reproduced from [18].

As shown in Figure 3.3(b), steep ion concentration gradients are present at the membrane–solution interface due to the high concentration of fixed charges within the ion-exchange membranes. These fixed charges attract mobile ions of opposite sign, referred to as counter-ions, while repelling ions of the same sign, referred to as co-ions. This asymmetric ion distribution gives rise to an electrostatic potential difference across the interface, known as the Donnan potential. This phenomenon

underlies the selective ion transport properties of ion-exchange membranes and is commonly referred to as ionic selectivity or Donnan exclusion.

The Donnan equilibrium, and therefore the selectivity of an ion-exchange membrane, depends on several key parameters:

- the concentration of fixed charges within the membrane,
- the valence of the co-ions,
- the electrolyte concentration in the adjacent solution,
- the affinity of the ion-exchange material for the counter-ions,
- the pH of the solution, which affects the degree of ionization of fixed charge groups, particularly in weak polyelectrolytes.

3.1.2 Transport number

The selective ion distribution is not just a static equilibrium effect, it also governs the dynamic transport behavior of the membrane when a driving force (e.g., a concentration or electric potential gradient) is applied. In such cases, the membrane does not allow all ions to pass through equally, but instead preferentially conducts counter-ions, resulting in a net ionic current dominated by one type of charge carrier. Base on the Maxwell-Stefan model, the diffusive/migrative ionic flux of the ionic species i under steady-state, isothermal and constant pressure in one dimensional directional, the driving force is the gradient of electrochemical potential:

$$J_i^{Diff/migra} = -\frac{D_i c_i}{RT}\frac{(d\bar{\mu}_i)_{T,p}}{dx}, \tag{3.13}$$

with D_i the diffusion coefficient [$\mathrm{m^2{\cdot}s^{-1}}$]. The total ionic flux is then the sum of the convection flux and the diffusive/migrative ionic flux

$$J_i^{Tot} = J_i = J_i^{Conv} + J_i^{Diff/migr} = c_i v - \frac{D_i c_i}{RT}\frac{(d\bar{\mu}_i)_{T,p}}{dx}, \tag{3.14}$$

with v the fluid velocity. The fraction of the current that is carried by a certain ion i is expressed by the ion transport or transference number which are given by:

$$T_i = \frac{z_i J_i^{Tot}}{\sum_i z_i J_i^{Tot}}, \tag{3.15}$$

and

$$t_i = \frac{T_i^{Tot}}{|z_i|} = \frac{|J_i^{Tot}|}{\sum_i z_i J_i^{Tot}}, \tag{3.16}$$

Here T_i and t_i are the transport and transference number of the component i and z_i its valence. The transport number T_i indicates the fraction of the total current that is carried by the ion i, and the transference number t_i indicates the number of moles of ion i transported per mole of electrons, i.e. per Faraday. The sum of the transport number or the transference number of all ions in a solution is 1. Unfortunately, in the literature the definition of the transport and the transference number is not used consistently and very often transference and transport number are mixed up.

The transport numbers of cations and anions in an aqueous salt solution do not differ very much. In an ion-exchange membrane, however, the situation is quite different. In addition to the ions of the electrolyte there are the "fixed" ions of the membrane. Since these ions are bound to the membrane matrix they are unable to contribute to the transport of electrical charges, i.e. the electrical current. Thus, their transport number is per definition 0. Furthermore, the concentration of the counterions, i.e. the ions which carry the opposite charge of the membrane is rather different from that of the coions, i.e. the ions which carry the same charge as the membrane. Their concentration depends on the fixed ion concentration of the membrane and the salt concentration of the solution in contact with the membrane as will be shown later. If the coions are completely excluded from the membrane the transport number of the counterion in the membrane is 1 and the membrane is strictly semipermeable.

3.1.3 Membrane potential

In order to place the analysis in a more simple framework, three different cases must be considered:

- a non selective membrane, with no fixed charge,
- a perfectly selective membrane,
- and a partially selective membrane.

For each case, two electrolyte solutions are separated by the membrane and the following hypothesis are also made:

- Electrolyte solutions of different concentrations on both sides: side 1 and side 2, c^{s1} and c^{s2}.
- Binary monovalent electrolyte (e.g., KCl or NaCl).
- Ideal solution behavior, no ion-ion interaction (activity $\simeq$ concentration, $a_i \simeq c_i$)

- Local electroneutrality.
- no pressure difference, i.e., $\Delta p = 0$.
- isothermal conditions.
- No water flux across the membrane (no osmosis or electroosmosis).

These assumptions imply that the solvent is at rest ($J_{\mathrm{H_2O}} = 0$), so that the potential difference arises solely from ionic diffusion and migration. The coupling between ion and solvent transport is therefore neglected, consistent with the classical Teorell–Meyer–Sievers (TMS) model [93].

3.1.3.1 Non selective membrane

If the membrane carries no fixed charge when immersed in water, its impact on the ionic flux is almost negligible. The ionic flux of species i inside the membrane is derived from (3.13) using (3.2), (3.5), and (3.6):

$$\begin{aligned} J_i^m &= -\frac{D_i^m c_i^m}{RT}\left(RT\frac{d\ln a_i}{dx} + z_i F\frac{d\varphi^m}{dx}\right) \\ &= -D_i^m\frac{dc_i^m}{dx} - \frac{z_i F}{RT}D_i^m c_i^m\frac{d\varphi^m}{dx}. \end{aligned} \tag{3.17}$$

This second expression is the one-dimensional Nernst–Planck equation, which describes the flux of ionic species i as the sum of diffusive and migrative contributions. Here, the dilute-solution (Debye–Hückel) limit is assumed, meaning $d\ln\gamma_i \simeq 0$, which is equivalent to treating the solutions as ideal.

Both ionic species diffuse across the membrane under the same initial driving force, namely the equality of chemical potentials $\mu_+ = \mu_-$. If the ions have different diffusion coefficients ($D_+ \neq D_-$), a charge imbalance develops across the membrane. In steady state and in the absence of an applied current, the total current density must vanish:

$$J = F(z_+J_+ + z_-J_-) = F(J_+ - J_-) = 0, \tag{3.18}$$

which gives

$$D_+^m\left(RT\frac{dc_+^m}{dx} + c_+^m F\frac{d\varphi^m}{dx}\right) = D_-^m\left(RT\frac{dc_-^m}{dx} - c_-^m F\frac{d\varphi^m}{dx}\right). \tag{3.19}$$

Assuming local electroneutrality,

$$c_+^m = c_-^m = c^m, \qquad \frac{dc_+^m}{dx} = \frac{dc_-^m}{dx} = \frac{dc^m}{dx},$$

the potential gradient becomes

$$\frac{d\varphi^m}{dx} = -\frac{RT}{F}\frac{D_+^m - D_-^m}{D_+^m + D_-^m}\frac{1}{c^m}\frac{dc^m}{dx}. \tag{3.20}$$

Integrating across the membrane thickness, from solution 1 to solution 2, gives the potential drop across the membrane:

$$\Delta\varphi_m = \Delta\varphi_{\text{Hen,diff}} = \varphi^{s2} - \varphi^{s1} = -\frac{RT}{F}\frac{D_+ - D_-}{D_+ + D_-}\ln\left(\frac{c^{s2}}{c^{s1}}\right), \tag{3.21}$$

where it is assumed that the membrane does not alter ionic mobilities, i.e. $D_i^m = D_i^{s1} = D_i^{s2} = D_i$. The resulting potential difference arises from the unequal mobilities of the ions and is known as the Henderson diffusion potential.

3.1.3.2 Perfectly selective membrane

The following assumptions are further made:

- An ion-exchange membrane is considered (e.g. a cation-exchange membrane with fixed negative charges X_-).
- The membrane is perfectly selective: co-ions (Cl^-) are completely excluded, and only counter-ions (K^+) can enter the membrane.
- Thermodynamic equilibrium is established at the membrane–solution interfaces (Donnan equilibrium).

When two electrolyte solutions of different ionic concentrations are separated by a permselective membrane, two Donnan potentials arise, one at each membrane–solution interface. Because the ion concentrations in the two solutions differ, the two Donnan potentials are not equal, resulting in a net potential difference between the two bulk solutions. This overall potential difference is referred to as the membrane potential. In contrast to the Donnan potential, which cannot be measured directly, the membrane potential can be measured experimentally.

While Eq. (3.19) remains valid, electroneutrality inside the membrane no longer implies $c_+^m = c_-^m$, since co-ions are completely excluded. Instead, electroneutrality requires

$$c_+^m = X_-.$$

As a consequence, a direct integration over the membrane thickness is no longer possible. The membrane potential is therefore expressed as

$$\begin{aligned}\Delta\varphi_m &= \varphi^{s2} - \varphi^{s1} \\ &= \underbrace{\varphi^{s2} - \varphi^{m2}}_{-\Delta\varphi_{\mathrm{Don},2}} + \underbrace{\varphi^{m2} - \varphi^{m1}}_{\Delta\varphi_{\mathrm{diff}}} + \underbrace{\varphi^{m1} - \varphi^{s1}}_{\Delta\varphi_{\mathrm{Don},1}} \\ &= -\Delta\varphi_{\mathrm{Don},2} + \Delta\varphi_{\mathrm{diff}} + \Delta\varphi_{\mathrm{Don},1}, \end{aligned} \tag{3.22}$$

where the membrane potential is composed of two Donnan potentials established at the membrane–solution interfaces and a diffusion potential arising from differences in ion transport within the membrane. The concentration and potential gradients across the membrane are schematically illustrated in Figure 3.4.

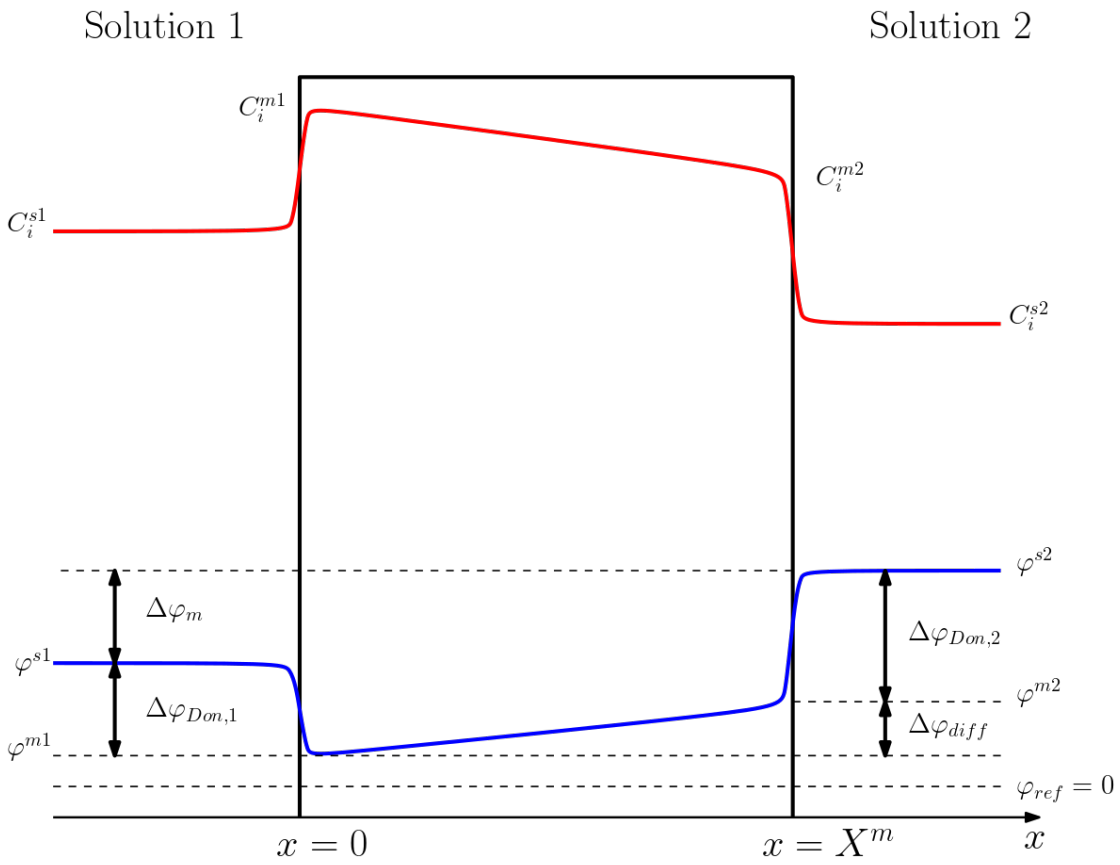


Figure 3.4: Schematic illustration of the concentration profiles and resulting potential differences for two solutions of different concentration separated by a permselective membrane. $\Delta\varphi_{\text{Don}}$, $\Delta\varphi_m$, and $\Delta\varphi_{\text{diff}}$ denote the Donnan potential, the membrane potential, and the diffusion potential, respectively. C is the concentration, x the spatial coordinate, and X_m the membrane thickness. Subscript i refers to the ion species, while superscripts s, m, 1, and 2 denote the bulk solution, the membrane phase, and solutions 1 and 2, respectively. Reproduced from [18].

Using the Donnan relation (3.10), Eq. (3.22) can be rewritten as

$$\Delta\varphi_m = -\frac{RT}{F}\ln\left(\frac{c_+^{s2}}{c_+^{m2}}\right) + \Delta\varphi_{\text{diff}} + \frac{RT}{F}\ln\left(\frac{c_+^{s1}}{c_+^{m1}}\right). \tag{3.23}$$

Although the origin of the diffusion potential in the above equation is analogous to that in the non-selective membrane case, the expression given in Eq. (3.21) is no longer applicable, since the membrane alters the ionic concentrations c_i^m and potentially the ion mobilities.

Under the assumption of a perfectly selective membrane, only one ionic species is allowed to diffuse through the membrane. As a result, no charge separation can occur due to differences in ionic mobility, and the diffusion potential vanishes:

$$\Delta\varphi_{\text{diff}} = 0.$$

For an ideal and symmetric membrane with a uniform fixed charge density X_-, the electroneutrality condition implies

$$c_+^{m1} = c_+^{m2} = X_-,$$

which simplifies Eq. (3.23) to

$$\Delta\varphi_m = \Delta\varphi_{\text{Nernst}} = -\frac{RT}{F}\ln\left(\frac{c_+^{s2}}{c_+^{s1}}\right). \tag{3.24}$$

This expression corresponds to the Nernst equation for a perfectly selective cation-exchange membrane and is also commonly referred to as the Planck potential.

3.1.3.3 Partially selective membrane

In reality, the membrane allows both ions to pass, but at different rates, meaning the membrane is never perfectly selective. In this case, let T_+ and T_- be transport numbers of the cation and anion, e.g. K^+ and Cl^-. Because both ions are now presents in the membrane, both will contributes to the electric field and so it is no longer possible use the Donnan potential as it has been done in (3.23). One approximation that is physically grounded, thermodynamically consistent, widely used in membrane science, biophysics, electrochemistry, and RED modeling is the approximation from the Teorell–Meyer–Sievers (TMS) model and earlier work by Planck [93, 94]. where it is assumed that the membrane potential is a weighted average of individual Nernst potentials using transport numbers:

$$\Delta\varphi_m = \Delta\varphi_{TMS} = -\frac{RT}{F}\sum_i T_i z_i \log\left(\frac{a_i^{s2}}{a_i^{s1}}\right), \tag{3.25}$$

with the additional assumptions that

- electric field is constant across the membrane,
- linear response regime,
- and an uniform transport numbers (independent of position).

For an ideal binary monovalent electrolyte,

$$\begin{aligned}\Delta\varphi_m = \Delta\varphi_{TMS} &= -\frac{RT}{F}T_+ \log\left(\frac{c_+^{s2}}{c_+^{s1}}\right) + \frac{RT}{F}T_- \log\left(\frac{c_-^{s2}}{c_-^{s1}}\right) \\ &= -\frac{RT}{F}(T_+ - T_-)\log\left(\frac{c^{s2}}{c^{s1}}\right) \\ &= -\frac{RT}{F}(2T_+ - 1)\log\left(\frac{c^{s2}}{c^{s1}}\right) \qquad (3.26) \\ &= (2T_+ - 1)\Delta\varphi_{Nernst} \qquad (3.27)\end{aligned}$$

where $c_+^{sj} = c_-^{sj}$ due to electroneutrality in the solutions. The model does not account for:

- position-dependent transport numbers,
- non-ideal activity coefficients,
- space charge effects, or concentrated solution effects,
- and coupling with water or co-ion transport in some systems.

Coherence between the models

The transport number can take value between 0 and 1. If the transport number for the cation is close or equal to 1, the membrane potential in (3.26) gives:

$$\Delta\varphi_m = \Delta\varphi_{TMS} \underbrace{=}_{T_+=1} -\frac{RT}{F}\log\left(\frac{c^{s2}}{c^{s1}}\right) = \Delta\varphi_{Nernst}, \qquad (3.28)$$

which is the potential for a perfectly selective cation exchange membrane (CEM), as expected for an ionic current composed of one type of ions (here the cation species). In the case if $T_+ = 0$, then we get the opposite results from (3.28), meaning it is a perfectly selective anion exchange membrane (AEM).

When the transport number $T_+ = 0.5$, the membrane potential becomes:

$$\Delta\varphi_m = \Delta\varphi_{TMS} \underbrace{=}_{T_+=0.5} 0. \qquad (3.29)$$

This is usually the representative of a non-selective membrane since it is neither cation or anion selective. However, the equation for the diffusion potential (3.21) is not recovered in this case because assuming $T_+ = 0.5$ in (3.15) implies $T_+ = T_-$, which means from equation (3.17) that

$$D_- = D_+. \qquad (3.30)$$

in practice, fort a salt, the ionic species never have perfectly similar diffusion coefficient. Thus, measuring a membrane potential of 0 with ionic species known to have different ionic mobilities indicates that the membrane is actually partially selective but that the diffusion potential in (3.22) is

$$\Delta\varphi_{diff} = \Delta\varphi_{Don,2} - \Delta\varphi_{Don,1}. \tag{3.31}$$

This indicates that the membrane impact on the ionic mobility and ionic concentration leads to a diffusion potential across the membrane opposite to the difference in the two Donnan potential.

If the membrane is actually known to have no impact on the ionic mobility nor the ionic concentration, in (3.23), the transport number can be changed as

$$\begin{aligned}\Delta\varphi_m &= -\frac{RT}{F}(T_+ - T_-)\log\left(\frac{c^{s2}}{c^{s1}}\right)\\ &= -\frac{RT}{F}\left(\frac{D_+}{D_+ + D_-} - \frac{D_-}{D_+ + D_-}\right)\log\left(\frac{c^{s2}}{c^{s1}}\right)\\ &= -\frac{RT}{F}\left(\frac{D_+ - D_-}{D_+ + D_-}\right)\log\left(\frac{c^{s2}}{c^{s1}}\right) = \Delta\varphi_{Hen,diff},\end{aligned} \tag{3.32}$$

and the membrane potential for a non selective membrane is recovered, which is consistent with the hypothesis made.

In conclusion, in order to assess the selectivity of a new membrane, it is important to use binary monovalent electrolyte with ionic mobilities similar to each other. This avoid the apparition of diffusion potential that could mask the effect of the membrane. In the literrature, this is the reason why KCl is often chosen over NaCl because of the ionic diffusion coefficient difference as shown in Table 3.1.

Ionic species	**Diffusion coefficient** $[\mathbf{10^{-9}m^2s^{-1}}]$
Na^+	1.334
K^+	1.96
Cl^-	2.032

Table 3.1: Diffusion coefficient comparison of ionic species [18, 95] .

3.1.4 Permselectivity

Membrane permselectivity is a key parameter for evaluating the performance of an ion-exchange membrane in a given separation or energy-conversion process. Commonly denoted by α or Ψ, it quantifies the ability of a membrane to preferentially transport ions of one charge while excluding ions of opposite charge. For

cation- and anion-exchange membranes, the permselectivity can be defined [18] as

$$\Psi^m = \frac{T_{\mathrm{co}}^m - T_{\mathrm{co}}}{T_{\mathrm{cou}}}, \tag{3.33}$$

where T_{co}^m is the transport number of the co-ion inside the membrane, T_{co} is the co-ion transport number in the bulk solution, and T_{cou} is the counter-ion transport number in the bulk solution.

Using Eq. (3.26) and normalizing the measured membrane potential $\Delta\varphi_m$ by the Nernst potential $\Delta\varphi_{\mathrm{Nernst}}$ corresponding to a perfectly selective membrane, the counter-ion transport number inside the membrane can be expressed as

$$T_{\mathrm{cou}}^m = \frac{1}{2}\left(\frac{\Delta\varphi_m}{\Delta\varphi_{\mathrm{Nernst}}} + 1\right). \tag{3.34}$$

Substituting this expression into Eq. (3.33) yields

$$\Psi^m = \frac{\frac{\Delta\varphi_m}{\Delta\varphi_{\mathrm{Nernst}}} + 1 - 2T_{\mathrm{cou}}}{2T_{\mathrm{co}}}. \tag{3.35}$$

For a symmetric 1:1 electrolyte such as KCl, the transport numbers of cations and anions in the bulk solution are approximately equal, i.e. $T_{\mathrm{co}} \simeq T_{\mathrm{cou}} \simeq 0.5$. Under this assumption, the permselectivity simplifies to first order as

$$\Psi^m \simeq \frac{\Delta\varphi_m}{\Delta\varphi_{\mathrm{Nernst}}}. \tag{3.36}$$

Permselectivity is therefore widely used as a practical metric to characterize membrane performance. Transport numbers can be determined experimentally using techniques such as Hittorf's method or chronopotentiometry. Since permselectivity depends strongly on electrolyte concentration, measurements must be performed over the relevant operational concentration range of the membrane in order to accurately assess its performance under practical working conditions [96, 97].

3.2 Ionic/electrical characteristic

The electrical response of an IEM can be characterized by measuring the current density as a function of the applied voltage, i.e., its current–voltage (I–V) relation. In the absence of any concentration difference ($c^{s1} = c^{s2}$), no diffusion potential exists across the membrane and its typical electrical response is shown in Figure 3.5. As can be seen, three distinct regimes are generally observed depending on the applied voltage [18, 98, 99].

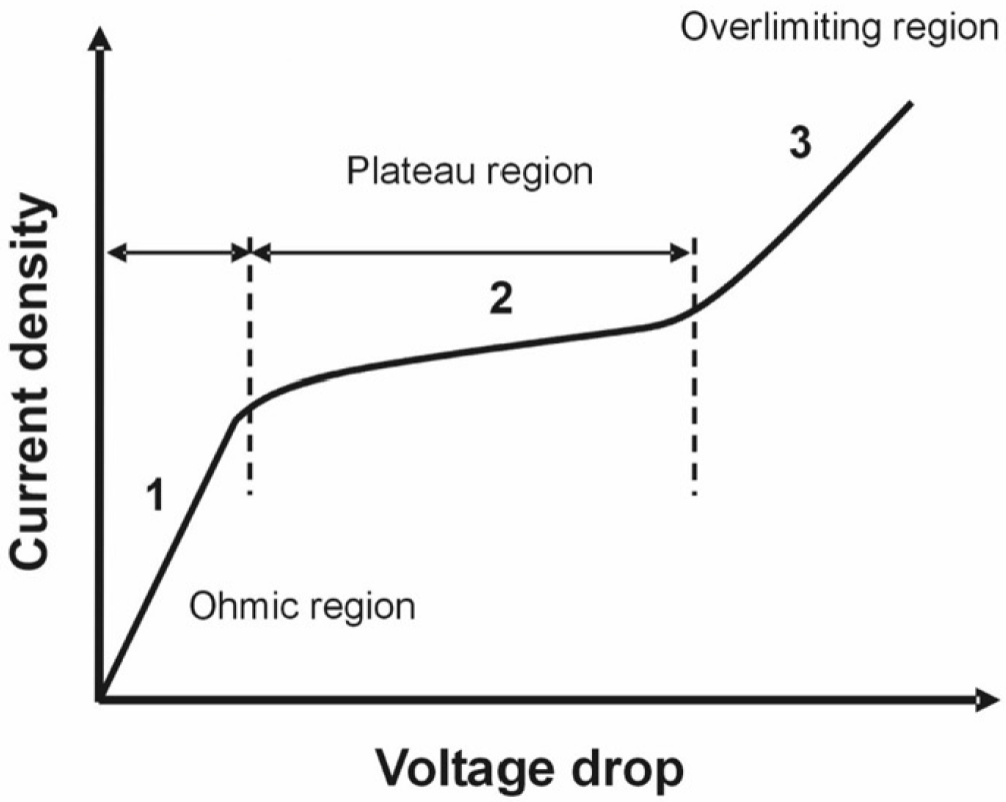


Figure 3.5: Schematic representation of the three characteristic regimes of the current–voltage (I–V) response of an ion-exchange membrane. [99].

For relatively small voltages, the response of the system is linear, corresponding to an Ohmic regime. Increasing the voltage leads to a plateau in the current density, referred to as the limiting current, which is associated with concentration polarization effects that deplete ions near the membrane surface. When the applied voltage exceeds this threshold, the system enters a third regime characterized by a renewed increase in current, called the overlimiting regime. This behaviour is typically attributed to additional transport mechanisms such as electroconvection, water dissociation, or surface conduction that overcome the diffusion limitation [99].

3.2.1 Linear Regime

The origin of the initial linear response can be understood from a thermodynamic description of ion transport. Ion motion in the system can be described by the

Nernst–Planck equation (3.17):

$$\mathbf{J}_i = -D_i \nabla c_i - \frac{z_i e}{k_B T} D_i c_i \nabla \varphi, \tag{3.37}$$

where D_i is the diffusion coefficient, z_i the ionic charge number, F the Faraday constant, R the gas constant, T the absolute temperature, c_i the concentration, and φ the electric potential. The total current density is obtained by summing over all ionic species:

$$\mathbf{J} = F \sum_i z_i \mathbf{J}_i. \tag{3.38}$$

At low applied voltages, the total potential difference across the system is small enough that the ionic composition in different regions (membrane and adjacent diffusion layers) does not differ appreciably from the equilibrium one. This situation corresponds to the *near-equilibrium approximation* described by Rubinstein [98], who noted that

> "for an infinitesimal voltage V, the ionic composition in different parts of the system does not differ appreciably from the equilibrium one, and the voltage–current curve remains nearly linear."

In this near-equilibrium regime, the electrochemical potential of each ionic species can be considered uniform (i.e. constant in space), and the local concentration follows the Boltzmann distribution:

$$c_i = c_i^{\infty} \exp\!\left(-\frac{z_i e \varphi}{k_B T}\right), \tag{3.39}$$

where e is the elementary charge, k_B the Boltzmann constant, T the absolute temperature, z_i the ionic charge number, and c_i^{∞} the concentration of species i in the bulk at the reference potential. This relation expresses how ions redistribute under an electric potential in order to maintain electrochemical equilibrium.

When a small external voltage is applied, a deviation from this equilibrium occurs and a net ionic flux develops. Substituting the Boltzmann concentration dependence into eq. (3.37) introduces an exponential coupling between concentration and potential. For small potentials such that $|z_i e\varphi / k_B T| \ll 1$, this exponential term can be linearized as

$$\exp\!\left(-\frac{z_i e \varphi}{k_B T}\right) \approx 1 - \frac{z_i e \varphi}{k_B T}. \tag{3.40}$$

Under this approximation, the concentration gradients remain weak and the Nernst–Planck equation simplifies to a linear relation between the ionic flux and the local potential gradient:

$$\mathbf{J}_i \approx -z_i u_i F c_i \nabla \phi, \tag{3.41}$$

with $u_i = D_i/(k_bT)$. Because $\nabla\phi = V/L$, with L the characteristic transport length, the total current, obtained by integrating over a surface A, therefore increases linearly with the applied voltage:

$$I = \frac{\kappa_{\text{eff}} A}{L} V, \tag{3.42}$$

which defines the Ohmic regime, where κ_{eff} is the effective ionic conductivity and A the active area [18].

The existence of this initial linear region and its interpretation as an Ohmic response are well established in the theory of electro-diffusion of ions [98] and confirmed experimentally for ion-exchange membranes [100–102]. In these studies, the linear portion of the I–V characteristic is shown to correspond to small potential differences where the system remains close to equilibrium, and deviations from linearity only appear once concentration polarization becomes significant. In this work, the applied potential is on the order of the Nernst potential and the approximation in (3.40) is valid.

3.2.2 Limiting regime and overlimiting region

Beyond the linear (Ohmic) regime, the current–voltage response of an ion-exchange membrane is governed by the development of concentration polarization (CP), which leads to two additional characteristic regions as the applied voltage increases. When an electric current flows through the membrane, charge is transported almost exclusively by counter-ions due to Donnan exclusion, whereas in the bulk electrolyte both ions contribute to conduction. This mismatch in ion transport numbers leads to the formation of diffusion boundary layers on both sides of the membrane, typically a few hundred micrometres thick [88].

Within these boundary layers, the salt concentration decreases on the ion-depleted side and increases on the enriched side, as illustrated schematically in Figure 3.6. As the applied voltage increases, the concentration at the depleted interface progressively drops because diffusion from the bulk solution cannot keep pace with ion migration through the membrane. Once the concentration at this interface approaches zero, ion transport becomes diffusion-limited, and the current can no longer increase despite further increases in applied potential. This marks the transition from the Ohmic region to the limiting current regime, a defining feature of CP-controlled ion transport across ion-exchange membranes. This defines the limiting current density I_{lim}, given by

$$I_{\text{lim}} = z_i F \frac{D_i c_b}{\delta}, \tag{3.43}$$

where D_i is the diffusion coefficient, c_b the bulk electrolyte concentration, and δ the thickness of the diffusion boundary layer. In this regime, concentration polarization

dominates and the I–V curve exhibits a nearly constant current plateau, as also depicted in Figure 3.5.

When the applied voltage exceeds the limiting value, additional nonlinear transport mechanisms become active, and the current increases again beyond I_{lim}. This region corresponds to the overlimiting regime, where strong electric fields near the depleted interface induce electroconvection, water dissociation, or surface conduction, thereby supplying extra charge carriers. As a result, the local electroneutrality assumption breaks down and the potential distribution becomes highly nonlinear [18]. This behaviour, first analyzed by Rubinstein [98] and later by Rubinstein and Zaltzman [103], marks the transition from near-equilibrium electro-diffusion to strongly coupled electrohydrodynamic transport.

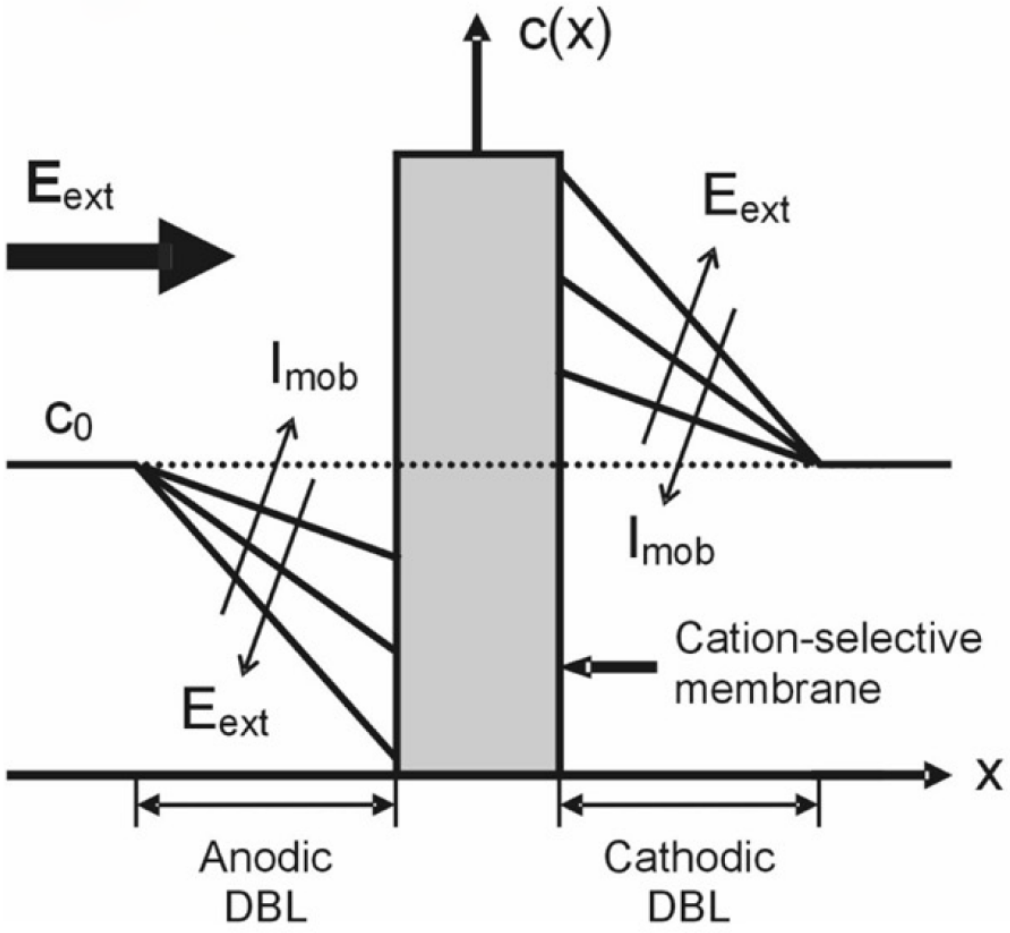


Figure 3.6: Schematic representation of the three characteristic regimes of the current–voltage (I–V) response of an ion-exchange membrane, including (1) concentration polarization (CP) near the membrane interface, (2) limiting current plateau, and (3) overlimiting region with electroconvective instability. Adapted from [99].

3.3 Polymer based IEM

Polymer Ion-exchange membranes are polymeric materials containing fixed ionic groups covalently bound to the polymer backbone. The immobilized nature of these groups gives rise to a net electrical charge within the membrane phase, typically referred to as the volume charge density. To maintain electroneutrality, the membrane absorbs mobile counter-ions from the surrounding electrolyte while

repelling co-ions of the same charge as the fixed sites. This selective ion uptake enables IEMs to facilitate the transport of specific ions while excluding others, a property critical to their application in electrodialysis, reverse electrodialysis (RED), fuel cells, and other electrochemical systems.

The distribution of fixed charges and their interaction with mobile ions and water strongly influence key transport properties, such as conductivity, permselectivity, and water uptake. These characteristics depend not only on the chemical identity of the polymer and functional groups, but also on the nanoscale morphology of the membrane, including the size and connectivity of hydrated ionic domains. The degree of confinement within these domains can lead to phenomena such as electrical double layer (EDL) overlap and non-ideal ion partitioning, both of which are central to the performance of modern IEMs.

3.3.1 Physical structure

Ion exchange membranes (IEMs) are generally categorized according to the nature of their charged functional groups. Cation-exchange membranes (CEMs) carry negatively charged groups such as sulfonic, carboxylic, or phosphonic acids, which permit cation transport while repelling anions. Conversely, anion-exchange membranes (AEMs) contain positively charged functional groups like ammonium or amine derivatives, allowing anion transfer while excluding cations [100].

From a structural standpoint, IEMs can be classified as homogeneous or heterogeneous. Homogeneous membranes exhibit a uniform charge distribution throughout the polymer matrix, whereas heterogeneous membranes consist of ion-exchange resin particles dispersed within an uncharged polymer binder, leading to a nonuniform charge structure [100].

Homogeneous membranes are typically produced either by copolymerization of monomers (e.g., styrene and divinylbenzene) followed by chemical functionalization, or by grafting functional monomers onto preformed polymer films or solutions. Heterogeneous membranes, in contrast, are fabricated by blending powdered ion-exchange resins with inert polymers such as polyvinyl chloride or acrylonitrile, followed by pressing or casting [100].

Recent advances in membrane design include polymer blending (e.g., fluorinated and non-fluorinated systems), pore-filling of porous supports with polymer electrolytes for improved stability and selectivity, in-situ polymerization using liquid monomers, and electrospinning of nanofibrous IEMs [100]. There also exist other polymer IEM structures, such as bipolar, amphoteric, and mosaic membranes, which will not be detailed in this work, as the focus is not on polymer membranes. More information can be found in Campione et al. [104] regarding IEMs in general, and in Tufa et al. [13] and Abidin et al. [105] for RED-specific studies.

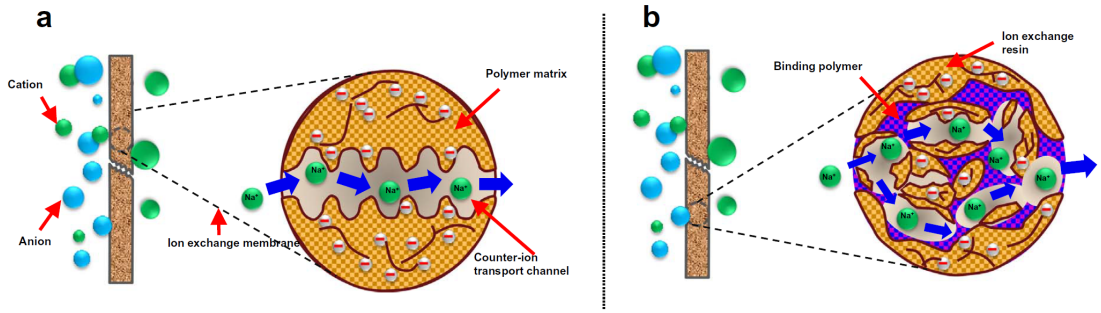


Figure 3.7: Schematic diagrams of the internal structure of (a) a homogeneous membrane in which fixed charges uniformly distribute in the polymer matrix and (b) a heterogeneous membrane in which charged domains of ion exchange resin mix with uncharged binding polymer. Taken from [100].

3.3.2 Characterization of polymer IEM

According to Mei and Tang [100], the performance of reverse electrodialysis (RED) systems is primarily governed by two intrinsic membrane properties: permselectivity and electrical resistance, both of which determine the attainable power output. Secondary parameters such as water content, ion exchange capacity (IEC), and fixed charge density (FCD) influence these main properties through their effects on ion transport and membrane structure.

Water content controls membrane swelling, mechanical stability, and ion mobility. High hydration generally enhances ionic conductivity but reduces permselectivity due to increased pore volume and structural loosening [106]. It is largely determined by the polymer composition, cross-linking degree, and external solution conditions.

The ion exchange capacity (IEC) quantifies the number of fixed ionic sites per unit mass of dry membrane, while the fixed charge density (FCD) represents the amount of fixed charge per gram of absorbed water. High IEC increases ionic selectivity but also promotes swelling, whereas high FCD improves electrostatic exclusion of co-ions and therefore enhances permselectivity [107]. The two parameters are interrelated, often requiring a balance between conductivity and selectivity.

Permselectivity measures the ability of an ion exchange membrane to selectively transport counter-ions while rejecting co-ions. Ideal membranes would have a permselectivity of one, but practical values are typically lower due to inevitable co-ion leakage. According to Donnan theory, increased FCD enhances permselectivity; however, this effect weakens in concentrated solutions where electrostatic interactions are screened.

Membrane resistance reflects the hindrance to ion migration through the polymer matrix and represents a major component of internal losses in RED stacks. It

depends on water content, ion concentration, and temperature, decreasing with higher hydration or temperature, but increasing with greater cross-linking or FCD. Experimental techniques such as chronopotentiometry (DC) and electrochemical impedance spectroscopy (AC) are typically used to evaluate area resistance and separate intrinsic membrane effects from boundary-layer contributions.

Overall, there exists a trade-off between permselectivity and resistance. Membranes with high conductivity often display lower selectivity, and vice versa. Therefore, achieving optimal RED performance requires careful tuning of membrane chemistry and microstructure, selecting IEMs that balance low area resistance with sufficient ion selectivity for the intended application [100].

3.3.3 Requirement for IEM for larger scale RED

According to Tufa *et al.* [13], ion exchange membranes (IEMs) are the core components of reverse electrodialysis (RED) systems and play a decisive role in determining power density, efficiency, and overall system performance. Optimal IEMs for RED applications should exhibit high permselectivity (above 95%), low area resistance (below 1 $\Omega{\cdot}cm^2$), and robust mechanical and chemical stability to ensure operational lifetimes of at least five years. Economic assessments indicate that membrane costs below approximately 4.3 €/m^2 are required for the financial viability of large-scale seawater RED plants [13].

Achieving low resistance and high ionic conductivity is essential, while maintaining high permselectivity is equally important to ensure efficient counter-ion transport and stable open-circuit voltage (OCV). These performance indicators depend on intrinsic electrochemical parameters such as the ion exchange capacity (IEC) and fixed charge density (FCD). Because both properties are closely linked to the polymer's molecular structure, a trade-off exists between ionic conductivity and selectivity. Additionally, minimizing water transfer across IEMs is necessary to prevent parasitic fluxes and osmotic losses [13].

Most IEMs used in electrochemical energy systems, such as fuel cells and water electrolyzers, are perfluorinated membranes optimized for high conductivity and chemical stability in acidic environments. In contrast, RED membranes operate under neutral conditions (pH $\approx$ 7), where Na^+ and Cl^- are the main charge carriers and divalent ions (e.g., Mg^{2+}, Ca^{2+}, SO_4^{2-}) can also affect transport. Consequently, RED-specific IEMs are generally thin, often unreinforced, and fabricated from hydrocarbon-based polymers to balance selectivity, mechanical robustness, and cost [13].

Despite recent progress driven by EU-funded projects such as *REAPower* and *RED-Heat-to-Power*, most experimental studies still rely on commercial IEMs originally developed for electrodialysis rather than membranes specifically tailored for RED operation [13].

3.3.4 RED at reduced Scale: implications for membrane design

The membrane performance criteria outlined above are primarily derived from large-scale RED installations targeting centralized salinity-gradient energy recovery. In such systems, membrane cost, long-term durability, and hydraulic efficiency dominate the design space.

When RED is considered at reduced scale, however, the relative importance of these constraints shifts. In miniaturized configurations, the absolute membrane area is limited, stack compression requirements are relaxed, and economic cost per square meter becomes less critical. Instead, parameters such as achievable voltage per membrane pair, internal resistance at low current densities, and compatibility with compact energy management systems gain prominence.

In contrast, nanofluidic RED (nRED) studies focus on single nanopores or highly porous membranes in which surface-charge-driven ion transport dominates as described in detail in Chapter 4. These investigations emphasize power density per unit area and electrokinetic enhancement mechanisms rather than membrane cost or multi-year durability.

This shift in research focus reflects a change in operational scale. Whereas conventional RED systems are designed for centralized installations operating with high volumetric flow rates , in reduced-scale configurations, the absolute membrane area is limited, and stacking numerous membrane pairs may not be practical. Under these constraints, maximizing open-circuit voltage per membrane pair and minimizing internal ionic resistance become increasingly important relative to cost per square meter.

Furthermore, when RED is considered for autonomous or distributed energy applications, system-level requirements differ from those of industrial-scale plants. Self-powered sensing platforms typically operate in the μW–mW range and rely on integrated energy management circuits to regulate voltage and buffer harvested energy [9–11]. In this context, membrane design must account not only for permselectivity and resistance, but also for voltage compatibility with low-power power management units and stable operation under low-flow conditions.

These considerations suggest that membranes optimized for large-scale RED may not be inherently optimal for miniaturized energy harvesting systems. A re-evaluation of membrane thickness, fixed charge density, and transport mechanisms is therefore warranted when targeting reduced-scale RED architectures.

3.4 State of the art for polymer IEM for RED

3.4.1 Conventional Polymer IEM

Ion-exchange membranes (IEMs) play a central role in determining the performance of reverse electrodialysis (RED) systems. At present, however, membranes specifically engineered for RED are not commercially available, in contrast to electrodialysis (ED), for which dedicated products exist. Consequently, most studies have relied on commercially produced IEMs originally developed for ED, fuel cells, or other electromembrane technologies [105]. Several works have assessed the feasibility of RED using these membranes, taking into account not only their electrochemical behavior but also their cost.

Reported power densities vary widely in the literature: many authors normalize their results to the total membrane area ($\mathrm{W\,m^{-2}}$), while others report power per cell pair, which effectively doubles the numerical value. A comparison of the performance of commercial IEMs tested in RED is summarized in Table 3.2. Most of these studies were conducted at the laboratory scale using single RED stacks, although a few pilot-scale demonstrations have also been reported.

The RED performance of commercial IEMs is strongly influenced by their electrochemical characteristics, particularly IEC and AR. It is important to note, however, that values reported for the same commercial membrane can differ substantially among publications. This variability is often attributed to differences in (i) production batches, (ii) membrane storage and age, (iii) measurement protocols, and (iv) the pre-treatment procedures applied before testing [105].

Table 3.2: List of commercial CEMs and AEMs tested for RED and their power output. α is the permselectivity. [a] Values computed based on T_+, no experimental validation.

Membrane	**Type**	**Configuration**	**Salinity ratio (dil./conc.)**	α [%]	**Power** [$\mathbf{W/m^2}$]	**Ref.**
Fuji-CEM Type 1	CEM	Single	0.1 / 4 M NaCl	95	3.77	[108]
Neosepta CMX	CEM	Single	0.1 / 4 M NaCl	100	3.23	[108]
CMX / PECH B1	CEM/AEM	Stack (5)	0.017 / 0.513 M NaCl	99.0 / 86.5	1.27	[109]
FKS / FAS	CEM/AEM	Stack (5)	0.017 / 0.513 M NaCl	94.2 / 89.4	1.11	[109]
FKS/FAS (commercial)	CEM/AEM	Stack (5)	0.017 / 0.5 M NaCl	95.0 / 89.4	0.45	[110]
Fumasep® dialysis microporous membrane	AEM	Single	1/ 30^{-1} M $CuSO_4$	-	7e-3	[111]
DuPont Nafion 117	CEM	Single	0.5 / 0.01 M NaCl	–	4.2[a]	[112]

3.4.2 Fabrication strategies for newly designed IEMs for RED

Conventional ion-exchange membranes (IEMs), which were originally developed for general electromembrane applications, have shown limited performance when evaluated in RED systems. This shortcoming has motivated extensive research into new membrane materials specifically suited for harvesting salinity-gradient energy at larger scales [105]. To meet the operational requirements of RED, a new generation of IEMs with tailored morphological architectures has been developed (Fig. 3.8). These novel designs rely on advanced fabrication strategies to control the type, distribution, and accessibility of fixed ionic groups within the membrane matrix.

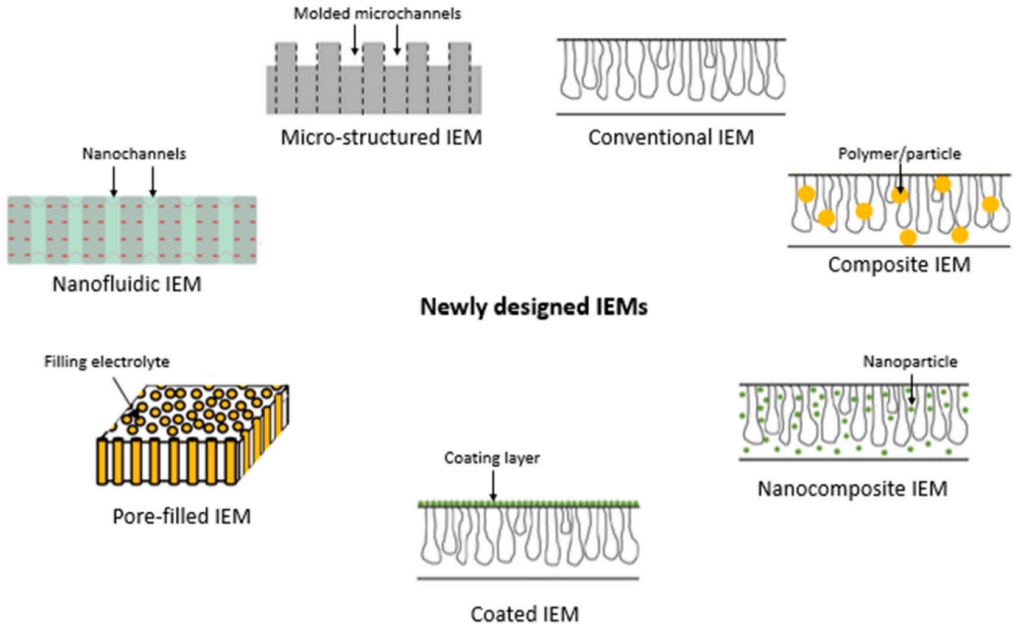


Figure 3.8: Different morphological structures of newly designed IEMs for RED. Reprinted from [105].

Chemical functionalisation is one of the most established strategies for improving the performance of polymer-based ion-exchange membranes (IEMs). Through reactions such as sulfonation, amination, or quaternisation, fixed ionic groups are introduced directly onto the polymer backbone, thereby enhancing ion-exchange capacity, increasing permselectivity, and reducing ionic transport resistance. These chemically treated IEMs include a wide range of sulfonated cation-exchange membranes, such as sulfonated poly(ether ether ketone) (SPEEK), sulfonated poly(phenylene sulfide

sulfone) (SPPSU), sulfonated poly(phenylene oxide) (SPPO), sulfonated poly(ether sulfone) (SPES), sulfonated polystyrene (SPS), and sulfonated poly(arylene ether sulfone) (SPAES).

Similarly, aminated anion-exchange membranes have been developed based on quaternised poly(epichlorohydrin)/polyacrylonitrile (PECH/PAN), poly(phenylene oxide) (PPO), poly(vinyl alcohol)–polyethylene blends (PVA–PE), and poly(arylene ether sulfone) (PAES). Because these modifications alter the intrinsic chemistry of the polymer matrix without relying on blending, grafting, pore filling, or composite structures, they form the class of conventional chemically functionalised IEMs described by Abidin [105]. These membranes constitute an important performance baseline for more advanced microstructured, grafted, composite, or nanostructured IEMs.

Thermal methods represent another approach to membrane optimisation and produce microstructured or carbonised IEMs through hot-pressing, casting into patterned moulds, or thermally induced crosslinking of precursor films. Such treatments reduce spacer shadow effects and improve hydrodynamics. Examples include microstructured Ralex membranes [113], microstructured Nafion and carbon membranes [56], and thermally stabilised poly(vinyl alcohol)/sulfosuccinic acid (PVA/SSA) composites [114].

Blending ion-conductive polymers with secondary polymers or inorganic nanophases enables the fabrication of homogeneous nanocomposites with enhanced conductivity and mechanical robustness. Typical additives include covalent organic frameworks (COFs), silica, metal oxides, fly ash, and carbon nanotubes (CNTs). Representative examples of such nanocomposite membranes are summarised in Table 3.3 and reported in Refs. [47, 115–121].

Finally, radiation- or UV-initiated graft copolymerisation within porous polyethylene (PE) or polypropylene (PP) substrates enables the fabrication of high-performance pore-filled membranes combining low area resistance with fast ion transport. This category includes KIER pore-filled cation- and anion-exchange membranes [122–124], PE-*g*-poly(2-acrylamido-2-methylpropane sulfonic acid) (PE-*g*-poly(AMPS)) and alkyltrimethylammonium chloride (ATAC)-based systems [124–126], polystyrene-grafted membranes [127, 128], and poly(ethylene-*co*-tetrafluoroethylene) (ETFE)-based grafted AEMs and CEMs [129]. Many of these membranes also feature surface patterning to enable spacer-free reverse electrodialysis (RED) operation.

Overall, these strategies provide a versatile toolbox for tailoring ion-exchange membranes to the specific requirements of RED. Recently developed membranes are summarised and grouped by fabrication method in Table 3.3.

Table 3.3: Experimentally measured RED performance of modified and nanocomposite ion-exchange membranes from recent studies, grouped by fabrication method following Abidin et al. [105]. Only membranes tested in physical RED cells or stacks are included.

Membrane	**Type**	**Config.**	**Salinity ratio**	α [%]	**Power [W/m^2]**	**Ref.**
Chemical treatment						
sPES-D (dense)	CEM	Single	0.1 / 4 M NaCl	95	3.92	[108]
sPES-P (porous)	CEM	Single	0.1 / 4 M NaCl	84	3.64	[108]
SPEEK65 / PECH B2	CEM/AEM	Stack (5)	0.017 / 0.513 M NaCl	89.1 / 87.2	1.28	[109]
SPEEK40 / PECH B2	CEM/AEM	Stack (5)	0.017 / 0.513 M NaCl	95.3 / 87.2	1.18	[109]
A-SPPO (AC-aligned)	CEM	Single	0.017 / 0.599 M NaCl	96.2	1.34	[49]
PECH B-1 (PECH/PAN)	AEM	Stack (5)	0.017 / 0.507 M NaCl	86.5	1.27	[45]
Thermal treatment						
Chevron-pressed cation-exchange membrane	CEM	Stack (5)	0.017 / 0.5 M NaCl	90-92	0.7	[113]
Microfluidic Nafion RED device	CEM	Microchannel	2000/1 mM KCl	—	0.755	[56]
PVA/SSA nanocomposite membrane	CEM	Stack (11)	0.017 / 0.5 M NaCl	90.4	1.02	[114]

Continued on next page

Membrane	Type	Config.	Salinity ratio	α [%]	Power [W/m^2]	Ref.
Blending / nanocomposite						
Nanocomposite SPPO/Fe_2O_3-SO_4^{2-}	CEM	Stack	0.017 / 0.5 M NaCl	87.7	1.3	[47]
SPPO/SiO_2-SO_3^-	CEM	stack	0.017 / 0.5 M NaCl	83.2	1.3	[115]
COF-interconnected nanofluidic membrane	CEM	Stack (paired with FAA-3)	0.01 / 0.5 M NaCl	—	0.45	[117]
Nanocomposite SPPO/Fe_2O_3 (CEM)	CEM	Stack (3)	0.01 / 0.5 M NaCl	85	0.4	[119]
Composite / nanocomposite PDDA/PVA (AEM)	CEM	stack (5)	0.017 / 0.5 M NaCl	87	0.5-0.6	[118]
Nanocomposite Nafion/SSWCNT (CEM)	CEM	Single	0.6/0.06 M NaCl	—	79e-3	[120]
Graft copolymerisation / pore-filled						
Thin pore-filled KIER-CEM1 / KIER-CEM2	CEM	Stack	0.017 / 0.58 M NaCl	97.8	2.4	[122]
Pore-filled PE-g-poly(AMPS–AMPSNa) (CEM)	CEM	Stack (12)	0.017 / 0.58 M NaCl	> 90	1.870	[125]

Continued on next page

Membrane	**Type**	**Config.**	**Salinity ratio**	α [%]	**Power [W/m^2]**	**Ref.**
Pore-filled Al_2O_3-g-poly(AMPSA) (CEM)	CEM	Pore-filled	0.017 / 0.51 M NaCl	99	17.3e-3	[130]
Pore-filled (PP-PE-PP)-g-poly(ATAC) (AEM)	AEM	Stack	0.017 /0 .507 M NaCl	95.9	1.8	[126]
Pore-filled PE-g-poly(VBTMA) (AEM)	AEM	Stack	0.017 / 0.5 M NaCl	93.8	1.5	[131]
Pore-filled PP-g-poly(AMPS) (AEM, amphoteric)	AEM	Stack	0.003 M NaCl+0.002 M Na_2SO_4/0.45 M NaCl+0.05M Na_2SO_4)	91	1	[132]
Pore-filled PE-g-poly(ATAC) (AEM)	AEM	Stack	0.017 / 0.507 M NaCl	95.5	1.5	[133]
Pore-filled PMP-g-polystyrene (AEM, second series)	AEM	Stack	0.1/5 M NaCl	—	2.1	[128]
PDDA/PVA (40:60)	AEM	Stack (5)	0.017 / 0.5 M NaCl	91.3	0.59	[110]

Chapter 4

Nanoporous IEM and nRED: physical interpretation

Inorganic porous ion-exchange membranes present also selective properties thank to surface charges inside the nano porous structure. They are emerging IEM and increasingly used in applications where high surface-to-volume ratio, enhanced ion selectivity, or fine control over ion transport is beneficial such as:

- Salinity Gradient Energy Harvesting, with scalability to micro- and nano-devices (e.g., μRED, nRED).
- Desalination & Ion Separation.
- Sensors and Lab-on-a-Chip Devices (e.g., ionic rectification, useful for sensing ionic concentrations, pH, or molecule detection).
- Biomedical Applications (e.g., mimic biological membranes, control of ion/-drug transport under electrical stimuli).

This chapter aims at explaining the physical origin the selective property of porous IEMs and their physical structure. First, at the nanoscale level, the origin of the charge inside the membrane when in contact with water in its structure is introduced. The implication regarding the creation of an electrical double layer inside the membrane structure and its specific ionic exclusion is presented. Finally, a state of the art regarding nanoporous membranes used in ionic selective purpose is presented with an emphasis regarding RED.

4.1 Electrical double layer

When a solid surface comes into contact with an electrolyte solution, an interfacial structure forms at the boundary, known as the electrical double layer

(EDL). This region plays a fundamental role in a wide range of electrochemical and physicochemical processes, including ion transport, surface interactions, and energy storage. The formation of the EDL begins with the generation of surface charges, which can arise from several mechanisms:

- Ionization of surface groups (e.g., acidic or basic functional groups on polymers or membranes),
- Ion adsorption from the electrolyte onto the surface,
- Or differences in electronic work function between materials and solutions.

To maintain electroneutrality, this surface charge attracts a compensating distribution of counterions (and sometimes co-ions) from the solution. These ions are not fixed but are distributed in a zone adjacent to the surface, creating a structure of alternating charge: a layer of fixed surface charges and a diffuse cloud of mobile ions, together forming the EDL.

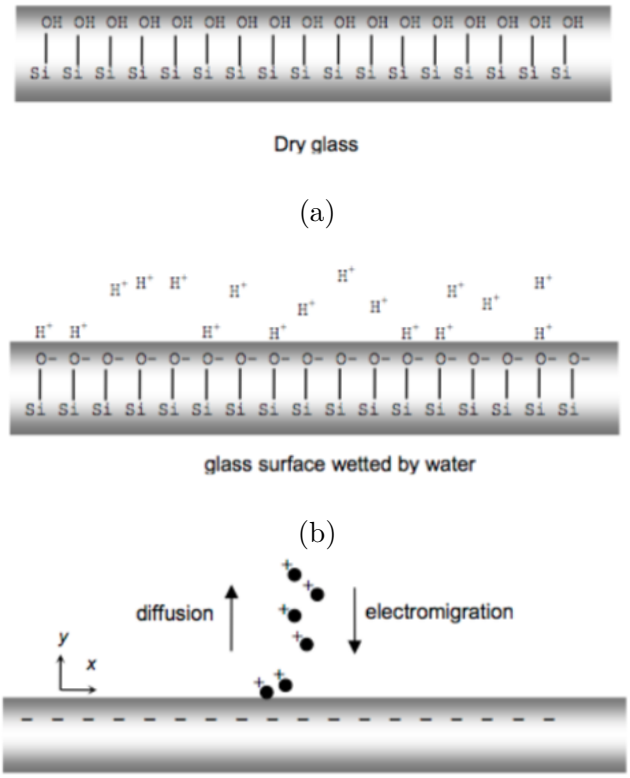


Figure 4.1: Surface ionization between silanol groups and water. (b) Dissociation of silanol groups in the above. (c) Formation of an electrical double layer by equilibrium between electromigration and diffusion. Reproduced from [134].

4.1.1 Planar description

Over the years, several theoretical models have been developed to describe the EDL, with 3 of most known presented in Figure 4.2:

- The Helmholtz model treats it as a simple capacitor with a single layer of counterions[135].
- The Gouy-Chapman model introduces a diffuse layer where ions follow a Boltzmann distribution[136, 137].
- The Stern model combines both concepts, distinguishing a compact layer of specifically adsorbed ions from a diffuse layer governed by electrostatic

interactions[138].

A key length scale in this context is the Debye length, which characterizes the thickness of the diffuse layer and depends on the ionic strength of the surrounding medium. One way to analyze each model is to try to solve the Poisson's equation, which relates the electric potential

$$\nabla(\varepsilon\nabla\varphi(\boldsymbol{r})) = -\rho(\boldsymbol{r}), \tag{4.1}$$

with $\rho(\boldsymbol{r})$ to the local charge density at point (r) and ε the permittivity of the medium. If the permittivity is assumed constant:

$$\nabla^2\varphi(\boldsymbol{r}) = -\frac{\rho(\boldsymbol{r})}{\varepsilon}, \tag{4.2}$$

Knowing the distribution of charge in each model, an expression for the potential can computed.

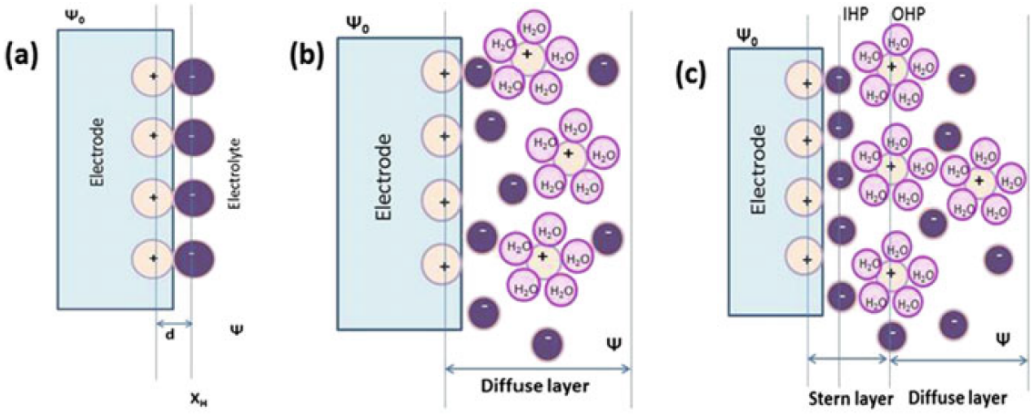


Figure 4.2: Theoretical models used to describe the electrical double layer: (a) a fixed layer of ions near the surface, known as the Helmholtz model; (b) a diffuse layer of ions extending into the solution, known as the Gouy–Chapman model; and (c) a combination of fixed and diffuse layers, known as the Stern model.

4.1.1.1 Hemlhotz model

The Hemlholtz model is the first model that has been proposed in 1853 [135]. It postulates that all counter-ions necessary to neutralize a charged surface are aligned in a single parallel layer at a certain distance from the membrane surface, which is

determined by the radius of the hydrated or unhydrated counterion. Similarly as a parallel plate capacitor, the potential decreases linearly away from the charge surface and a potential difference $\Delta\varphi$ can be calculated base on the surface charge density:

$$\Delta\varphi = \frac{4\pi d}{\varepsilon}\sigma, \tag{4.3}$$

where σ the surface charge density and d the thickness of the double layer (e.i. the thickness of the capacitor). However, the Hemlholtz model is far too simple. For example, it neglects the thermal motion of the solution. Louis Georges Gouy in 1910 and David Leonard Chapman in 1913 [136, 137] both observed that the capacitance of the double layer was dependent on the applied voltage to the surface and the ionic concentration.

4.1.1.2 Gouy-Chapman model

In the Gouy-Chapman model, a diffuse model is introduced for the double layer. The total number of counter-ions in this double layer is still equal to the fixed charge of the surface, but their distribution now results from the equilibrium between electro-migration and diffusion. In an electrolyte, the charge density comes from mobile ions. Assuming Boltzmann statistics for ions

$$c_i(\boldsymbol{r}) = c_i^{\infty}\exp\left(-z_i\frac{e\varphi(\boldsymbol{r})}{k_BT}\right), \tag{4.4}$$

with e is the elemental charge, k_B the Boltzmann's constant, T the absolute temperature of the solution, c_i^{∞} the concentration of the ionic species i in the bulk far from the surface and z_i the net charge of ions i. The charge density is expressed as

$$\rho(\boldsymbol{r}) = \sum_i z_i e c_i(\boldsymbol{r}) = \sum_i z_i e c_i^{\infty}\exp\left(-z_i\frac{e\varphi(\boldsymbol{r})}{k_BT}\right). \tag{4.5}$$

Injecting (4.5) into (4.1) gives

$$\nabla^2\varphi(\boldsymbol{r}) = -\frac{\rho(\boldsymbol{r})}{\varepsilon} = -\frac{e}{\varepsilon}\sum_i z_i c_i^{\infty}\exp\left(-z_i\frac{e\varphi(\boldsymbol{r})}{k_BT}\right). \tag{4.6}$$

This is the nonlinear 3D the Poisson-Boltzmann (PB) equation equation, which usually requires numerical methods to solve in complex geometries. A dimensionless form of the potential in (4.6) can be written with

$$\Psi = \frac{e\varphi}{k_BT}, \tag{4.7}$$

which gives

$$\nabla^2\Psi(\boldsymbol{r}) = -\sum_i \frac{z_i c_i^\infty}{\sum_j z_j^2 c_j^\infty}\kappa^2 \exp\left(-z_i\Psi(\boldsymbol{r})\right), \tag{4.8}$$

with

$$\frac{1}{\kappa} = \lambda_D = \sqrt{\frac{\varepsilon k_B T}{\sum_i z_i e c_i^\infty}} \tag{4.9}$$

which is known as the Debye length λ_D. It represents the scale of the length required for a group of ions to screen the effect of a charge carrier (e.g., a charge surface) or equivalently the scale of how far charge carrier's net electrostatic effect persists in electrolytes solution. For a binary monovalent electrolyte, if electroneutrality is assumed in the bulk $c_+^\infty = c_-^\infty = c^\infty$, at $c^\infty = 1$ mM, with $\varepsilon_{\text{water}} \simeq 78\varepsilon_0$, $\lambda_D \simeq 13$ nm.

For a binary monovalent electrolyte with the assumption of electroneutral bulk, (4.5) becomes

$$\rho(\boldsymbol{r}) = ec^\infty\left(\exp\left(-\Psi(\boldsymbol{r})\right) - \exp\left(\Psi(\boldsymbol{r})\right)\right), \tag{4.10}$$

and (4.8) becomes

$$\nabla^2\Psi(\boldsymbol{r}) = -\kappa^2 \sinh\left(\Psi(\boldsymbol{r})\right), \tag{4.11}$$

If the geometry of the interface is such that the radius of curvature of the solid/liquid interface is significantly larger than the thickness of the Debye layer the gradients are mostly oriented in a constant direction x normal to the interface:

$$\frac{d^2\Psi(x)}{dx^2} = -\kappa^2 \sinh\left(\Psi(x)\right), \tag{4.12}$$

In dilute electrolyte solutions and weak surface charges, where the electric potential is low compared to thermal energy (Debye–Hückel regime),

$$\left|\frac{z_i e\varphi}{k_B T}\right| \ll 1, \tag{4.13}$$

and (4.12) can be linearised as

$$\frac{d^2\Psi(x)}{dx^2} = -\kappa^2\Psi(x), \tag{4.14}$$

Solving (4.14),

$$\Psi(x) = \Psi_0 e^{-x/\lambda_D}, \tag{4.15}$$

with the boundary conditions that $\Psi(x) \underbrace{=}_{x\to\infty} 0$ (bulk potential) and $\Psi(0) = \Psi_0$. (solid/liquid interface). In the dimension form,

$$\varphi(x) = \zeta e^{-x/\lambda_D}, \tag{4.16}$$

with ζ is the "zeta"-potential of the liquid/solid interface ($\zeta \simeq -0.1$V for water on glass). The relation between the zeta-potential and the surface charge density can be found using the Gauss law. At a charged interface, Gauss law gives

$$\frac{d\varphi}{dx}|_{x=0^+} = -\frac{\sigma}{\varepsilon} \rightarrow \frac{d\Psi}{dx}|_{x=0^+} = -\frac{-e\sigma}{\varepsilon k_B T}. \tag{4.17}$$

Multiplying both side of (4.12) by $\frac{d\Psi}{dx}$ and integrating once gives

$$\left(\frac{d\Psi(x)}{dx}\right)^2 = 2\kappa^2 \left[\cosh\left(\Psi(x)\right) - 1\right], \tag{4.18}$$

and evaluating at $x = 0$,

$$\sigma_{planar,1:1} = \sqrt{8\varepsilon k_B T c^\infty} \sinh\left(\frac{e\zeta}{k_B T}\right), \tag{4.19}$$

which is the relation between the surface charge density and the zeta potential in a monovalent electrolyte for a planar surface. In dilute electrolyte solutions and weak surface charges, where the electric potential is low compared to thermal energy,

$$\sigma_{planar,1:1,l} \simeq \frac{\varepsilon\zeta}{\lambda_D}. \tag{4.20}$$

which is the relation between the surface charge density and a low zeta potential in a monovalent electrolyte for a planar surface (Debye–Hückel regime).

4.1.1.3 Stern model

Finally, there exists another model for the double charge layer which is the mostly used one. In the the Gouy-Chapman model, ions are considered as punctual charges and according to the Poisson equation, they can be as unrealistically close as possible to the charge surface, especially at large ion concentrations or large applied electrode potentials. This model leads to the prediction of enormous double-layer capacitances that cannot be observed experimentally. Thus Otto Stern suggested a combination of the Helmholtz model with the Gouy-Chapman model [138]. In Stern's model, some ions adhere to the surface as suggested by Helmholtz, constituting an internal Stern layer, while some ions form a Gouy-Chapman diffuse layer. Consequently, as shown in Figure 4.3, the variation of the potential decreases linearly close to the surface as in a plane capacitor, until it reaches the "zeta"-potential and then decreases exponentially following eq. (4.16). In this case, ζ

refers to the potential at the shear plane, where liquid begins to flow relative to the surface (i.e., hydrodynamic slip plane). Thus, in this model, Ψ_0 and $\Psi_d(=\zeta)$ are used to indicate the potential at $x = 0$ and $x = d$ from the solid-liquid interface, where d is the thickness of the Stern layer.

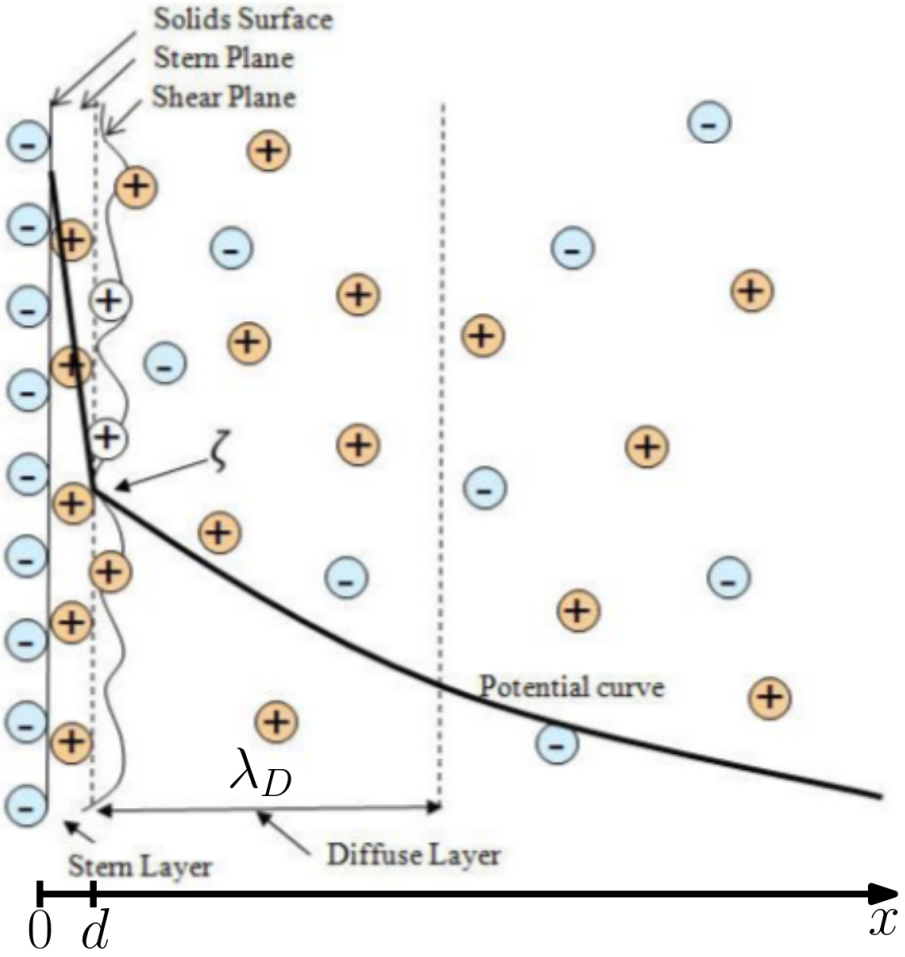


Figure 4.3: Variation of the electric potential in the double electric charged layer, based on the Gouy-Chapman-Stern model. Taken from [139].

4.1.2 Influence of parameters

4.1.2.1 Surface charge density

In the expression (4.9), the surface charge density does not appear. The Debye

length is a representative length of the effect of the competition between electrostatic attraction and diffusion, and thus mainly depends on the ionic strength of the solution and does not depends on the surface charge density. However, the surface charge density still play an important roll because it dictates the number of ions near the surface (i.e. how much screening is required by the ions in the solution).

In the Debye-Hückel regime, (4.14) is a linear ODE so the shape of the solution is fixed by the equation. The boundary condition $\Psi(0) = \zeta$ fixes only the magnitude. Thus in the low potential regime, based on (4.20), the surface charge density only plays a role in the magnitude of the electric potential. When the surface charge density is larger, the potential increases and the assumption in (4.13) is no longer valid. Analysing (4.12), the differential equation is not linear and the shape of the function is dependant on the boundary condiiton $\Psi(0) = \zeta$. From (4.19), increasing the surface charge density increases the zeta-potential and impacts the shape of the electrical potential $\Psi(x)$ such that a higher σ induces the potential to rise more steeply near the wall but decays more slowly (longer "tail") compared to the linear case with a similar increase in σ. This is known as nonlinear compression or extension occurs depending on σ. Even though the decay isn't purely exponential anymore, the asymptotic decay length still is fixed by λ_D.

4.1.2.2 Temperature

The distribution of ions in the electrical double layer (EDL) is governed by the Boltzmann equation:

$$c_i(x) = c_i^{\infty} \exp\left(-\frac{z_i e \psi(x)}{k_B T}\right), \tag{4.21}$$

where $c_i(x)$ is the local ion concentration, c_i^{∞} is the bulk concentration, z_i is the ionic valency, e is the elementary charge, $\psi(x)$ is the electrostatic potential, k_B is the Boltzmann constant, and T is the temperature. As the temperature increases, the thermal energy $k_B T$ becomes larger, reducing the relative influence of the electrostatic energy term $z_i e \psi$. As a result, the exponential accumulation of counter-ions near a charged surface is weakened: ions become less localized, their distribution becomes more diffuse, and the electrostatic potential decays more gradually. Physically, higher thermal agitation tends to spread out the ions, counteracting the electrostatic attraction toward the charged surface.

4.1.2.3 pH

Many surfaces, especially in polymer membranes or oxides, carry acidic or basic functional groups that can gain or lose protons depending on the local pH and are

called amphoteric materials. Surface charge regulation is commonly described using surface complexation models such as the Constant Capacitance Model (CCM), the Diffuse Layer Model (DLM), or the Triple Layer Model (TLM) [140–142]. For oxide-based surfaces, a fundamental reaction is the protonation/deprotonation of surface hydroxyl groups. In this work, SiO_2 is the material of interest:

$$\mathrm{SiOH} \rightleftharpoons \mathrm{SiO^-} + \mathrm{H^+}, \qquad K_A = \frac{a_{\mathrm{H^+}} N_{\mathrm{SiO^-}}}{N_{\mathrm{SiOH}}}; \tag{4.22}$$

$$\mathrm{SiOH} + \mathrm{H^+} \rightleftharpoons \mathrm{SiOH_2^+}, \qquad K_B = \frac{N_{\mathrm{SiOH_2^+}}}{a_{\mathrm{H^+}} N_{\mathrm{SiOH}}}; \tag{4.23}$$

where

$$N_{Total} = N_{\mathrm{SiO^-}} + N_{\mathrm{SiOH_2^+}} + N_{\mathrm{SiOH}}. \tag{4.24}$$

N_{Total}, represents the total number of site densities of functional groups on the surface. $N\mathrm{SiO^-}$, $N\mathrm{SiOH_2^+}$ and $N\mathrm{SiOH}$ are, respectively, the surface site densities of $\mathrm{SiO^-}$, $\mathrm{SiOH_2^+}$ and SiOH in units of site nm^2. N_{Total}, represents the total number of site densities of functional groups on the surface.The chemical equilibrium constants, K_A and K_B are 2.510×10^{-8} (mol/L) and 1.258×10^{-2} (L/mol), respectively[143]. The activity of $\mathrm{H^+}$, $a_{\mathrm{H^+}}$, may be obtained via the product of its concentration in the activity coefficient, $\gamma_i[\mathrm{H^+}]$.

The surface charge density of silica, σ_s can be obtained using the following equation

$$\sigma_s = F(N_{\mathrm{SiOH_2^+}} - N_{\mathrm{SiO^-}}), \tag{4.25}$$

with F the Faraday constant. Using (4.22)-(4.24),

$$\sigma_s = -FN_{Total}\frac{K_A - K_B a_{\mathrm{H^+}}^2}{K_A + a_{\mathrm{H^+}} + K_B a_{\mathrm{H^+}}^2}. \tag{4.26}$$

At low pH, acidic groups tend to be protonated (neutral), and basic groups are positively charged. At high pH, acidic groups become negatively charged, and basic groups tend to be deprotonated (neutral). This leads to a pH-dependent surface charge density, typically described by titration curves or surface pK_a values and the notion of the point of zero charge PZC. The PZC is the value of the pH that leads to a net surface charge density $\sigma_s = 0$.

The surface charge regulates the electrostatic potential at the surface, ψ_0, and determines the shape of the EDL. In consequences, the structure and properties of the electrical double layer (EDL) are strongly influenced by the pH of the surrounding electrolyte, especially when the surface has ionizable groups (e.g., –COOH, –OH, $–NH_2$, $–SO_3H$). The key effect is that pH determines the degree of surface charge, which in turn shapes the EDL potential and ion distribution.

4.1.2.4 Ion valency (z_i)

Multivalent ions (e.g., Ca^{2+}, Al^{3+}) screen the surface charge more effectively than monovalent ions such as Na^+ or Cl^-. This is because the electrostatic attraction between the surface and counter-ions increases with the ion valency z_i. As a result, multivalent ions can lead to a more compact electrical double layer, with higher counter-ion density near the surface. However, in such cases, ion–ion correlation effects become significant, especially for divalent and trivalent ions. These effects can lead to phenomena that lie beyond classical mean-field theories like the Poisson–Boltzmann (PB) equation:

- Charge inversion: where the accumulated counter-ions overcompensate the surface charge, leading to an effective reversal of sign.
- Over-screening: where the local electric field changes sign multiple times, creating oscillatory potential profiles.

Such effects require more advanced theoretical models, such as those including ion correlations, density functional theory (DFT), or simulations (e.g., Monte Carlo, molecular dynamics).

4.1.3 Confined geometry

When transitioning from planar interfaces to nanoconfined environments, such as cylindrical nanopores, nanotubes, or narrow slits, the behavior of the electrical double layer (EDL) changes significantly due to both geometrical and physical constraints. The curvature introduced by confinement alters the spatial distribution of the electrostatic potential, requiring a shift from cartesian to cylindrical or spherical coordinate systems for accurate modeling. Moreover, when the pore size becomes comparable to or smaller than the Debye length, EDL overlap occurs, leading to a fully charged environment where coion exclusion and counter-ion enrichment dominate [99], as shown in Figure 4.4b.

In cylindrical coordinates (radial direction r), assuming radial symmetry and no angular/axial dependence, the linearized PB becomes:

$$\frac{1}{r}\frac{d}{dr}\left(r\frac{d\Psi}{dr}\right) = \kappa^2\Psi, \tag{4.27}$$

or more explicitly

$$\frac{d^2\Psi}{dr^2} + \frac{1}{r}\frac{d\Psi}{dr} = \kappa^2\Psi. \tag{4.28}$$

The solution is in terms of modified Bessel functions:

$$\Psi(r) = AI_0(\kappa r) + BK_0(\kappa r), \tag{4.29}$$

where I_0 and K_0 are the modified Bessel functions of the first and second kind, respectively. $I_0(\kappa r)$ grows exponentially with r and $K_0(\kappa r)$ decays exponentially with r. Constants A and B depend on boundary conditions. Considering a pore of radius a, the boundary are

$$\Psi(a) = \zeta, \tag{4.30}$$

$$\Psi(0) < \infty. \tag{4.31}$$

Since $K_0(r) \to \infty$ ar $r \to 0$, $B = 0$ to avoid divergence at $r = 0$. The solution is then

$$\Psi(r) = \zeta \frac{I_0(\kappa r)}{I_0(\kappa a)}. \tag{4.32}$$

The asymptoptique behvior of the Bessel function as follow:

$$I_0(x) \simeq \frac{e^x}{\sqrt{2\pi x}}, \quad \text{for } x \gg 1, \tag{4.33}$$

and

$$I_0(x) \simeq 1 + \frac{x^2}{4} + ... \quad \text{for } x \ll 1. \tag{4.34}$$

For $\kappa a \gg 1$ or $a \gg \lambda_D$(large pore radius or high ionic concentration),

- Close to the wall , $r \to a$, (4.32) behaves as

$$\Psi \simeq \zeta \frac{I_0(\kappa r}{I_0(\kappa a)} \simeq \zeta e^{\kappa(r-a)} \sqrt{\frac{a}{r}} \simeq \zeta e^{\kappa(r-a)} \tag{4.35}$$

  For large pore radius a, the potential decays exponentially close to the pore wall toward the center, similarly as in the planar case (4.16).

- Close to the center, $r \to 0$

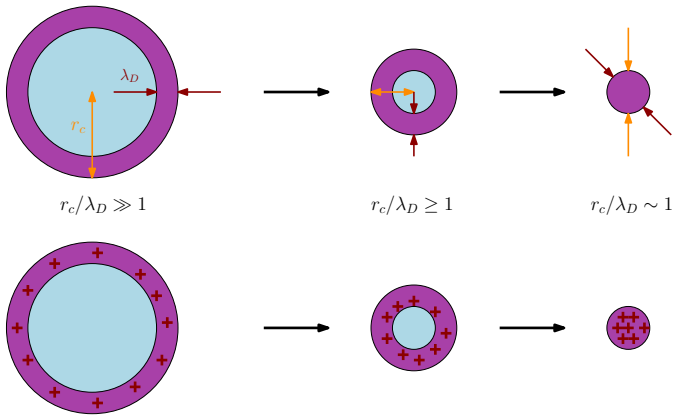
$$\Psi \simeq \zeta \frac{I_0(\kappa r)}{I_0(\kappa a)} \simeq \zeta \frac{1 + \frac{(\kappa r)^2}{4}}{I_0(\kappa a)}. \tag{4.36}$$

  For $\kappa a \gg 1$, the potential is flat, gently curved but highly suppressed in value by $I_0(\kappa a) \gg 1$, thus $\Psi(0) \simeq 0$.

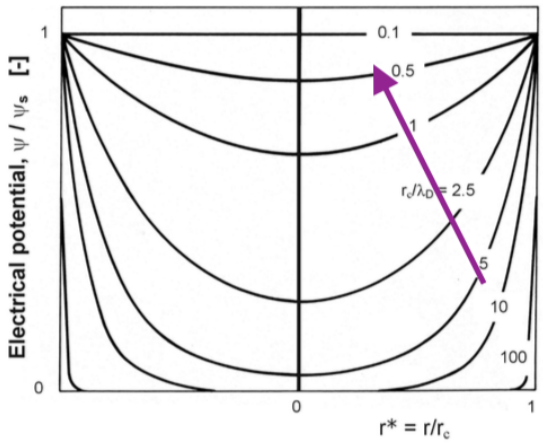
This is exactly what it is expected in large pores or high salt (small Debye length): strong screening, little overlap and potential localized near the wall. If $\kappa a \leq 1$ or $a \leq \lambda_D$, κr is also small and (4.32) behaves as

$$\Psi(r) = \zeta \frac{1 + \frac{(\kappa r)^2}{4}}{1 + \frac{(\kappa a)^2}{4}}, \tag{4.37}$$

which is almost flat for $\kappa a \ll 1$, i.e., very small radius or low ionic concentration. In this situation, the potential in the center is significant, almost equals to the one at the pore wall, meaning $\Psi(0) \simeq \zeta$.The electrical potential profile is shown in Figure 4.4b for different κa (or a/λ) ratio.



(a)



(b)

Figure 4.4: (a) Overlap of the EDL when $r_c \to \lambda_D$. (b) Cross-sectional distribution of electrical potential in a channel (normalized by the surface potential $\psi_s = \psi_0$) for different values of r_c/λ_D, radius over Debye length. Reproduced from [99].

Because of the nanoconfinement, EDLs from opposite walls merge, the entire pore is charged and there is no electroneutral bulk. There is depletion or enrichment throughout pore and the potential flattens or plateau. The transport behavior is surface governed, meaning the pore is selective to the ionic species because only counterions with respect to the surface charge fit energetically.

4.1.4 Breakdown of key assumptions with confinement

4.1.4.1 Dielectric constant in confined geometries

As confinement increases, PB equation is still valid under mean-field and continuum assumptions [144], but fails at extremely high confinement (<1 nm) due to ion correlations, finite ion size, dielectric breakdown [145, 146]. In standard electrostatics, we assume the dielectric permittivity ε of water is constant and equal to 78.5 (relative) at room temperature. However, this assumption breaks down near surfaces and under nanoconfinement for several reasons:

- Water structuring near interfaces: Water molecules near charged or hydrophobic surfaces form ordered layers. This restricts their ability to reorient in response to an electric field as they would normally do [147].
- Nanoconfinement and finite space: In nanopores (<10 nm), water is not bulk-like. The entire dielectric environment is altered due to restricted volume and interactions with both walls [148].
- High electric fields: Strong surface charges can saturate water polarization, further reducing the effective dielectric constant.

These reasons explain the reduction of local permittivity close to the surface. Experimental evidence with atomic force microscopy (AFM) [149], Surface Force Apparatus (SFA) [150] and X-ray reflectivity show layers of water near interfaces with reduced dielectric response. Molecular dynamics simulations confirm that water near hydrophilic/hydrophobic or charged surfaces has reduced ε over 0.2–1 nm. (as low as 2–10) [151–154].

In Poisson's equation (4.1), if the permittivity is spatially variable,

$$\varepsilon\nabla^2\varphi + (\nabla\varepsilon)\nabla\phi = -\rho. \tag{4.38}$$

This introduces a dielectric gradient term, which couples spatial changes in permittivity to the electrostatic potential. It is possible to study numerically these dielectric shifts mentioned in [151–154] and analyse their impact on the potential by introducing model for the permittivity such as

$$\varepsilon(r) = \begin{cases} \varepsilon_{\text{low}}, & \text{for } r \leq a - \delta \\ \varepsilon_{\text{bulk}}, & \text{for } r > a - \delta \end{cases} \tag{4.39}$$

with δ is the thickness of the low-permittivity interfacial layer near the solid surface and a the pore radius. This is a step function model often used in modified PB because it captures the main effects of dielectric shift. A dielectric shift, with lower permittivity near the wall, induces a stronger local electric field for the same surface charge. It also reduces the screening effect, thus the decay is shorter and λ_D is shorter [151, 154].

In conclusion, nanoconfinement leads to a break down of the classical PB model. Many models have been proposed as modified PB to include for the finite size of the ions [145, 146], interaction between ions [155]. It is possible to improve the description of ionic interaction with the surface in a nanoconfined environment using modified PB, Density Functional Theory (DFT), or Molecular Dynamics (MD). These eventually show modifications of the electrical double thickness, dielectric constant and ionic distribution closer to what observed.

4.1.4.2 Ionic mobility

In nanoconfined systems, the assumption of bulk ionic mobility is no longer valid. When pore sizes approach the Debye length, electrical double layers (EDLs) overlap and lead to asymmetric ion transport, where counter-ions dominate and coions are strongly excluded. Moreover, steric effects arise because hydrated ions occupy a finite volume, which restricts their ability to approach charged surfaces and alters their diffusion compared to the bulk. These excluded-volume effects are commonly incorporated through modified Poisson–Nernst–Planck (PNP) or lattice-gas models [156, 157]. In addition, near charged walls the viscosity of interfacial water is higher, lowering the local diffusion coefficient, as confirmed by molecular dynamics (MD) simulations [151, 158]. A related parameter often used to characterize the importance of surface conduction relative to bulk conduction is the Dukhin number (Du), which increases strongly when EDLs overlap, indicating that transport becomes dominated by counter-ion motion in the interfacial region [159, 160]. Together, these effects demonstrate that ionic mobilities in nanopores are not constant but depend on confinement, EDL overlap, and surface interactions.

4.1.4.3 Surface charge density

In the planar surface model for the electrical double layer, the equation for the surface charge density (4.26) suggests that its value is determined by the pH of the solution only. However, in confined spaces, the surface charge has been shown to also depends on the ionic concentration of the solution, the dimension and the shape of the confined geometry [143, 161–170]. More specically for silica material, many of the studies use eqs. (4.22), (4.23) and (4.26) to determine the surface charge density. Because of the EDL overlap, the selective exclusion appears in confined space, which

impacts the adsorption desorption of ionic species, included H^+ and OH^-. Thus, the ionic concentration impacts the surface charge density as it directly impacts the EDL overlap. Ma et al.[171] examined electroosmotic flow in nanochannels and showed that electric double layer (EDL) overlap strongly influences zeta potential, surface proton concentration, and conductivity, particularly in thin channels under low salt and pH conditions.

Interaction between the amphoteric group also becomes more important when the scale of the geometry goes down to the nanometer range. From a theoretical standpoint, Atalay et al.[170] explored the surface charge characteristics of two charged silica structures, namely, a nanoparticle positioned at a certain distance from a silica plate. They demonstrated that due to curvature effects, the silica plate exhibited a lower surface charge than the nanoparticle. Along similar lines, Sen and Barisik [169] investigated nanochannel surface charge under varying electrolyte conditions and reported that both curvature and axial EDL overlap between the reservoir and the channel significantly affected the surface charge density.

Ozcelik and Barisik [165] further examined the impact of surface patterning on charge distribution. They showed that both local and average surface charge densities are controlled by EDL overlap and surface curvature. Specifically, reducing the diameter of surface roughness enhanced EDL overlap in the patterned pores, leading to a reduced surface charge in the pits compared to the tips. The curvature at the tips, however, increased the local surface charge. Introducing an overlap ratio parameter (λ/DR), where λ represents the EDL thickness and DR the roughness diameter, they found that when λ/DR exceeded 0.2, the average surface charge on rough patterned surfaces became lower than that of flat ones.

In a related study, the surface charge density of nanoparticles with periodically repeating concave and convex features was evaluated[166]. The results revealed that roughness greater 2 nm than caused decreases in charge for concave regions and increases for convex ones. Moreover, the average surface charge density of such rough surfaces approached that of a smooth nanoparticle. They introduced a scaling parameter, defined as $(DR/\lambda) \times (DR/D_p)$, with D_p denoting the roughness periodicity, to describe how EDL overlap and curvature collectively influence the average surface charge.

In a more recent study, Ezat Keshavarzi et. al.[143] analyzed numerically the surface charge regulation on the concave wall of a spherical silica pore. This study is very important for the thesis as it represents the closest situation to the nanopore. The electrolyte solution was a mixture of KCl and either HCl or KOH for the acidic or basic solution respectively. Three different ionic concentration, 0.001M, 0.05M, 0.1M 0.5M were analysed in different pH conditions. Their main results for the surface charge density with respect to the pore size, for different ionic concentrations are shown in Figure 4.5 for a basic solution and in Figure 4.6 for a

acidic solution.

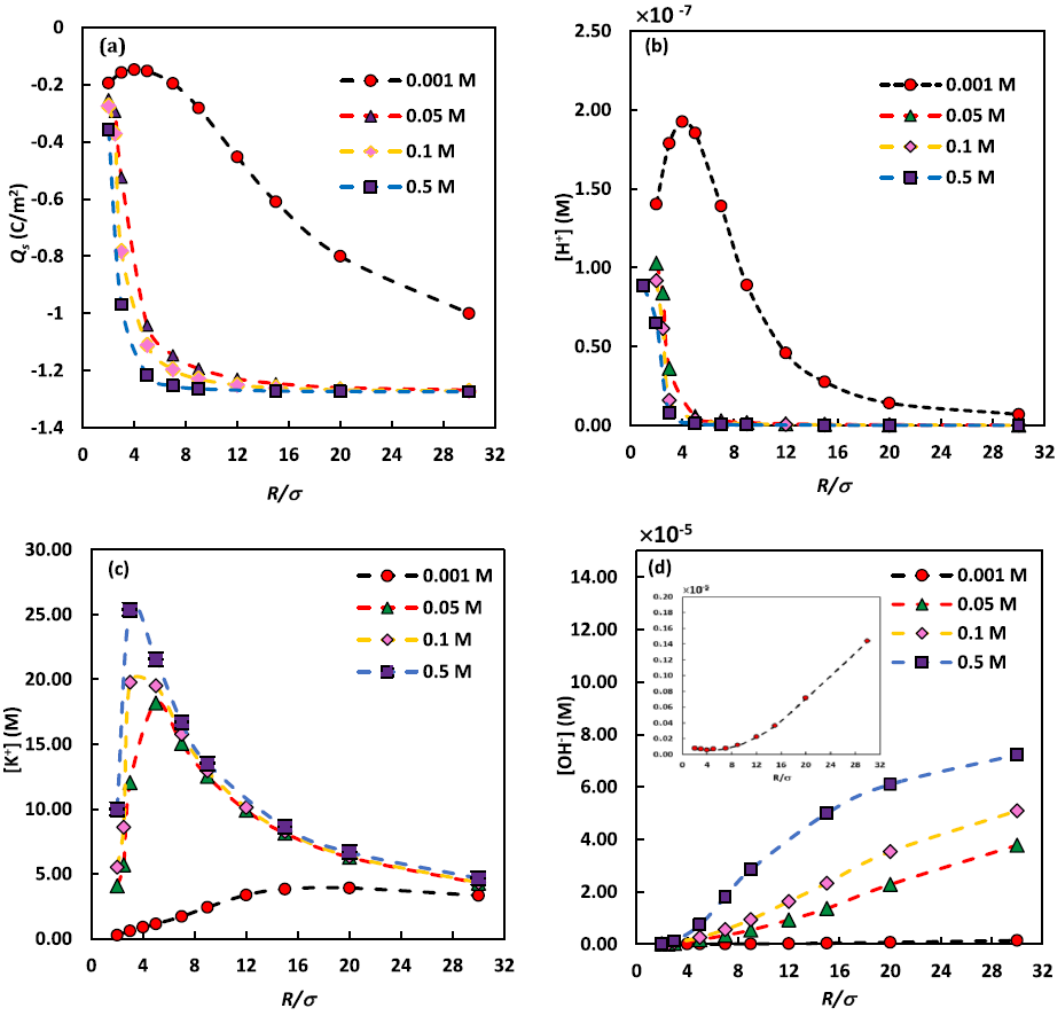


Figure 4.5: (a) Surface charge density as a function of pore size R and the average concentrations of (b) H+, (c) K^+, and (d) OH^- for different KCl concentrations, including 0.001, 0.05, 0.1, and 0.5 M and pH=10. The inset plot in this figure enlarges the behavior of OH^- versus pore size. $\sigma = 0.3$ nm. Taken from [143].

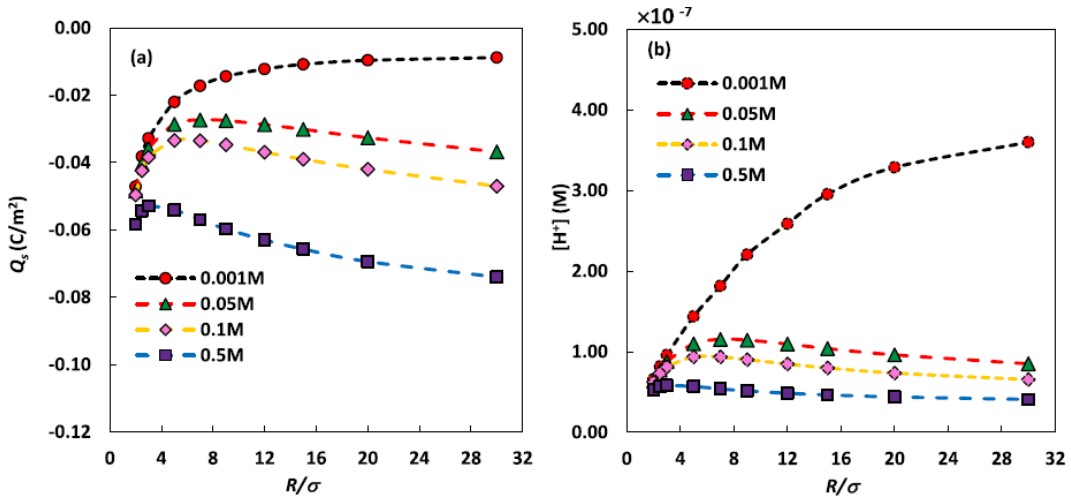


Figure 4.6: (a) Surface charge density and (b) average concentrations of H^+ as a function of pore size R for different concentrations of KCl equal to 0.001, 0.05, 0.1, and 0.5 M and pH = 6.5. $\sigma = 0.3nm$. Taken from [143].

In that work, the electrolyte confined in the silica nanopore is modeled using the modified fundamental measure theory (MFMT) in the framework of the restricted primitive model (RPM), combined with a surface reaction model (SRM). In this approach, ions are represented as charged hard spheres of equal size (σ = 0.3 nm), and the free energy of the system includes contributions from ideal entropy, Coulomb interactions, hard-sphere excluded volume, and electrostatic correlations. The density distributions of the ions inside the pore are obtained self-consistently by solving the Euler–Lagrange equations, while the surface chemistry is accounted for through the protonation and deprotonation equilibria of silanol groups on the silica wall. This coupling ensures that the surface charge density is not imposed but instead emerges from the interplay between electrostatics, steric effects, and chemical equilibrium.

Within this framework, both K^+ and H^+ act as counterions to the negatively charged silica surface. Since they are modeled as equal-size monovalent spheres, their steric exclusion and Coulomb attraction to the wall are identical. The crucial difference arises from their roles: H^+ directly participates in the surface equilibrium of silanol groups (eq. (4.22)), while K^+ merely screens the negative charge electrostatically. Consequently, the competition between these two ions is determined mainly by their relative abundance in the bulk. At low salt concentrations, bulk $[K^+]$ is small, so H^+ dominates adsorption and the surface charge density essentially follows the pH through silanol regulation. At high salt concentrations, the overwhelming excess of K^+ makes it the dominant counterion, displacing H^+ from the pore and increasing the absolute surface charge density. This explains the behavior

in Fig. 4.5, where surface charge grows in magnitude with salt concentration as K^+ crowds the pore wall.

The dependence on pore size adds another layer of complexity. In basic solutions (pH $\approx$ 10), bulk [H^+] is extremely low, but confinement alters its local density inside the pore. For moderately small pores, strong confinement enhances counterion selectivity, pulling H^+ and K^+ toward the wall. Even though H^+ is rare in the bulk, its local concentration inside the pore increases relative to bulk due to confinement. However, when the pore radius is reduced further into the ultra-small regime, steric crowding and the sheer abundance of K^+ cause H^+ to be displaced again. At the same time, a small but non-negligible amount of OH^-, normally excluded as a coion, can penetrate the pore due to correlation effects and weakened selectivity at extreme confinement. This competition results in a non-monotonic dependence of H^+ concentration on pore size: it rises with moderate confinement and then falls again when the pore becomes too small. The surface charge density follows this trend, decreasing initially as more H^+ is present (favoring reprotonation), then increasing again as H^+ is suppressed and OH^- appears, leading to stronger deprotonation. At very low salt concentration (1 mM), this explains why $|Q_s|$ first decreases and then rises as pore size shrinks in basic solutions (Fig. 4.5).

In acidic solutions (pH $\approx$ 6.5), the situation differs because bulk [H^+] is relatively high. Here, both H^+ and K^+ act as counterions, while Cl^- serves as the co-ion. In this case, H^+ competes more effectively with K^+ for adsorption. The resulting surface charge density shows a maximum as a function of pore radius (Fig. 4.6) for moderate salt concentration (0.05 M, 0.1 M and 0.5 M). For small pores, confinement enhances H^+ adsorption, shifting the surface equilibrium toward reprotonation and lowering the absolute surface charge. As the pore radius increases, H^+ concentration inside the pore initially rises, reaching an optimum where adsorption is strongest. Beyond this size, confinement weakens, co-ions such as Cl^- can enter more easily, and the relative density of H^+ decreases, shifting the equilibrium toward deprotonation and lowering the surface charge. At very low salt concentrations (0.001 M KCl), the behavior is different: [H^+] continues to increase monotonically with pore size, and thus $|Q_s|$ decreases steadily with no maximum observed.

In summary, the model captures how surface charge regulation emerges from the competition between K^+ and H^+ under different conditions. At low salt, H^+ controls the regulation through direct participation in silanol chemistry, while at high salt, K^+ dominates due to its bulk abundance. In basic solutions, the confinement effect produces a non-monotonic trend: H^+ increases at intermediate pore sizes but is suppressed in ultra-small pores, leading to a U-shaped dependence of surface charge. In acidic solutions, H^+ is more abundant and competes strongly with K^+, giving rise to a peak in surface charge as a function of pore size, except at very

low salt where [H^+] rises continuously. These results highlight the subtle balance between ion competition, confinement, and surface chemistry in determining charge regulation within silica nanopores.

It should be emphasized, however, that in this model all ions were treated as equal-size hard spheres ($\sigma = 0.3$ nm). In reality, hydrated ion sizes differ significantly: H^+ (often existing as hydronium or via Grotthuss transport) is effectively smaller, while K^+, Cl^-, and OH^- have larger hydrated radii. If such size differences were included, the predicted adsorption and surface charge regulation would likely change. Smaller H^+ ions could approach the silica surface more closely and occupy regions inaccessible to larger ions, thereby enhancing their influence on protonation–deprotonation equilibria. Conversely, bulkier ions such as K^+ or Cl^- would experience stronger steric exclusion in confined pores, reducing their ability to compete with H^+. As a result, incorporating realistic ion sizes would likely shift the balance between chemical regulation and electrostatic screening, altering the shape of the $|Q_s|$ versus pore size curves and amplifying the asymmetry between acidic and basic regimes [172–174].

4.2 Inorganic porous IEM

A particularly important class of ion-exchange membranes consists of nanoporous/-nanostructured materials, which encompass a broad class of materials in which ion transport occurs through nanoscale charged domains or pores, typically ranging from sub-nanometer to tens of nanometers in size. Classical examples include track-etched polymer films, anodic alumina (AAO) and self-assembled block copolymer membranes. Beyond these, several other architectures also exhibit nanostructure-governed transport, such as mesoporous oxides, graphene oxide and other two-dimensional (2D) layered materials, metal–organic or covalent–organic framework (MOF/COF) membranes, and electrospun nanofiber networks. In all these systems, when the Debye length becomes comparable to the pore radius, electrical double layer (EDL) overlap leads to surface-charge-dominated conduction and enhanced ion selectivity.

In these systems, surface charge arises primarily from the adsorption of ions or the dissociation of surface functional groups on the pore walls. When an electrolyte solution fills the pores, the interaction between the fixed surface charge and mobile ions leads to the formation of overlapping electrical double layers (EDLs) within the confined geometry. Due to the small pore size relative to the Debye length, co-ions are effectively excluded from the pore interior, and counter-ions dominate the transport. This results in strong ion selectivity, similar to that observed in polymeric IEMs, but governed here by interfacial electrostatics within the pore space. Additionally, the combination of nanoconfinement, surface charge, and electrolyte

composition gives rise to distinct electrostatic phenomena such as Donnan exclusion, permselectivity, and modified ion mobility, which are central to the membrane's function in separation, energy conversion, and sensing applications.

4.2.1 Track-etched membranes (TEMs)

Track-etched membranes (TEMs) are precision porous films produced by irradiating thin polymer foils with energetic heavy ions and subsequently chemically etching the latent tracks. This technique allows for exceptional control over the pore size, geometry, and density, enabling the fabrication of membranes with well-defined transport and retention characteristics as seen in Figure 4.7 [175].

The formation of pores in track-etched membranes involves two main stages: irradiation and chemical etching. In the irradiation step, energetic ions traverse the polymer film, leaving behind narrow damage trails, so-called latent tracks, along their paths. Two irradiation methods are typically used. The first employs fission fragments from isotopes such as ^{235}U or ^{252}Cf, producing almost isotropic track distributions at relatively low cost. However, this approach is limited by the restricted penetration depth of fission fragments and by radioactive contamination of the foils. The second method utilizes heavy-ion beams from particle accelerators. This route offers superior control over the ion energy, angle of incidence, and fluence, allowing for uniform and parallel track arrays with tunable density (up to 10^9–10^{10} cm^{-2}). Moreover, it eliminates the issue of radioactivity and enables the use of thicker foils [175].

Following irradiation, the latent tracks are converted into open pores by selective chemical etching. The etching process is governed by two rates: the track etch rate V_T and the bulk etch rate V_B. The ratio V_T/V_B determines the resulting pore geometry, which may range from conical to cylindrical or funnel-like depending on the etching conditions. Alkali solutions are commonly used as etchants for polyethylene terephthalate (PET) and polycarbonate (PC). Factors influencing the etch rate include the chemical composition and temperature of the etchant, the type and energy of the bombarding ions, and post-irradiation treatments such as ultraviolet sensitization or solvent exposure. The addition of surfactants can further modify the pore morphology by controlling local dissolution and surface adsorption [175].

Polyethylene terephthalate (PET) and polycarbonate (PC) are the most widely used materials for track-etched membranes. PET offers good mechanical strength, chemical stability, and hydrophilicity, with a simple and reproducible etching process that yields pores from tens of nanometers to several micrometers. PC is more sensitive to irradiation, which allows the fabrication of extremely small pores (down to ∼10 nm) without the need for UV sensitization, though it has lower resistance to organic solvents. Other polymers, such as polypropylene (PP),

polyvinylidene fluoride (PVDF), and polyimides (PI), have also been investigated for specific chemical or thermal applications, although their processing is more complex and less economically viable [175].

The resulting membranes exhibit a highly uniform pore size distribution and a simple pore geometry that can be accurately modeled by classical transport equations such as Poiseuille or Knudsen flow. The pore diameter typically ranges from 10 nm to tens of micrometers, while the pore density can be varied between 1 and 10^{10} cm^{-2}. Their structure is commonly verified by scanning electron microscopy, gas and liquid permeability tests, and bubble-point measurements. These membranes are usually used as "screen filters," where retention is mainly determined by the relationship between pore size and particle size. Surface adsorption phenomena, however, can strongly influence their filtration performance, especially for proteins or charged solutes, giving them selective properties [175].

The surface properties of track-etched membranes can be further tailored by various modification techniques. Hydrophilization can be achieved by adsorption of polyvinylpyrrolidone or plasma oxidation, while hydrophobicity can be imparted by coating with silicone or paraffin oils. More advanced functionalization is possible through radiation-induced graft polymerization of monomers such as methacrylic acid or *N*-vinylpyrrolidone, introducing ionizable or stimuli-responsive groups that alter the electrochemical and wettability properties of the pores [175].

Track-etched membranes find applications in process and laboratory filtration, cell and tissue culture, and as templates for the synthesis of micro- and nanostructures such as metallic or polymeric nanowires. Their precisely defined pore geometry also makes them valuable model systems for studying transport of ions, molecules, and fluids through confined channels. Despite their higher production cost compared to phase-inversion polymer membranes, track-etched membranes remain indispensable wherever reproducibility, monodispersity, and geometric precision are required [175].

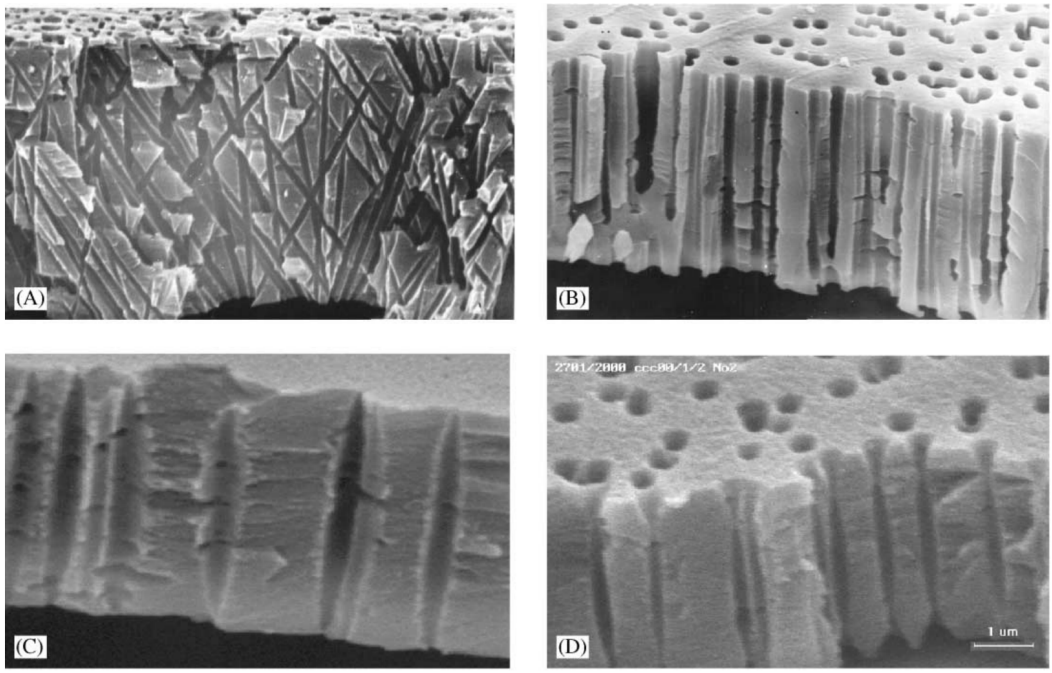


Figure 4.7: Examples of porous morphologies obtained in thin polymeric films through various irradiation and chemical etching techniques include: (A) a polycarbonate track-etched membrane (TM) exhibiting cylindrical, non-parallel pore channels; (B) a polypropylene TM featuring slightly conical pores that taper toward the center; (C) a polyethylene terephthalate TM with elongated, cigar-shaped pores; and (D) a polyethylene terephthalate TM displaying characteristic "bow-tie" pore geometries. Taken from [175].

4.2.2 Anodic Aluminum Oxide (AAO) membranes

Anodic aluminum oxide (AAO) is a self-organized porous alumina formed by electrochemical anodization of aluminum. Its highly ordered, vertically aligned nanopore arrays exhibit tunable pore diameter, interpore distance, wall thickness, and membrane thickness, enabling use as robust nanofluidic platforms, lithographic masks, and templates for one-dimensional nanostructures and sensor architectures as seen in Figure 4.8. Porous AAO is distinguished from compact "barrier" alumina by its open, hexagonally arranged cells terminating in a thin barrier layer at the metal/oxide interface [73].

The pore geometry in AAO is set by the anodization conditions: electrolyte (commonly sulfuric, oxalic, or phosphoric acids), voltage waveform and magnitude, bath temperature, time, and aluminum purity. Interpore distance grows approxi-

mately proportionally with the applied voltage, and larger voltages generally yield larger pores and cell sizes. Conventional operation uses direct-current anodization (DCA) under mild anodization (MA) at low temperatures (about -5 to $15\,^{\circ}\mathrm{C}$) to limit Joule heating and preserve order. For higher growth rates, hard anodization (HA) employs elevated fields and currents, often increasing oxide growth by an order of magnitude versus MA while maintaining long-range order when carefully cooled and controlled. In addition to pure DC, pulse, reverse-pulse, and hybrid-pulse anodization (HPA) waveforms can tailor heat load and ion transport, widening the viable parameter window (including operation at $\sim$20–30 $^{\circ}\mathrm{C}$) and enabling use of lower-purity Al when needed.

The benchmark route to highly ordered AAO is the two-step anodization method. After mechanical polishing and electropolishing, a first anodization creates a disordered porous oxide. This oxide is chemically stripped, leaving a nanoconcave imprint in the Aluminium. A second anodization then replicates this pre-pattern to yield a hexagonally ordered pore array with narrow size distribution. While two-step anodization remains the mainstream for high-regularity templates, it entails long processing times and typically relies on high-purity Al. Alternatives include pre-texturing the Al (e.g., nanoimprint) to direct ordering in a single anodization, and depositing/sputtering Al on other substrates (Si, glass) to integrate AAO directly onto devices.

Post-treatments refine geometry and functionality. Pore widening (typically in phosphoric acid) increases pore diameter after growth with minimal loss of order, while barrier-layer thinning/opening enables through-pores for free-standing membranes or membrane-supported transport. Temporal modulation of voltage or electrolyte allows shape engineering, cylindrical, conical, bamboo-like or branched channels, useful for optical interference platforms, ionic rectification, or plasmonic/SERS(Surface-Enhanced Raman Scattering) substrates. Overall membrane thickness (and thus aspect ratio) is field/time controlled; long tubes with aspect ratios $\gg 100$ are routine with appropriate heat management.

Detachment to obtain freestanding, through-hole AAO membranes typically proceeds by selective dissolution of the underlying Al followed by barrier-layer removal; newer rapid schemes combine optimized potentiostatic steps with tailored electrochemical polishing to release multiple membranes efficiently. In practice, the choice among MA, HA, and pulse/hybrid waveforms is dictated by the desired trade-off between throughput, order, substrate constraints, and the final application (e.g., nanowire growth, optical interference sensors, humidity/gas capacitive sensors, and SERS platforms). With continued advances in waveform engineering and substrate integration, AAO remains a versatile, scalable route to precision nanoporous architectures for sensing and templated nanomanufacturing [73].

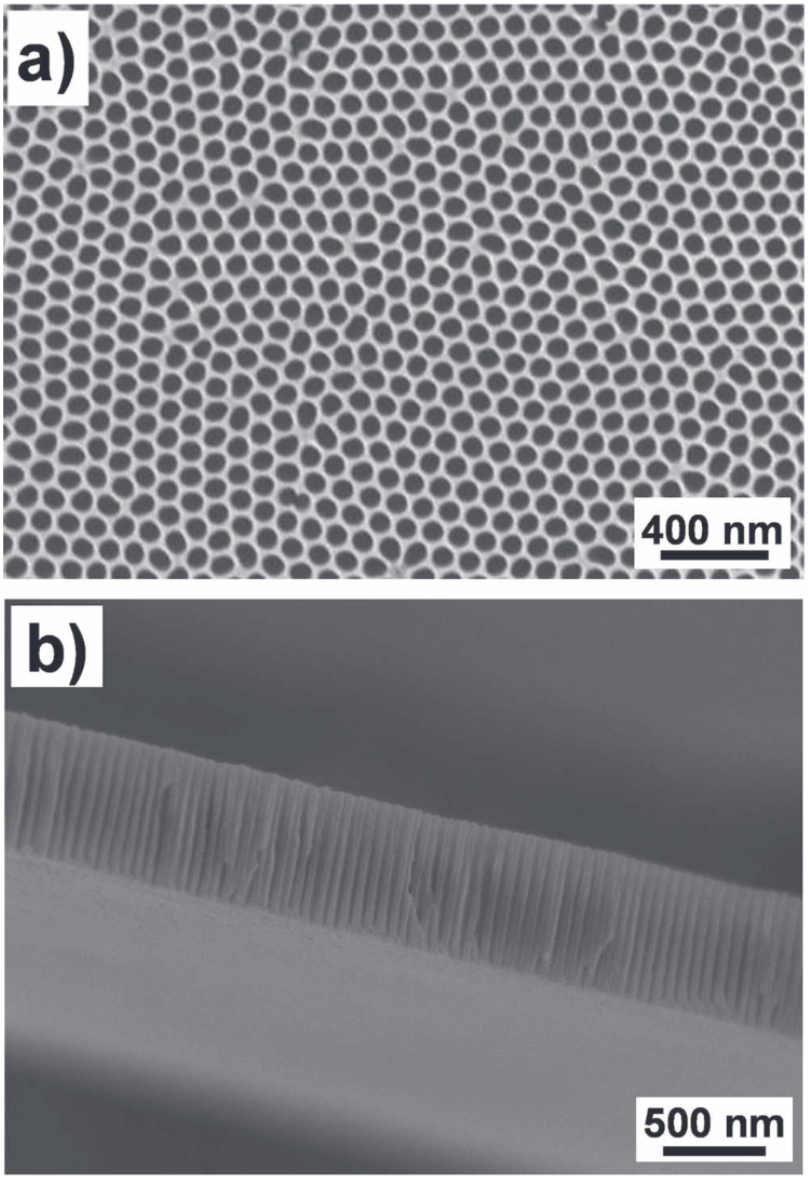


Figure 4.8: a) Scanning electron microscopy (SEM) image of an AAO membrane with pore size of ca. 80 nm and cell wall thickness of ca. 20 nm. b) SEM image showing the cross section of an AAO template with membrane thickness of 1 μm. Taken from [176].

4.2.3 Block Copolymer Membranes

Block copolymer (BCP) membranes exploit microphase separation to form isoporous nanochannels with narrow pore-size distributions (Figure 4.9) [177]. The mainstream fabrication route is SNIPS (self-assembly coupled with nonsolvent-induced phase separation): a BCP dope is cast on a support, brief solvent evaporation preorganizes the domains, and immersion in a nonsolvent bath freezes an isoporous top layer over a porous substructure. Pores are opened and tuned by selective swelling or by removing a sacrificial block; higher swelling temperatures generally enlarge pores by enhancing block solvation.

Beyond SNIPS, solution or machine casting can deposit a dense BCP layer that is subsequently nanoperforated by controlled swelling/etching. This route is compatible with roll-to-roll supports (e.g., nonwovens) and improves throughput. Ordering during film formation can be tightened using additives (such as metal-ion complexation with pyridyl blocks) that stabilize micelles in the casting solution. Dynamic-covalent BCPs offer another lever: reversible linkages establish order during casting and are later cleaved to generate pores with built-in functionality.

The isoporous "skin" typically consists of vertical cylindrical channels arranged in a short-range hexagonal lattice as seen in Figure 4.9; pore diameter is set by block ratio and molar mass and is further refined by solvent system, evaporation time, nonsolvent composition, and post-swelling. Reported diameters span from sub-5 nm up to a few hundred nanometers depending on chemistry and protocol. Triblock and ABC systems broaden accessible morphologies (cylinders, lamellae, gyroid) and improve mechanical robustness while allowing distinct chemistries at the pore wall.

Key knobs are block architecture and molecular weight, casting solvent selectivity, evaporation history, nonsolvent exchange conditions, additives/complexants, and optional thermal or chemical post-treatments. Structure and order are assessed by AFM/TEM/SEM and SAXS (Small-Angle X-ray Scattering), while permeance measurements combined with simple Poiseuille/Darcy analysis provide effective pore sizes. In practice, careful control of solution chemistry and thermal history yields reproducible, defect-lean membranes with tunable pore diameters and narrow distributions [177].

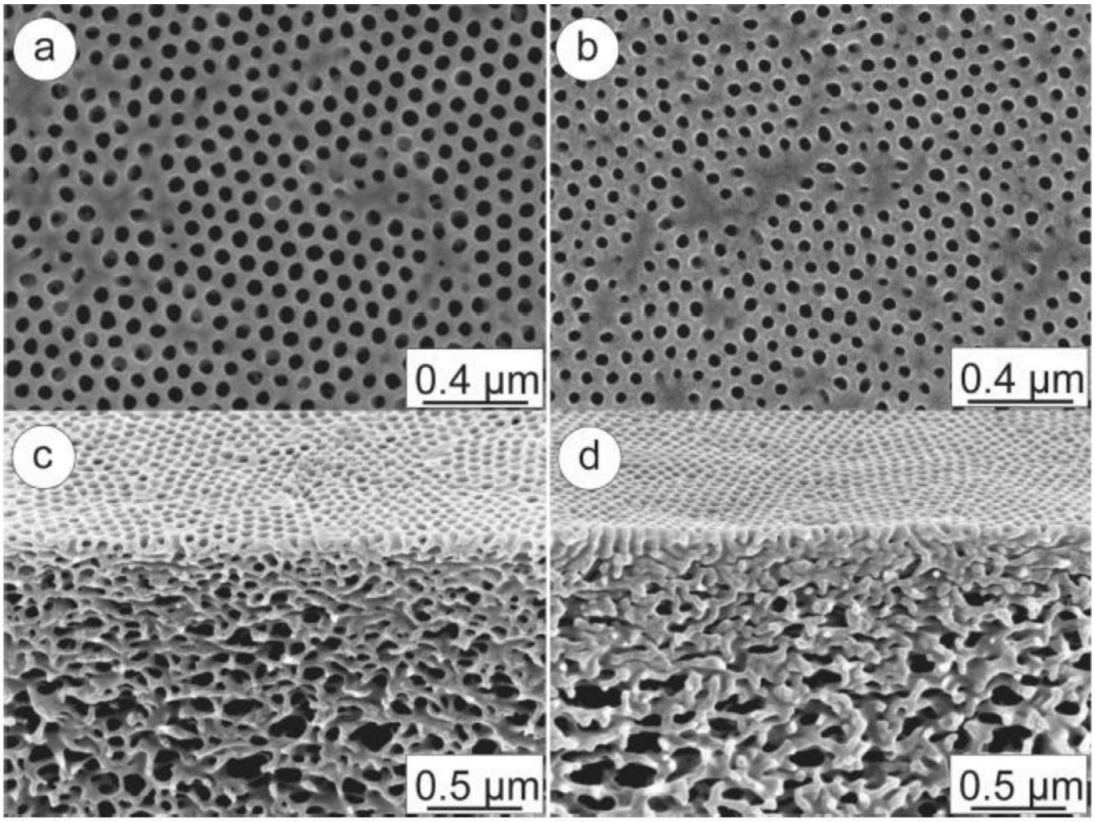


Figure 4.9: SEM images of block copolymer (BCP) membranes based on polystyrene-*b*-poly(4-vinylpyridine) (PS-*b*-P4VP). (a,b) Top-view images showing the isoporous membrane surface with short-range hexagonal ordering of cylindrical nanopores for (a) the bare PS-*b*-P4VP membrane and (b) the PS-*b*-P4VP membrane modified with polydopamine and pNIPAM-NH_2. (c,d) Cross-sectional images revealing the asymmetric membrane architecture, consisting of a thin isoporous skin layer with vertically oriented cylindrical nanochannels supported by a thicker, less-ordered porous substructure, for (c) the bare membrane and (d) the modified membrane. Adapted from [177].

4.2.4 Other nanostructured ion-exchange materials: structures and fabrication

Beyond block copolymers, AAO, and track-etched films, several classes of nanostructured materials have emerged as ion-exchange membranes (IEMs) by virtue of their intrinsic or engineered nanochannels and their compatibility with thin-film processing on porous supports [102, 178]. A first family comprises porous crystalline frameworks such as metal–organic frameworks (MOFs) and covalent organic

frameworks (COFs), whose Angström-to-nanometer pores are commensurate with hydrated ions. In composite MOF membranes, a thin selective layer is created on a mechanically robust substrate (Figure 4.10) using hydrothermal growth, secondary growth from seeds, contra-diffusion across the substrate, electrodeposition, chemical vapor deposition, or slurry-based routes such as vacuum filtration and doctor-blade casting. Hydrothermal methods are widely used but can yield micrometer-thick layers with reproducibility challenges, whereas electrodeposition and CVD enable thinner, more uniform skins at higher cost and complexity; by contrast, contra-diffusion, vacuum filtration, and doctor-blade casting offer scalable pathways to conformal MOF or MOF–polymer films with tunable thickness from the tens of nanometers to hundreds of micrometers. The resulting crystalline networks provide size- and charge-governed transport, although water stability and defect control remain central issues for long-term operation.

COF membranes extend this concept to fully organic lattices that integrate designed proton- or ion-hopping sites into sub-nanometer channels. Acid doping and oriented channel alignment have delivered large increases in anhydrous proton conductivity, and COFs have been integrated into membrane–electrode assemblies for proton-exchange fuel cells; nevertheless, sustaining crystallinity and linkage stability in hot, acidic or basic environments remains a key challenge that motivates continued chemistry refinement and film-thinning strategies.

A second family uses two-dimensional carbons and nanotubes to build ion pathways with minimal thickness and controllable interfacial chemistry. Laminar graphene oxide (GO) films form stacked galleries whose interlayer spacing and surface charge can be tuned during assembly, producing ultrathin selective skins that suppress fuel or ion crossover while maintaining ionic conduction; in parallel, networks of carbon nanotubes (CNTs) can be aligned or percolated to create long-range conduits for ion transport and to reinforce polymer matrices mechanically. These carbon-based layers are often deployed as top coatings or as intermediate scaffolds that guide the growth and adhesion of other selective phases, yielding composite IEMs that couple fast transport with improved robustness.

A third direction pursues composite and pore-filled membranes that engineer ion-transport channels at polymer–filler interfaces or within nanoconfined pores. In filler-integrated systems, nanofillers such as polyaniline nanofibers, CNTs, or sulfonated GO induce self-organization of ion-exchange groups along the interface, creating continuous ion-transport nanochannels that enhance conductivity while limiting swelling and improving mechanical stability. Pore-filled membranes infuse ion-conductive polyelectrolytes into a porous substrate and then immobilize and orient the functional groups; recent covalent-bonding–triggered filling establishes well-ordered channels that raise conductivity and durability by simultaneously restraining water uptake and preserving channel continuity. These strategies are

attractive because they decouple mechanical support from selective transport, enabling thin active zones without sacrificing dimensional stability.

Finally, artificial surface nanostructuring translates bioinspired channel geometries to the membrane–solution interface to reduce boundary-layer resistance while preserving permselectivity. Electrochemically grown, electro-ionically conductive nanocones of polyaniline on conventional IEMs exemplify a rapid and scalable approach: by generating counter-rotating microvortices at the surface, these nanocones thin the polarization layer and boost cation permeation and Na^+/Mg^{2+} selectivity. More generally, controlled surface patterning and functionalization by plasma, electroless deposition, or sputtering enable charged, hydrophilic, or metallic coatings within or atop nanochannels, providing additional levers to tune interfacial transport without thickening the selective layer.

In summary, framework membranes (MOFs/COFs), 2D carbons and nanotubes, filler-integrated and pore-filled composites, and bioinspired surface nanostructures each offer distinct fabrication toolkits and structure–transport couplings that complement traditional IEMs. Their shared objective is an ultrathin, defect-lean, strongly charged nanochannel network whose characteristic size matches hydrated ions while maintaining mechanical integrity under operating hydration and potential gradients. More detailed can be found in [102, 178].

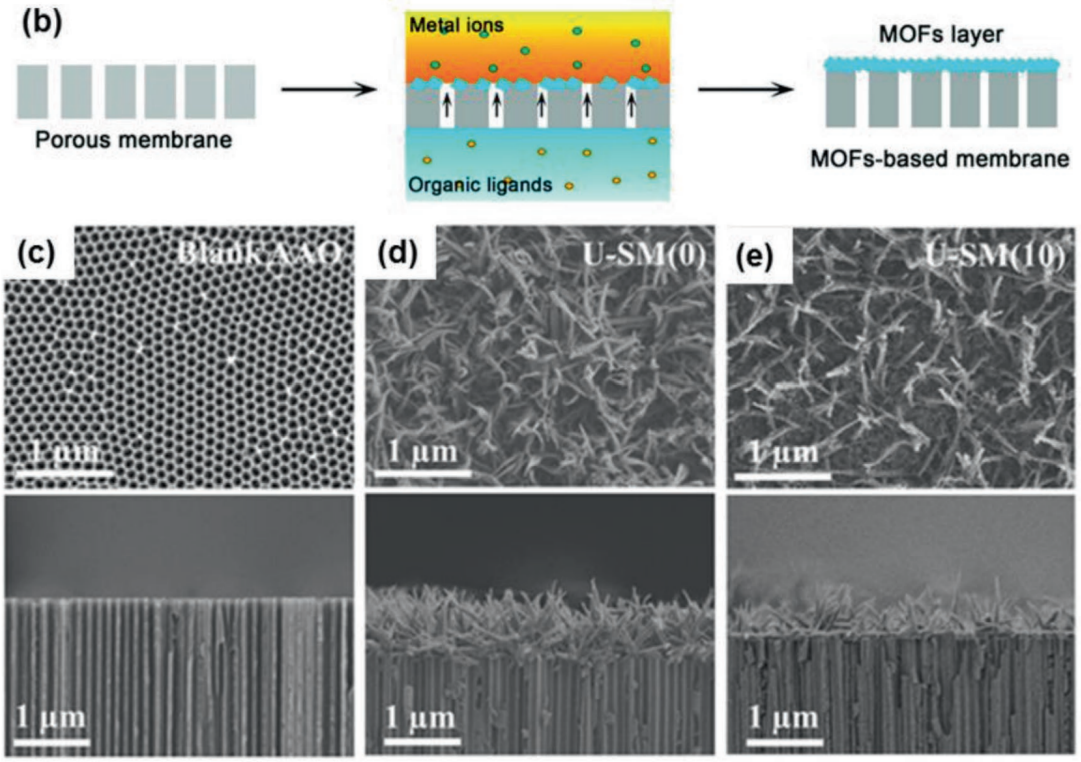


Figure 4.10: b) A schematic illustration exhibiting the crystallization of MOF nanostructures as a thin layer on a porous substrate surface. c–e) SEM micrographs of a blank AAO, U-SM(0) and U-SM(10), respectively, showing grown MOF nanostructures on the substrate surface. The cross-sectional SEM images showing a nanostructured thin MOF layer. Taken from [102].

4.3 Techniques for improving ion selectivity and membrane resistance

The performance of ion-exchange membranes (IEMs) depends critically on their ability to achieve high ion selectivity while maintaining low electrical resistance. Improving these properties requires balancing charge transport, interfacial phenomena, and structural stability. Two main approaches are generally used: (*i*) surface modification, which tailors the chemical and electrostatic properties of the membrane surface or pore walls, and (*ii*) geometry modification, which alters the membrane morphology or pore structure to optimize transport under nanoscale confinement.

4.3.1 Surface Modification

Surface modification aims to tune the interfacial chemistry and charge density of IEMs without significantly altering their bulk morphology. These methods improve counter-ion affinity, suppress co-ion leakage, enhance fouling resistance, and can even reverse charge polarity.

A comprehensive review by Khoiruddin and Wenten [179] details classical surface modification approaches applied to both cation and anion exchange membranes, including plasma treatment, UV-induced grafting, interfacial polymerization, and electrodeposition. Such methods alter the surface charge density or hydrophilicity and have been widely used to enhance permselectivity and electrochemical stability.

Another widely used strategy is the incorporation of nanomaterials or fillers into the polymer matrix to form hybrid or composite IEMs. Alabi et al. [180] reviewed the use of nanoparticles such as SiO_2, TiO_2, graphene oxide (GO), and carbon nanotubes (CNTs) to improve mechanical strength, selectivity, and ion conductivity while minimizing swelling. Kotoka et al. [181] further demonstrated how surface functionalization and nanoparticle embedding can selectively enhance monovalent ion transport in anion-exchange membranes (AEMs). More recently, Kumar et al. [182] showed that surface coating of cation-exchange membranes (CEMs) with conductive polymers such as polyaniline or polypyrrole can improve ionic conductivity and interfacial stability.

Recent developments have also explored atomic layer deposition (ALD) as a precise surface modification method for IEMs and related ion-conducting membranes. ALD enables conformal deposition of sub-nanometer oxide coatings (e.g., Al_2O_3, TiO_2) on internal pore surfaces, finely tuning surface charge and hydrophilicity without clogging pores. Toikkanen et al. [183] applied ALD to coat Nafion membranes with Al_2O_3, reducing methanol crossover and improving stability. Wormser et al. [184] demonstrated that ultrathin ALD oxide coatings can tune the electrostatic surface charge of cation-exchange membranes to achieve enhanced monovalent selectivity. Xiong et al. [185] provided a comprehensive review on ALD for membrane modification, emphasizing its potential for precise control over surface functionality in charged and hybrid systems.

Composite strategies combining polymer and inorganic components have also been developed. Cao et al. [186] fabricated layer-by-layer (LBL) assembled AEMs with an ultrathin composite surface layer that improved antifouling and ion selectivity. Similarly, Rakhshani et al. [187] and Charyton et al. [188] reported phase-inverted composite AEMs in which an ionomeric active layer was formed atop a porous substrate, improving mechanical robustness and electrochemical performance.

4.3.2 Geometry modification

Geometry modification involves engineering the membrane's physical structure, its thickness, pore diameter, and shape, to control ionic transport pathways and electric field distribution. By reducing diffusion lengths and enhancing confinement, geometric optimization can simultaneously lower resistance and increase selectivity.

Composite membranes with an active thin layer supported on a porous substrate are widely used to reduce ohmic resistance. Such architectures maintain high selectivity while minimizing transport distance [102]. Further control can be achieved by tailoring the pore geometry to exploit asymmetric electrostatic effects. Conical, step, and bullet-shaped nanopores exhibit directional ion transport and ionic current rectification due to asymmetric EDL overlap along the pore axis as seen in Figure 4.11 [189, 190]. Track-etched polymer films and anodic alumina (AAO) membranes are prototypical platforms for generating such geometries with nanometer precision, enabling studies of surface-charge-governed ion transport [78, 190, 191].

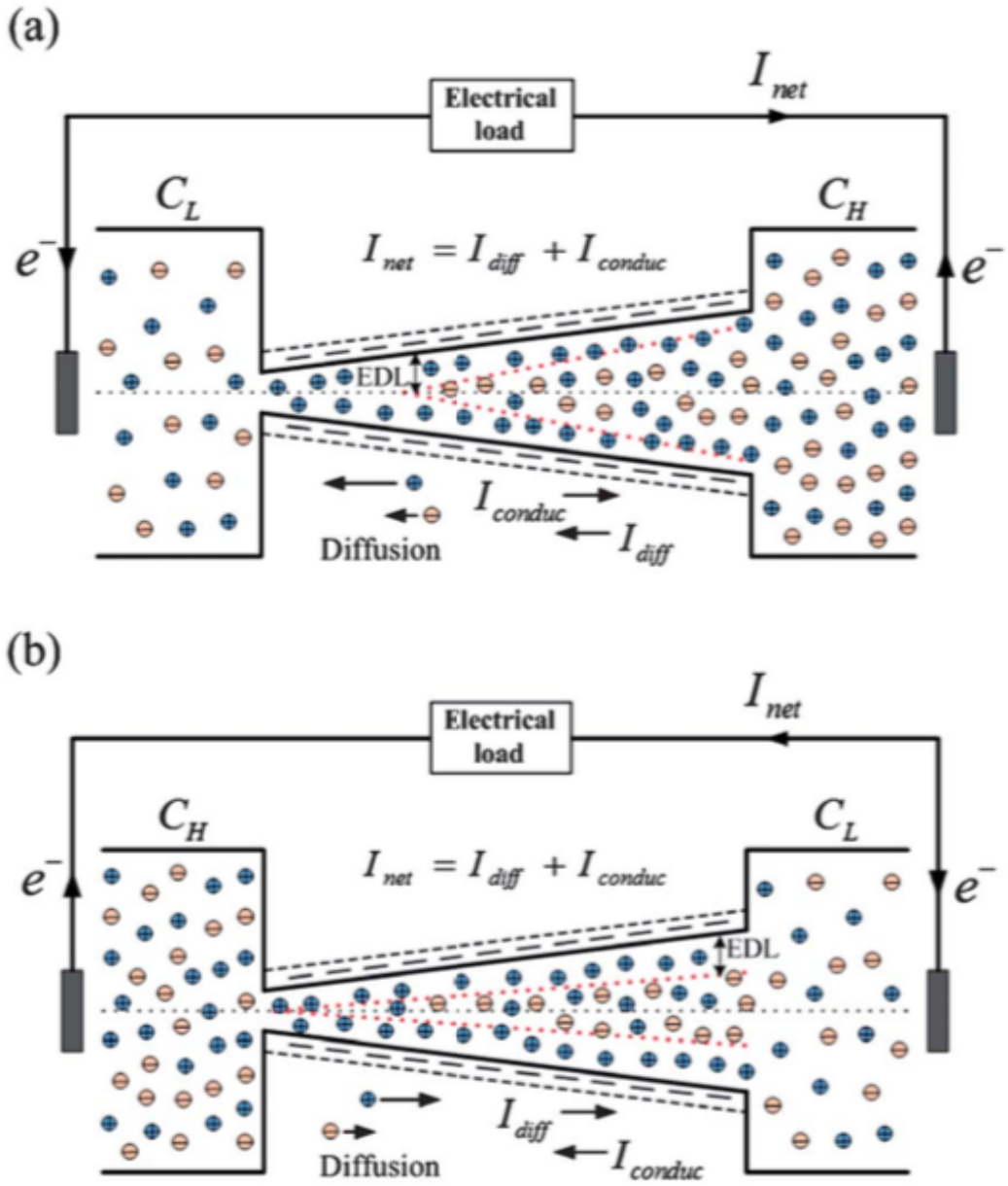


Figure 4.11: Schematic representation of power generation in negatively charged nanopore as a result of reverse electrodialysis (RED). (a) Ion diffusion through nanopore from base side to tip side under effects of concentration gradient. (b) Ion diffusion through nanopore from tip side to base side under effects of concentration gradient. Due to the geometrical effect and different concentration gradient, a different degree of electrical double layer (EDL) overlap occurs between the walls of the nanopore in the two cases. Taken from [192].

A notable example of geometric optimization is the anisotropic anodic aluminum oxide (AAO) membrane developed by Lee et al. [65]. This design integrates a thin active layer of small nanopores atop a supporting layer with larger pores, combining high ion selectivity with low electrical resistance. Experimental results demonstrated that such anisotropic membranes yield a maximum power density of 15.0 mW m^{-2}, which is 7.2 times higher than that of isotropic AAO membranes. The performance enhancement was attributed to increased diffusion potential (due to the high surface charge and small pore diameter of the active layer) while maintaining low overall resistance because of the short active layer thickness. The study further showed that the length of the active layer is a more critical parameter than its pore diameter, and that optimal performance is achieved when the low-concentration solution contacts the active layer side. This asymmetric nanoporous configuration shows how combining structural anisotropy with nanoscale confinement can significantly enhance ion selectivity and power generation in reverse electrodialysis.

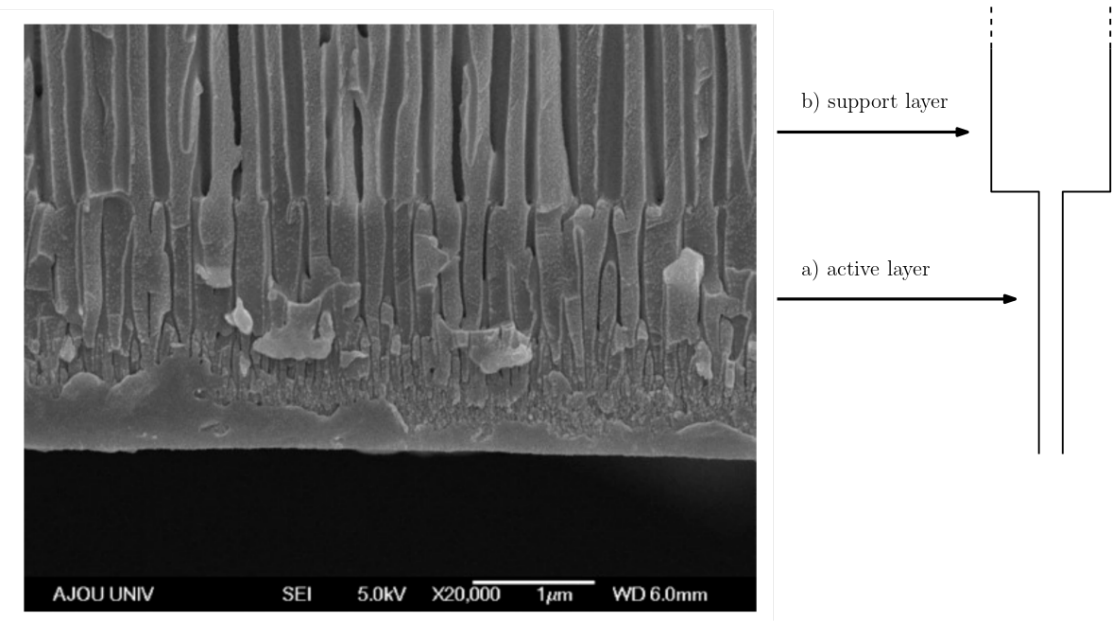


Figure 4.12: Scanning Electron Microscope (SEM) cross-sectional view of the anisotropic nanoporous anodic aluminum oxide membrane: (a) active layer side; (b) support layer side. Taken from [65] .

4.4 State of the art for nanoporous and nanochannel systems for RED

Nanoporous and nanochannel systems represent a fundamentally different class of membranes for salinity-gradient energy harvesting compared with polymer-based ion-exchange membranes. Instead of relying on fixed ionic groups embedded within a hydrated polymer matrix, these membranes exploit nanofluidic transport in structurally defined pores, where ion selectivity is governed by surface-charge-driven electric double layer (EDL) interactions. Materials such as anodic aluminium oxide (AAO), porous silicon (PSi), track-etched polycarbonate, and two-dimensional lamellar frameworks provide well-controlled pore sizes in the nanometre range, enabling strong overlap of EDLs under dilute conditions and thereby promoting counter-ion selectivity without the need for chemical functionalisation. These systems have attracted considerable attention due to their ability to achieve high intrinsic selectivity and ion-rectification effects at the single-pore level.

A wide variety of nanofluidic structures have been developed to convert salinity gradients into electrical power, and their performance depends strongly on membrane geometry, surface chemistry, and fabrication method. Early studies on straight cylindrical nanopores, such as anodic alumina oxide or track-etched polycarbonate, demonstrated that even simple pores can exhibit ion selectivity when their diameters are sufficiently small for electric double layer overlap [54, 193]. These membranes typically show moderate power densities, limited mainly by their relatively large thickness and low pore density. Conical nanopores introduced through asymmetric track-etching significantly improved selectivity due to their tapered geometry, enabling rectification and enhanced diffusion potentials, although their effective power remains constrained by small active areas [52, 67].

More advanced strategies rely on engineered surface chemistry to strengthen ion selectivity beyond what geometry alone provides. For instance, coating alumina nanochannels with polyelectrolytes or ionic liquids can dramatically increase surface charge density and reduce co-ion leakage, thereby shifting the transport regime from purely geometric confinement to strong electrostatic control [66]. These surface-modified inorganic nanochannels remain nanofluidic in nature, as the pores stay open and ion transport is governed by electric double layer regulation at the solid–liquid interface.

Beyond synthetic inorganic substrates, naturally occurring nanofluidic structures have recently emerged as a promising category within this field. Ionized wood membranes, for example, exploit the intrinsic 1–5 nm nanochannels formed by aligned cellulose nanofibrils and achieve ion selectivity through surface functionalisation with quaternary ammonium or carboxylate groups, effectively behaving as inorganic-like nanochannels rather than polymeric IEMs [194]. Similarly, silk

nanofibril membranes form densely packed protein-based nanochannels that exhibit surface-charge-regulated ion transport analogous to that of synthetic nanofluidic systems [195]. These natural nanofibrillar scaffolds broaden the materials palette available for nanofluidic RED, demonstrating that rigid organic frameworks can achieve nanofluidic behaviour typically associated with inorganic membranes.

Another major direction has been the design of hybrid or composite nanofluidic membranes that combine multiple structural length scales. Anisotropic membranes, in which an ultrathin selective layer is supported by a highly permeable scaffold, reduce internal resistance while maintaining strong ion exclusion [65]. This architecture, inspired by commercial IEMs, yields significantly higher power density than isotropic nanoporous films. Even more complex hybrid systems, such as block-copolymer layers deposited on conical PET pores or MXene-based asymmetric stacks, exploit both charge polarity contrast and geometric asymmetry [55, 196]. These structures act as nanofluidic diodes, suppressing concentration polarisation and enabling highly directional ion transport, which leads to substantial gains in harvested power.

Ultrathin selective layers deposited by spin-coating, interfacial polymerisation, LbL assembly, or block-copolymer coating create nanoscale ion-transport channels on porous supports. Representative coated systems include COF/dye-coated CEMs [197], PET/PS-b-P4VP nanofluidic AEMs [55], and PDDA/ABN-based coated AEMs [198].

Two-dimensional and nanolamellar materials constitute another rapidly expanding class of nanofluidic membranes. Graphene oxide laminates provide angstrom-scale channels with exceptional monovalent selectivity [199], while holey graphene and graphene-derived nanofluidic structures introduce well-defined through-nanopores that further reduce transport resistance and enhance selectivity [200]. The stacked or perforated morphology of these two-dimensional materials creates extremely short transport pathways, enabling high power densities compared with conventional nanoporous substrates. Similarly, nanochannels formed through the packing of nanoparticles create continuous yet tortuous pathways with high effective surface area, enabling strong electric double layer regulation and high normalised power densities [201, 202].

Table 4.1 reports the power densities from the studies mentioned above. Overall, the literature shows a clear trend: membranes that combine high selectivity (through charge regulation, functionalisation, or asymmetric design) with low resistance (via ultrathin selective layers, high pore density, or two-dimensional channels) consistently outperform traditional nanoporous structures. This explains the several-orders-of-magnitude variation in reported power densities and highlights the critical role of nanofluidic architecture in the development of next-generation salinity-gradient energy harvesting systems.

Table 4.1: Power density of nanochannels and nanopores at different salinity gradients. [a] Values extrapolated from the single pore output power. No confirmation of these values.

Salinity ratio	**Nanochannels / nanopores type**	**Configuration & geometry (membrane / single pore; pore size; area)**	**Power density [W/m^2]**	**Ref.**	**Year**
100000 (KCl)	Blind-Hole AAO	mem.; 45; 13.4 mm^2	0.28e-3	[203]	2024
1000 (1 M/1 mM KCl)	Track-etched polycarbonate	mem.; 15 nm; 78.5 mm^2	0.58e-3	[193]	2013
10000 (10/0.001 mM NaCl)	Silk nanofibril (SNF) nanochannels (SO_3H / IL)	mem.; eff. nanochannels $\sim$ 3–6 nm; 10.75 cm^2	0.59e-3	[195]	2021
10 (0.1/0.01 M NaCl)	Silica coated on alumina substrate	mem.; not given; 17.3 cm^2	1e-3	[204]	2016
3000 (300/0.1 mM KCl)	Paper based capillary	mem.; dense Nafion; 0.2 cm^2	2.8e-3	[205]	2015
0.01/0.6 (NaCl)	Ionized wood nanochannels (cellulose nanofibrils)	mem.; 1.4 nm (p-Wood) / 5.1 nm (n-Wood); 1 cm^2	5.14e-3	[194]	2020
10 (100/10 mM NaCl)	AAO nanopores	mem.; 20 nm; 82 mm^2	6.6e-3	[54]	2013
100 (10/0.1 mM KCl)	Nanochannels formed by packed nanoparticles	mem.; nano-interstices 15-105 nm; 200x200 μm^2	8e-3	[201]	2015
50 (0.5/0.01 M NaCl)	Anisotropic nanoporous AAO membranes	mem.; active: 2 nm/ support: 100 nm;19.6 mm^2	1.5e-2	[65]	2020

Continued on next page

Salinity ratio	**Nanochannels / nanopores type**	**Configuration & geometry (membrane / single pore, pore size, area)**	**Power density [W/m^2]**	**Reference**	**Year**
50 (0.5/0.01 M NaCl)	Hybrid BCP-coated conical PET nanochannels	mem.; PET conical pores 50–500 nm/ BCP layer 10 nm	0.35	[55]	2015
50 (0.5/0.01 M NaCl)	Layer-by-layer membranes	mem.; layered ANF/BN nanochannels (few nm); 3.14 mm^2	0.6	[198]	2020
50 (0.5/0.01 M NaCl)	Graphene oxide (GO) nanochannels	mem.; 0.9-1 nm; 0.8 mm^2	0.77	[199]	2016
50 (0.5/0.01 M KCl)	Confined ionic-liquid AAO membranes	mem.; AAO 80-100 nm; 3.14 mm^2	5.07	[66]	2024
1000 (1 M/1 mM KCl)	Silica nanochannels	Nanochannel array; H = 4-80 nm/ W = 25 μm/ L = 140 μm; 10 channels	7.7	[53]	2010
1000 (1 M/1 mM KCl)	Holey graphene-like (HGN) subnanometer pores	mem.; $<$ 1 nm; 3.14 μm^2	$\simeq$ 10	[200]	2020
1000 (100/1 mM KCl)	Packed nanoparticle nanochannels	mem.; silica nanoparticles 100-500 nm (best: 100 nm); 415 μm^2	28.2	[202]	2013
50 (0.5/0.01 M NaCl)	COF nanoporous membranes	mem.; 0.72 nm; cm-scale membrane	51.4	[197]	2021

Continued on next page

Salinity ratio	**Nanochannels / nanopores type**	**Configuration & geometry (membrane / single pore, pore size, area)**	**Power density [W/m^2]**	**Reference**	**Year**
500 (0.5/0.01 M NaCl)	Asymmetric MXene/AAO/-Nafion (MOF) membrane	mem.; AAO pore $\simeq$ 50 nm; MXene $\simeq$ 182 nm; Nafion $\simeq$ 97 nm; 0.03 mm^2	65.6	[196]	2025
1000 (1 M/1 mM KCl)	Track-etched conical nanopore	Single nanopore; D_{tip} = 10-40 nm; D_{base} = 1.2-1.5 μm; π(20 nm)^2	8.3e3–1.43e1	[67]	2011
1000 (1 M/1 mM KCl)	Track-etched conical nanopore	Single nanopore; D_{tip} : 20-50 nm/ D_{base}: 1-2 μm	2e4–2.6e3[a]	[52]	2010

4.5 Discussion and outlook

In this chapter, the operating principle of reverse electrodialysis (RED) was introduced. This technique converts salinity-gradient energy into electrical power by transporting ions through alternating cation- and anion-exchange membranes. The characteristics of the ion-exchange membranes (IEMs) are therefore central to system performance: they must sustain a high membrane potential while simultaneously permitting a high ionic flux. Conventional IEMs, originally designed for electrodialysis, generally exhibit excellent permselectivity but relatively high area resistance, which limits the achievable power density in RED. Numerous chemical, structural, and composite-based modification strategies have been explored to address these limitations. While significant progress has been achieved, further improvements are required to make RED competitive as a large-scale energy-harvesting technology. Moreover, these polymer membranes remain dependent on water uptake for ion transport and are susceptible to swelling, fouling, and long-term chemical degradation.

From a microfabrication perspective, conventional polymer IEMs are also difficult to integrate directly into MEMS platforms due to limitations in thermal stability, mechanical robustness, and process compatibility. This motivates the exploration of alternative membrane concepts that could bridge nanoscale ionic transport with microdevice integration.

Single-nanopore studies have demonstrated exceptional intrinsic performance, combining high selectivity, low internal resistance, and in some cases very high power densities. Efforts to upscale these principles to membrane-scale devices have employed porous substrates such as anodic aluminium oxide (AAO) [54] and track-etched polymer films [193]. However, the resulting power densities remain significantly lower than those obtained with polymer IEMs. A major limiting factor is the requirement for electric double layer (EDL) overlap to achieve strong selectivity; this typically demands either very small pore diameters or low electrolyte concentrations. Both constraints reduce the number of charge carriers available for conduction, and thus inherently limit the achievable power.

Several design strategies have been proposed to mitigate this trade-off. One promising direction is the introduction of asymmetric or conical nanopores, where the active ion-selective region is confined to a very thin zone of the membrane. This approach maintains high selectivity while reducing the overall ionic path length, thereby decreasing resistance. Conical or otherwise asymmetric pores, achieved either through controlled track-etching, plasma shrinking, or by applying ultrathin coatings, have shown improved performance and directional ion transport [52, 67]. More recent hybrid architectures, such as anisotropic nanoporous structures with thin selective layers or MXene/AAO combinations, further illustrate how geometry and surface charge can be co-designed to enhance RED performance [65, 196].

Nevertheless, substantial progress is still required to reach the power densities of state-of-the-art polymer IEMs while preserving the structural, chemical, and processing advantages of inorganic nanoporous materials.

Chapter 5

Porous silicon membranes as ion exchange membranes

5.1 Porous silicon: fundamentals and membrane

Silicon (Si) technology has dominated microelectronics for more than half a century. Not only is silicon the second most abundant element on earth, but it also possesses an ideal balance between performance and stability [206]. In recent decades, microelectronics has expanded beyond digital circuits into so-called More-than-Moore devices for sensing, optics, radio frequency (RF), MEMS, and power electronics. To enable this diversification of applications, the functionality of silicon technology was extended, and the porosification of silicon emerged as a simple and inexpensive route to broaden its use.

Porous silicon (PSi) exhibits properties that differ remarkably from those of bulk Si and can be fine-tuned by adapting the porous morphology. It was first discovered in the mid-1950s by Arthur and Ingeborg Ulhir, who accidentally fabricated the first porous silicon film while studying surface polishing techniques [206]. The discovery was largely forgotten until the late 1980s, when the observation of quantum confinement effects in PSi reignited interest in its unique physical and optical properties [206]. Among the many research avenues that followed, the fabrication of porous silicon membranes (PSiMs) rapidly gained traction as an effective way to create permeable Si-based structures for transport, filtration, and sensing applications [79, 206].

Porous silicon membranes (PSiMs) are gaining increasing attention due to their tunable physical, chemical, and structural properties, which make them attractive for applications in sensing, biomedical engineering, and energy conversion. They are typically fabricated by electrochemical etching of silicon wafers or through microfabrication techniques such as dry/wet etching and lithography. Various

configurations exist, including freestanding, self-supported, lateral, and microfabricated membranes, each with specific advantages in terms of robustness, integration, and scalability [206]. The morphology of PSiMs can be precisely controlled: they may be ultra-thin or several hundred micrometres thick, and their pores can range from micro- to macroporous, depending on the etching parameters and substrate doping.

The structural parameters of PSiMs, particularly porosity, pore size, and thickness, strongly affect their physical behaviour. Increasing porosity reduces mechanical strength and thermal conductivity but enhances mass transport and optical tunability [79]. PSiMs also exhibit low dielectric losses, high resistivity, and adjustable refractive indices, enabling integration into optical and electronic devices. They are biocompatible and biodegradable, although surface modification (e.g., silanisation, oxidation, or hydrocarbonisation) is often necessary to ensure stability in aqueous or physiological environments [206].

Key application domains include:

- Biomedical engineering: scaffolds for tissue regeneration, drug delivery systems, and biosensing platforms.
- Sensing: optical, electrochemical, and nanopore-based sensors for gases, biomolecules, and DNA.
- Energy devices: ion-exchange membranes, electrodes, and catalytic supports for micro fuel cells and batteries.
- Microelectronics: MEMS and RF components benefiting from thermal insulation and low dielectric losses.

Despite progress, integration challenges remain, particularly regarding mechanical fragility, reproducibility, and CMOS compatibility. However, PSi offers a decisive advantage over non-silicon templates such as anodic aluminium oxide (AAO): it can be fabricated directly within standard silicon microfabrication lines. Industrial processes such as Bosch's Advanced Porous Silicon Membrane (APSM) technology already demonstrate CMOS-compatible integration for pressure sensors. Recent developments by Barillaro *et al.* [207, 208], Capelle *et al.* [209, 210], and Scheen *et al.* [211] have extended this compatibility to gas and RF devices. Moreover, Tuyaerts *et al.* [212, 213] recently achieved low-temperature ($<150\,^{\circ}\mathrm{C}$) post-fabrication porosification on standard-resistivity silicon substrates, maintaining CMOS front-end integrity and exhibiting excellent RF performance.

Overall, these advances confirm that PSiMs bridge the gap between nanostructured porous materials and microelectronic technologies, establishing them as a versatile and integrable platform for next-generation devices.

5.1.1 PSi fabrication

The strong and continued scientific interest in porous silicon (PSi) arises from its remarkable versatility and tunable properties. A wide range of fabrication techniques allows precise control over its structural characteristics. For instance, pore diameters can range from a few nanometers to several tens of micrometers, while film thickness may vary from the nanometer to the micrometer scale. Additional parameters such as porosity, pore distribution, and pore geometry can also be finely adjusted through processing conditions.

Several fabrication routes are available for producing PSi, most of which are based on either dry etching or electrochemical methods. In dry etching, a hard mask is employed to define the desired pattern, which is subsequently transferred into the silicon substrate by anisotropic plasma etching. The electrochemical approach, on the other hand, primarily comprises two methods: electrochemical etching and stain etching. The latter is based on spontaneous electroless etching of silicon in an oxidizing hydrofluoric acid (HF) solution [214]. When combined with metal films or nanoparticles, the process is referred to as Metal-Assisted Chemical Etching (MACE) [215]. However, since no recent studies on MACE-fabricated PSi membranes have been reported, the present work focuses exclusively on electrochemical and dry-etching methods.

Porous silicon is produced through the electrochemical etching of crystalline silicon in aqueous or non-aqueous electrolytes containing hydrofluoric acid (HF). Although the chemical dissolution of silicon in HF solution is thermodynamically possible, the process proceeds extremely slowly unless an oxidizing agent (such as O_2 or NO_3^-) is present or the oxidation reaction is electrochemically driven. This slow reaction rate is mainly attributed to the formation of surface hydrides, which passivate the surface and hinder corrosion kinetics. During etching in HF-based solutions, the freshly exposed silicon surface becomes hydrogen-terminated, as illustrated in Figure 5.1. Residual oxides and fluorides are efficiently removed by the HF electrolyte [80].

Electrochemical etching requires two electrodes, where oxidation occurs at the anode and reduction at the cathode. A schematic of a typical two-electrode cell is shown in Figure 5.2. In this setup, the silicon substrate acts as the anode (working electrode), while a platinum electrode is commonly used as the cathode. The etching apparatus is constructed from HF-resistant materials such as Teflon® or polyether ether ketone (PEEK) to ensure chemical compatibility [79, 80].

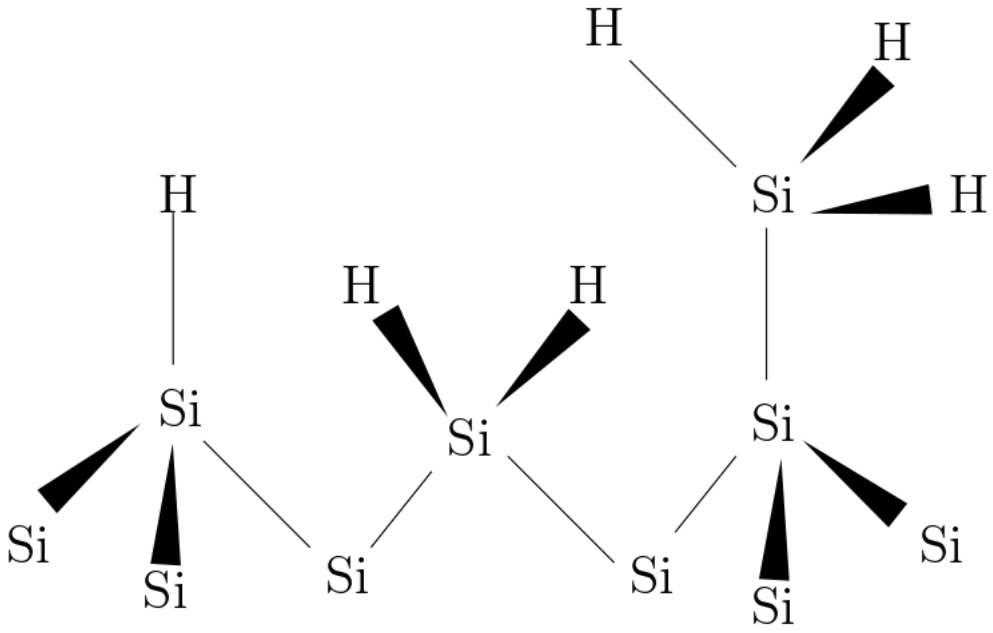


Figure 5.1: Hydrides on the porous silicon surface. Three types of surface hydrides are depicted: SiH, SiH2, and SiH3. Adapted from [206].

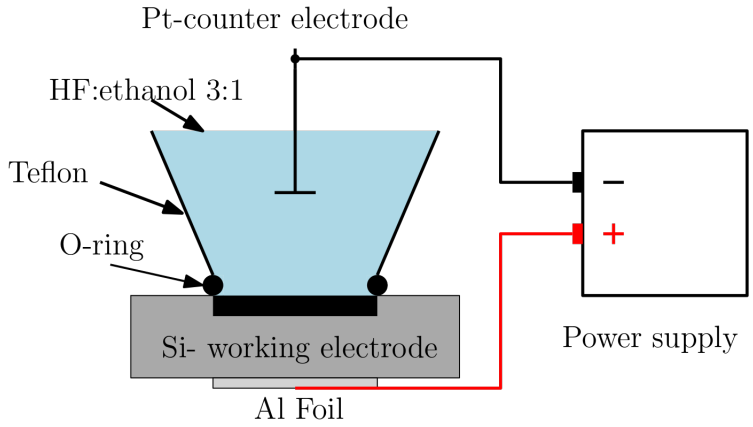


Figure 5.2: Schematic representation of a two-electrode electrochemical cell for the formation of porous silicon, illustrating the main oxidation and reduction half-reactions occurring during the etching process. Adapted from [206].

During the electrochemical etching of silicon, two distinct regimes can be identified: pore formation and electropolishing, as illustrated in Figure 5.3. In the pore formation regime, holes reaching the pore tips weaken the Si–H surface bonds, enabling localized dissolution of silicon, which is governed by the following reaction pathways:

- a simplified valence-2 dissolution pathway:

$$\mathrm{Si} + 2h^+ + 2F^- \rightarrow \mathrm{SiF_2}, \tag{5.1}$$

- which further reacts to give the overall dissolution reaction:

$$\mathrm{Si} + 6HF + 2h^+ \rightarrow \mathrm{H_2SiF_6} + H_2 \uparrow + 2H^+. \tag{5.2}$$

Because these reactions are hole-driven, the formation of an electronic barrier at the pore walls suppresses further hole injection, thereby passivating the walls against continued etching. In contrast, the enhanced electric field at the pore tip promotes hole accumulation, sustaining localized dissolution and pore propagation.

As the applied current density increases, the pore walls progressively thin until adjacent pores merge, marking the onset of the electropolishing regime at a current called the electropolishing current J_{EP}. Above this current, the regime is governed by the following reaction equations:

- the silicon surface is first oxidized:

$$\mathrm{Si} + 2\mathrm{H_2O} \rightarrow \mathrm{SiO_2} + 4\mathrm{H^+} + 4\mathrm{e^-}, \tag{5.3}$$

- The freshly made oxide is then dissolved by hydrofluoric acid:

$$\mathrm{SiO_2} + 6\mathrm{HF} \rightarrow \mathrm{H_2SiF_6} + 2\mathrm{H_2O}. \tag{5.4}$$

  This two-step sequence, surface oxidation followed by chemical dissolution, ensures uniform material removal.

When analyzing the current–potential characteristics of silicon in an HF-based electrolyte, the current initially rises exponentially with increasing potential until a peak is reached. It then slightly decreases before gradually increasing again at higher potentials, as shown in Figure 5.4 [80]. The transition between these two regimes, each described by a distinct reaction mechanism, as also indicated in Figure 5.4, depends on several factors, including the substrate doping level, crystalline orientation, electrolyte composition, and temperature. However, it is primarily governed by the ratio of applied current density to fluoride ion concentration [79]. Although slight surface roughening may occur, electropolishing typically removes silicon atoms uniformly, resulting in a smooth and polished surface [80].

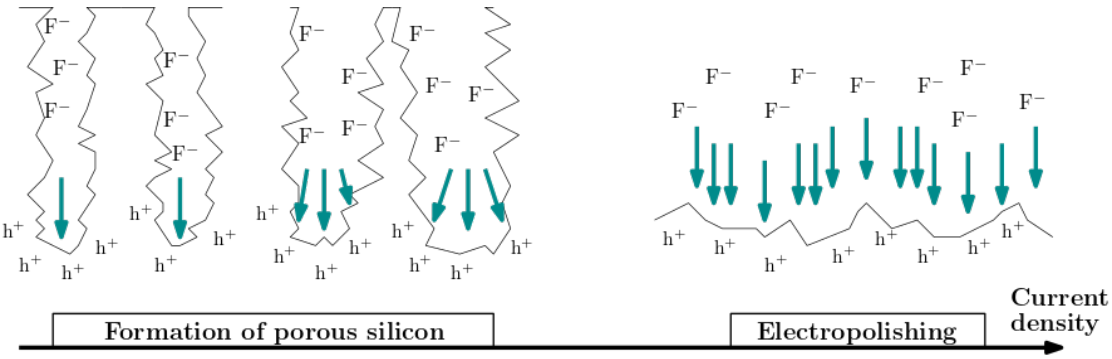


Figure 5.3: Mechanism of pore formation with increasing current densities. Adapted from [206].

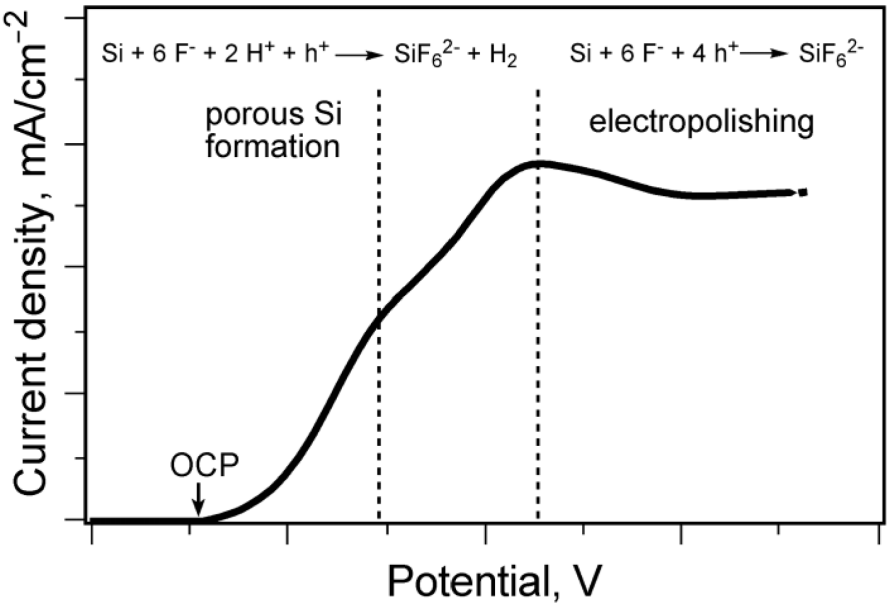


Figure 5.4: General current density versus applied potential curve for the electrochemical etching of silicon in an HF-based electrolyte, illustrating the regimes of porous silicon formation and electropolishing. The label "OCP" denotes the open-circuit (rest) potential of the silicon electrode. Adapted from [80].

Furthermore, several general characteristics are commonly observed during porous silicon formation [80]:

- Pores typically nucleate uniformly across the silicon surface without long-range order, unless the wafer has been deliberately pre-patterned.

- The electric current is concentrated near the pore tips, promoting localized dissolution at these regions.
- The pore walls tend to become passivated over time, resulting in preferential silicon dissolution at the interface between the porous and crystalline silicon layers.
- Once formed, pores remain stable and do not undergo reconstruction or redistribution.
- The final structure exhibits a distribution of pore diameters rather than a single, uniform pore size.

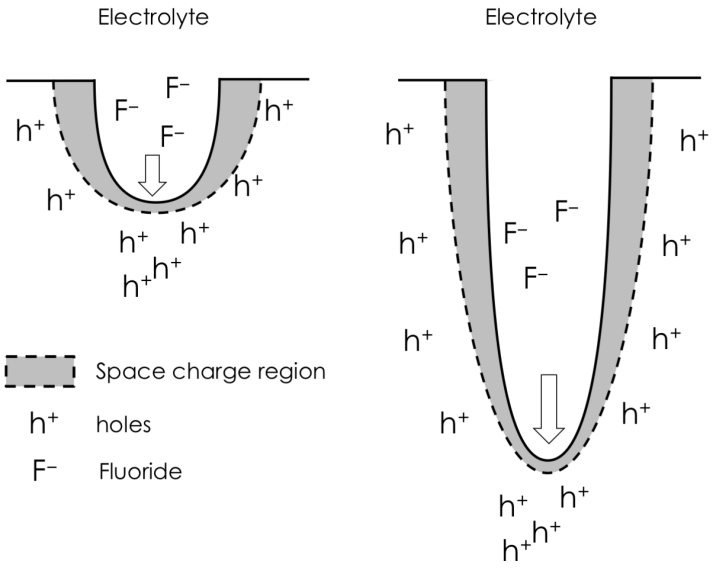


Figure 5.5: Illustration of the pore growth via the formation of a space charge region that tends to passivate the pore wall and induce the etching of the pore tip. Reprinted from [216].

Transitional layer

At the onset of electrochemical anodization, porous silicon (PSi) formation often begins with the development of a near-surface transitional layer. This region is typically described as a thin and relatively compact porous layer characterized by very small pore openings, generally below 10 nm, and a porosity lower than that of the subsequently formed porous film. Due to its restricted pore size, this transitional layer limits the penetration of larger molecular species from the

electrolyte and hinders the establishment of a homogeneous porous network. As a result, the pore diameter and porosity in this initial region may differ from the steady-state morphology, which is otherwise primarily governed by the applied current density [217]. The expected pore morphology is illustrated in Figure 5.6.

The transitional layer forms during the early, non-steady stage of anodization and its thickness has been reported to depend on several parameters, including current density, substrate resistivity (i.e., doping level), electrolyte composition, surface condition, and impurities [217]. Although no single value can be assigned, reported thicknesses in the literature typically range from a few tens to a few hundreds of nanometers. For instance, Unagami reported a maximum thickness of approximately 200 nm for p-type silicon anodized at 100 $\mathrm{mA{\cdot}cm^{-2}}$ on 0.02 $\Omega{\cdot}$cm substrates, with significantly smaller values observed for both lower and higher resistivities [217].

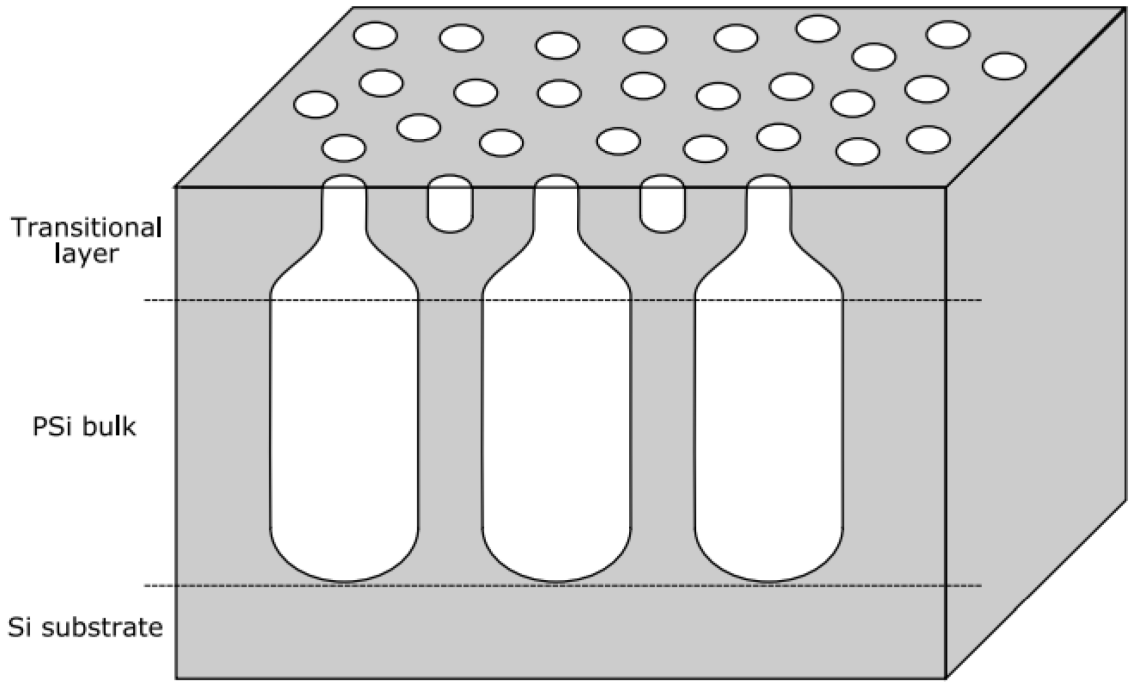


Figure 5.6: Schematic representation of pore morphology during porous silicon formation. After nucleation, some pores do not propagate into the bulk, while others expand both in diameter and depth, resulting in a dense transitional layer above a more homogeneous PSi bulk layer. Adapted from [217].

The presence of this compact near-surface region is undesirable, as it introduces

structural inhomogeneity and can limit mass transport within the porous layer. To suppress its influence, a sacrificial layer strategy is commonly employed. In this approach, an initial porous silicon layer is deliberately formed under anodization conditions chosen to promote rapid pore initiation and to reach the steady-state pore propagation regime as quickly as possible. This sacrificial layer is subsequently removed by wet chemical etching in alkaline solutions, most commonly potassium hydroxide (KOH) or sodium hydroxide (NaOH) [217]. Following its removal, a second anodization step yields a porous silicon layer exhibiting a more homogeneous pore morphology from the top surface onward.

5.1.2 PSi characterisation

The morphology of porous silicon (PSi) is primarily defined by three parameters: pore size, layer thickness, and porosity [217]. As discussed previously, multiple fabrication parameters influence pore formation, and consequently, the final structure and morphology of PSi strongly depend on their selection.

5.1.2.1 Pore size

The first key parameter is the pore size. According to the classification established by the International Union of Pure and Applied Chemistry (IUPAC) [218], PSi can be categorized as follows:

- Micropores: $d < 2$ nm
- Mesopores: $2 < d < 50$ nm
- Macropores: $d > 50$ nm

Table 5.1: Effect of wafer doping concentration on the pore size of porous silicon (PSi), adapted from [206] [80].

Wafer type	**Doping concentration (cm^{-3})**	**Typical pore size / morphology**
n-doped Si	$< 10^{18}$	Wide range, from nanometres to micrometres
p-doped Si	$< 10^{15}$	Large pores in the μm range, often with nanometric pores within
p^+ Si	10^{15}–10^{18}	1–10 nm
p^{++} and n^{++} Si	$> 10^{19}$	10–100 nm

The applied current density has a major influence on both pore size and growth rate. Lower applied current densities generally result in the formation of smaller

pores [219–221]. The pore dimensions and morphology can be characterized using high-resolution imaging techniques such as transmission electron microscopy (TEM), scanning electron microscopy (SEM), or atomic force microscopy (AFM) [80, 222, 223].

5.1.2.2 Pore depth and porosity

The second defining feature of porous silicon (PSi) morphology is the pore depth or layer thickness, which is directly related to the etching duration. For a constant current density, longer etching times yield thicker porous layers; in fact, doubling the etching time approximately doubles the layer thickness. However, at greater depths, diffusion limitations can deplete the local HF concentration, thereby altering the growth rate and disrupting the linear correlation between etching time and layer thickness [217].

The third morphological characteristic is porosity, defined by the International Union of Pure and Applied Chemistry (IUPAC) as the ratio between the total pore volume (V_p) and the apparent sample volume (V). Porosity can be further categorized as follows:

- Open porosity: volume of pores that are accessible to a given probe molecule.
- Closed porosity: volume of pores that are inaccessible to the probe molecule.
- Total porosity: the sum of open and closed porosities, representing both accessible and inaccessible pore volumes.

Since porous silicon (PSi) is formed through the electrochemical corrosion of crystalline silicon, all pores in a freshly etched sample initially contribute to an open-porous structure, with no inaccessible regions. However, subsequent surface modification or passivation treatments can partially seal the pore openings, resulting in the formation of closed porosity [80]. This distinction is particularly relevant for ion exchange purpose, as the ionic flow may be hindered by block pores. In this work, however, passivation may have a limited impact as it consists in oxidation of the porous silicon layer into SiO2.

The formation of pores in porous silicon is governed by a combination of several parameters, including the electrolyte composition, dopant type and concentration, applied voltage, temperature, and illumination conditions [80]. Although extensive research has been conducted, a complete understanding of the mechanisms controlling porous silicon morphology remains elusive, as the porosification process involves a complex interplay of numerous factors [224]. Nevertheless, certain general trends have been consistently observed and are summarized in Table 5.2.

Table 5.2: Effect of anodization parameters on porous silicon (PSi) formation. Adapted from [225].

Increase of	**Parameter**		
	Porosity	**Etching rate**	**Critical current**
HF concentration	Decreases	Decreases	Increases
Current density	Increases	Increases	–
Anodization time	Increases	Nearly constant	–
Temperature	–	–	Increases
Wafer doping (p-type)	Decreases	Increases	Increases
Wafer doping (n-type)	Increases	Increases	–

The gravimetric method is a classical approach to determine both the porosity and thickness of porous silicon (PSi) layers. It relies on the high reactivity of PSi toward alkaline solutions (e.g., KOH or NaOH) compared to bulk crystalline silicon due to its large surface area. The sample mass is recorded before porosification (m_1), after porosification (m_2), and after removal of the porous layer (m_3). Using the etched surface area A and the density of silicon ρ_{Si}, porosity (P) and layer thickness (L) are calculated as:

$$P = \frac{m_1 - m_2}{m_1 - m_3}, \qquad L = \frac{m_1 - m_3}{A\,\rho_{\mathrm{Si}}} \tag{5.5}$$

This method, however, is destructive. Cross-sectional SEM imaging, often used for measuring thickness, is also destructive. To avoid this, the Spectroscopic Liquid Infiltration Method (SLIM) provides a non-destructive alternative based on Reflective Interferometric Fourier Transform Spectroscopy (RIFTS).

In SLIM, the reflectance spectrum of the PSi layer is recorded twice—first with air and then with a solvent filling the pores—using a broadband light source and a spectrometer coupled through an optical fiber (Figure 5.7a). The resulting spectra display Fabry–Pérot fringes (Figure 5.7b), and their Fourier transform yields a frequency peak corresponding to the effective optical thickness (EOT):

$$EOT = 2nL \tag{5.6}$$

where n is the average refractive index and L the layer thickness. The EOT values from both spectra are then analyzed using the Bruggeman or Looyenga effective medium models to extract the porosity and thickness of the PSi layer [80].

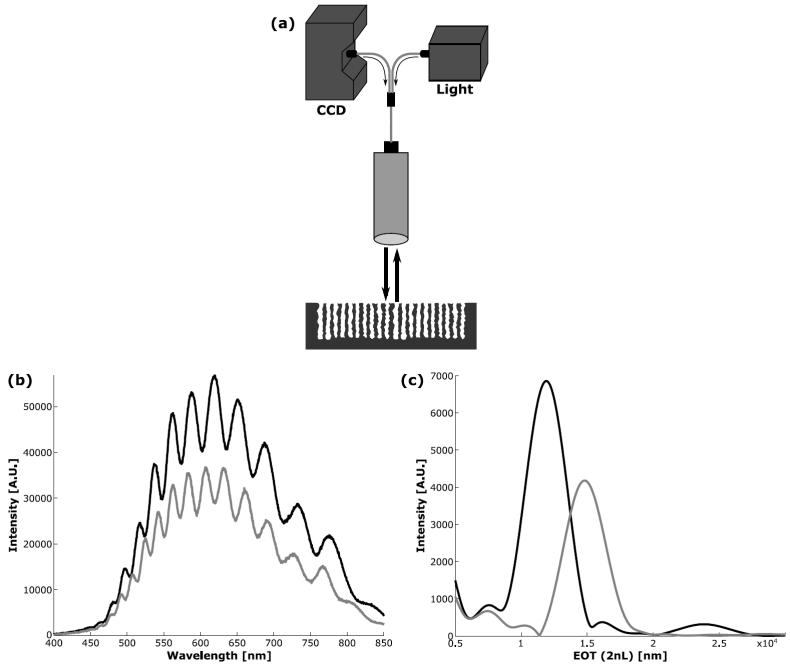


Figure 5.7: Schematic illustration of the working principle of the Spectroscopic Liquid Infiltration Method (SLIM) based on white-light reflectance interferometry. (a) White light from a halogen source passes through a bifurcated optical fiber and is focused normally onto the PSi surface using bi-convex lenses. The reflected beams from the top and bottom interfaces are collected through the same optical path and directed toward a CCD spectrophotometer. (b) Representative reflectance spectra showing interference fringes produced by double reflection at the interfaces. The black and grey traces correspond to PSi measured in air and in ethanol, respectively. (c) Fourier transforms of the reflectance spectra from (b), yielding a peak whose position represents the effective optical thickness ($2nL$). Adapted from [217].

5.1.2.3 Morphology

The pore morphology in porous silicon (PSi) is strongly influenced by the anodization parameters, as well as by the doping level and crystalline orientation of the silicon substrate. Depending on these factors, pores may be straight or branched, and their cross-sections can vary from cylindrical to pyramidal shapes. A wide range of microstructures can therefore be obtained, as illustrated in Figure 5.8. In some cases, PSi layers exhibit a stratified structure, where different morphologies appear along the depth of the film.

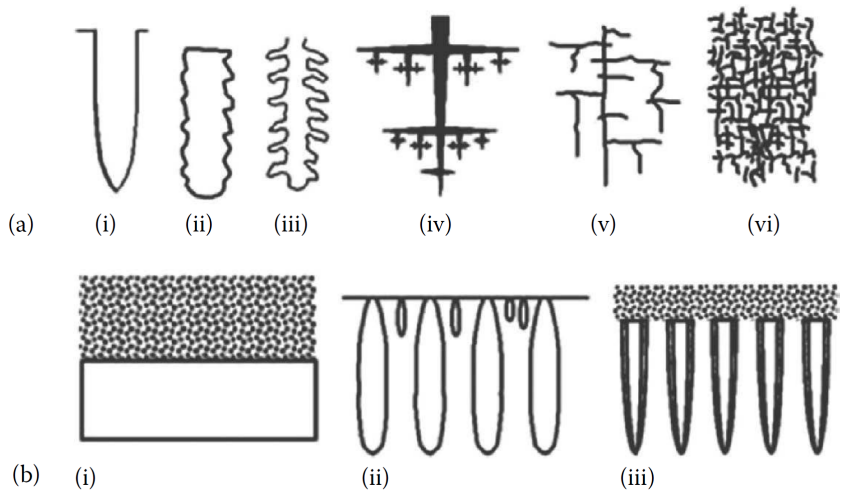


Figure 5.8: Variants of porous silicon (PSi) microstructures obtained under different anodization conditions. (a) Examples of pore branching: (i) smooth pore walls; (ii) branches shorter than the main pore diameter; (iii) secondary branching only; (iv) dendritic branching; (v) primary pores with second- and third-level branches; (vi) dense, randomly distributed short branches. (b) Depth-dependent variations in PSi morphology: (i) single layer of microporous silicon; (ii) single layer of macroporous silicon with smaller surface pores; (iii) microporous layer formed on top of a macroporous layer. Adapted from [224].

5.2 Porous silicon membranes

The following section is largely based on the review and research work of Roselien Vercauteren [79], which provides a comprehensive overview of the fabrication methods, structural characteristics, and applications of porous silicon membranes (PSiMs). Her work serves as the principal foundation for the present synthesis, which has been adapted and expanded to fit the scope and objectives of this thesis.

5.2.1 Porous membranes fabrication techniques

Porous silicon membranes (PSiMs) are obtained by detaching the porous silicon (PSi) layer from the underlying crystalline silicon substrate. This process opens the pore channels, enabling flow-through configurations suitable for various applications. Several fabrication strategies have been developed to produce PSiMs, which can be broadly classified into two categories: those based on electrochemical etching for porosification and those relying solely on microfabrication techniques,

as summarized in Figure 5.9.

Electrochemically etched PSi membranes can be fabricated through four main approaches [79]:

- Through-wafer: anodization performed across the full thickness of a standard silicon wafer [226];
- Free-standing: anodization limited to a defined region of the wafer, followed by release of the porous matrix through electropolishing of a thin cavity beneath it [227];
- Self-supported: microfabrication steps used to define cavities either before or after anodization [228];
- Lateral: pore channels oriented parallel to the wafer surface are produced using a combination of anodization and microfabrication techniques [229].

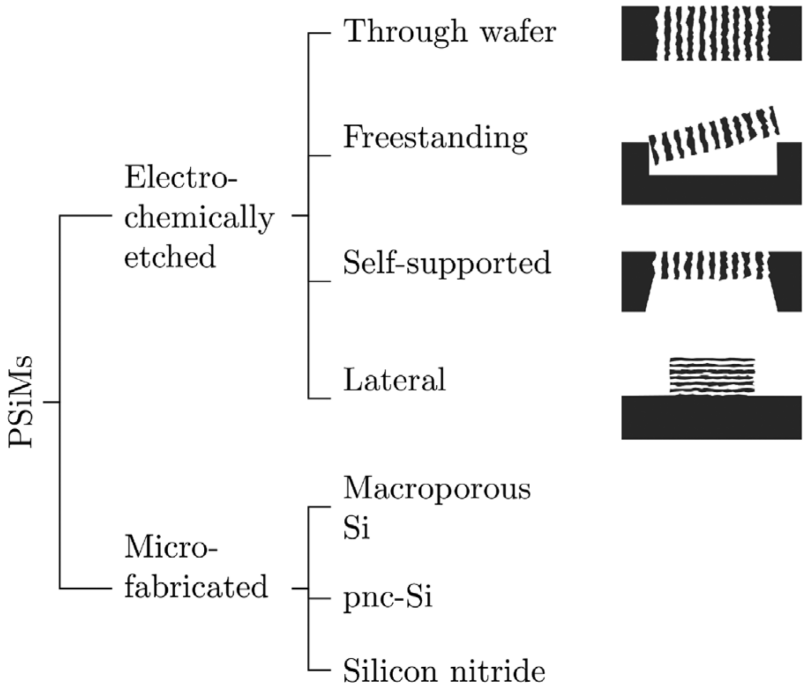


Figure 5.9: Summary of porous membranes fabrication techniques. Taken from [206].

Highly controlled pore geometries can also be achieved in membranes fabricated exclusively through microfabrication techniques, without the use of electrochemical

etching. These non-anodized porous membranes can be classified into three main categories [79]:

- Macroporous silicon membranes: produced via photolithography followed by dry etching [230];
- Nanoporous silicon nitride membranes: fabricated using similar lithographic and dry-etching processes [231];
- Porous nanocrystalline silicon (pnc-Si) membranes: formed spontaneously during rapid thermal annealing of amorphous silicon as nanocrystals nucleate within the film [232].

The first approach is through-wafer anodization, in which the entire thickness of a standard silicon wafer is anodized [211, 226, 233–235]. Although this method can yield fully porous wafers, it is generally time-consuming and highly sensitive to HF concentration variations, which often result in membrane non-uniformity. The second method produces freestanding membranes by anodizing a selected region of the wafer and subsequently releasing the porous layer through electropolishing of a thin cavity beneath it (see Section 5.2.1.1). This technique offers a straightforward fabrication route but yields membranes that are fragile and difficult to handle. A third configuration, known as self-supported membranes, combines anodization and microfabrication steps to create support cavities either before or after porosification (see Section 5.2.1.2). Finally, lateral membranes are fabricated by orienting the pores parallel to the wafer surface through a combination of anodization and microfabrication methods (see Section 5.2.1.3). Although self-supported and lateral PSiMs require additional microfabrication steps, they provide enhanced mechanical stability and can be more easily integrated into device architectures.

As previously discussed, one of the main advantages of porous silicon lies in the tunability of its structural properties through fabrication parameters, a feature that extends to PSi membranes. While the removal of the underlying bulk substrate does not modify the intrinsic material characteristics of PSi, it can significantly affect the performance of PSi-based devices.

In addition to electrochemical etching, alternative fabrication routes can also be employed to produce porous membranes with highly controlled pore geometries. These non-electrochemical approaches rely on advanced microfabrication techniques such as lithography, dry or wet etching, thin-film deposition, or thermal annealing. Three main types of non-anodized porous membranes are generally distinguished: macroporous silicon membranes, nanoporous silicon nitride membranes, and porous nanocrystalline silicon (pnc-Si) membranes. These non-anodized membrane structures are discussed in more detail in Section 5.2.1.4.

5.2.1.1 Free-standing PSiMs

Freestanding porous silicon membranes (PSiMs) are produced by electrochemically etching a defined region of a silicon substrate, followed by the lift-off of the porous layer. Several strategies have been developed for membrane detachment. The most common approach involves electropolishing a thin cavity beneath the porous region by applying one or more high-current pulses at the end of the anodization process. The amplitude of these current pulses can be reduced by lowering the hydrofluoric acid (HF) concentration in the electrolyte [236].

An alternative method, proposed by Preobrazhenskiy *et al.*, employs an alkaline potassium hydroxide (KOH)-based solution to detach the membrane, which simultaneously increases the porosity of the porous layer [237]. Mechanical lift-off is also possible, achieved by supporting the porous region on adhesive tape [227] or on a polydimethylsiloxane (PDMS) film [238], as shown in Figure 5.10. Another advantage of freestanding PSiMs, also illustrated in Figure 5.10, is the potential for substrate reuse: the same silicon wafer can be recycled for the fabrication of multiple membranes [227, 239].

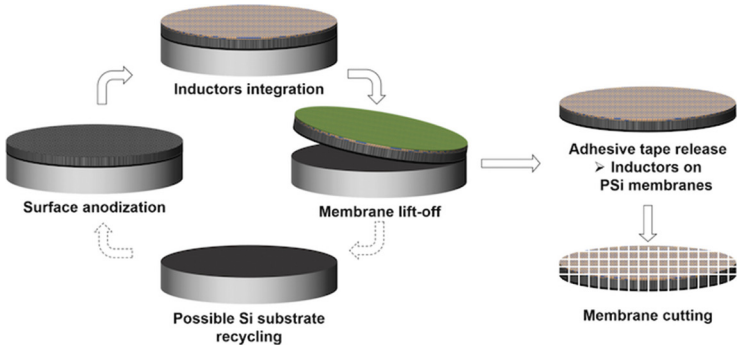


Figure 5.10: Illustration of the mechanical detachment of a PSi membrane and the possible recycling of the silicon substrate. Reprinted from [227].

However, freestanding PSiMs often exhibit a strong spatial anisotropy in their morphological features. Due to the directional nature of electrochemical etching and carrier depletion during prolonged etching, porosity gradients may develop across the surface or through the thickness of the membrane.

The integration potential of freestanding PSiMs is extensive and includes applications in electronics, microfluidics, and sensing. Electrical integration can be achieved by depositing conductive layers directly onto the porous membrane (Figure 5.11a. Reported examples include vacuum-evaporated gold [240], electroplated copper [237, 241], and sputtered indium tin oxide (ITO) [240, 242]. Freestanding PSiMs have also been successfully incorporated into more complex architectures.

Cencha *et al.* fabricated an anodic aluminium oxide (AAO)–PSi hybrid membrane using capillary forces to attach the PSi layer to the alumina substrate [243], illustrated in Figure 5.11b.

For microfluidic integration, PDMS can be cast on top of the still-attached PSi film, serving as a mechanical support during detachment [236, 244–246], as depicted in Figure 5.11c. Another strategy involves transferring detached membranes onto different substrates such as other PSi layers [247], gold slides [248], ITO-coated glass [249], plain glass [250–252], or poly(ethylene glycol) diacrylate (PEGDA) matrices [253, 254], shown in Figure 5.11d.

Recent advances have further expanded PSiM functionality toward microfluidic sensing. Gevers *et al.* [255] integrated large-pore ($\sim$67 nm) freestanding PSiMs into sealed microfluidic systems (Figure 5.11e, enabling flow-through decoration of the membranes with presynthesized gold nanoparticles (Au NPs). This configuration achieved homogeneous nanoparticle distribution throughout the membrane thickness, eliminating clogging and aggregation typically observed with drop-casting or immersion methods. The resulting membranes exhibited improved optical sensitivity and signal reproducibility during Reflective Interferometric Fourier Transform Spectroscopy (RIFTS) measurements.

More recently, An *et al.* [256] demonstrated a Porous Silicon on Paper platform for label-free optical sensing. In their approach, open-ended PSi freestanding membranes were transferred onto paper substrates, which provided both structural support and a passive capillary-driven flow mechanism, eliminating the need for external pumps or microfluidic channels. The system enabled rapid, quantitative detection of streptavidin proteins with a fourfold increase in sensitivity and a twofold reduction in response time compared to traditional on-substrate PSi sensors. This innovation highlights the potential of paper-supported PSi membranes for low-cost, point-of-care diagnostic devices (Figure 5.11f).

Freestanding PSiMs can also act as templates for nanostructure growth. De La Luz-Merino *et al.* demonstrated the electrodeposition of $CuInSe_2$ nanowires onto glass or transparent conductive oxide (TCO)-supported PSiMs, forming hybrid materials with potential applications in solar energy conversion [257].

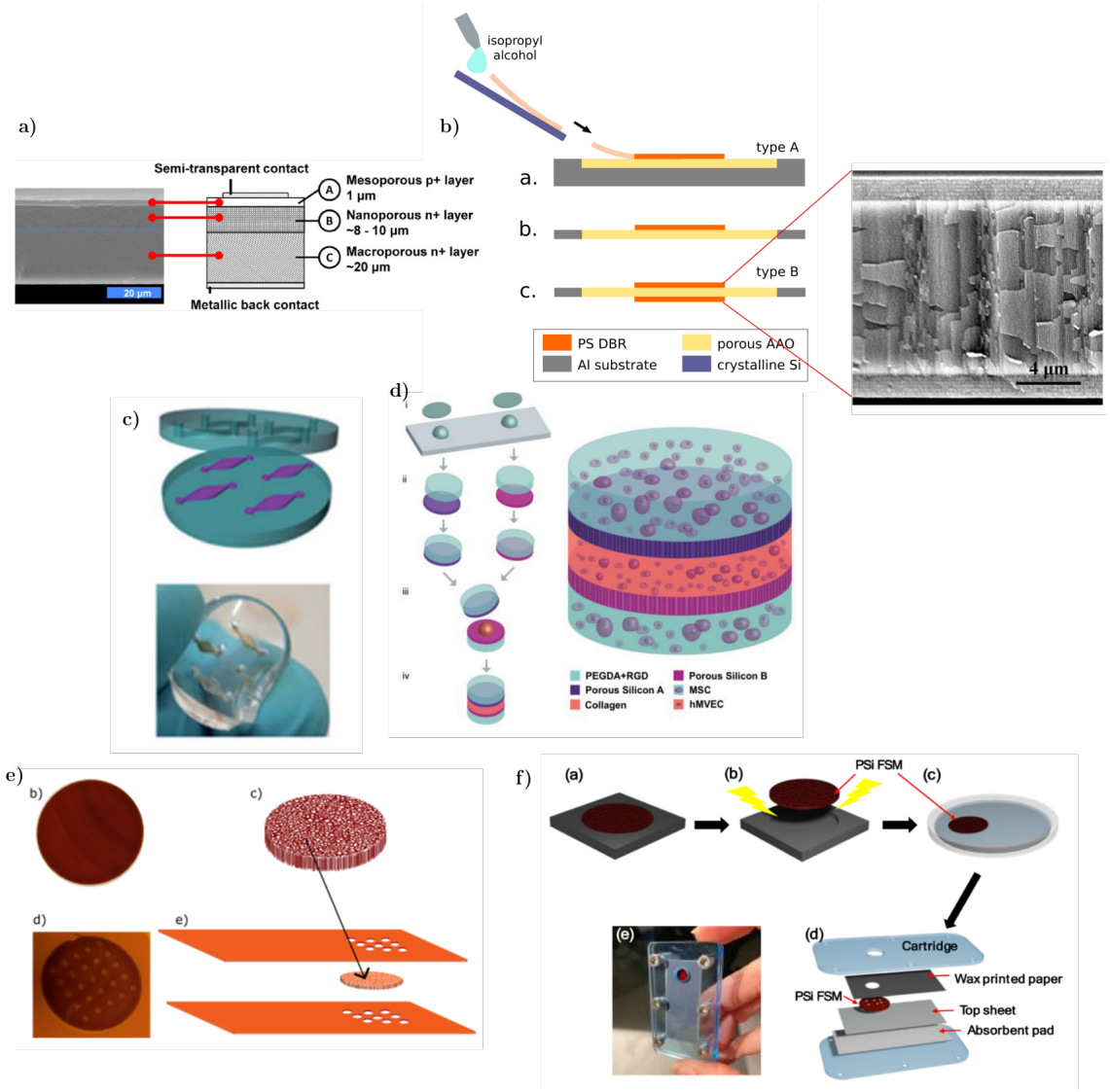


Figure 5.11: Examples of integration strategies for freestanding porous silicon membranes (PSiMs). (a) Electrical integration through metal deposition and substrate reuse. Taken from [240]. (b) Composite anodic aluminium oxide (AAO)–PSi hybrid membrane fabricated using capillary attachment. Taken from. Taken from [243]. (c) Microfluidic integration by casting PDMS on top of a still-attached PSi film, which serves as mechanical support during detachment. Taken from [244]. (d) Transfer of detached PSiMs onto various substrates, including gold, glass, or PEGDA matrices. Taken from [254]. (e) Flow-through microfluidic configuration for in situ decoration of large-pore PSiMs with gold nanoparticles (Au NPs), enhancing optical sensing performance. Taken from [255]. (f) Porous silicon integrated onto paper substrates for rapid, low-cost diagnostic testing. Taken from [256].

5.2.1.2 Self-supported PSiMs

Self-supported porous silicon membranes (PSiMs) were developed to meet the demand for mechanically robust structures with high optical quality [258]. Conventional freestanding or through-wafer membranes often fail to satisfy these requirements, as they typically exhibit strong spatial anisotropy and pronounced porosity gradients. In the self-supported fabrication approach, microfabrication techniques are employed to define cavities within the silicon substrate either before or after the electrochemical etching process. Depending on the doping level and type of the silicon wafer, either wet or dry etching methods can be used to create these support cavities.

Figure 5.12 illustrates a representative process used for the fabrication of self-supported porous silicon membranes (PSiMs) based on wet etching of a standard silicon wafer. (a–b) Both sides of the wafer are first coated with silicon nitride (Si_3N_4) and covered with a photoresist layer. (c–f) The Si_3N_4 layers are then patterned through standard photolithography followed by buffered oxide etching (BOE). (g) The exposed regions are etched in potassium hydroxide (KOH) to form a cavity, leaving only a thin silicon layer, typically a few micrometres thick, at the bottom. (h) The remaining silicon nitride is subsequently removed by BOE. (i) Finally, electrochemical anodization is performed to generate the porous silicon structure.

Similar microfabrication workflows have been reported in several studies [259–264], yielding self-supported PSiMs with morphologies comparable to those shown in Figure 5.13a–b.

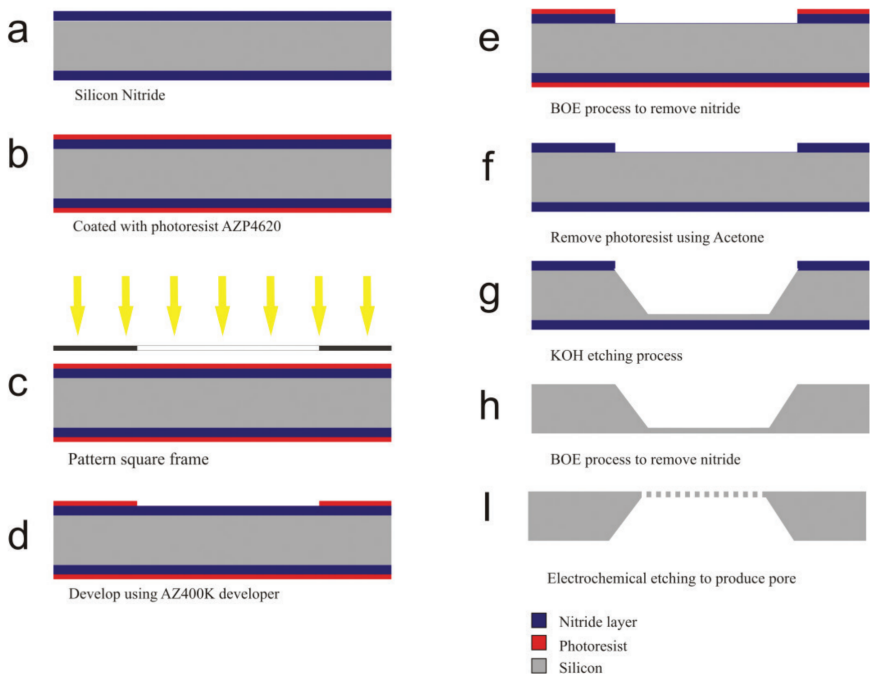


Figure 5.12: Fabrication processes for self-supported PSiMs using combinations of dry, wet and electrochemical etching on standard silicon substrates, adapted from [262]

An alternative to wet etching for cavity formation is the introduction of a sacrificial porous silicon layer on the backside of the wafer [265]. In some fabrication schemes, an additional dry etching step is applied after anodization to produce a fully porous membrane [266]. This step is necessary because, following electrochemical etching, typically only a limited number of pores reach the backside of the membrane. Once the first channels penetrate through, the electrical current preferentially flows along these low-resistance pathways, effectively halting further pore propagation and preventing complete porosification [267].

In other fabrication approaches, the silicon wafer is first anodized over a defined area and thickness, after which the membrane is opened from the backside. This can be accomplished using dry etching techniques, most commonly Deep Reactive Ion Etching (DRIE) [258, 268–272], as illustrated in Figure 5.13c. For such processes, it is often advantageous to oxidize the porous silicon layer prior to etching, as oxidation can lower the etch rate of the porous matrix and promote a more uniform membrane structure. Alternatively, mechanical thinning or backside grinding has also been employed to open the membrane [273–277].

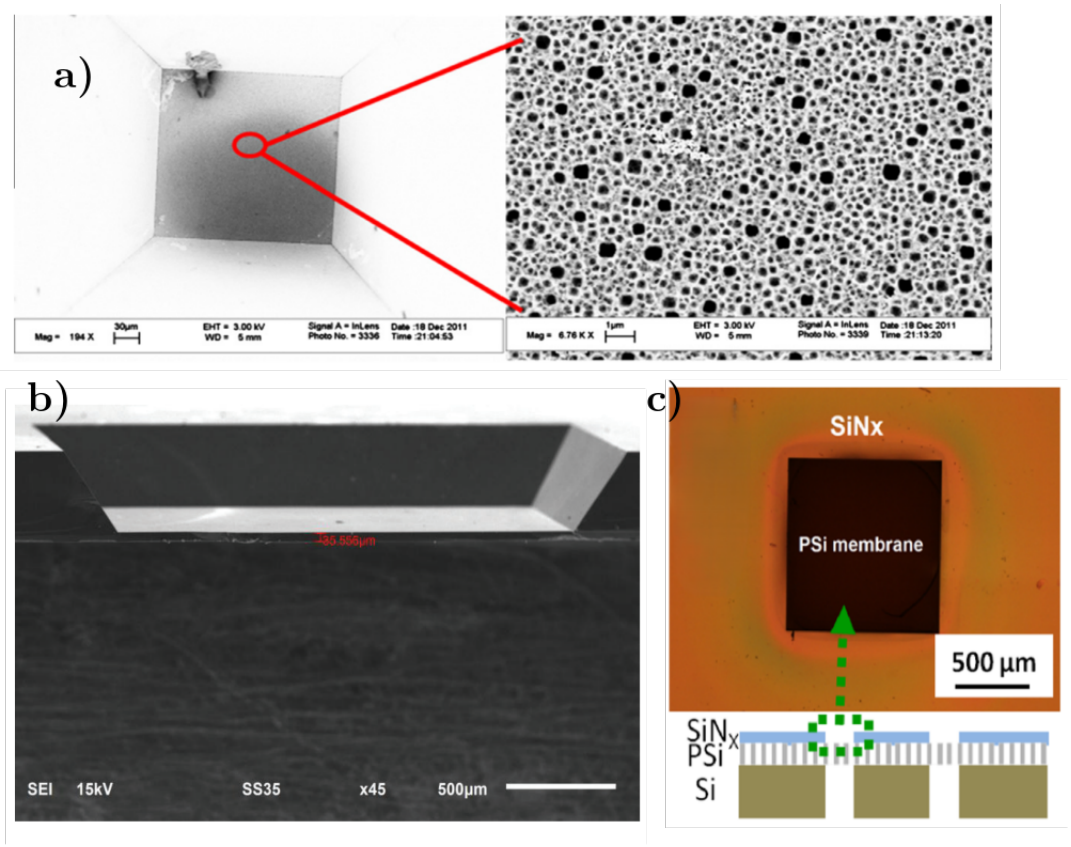


Figure 5.13: Examples of self-supported PSiMs(a) Top view of a mesoporous membrane created via wet etching reprinted from [278]; (b) Top view of a PSiMs created via wet etching, reprinted from [262]; (c) Top view and schematic view of a PSiMs fabricated using DRIE after anodisation, reprinted from [268].

In certain studies, Silicon-On-Insulator (SOI) substrates are preferred over conventional bulk silicon, as the thin top silicon layer, often referred to as the device or active layer, acts directly as the membrane. The underlying handle layer (the thick silicon support) is selectively removed using wet or dry etching techniques prior to electrochemical anodization [279–281], as illustrated in Figure 5.14.

In the process shown, a single nanopore is fabricated within the device layer of the SOI wafer. (a–d) A Si_3N_4 masking layer is deposited and patterned, followed by KOH wet etching of the handle layer. (e) The intermediate SiO_2 layer is then etched to expose the top silicon. (f–h) A new Si_3N_4 mask is deposited and patterned on the front side of the wafer. (i–j) This mask is further defined to localize the pore position. (k) A pre-patterning step using KOH wet etching defines the initial pore geometry. (l) Finally, electrochemical etching is performed to form the single nanopore.

Comparable processes have been used to produce membranes containing multiple nanopores [282, 283]. Moreover, the front-side KOH pre-patterning step is commonly applied for the fabrication of macroporous structures, as it promotes highly uniform pore shapes and sizes.

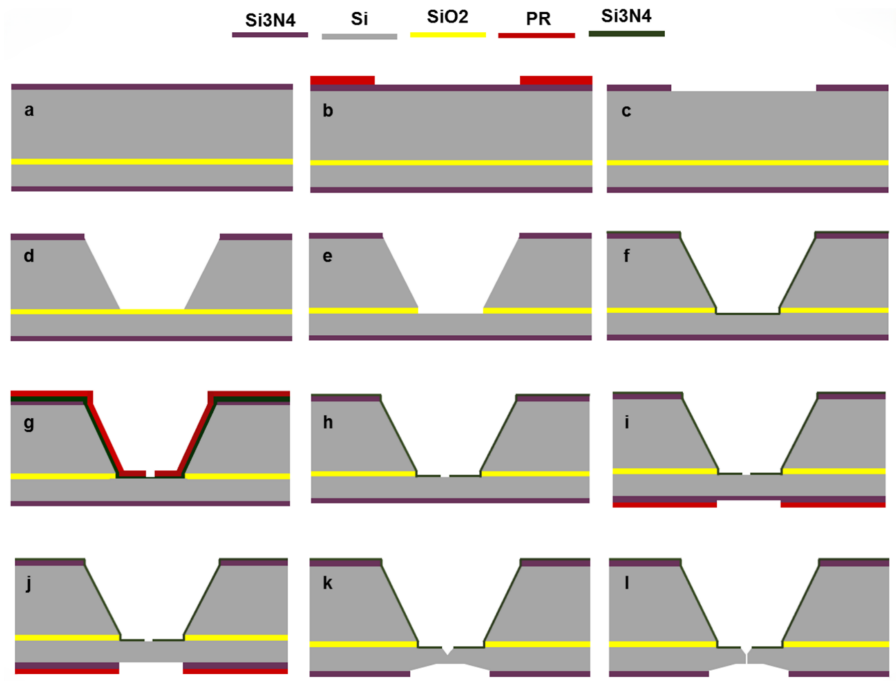


Figure 5.14: Fabrication processes for self-supported PSiMs using combinations of dry, wet and electrochemical etching on SOI substrates, reprinted from [279]

The integration of self-supported porous silicon membranes (PSiMs) into functional devices is generally more straightforward than that of freestanding PSiMs. Their enhanced mechanical stability and ease of handling allow their incorporation into reusable, custom-built setups that can include fluidic chambers, microchannels, and electrodes [259, 269, 270, 274, 275, 283]. For device-level integration, polydimethylsiloxane (PDMS) is often employed as a flexible and conformal sealing material [258, 260, 261, 268]. Other compatible substrates include glass slides [284], carbon-paper electrodes [273], and poly(methyl methacrylate) (PMMA) holders [263, 264]. Self-supported PSiMs can also function as support substrates onto which microdevices or functional layers are transferred [265].

Hybrid PSi structures have been developed by incorporating additional materials into the porous matrix. Examples include the chemical vapor infiltration of graphene [276] and the growth of carbon nanotubes (CNTs) via thermal chemical vapor deposition [285]. Metals can likewise be integrated within the porous

framework to enhance electrical or catalytic performance. For instance, platinum was deposited by immersion plating on PSi to act as a catalyst for micro fuel cell electrodes. When applied before backside membrane opening, the Pt layer simultaneously served as an etch-stop barrier during plasma processing [286, 287]. Other metallization strategies for improving electrode conductivity include the sputtering or electrodeposition of titanium, nickel, or gold layers [288].

5.2.1.3 Lateral PSiMs

To further enhance device integration, lateral porous silicon membranes (PSiMs) have been developed using Silicon-On-Insulator (SOI) substrates, in which the pores are oriented parallel to the wafer surface [229]. The process introduced by Leïchlé and co-workers involves four main steps: (1) microchannels surrounding the future membrane are defined by dry etching; (2) a Cr/Au working electrode is deposited and patterned where anodization will begin; (3) lateral porous silicon is formed by electrochemical etching, using the patterned metal as the anode and a platinum wire as the cathode; and (4) the Cr/Au layer is removed, fluidic ports are opened by sandblasting, and the device is sealed through anodic bonding.

The resulting lateral PSiM, shown in Figure 5.15 a), exhibits horizontally aligned pores. This orientation is governed by the electric field lines established during anodization: since the metal electrode is placed on the vertical sidewall, the current flow, and thus pore propagation, runs parallel to the substrate surface.

A subsequent refinement of the technique was proposed by He *et al.* [289], who employed ion implantation to predefine the region in which the porous layer develops. This approach enables more precise localization of the membrane within the SOI device layer but limits the achievable membrane thickness, since the anodized region cannot extend beyond the depth of the implanted dopant profile.

Building on these concepts, Vasconcellos *et al.* [290] introduced a powerful extension of the method that allows the fabrication of multiple porous silicon membranes exhibiting different pore morphologies on a single microfluidic chip. Their strategy relies on selective ion implantation to locally modulate the dopant concentration in the SOI device layer prior to anodization. Because pore size and porosity in PSi strongly depend on doping level, this enables membranes with distinct structures, such as flow-over and flow-through architectures, to be produced simultaneously during a single anodization step. Using this approach, pore sizes between 25–50 nm and porosities from 65% to 90% were achieved within the same device as shown in Figure 5.15 b), significantly simplifying fabrication and enabling compact lab-on-chip platforms combining separation, filtration, and sensing functionalities.

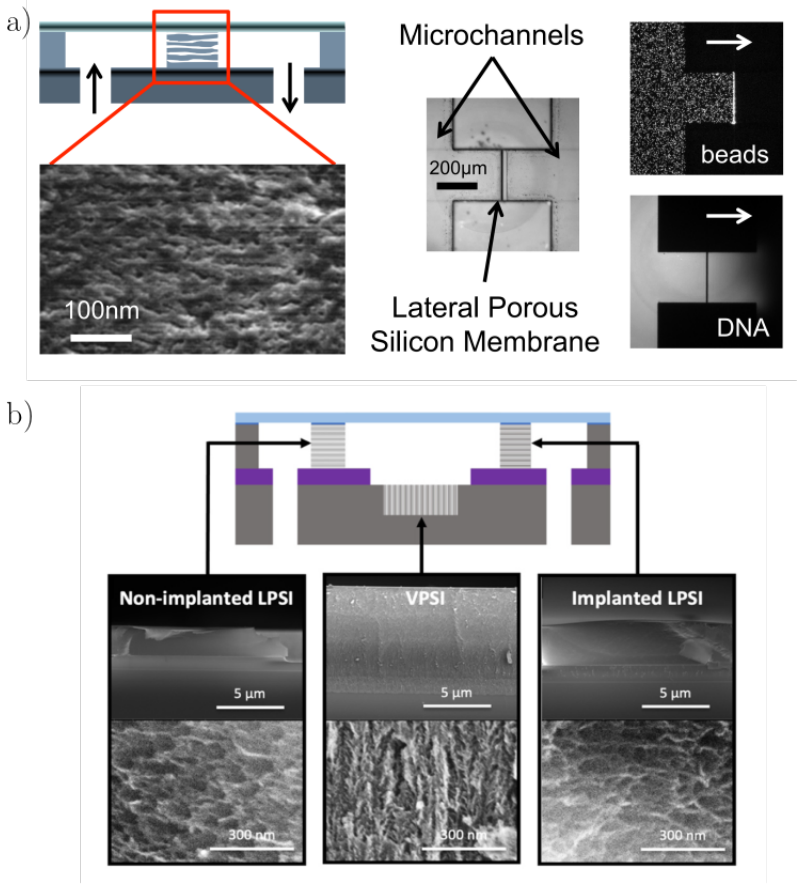


Figure 5.15: a) Schematic view and SEM images from a lateral PSiM, reprinted from [229]. In terms of physical properties, the obtained membrane is about 20 μm-high and the pores are 10 μm-long. b) SEM images of the cross-section of different porous silicon elements fabricated with a single anodization step (1:1 HF:ethanol, 225 mA/cm2, 60 s) on a 2 μm SOI chip. Taken from [290].

5.2.1.4 Microfabricated porous membranes

Porous silicon membranes (PSiMs) can also be fabricated without relying on electrochemical etching. To obtain membranes with highly defined geometries, a combination of photolithography and reactive ion etching (RIE) is often employed [232, 291–294]. This approach offers the advantage of precisely controlling both the pore diameter and spatial periodicity through the photolithographic pattern, as illustrated in Figure 5.16a. By combining electron-beam lithography with deep reactive ion etching (DRIE), pore diameters as small as 130 nm have been achieved [295–297].

In addition to conventional photoresist masks, block copolymers have been

utilized as self-assembled templates, where arrays of iron oxide nanodots serve as nanoscale etch masks during DRIE [298, 299]. However, this technique tends to produce a high density of structural defects, leading to variations in pore ordering and diameter uniformity.

Directly patterning channels into silicon substrates is often a highly time-consuming process, particularly when electron-beam lithography is employed. This limitation has motivated the development of alternative fabrication approaches. One such method involves the spontaneous formation of pores during the rapid thermal annealing (RTA) of amorphous silicon films. The resulting structures, referred to as porous nanocrystalline silicon (pnc-Si) membranes, form as nanocrystals nucleate and grow within the amorphous silicon matrix during annealing [232, 300]. As illustrated in Figure 5.16b, this technique enables the fabrication of extremely thin, mesoporous membranes with well-defined and uniform pore networks.

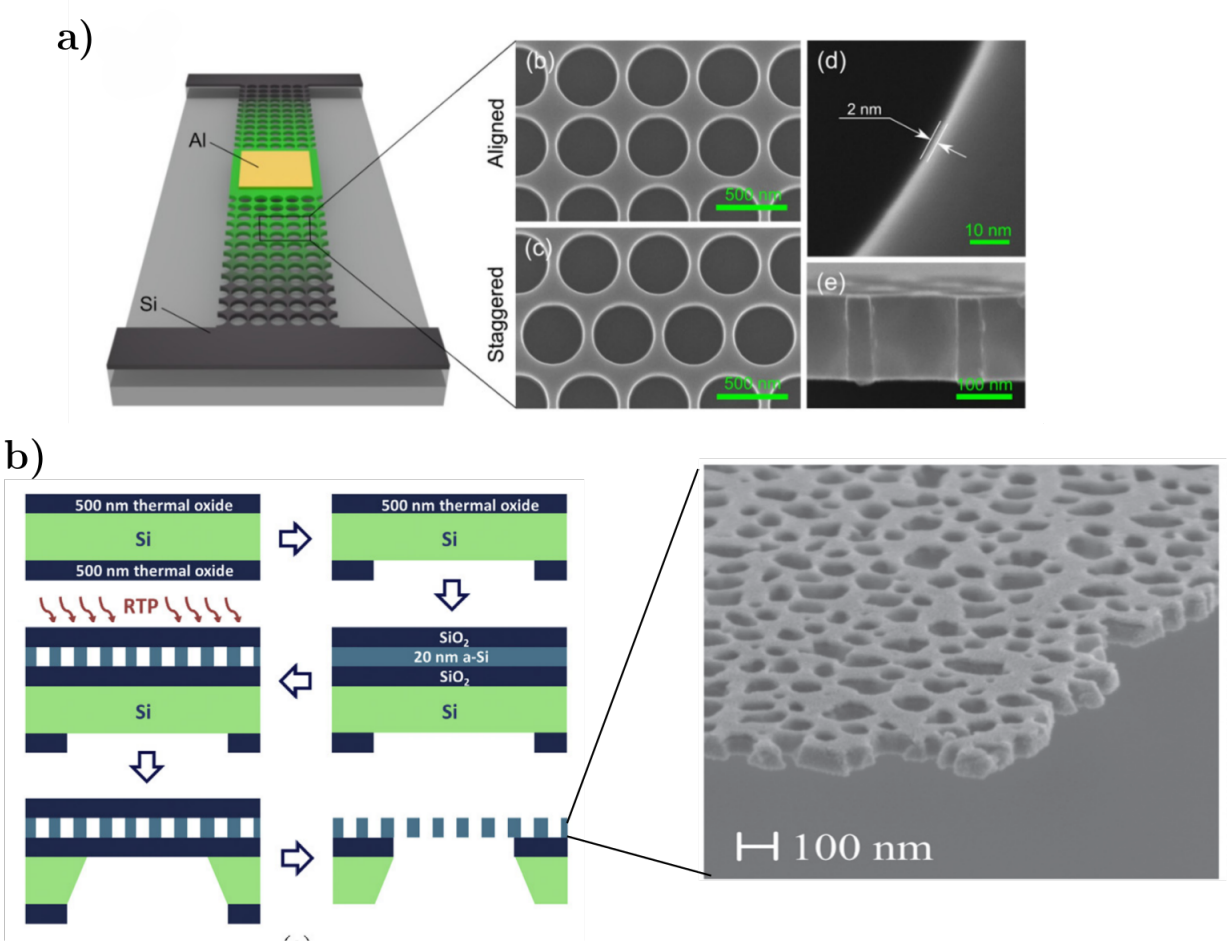


Figure 5.16: Microfabricated PSiMs: (a) macroporous membrane prepared using standard microfabrication techniques like e-beam lithography and RIE, reprinted from [296]; (b) pnc-Si membrane, reprinted from [232].

A final category of microfabricated porous membranes, often regarded as a hybrid form of PSiM, is the nanoporous silicon nitride (Si_3N_4) membrane. These membranes are fabricated using similar microfabrication techniques to those applied for plain silicon membranes, including optical lithography and dry etching [231, 299, 301, 302]. Alternatively, focused ion beam (FIB) milling can be employed to directly perforate nanoscale holes through the membrane [303, 304]. Hybrid configurations have also been demonstrated, in which nanoporous Si_3N_4 membranes are combined with porous nanocrystalline silicon (pnc-Si) layers, where the latter acts as a structural template for the dry etching of the nitride film [232, 305, 306].

5.2.2 Properties

The unique appeal of porous silicon (PSi) lies in its ability to modify the intrinsic properties of bulk silicon through the introduction of nano- and microscale porosity. These properties are highly tunable, primarily by adjusting the structural characteristics of the porous matrix. By carefully controlling key morphological parameters, such as porosity, pore diameter, and layer thickness, the mechanical, chemical, electrical, thermal, and optical properties of PSi can be tailored to specific applications. Further modification is possible by detaching the PSi layer from the bulk substrate, thereby eliminating substrate-induced effects. Although substrate removal does not alter the intrinsic characteristics of the porous silicon itself, it can significantly influence the overall performance of PSi-based devices.

In the context of this work, the discussion will focus primarily on the mechanical and chemical properties of PSi and PSi membranes (PSiMs), as these are the most relevant to their fabrication and stability. Other aspects, such as mass transport and optical and optoelectronic properties, are not addressed here but have been extensively reviewed.

5.2.2.1 Mechanical properties

Monocrystalline silicon exhibits exceptional mechanical performance, characterized by a Knoop hardness of approximately 8.5 GPa (compared to 6.5 GPa for steel) [307], a high yield strength near 7 GPa, and a relatively low fracture toughness of about 1 MPa $\cdot$ m$^{1/2}$ [308]. It should be noted that single-crystal silicon possesses cubic elastic symmetry and therefore exhibits orientation-dependent mechanical properties. Porosification, however, significantly alters these properties, primarily depending on three morphological parameters: porosity, pore size, and layer thickness. Understanding and optimizing the mechanical response of PSi and PSi membranes (PSiMs) is crucial for reliable device fabrication, as deformation or cracking can affect both chemical reactivity and device durability [309–311].

The stiffness of PSi is commonly characterized by its Young's modulus. However, because monocrystalline silicon is elastically anisotropic and electrochemically etched pores are typically aligned along a preferential direction, porous silicon is more rigorously described as an orthotropic material. Consequently, the Young's modulus is direction-dependent (E_x, E_y, E_z), although many experimental studies report an effective modulus corresponding to the loading direction considered. In all cases, the stiffness decreases with increasing porosity and depends on pore geometry, particularly branching. Experimental and FEM-based analyses consistently describe this dependence by a power-law relationship [312]:

$$E_i = E_{i,0}(1-\phi)^{m_i}, \tag{5.7}$$

where ϕ is the porosity, i denotes the principal material direction, and m_i is a structural parameter generally ranging between 1 and 3 depending on pore morphology [299, 313, 314].

Residual mechanical stress is another key consideration. Tensile stress accumulates during electrochemical etching and is partially relieved upon membrane detachment, often resulting in membrane bending [314, 315]. Typical residual stresses in PSi-based and related membranes are on the order of 10–100 MPa [299].

Finite element modeling and experimental testing show that the mechanical strength and deflection behavior of PSiMs strongly depend on thickness and membrane area: thinner membranes experience higher deflection and Von Mises stress under pressure, while smaller membranes withstand greater loads [303, 316, 317]. Mechanical robustness can be improved by reducing pore size and overall porosity, design strategies verified experimentally on both pnc-Si and nanoporous Si_3N_4 membranes [299, 303].

5.2.2.2 Chemical stability in ionic aqueous solutions

The chemical stability of porous silicon (PSi) and porous silicon membranes (PSiMs) in aqueous and ionic environments is a critical factor for their long-term use in sensing and electrochemical applications. Freshly etched PSi is highly reactive due to the presence of surface hydrides and rapidly oxidizes upon contact with water. This oxidation leads to the formation of a thin silicon oxide (SiO_2) layer, which subsequently undergoes hydrolytic dissolution according to the following reactions:

$$Si + 2H_2O \rightarrow SiO_2 + 2H_2 \tag{5.8}$$

$$SiO_2 + 2H_2O \rightarrow Si(OH)_4 \tag{5.9}$$

This oxidative–hydrolytic process is strongly pH-dependent: it proceeds slowly under acidic or near-neutral conditions but accelerates significantly in alkaline or highly ionic solutions [318]. At physiological pH, the dissolution rate of mesoporous silicon is relatively low, although prolonged exposure to electrolyte solutions can still induce gradual degradation of the porous framework. The dissolution behaviour of porous silicon depends not only on porosity (and thus internal surface area and pore-wall thickness), but also critically on the surface state, i.e., whether the material is freshly etched (hydride-terminated) or pre-oxidised/treated. In air-aged porous silicon films (stored in air for less than one week prior to testing), Anderson *et al.* [318] observed a strong porosity dependence at pH 7 and 25 °C: medium-porosity films (62%) showed limited dissolution over 24 h (6.9 ± 0.9%), whereas high- and very-high-porosity films (83% and 88%) exhibited substantially greater dissolution, reaching 61.3 ± 7.6% and 45.5 ± 3.3%, respectively, over the

same period. In contrast, for *native* (unoxidised) porous silicon, much faster initial degradation can occur because the hydride-terminated surface is directly attacked and concurrently oxidised in aqueous media. For example, Wang *et al.* [319] reported that native mesoporous silicon particles (porosity ∼70%) in Tris buffer (pH 7.2, 37 °C) dissolved extremely rapidly, with ∼52% mass loss occurring before the first 5 min sampling point, accompanied by hydrogen bubbling, while more oxidised (thermally treated) samples dissolved more slowly and approximately linearly over time. These observations indicate that the "fresh" hydride-terminated state represents a kinetic extreme with rapid initial dissolution, whereas air-aged or oxidised porous silicon exhibits slower, cumulative degradation, with the magnitude strongly amplified at high porosity.

To enhance stability, several surface modification strategies have been explored for both PSi layers and PSiMs. Among these, thermal oxidation [320], hydrosilylation [321], atomic layer deposition (ALD) [322], and thermal hydrocarbonization [323] have shown varying degrees of success. However, not all methods are suitable for thin freestanding membranes. For instance, thermal oxidation can cause volumetric expansion of the SiO_2 network, leading to warping or fracture of mesoporous PSiMs [272].

To mitigate such issues, Baraket et al. [272] demonstrated that a combination of standard wet chemical treatments (RCA-1 and RCA-2) followed by silanization significantly improved chemical stability in ionic aqueous environments, while preserving both structural integrity and surface reactivity. Other stabilization strategies, such as thermal hydrocarbonization [324], silanization [325], or hydrosilylation [254], have also been successfully applied to PSiMs. While hydrocarbonized surfaces initially reduce wettability and reactivity, simple pre-incubation in electrolyte or physiological solutions was shown to restore both hydrophilicity and chemical stability [324].

5.2.3 Applications

The primary applications of porous silicon membranes (PSiMs) can be broadly classified into five domains: microfluidics, biomedical applications, sensing, energy conversion, and electronics. Table 5.3 summarises representative PSiM-based devices reported in the literature across these fields. The widespread use of PSiMs stems from their unique combination of properties, including tunable porosity, high surface area, and compatibility with standard silicon processing technologies. However, several intrinsic characteristics can also pose challenges to practical implementation. In particular, the limited mechanical stability of PSiMs remains a significant obstacle to their large-scale integration, highlighting the need for a detailed understanding of the parameters governing their structural robustness.

Microfluidic applications of porous silicon membranes (PSiMs) primarily exploit

their structural characteristics. The most common use is in filtration, enabled by the open-ended and highly ordered pore structure. Since the pore diameter can be precisely tuned during fabrication, PSiM-based filters typically operate via size-selective separation [229, 261, 289, 326, 327]. In these systems, mesoporous membranes are most often employed, allowing only small, nanometre-scale species to permeate through the membrane. In addition to size exclusion, charge-based filtration can also be achieved, as PSiMs exhibit ion permselectivity in charged electrolyte environments when an external electric field is applied [327].

Porous silicon membranes (PSiMs) are widely explored in the biomedical field owing to their biocompatibility and controllable surface chemistry. They are primarily employed as scaffolds for cell culture and in tissue engineering, where the tunable porosity facilitates nutrient transport and cell adhesion. Additional biomedical applications include drug delivery patches [253], hemodialysis membranes [328], DNA purification devices [269, 270], and supports for pore-spanning lipid membranes used in membrane biophysics and biosensing studies [329–335].

Sensing and diagnostics represent one of the most prominent application areas for porous silicon membranes (PSiMs), particularly for mesoporous structures. Their suitability arises from the combined influence of their physical, optical, mass transport, and surface chemical properties. In such membranes, analyte solutions can flow through the porous network, while target molecules are selectively retained, either by size exclusion or by specific interactions with the pore walls. These processes can be monitored through measurable changes in the optical or electrical response of the membrane.

PSiM-based sensors are generally classified into two categories: gas sensors and biosensors. Gas sensors are typically employed for detecting solvent vapours and volatile organic compounds [336–338], whereas biosensors leverage the high surface area and tunable pore chemistry of PSiMs for the specific detection of biomolecules and pathogens.

The unique electrical properties and intrinsic permselectivity of porous silicon (PSi) have also inspired its use in various energy-related applications. A recurrent example is the employment of PSi membranes (PSiMs) as the base material for microfuel cells [339]. PSiMs have further been investigated as anodes for lithium-ion batteries, offering several advantages: the formation of a $Li_{22}Si_5$ alloy enables a very high specific capacity; they exhibit a low discharge potential; and by tailoring the structural properties, they can sustain numerous charge–discharge cycles. Additionally, the abundance and low cost of silicon make these membranes economically attractive for large-scale production [340, 341]. A comprehensive overview of PSiM-based anodes for lithium-ion batteries has been presented by Luais *et al.* [342]. Beyond these applications, the ion transport and permselective characteristics of PSiMs also make them promising candidates for use as ion-

exchange membranes. This aspect will be discussed in more detail in Section **??**.

The final domain of application considered in this section is electronics. The inherently low thermal conductivity of porous silicon membranes (PSiMs) makes them suitable substrates for thermal microdevices, such as micro-heaters [265, 284, 343]. PSi has also been extensively employed for radio-frequency (RF) isolation, either as a thin film or in membrane form [227]. Its interest in RF applications arises from its reduced effective resistivity and permittivity compared to bulk silicon, which translate into lower electromagnetic losses, diminished crosstalk, and significantly weaker signal harmonic distortion. However, the same low thermal conductivity that benefits thermal insulation can be disadvantageous in RF circuits, as it promotes self-heating of the integrated components. Additional microelectronic applications include optoelectronic devices, such as wavelength modulators [344] and light-emitting capacitors [249].

Table 5.3: Recent advances in the application fields of porous silicon membranes

Application field	**Membrane characteristics**	**Membrane thickness**	**Detailed application**	**Ref.**
Notes: C, F, FT, L, M, S = Commercial, Freestanding, Full Thickness, Lateral, Microfabricated, Self-supported.				
Microfluidics	M, mesoporous	15 nm	Size and charge selective filtration	[345]
	S, mesoporous	5 µm	Filtration of small biological molecules from mixtures	[261]
	L, mesoporous	10–20 µm	Size and charge selective filtration	[229, 289, 326, 327, 339]
	S, macroporous	215 µm	Electro-osmotic pump	[274]
Medical	F, macroporous	4.29 µm	Drug delivery patch and optical monitoring of drug release	[253]
	M, macroporous	50–60 nm	Culture of human umbilical vein vascular endothelial cells	[306]
	M, macroporous	500 nm	Reconstruction of the intestinal barrier of a trout via cell culture	[301]
	M, mesoporous	75 nm	Small-format hemodialysis with high toxin elimination capabilities	[328]
	M, macroporous	30 µm	Transmigration assay for cancer cells	[292]
	F, mesoporous	276 µm	Scaffold for culture of oral mucosal epithelial cells	[325]
	C, macroporous	1–10 µm	Support for the investigation of pore-spanning lipid membranes	[329–334, 337]
	M, mesoporous	30 nm	Cell culture of endothelial cells	[231]
	F, macroporous	12–15 µm	Tissue scaffold integrated with cell-laden hydrogel biomaterials	[254]
	M, macroporous	5 µm	Lung-on-chip microfluidic device	[346, 347]
	M, macroporous	10 µm	Culture of intestinal epithelial cells	[293]
	S, macroporous	130–150 µm	Mechanical cell lysis and DNA isolation	[269, 270]
	F, mesoporous	4–5 µm	Implantable scaffold for cell culture	[324]
	F, mesoporous	10–25 µm	Porous-silicon biomembrane for lung-on-a-chip; supports epithelial/endothelial co-culture	[348]
Sensing	S, macroporous	$\leq$50 µm	Electrophysical NO_2 gas detector	[266]

Continued on next page

Application field	Membrane characteristics	Membrane thickness	Detailed application	Ref.
Notes: C, F, FT, L, M, S = Commercial, Freestanding, Full Thickness, Lateral, Microfabricated, Self-supported. (continued)				
	F, mesoporous	1.7 µm	Silver-modified sensor for SERS-based detection of miRNA	[236]
	L, mesoporous	10 µm	Interferometric transducer for solvent detection	[338]
	F, mesoporous	1.6 µm	Optical detection of ethanol vapour	[336]
	S, mesoporous	2.5 µm	Impedance spectroscopy of the formation of a lipid membrane	[280, 281]
	F, mesoporous	29 µm	Electrostatic isopropanol vapour sensor	[337]
	F, meso-/macroporous	5.5 µm	Optical detection of Bovine Serum Albumin	[349]
	F, mesoporous	17–21 µm	Optical detection of dissolved gas concentrations in liquids	[350]
	M, mesoporous	50 nm	Nanopore-based sensing of DNA translocation	[305]
	S, mesoporous	20 µm	Multi-assay solvent vapour optical detection	[351]
	F, mesoporous	870 nm	Multianalyte detection using silver-decorated sensors	[245, 246]
	M, mesoporous	15 nm	Optical detection of Bovine Serum Albumin permeation	[352]
	F, meso-/macroporous	4.5 µm	Electrochemical detection of MS2 bacteriophage	[248]
	F, meso-/macroporous	4.5 µm	Label-free electrochemical detection of bacterial toxin	[353]
	M, meso-/macroporous	50 nm	Electrochemical detection of ion-transfer across the PSiM	[303]
	C, macroporous	475 µm	3D liquid core sensor array	[354]
	S, mesoporous	340 nm	DNA translocation detection	[282, 283]
	M, macroporous	50 µm	Immunoassay for specific leukocyte subsets	[294]
	S, macroporous	1–3 µm	Transmembrane proteins sensing	[278]
	C, meso-/macroporous	10–15 nm	DNA translocation detection	[355–357]
	F, mesoporous	19.9 µm	Optical aptasensors with multiple target-binding sites	[358]
	S, mesoporous	4–15 µm	Optical detection of enzyme adsorption and streptavidin binding	[258, 268, 359]

Continued on next page

Application field	Membrane characteristics	Membrane thickness	Detailed application	Ref.
Notes: C, F, FT, L, M, S = Commercial, Freestanding, Full Thickness, Lateral, Microfabricated, Self-supported. (continued)				
	F, micro/macroporous	10–30 µm	Wide-gap absorber for solar cells	[240, 242]
	S, mesoporous	≤70 µm	Implantable glucose biofuel cell	[272]
	S, mesoporous	5–20 µm	Ion-exchange membrane for micro fuel cells	[360]
	S, mesoporous	50 µm	Anion exchange membrane for glucose/O_2 micro fuel cell	[259]
	S, macroporous	125 µm	Membrane–electrode assembly for H_2/air-fed micro fuel cells	[273]
	S, macroporous	230 µm	Microfluidic electric generator	[274]
	S, mesoporous	13 µm	Monolithic Si electrode for micro fuel cells	[287, 361]
	F, macroporous	50 µm	Anode for lithium-ion batteries	
	F, mesoporous	200 µm	Anode for lithium-ion batteries	[362]
	M, macroporous	5 µm	Electrode grids for micro fuel cells	[288]
	S, micro/macroporous	210 µm	High-conductivity electrodes for micro fuel cells	[276]
	M, macroporous	280 µm	Ion-exchange membrane for photoelectrochemical cell	[360]
	S, macroporous	50 µm	Electrode for methanol micro fuel cell	[285]
	S, macroporous	60 µm	Cathode for self-breathing micro fuel cells	[271]
	FT, meso-/macroporous	500 µm	Membrane–electrode assembly for hydrogen/oxygen micro fuel cells	[234, 235]
	S, mesoporous	100 µm	Proton exchange membrane for methanol micro fuel cells	[263, 264]
	S, meso/macroporous	80–100 µm	Pervaporation membrane for methanol vapour-fed micro fuel cells	[260]
	F, mesoporous	28 µm	Freestanding porous Si membrane anode for lithium-ion batteries; specific capacity ≃1870 mA h g^{-1}, Coulombic efficiency ≃ 94% after 80 cycles	[363]
Electronics	F, mesoporous	46 µm	RF insulating and supporting substrate for microfabricated inductors	[227]
	S, mesoporous	10 µm	MEMS-based superheated loop heat pipes	[284]

Continued on next page

Application field	**Membrane characteristics**	**Membrane thickness**	**Detailed application**	**Ref.**
Notes: C, F, FT, L, M, S = Commercial, Freestanding, Full Thickness, Lateral, Microfabricated, Self-supported. (continued)				
	M, macroporous	600 nm	Thermal management device	[343]
	S, mesoporous	300 µm	Thermal isolation layer for high-temperature micro-hotplates	[265]
	F, macroporous	2.46 µm	Flexible optoelectronics device	[249]
	F, mesoporous	1.92 µm	Modulator for photodetector	[251, 252]
	FT, mesoporous	380 µm	CMOS-compatible RF insulating substrate	[236]

5.2.4 Discussion and outlook

The literature reviewed above demonstrates that porous silicon can be reproducibly fabricated, chemically functionalized, and integrated into microfabricated electrochemical devices. In most reported systems, however, ion transport is achieved either through infiltration of polymer electrolytes (e.g., Nafion) or through surface functionalization aimed at proton conduction in fuel cells. In these configurations, the porous silicon matrix primarily acts as a mechanical scaffold, while the ion-exchange functionality arises from grafted ionic groups or infiltrated polymers. The dominant transport mechanism is therefore bulk proton conduction rather than permselective ion transport under concentration gradients.

For salinity-gradient energy conversion, such as reverse electrodialysis (RED), the requirements differ fundamentally. Rather than maximizing proton conductivity, the membrane must:

- Sustain a concentration gradient,
- Exhibit high counter-ion permselectivity,
- Minimize co-ion leakage,
- Operate under neutral salt solutions (e.g., NaCl), rather than acidic environments.

None of the fuel-cell-oriented porous silicon membranes reviewed above were designed with these constraints in mind.

A key parameter that remains largely unexplored in this context is electrical double layer (EDL) overlap inside nanoscale pores. In mesoporous structures with pore diameters between 20 and 100 nm, the Debye length in typical saline solutions (approximately 1 nm in 0.1 M NaCl) is much smaller than the pore radius. As a result, the electrical double layer occupies only a thin region near the pore wall, while the pore core remains essentially electroneutral. Under these conditions, ion transport is primarily diffusive and bulk-like rather than surface-charge dominated, and permselectivity remains weak unless a high density of fixed ionic groups is introduced.

In contrast, when pore diameters approach only a few Debye lengths (typically $\leq$10 nm under moderate ionic strength), the electrical double layers originating from opposite pore walls overlap. In this nanofluidic regime, transport becomes strongly surface-charge controlled: counter-ions dominate within the pore, co-ion exclusion is enhanced, and the membrane can behave as an intrinsically ion-selective medium even without polymer infiltration. This mechanism is well established in anodic aluminum oxide nanofluidic membranes and synthetic nanopores, yet it

has not been systematically exploited in porous silicon for salinity-gradient energy conversion.

Although prior μDMFC studies did not explicitly target EDL overlap, they provide several important insights relevant to RED. First, they confirm that high-aspect-ratio pores extending across hundreds of micrometers can be fabricated reproducibly. Second, they demonstrate that internal surface chemistry within deep porous structures can be controlled through silanization or sulfonation. Third, they establish compatibility with microfabrication processes and monolithic device integration. Notably, reports of improved electrochemical performance in smaller-pore electrodes suggest that reducing pore dimensions enhances interfacial control and transport efficiency, a trend consistent with nanofluidic theory.

Therefore, rather than relying primarily on polymer infiltration, the present work adopts a different design philosophy. The approach is based on:

- Selection of a silicon substrate and doping level optimized for controlled nanoscale pore formation,
- Targeting pore diameters in the regime where EDL overlap becomes significant,
- Exploiting the intrinsic surface charge of oxidized silicon to induce permselectivity,
- Transforming porous silicon from a proton-conducting scaffold into a nanofluidic ion-exchange medium suitable for RED.

The following chapter introduces the rationale behind the selected silicon substrate, including its resistivity, and electrochemical etching behavior, and explains how these parameters enable the fabrication of pores tailored for surface-charge-dominated ion transport.

Chapter 6

Porous silicon characteristics for nRED

6.1 Motivation

The objective of this chapter is to study the ionic characteristic of the pores inside the porous membrane under a concentration gradient. Following the analysis serves as a basis for the criteria of the fabrication process of the porous layer, mainly the current density during the electrochemical etching steps. The analysis requires first to observe the structure of the pores and to then model them numerically based on hypothesis.

6.2 Materials and methods

6.2.1 Porous silicon study and characterisation

6.2.1.1 Porous silicon samples fabrication

Porous silicon (PSi) layers were fabricated by electrochemical anodization of double-side polished, boron-doped silicon wafers (100 orientation, 0.9–1 $m\Omega \cdot cm$, 380–400 µm thick; ZHONGGUI Semiconductor (Yangzhou) Co., Ltd. (China)). Etching was performed in a custom-made single-compartment Teflon cell equipped with a platinum coil counter-electrode and controlled by a Keithley 2460 SMU controlled with predefined script. The electrolyte consisted of a hydrofluoric acid (HF, 49%, Chem-Lab NV) and ethanol mixture in a 3:1 volume ratio.

The anodization process began with the formation of a sacrificial layer, etched at a current density similar to the one used for the porous layer. The etching time were between 60 s to 600 s for current between 300 mA/cm^2 to 3 mA/cm^2

respectively. The layer was then subsequently removed in a 2 M aqueous KOH solution until gas evolution ceased. This preliminary step improved pore uniformity by eliminating the dense transitional layer. After rinsing once with deionised water and twice with 2-propanol, the sample was re-etched at current densities ranging from 3 to 300 mA $\cdot$ cm^{-2}. Most samples were anodized for 60 s, while others were processed for shorter or longer durations to study morphology dependence on etch time. Following anodization, the PSi samples were rinsed three times in 2-propanol and gently dried under a nitrogen flow.

6.2.1.2 PSi characterisation

The PSi samples were initially characterised optically using the SLIM technique, as described in Section 5.1.2.2, to estimate both the porosity and the thickness of the porous layers. Measurements were performed with a fibre-coupled Ocean Optics JAZ spectrometer and a 10 mW halogen light source. The acquired reflectance spectra, which exhibit Fabry–Pérot interference fringes, were analysed by applying a Fourier transform over the 450–850 nm wavelength range.

Morphological characterisation was carried out using a Carl Zeiss Ultra 55 scanning electron microscope (SEM), in both cross-sectional and top-view configurations. The cross-section images were used to verify the membrane thickness, while the top-view images enabled analysis of the pore size distribution. For this purpose, SEM micrographs were processed in ImageJ: after calibrating the image scale and cropping the region of interest, the images were converted to binary format using carefully selected threshold values to best reproduce the original contrast. The *Analyse Particles* tool was then applied to extract the average Feret diameter of the pores, providing an estimate of the pore size for each PSi sample.

6.2.2 Modelling of a single Si pore ionic I–V characteristic

Similarly as done in the development of B. D. Kang et. al. [364], ion transport through charged nanofluidic channels is described within the continuum framework, which provides an adequate approximation for length scales above approximately 5 nm [365, 366]. The electric potential distribution φ inside the pore is governed by the Poisson equation:

$$\varepsilon_0 \varepsilon_r \nabla^2 \varphi = -zF(c_+ - c_-), \tag{6.1}$$

where c_+ and c_- denote the cation and anion concentrations, z the ionic charge number, ε_0 the vacuum permittivity, ε_r the dielectric constant of water, and F the Faraday constant.

The total flux of each ionic species is composed of contributions from diffusion,

electromigration, and convection:

$$\bar{J}\pm = D\pm\left(\mp\frac{zFC_{\pm}}{RT}\nabla\varphi - \nabla C_{\pm}\right) \tag{6.2}$$

where $\bar{J}_+$ and $\bar{J}_-$ represent the cation and anion fluxes, D_+ and D_- are their respective diffusion coefficients, R is the universal gas constant, T is the absolute temperature, and $\bar{u}$ is the velocity vector. The diffusivities of potassium and chloride ions are taken as $D_+ = 1.96 \times 10^{-9}$ m^2/s and $D_- = 2.0 \times 10^{-9}$ m^2/s, respectively. For steady-state transport, the fluxes satisfy the continuity equation:

$$\nabla \cdot \bar{J}_{\pm} = 0 \tag{6.3}$$

The motion of the incompressible electrolyte, driven by both the electric potential and the pressure gradient, is described by the modified Stokes equation together with the continuity condition:

$$0 = \nabla p + \mu\nabla^2\bar{u} + zF(c_+ - c_-)\nabla\varphi \tag{6.4}$$

$$\nabla \cdot \bar{u} = 0 \tag{6.5}$$

where p is the pressure and μ the dynamic viscosity. In Eq. (6.4), the inertial terms of the Navier–Stokes equations are omitted, since the Reynolds number for solution flow through nanopores is typically very small.The last term in eq. (6.4) represents an electrohydrodynamic body-force term, usually important for electroosmotive flow studies. These equations highlight the strong coupling between ionic transport and fluid flow.

The full set of governing equations (6.1)-(6.5) is solved numerically under boundary conditions. At the pore wall, the conditions are specified as:

$$\nabla^{\perp}\varphi = -\frac{\sigma_s}{\varepsilon_0\varepsilon_r}, \quad \bar{J}_{\pm}^{\perp} = 0, \quad \bar{u} = 0 \tag{6.6}$$

where σ_s is the surface charge density and $\perp$ denotes the normal to the wall.

Numerical simulations are carried out using the finite element method. The computational domain is discretized into non-uniform quadrilateral elements, and the Multifrontal Massively Parallel Sparse (MUMPS) direct solver is employed within COMSOL (version 6.2). COMSOL provides a robust platform for modeling coupled physical phenomena governed by ordinary and partial differential equations [367, 368]. In addition to its built-in physics-based modules, it also supports custom PDE implementations, either directly or via weak formulations [368].

Finally, the ionic current through the nanopore, I_{pore}, is obtained by integrating the current density across the pore cross-section:

$$I_{pore} = \int zF(\bar{J}_- - \bar{J}_+)d\bar{A} \tag{6.7}$$

6.2.2.1 Cylindrical pore

We made the following assumption to model the pore: we consider a charged cylindrical nanopore of length L and radius r_{pore}, connecting two identical reservoirs, as illustrated in Figure 6.1. The pore walls carry a uniform and constant surface charge density σ_s. Both reservoirs contain aqueous potassium chloride (KCl) solutions but at different bulk concentrations, c_H and c_L, with $c_H > c_L$. No external pressure gradient is imposed between the two sides. A cylindrical coordinate system (r, z) is adopted, with its origin at the left pore entry.

Chosen parameter ranges used in the simulations are shown in Table 6.1 and the justification for the assumptions and the range of values are given in the following part.

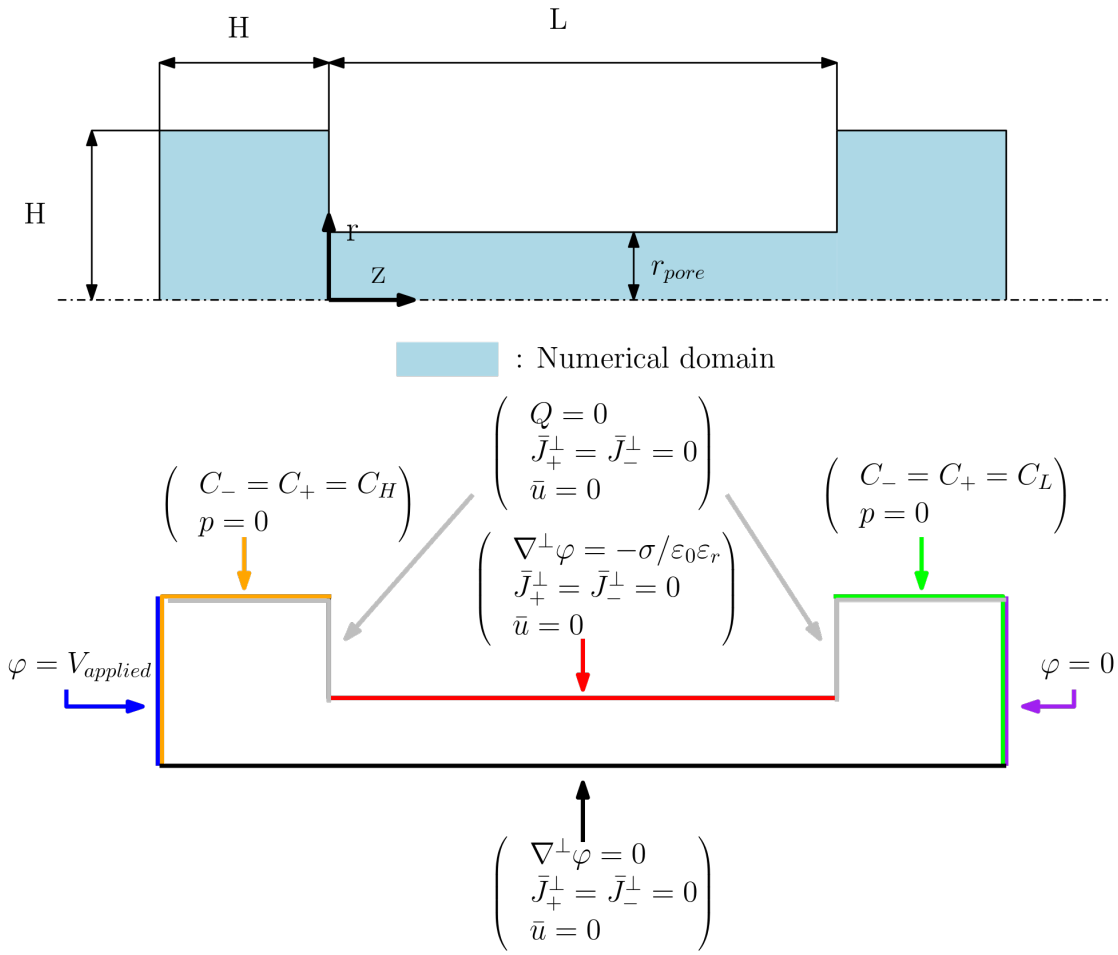


Figure 6.1: Schematic of the numerical domain (top) and the boundary conditions (bottom) used for the numerical simulation.

Table 6.1: Chosen parameter ranges used for the numerical simulations. The number of nodes (1 325 703) was selected as sufficient to ensure convergence.

Parameter	**Metric range**	**Variability**
r_{pore}	15 nm	variable
L	0.8 μm	fixed
H	0.1 μm	fixed
$\sigma_{s,h}$	-4 mC/m^2	fixed
$\sigma_{s,l}$	-0.4 mC/m^2	fixed
C_i	S1: 0.1 mM	fixed
	S2: 1 mM	fixed
	S3: 10 mM	fixed
ϵ_r	80	fixed
D_- (Cl^-)	2.032×10^{-9} m^2/s	fixed
D_+ (K^+)	1.96×10^{-9} m^2/s	fixed

Details of the variable and fixed parameters

The range of values chosen in Table 6.1 is based in the experimental observations in 6.3, convergence issues and the literature.

- The pore size range r_{pore} is based on the SEM observations in Fig. 6.7, which show that the pores obtained with the substrate used in this work vary between 11 nm and 45 nm in diameter

- The length L is fixed based on a trade-off between computation time and the convergence of the electrical potential generated by EDL overlap. On the one hand, simulating the actual membrane thickness, which is on the order of tens of micrometres, would require excessive computation time, and the model length must therefore be reduced. On the other hand, if the pore is too short, the electrical potential induced by the surface charges may not fully develop because of the influence of both pore entrances. This minimal length depends on boundary conditions such as surface charge density and ionic concentration, but a value above approximately 500 nm is generally sufficient. For this reason, a length of 0.8 µm was chosen. To recover the results corresponding to the actual membrane thickness, we take advantage of the linear behavior of the system, as discussed in Section 3.2.1.

- The size of the reservoir H was also chosen as a trade-off between computation time and the influence of boundary conditions on the solution. On the one hand, if H is too small, the boundary conditions affect both the concentration

profiles and the electrical potential inside the pore. On the other hand, if H is too large, the computation time increases unnecessarily. For reservoir sizes above approximately 50 nm, the influence of the boundary conditions becomes negligible, as they are sufficiently far from the pore entrance.

- The two surface charge densities were chosen based on values reported in the literature. Experimentally, this parameter is challenging to determine, as it depends on the measurement method and on the quality and conformity of the silica layer. Most reported values for the surface charge density of silica correspond to planar surfaces or nanoparticles. However, the situation in this work is different, as the space is confined and, as discussed in Section 4.1.4.3, the surface charge density in confined geometries depends not only on the pH of the solution, but also on the pore size and the ionic environment. Consequently, values obtained for planar surfaces or nanoparticles are not necessarily representative for nanopores, and assumptions must therefore be made. First, the surface charge density of SiO_2 should be negative because the point of zero charge (PZC) of silica is around pH 2, while the experiments are performed near pH 6, typical for aqueous solutions [369–371].

  Reported surface charge densities for oxide nanoparticles and oxide surfaces in water generally range from -10 to -100 mC/m^2 depending on pH, ionic strength, and electrolyte composition [372–375]. Values between -20 and -40 mC/m^2 are typically found for spherical silica beds at pH 6–7 in water [372, 373]. Numerically, Keshavarzi et al. [143] showed that the absolute value of the surface charge density in nanopores decreases with pore size under low ionic concentration. As illustrated in Fig. 4.6, their results indicate values ranging from approximately -40 mC/m^2 for pores of 1 nm down to -5 mC/m^2 for pores of 7.5 nm at 1 mM concentration. Since this study is closest to our conditions in terms of confinement and ionic strength, and given that our pore sizes range from 11 nm to 45 nm, surface charge densities between approximately -4 and -0.4 mC/m^2 appear reasonable. Two values of -4 mC/m^2 and -0.4 mC/m^2 were therefore chosen as lower and upper limits respectively.

- The ionic solution chosen was KCl. To obtain significant electrical double-layer overlap for the target pore-size range of 10–100 nm, concentrations between 0.1 mM and 10 mM were selected. These correspond to electrical double-layer thicknesses ranging from approximately 30.4 nm down to 3.0 nm, respectively.

  The choice of KCl is common in reverse electrodialysis studies because the diffusion coefficients of K^+ and Cl^- are nearly identical, which minimizes

unwanted electrochemical potential noise. In non-selective membranes, differences in ion mobilities can produce a membrane potential, known as the Henderson diffusion potential, even when no true ionic selectivity is present. This artificial potential can lead to the erroneous interpretation that a membrane is partially selective, as discussed in Section 3.1.3.1, and should therefore be minimized.

Using the diffusion coefficients listed in Table 3.1, the expected Henderson diffusion potentials computed from Eq. (3.21) for KCl are given in Table 6.2. These values represent the maximum possible contribution of ionic mobility differences, since they correspond to the case of a completely non-selective membrane. For selective membranes, the effect is significantly smaller. Consequently, the influence of the Henderson potential is considered negligible in this work.

KCl Concentration ratio	**Henderson potential [mV]**
S1/S2	1.1
S2/S3	1
S1/S3	2.1

Table 6.2: Henderson potential values for different concentration ratios of KCl solutions. S_i are given in Table 6.1.

- The relative permittivity of water is typically taken as 80 in most studies of ionic conduction in nanopores. For very small pores (below 10 nm), it has been shown that water permittivity is altered due to confinement effects, as discussed in Section 4.1.4.1. Similarly, ionic diffusion coefficients may also be affected by confinement, as detailed in Section 4.1.4.2. Since the pore sizes used in this work range from 11 nm to 45 nm (see Section 6.3.1), we assumed that the relative permittivity of water and the ionic diffusion coefficients remain equal to their bulk (non-confined) values. This assumption may not strictly hold in the vicinity of the pore walls.

A MATLAB (MathWorks) routine was developed in-house to define the COMSOL geometry and constraints, and to perform multiple simulations in series on the UCLouvain cluster machines. The main parameters explored in these simulations are the pore radius R and the concentration ratio S_i/S_j ($i, j = 1, 2, 3$ and $i \neq j$), as these are the two controllable factors in the experimental workflow: the pore size is adjusted through the etching current density during fabrication, while the concentration ratio is selected through the choice of electrolyte solutions. The objectives of the simulations are the following:

- to determine the influence of each parameter on the ionic transport properties of the pore;
- to identify which concentration ratio optimizes the power density;
- to determine which pore size maximizes the power output.

6.3 Results

6.3.1 Porous layer properties

The choice of such a highly doped substrate is motivated by its influence on the anodic dissolution mechanism. As reported by Herino *et al.* [376], porous layers formed on heavily doped p-type silicon exhibit larger and more uniform pores (2–9 nm for 10 mΩ·cm) than those obtained on lightly doped substrates (<2 nm for 1000mΩ·cm), owing to the higher hole availability at the pore tips. Subsequent studies confirmed that p^{++} silicon allows stable pore propagation, avoids electropolishing, and ensures a homogeneous current distribution across the wafer [377, 378]. These properties are essential for the aim of producing well-ordered, interconnected porous layers suitable for membranes of pore between 10 and 50 nm .

The electrolyte composition also plays a decisive role in controlling pore uniformity and layer quality [379–381]. A mixture of HF:EtOH = 3:1 (v/v) was employed, as this ratio is widely adopted for mesoporous PSi formation on highly doped p-type substrates [80, 377]. Ethanol enhances wetting and gas removal from the porous network, improving homogeneity and reducing pore coalescence. This composition has also been extensively optimized and characterized within our laboratory, providing a reliable and reproducible basis for membrane fabrication. Another important feature is porosity: the higher the porosity, the higher the number of available pore to participate in the ionic conduction, thus higher ionic current and lower ionic resistance, increasing the maximal output power.

A series of PSi samples were fabricated using different anodization conditions. The primary parameter investigated was the current density, as it is well established that pore dimensions increase with increasing current density [382]. In this work, the maximum current density was limited to 150 mA/cm^2, since higher values produced layers that were overly porous and mechanically fragile. For all samples, the transitional layer was removed by wet etching prior to the main electrochemical etch, following standard procedures reported in the literature [219, 383].

The PSi samples were first characterised optically using the SLIM method to extract the porosity and thickness of the porous layers. The layer thicknesses obtained from SLIM were subsequently confirmed by cross-sectional SEM imaging.

An example is shown in Figure 6.2 for a sample etched at 3 mA/cm^2, where the porous layer is approximately 1.6 µm thick and exhibits a straight but branched pore morphology.

For comparison across samples, the results are expressed as an etch rate rather than absolute thickness. As shown in Figure 6.4, the etch rate increases with current density, displaying an approximately linear dependence. A similar trend is observed for porosity: Figure 6.5 shows that the porosity also rises linearly with current density. The highest average porosity obtained was about 81%, with some individual measurements reaching up to 90%. These trends, an increase in both etch rate and porosity with increasing current density, are consistent with previous observations reported in the literature for similar substrates [206, 224].

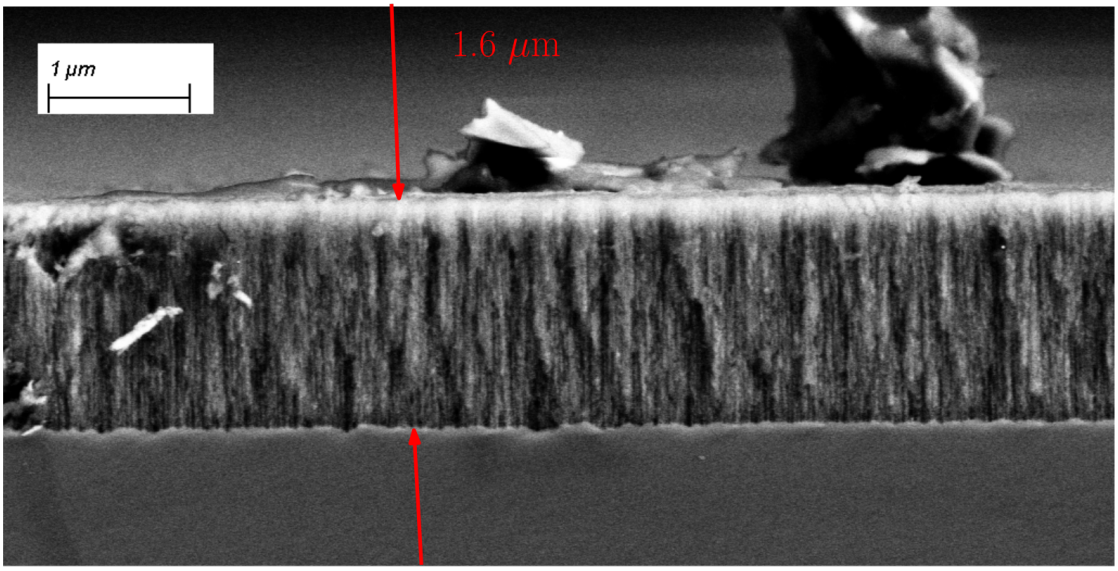


Figure 6.2: Cross-section SEM images PSi layer etched on a p++ wafer (0.9-1 mΩcm) at 3 mA/cm^2 for xx s in HF:etOH 3:1 in volume.

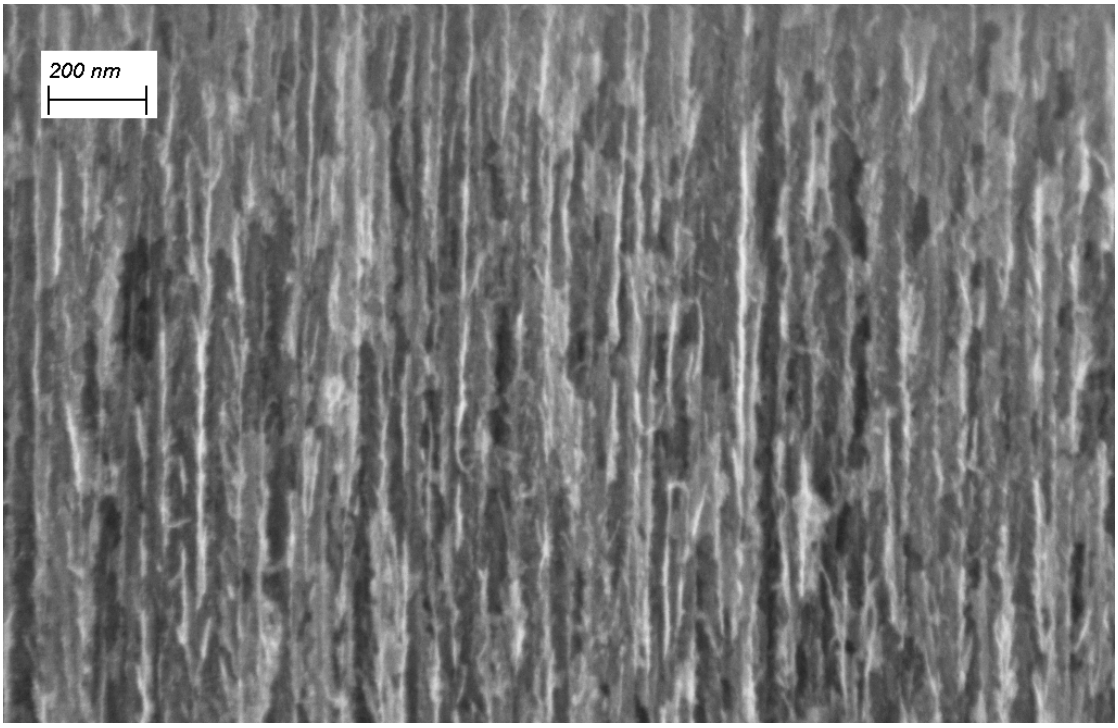


Figure 6.3: Cross-section SEM images PSi layer etched on a p++ wafer (0.9-1 mΩcm) at 50 mA/cm^2 in HF:etOH 3:1 in volume.

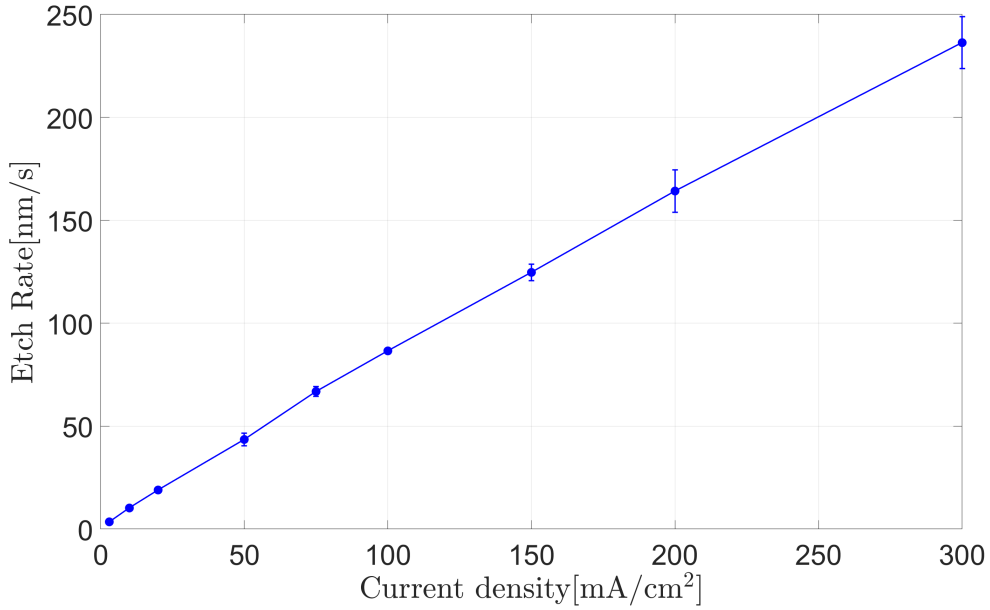


Figure 6.4: Calculated etch with varying current densities, on a p++ Si wafer (0.9-1 mΩ cm) in HF:etOH 3:1 in volume, based on SLIM measurements.

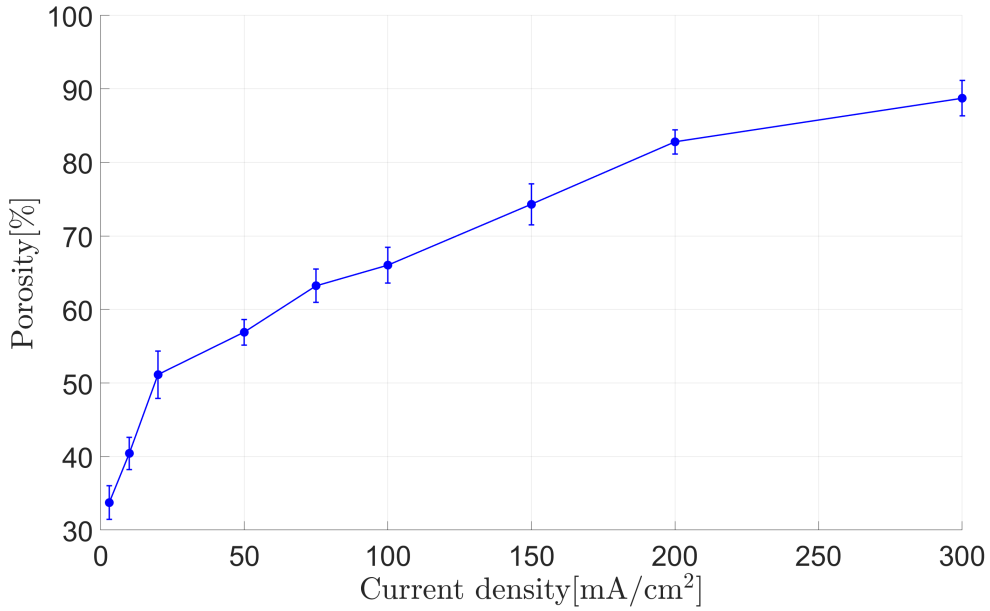


Figure 6.5: Calculated porosity with varying current densities, on a p++ Si wafer (0.9-1 mΩ cm) in HF:etOH 3:1 in volume, based on SLIM measurements.

The pore sizes of the PSi samples were evaluated from top-view SEM images. Representative micrographs acquired at various current densities are shown in Figure 6.6. Only a slight increase in pore diameter is observed between 50 and 100 mA/cm^2, whereas the enlargement becomes much more pronounced at higher current densities like 200 mA/cm^2. In contrast, the pore wall thickness appears largely unaffected by the current density. This is consistent with previous reports, which indicate that wall thickness is primarily governed by the substrate doping level and the HF concentration of the electrolyte, rather than by the anodization current density [206, 224]. This only execption found is at very low current density (3 mA/cm^2), where the pore wall appears much thicker than at higher current density.

Image analysis of the SEM micrographs yielded the average pore diameter for each current density, as shown in Figure 6.7. As with porosity and etch rate, the pore diameter increases with current density; however, the dependence appears quadratic rather than linear. This behaviour has also been reported in previous studies [206, 224]. In addition, the distribution of pore sizes broadens at higher current densities: although the average pore diameter at 200 mA/cm^2 remains below 50 nm (and thus within the mesoporous regime), isolated pores as large as 100 nm were observed in some samples. All the properties above are summarized in Table 6.3.

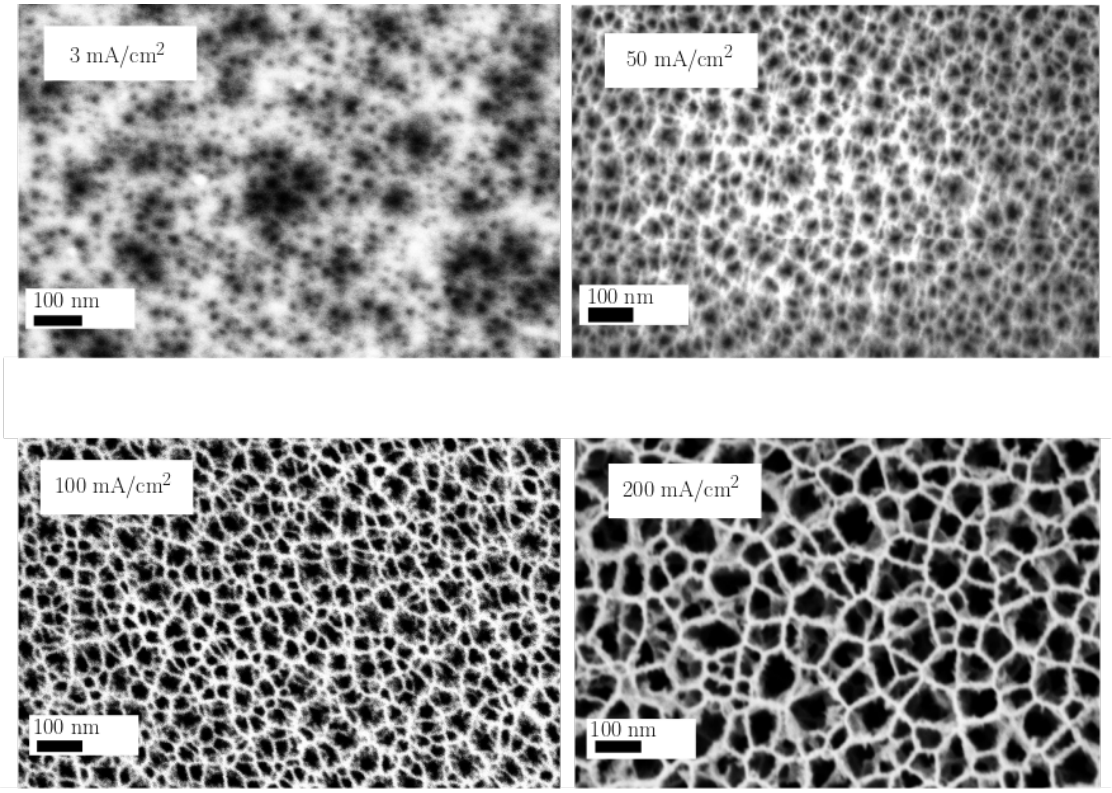


Figure 6.6: Top view SEM observations of porous silicon produced with different current densities: 3, 50, 100 and 200 mA/cm^2. The PSi was etched on a p++ Si wafer (0.9-1 m cm) in HF:etOH 3:1 in volume. Samples thickness are thin, between 1 μm to 3 μm. The scale bar represents 100 nm.

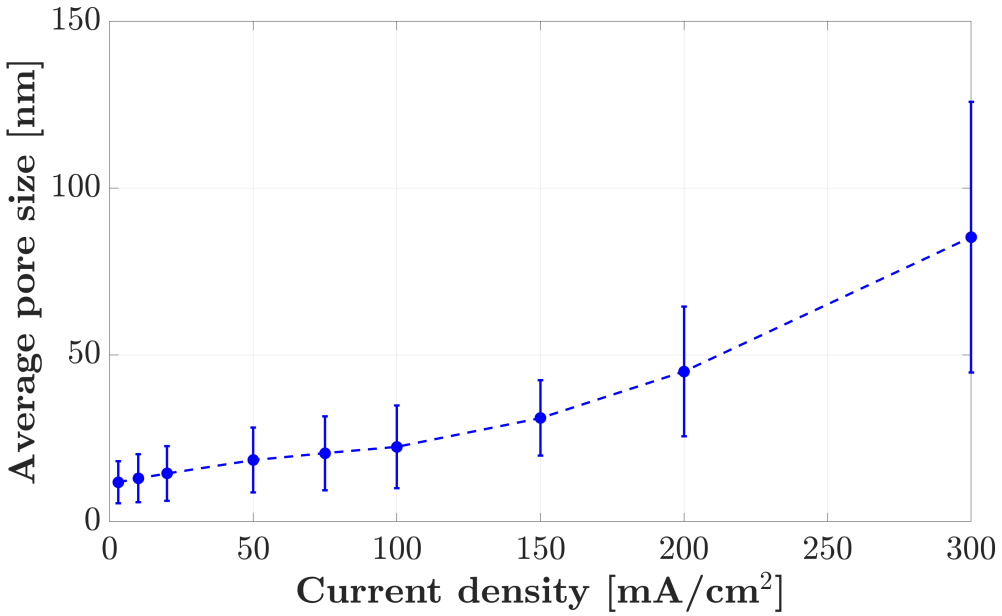


Figure 6.7: Properties of PSi samples etched at different current densities, on a p++ Si wafer (0.9-1 m cm) in HF:etOH 3:1 in volume; these values were extracted from SLIM measurements and SEM observations.

Table 6.3: Morphological characteristics of porous silicon (PSi) as a function of current density.

Current density [mA/cm^2]	**Etch rate** [nm/s]	**Pore size,** d_p [nm]	**Porosity,** ε_p [%]
3	3.51 ± 0.03	11.8 ± 6.3	33.73 ± 2.30
10	10.23 ± 0.55	13.0 ± 7.2	40.43 ± 1.78
20	18.98 ± 0.69	14.5 ± 8.2	51.13 ± 2.61
50	43.01 ± 2.77	18.5 ± 9.72	56.90 ± 1.39
75	66.82 ± 1.93	20.5 ± 11.1	63.23 ± 1.88
100	86.54 ± 0.36	22.4 ± 12.4	66.03 ± 2.36
150	124.69 ± 3.23	31.1 ± 11.29	74.30 ± 2.80
200	164.20 ± 8.67	45.0 ± 19.45	82.80 ± 1.68
300	236.27 ± 10.30	85.3 ± 40.54	88.73 ± 2.45

6.3.2 Simulation of ionic I–V characteristics

First, the simulation was run for a pore radius $r_{\text{pore}} = 15$ nm and $\sigma_{s,h}$ in an open-circuit configuration, such that the solutions equilibrate freely and no net current flows at equilibrium. This requires imposing a constraint on the system to determine the value of V_{applied} that forces the ionic current to zero. The resulting distributions of cations, anions, and electric potential are shown in Fig. 6.8. As expected, the negative surface charge on the pore wall attracts cations and repels anions, thereby creating a cation-selective nanopore. A radial cross-section (taken at mid-length of the pore) of the potential distribution, shown in Fig. 6.9, reveals the characteristic exponential decay of the electric double layer away from the pore wall. Due to confinement, however, the overlap between the double layers from opposite walls slows down this decay compared to the simple exponential profile predicted in bulk conditions, as discussed in Section 4.1.3.

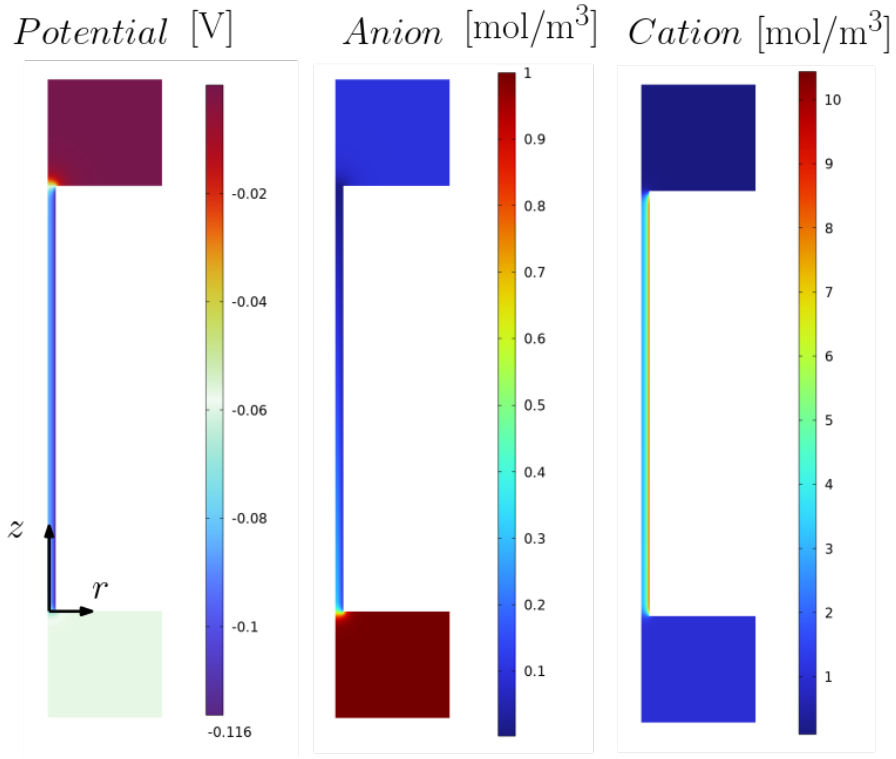


Figure 6.8: Numerical distributions of the electrical potential, anion concentration, and cation concentration inside the nanopore in an open-circuit configuration. Numerical parameters: $r_{\text{pore}} = 15$ nm, $\sigma_{s,h}$, $C_H = \text{S2}$, and $C_L = \text{S1}$.

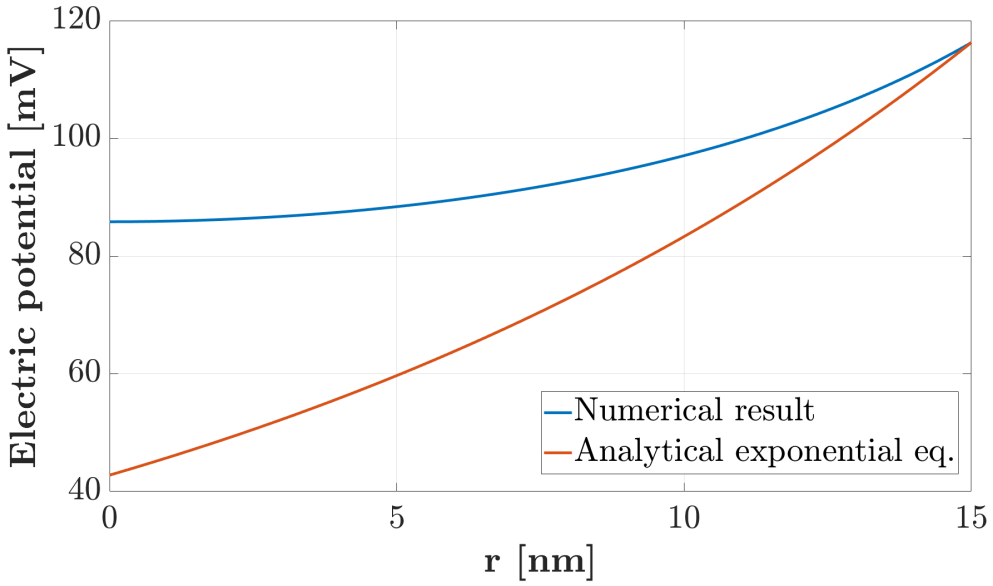


Figure 6.9: Cross-sectional profile of the electrical potential at $z = L/2$ (blue), compared with the analytical exponential decay (red) characterized by the Debye length λ_D. Numerical parameters: $r_{\text{pore}} = 15$ nm, $\sigma_{s,h}$, $C_H = \text{S2}$, and $C_L = \text{S1}$.

The transport of charge inside the pore is mainly carried by cations. The distributions of cations and anions along the central axis of the pore, shown in Fig. 6.10, further highlight the selective properties of the nanopore. As discussed in Section 3.1.1, and analogously to polymer membranes containing fixed charges in their matrix, the surface charge inside the pore induces concentration gradients between the pore interior and the adjacent solutions. This leads to the formation of two Donnan potentials, one at each pore entrance, as illustrated in Fig. 6.11. The resulting potential difference across the pore corresponds to the membrane (or pore) potential, E_m or $\Delta\varphi_m$, given by Eq. 3.27:

$$E_m = -\frac{RT}{F}(2T_+ - 1)\log\left(\frac{c^{s2}}{c^{s1}}\right) = -54[mV]. \tag{6.8}$$

The transport number T_+ of the nanopore can then be deduced using eq. (2.14),

$$T_+ = \frac{57.15[mV]F}{2RT\log\left(\frac{c^{s2}}{c^{s1}}\right)} + \frac{1}{2} = 0.991, \tag{6.9}$$

as well as the permselectivity

$$\Psi = \frac{-57.15[mV]}{\Delta\varphi_{Nernst}} = 0.981, \tag{6.10}$$

which is considered very good.

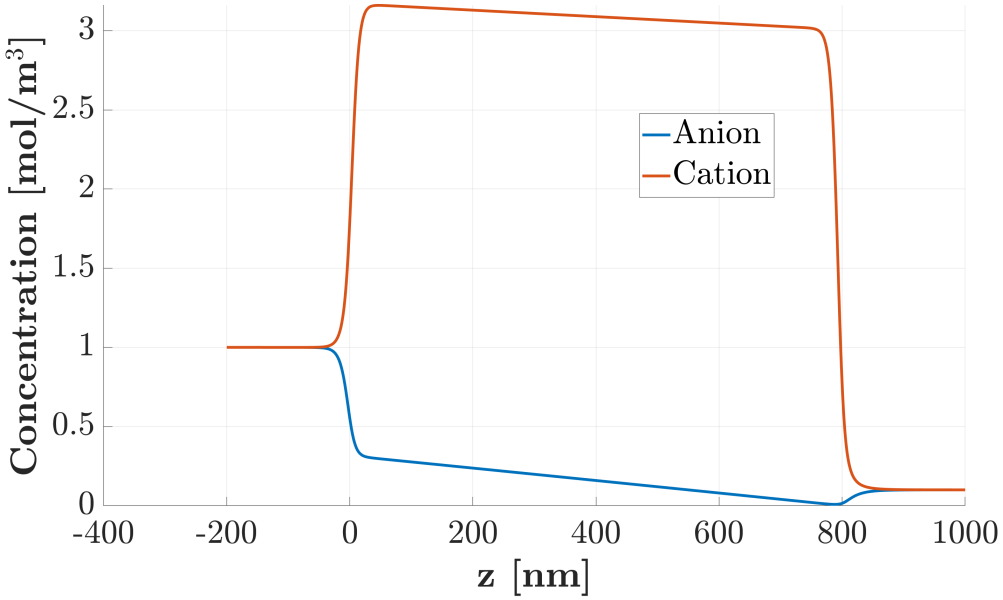


Figure 6.10: Axial profiles of the anion and cation concentrations at $r = 0$ in an open-circuit configuration. Numerical parameters: $r_{\text{pore}} = 15$ nm, $\sigma_{s,h}$, $C_H = \text{S2}$, and $C_L = \text{S1}$.

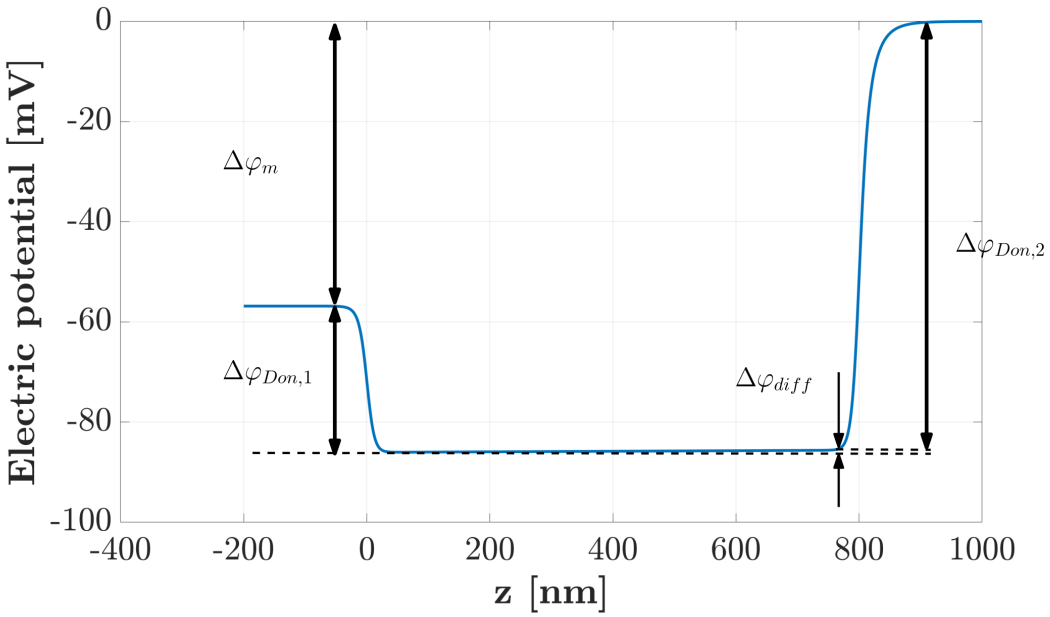


Figure 6.11: Axial profile of the electrical potential at $r = 0$ in an open-circuit configuration. Numerical parameters: $r_{\text{pore}} = 15$ nm, $\sigma_{s,h}$, $C_H = \text{S2}$, and $C_L = \text{S1}$.

In a second step, the I–V characteristics were determined by applying an external voltage V between -70 mV and 0 V. Figure 6.12 shows the results for the concentration ratio S1/S2. A clear linear relationship between the applied voltage and the ionic current is observed. When the applied voltage equals the membrane potential, the net current is zero. The short-circuit current corresponds to the condition $V_{\text{applied}} = 0$ V.

The slope of the I–V curve gives the ionic conductance of the nanopore. Equivalently, it can be computed as the ratio between the short-circuit current and the membrane potential.

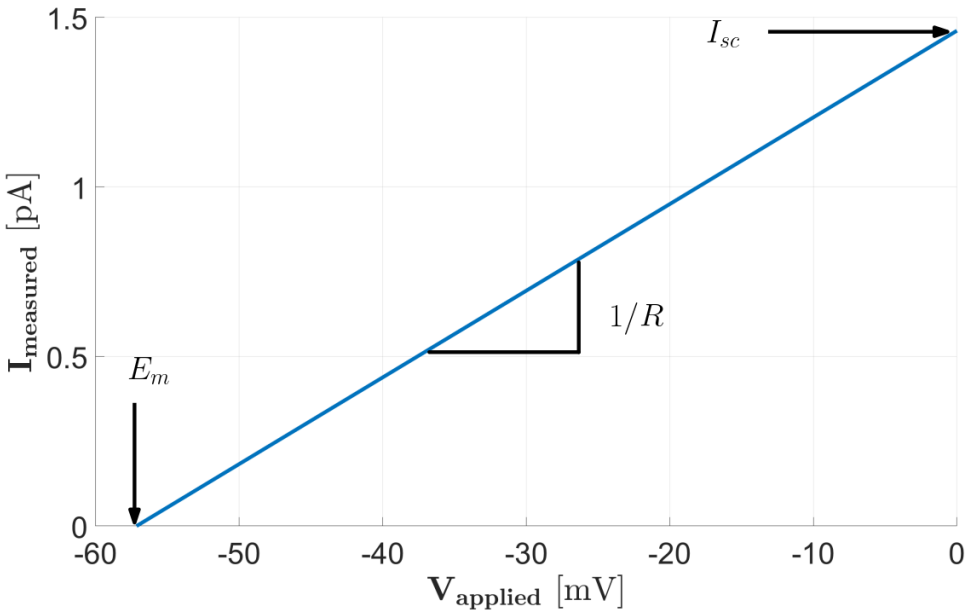


Figure 6.12: Measured current as a function of the applied voltage. Numerical parameters: $r_{\text{pore}} = 15$ nm, $\sigma_{s,h}$, $C_H = \text{S2}$, and $C_L = \text{S1}$.

6.3.2.1 Pore size study – High surface charge density

The pore-radius range chosen for the numerical analysis was 10 nm to 200 nm, corresponding to pore diameters between 20 nm and 400 nm. This diameter range is larger than the pore sizes observed by SEM, but for convergence reasons it was difficult to obtain stable numerical results for pore radii smaller than 10 nm at this surface charge density. The resulting I–V characteristics are shown in Fig. 6.13, and the corresponding key metrics are summarized in Table 6.4.

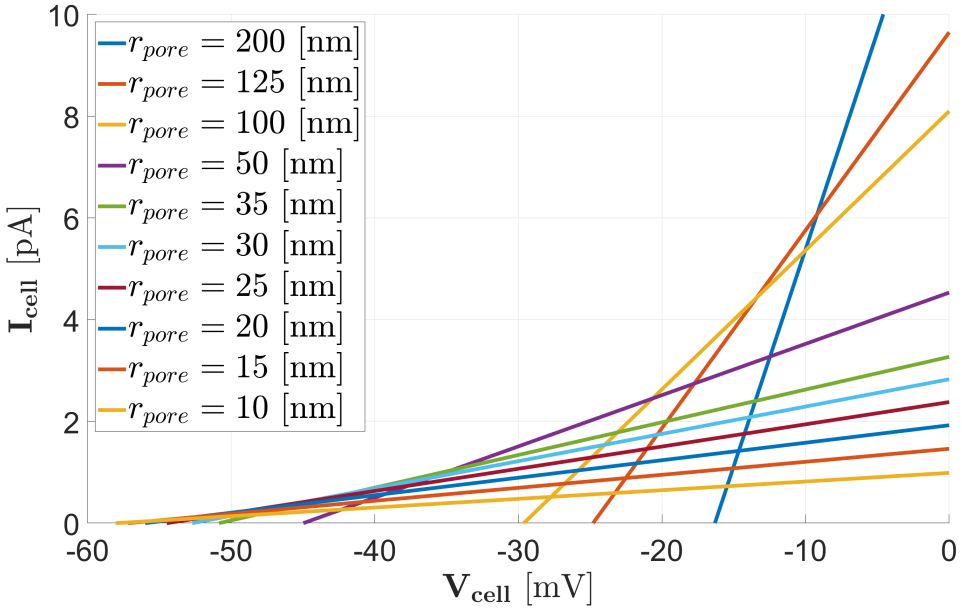


Figure 6.13: Computed current as a function of the applied voltage for different pore sizes. Numerical parameters: $\sigma_{s,h}$, C_H = S2 and C_L = S1.

Table 6.4: Computed or derived metrics for a nanopore under C_H = S2 and C_L = S1 as a function of pore radius and $\sigma_{s,h}$. I_{sc} is the short-circuit current, E_m the membrane potential, R the pore resistance, $P_{\max}$ the maximum output power, T_+ the cation transport number, and Ψ the permselectivity.

r_{pore} **[nm]**	I_{sc} **[pA]**	E_{m} **[mV]**	R **[GΩ]**	$P_{\max}$ **[fW]**	T_+ **[-]**	ψ
10	0.988	-57.990	58.714	14.319	0.998	0.996
15	1.461	-57.146	39.124	20.867	0.991	0.981
20	1.923	-55.963	29.095	26.910	0.980	0.961
25	2.379	-54.464	22.895	32.391	0.968	0.935
30	2.827	-52.693	18.637	37.246	0.952	0.905
35	3.268	-50.831	15.555	41.527	0.936	0.873
50	4.531	-44.969	9.925	50.938	0.886	0.772
100	8.097	-29.622	3.658	59.963	0.754	0.509
125	9.648	-24.802	2.571	59.821	0.713	0.426
200	13.913	-16.316	1.173	56.752	0.640	0.280

When the pore radius increases, the absolute value of the membrane potential

$|E_m|$ decreases, indicating a reduction in selectivity due to weaker EDL overlap, as shown in Fig. 6.14. In contrast, the ionic resistance decreases with increasing pore size, similar to the behaviour of a conventional electrical resistor. This reduction in resistance is much more pronounced than the decrease in $|E_m|$, which results in a higher short-circuit current I_{sc} for larger pores. However, this trend has a limit: for sufficiently large pores, $|E_m| \to 0$, which implies $I_{sc} \to 0$. In this regime, the pore becomes non-selective and behaves as a simple ionic resistor.

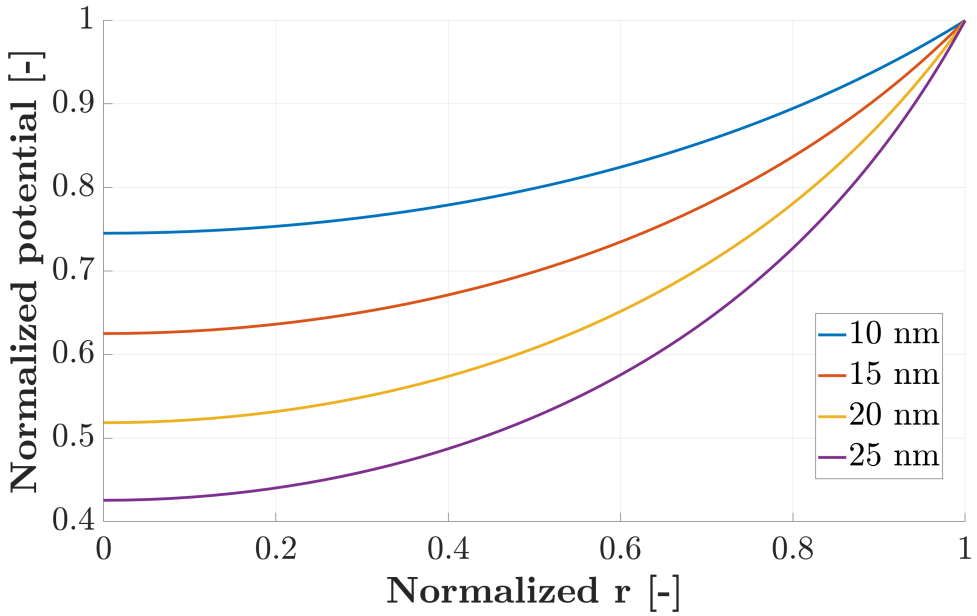


Figure 6.14: Cross-sectional profiles of the normalized electrical potential at $z = L/2$ for different pore radii. Numerical parameters: $\sigma_{s,h}$, C_H = S2 and C_L = S1.

Analyzing the maximum power output using Eq. (2.9), Fig. 6.15 shows that a nanopore exhibits an optimal pore radius that maximizes the generated power when all other parameters are kept constant. Starting from $r_{\text{pore}} = 10$ nm, increasing the pore radius initially leads to an increase in the maximum power because the reduction in E_m is compensated by a more rapid decrease in the pore resistance R. This trend continues until a point at which the decrease in E_m, and therefore in selectivity, becomes too pronounced, causing the maximum power to decline.

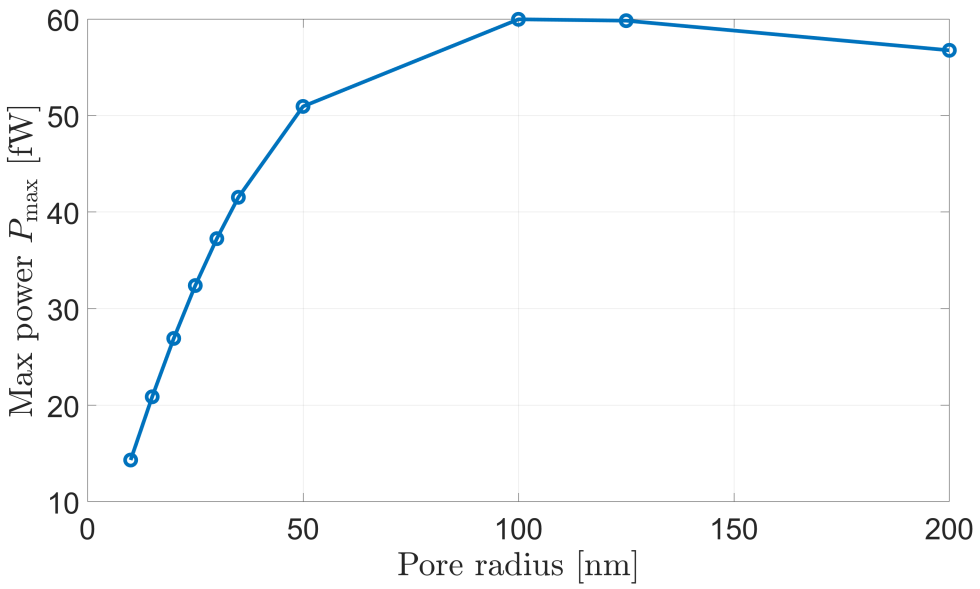


Figure 6.15: Computed maximum power output of the nanopore under $\sigma_{s,h}$, C_H = S2 and C_L = S1 as a function of the pore radius.

From single pore analysis to full scale membrane

The analysis of the maximum power as a function of pore size indicates the existence of an optimal radius, around 100 nm in Fig. 6.15, which maximizes the power output. This optimal radius is nevertheless much larger than the targeted pore-size range. However, a single nanopore does not accurately represent the behaviour of a full-scale membrane, since additional parameters must be taken into account when the membrane consists of a collection of pores.

To relate the single-pore results to membrane-scale behaviour, the total number of pores per unit area must be considered. In order to compute the power output of the membrane, both E_m and R must first be estimated at the membrane level. In a simplified view, the membrane can be modelled as an array of parallel pores with a well-defined average pore radius, where each pore behaves as a voltage source E_m in series with an internal resistance R_{pore}.

Assuming that the membrane potential is equal to that of a single pore (since voltage sources in parallel share the same potential), the membrane resistance is simply the pore resistance divided by the total number of pores:

$$R_{\text{membrane}} = \frac{R_{\text{pore}}}{N_{\text{pore}}}, \tag{6.11}$$

where N_{pore} is the number of pores per unit surface area.

In terms of maximum power density, this implies that the maximum power of a full-scale membrane is

$$P_{\text{max,membrane}} = P_{\text{max,pore}}\, N_{\text{pore}}. \tag{6.12}$$

Theoretically, for a membrane with a given surface area, the porosity and the pore size allow estimating the total number of pores. At constant porosity, decreasing the pore size increases the number of pores that can fit within the same surface area. Thus, it would appear advantageous to favour a large number of smaller pores, since many efficient small pores should outperform a few larger ones. However, in porous silicon, selecting a target pore size through the etching current density simultaneously fixes the porosity, as shown in Tab. 6.3. The number of pores per unit area, N_{pore}, can be estimated from the porosity ε_p (Tab. 6.3) and the average pore diameter d_p using

$$N_{\text{pore}} = \frac{4\varepsilon_p}{\pi d_p^2}. \tag{6.13}$$

Figure 6.16 shows that, on a given surface area, there are at least six times more pores with diameters below 10 nm than above 20 nm. Based on Eq. (6.12), the resulting impact on power density at the membrane level is presented in Fig. 6.17. In this analysis, the maximum power of a single nanopore (Fig. 6.15) was interpolated and used to estimate the maximum power for the experimentally observed pore diameters d_p. Within this simplified framework, the pore diameter that maximizes the membrane power density is approximately 15 nm, which lies within the target experimental range (11–45 nm).

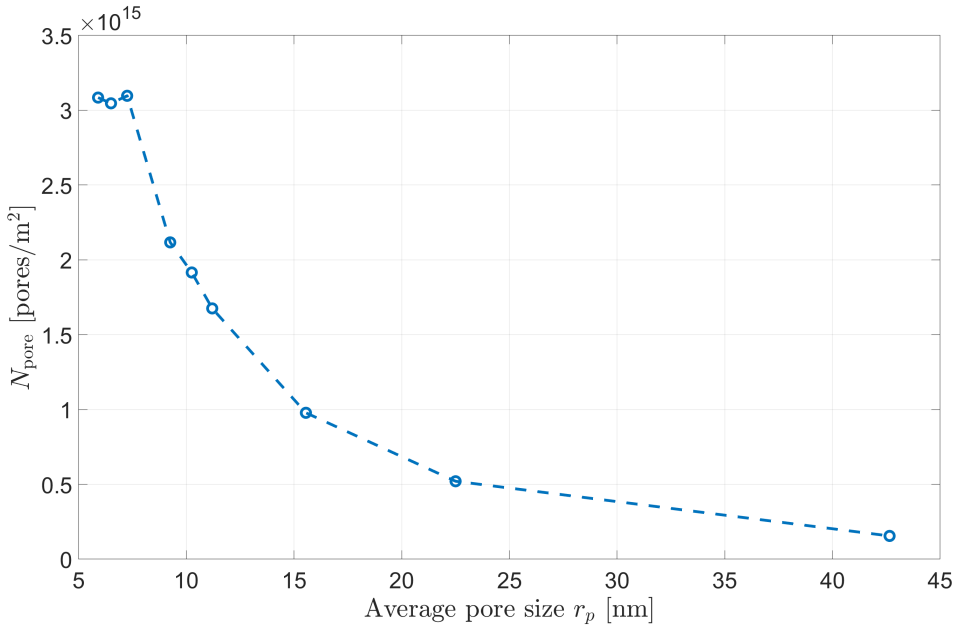


Figure 6.16: Theoretical pore density per unit area as a function of pore size. The pore density is computed from the measured porosity ε_p and pore radius r_p.

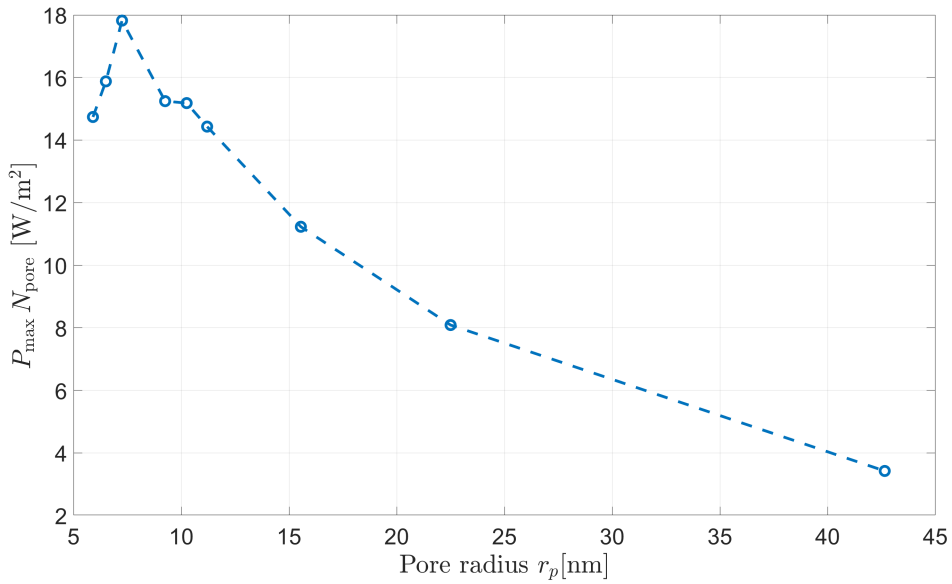


Figure 6.17: Theoretical maximum power density as a function of pore size for $\sigma_{s,h}$, C_H = S2 and C_L = S1. The power values are extracted from numerical simulations of a single pore, and the pore density per unit area is computed from the measured porosity and pore radius.

6.3.2.2 Concentration ratio study – High surface charge density

We analyzed the influence of the concentration ratio for a nanopore with a 15 nm radius, as shown in Fig. 6.18. Table 6.5 summarizes the key metrics extracted from the simulations. We observe that $|E_{m,\text{S1/S2}}| > |E_{m,\text{S2/S3}}|$. From Eq. (3.26), this corresponds to a higher cation transport number $T_{+,\text{S1/S2}}$ compared to $T_{+,\text{S2/S3}}$, which is a direct consequence of the larger Debye length λ_D (cf. Eq. (4.9)) associated with the lower concentration in S1/S2, and thus a stronger EDL overlap, as shown in Fig. 6.19.

Replacing S1 with S3 leads to a lower selectivity ($T_{+,\text{S1/S3}} < T_{+,\text{S1/S2}}$), but the pore still exhibits a higher absolute membrane potential $|E_{m,\text{S1/S3}}|$ because the larger concentration ratio compensates for the reduction in selectivity.

In terms of ionic resistance and short-circuit current, higher concentrations lead to lower ionic resistance: $R_{\text{S2/S3}} < R_{\text{S1/S3}} < R_{\text{S1/S2}}$. This is a direct consequence of the greater number of charge carriers available to conduct current inside the pore. Despite this trend, we observe that $I_{sc,\text{S1/S3}} > I_{sc,\text{S2/S3}}$ because the I–V curve for S1/S3 is shifted further to the left, as $|E_{m,\text{S1/S3}}|$ is the highest. This higher membrane potential results in a larger short-circuit current.

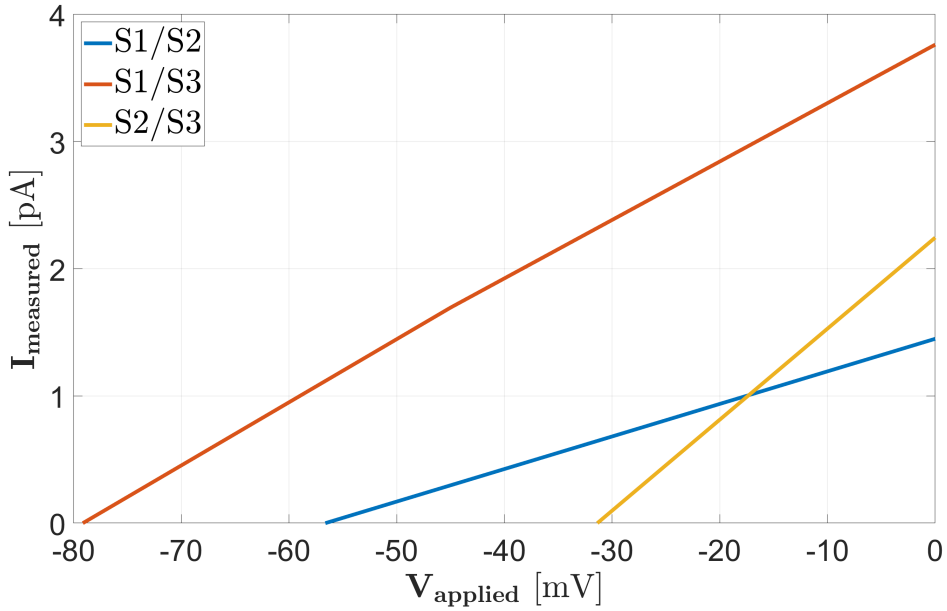


Figure 6.18: Computed current as a function of the applied voltage for different concentration ratios. Numerical parameter: $r_{\text{pore}} = 15$ nm and $\sigma_{s,h}$.

Table 6.5: Computed or derived metrics for a nanopore under different concentration ratios for $r_{\text{pore}} = 15$ nm and $\sigma_{s,h}$. I_{sc} is the short-circuit current, E_m the membrane potential, R the pore resistance, P_{max} the maximum output power, T_+ the cation transport number, and Ψ the permselectivity.

Concentration	I_{sc} **[pA]**	E_{m} **[mV]**	R **[GΩ]**	P_{max} **[fW]**	T_+ **[-]**	$\boldsymbol{\psi}$
S1/S2	1.461	-57.146	39.124	20.867	0.991	0.981
S1/S3	3.756	-79.912	21.276	75.038	0.844	0.686
S2/S3	2.245	-31.367	13.974	17.603	0.769	0.539

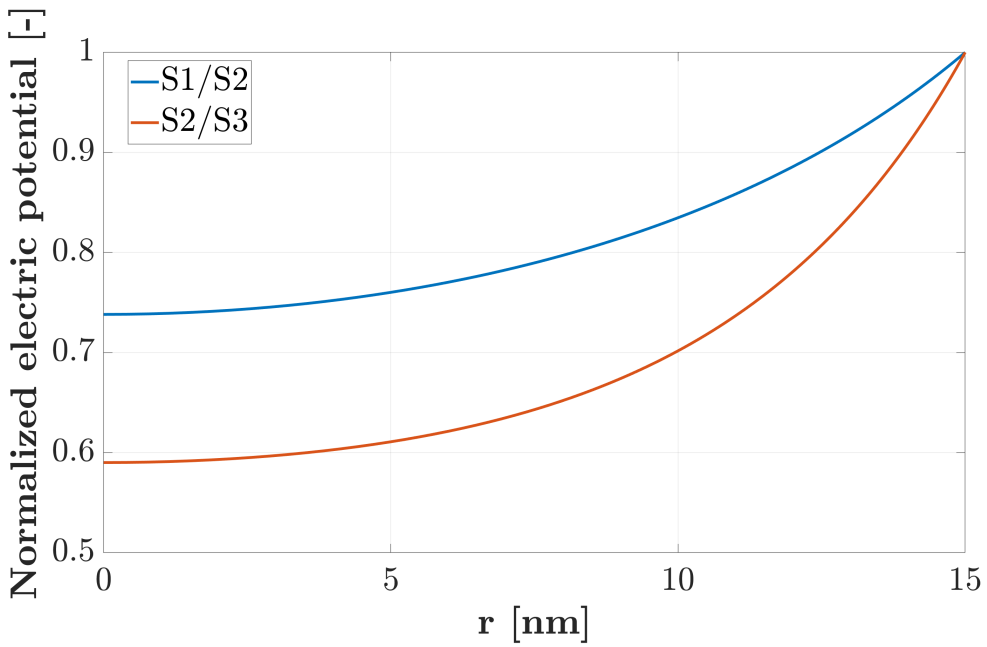


Figure 6.19: Cross-sectional profiles of the normalized electrical potential at $z = L/2$ for two different concentration ratios such that S2/S3 = 10 × S1/S2. Numerical parameter: $r_{\text{pore}} = 15$ nm and $\sigma_{s,h}$.

6.3.2.3 Pore size study – Low surface charge density

When the surface charge density is reduced, it becomes possible to study a lower pore-size range. Figure 6.20 shows the resulting I–V curves, and Table 6.6 summarizes the corresponding metrics. The trends observed for the dependence of the membrane potential E_m and the ionic resistance on the pore radius remain consistent with those obtained for a higher surface charge density. However, for a given pore size, the membrane potential is lower when the surface charge density is smaller. This results from a weaker electrical double layer (EDL) overlap, which reduces the Donnan potentials at the pore entrances, as illustrated in Figure 6.21. Additionally, the membrane potential decreases more rapidly with increasing pore size when the surface charge density is lower.

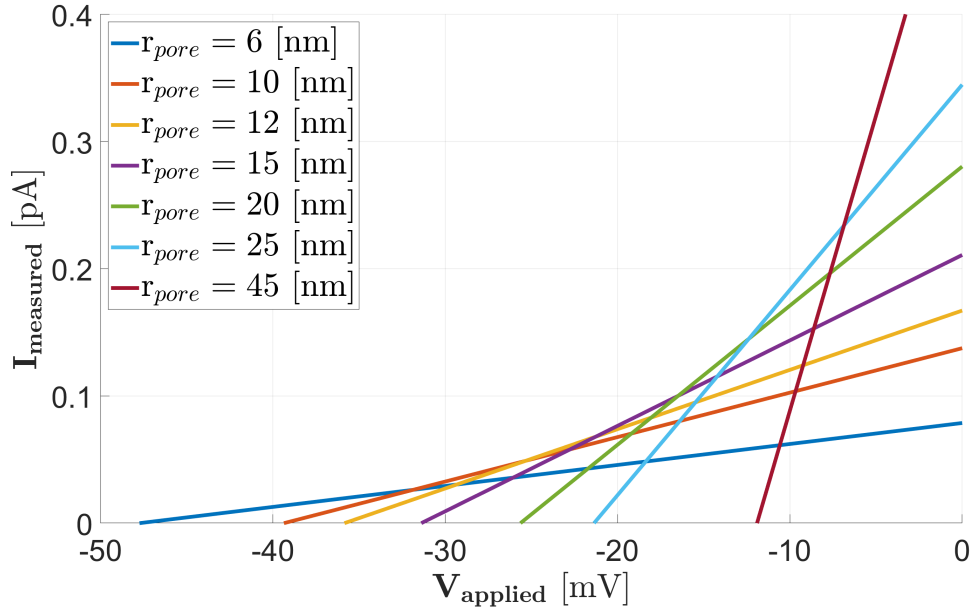


Figure 6.20: Computed current as a function of the applied voltage for different pore sizes. Numerical parameters: $\sigma_{s,l}$, C_H = S2 and C_L = S1.

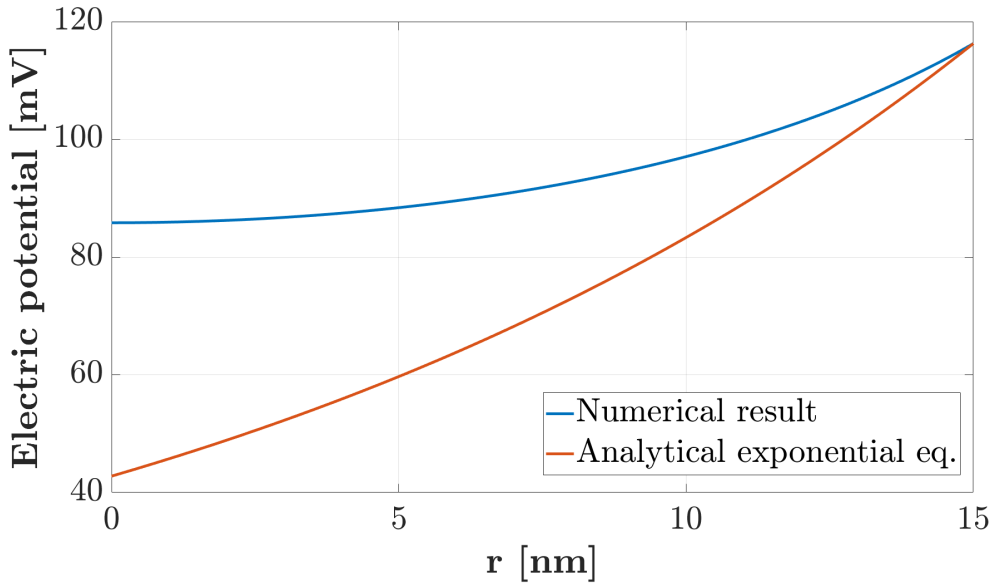


Figure 6.21: Axial profile comparison of the electrical potential at $r = 0$ in an open-circuit configuration between a pore with a high or low surface surface charge density σ_s. Numerical parameters: $r_{\text{pore}} = 15$ nm, $\sigma_{s,h}$, C_H = S2, and C_L = S1.

The ionic resistance is also larger when the surface charge density is reduced, because fewer counter-ions are required to compensate the surface charges inside the pore, as shown in Fig. 6.22. The maximal output power for a lower surface charge density is likewise reached at a smaller pore radius, indicating that the degradation of the membrane potential with increasing pore size outweighs the decrease in ionic resistance. In other words, the loss of selectivity becomes the dominant factor governing the power output.

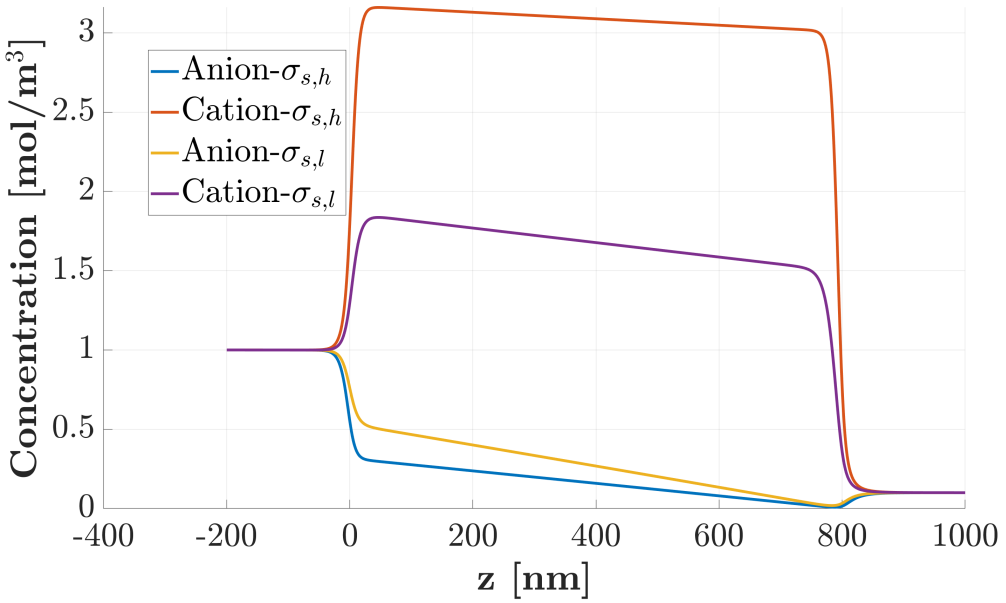


Figure 6.22: Axial profiles comparison of the anion and cation concentrations at $r = 0$ in an open-circuit configuration between a pore with a high or low surface surface charge density σ_s . Numerical parameters: $r_{\text{pore}} = 15$ nm, $\sigma_{s,h}$, $C_H = \text{S2}$, and $C_L = \text{S1}$.

Table 6.6: Computed or derived metrics for a nanopore as a function of pore radius, $\sigma_{s,l}$ and concentration S1/S2. I_{sc} is the short-circuit current, E_m the membrane potential, R the pore resistance, $P_{\max}$ the maximum output power, T_+ the cation transport number, and Ψ the permselectivity.

r_{pore} **[nm]**	I_{sc} **[pA]**	E_{m} **[mV]**	R **[GΩ]**	$P_{\max}$ **[fW]**	T_+ **[-]**	ψ
6	0.079	-47.721	606.308	0.939	0.910	0.819
10	0.138	-39.352	286.164	1.353	0.838	0.676
12	0.167	-35.843	214.487	1.497	0.808	0.615
15	0.211	-31.386	148.871	1.654	0.769	0.539
20	0.280	-25.634	91.430	1.797	0.720	0.440
25	0.345	-21.365	61.972	1.841	0.683	0.367
45	0.552	-11.906	21.554	1.644	0.602	0.204

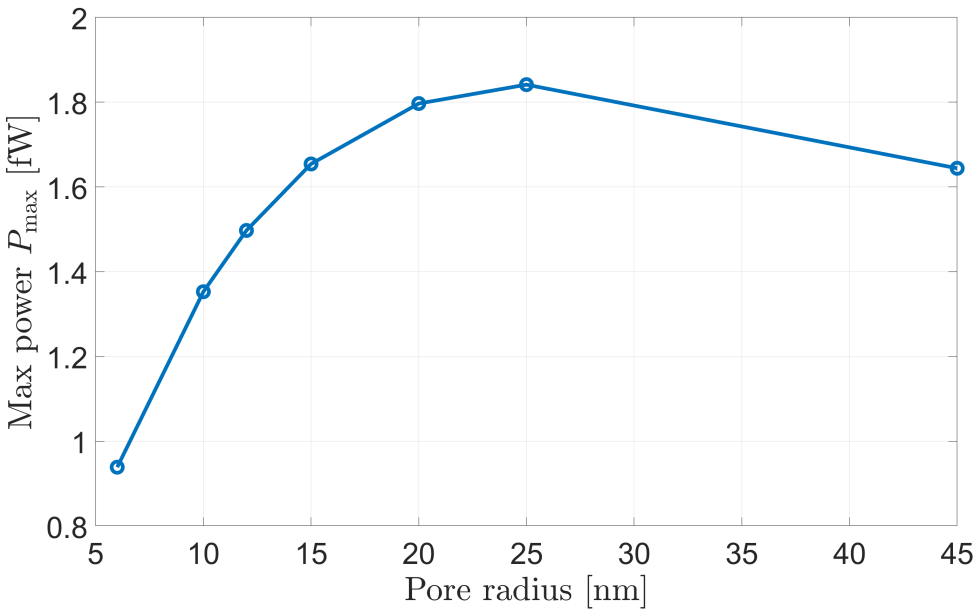


Figure 6.23: Computed maximum power output of the nanopore under $\sigma_{s,l}$, C_H = S2 and C_L = S1 as a function of the pore radius.

From single pore analysis to full scale membrane

If we perform the same analysis for the maximal output power density of a full-scale membrane as in the case with a higher surface charge density, the optimal

pore radius remains close to 7.5 nm. This results from the significantly larger number of pores at this size, which compensates for the lower individual power output of each pore. This finding highlights that pore density is a critical parameter when selecting or designing a substrate for RED applications.

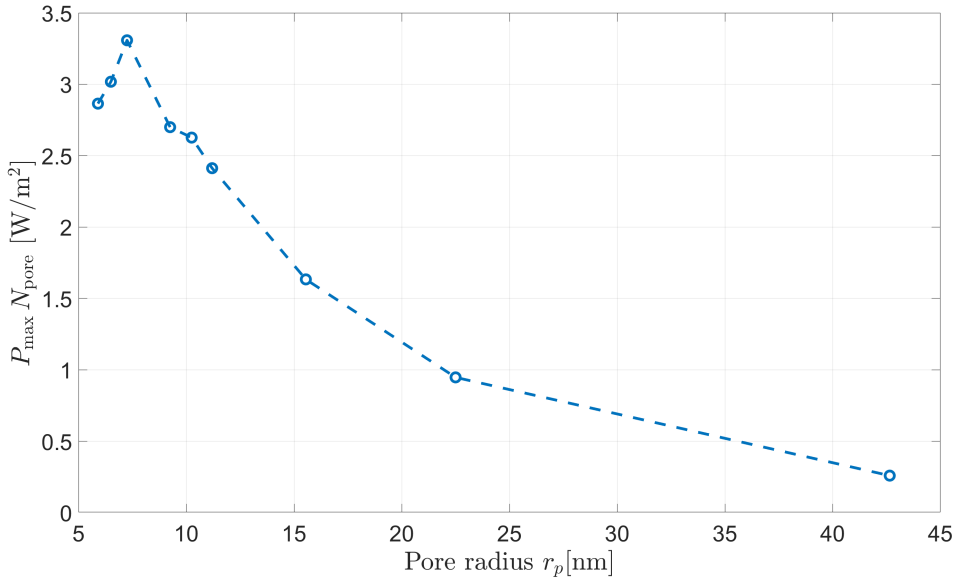


Figure 6.24: Theoretical maximum power density as a function of pore size for $\sigma_{s,l}$. The power values are extracted from numerical simulations of a single pore, and the pore density per unit area is computed from the measured porosity and pore radius.

6.3.2.4 Concentration ratio study – Low surface charge density

The I–V characteristics for the nanopore at different concentration ratios with a reduced surface charge density are shown in Fig. 6.25, and the corresponding metrics are summarized in Table 6.7. When the absolute surface charge density is decreased, the influence of the concentration ratio becomes more pronounced. Increasing the concentration reduces the thickness of the electrical double layer, and when combined with a lower surface charge density, the pore becomes significantly less selective.

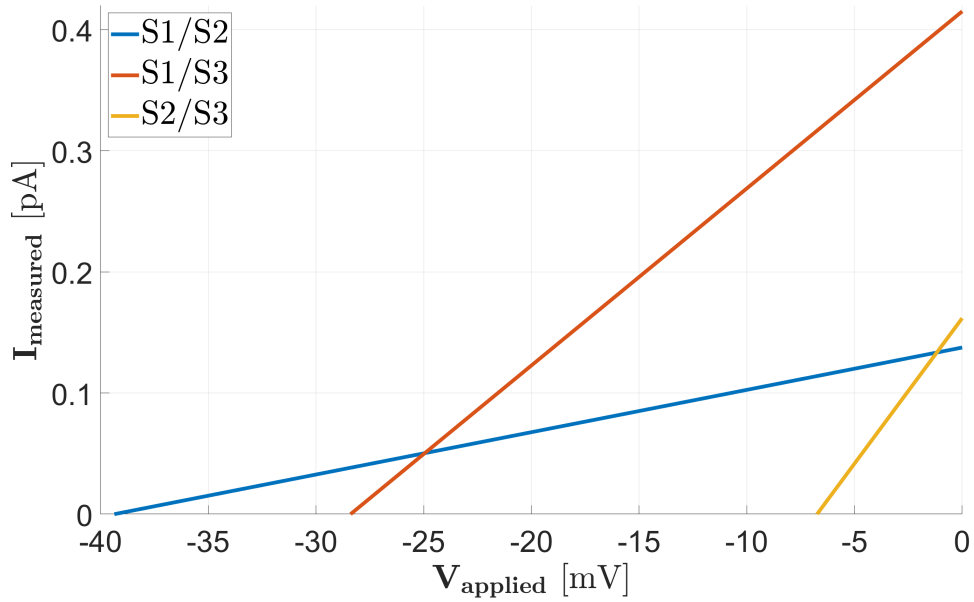


Figure 6.25: Computed current as a function of the applied voltage for different concentration ratios. Numerical parameter: $r_{\text{pore}} = 10$ nm and $\sigma_{s,l}$.

Table 6.7: Computed or derived metrics for a nanopore under different concentration ratios for $r_{\text{pore}} = 10$ nm and $\sigma_{s,l}$. I_{sc} is the short-circuit current, E_m the membrane potential, R the pore resistance, P_{max} the maximum output power, T_+ the cation transport number, and Ψ the permselectivity.

Concentration	I_{sc} **[pA]**	E_{m} **[mV]**	R **[GΩ]**	P_{max} **[fW]**	T_+ **[-]**	ψ
S1/S2	0.138	-39.352	286.164	1.353	0.838	0.626
S1/S3	0.415	-28.395	68.410	2.947	0.622	0.244
S2/S3	0.162	-6.736	41.651	0.272	0.558	0.116

6.4 Discussion

In this chapter, a first analysis was carried out to guide the choice of fabrication parameters for porous silicon membranes, with the aim of operating under conditions that maximise the power output in reverse electrodialysis. The structural properties of the porous layer were first investigated to determine the achievable pore-size range. Because pore size and porosity are intrinsically linked for a fixed choice of HF–alcohol solution, this relationship constrains the total number of pores per unit

surface area and therefore influences the theoretical maximum power density of the membrane. To modify the relationship between pore size and porosity, alternative substrates and/or different electrolyte compositions for the electroetching could be considered.

In a second step, a numerical model of a charged nanopore was used to study the ionic transport properties and to compute the theoretical maximum power output. The results show clearly that pore size strongly affects the power performance and therefore provides guidance for selecting the target pore-size range, and by extension the etching current density during fabrication. Although smaller pores yield lower individual power outputs, their much higher number per unit area allows them to outperform larger pores at the membrane scale. Pores with diameters below 20 nm are therefore expected to provide the highest power densities.

Several assumptions underlying this analysis must, however, be discussed. In the present study, the surface charge density was assumed constant and uniform, even though it has been shown to depend on both pore size and ionic concentration [143]. Yun Do Kim *et al.* [384] solved the Nernst–Planck–Poisson (NPP) equations for a charged alumina nanopore, determining the surface charge from an equilibrium model similar to Eq. (4.26), but using only the solution pH as a parameter. Their model did not account for local curvature or confinement effects, which are expected to play an important role at the nanoscale. A more accurate approach would consist of coupling the surface-charge model of Keshavarzi *et al.* [143] directly to the NPP solver. This would require knowledge of the equilibrium constants and the surface-site density of the actual porous silicon, which could in principle be determined experimentally. The model also requires assigning finite ion sizes, which would significantly increase the computational cost due to the large simulation domain. Given that the present thesis is primarily experimentally oriented, such a numerically intensive extension was not pursued. Instead, a simplified approach incorporating only a surface–complexation description of the surface chemistry is explored in Chapter 8.

Another possibility would be to tabulate the surface charge density as a function of ionic concentration and pore size. Although no direct measurement technique exists to obtain these values inside nanopores, an indirect approach based on electro-osmosis could be used. This method, explored during the Master's thesis of Laura Dubus, is briefly presented in Section B.

The upscaling model used to relate single-pore results to full membranes also relies on the assumption that the membrane behaves as an array of perfectly parallel, independent pores. This approximation neglects structural features such as pore branching and pore spacing. Pore branching occurs when neighbouring pores merge or connect during electrochemical etching, a phenomenon that becomes more frequent at high current densities due to increased porosity. Its consequences

depend on both the resulting geometry and the concentration conditions [385, 386]. Merging increases tortuosity and may hinder ionic transport, but it can also provide additional pathways and reduce dead-end pores, limiting resistance increases [385].

Pore inter-distance also affects concentration polarisation (CP) at membrane entrances. Su *et al.* [64] showed that membranes with large inter-pore spacing (>500 nm, $< 10^6$ pores/cm^2) can be described well by extrapolating single-pore results, whereas membranes with smaller spacing exhibit strong interactions between neighbouring pores, modifying the local concentration and therefore the resistance. Although the porous silicon samples etched at 3 mA/cm^2 contain smaller pores that should reduce CP, the pore spacing in all samples is below 20 nm, and the pore densities exceed 10^6 pores/cm^2; CP effects therefore cannot be neglected.

A refined description of these effects would require a full 3D model accounting for pore branching, tortuosity, and inter-pore interactions. However, this would involve extremely large computational domains for potentially few insight regarding the membrane properties.

Considering the results of the present study, three different etching current densities were selected based on the pore sizes they produce, as shown in Table 6.8. The membrane thickness was chosen according to mechanical constraints in order to ensure structural integrity and avoid mechanical failure. Based on the work of Vercauteren [206], who used a similar silicon substrate, a thickness of 90 µm was found to be sufficient to withstand the pressure associated with water flow through the membrane for her fluidic set-up.

Table 6.8: Chosen morphological characteristics of the porous silicon (PSi) layer for the membranes. Three different membranes were fabricated.

Current density [mA/cm^2]	**Pore size,** D_p [nm]	**Porosity,** ε_p [%]
3	11.8 ± 6.3	33.73 ± 2.30
50	18.5 ± 9.72	56.90 ± 1.39
100	22.4 ± 12.4	66.03 ± 2.36

6.5 Conclusion

In this chapter, the objective was to investigate the I–V characteristics of porous silicon membranes through a numerical analysis of a single charged nanopore under salinity gradient conditions. This study constitutes the first step toward establishing a physics-based understanding of ionic transport in porous silicon within the framework of nanofluidic reverse electrodialysis (nRED).

Structural characterization of porous layers fabricated from highly p^{++}-doped silicon substrates revealed that pore radius and porosity are intrinsically linked to the electrochemical porosification current density. Lower current densities produce smaller pores and reduced porosity. From a transport perspective, these small pores operate in a surface-charge-dominated regime where electric double layer (EDL) overlap enhances ion selectivity and increases the membrane potential. However, this enhancement occurs at the expense of higher ionic resistance.

The numerical results highlight a fundamental trade-off between permselectivity and ionic conductance, leading to the existence of an optimal pore radius that maximizes output power density. When extending the analysis from a single pore to a porous membrane, pore density becomes a critical parameter. Accounting for porosity suggests that membranes with pore diameters below 20 nm are particularly promising, as the increased pore density compensates for the higher individual pore resistance at the macroscopic scale.

Although the model assumes a constant surface charge density and neglects structural complexities such as pore tortuosity, branching, and concentration-dependent surface chemistry, it provides a first-order performance map linking fabrication parameters to electrochemical output. This establishes theoretical performance limits for porous silicon membranes in nRED and identifies a targeted fabrication window for subsequent experimental validation.

Overall, this chapter lays the theoretical foundation for the thesis by quantifying how pore geometry and surface charge govern ionic transport and power generation. It thereby supports the central hypothesis that porous silicon, when engineered within the appropriate nanometric regime, can function as a viable ion-exchange membrane for nanofluidic reverse electrodialysis.

Chapter 7

Process for porous silicon membrane fabrication and analysis as membranes for nRED

7.1 Introduction and motivation

The previous chapter focused on selecting porous silicon characteristics that maximize nRED performance, based on a theoretical study of a single nanopore using numerical simulations. The present chapter focuses on the experimental validation of these theoretical predictions.

Nano-porous reverse electrodialysis (nRED) is a method for generating electricity from the mixing of fresh and saltwater, similar to conventional reverse electrodialysis (RED), but relying on nanoporous membranes to enhance performance through higher ionic selectivity and increased ionic current, as described in Chapter 4. However, as discussed in Section 4.5, the performance of nanoporous membranes remains below that of conventional polymer membranes in terms of power density. Existing studies have mainly focused on track-etched membranes and anodic aluminum oxide (AAO) as base materials, while no study to date has investigated porous silicon membranes for RED applications.

Porous silicon nevertheless presents several attractive features, as its pore size and porosity can be precisely tuned during the electrochemical etching process. Compared to AAO and track-etched membranes, porous silicon also offers advantages for integration into MEMS-based energy harvesters, since it does not require additional transfer or bonding steps for membrane integration, as discussed in Section 5.

This chapter therefore focuses on the fabrication and characterization of porous silicon membranes for ionic selectivity. Two fabrication routes are investigated: a

self-supported membrane, based on the work of R. Vercauteren [206], and a free-standing membrane. The second approach was developed in response to limitations encountered with the first method, which are detailed in this chapter. Finally, the performance of the fabricated pSi membranes is evaluated in a custom-made RED cell, and the experimental results are compared with the numerical trends established in the previous chapter.

7.2 Materials and experimental set-up

7.2.1 Materials: pSi membrane

The substrates consisted of double-side polished, heavily boron-doped (p++), "100"-oriented silicon wafers, with a resistivity of 0.9–1 mΩ·cm and a thickness in the range of 380–400 µm. The wafers were supplied by ZHONGGUI Semiconductor (Yangzhou) Co., Ltd. (China).

7.2.2 Materials: set-up for characterisation

The set-up is shown in Fig. 7.1 and consists of the membrane sandwiched between two cells filled with ionic solutions of different concentrations. Two O-rings (10.82 × 1.78 mm) ensure that no leakage occurs and that no ionic short-circuit is possible.

Two Ag/AgCl reference electrodes (C2015B1) were purchased from Ossila Ltd., and two platinum mesh electrodes (CS913) were obtained from Wuhan Corrtest Instruments Corp. Ltd. A 5 M sodium chloride solution was purchased from Merck.

Cation- and anion-exchange membranes (Fumasep® FKS-30 and Fumasep® FAS-30) were purchased from Fumatech. Each membrane was cut from a single sheet and soaked in KCl solution to hydrate the polymer and remove the polyethylene glycol protection layer. The Fumatech membranes were placed directly against the O-ring. The membrane area defined by the inner diameter of the O-ring corresponds to an apparent exposed area of approximately 92 mm^2 when viewed perpendicular to the membrane plane. Owing to fluid penetration underneath the O-ring, the membrane surface accessible to the solution extends beyond this geometric boundary. In the absence of applied pressure, the accessible area can reach approximately 125 mm^2, while under typical sealing pressure required to prevent leakage, the effective liquid-accessible membrane area is estimated to be around 115 mm^2.

Aluminium oxide (AAO) membrane filters (13 mm diameter) were purchased from Sterlitech. Although the nominal pore size specified by the manufacturer is 20 nm, our measurements revealed that the majority of the membrane thickness

exhibits pore diameters closer to 200 nm, with only a thin top layer showing 20 nm pores. The membrane thickness is 60 μm and the average porosity is 37%. The AAO membranes were sealed in the same manner as the free-standing pSi membranes.

7.2.2.1 Set-up: sensing data acquisition

Two Ag/AgCl reference electrodes were used to measure the difference in electrochemical potential across the membrane. They were placed as close as possible to the membrane. Silver/silver chloride (Ag/AgCl) reference electrodes are widely used in electrochemical measurements due to their stable and well-defined potential, which is governed by the reversible redox equilibrium between metallic silver and silver chloride. The use of potassium chloride as an internal electrolyte ensures high ionic conductivity and minimizes liquid junction potentials, resulting in low noise and rapid potential stabilization. Unlike mercury-based reference electrodes, Ag/AgCl electrodes are non-toxic and environmentally benign, making them suitable for both laboratory and field applications. They exhibit good long-term stability, reproducibility within a few millivolts, and compatibility with a wide range of aqueous electrolytes. Owing to their robustness, simplicity, and low cost, Ag/AgCl reference electrodes remain the most practical and reliable choice for potentiometric and impedance-based electrochemical measurements [83, 387].

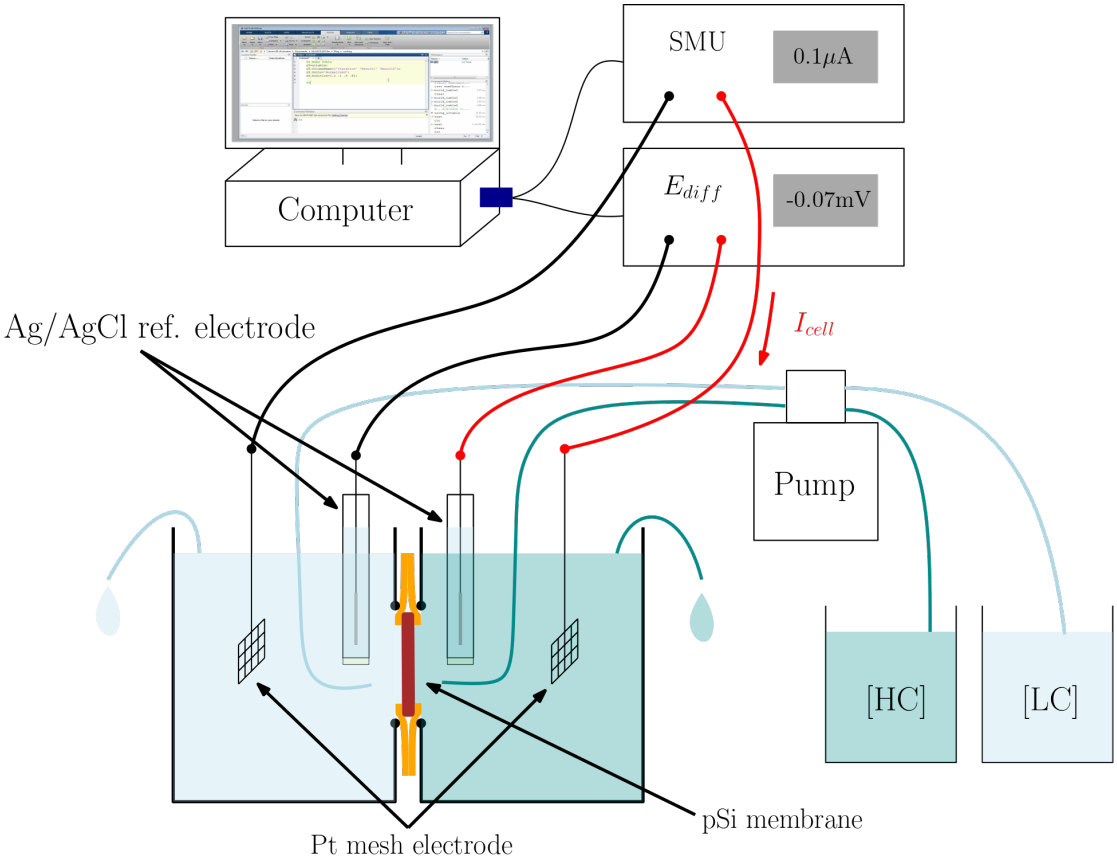


Figure 7.1: Schematic of the measurement setup. The FS-PSi membrane is clamped between two half-cells filled with KCl electrolyte with high (HC) or low (LC) concentration, and sealed by O-rings to prevent leakage and ionic short-circuiting. Two Ag/AgCl reference electrodes are connected to a multimeter to monitor the membrane potential, while two Pt mesh electrodes are driven by a SMU to apply voltage or current and record the ionic current through the membrane. Both instruments are computer-synchronized. The electrolyte is continuously refreshed near the membrane surfaces using peristaltic pumps to reduce concentration polarization.

The silver/silver chloride (Ag/AgCl) reference electrode is typically constructed from a silver wire that is electroplated with a thin layer of silver chloride and subsequently immersed in a 3.5 M or saturated potassium chloride (KCl) solution. The electrolyte is generally contained within a glass tube that terminates in a porous glass frit, which serves as a liquid–liquid junction to enable ionic exchange between the internal solution and the external electrolyte. This configuration yields a straightforward and robust electrode design, commonly used in electrochemical measurements. A schematic representation of a standard Ag/AgCl reference

electrode is shown in Figure 7.2.

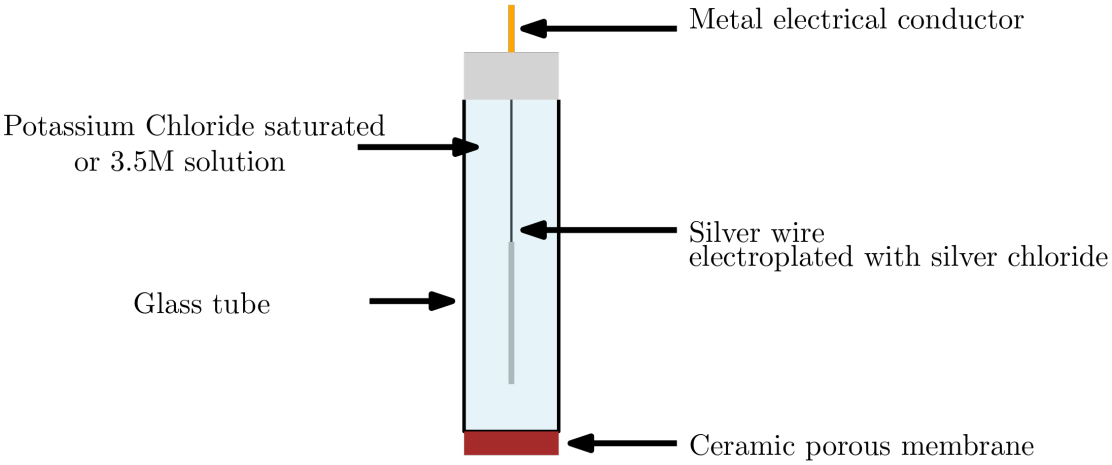


Figure 7.2: Schematic of an Ag/AgCl reference electrode.

When carefully prepared and properly maintained, Ag/AgCl reference electrodes exhibit exceptionally stable potentials, with variations below 0.02 mV under controlled laboratory conditions [83]. Their performance can, however, be influenced by aging of the AgCl layer, oxygen exposure, electrolyte impurities, and light-induced reactions, which may slightly alter the Ag/AgCl equilibrium. Despite these effects, Ag/AgCl electrodes remain the most reliable and reproducible reference system due to their well-defined and reversible redox behavior. Recent quantitative studies have shown that their intrinsic electrochemical noise is extremely low: Riistama *et al.* [388] measured root-mean-square noise voltages of 0.08–0.45 mV over 0.5–500 Hz, confirming the dominance of low-frequency $1/f$ components below 10 Hz, while Zhang *et al.* [389] reported self-noise levels of only a few $\mathrm{nV}/\sqrt{\mathrm{Hz}}$ at 1 Hz in seawater for optimized Ag/AgCl electrodes. These values represent the state of the art in reference electrode stability, making Ag/AgCl systems ideally suited for high-sensitivity electrochemical and impedance measurements where microvolt-level noise control is essential.

For the application of a precise external current or voltage, mesh platinum electrodes were chosen. These electrode are inert electrode, meaning it does not readily undergo oxidation or reduction under normal electrochemical conditions and thus will not contaminate the solutions. The potential is never measured with these electrodes.

The Ag/AgCl electrodes were connected to a Keithley DMM7510 7.5-digit multimeter to measure the membrane potential and the two platinum mesh electrodes were connected to a Keithley 2450 SMU to apply either an external voltage or current. Both instruments were computer-controlled with Matlab and a GBIP

connection to synchronize sourcing and measurement times. The external voltage was applied every 0.4 s, and the membrane potential was measured with NPLC = 3. This parameter allowed to limit the noise to be less than 1 mV. To minimize concentration polarization (see 3.2.2), the solutions were stirred using two peristaltic pumps delivering flow close to the membrane surface. The room temperature was maintained at 22 °C, and the pH of the solution was measured at 5.7.

7.2.2.2 Ionic solutions

Solutions were prepared by dilution from a 5 M KCl stock solution, obtained by dissolving 372.756 g of KCl in 1 L of deionized water. Concentrations were determined from ionic conductivity measurements using a Conductivity Meter (SEVENCOMPACT S230). Table 7.1 summarizes the three different concentrations used in this work.

Table 7.1: Different KCl concentrations used in this work and their measured ionic conductivity for reference.

Solution name	**Concentration [M]**	**Conductivity [μS/cm]**	**Activity $\gamma_\pm$** KCl [-][390]
S1	1×10^{-4}	17.4	0.988[a]
S2	1×10^{-3}	178.1	0.965
S3	1×10^{-2}	1806	0.900

[a] Extrapolated from S2 and S3 using $f(x) = 1 - \exp\big(-0.516 + 0.343 \ln x - 0.00985(\ln x)^2\big)$ with x the concentration in mol/L.

7.3 Self-supported porous silicon membranes: fabrication and characterisation

7.3.1 Self-supported porous silicon membranes: fabrication

Porous silicon (pSi) membranes were fabricated in the cleanroom facility of the Wallonia Infrastructure Nano Fabrication platform (Winfab, UCLouvain). Figure 7.3 summarises the process flow used for the fabrication of the self supported porous silicon (PSi) membranes. The procedure begins with a standard cleaning sequence in a freshly prepared piranha solution (H_2O_2:H_2SO_4, 2:5), followed by two rinsing steps in continuously flowing deionised (DI) water for 20 min each. The native oxide is subsequently removed in a 2% HF bath until the silicon surface becomes hydrophobic. A 90 nm SiO_2 layer is then grown by wet thermal oxidation

at 1000 °C, after which a 500 nm polycrystalline silicon (PolySi) film is deposited at 620 °C using LPCVD.

Patterning is performed by i-line optical lithography (positive resist AZ® MIR™ 701, MicroChemicals GmbH), followed by RIE to open the PolySi layer and clear it from the rear side of the wafer. The exposed SiO_2 at the bottom of the etched features is removed in diluted HF (5% v/v). This patterned SiO_2/PolySi bilayer subsequently acts as the hard mask during the electrochemical formation of porous silicon [206].

A second lithography step is carried out on the backside using a negative resist (AZ® nLOF™ 5510), forming a lift-off stencil for aluminium evaporation. Al deposition is performed in an e-gun VST system, producing a 300 nm film that serves both as a backside etch mask and as an electrical contact during anodization.

Porosification is carried out in a custom Teflon® single-bath etch cell using a platinum coil counter-electrode, an aluminium working electrode, and a Keithley DC power supply (Model 2460) operated as a current source. Etching is performed in an HF (49%):ethanol electrolyte (3:1 vol. ratio) following a two-step sequence. (i) Formation and removal of a sacrificial porous layer using a current density identical to that applied in the subsequent etching step. The sacrificial layer is etched for 60 s and then removed in 1 M KOH until the reaction ceases. This procedure serves as an efficient cleaning step, providing clean and reproducible surfaces [383], as discussed in Section 5.1.1. (ii) Etching of the porous layer using the etch-stop technique (10 s current on, 2 s current off) at one of the selected current densities (see Table 6.8). The total number of cycles is defined in Table 7.2 for each current density. The etch-stop technique allows regeneration of the HF concentration at the pore tips during the pause period [391]. The off-time was chosen to be short compared to the pore growth time, but long enough to allow partial restoration of the HF concentration at the pore tips by diffusion. Using $t_D \sim L^2/D_{\text{eff}}$ with a characteristic diffusion length on the order of the porous layer thickness ($L \sim 10$–$100\ \mu$m) and a molecular diffusion coefficient for small species in liquid electrolytes of $D \sim 10^{-5}\ \text{cm}^2\,\text{s}^{-1}$ (with D_{eff} reduced in porous media by tortuosity), the resulting diffusion time scale ranges from sub-second values at early stages to several seconds or more for thick layers. Therefore, a 2 s pause is sufficient to mitigate HF depletion during the initial growth but may become limiting as the porous layer approaches $\sim$90 μm.

Table 7.2: Parameters for the electrochemical etching of the porous layer for the different membranes.

Current density [mA/cm^2]	**Sacrificial time**	**Number of cycles**	**Predicted thickness [μm]**
3	120	3,340	117.1
50	60	213	92.68
100	30	112	96.93

After anodization, the wafer is thermally oxidised in a Heraeus furnace under a 1.5 L min^{-1} O_2 / 1.2 L min^{-1} N_2 atmosphere at 250 C for 30 min. This mild oxidation step stabilises the porous matrix while limiting thermally induced stresses. The resulting thin oxide layer also protects the porous region during the final backside pattern transfer, performed by DRIE until the PSi membrane becomes exposed.

The fabricated membranes are produced either as 4 mm^2 squares or as circular membranes of 3.14 mm^2. Each membrane is located on a 1 cm^2 die, yielding 32 devices per 3-inch wafer. Final membrane thicknesses range from 65 to 100 μm depending on membrane size, wafer position, and batch variations. Thinner structures were avoided due to their tendency to deform or crack during subsequent processing.

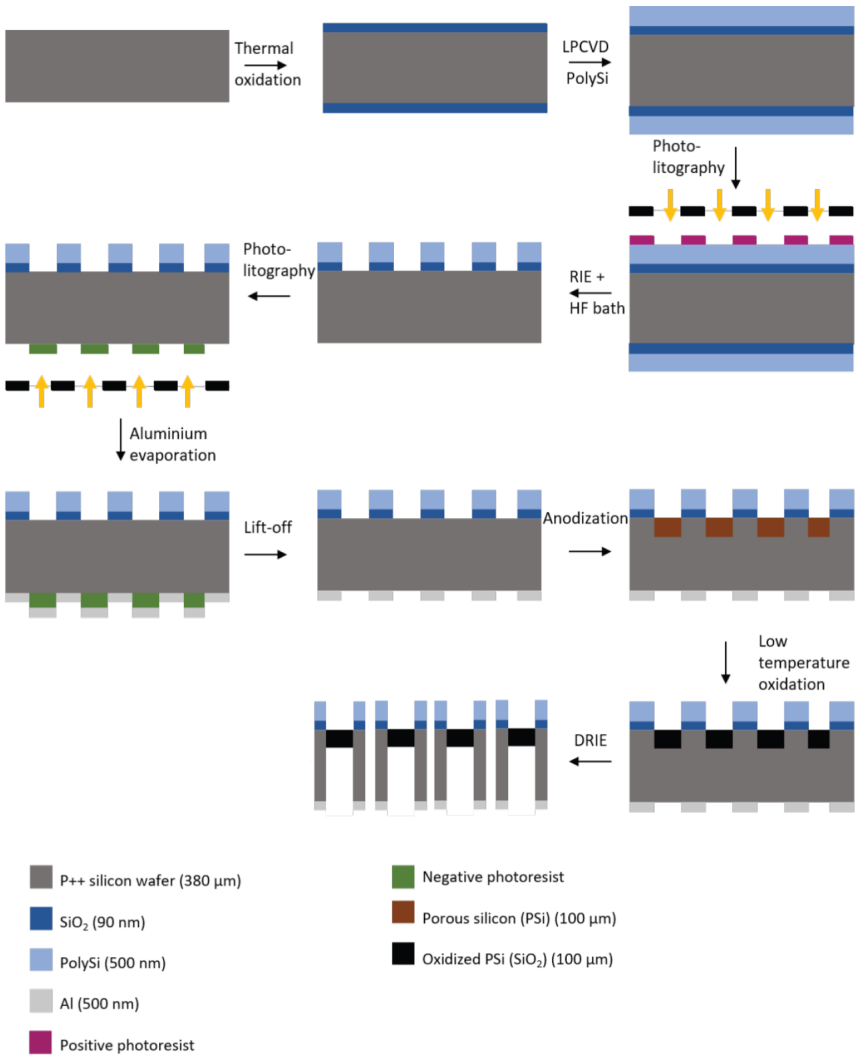


Figure 7.3: Schematic illustration of the manufacturing process of PSi membranes. Starting from a cleaned 3-in diameter highly doped silicon wafer, the process goes through the following steps: (1) thermal oxidation, (2) deposition of a polysilicon layer (PolySi) using Low Pressure Chemical Vapour Deposition (LPCVD); (3) positive photolithography on the frontside and opening of the PolySi and SiO_2 layers using Reactive Ion Etching (RIE) and diluted HF respectively; (4) negative photolithography on the backside, evaporation of an aluminium mask and lift off of the resist; (5) formation of the porous silicon layer by electrochemical etching; (6) low temperature thermal oxidation; and finally (7) opening of the membrane using Deep Reactive Ion Etching (DRIE). Modified from [206].

The main objective of an ion-selective membrane in a reverse electrodialysis

system is to ensure the selective passage of ions, regardless of its overall performance. Therefore, the primary target in the fabrication of porous silicon membranes was to avoid any defects or cracks in the porous layer, as these would lead to regions of very low ionic selectivity and result in ionic short-circuits.

7.3.1.1 Characterisation: front side

For low electroeching current (below 50 mA/cm^2), the membranes usually ended up clean from the top view (the side initially exposed to the HF during the etching) as seen in Figure 7.4. All over the unmasked area, the porous layer kept the desired characteristics, like pore size and porosity, as seen in Figure 7.5, although the pore walls got slighty thicker due to the thermal oxidation.

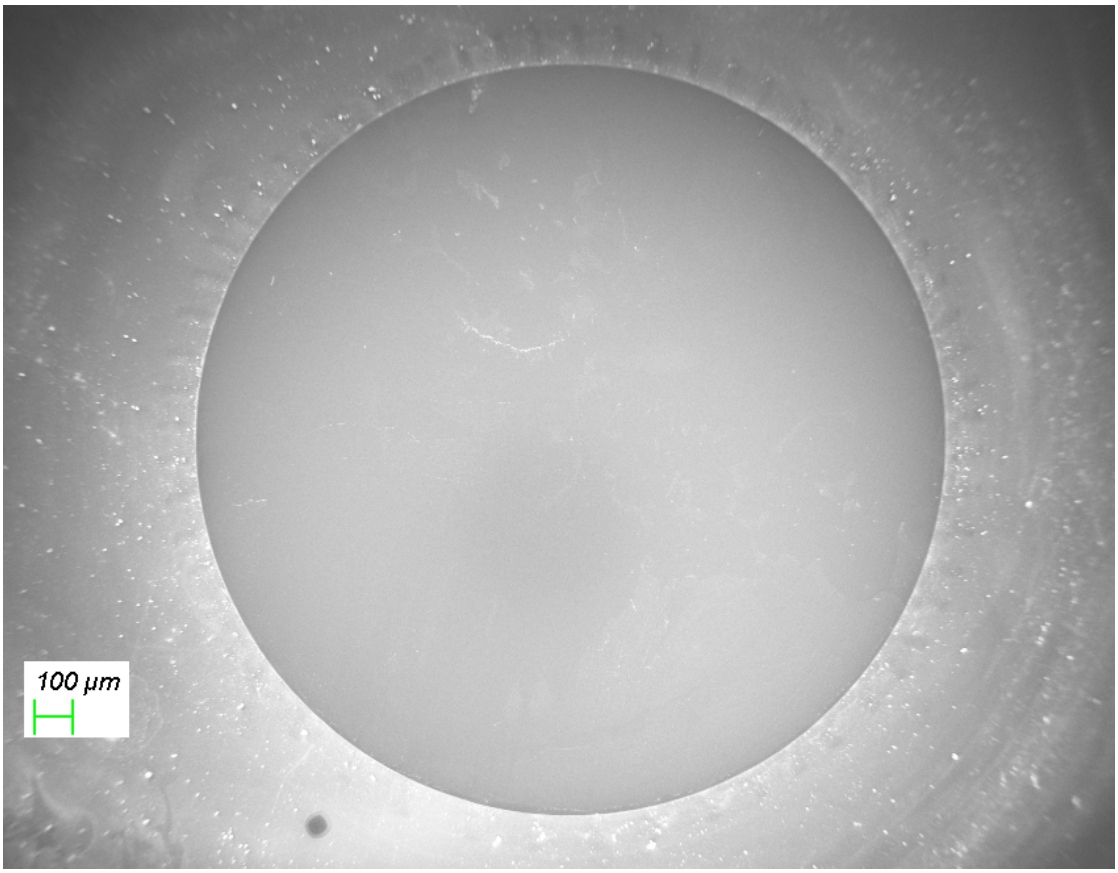


Figure 7.4: Top view SEM image of a self-supported porous silicon membrane.

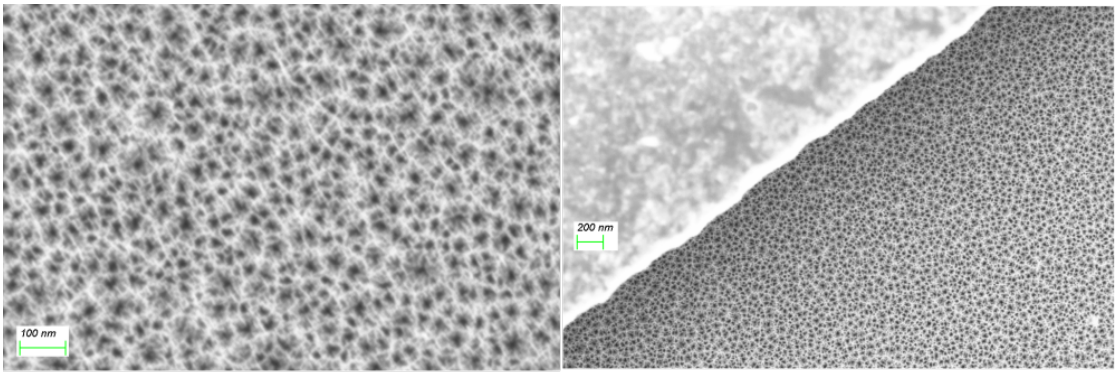


Figure 7.5: Top view SEM image of a self-supported porous membrane obtained with 50 mA/cm^2. Image taken a) in the central region and b) close to the membrane edge.

Membranes obtained with higher current densities tended to develop cracks, most often near the membrane edge. These defects originate immediately after the porosification step, as confirmed by the SEM images in Fig. 7.6. Thermal expansion during oxidation generally did not increase the crack size, as illustrated in the same figure.

The defects appear at the periphery of the membrane, close to the bulk support, and are most likely caused by stress release during the drying of isopropanol after rinsing the HF solution. As explained in [392–394], porous structures can experience large capillary forces when the rinsing liquid evaporates. As illustrated in Fig. 7.7(a), the capillary pressure exerted on the pore walls depends on the liquid–solid contact angle θ, the liquid–vapor surface tension γ, and the pore diameter D. It is given by the Laplace pressure

$$\Delta P = P_1 - P_2 = \frac{4\gamma \cos\theta}{D},$$

which increases as evaporation progresses, since the contact angle θ typically decreases as the liquid film thins.

Belmont *et al.* [393] reported that cracking occurs when the elastic energy stored in the porous layer due to capillary pressure exceeds the interfacial fracture energy of the silicon layer. They derived the following expression for the critical thickness:

$$h_c = \left(\frac{r}{\gamma_{LV}}\right)^2 E_{Si}(1-\varepsilon_p)^3\gamma_{Si}, \tag{7.1}$$

where r is the pore radius, γ_{LV} the liquid–vapor surface tension, E_{Si} the Young's modulus of silicon, γ_{Si} the surface energy of silicon, and ε_p the porosity.

For samples etched at 100 mA/cm^2, the porosity ε_p is high and the critical thickness h_c becomes relatively small, even when using isopropanol, which has a low surface tension γ_{LV}. Since measurements are carried out in water (higher γ_{LV}), the likelihood of crack formation during handling becomes even greater. For this reason, each membrane must be rinsed in isopropanol immediately after any experiment to preserve its structural integrity.

Furthermore, attempting to use even higher current densities would increase the pore size r but also increase the porosity ε_p, which would further reduce h_c. Thus, either the membrane thickness must be reduced (at the expense of mechanical stability), or critical-point drying must be employed to avoid cracking during the drying phase.

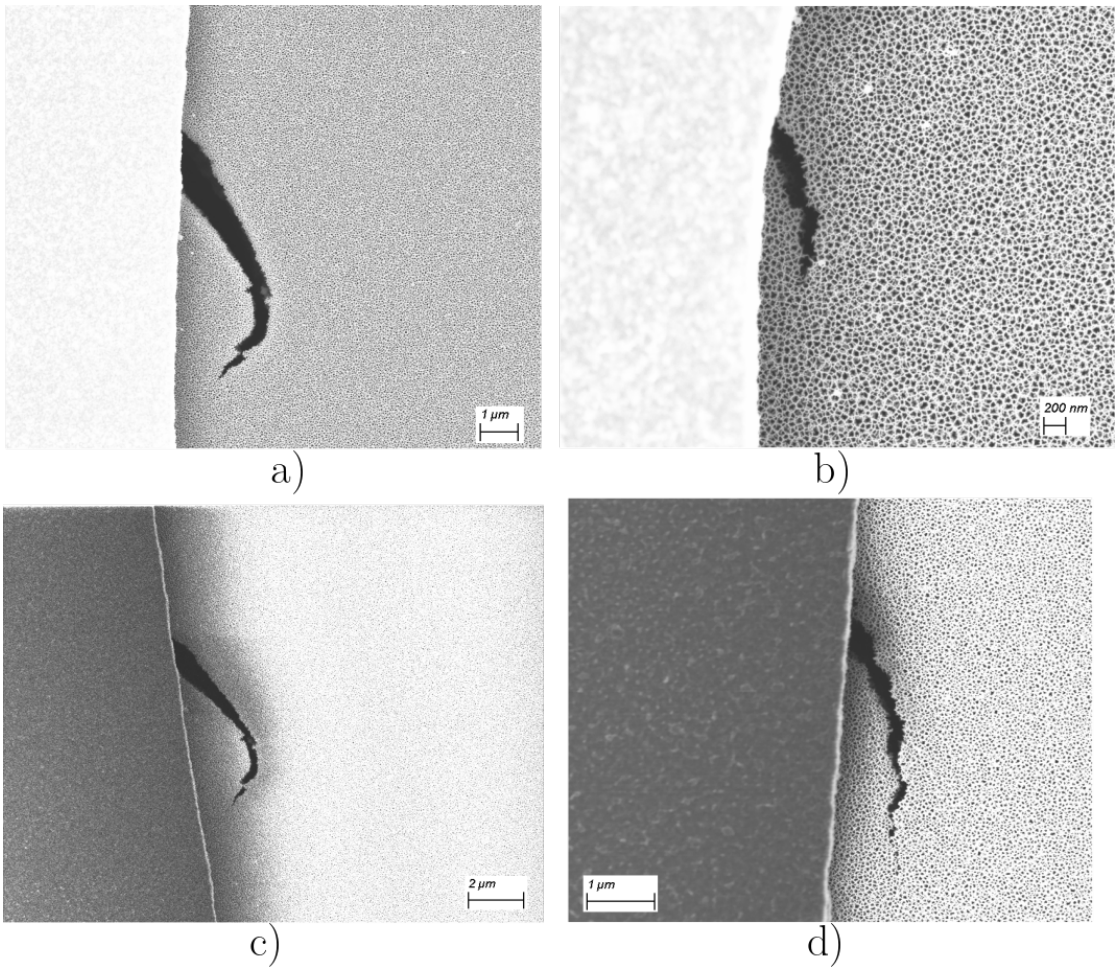


Figure 7.6: Top view SEM image of a self-supported porous membrane obtained with 100 mA/cm^2. Image taken before (a) and b)) and after (c) and d)) the oxidation step close to the membrane edge.

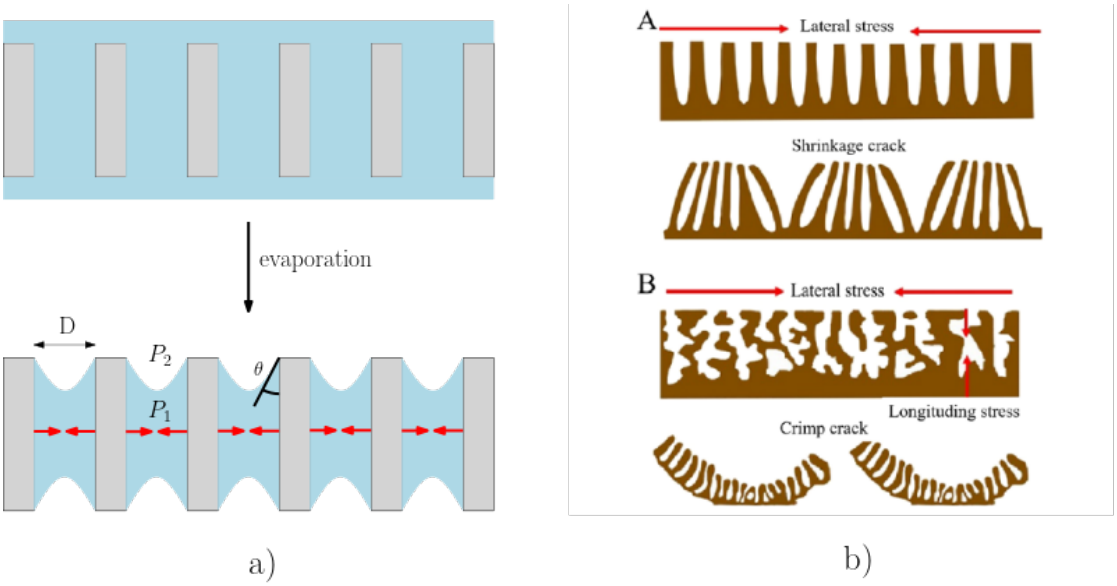


Figure 7.7: a) Formation of capillary pressure inside a pore during liquid evaporation. P_1 denotes the pressure within the liquid, P_2 the pressure in the surrounding air, θ the contact angle at the liquid–solid interface, and D the pore diameter. b) Geometry- and porosity-controlled model describing surface cracking behaviour in porous silicon (pSi) [394].

7.3.1.2 Characterisation: back side

The backside is released when the DRIE etches away the bulk silicon beneath the porous layer, thereby opening the pores from both sides. The main drawback of this method is that the number of cycles required to fully open all backside pores cannot be determined precisely, because the etch rate depends on the plasma conditions inside the chamber as well as on the uncertainty in the porous-layer thickness. For this reason, the etch is performed in two stages. First, based on the estimated etch rate, most of the bulk silicon is removed, leaving only a few micrometres above the porous layer. Then, the etching proceeds in small groups of cycles; after each group, the wafer is inspected to check whether the porous layer has been exposed.

Three issues were observed with this DRIE approach. First, the backside of the membrane is not uniformly etched, as shown in Fig. 7.8. This non-uniformity limits the number of pores that are fully opened and therefore reduces the effective pore density available for ionic transport in the RED system. To further release the remaining pores, more cycles are required and this has an impact on the porous layer.

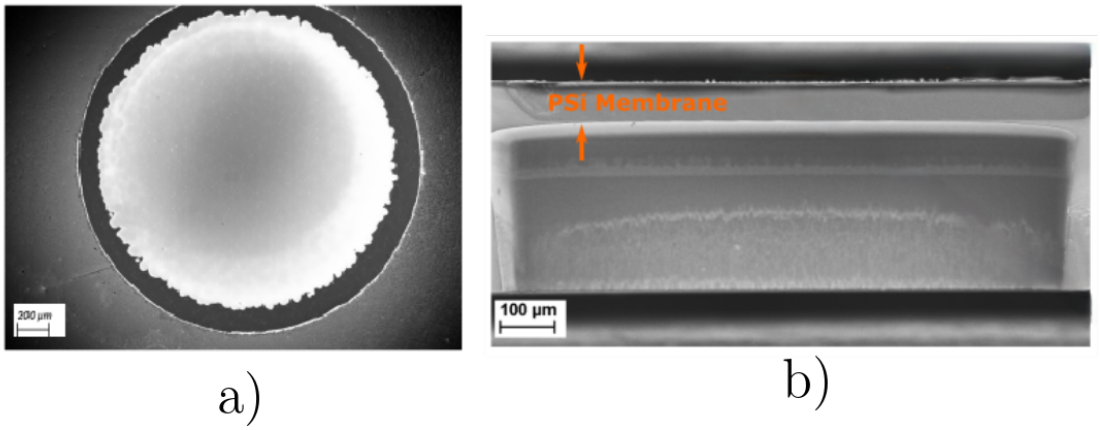


Figure 7.8: a) Back-side SEM image of a self-supported porous silicon membrane after the DRIE release. The silicon substrate is not uniformly etched away, leaving regions where pores remain unopened. b) Cross-section of the self-supported porous silicon membrane. The membrane is thinner at the center than near the edges due to the non-uniformity of the DRIE etch.

The second issue is the impact of the DRIE plasma on the porous layer. Although SiO_2 is etched more slowly than Si, its high specific surface area and thin pore walls make it sensitive to plasma exposure. Test runs in which a porous layer was exposed to two DRIE cycles show that the porosity and pore size are altered, as illustrated in Fig. 7.9. Cross-sectional images further reveal a deformed porous region approximately 500 nm thick, also visible in Fig. 7.9. Such deformation can reduce the number of pores that are properly opened.

Because of variations in porous-layer thickness, fluctuations in the DRIE etch rate, and the intrinsic non-uniformity of the etch, it is nearly impossible to stop the process exactly at the moment the membrane becomes fully released. As a result, the porous layer is unavoidably exposed to additional DRIE cycles, increasing the extent of plasma-induced damage.

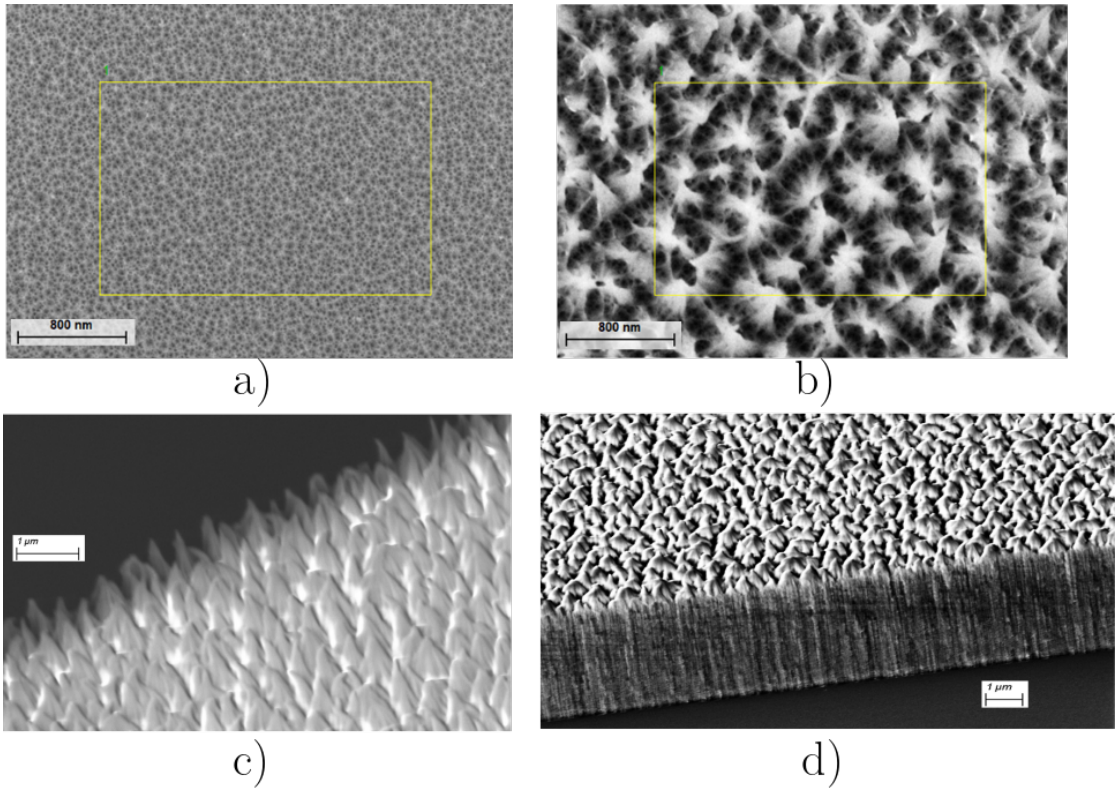


Figure 7.9: SEM images of a porous layer obtained at 50 mA/cm^2, a) before any DRIE cycles and b) after 3 cycles of DRIE. c) d) Cross section images of a porous layer after DRIE cycles. The affected layer shows small pyramids.

Lastly, an unexpected effect from the DRIE was noticed later during the thesis. The impact of the DRIE was not limited to the structural modification of the pores, but also affected their surface chemistry. The Bosch DRIE process consists of two alternating steps. The first is a passivation step, during which a fluorocarbon polymer layer (CF_x) is deposited from the C_4F_8 plasma. This polymer coats all surfaces and prevents lateral etching. The second step is the etch step, where ion bombardment removes the polymer only at the bottom of the pores, exposing the silicon. Fluorine radicals generated from the SF_6 plasma then etch the silicon vertically. Because the removal of the CF_x polymer is anisotropic, a fraction of this fluorocarbon layer remains on the sidewalls after the DRIE cycles. This results in a non-homogeneous surface chemistry inside the porous layer, with silicon partially covered by residual fluorocarbon.

To verify this, the chemical composition of the porous layer was analysed using EDX in the SEM, comparing samples exposed to different numbers of DRIE cycles. Table 7.3 shows the atomic percentages of silicon, fluorine, and oxygen obtained from top-view EDX scans over a defined area. A first observation is that fluorine is

detected even on samples that were not subjected to DRIE. This fluorine originates from the electrochemical etching process in HF and is uniformly distributed across the porous layer, as confirmed by the cross-section EDX analysis presented later in this section.

When the samples undergo DRIE, the proportion of fluorine increases with the number of cycles. This indicates the accumulation of fluorocarbon residues inside the porous matrix, rather than simple "implantation" of fluorine atoms. This effect appears to depend on the morphology of the porous layer: samples fabricated at lower current density (5 mA/cm^2), which have smaller pore sizes and lower porosity, show a reduced increase in fluorine content, likely due to limited plasma penetration and reduced polymer deposition inside narrower pores.

Elem.	**50 mA/cm^2 no DRIE**	**50 mA/cm^2 DRIE (3 c.)**	**50 mA/cm^2 DRIE (6 c.)**	**5 mA/cm^2 DRIE (3 c.)**
O	39.92 ±6.31	46.34 ±6.40	46.09 ±7.53	40.98 ±5.89
F	2.15 ±0.87	5.68 ±1.43	7.87 ±2.22	4.60 ±1.31
Si	57.93 ±4.93	47.98 ±3.94	46.04 ±4.29	54.42 ±4.30

Table 7.3: Atomic percentage (at.%) of elements with 1-sigma errors for all samples, showing the evolution of the porous silicon layer composition before and after different numbers of DRIE cycles.

Cross-sectional EDX images reveal how deeply fluorine is implanted inside the porous layer, as shown in Fig. 7.10. Based on the measurements, fluorine originating from the DRIE process is detected up to approximately 1 μm into the porous layer, which corresponds roughly to the thickness of the deformed region observed in Fig. 7.9.

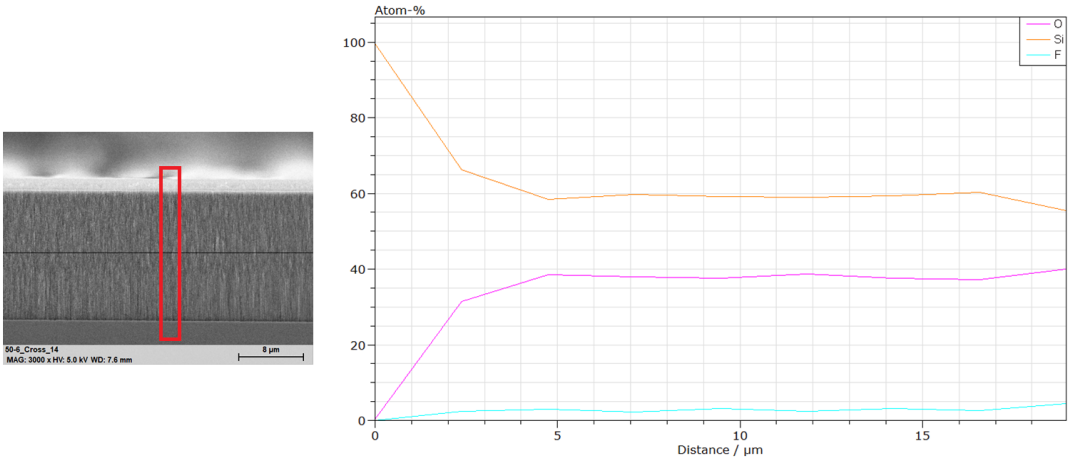


Figure 7.10: Cross section EDX image of a oxidized porous silicon layer (left) showing the composition in atomic percentage of Oxigen (purple), Silicon (orange) and Fluorine (blue).

7.3.2 Self-supported porous silicon membranes: I–V results

7.3.2.1 Methods for sensing data

Each membrane was briefly immersed (30 s) in a KCl solution before being placed in the microfluidic cell. The data presented for the self-supported porous silicon membranes correspond to raw measurements. As discussed in the following section, the variability observed between successive measurements over time makes a rigorous statistical analysis difficult.

7.3.2.2 Characterisation: I–V results

The first tests performed on the membranes were I–V measurements under the S1/S2 concentration ratio. Issues related to the DRIE-induced damage were identified when testing the symmetry of the membranes. In principle, these membranes should be symmetric across their thickness, since the porosification current density was kept constant during fabrication. However, as shown in Fig. 7.11, different I–V characteristics were obtained depending on which side of the membrane faced the high- or low-concentration solution, a behaviour that was not expected.

The asymmetric nature of the membranes was further confirmed by performing I–V measurements with identical solutions on both sides. Instead of producing a linear, symmetric curve, the membrane exhibited a diode-like response, as seen in Fig. 7.12. Such rectifying behaviour can be reproduced numerically by introducing

a small region of the nanopore with an opposite surface charge density, as illustrated in Fig. 7.13.

The physical origin of this behaviour is the formation of a nanopore with two regions of opposite surface charge densities, $\sigma_{s,+}$ and $\sigma_{s,-}$. In such a configuration, the direction of the applied electric field influences whether ions accumulate or are depleted inside the pore. When the electric field points toward the right (relative to the $\sigma_{s,+}$–$\sigma_{s,-}$ junction), anions in the $\sigma_{s,+}$ region are pushed out of the pore and only few can enter from the $\sigma_{s,-}$ side, as they must overcome a large potential barrier. A similar situation occurs for cations in the $\sigma_{s,-}$ region. The pore therefore becomes depleted of charge carriers, resulting in a very low ionic current.

When the direction of the applied electric field is reversed, the situation in both regions is inverted: ions accumulate instead of being expelled, and the pore becomes enriched in charge carriers. Consequently, the ionic current increases significantly. This ionic rectification mechanism closely resembles the I–V response of a semiconductor diode. In this analogy, anions and cations behave similarly to electrons and holes, while the surface charge density plays the role of the doping concentration that determines the dominant charge carrier in each region. Both carriers must cross the potential barrier at the $\sigma_{s,+}$–$\sigma_{s,-}$ junction, which is effectively lowered or raised depending on the direction of the applied electric field.

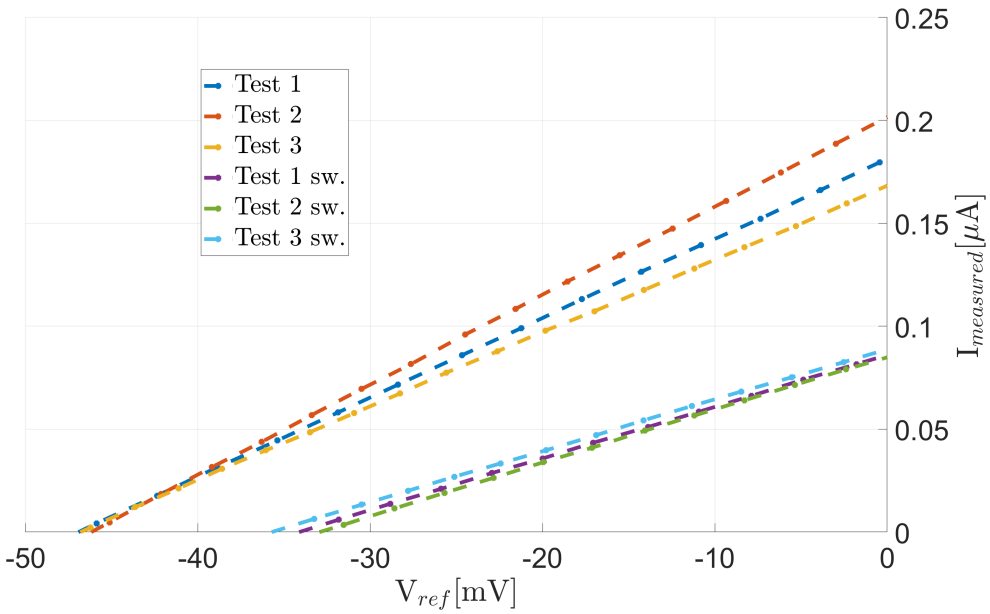


Figure 7.11: I–V tests were performed on a 50 mA/cm^2 self-supported porous silicon membrane under an S1/S2 concentration ratio. The I–V characteristics, such as the membrane potential E_m and the short-circuit current I_{sc}, depend on which side of the membrane faces the low-concentration solution. In Tests 1, 2, and 3, the back side of the membrane was facing the low-concentration side (S1). In Tests 1, 2, and 3 (sw), the concentration ratio was switched with respect to the membrane orientation. Membrane area is 3.1416 mm^2.

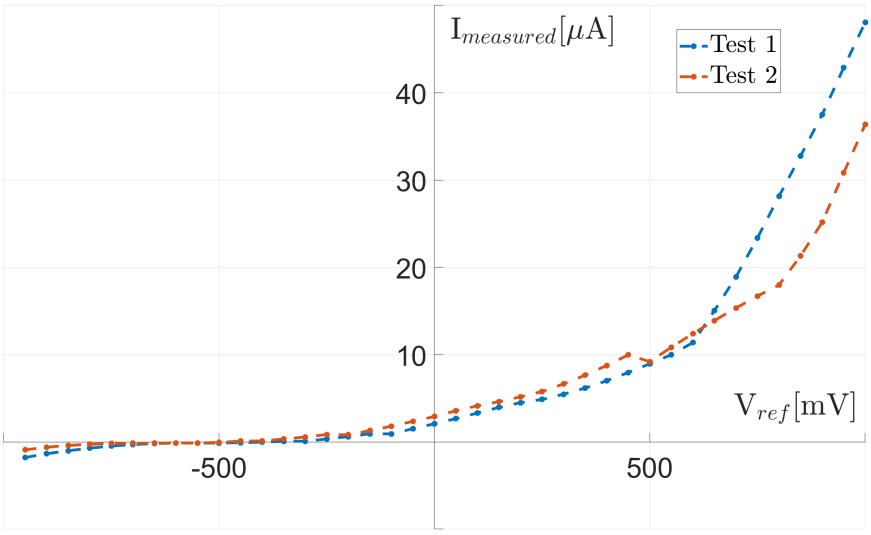


Figure 7.12: I–V test run on a freshly made 50 mA/cm^2 self supported porous silicon membrane in S3 solution on both sides. Test 1 and Test 2 were performed with a 5 min interval between them. The I–V response shows a diode like behaviour. Membrane area is 3.1416 mm^2.

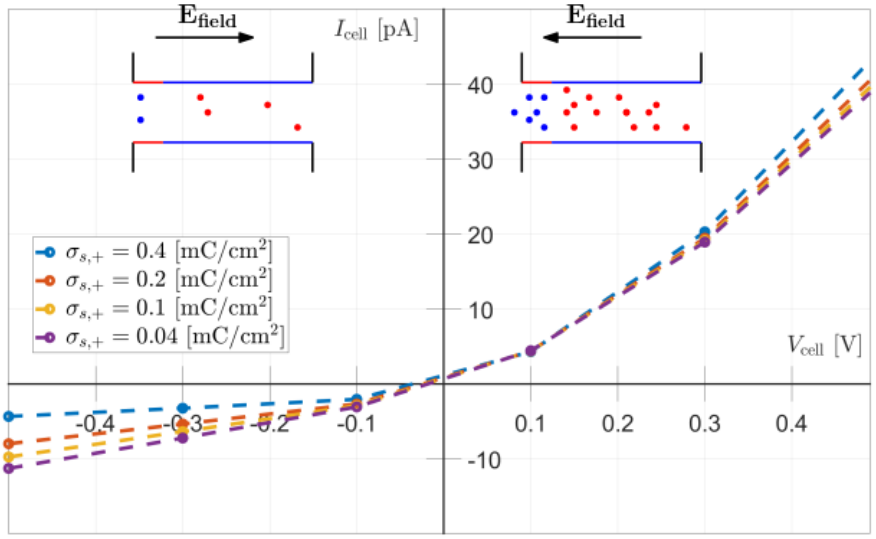


Figure 7.13: Numerical I–V characteristics of a nanopore with a negative surface charge density and a small region of opposite (positive) surface charge density of varying magnitude. A diode-like rectification behaviour is observed. The ICR decreases as the magnitude of the positive surface charge density is reduced. Parameter: $\sigma_{s,-} = -4$ mC/m^2, r=20 nm and S2 concentration.

With the newly added region of opposite surface charge density, we also show numerically in Fig. 7.14 that the I–V characteristic of a nanopore can exhibit an asymmetric behaviour similar to that observed experimentally in Fig. 7.11.

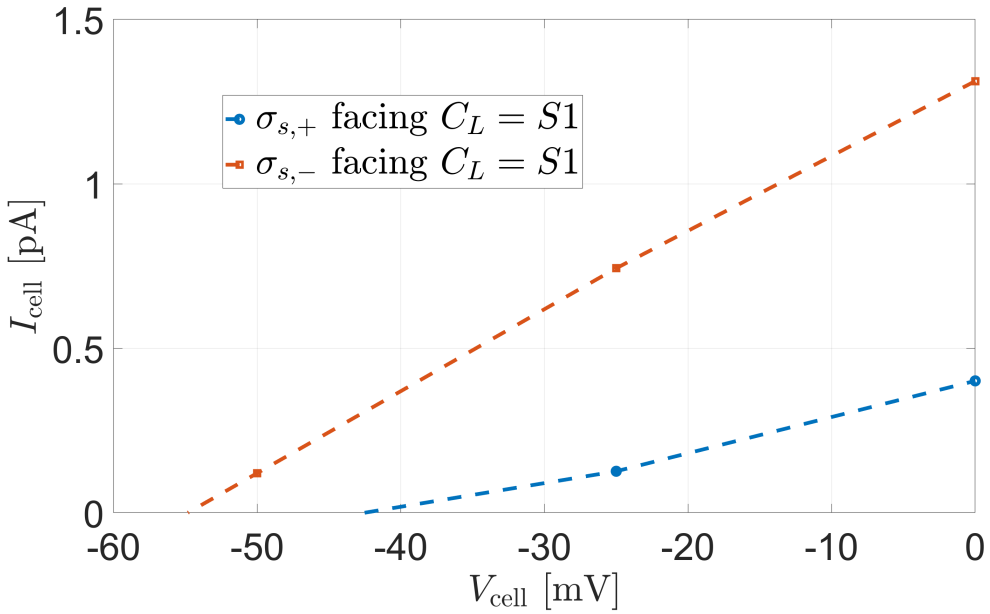


Figure 7.14: Numerical I–V characteristics of a nanopore with a negative surface charge density and a small region of opposite (positive) surface charge density of varying magnitude with a concentration ratio S1/S2. The I–V characteristics depends on which side is facing the low concentration side S1.

The ICR ratio is larger at higher ionic concentrations, which may be related to a concentration-dependent change in the surface charge of the DRIE-exposed side of the membrane. The diode-like behaviour also decreases over time when the membrane is kept in solution, as shown in Fig. 7.15, indicating an evolution of the surface chemistry. Numerically, when the added region with opposite surface charge density is assigned a reduced absolute charge, the ICR ratio decreases as well, as shown in Fig. 7.13.

This reduction in surface charge could be linked to the gradual hydrolysis of Si–F and Si–O–F species formed on the porous layer during DRIE. These species are not stable in aqueous environments and convert to silanol groups (Si–OH), which reduces the magnitude of the surface charge. In contrast, the fluorocarbon polymer (CF_x) deposited during the C_4F_8 passivation step is chemically stable in water and does not dissolve, although its partial oxidation or rearrangement may still influence the surface over time. This combination of processes may explain the time-dependent evolution of the ICR ratio observed in Fig. 7.15. Although the ICR decreases over time, it remains observable even after the membrane has been immersed in solution for more than two hours.

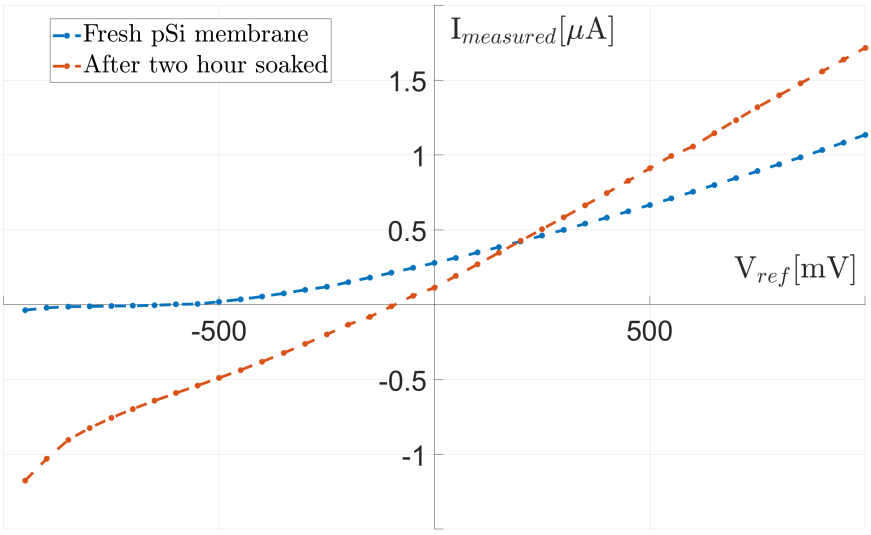


Figure 7.15: Comparison of the I–V characteristics in S1 solution of a freshly made 50 mA/cm^2 self supported membrane versus a soaked membrane for over 2 hour in DI solution. Membrane area is 3.1416 mm^2.

Interestingly, as shown in Fig. 7.16, this diode-like behaviour leads to a memory effect when examining the hysteresis response of a membrane that has not been soaked in water for an extended period. The slow response of the ions to changes in the applied electric field, combined with the asymmetric behaviour of the pore, is the main origin of this hysteresis.

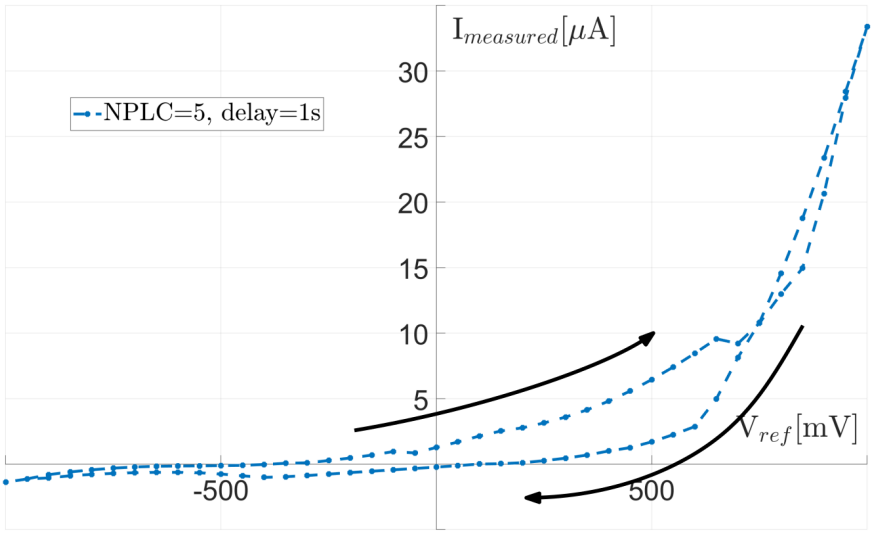


Figure 7.16: Hysteresis response of freshly made 50 mA/cm^2 self-supported porous membrane in S3.

7.3.3 Discussion

As a first step toward evaluating porous silicon membranes as ion-exchange membranes (IEMs) for RED applications, self-supported membranes were tested. However, two major issues were identified.

The first issue concerns the mechanical stability requirement. To avoid membrane rupture, a thickness of approximately 90 μm must be maintained, which limits the porosity that can be achieved during electrochemical etching. For porosities above a certain thickness threshold, cracks appear during the drying of liquid within the porous layer, typically near the membrane anchor where stress concentrations are highest. Critical-point drying could alleviate this problem and allow the use of higher-porosity membranes, but it would need to be performed after each measurement cycle in the RED set-up, greatly complicating operation.

The second issue is the impact of the DRIE process on the porous layer. DRIE not only alters the structural integrity of the porous silicon but also modifies its surface chemistry. During the passivation steps of the Bosch process, a fluorocarbon polymer (CF_x) is deposited from the C_4F_8 plasma, and a fraction of this polymer remains on the pore walls after etching. In addition, Si–F and Si–O–F species can form on the exposed silicon surfaces during the SF_6 etch step. These residues penetrate into the porous network to the extent that plasma species can access the

pores, resulting in an inhomogeneous and partially fluorinated surface.

This contamination modifies the I–V response, causing the membrane to behave as an ionic diode. The effect is uncontrolled and evolves over time as the membrane remains soaked in solution: Si–F and Si–O–F groups hydrolyse to silanols (Si–OH), while the CF_x polymer remains chemically stable but may undergo slight surface oxidation. These changes lead to a progressive reduction of the surface charge and therefore to a time-dependent I–V behaviour, making the membrane unsuitable for establishing stable and reproducible electrochemical characteristics.

An oxygen plasma treatment after DRIE could help remove part of the CF_x contamination; however, the porous structure would still be affected by the etching step, and the chemical state of the surface would continue to evolve once immersed in solution.

7.4 Free-standing porous silicon membranes: fabrication and characterisation

7.4.1 Free-standing porous silicon membranes: fabrication

Figure 7.17 summarises the process flow used for the fabrication of the free-standing porous silicon (fs-PSi) membranes. The electrochemical cell for the free-standing membranes is smaller and only small die can fit into the cell. Thus, prior to any process step, each 3 inch wafer is cut into small die of around 3×3 cm.

The silicon dye is sandwiched between an O-ring and an aluminium foil that insure leakage proof and good electric contact respectively. The O-ring in Figure 5.2 delimited the exposed area to the electrolyte, no prior masking is required in this work. The exposed area is a circle of 27 mm^2.

Porosification After a standard cleaning sequence, the process begins with the etching of a sacrificial layer similarly as presented in 7.3.1. After removing the sacrificial with KOH, the porous layer is etched with the same conditions as in 7.3.1.

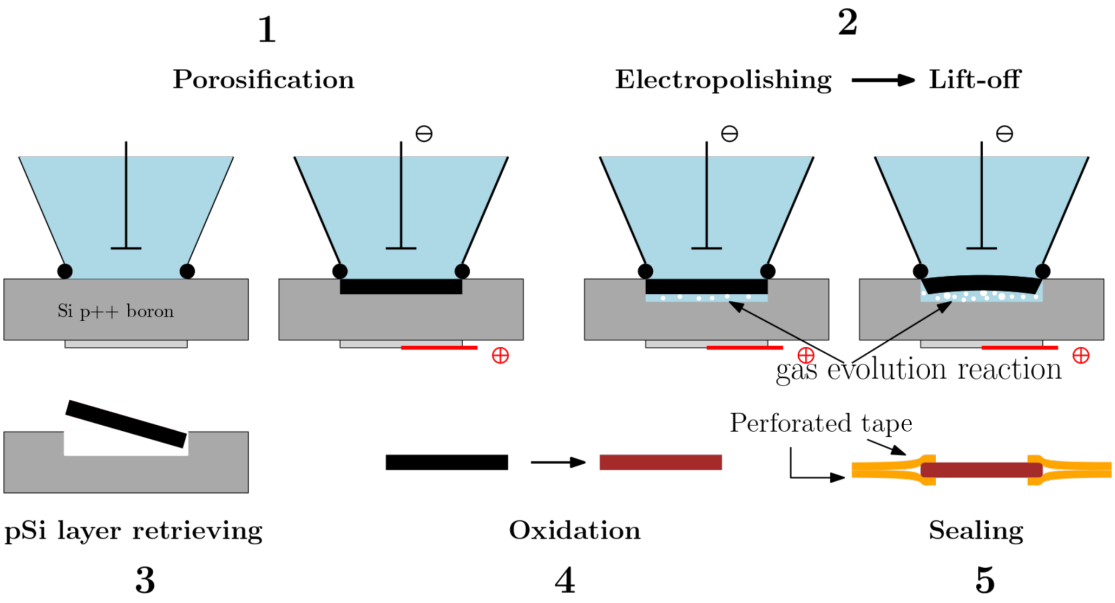


Figure 7.17: Schematic of the process flow for free-standing porous silicon membrane: 1) Electrochemical etching of the Si with a specific current density over a given period of time to reach the desired thickness and porosity. 2) An electropolishing current is applied for a short period until lift-off of the porous layer is achieved. 3) The pSi flake is cleaned in isopropanol and retrieved from the substrate. 4) The flake is then oxidized in an oven at 250 °C. 5) The flake is sealed with a perforated hydrophobic tape for easier handling.

Lift-off In this work, we decided to apply a step increase in the current density as in [395]. The current was 444 mA/cm^2, determined to be in the electropolishing regime by direct observation in the SEM.

After 10 seconds of no current, different lift-off current density times for each sample were applied. They were determined through experimental observations. For the samples obtained with a current density of 3 mA/cm^2, 50 mA/cm^2 and 100 mA/cm^2, 3 s, 4 s and 6 s respectively were found as sufficient to obtain a clean lift-off without any damage to the porous layer.

After the lift-off is finished, the membrane is rinsed in IPA and kept for 2 min in IPA and then dried. This step is important to avoid stress from the surface tension of any etching solution remaining inside the porous layer.

Oxidation The free-standing membranes are then oxidized in an oxygen environment for 1 hour at 250 °C. The final part of the process is to seal the free-standing membrane with tap with a hole for easier handling of the porous flake and avoid to put direct pressure on the porous material. The area of the exposed membrane

after sealing is 11.95 mm^2.

7.4.1.1 Characterisation: Lift-off analysis

Several fabrication techniques for free-standing silicon membranes have been described in the literature [395–399]. Such membranes have been predominantly used to investigate the optical and optoelectronic behavior of porous silicon. Reported methods include a two-stage process [396, 397] in which the current density is abruptly increased into the electropolishing regime, a single-step technique [395] where the porous layer detaches spontaneously, and a more recent two-step approach [399] that employs a gradual ramping of the current density at a defined rate.

The origin of the lift-off is not yet fully understood. In [250, 395], they originally proposed that the fast increase in current consumes locally the HF faster than it can be resupplied by the above solution and the detachment occurs due to the rapid accumulation of gas under the porous layer. This induces a sudden increase in the measured voltage shown in Figure 7.18. The origin of the gas was attributed to the formation of H_2 molecules during the etching, but it could also be the additional formation of O_2 as proposed in [399].

Another possible explanation formulated later by the same group as in [395] explained that the sudden increase in measured voltage (Figure 7.18) could be attributed to a sudden depletion of HF in the electrolyte. This leads to the formation of a high porosity layer, that can then lift-off. Once the layer is lift-off, the HF can be resupply again and the measured voltage drops back.

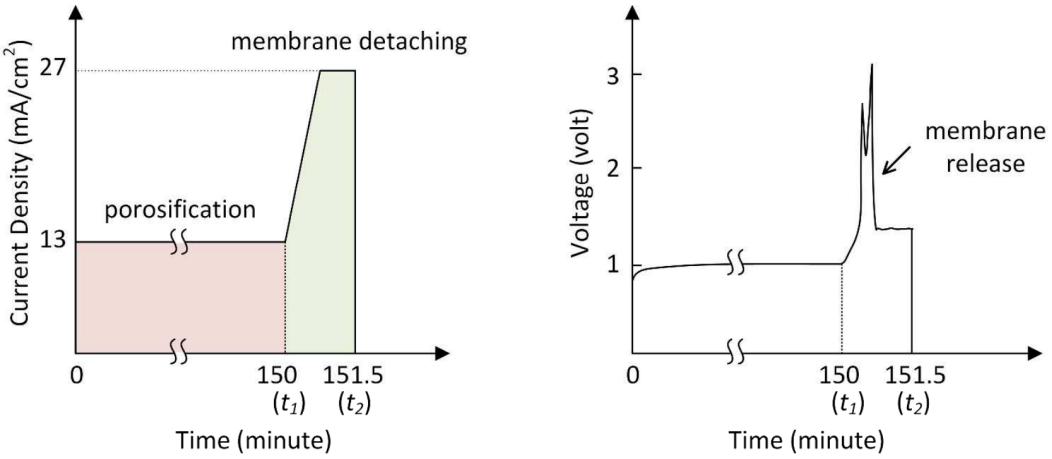
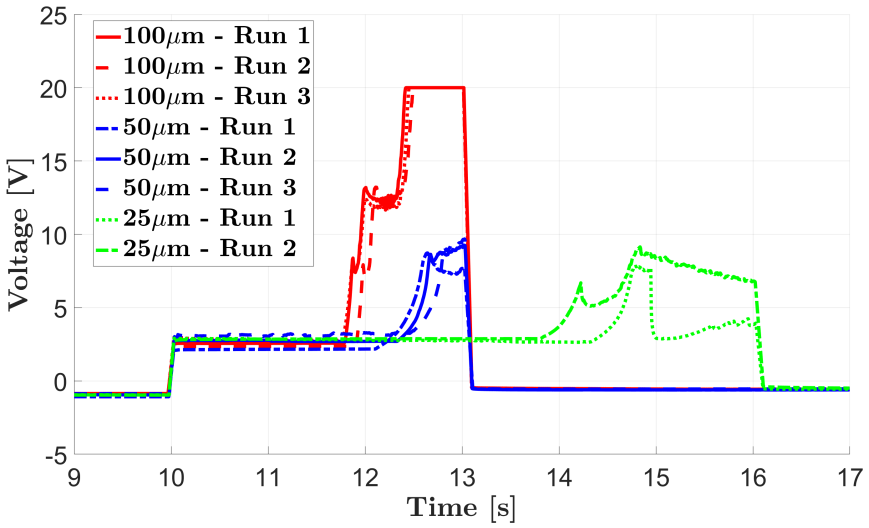


Figure 7.18: (Left) temporal profile of the imposed current density, and (right) a representative voltage response during porosification and subsequent current ramping for porous layer detachment. Reprinted (adapted) with permission from [250].

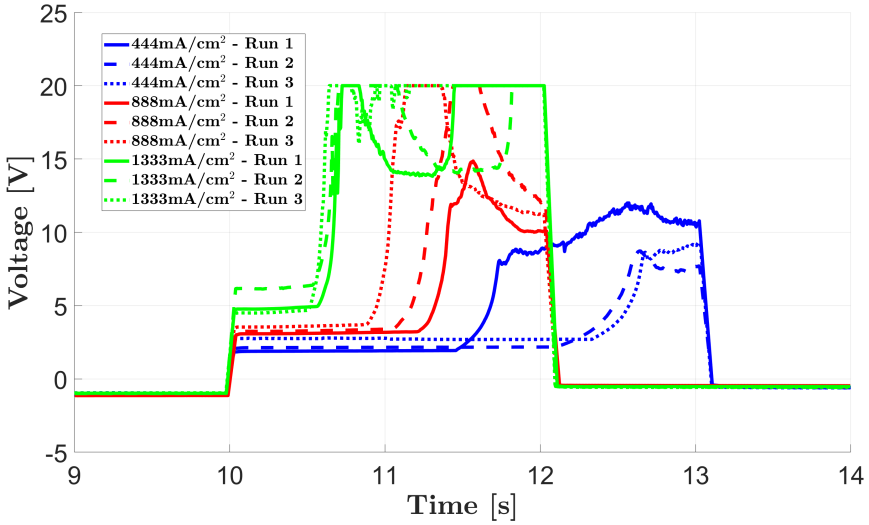
Both [399] and [250] used a ramp-up of the applied current for better control and reproducibility of the porous layer lift-off because this method doesn't depend on the thickness and porosity of the porous layer. In our case, we decided to rather apply a a 'step' increase in the current density as in [395]. The current was 444 mA/cm^2, determined to be in the electropolishing regime by direct observation in the SEM. Since a ramp up of current would mean that the current is initially low, we would create first a thin transitional layer with locally a different porosity (i.e., average pore diameter) than what the desired one. This would create undesired anisotropy along the membrane thickness.

The prior work was to determine the conditions for lift-off of the porous layer. Several parameters have been chosen such as the membrane thickness and the applied current density for the lift-off. For each case, the time for the sudden voltage increase was recorded and lift-off was noticed. The results are shown in Figures 7.19a and 7.19b, respectively.

Observations revealed that if the lift-off current application time is shorter than the appearance of the peak voltage, then no spontaneous lift-off is observed. Small pressure with a diamond tip on the side of the porous afterward induces the separation of the layer from the substrate. If the lift-off current is applied for longer than the time at which the voltage peak appears, the porous layer usually ends up breaking.



(a)



(b)

Figure 7.19: Measured voltage over time during the electropolishing step for porous-layer lift-off. A constant current was imposed, and the sharp voltage peak indicates lift-off of the porous layer. All porous layers were obtained at the same current density (50 mA/cm^2). (a) Comparison of peak-voltage appearance time for different porous layer thicknesses. The applied current was 444 mA/cm^2; (b) comparison for different electropolishing currents.

While the explanation for the apparition of the voltage peak based on the

depletion of HF is reasonable [398], it does not explain in our case why the porous layer suddenly detached from the substrate. Thus, similarly to [395], we also proposed to explain the observations based on the sudden accumulation of gas. More specifically, we supposed that the rate of gas accumulation is the main factor for lift-off. Indeed, for thicker membrane, one could expect the breaking point time to be longer. But in practice, with the same lift-off current, the time required for lift-off decreases. One explanation is then: when lift-off current is applied, the gas has no choice but to leave through the porous layer. The accumulation of gas is then faster with thicker membrane because the release rate through the membrane is slower.

To further confirm that the lift-off occurs due to a sudden accumulation of gas, we applied the same lift-off current with the same total amount of time but with the etch-stop technique. No sharp peak in voltage (over 3V) is observed as seen in Figure 7.20 and no lift-off of the membrane is noticed afterwards. Interestingly, the SEM image revealed that a cavity has been created under the porous layer, as shown in Figure 7.21. This indicates that the sides of the membrane still hold the membrane to the substrate.

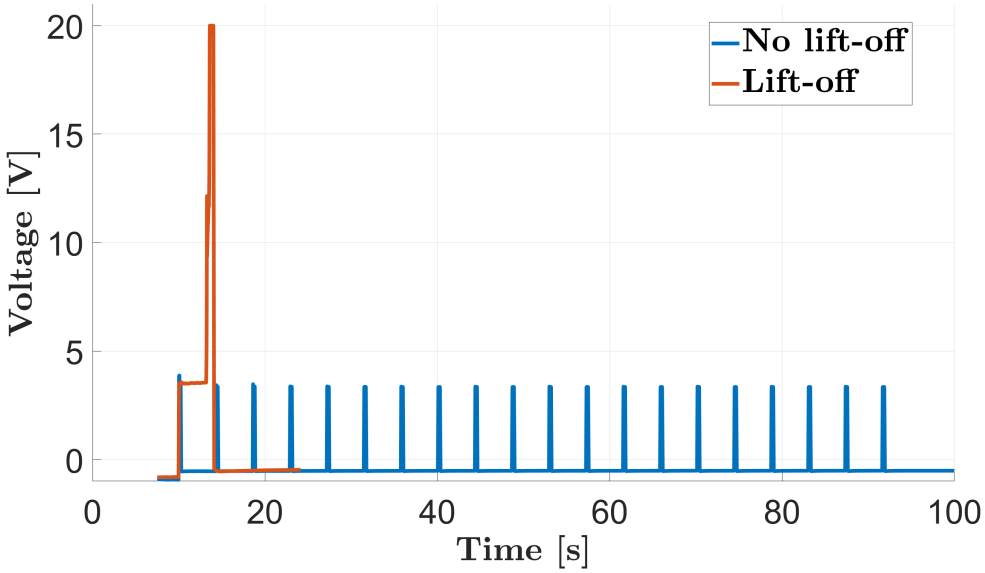


Figure 7.20: Measured voltage during the application of the lift-off current (444 mA/cm^2) with the etch stop technique in blue (20 cycles of 0.2 second with 4-second etch stops) and continuous 4 seconds in red.

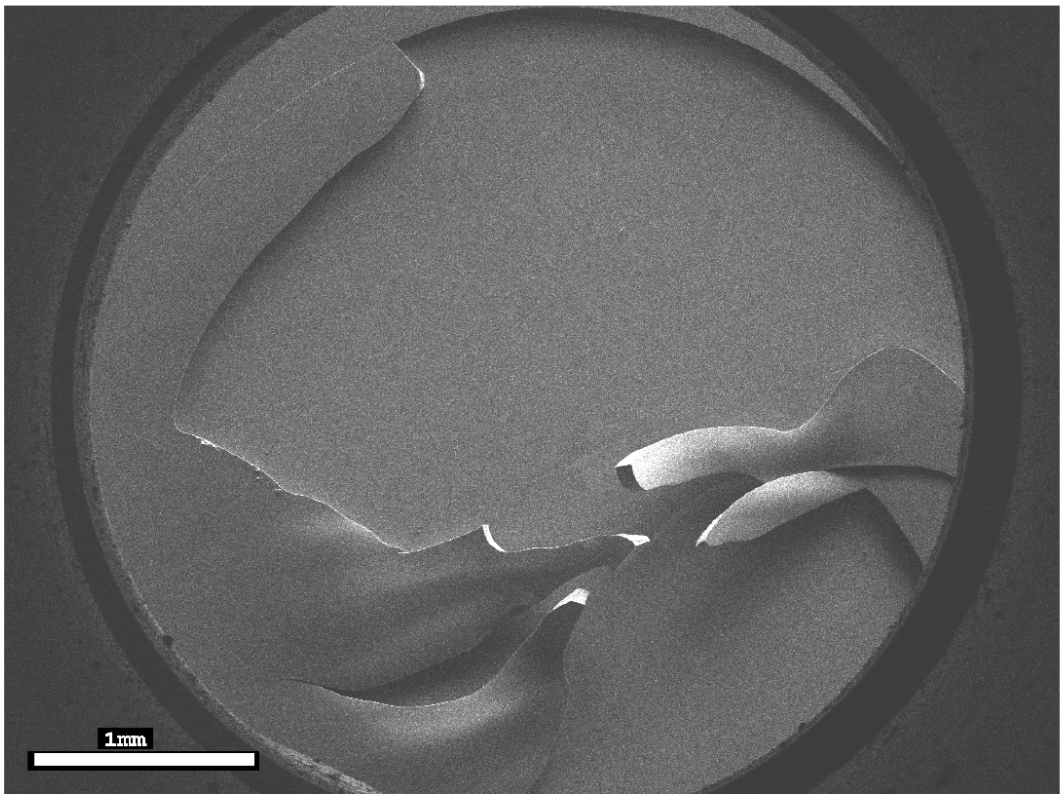


Figure 7.21: Top view SEM image of a pSi layer which underwent etch stop cycle of 0.2 seconds with 444 mA/cm^2 and 4 seconds of no current. Bar scale is 1 mm.

This region corresponds to the area under the O-ring, where the etching conditions differ from those in the central part of the membrane. As discussed in [224], the electric field lines, which determine the current distribution, at the edges of the porous region depend on the type of mask used during porosification. In our case, no lithographic mask is present; the only constraint is the mechanical pressure from the O-ring on the substrate. Because the substrate has a very low resistivity, the electric field lines can spread more widely near the edges, resulting in a lower effective current density in this region.

As shown in Fig. 7.22, the substrate exhibits residual porosity near the borders, whereas the central region shows no visible pores, which is indicative of electropolishing. Cross-sectional images of the porous layer before and after lift-off (Fig. 7.23) further reveal that the layer is thinner toward the edges of the porous region. This suggests that the border areas are etched at a slower rate (i.e., subjected to a lower current density). These less-porosified edge regions remain mechanically stronger during the electropolishing step, which may explain why the porous layer continues to adhere at the periphery.

In the test run shown in Fig. 7.20, the gas generated during etching was able to escape through the porous structure, preventing any significant pressure build-up. As a result, the pressure was never sufficient to lift the membrane from the substrate.

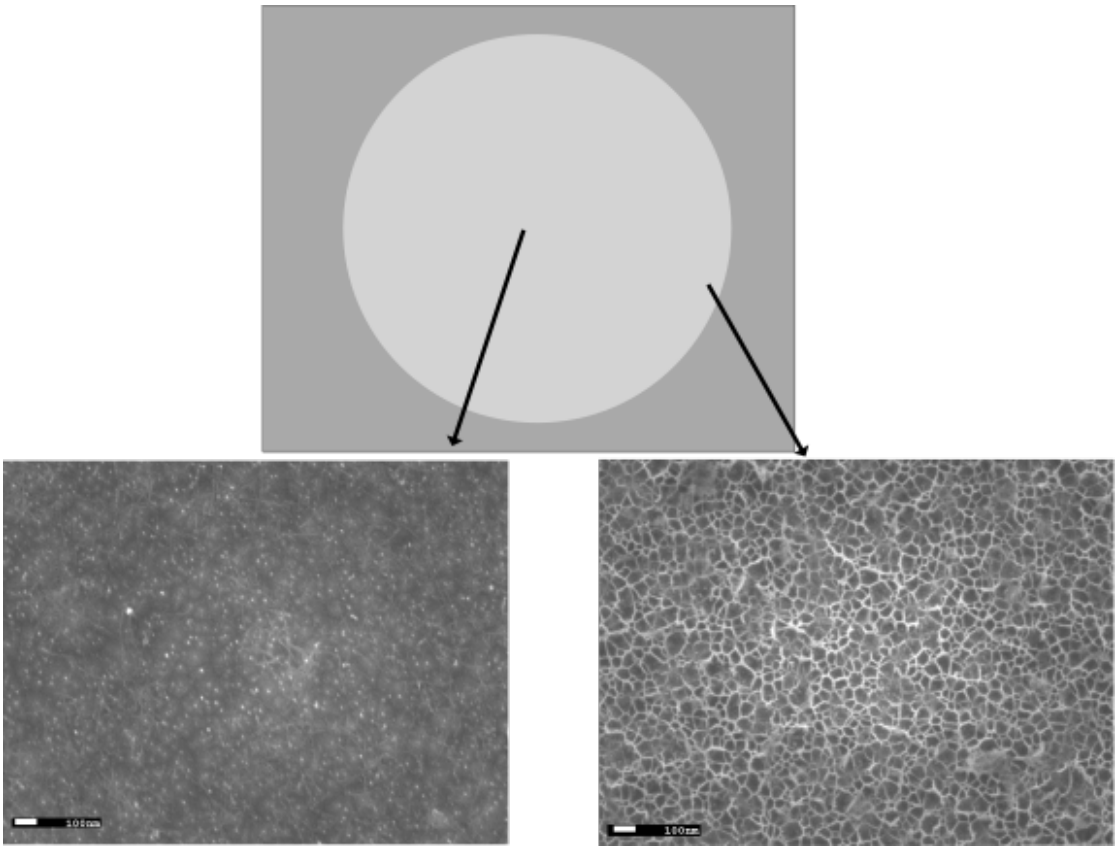


Figure 7.22: Top-view SEM images of the substrate after the lift-off process. The surface roughness differs between the central region and the area near the edges due to the variation in electrochemical etching conditions (i.e., local current density).

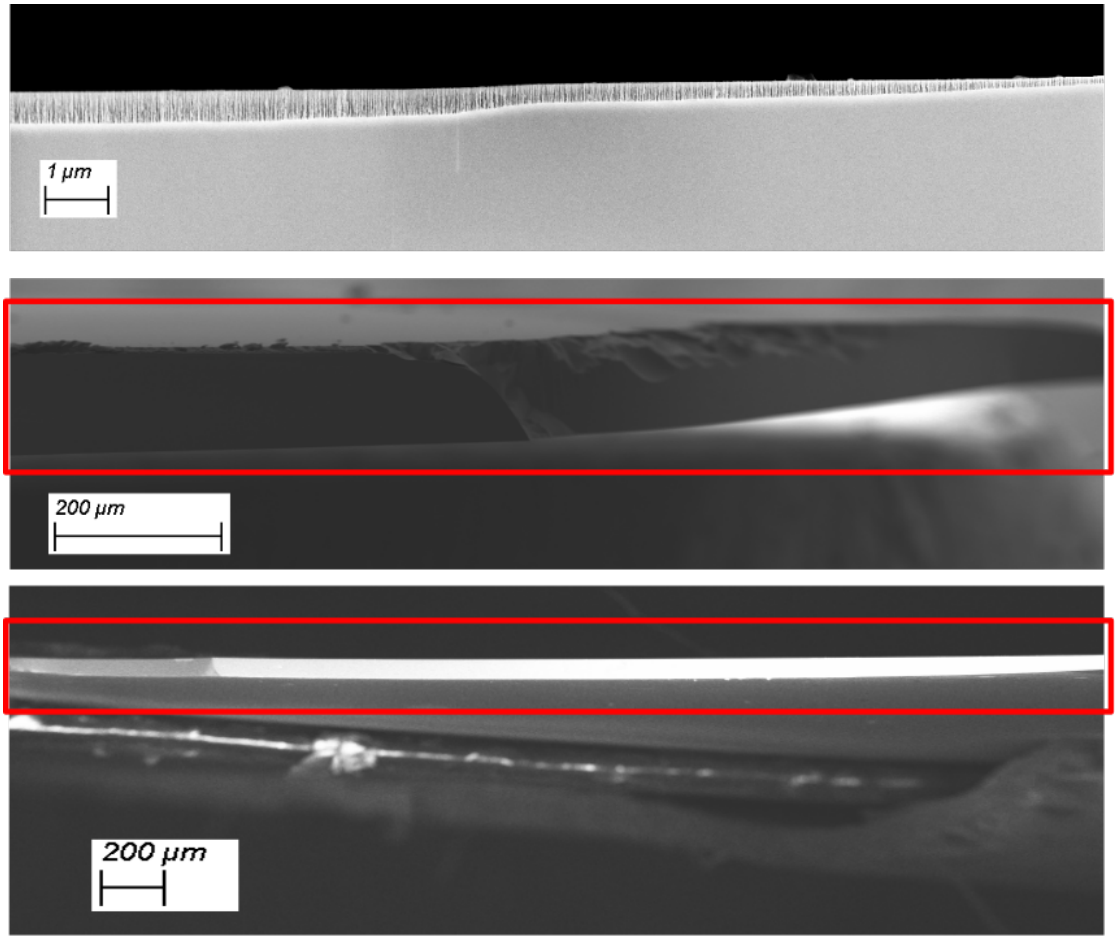


Figure 7.23: Cross-section SEM images of different porous layer:(Top)50 mA/cm^2, 120 s, porous silicon layer. (Middle and bottom) 50 mA/cm^2 free-standing porous membrane. The edges are always thinner than in the center.

Our explanation for the lift-off is that when the applied current density is suddenly increased, the demand for holes (h^+) at the silicon surface rises abruptly. In order to sustain the enhanced dissolution rate, fluoride ions must be supplied rapidly from the electrolyte. If the transport of HF by diffusion or convection cannot immediately meet this demand, the local HF concentration at the Si/electrolyte interface decreases. This transient depletion leads to the build-up of partially oxidized surface species (e.g., Si–H, Si–OH), the accumulation of a thin oxide layer, and in some cases the initiation of a cavity or depleted zone at the interface.

Under these conditions, gas evolution behaviour also changes. At the front of the cavity, where HF is locally depleted, the valence-4 oxidation–dissolution pathway becomes less efficient because the removal of SiO_2 by HF is hindered. As a result, excess holes are consumed in side reactions, most notably proton reduction,

which produces molecular hydrogen:

$$2H^+ + 2e^- \quad \rightarrow \quad H_2 \uparrow \tag{7.2}$$

This reaction gives rise to localized hydrogen bubble nucleation inside the cavity. The bubbles can further obstruct HF transport, thereby amplifying the depletion effect and accelerating cavity growth. Importantly, this transient hydrogen evolution represents an exception to the typical electropolishing regime seen in (5.4), where dissolution proceeds uniformly via oxide-mediated reactions and gas formation is minimal.

7.4.1.2 Characterisation: PSi layer structure

First we checked the cross section thickness. As shown in Table 7.4, the porous layer thicknesses measured from cross-sectional SEM images are systematically lower than the values predicted from the number of etching cycles and the etch rates determined by SLIM. This indicates a progressive reduction of the effective etch rate during porosification. One contributing factor is the use of a fixed off-time in the etch-stop protocol. While a 2 s pause is sufficient to partially restore the HF concentration at the pore tips during the early stages of etching, the characteristic diffusion time for HF replenishment increases with pore depth according to $t_D \sim L^2/D$. For porous layers approaching $\sim$90 μm, this time scale becomes comparable to or longer than the pause duration, leading to incomplete HF replenishment at the pore tips during the later stages of etching. As a result, dissolution becomes increasingly transport-limited, reducing the effective etch rate and yielding thinner layers than predicted.

In addition, the discrepancy between predicted and measured thickness is more pronounced at low current density, where the total etching duration is significantly longer. This trend suggests the presence of slow, time-dependent effects acting on the electrolyte at the macroscopic scale. In particular, partial evaporation of the electrolyte during long etching times would increase the bulk HF concentration, which is known to reduce the porous silicon growth rate under hole-limited conditions. This global change in electrolyte composition is distinct from the local HF depletion occurring at the pore tips and primarily affects samples etched over extended durations.

Table 7.4: Parameters for the electrochemical etching of the porous layer for the different membranes. The predicted and the measured porous layer thickness are also shown.

Current density [mA/cm^2]	**Number of cycles**	**Predicted thickness [μm]**	**Measured thickness [μm]**
3	3,340	117.1	90.58
50	213	92.68	90.15
100	112	96.93	94.30

We also check the back of the flake, which is the side that is attached to the substrate before the electropolishing occurs for the lift-off step. Figure 7.24 shows a comparison of the top and the back side. We observed that the back side has pore with average size larger than the top. This has also been observed in another study by Solanki et. al. [398] and is a consequence of side etching during the early phase of the electropolishing phase as schematically shown in Figure 7.25. Such pore enlargement is only a few nanometer deep into the porous layer and its impact should be unnoticeable for the IV characteristic.

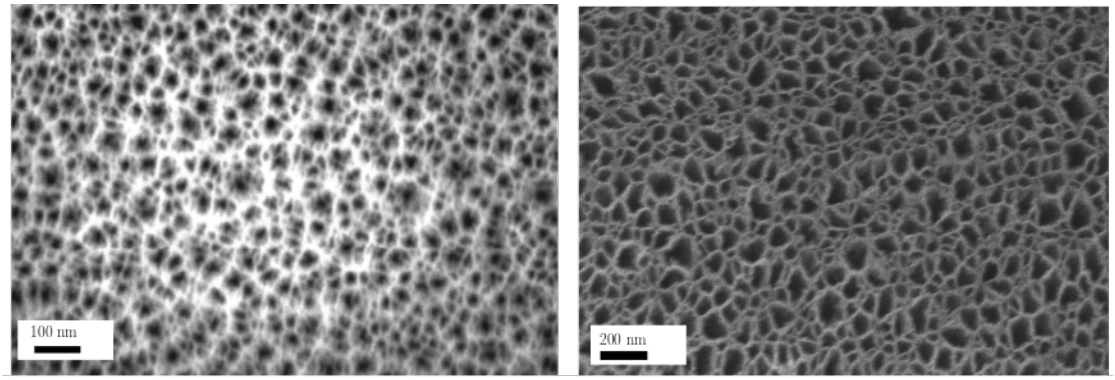


Figure 7.24: SEM image of top view (left) and back-side view of a 50 mA/cm^2 free standing porous silicon membrane.

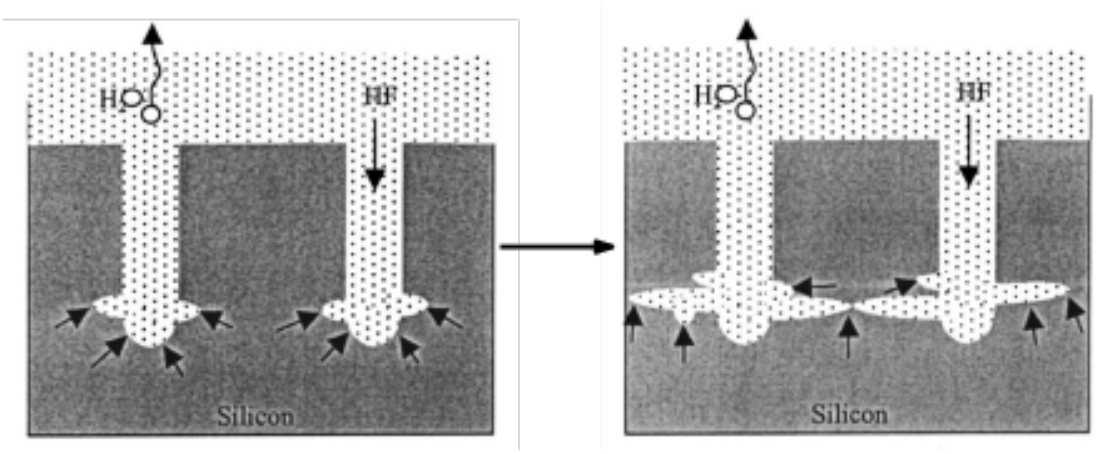


Figure 7.25: Schematic explaining the mechanism for pore widening on the bottom side of a porous silicon flake The bottom of the pore, in contact with the HF-depleted electrolyte, exerts high impedance in the current path. In order to minimize the impedance, the current flows over an enlarged area around the tip. The dissolution effectively occurs at the position where the HF is available. Therefore, apart from some dissolution at the pore tip, silicon gets dissolved a little bit above. This effectively increases the pore size and hence the layer porosity at that position [398].

7.4.2 Free-standing porous silicon membranes: I–V results

7.4.2.1 Methods for sensing data

Since the membrane fabrication is now validated for the free-standing pSi membranes, the study can continued. The first measurement consisted of an I–V test performed with identical electrolyte concentrations on both sides of the membrane to verify its structural symmetry. As shown in Figure 7.26, the free-standing membrane exhibits a linear current–voltage response with no observable rectification, confirming that the membrane behaves symmetrically under these conditions. This result also provides further evidence of the impact of the DRIE step on the integrity of the porous silicon layer.

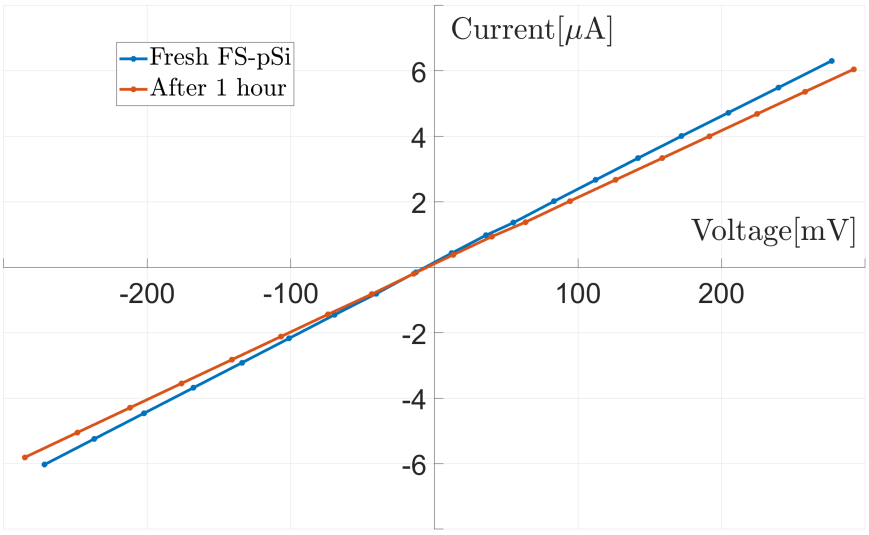


Figure 7.26: I–V characteristics in S2 solution of a freshly made 50 mA/cm^2 fs-pSi membrane and the same membrane soaked in water for 1 hour. Membrane area is 11.95 mm^2.

The main parameters examined in this work to analyse the I–V characteristics of the free-standing porous silicon membranes are the electrolyte concentration and the average pore size.

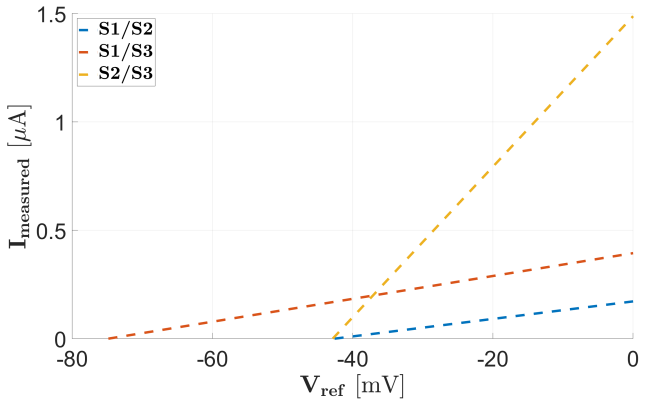
Each membrane was immersed in a KCl solution for at least 5 min before being placed into the μfluidic cell. This ensured complete wetting of the membrane and allowed sufficient time for protonation/deprotonation of surface hydroxyl groups to equilibrate, thereby minimizing measurement drift.

For a given concentration gradient C_H/C_L, measurements were repeated every 1 min, at least five times, to check for temporal drift. The membrane orientation was then reversed with respect to the solutions to test for asymmetry. Using the least-squares method, each measurement was interpolated, and the diffusion potential E_{diff} and short-circuit current I_{sc} were extracted.

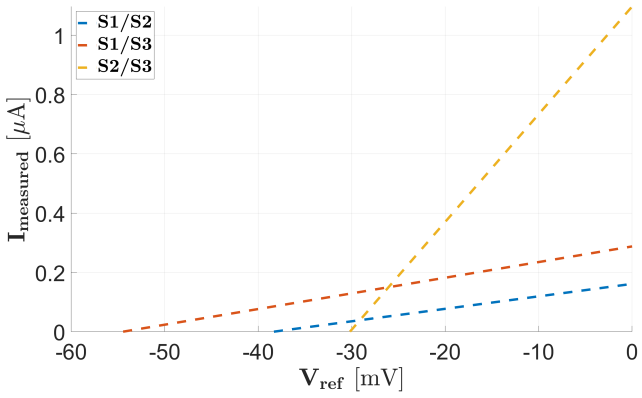
7.4.2.2 Experimental results: impact of the concentration ratio

The results obtained for the membranes etched at 3 mA cm^{-2}, 50 mA cm^{-2}, and 100 mA cm^{-2} are shown in Figures 7.27a, 7.27b, and 7.27c, respectively, for the

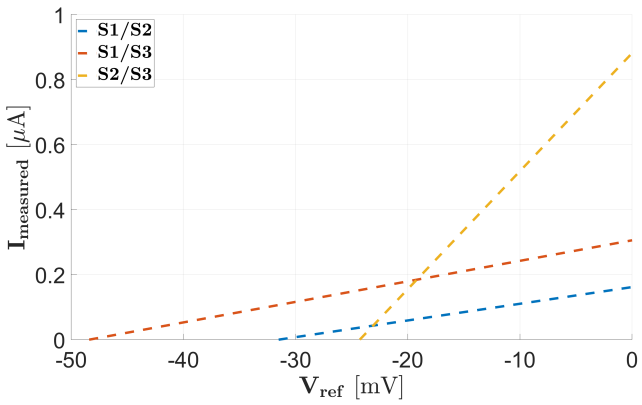
three tested concentration gradients. A summary of the key experimental metrics is provided in Table 7.8.



(a)



(b)



(c)

Figure 7.27: Experimental mean linear regression I–V curves at different concentration ratios for (a) 3 mA/cm^2, (b) 50 mA/cm^2, and (c) 100 mA/cm^2. Membrane area is 11.95 mm^2.

For all three samples, the overall tendency is similar. Between S1/S2 and S2/S3, the absolute $|E_m|$ is higher for S1/S2, reflecting stronger selectivity according to (2.14). Between S1/S3 and S1/S2, the selectivity is weaker for S1/S3, but the absolute $E_{m,S1/S3}$ is still the highest because of the larger concentration ratio. In terms of resistance, it is lower for S2/S3 than for S1/S2, which implies $I_{sc,S2/S3} > I_{sc,S1/S2}$, consistent with the single-pore analysis. We also observe that the ionic resistance is lower for S1/S3 than for S1/S2. However, $I_{sc,S1/S3}$ is lower than $I_{sc,S2/S3}$ despite the higher absolute E_m for S1/S3. Numerically, it is rather found that $I^{\text{num}}_{sc,S1/S3}$ is greater than $I^{\text{num}}_{sc,S2/S3}$ s seen in Figure 6.25 and 6.18. Experimentally, we found that $R_{S1/S3}/R_{S2/S3} \simeq 6.5$ while numerically it was 1.6.

Numerically, under the initial assumption of a uniform and constant surface charge density, it is not possible to reproduce the tendency regarding the experimental resistance. The reason is that this model neglects the relation between surface charge density and local ionic concentration. Several studies have shown that the higher the ionic concentration in confined spaces such as nanopores, the higher the surface charge density [143, 170]. For silica, the surface charge originates from the protonation and deprotonation of hydroxyl groups as detailed in (4.26), and the local ionic concentration affects also the equilibrium.

A simple first-order correction to account for this relation is to divide the nanopore into two halves and assign a surface charge density to each half according to the concentration on the adjacent side, as illustrated in Fig. 7.28.

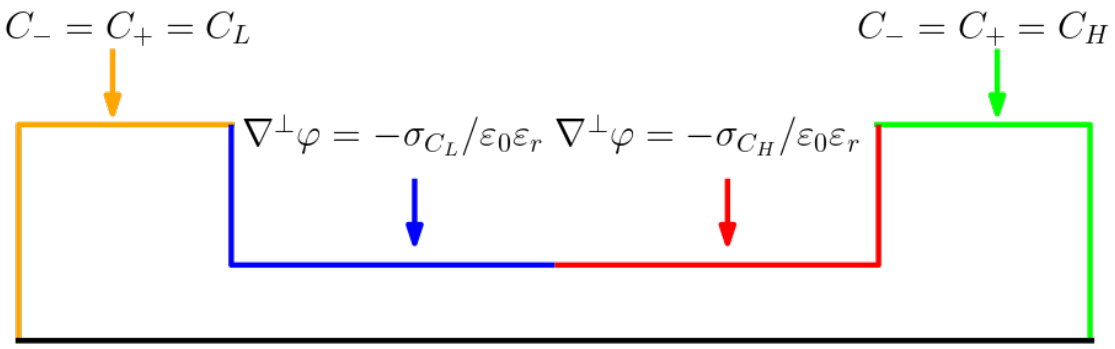


Figure 7.28: Modified surface charge density boundary conditions used in the numerical simulation to account for the relation with solution concentration.

Table 7.5: Surface charge density values chosen with respect to local concentration for the modified surface charge density boundary conditions as shown in Figure 7.28.

Concentration	**Surface charge density [mC/m^2]**
S1/S2	$-0.4/-0.6$
S1/S3	$-0.6/-3.2$
S2/S3	$-1.6/-3.4$

The results for a 10 nm pore radius (pore size in between 50 and 100 mA/cm^2) are shown in Fig. 7.29. With the updated surface charge density values, the I–V trends more closely match those in Fig. 7.27, confirming the importance of including the dependence of surface charge density on concentration.

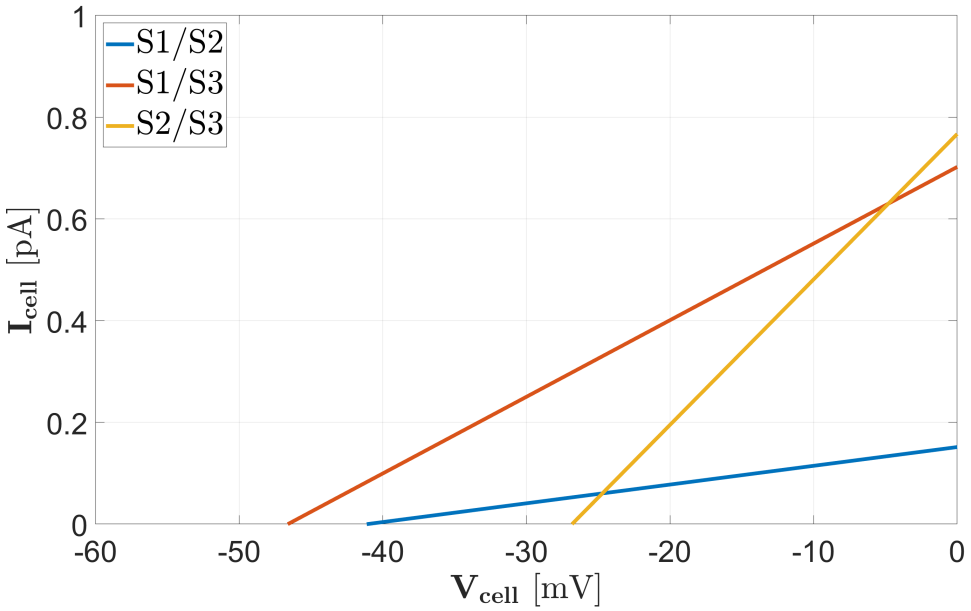
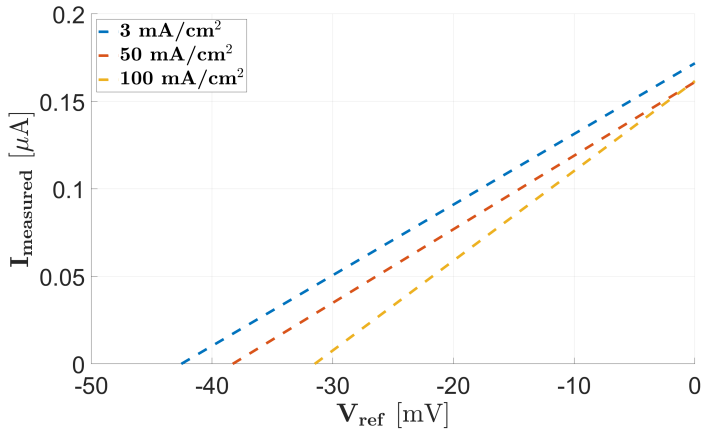


Figure 7.29: Numerical results for a 15 nm pore size at different concentration ratios with surface charge density adapted to the concentration as presented in the modified numerical model Fig.7.28.

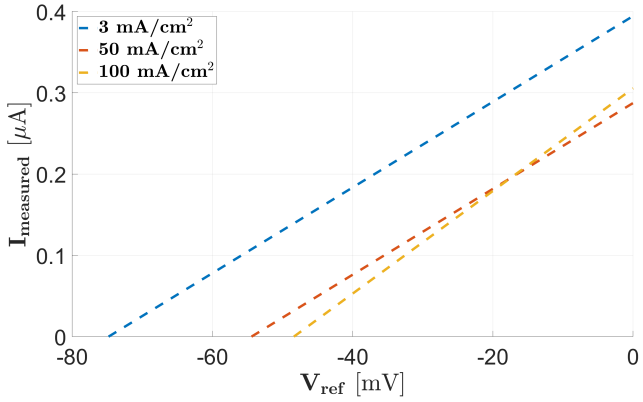
7.4.2.3 Experimental results: impact of the average pore size

The second parameter analyzed experimentally was the average pore size, adjusted by controlling the current density during electrochemical etching. The

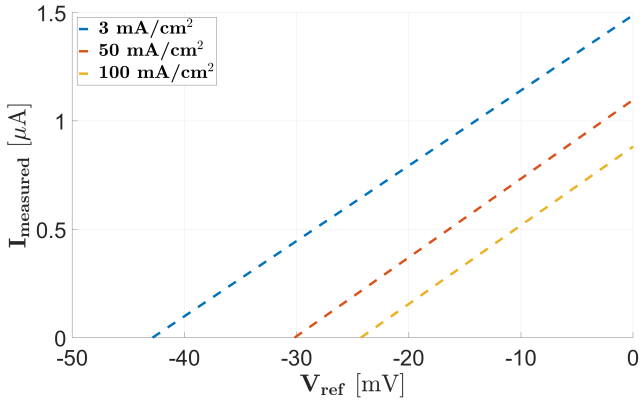
I–V results comparing membranes etched at different current densities for a given concentration ratio are shown in Fig. 7.30a, 7.30b, and 7.30c for S1/S2, S1/S3, and S2/S3, respectively. For all three concentration ratios, the membranes with the smallest average pore radius exhibit the highest absolute E_m due to stronger EDL overlap, consistent with the numerical results. Likewise, numerical simulations predict a decrease in ionic resistance with increasing pore size.



(a)



(b)



(c)

Figure 7.30: Experimental mean linear regression I–V curves with membrane obtained at different electroetching current density for (a) S1/S2, (b) S1/S3, and (c) S2/S3. Membrane area is 11.95 mm^2.

In order to analyse whether the numerical simulations reproduce the experimental results, the total number of pores must be taken into account. Using Eq. (6.11) together with the single-pore values from Table 6.6, an estimate of the membrane-scale resistance was obtained (Table 7.6). The difference in absolute magnitude between the measured and estimated resistances can be attributed to several factors that were neglected in the simplified model. These include the actual membrane thickness (90 μm instead of 0.8 μm in the simulations), concentration polarization effects, and the real three-dimensional membrane structure. As discussed in Sec. 6.4, all of these factors tend to increase the effective membrane resistance. However, because all membranes share a comparable thickness, exhibit similar porous structures, and because stirring limits concentration polarization, we expect these effects to influence each membrane in a similar manner.

For the concentration ratio S1/S2, increasing the pore size (i.e., increasing of the electrochemical etching current density) leads to the same qualitative trend in both the measured and estimated membrane resistances. However, when higher concentrations are involved, such as in S1/S3 and S2/S3, the estimated resistance decreases much faster than the measured resistance. This discrepancy is more pronounced for S2/S3 than for S1/S3.

Solution	**Current density**	$\mathbf{R \cdot A}$	$\mathbf{R_{est}}$
S1/S2	3	2.9761	1.840×10^{-4}
	50	2.8545	1.556×10^{-4}
	100	2.3710	1.410×10^{-4}
S1/S3	3	2.2914	5.237×10^{-5}
	50	2.2967	3.958×10^{-5}
	100	1.9107	3.302×10^{-5}
S2/S3	3	0.3448	2.743×10^{-5}
	50	0.3309	2.111×10^{-5}
	100	0.3320	1.783×10^{-5}

Table 7.6: Measured membrane area resistance ($R \cdot A$) and estimated resistance from nanopore scaling eq. (6.11) ($R_{\text{est}} = R_{\text{pore}}/N_{\text{pore}}$) for each concentration ratio and current density. Both area resistances are expressed in [$\Omega \cdot$ m^2].

Likewise, from the known dependence of the surface charge density on the local ionic concentration, a similar dependence must also exist with respect to the pore size. As discussed in Sec. 4.1.4.3, confinement inside a nanopore introduces a coupled dependence on both pore size and local concentration. For silica surfaces, the negative surface charge density generally decreases with increasing pore size

for concave geometries [143, 165]. However, at very low concentrations and under acidic pH, conditions relevant to the present study, the absolute surface charge density increases as the pore size decreases (Fig. 4.6). As shown in the previous chapter, a reduction in the absolute surface charge density results in a numerical increase in the ionic resistance.

Considering, for example, the concentration ratio S1/S3, if the surface charge density is scaled with respect to the pore size, as presented in Table 7.7, the decrease in the estimated resistance with increasing pore size becomes noticeably less pronounced compared to the case without scaling (Table 7.6).

Current density [mA/cm^2]	$\sigma_{s,C_L}/\sigma_{s,C_H}$ [mC/m^2]	$\mathbf{R \cdot A}$	$\mathbf{R_{est}}$
3	0.5/0.5333	2.2914	4.875×10^{-5}
50	0.3478/0.25	2.2967	3.887×10^{-5}
100	0.3404/0.2222	1.9107	3.329×10^{-5}

Table 7.7: Measured membrane area resistance ($R \cdot A$) and estimated resistance obtained from nanopore scaling ($R_{\text{est}} = R_{\text{pore}}/N_{\text{pore}}$) for each concentration ratio and current density, accounting for the dependence of the surface charge density on the pore size. Both area resistance are expressed in [Ω·m^2].

7.5 Performances comparison with other membranes and discussion

7.5.1 Performances comparison

In order to fairly compare the performance of the free-standing porous silicon (fs-pSi) membranes, identical tests were carried out on three reference membranes: a cation-exchange membrane (CEM, Fumasep FKS-30), an anion-exchange membrane (AEM, Fumasep FAS-30), and a commercial AAO membrane. Their respective performances are summarised in Table 7.8.

The membrane potentials measured for the Fumasep membranes were generally high, reflecting strong ion selectivity. According to the manufacturer's datasheet, the FKS-30 exhibits a Na^+ selectivity above 98% and the FAS-30 shows Cl^- selectivity above 90% when tested in 0.5 M NaCl under symmetric conditions (i.e. without a concentration gradient). Assuming these values correspond to permselectivity, our measurements yield maximal permselectivities of 89.5% for FKS-30 under the S2/S3 condition and 90.9% for FAS-30 under S1/S3, calculated using Eq. (3.36).

The supplier specifies an area resistance below 1.5 $\Omega \cdot \text{m}^2$ for both membranes in 0.5 M NaCl. In our measurements, the lowest area resistances were approximately

2.2–2.3 $\Omega \cdot m^2$ under the S2/S3 concentration ratio, with higher values observed at lower concentrations. As expected for polymer IEMs, their performance was best when operated with the higher-salinity S2 and S3 solutions.

When comparing the polymer membranes with our fs-pSi membranes, we observe that the fs-pSi membranes exhibit lower membrane potentials but significantly lower area resistances. These differences primarily arise from the contrasting structural and physicochemical properties of dense polymer ion-exchange membranes versus nanoporous silicon membranes. The fs-pSi membranes rely on nanoscale electrostatic selectivity generated by surface charge and confinement, whereas polymer membranes rely on fixed ionic groups embedded in a hydrated polymer matrix, resulting in inherently different transport behaviour.

Regarding the membrane potential, polymer membranes contain a high density of fixed charges throughout the polymer matrix. These fixed charges create strong Donnan exclusion, which maintains high ion selectivity even at elevated bulk concentrations. In contrast, selectivity in nanoporous membranes such as fs-pSi originates from electrical double layer overlap inside the nanopores. When the Debye length is comparable to the pore radius, co-ions are excluded and counter-ions dominate transport. As the external concentration increases, the Debye length decreases and the electrical double layer becomes thinner, reducing the degree of overlap. This decreases the effective selectivity of the nanopores and results in a lower membrane potential.

For the ionic resistance, the trend is opposite. In polymer membranes, ion transport occurs through hydrated nano-domains whose mobility is influenced by polymer chemistry, water uptake, and the density of fixed charges. These factors often lead to relatively high intrinsic ionic resistance. In fs-pSi, ions migrate through straight nanopores with low tortuosity and minimal steric hindrance. Even when partial electrical double layer overlap exists, the accessible transport pathways remain wider and less resistive than those in dense polymer matrices. Consequently, fs-pSi membranes show much lower area resistance, which is beneficial for reverse electrodialysis, since total stack resistance directly limits the achievable power output.

Overall, polymer membranes maintain high selectivity but at the cost of higher resistance, whereas fs-pSi membranes exhibit lower selectivity at high concentration but offer much lower resistance, allowing higher current densities and improved performance in microscale RED systems.

The AAO membrane behaved similarly to the fs-pSi membranes, but exhibited a positive membrane potential. This is due to its positive surface charge density at the measured pH, causing it to act effectively as an anion-exchange membrane (AEM). However, its performance was very poor, mainly because its pore size is extremely large compared to the Debye length, resulting in negligible electrical

double-layer (EDL) overlap and therefore weak ion selectivity.

7.5.2 Model analysis and roads for improvement

The model used to describe ionic conduction and the selective properties of porous silicon was based on the assumption of a fixed surface charge density on a straight cylindrical nanopore. While this simplified model provided valuable insight and allowed us to interpret the trends observed in the I–V measurements, it remains limited and cannot fully account for several features of the experimentally measured ionic resistance.

We propose that these discrepancies arise from a dependence of the surface charge density on both the local ionic concentration and the pore size. When the surface charge density was adjusted according to these parameters, the numerical simulations showed much better agreement with the experimentally observed trends, supporting our physical interpretation.

These findings highlight the complexity of the relationship between surface charge, concentration, and pore radius. If one aims to perform a rigorous optimisation study, a more complete surface-charge model must be incorporated. Such a model should not assume a fixed surface charge density; instead, it should determine it self-consistently by solving the underlying chemical equilibrium at the pore surface. As discussed in Section 6.4, this approach would still require knowledge of the relevant equilibrium constants, which must be obtained experimentally. A numerical model which includes this is tested in the next chapter.

7.6 Conclusion

In this chapter, porous silicon membranes were fabricated and experimentally characterized within the framework of nanofluidic reverse electrodialysis (nRED). This work constitutes the experimental realization of the benchmarking platform introduced in the thesis objectives and provides the first systematic evaluation of porous silicon membranes under controlled salinity gradients.

Two fabrication strategies were investigated: self-supported membranes and free-standing membranes. Although the self-supported process previously demonstrated the ability to produce multiple membranes per wafer, the final deep reactive ion etching (DRIE) step significantly altered the structural and electrical properties of the porous layer. The incomplete and non-uniform pore opening reduced the effective pore density, while the emergence of time-dependent ionic rectification prevented reproducible electrochemical characterization. These limitations rendered the approach unsuitable for reliable RED benchmarking.

Membrane Type	**Solutions ratio**	$\mathbf{E_m}$ **[mV]**	$\mathbf{I_{sc}}$ **[μA]**	$\mathbf{R \cdot A}$ **[$\Omega \cdot$ m^2]**	$\mathbf{T_+}$ (2.14) [-]	$\mathbf{P_{max}}$ (2.9) **[mW/m^2]**	$\boldsymbol{\eta}_{\max}$ (2.13) [%]
3	S1/S2	-42.54	0.1718	2.9761	0.8690	0.1536	27.24
	S1/S3	-74.80	0.3944	2.2914	0.8278	0.6190	21.49
	S2/S3	-42.80	1.4877	0.3448	0.8793	1.3343	28.77
50	S1/S2	-38.29	0.1611	2.8545	0.8321	0.1306	22.06
	S1/S3	-54.40	0.2874	2.2967	0.7385	0.3332	11.37
	S2/S3	-30.20	1.0968	0.3309	0.7672	0.7087	14.28
100	S1/S2	-31.49	0.1616	2.3710	0.7732	0.1078	14.92
	S1/S3	-48.40	0.3055	1.9107	0.7120	0.3133	8.99
	S2/S3	-24.30	0.8814	0.3320	0.7149	0.4557	9.24
Fumasep® FKS-30	S1/S2	-45.7	0.3462	15.1695	0.8961	3.44e-02	31.38
	S1/S3	-104.6	0.6804	17.6875	0.9585	0.15479	42.05
	S2/S3	-52.1	2.6019	2.3038	0.9615	0.29482	42.59
Fumasep® FAS-30	S1/S2	35.2	-0.2076	19.5047	0.1946	1.59e-02	18.65
	S1/S3	105.9	-0.7305	16.6667	0.0361	0.16813	43.04
	S2/S3	43.0	-2.2400	2.2050	0.1195	0.20900	28.96
AAO	S1/S2	7.4	-0.0423	2.0784	0.4362	6.50e-03	0.80
	S1/S3	12.0	-0.1103	1.2972	0.4476	2.76e-02	0.50
	S2/S3	9.9	-0.4031	0.2924	0.4127	8.32e-02	1.53

Table 7.8: Experimental average results for the different membranes. Columns 3–4 (E_{m}, I_{sc}) contain average measured quantities, while columns 5–8 ($R \cdot A$, T_+, $P_{\max}$, $\eta_{\max}$) report average values obtained by extrapolation (linear regression) or calculation. Fs-pSi membrane area is 11.95 mm^2. Polymer IEM membrane area is 115 mm^2.

To overcome these issues, free-standing porous silicon membranes were developed using a controlled porosification followed by electropolishing lift-off, thereby eliminating the need for DRIE. The lift-off mechanism was analysed under different electropolishing conditions to improve process stability and reproducibility. Although thickness variations were observed across the membrane area, the porous structure remained largely preserved, and the resulting membranes exhibited stable, non-rectifying I–V characteristics suitable for quantitative RED analysis.

Three free-standing membranes fabricated at 3, 50, and 100 mA/cm^2 were evaluated under three salinity gradients. Their I–V responses followed the qualitative trends predicted by the numerical model developed in the previous chapter, confirming the relevance of the surface-charge-dominated transport framework. However, quantitative discrepancies revealed the limitations of the constant surface charge assumption. Improved agreement was achieved by introducing a pseudo-adaptive surface charge density dependent on electrolyte concentration and pore size, indicating that surface chemistry and confinement effects play a dynamic role in porous silicon membranes.

Most importantly, when benchmarked against commercial polymer ion-exchange membranes tested in the same RED setup, the free-standing porous silicon membranes demonstrated superior performance. The membrane fabricated at 3 mA/cm^2 achieved a maximum power density of 1.3 mW/m^2 under the S2/S3 concentration ratio, compared to 0.29 mW/m^2 for the Fumasep® FKS-30 membrane under identical conditions.

These results provide the first experimental validation of porous silicon as a functional ion-selective membrane for nanofluidic reverse electrodialysis. By coupling fabrication control, systematic benchmarking, and model refinement, this chapter directly advances the thesis objective of bridging nanofluidic transport theory and CMOS-compatible membrane technology, and establishes a concrete pathway toward optimized porous silicon energy harvesters.

Chapter 8

Routes for improved pSi membrane for nRED

8.1 Introduction and motivation

The previous chapter presented the first experimental results obtained with fs-pSi membranes fabricated at different current densities. Membranes with smaller pores exhibited higher selectivity but also higher area resistance, whereas membranes with larger pores showed the opposite behaviour. Numerically, assuming a constant surface charge density, an optimal pore size emerged, indicating a trade-off between selectivity and pore resistance. Experimentally, however, the pore-size dependence of the surface charge density, combined with the higher pore density in small-pore membranes, resulted in the smallest-pore fs-pSi membrane displaying the best overall performance, despite its comparatively high area resistance. These observations further underline the need for an adaptive surface-charge model rather than a fixed-charge approximation.

To improve the performance of fs-pSi membranes, one straightforward approach would be to reduce their thickness in order to lower the area resistance. However, such thinning compromises mechanical stability. A commonly adopted strategy is therefore to introduce a support layer: as discussed in 4.3.2, several studies have shown that combining a mechanically robust support with a thin, highly selective active layer can significantly improve membrane power output. In such composite structures, the active layer provides high selectivity while the support layer ensures low ionic resistance.

In this chapter, leveraging the fabrication flexibility of porous silicon, we first fabricate and characterise fs-pSi membranes consisting of a thin, highly selective top layer supported by a thicker, lower-resistance porous layer. We then numerically analyse the impact of using an adaptive surface-charge model based on local

chemical equilibria, with the goal of understanding and predicting the membrane behaviour more accurately.

8.2 Fs-pSi step membrane: numerical analysis, fabrication and I–V results

8.2.1 Fs-pSi step membrane: numerical analysis

8.2.1.1 Numerical model

As shown in Section 6, high selectivity in nanopores is achieved for small pore sizes, whereas low ionic resistance is obtained with larger pores. For nanoporous membranes, engineering a variation in pore size is therefore a natural strategy to create an active layer on top of a support layer. Several configurations have been proposed in the literature, as reviewed in [400], where different tapered or composite pore geometries are compared in terms of their achievable power output (Fig. 8.1). Among the geometries analysed, the bullet-shaped pore yielded the highest power, indicating that the active selective region should remain as thin as possible so that its high resistance does not dominate the overall transport while its strong selectivity is still retained.

Motivated by these observations, we selected a step-nanopore geometry, shown in Fig. 8.2, consisting of a short, highly selective pore section of small radius r_{act} connected to a longer support pore with a larger radius r_{supp}. For a fixed total pore length L, we numerically investigated the influence of the active-layer length on the transport properties and performance. The simulation parameters are summarised in Table 8.1. In this first-order study, the surface charge density was kept uniform along the pore walls to isolate the geometric effects.

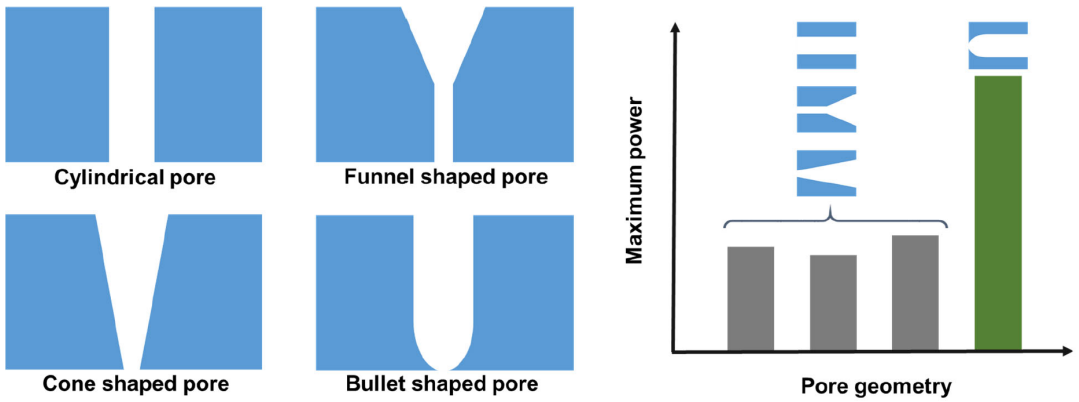


Figure 8.1: Schematic representation of different pore geometries in track-etched membranes. the bullet shaped pore generates higher power compared to the pores of other geometry. Taken from [400]

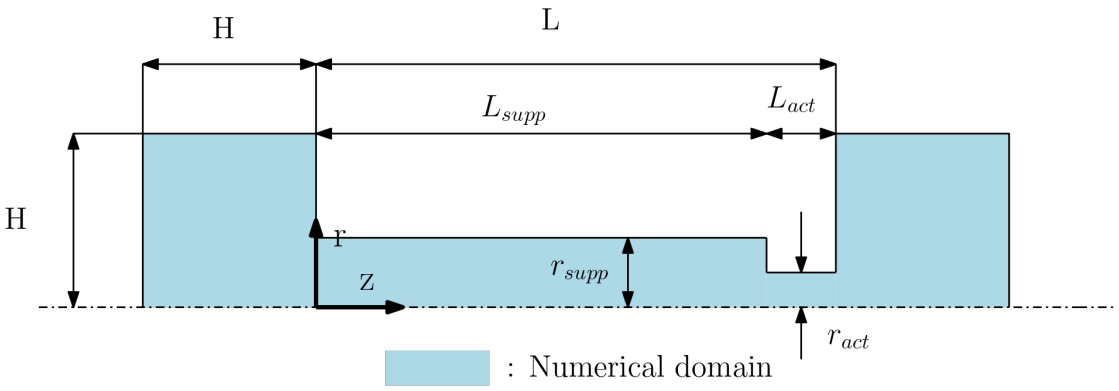


Figure 8.2: Schematic of the numerical domain used to study the step-shaped nanopore. r_{act} and L_{act} represents the pore size and the length of the active layer. r_{supp} and L_{supp} represents the pore size and the length of the support layer.

8.2.1.2 Numerical results

The maximum output power was computed using (2.9) from the I–V characteristics for different active-layer lengths, ranging from a very thin layer to a configuration where the entire pore consists of the active layer. As shown in Fig. 8.3, an optimum exists when the active-layer length is around 150 nm, corresponding to approximately 18% of the total pore length. When the active layer becomes too long, the gain in selectivity no longer compensates for the increase in ionic resistance. Conversely, if the active layer is too short, the improvement in selectivity

Table 8.1: Typical values used for the numerical simulation of the step-shaped nanopore.

Parameter	**Metric range**	**Variability**
r_{supp}	12 nm	fixed
r_{act}	6 nm	fixed
L	0.8 μm	fixed
H	0.1 μm	fixed
σ_s	-0.4 mC/m^2	fixed
C_i	S1: 0.1 mM	fixed
	S2: 1 mM	fixed
ϵ_r	80	fixed
D_- (Cl^-)	2.032×10^{-9} m^2/s	fixed
D_+ (K^+)	1.96×10^{-9} m^2/s	fixed

is insufficient compared to the additional resistance introduced by the narrower pore section.

Numerically, increasing the active-layer length causes the power output to converge toward that of a cylindrical pore with radius $r = 6$ nm, as expected. However, reducing the active-layer length does not make the system converge to the behaviour of a cylindrical pore with radius $r = 12$ nm. Even when the influence of the active layer on selectivity becomes negligible, its presence still constitutes a physical constriction to ionic transport. As a result, even a 1 nm-thick active layer imposes a significant resistance penalty. This explains why the optimum output power obtained for the step pore ($r_{\text{act}} = 6$ nm, $r_{\text{supp}} = 12$ nm) is approximately 1.47 fW, which is lower than that of a fully cylindrical pore of radius $r = 12$ nm, 1.497 fW (see Table 6.6).

Numerically, in term of power output, it appears that adding an active layer on top of a support layer does not improve the performance compared with having no active layer at all. However, as shown in Fig. 6.16, the estimated number of pores in the support layer (9.25 nm at 50 mA/cm^2 and 11.2 nm at 100 mA/cm^2) is significantly lower than in the active layer (5.8 nm at 3 mA/cm^2). This implies that one larger pore in the support layer connects to multiple smaller pores in the active layer, a configuration that is confirmed by the cross-sectional SEM image in Fig. 8.5.

As a consequence, the numerical model used in Fig. 8.2 overestimates the actual resistance of the membrane, since it assumes a single one-to-one pore connection. In reality, several active-layer pores feed into each support pore, reducing the effective resistance. Therefore, an improvement in power output is expected experimentally even though the simplified numerical model does not predict it.

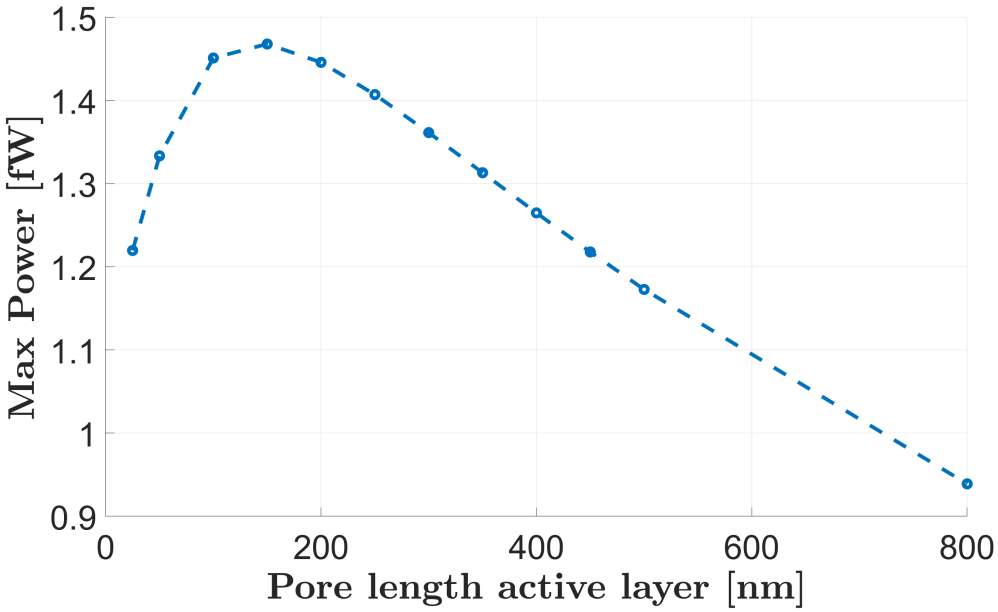


Figure 8.3: Maximun output power as a function of the active layer length for a step-shaped nanopore.

8.2.2 FS-pSi step membrane: fabrication and I–V results

8.2.2.1 FS-pSi step membrane: fabrication

The fabrication procedure follows the same steps described in Section 7.4.1, with one key modification. Instead of applying a single constant current density during porosification, the electrochemical etching is performed in two sequential current steps:

- A first etching step at a controlled low current density produces the active layer. The duration of this step is determined from the etch rate and the desired active-layer thickness.
- A second etching step at a higher current density is then applied for a longer period to form the support layer.

With this approach, the top portion of the membrane acts as the active layer, while the bottom portion becomes the support layer. This method also helps prevent the unwanted pore enlargement that typically occurs during lift-off, as previously observed in Fig. 7.25.

Three membranes were fabricated, and their processing parameters are listed in Table 8.2. For all membranes, the active layer was etched at 3 mA/cm^2, as

this condition yielded the best selectivity in Section 7.8. Two membranes share the same active layer but differ in the support-layer etching current (50 mA/cm^2 and 100 mA/cm^2). A third membrane also uses a 100 mA/cm^2 support layer but includes a thicker active layer. The total membrane thickness was maintained at approximately 90 μm for all samples.

The chosen active-layer thickness, between one-tenth and one-fifth of the total membrane thickness, is motivated by the numerical results presented in Section 8.2.1.2.

Table 8.2: Parameters for the electrochemical etching of the free-standing porous layer with step-shaped pores for the different membranes.

Current density act–supp [mA/cm^2]	**Number of cycles active layer**	**Number of cycles support layer**
3–50	334	201
3–100-a	334	99
3–100-b	668	86

Fs-pSi step membrane: Porous Structure Cross-sectional images in Figs. 8.4 and 8.5 reveal a clear distinction between the thin porous active layer (top) and the thicker support layer (bottom). In Fig. 8.5, a single pore from the support layer branches into multiple smaller pores in the active layer.

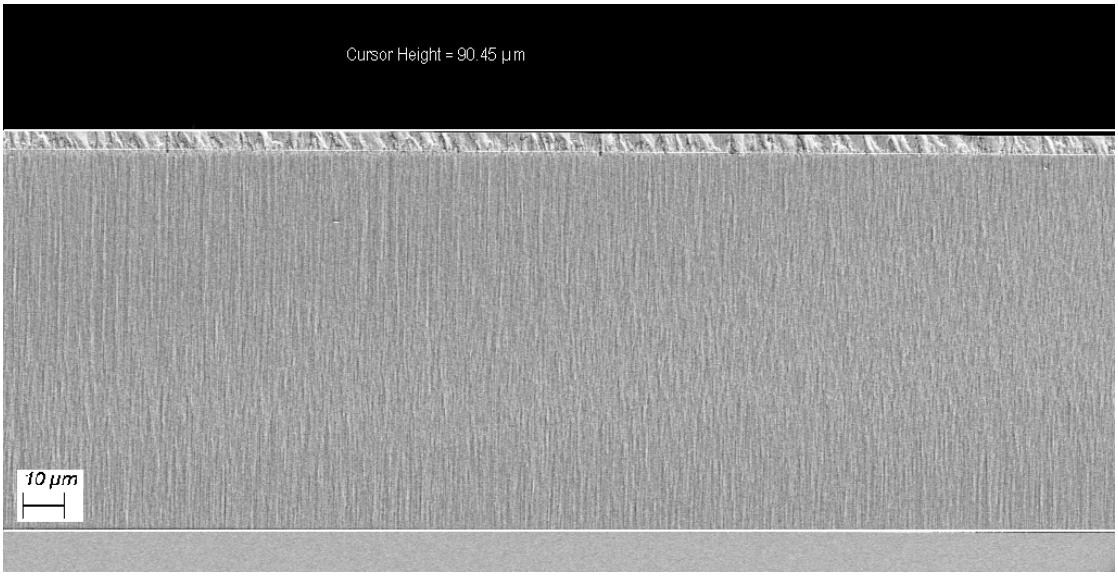


Figure 8.4: Cross-sectional SEM image of a porous silicon layer obtained by controlling the electrochemical etching current density to form a thin, low-porosity active layer (top) on top of a thicker, high-porosity support layer (bottom). The active layer was etched at 3 mA/cm^2, while the support layer was produced at 50 mA/cm^2.

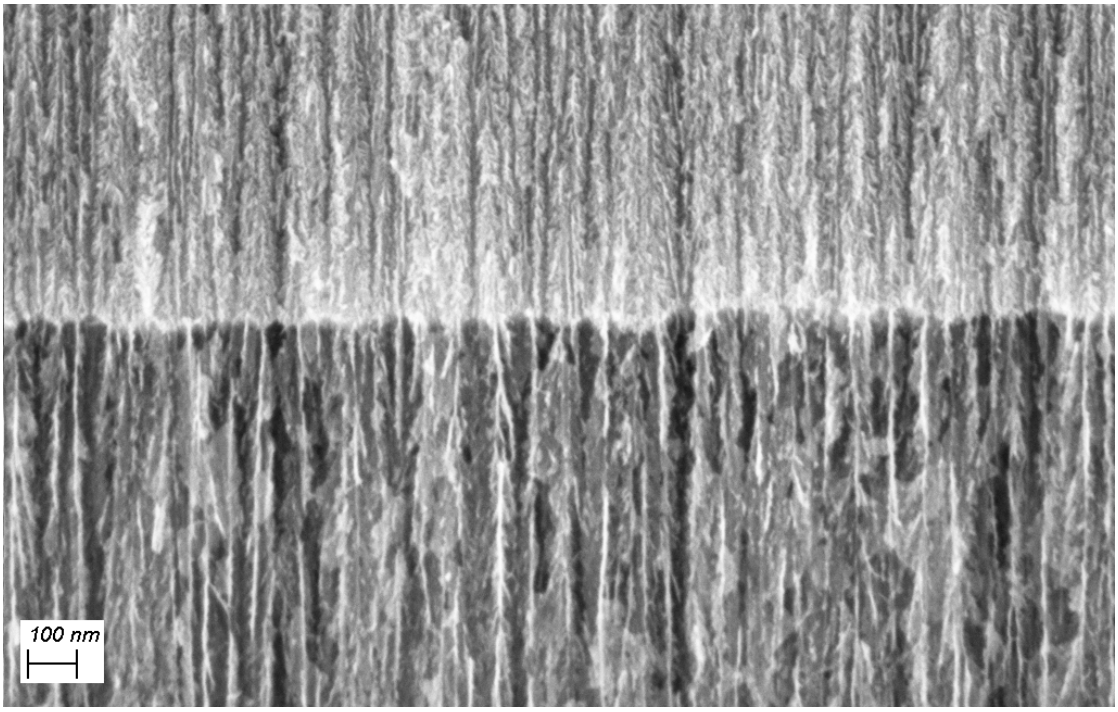


Figure 8.5: Zoomed cross-sectional SEM image of the junction between the active and support layers in a porous silicon structure fabricated by controlled electrochemical etching. The active layer (top), characterized by smaller pores and lower porosity, was formed at 3 mA/cm^2, while the support layer (bottom), with larger pores and higher porosity, was produced at 50 mA/cm^2.

8.2.2.2 Fs-pSi step membrane: I–V results

The I–V characteristics are reported in Table 8.3. Comparing the membranes with active layers (3–50 mA/cm^2 and 3–100 mA/cm^2) to the corresponding membranes without an active layer in Table 7.8, we find that in all cases the membrane potential is improved when the active layer is present. As expected, the ionic resistance increases when the active layer is added, since this thin layer introduces an additional resistive region. However, the gain in membrane potential outweighs the increase in resistance, resulting in a higher maximum power density overall.

A comparison between membranes 3–100–a and 3–100–b shows that a thicker active layer yields better performance, and surprisingly, an even lower ionic resistance. This behaviour does not follow the trend predicted by numerical simulations (Fig. 8.6), where the ionic resistance increases with the active-layer pore length.

Despite the improved characteristics observed for the 50 mA/cm^2 and 100 mA/cm^2 membranes with an active layer compared to their counterparts without one, their maximum output power remains similar to or lower than that of the membrane

etched entirely at 3 mA/cm^2. Only the 3–50 mA/cm^2 membrane under the S1/S2 concentration ratio exhibited a higher power density.

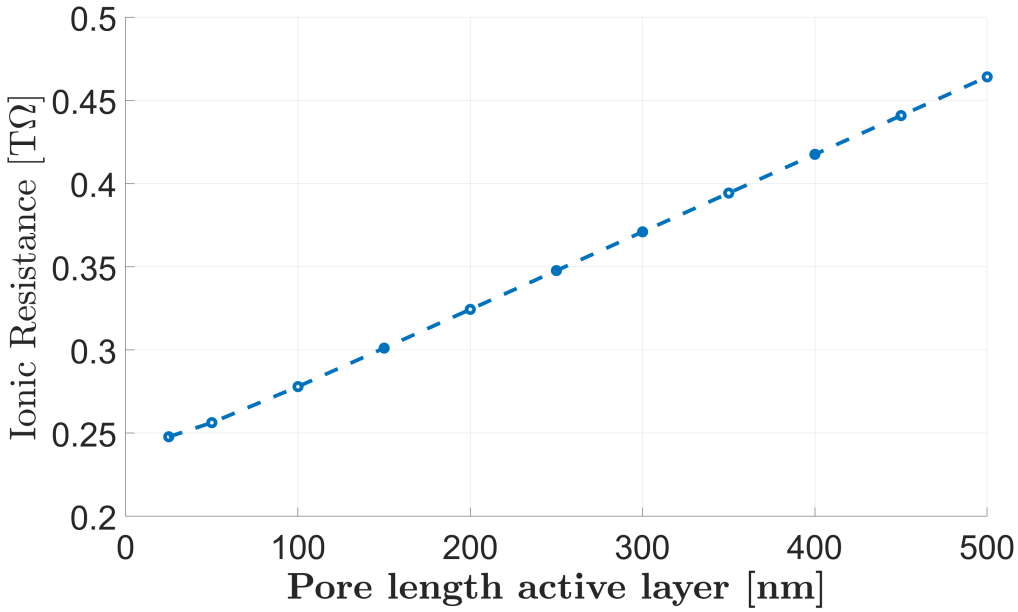


Figure 8.6: Numerical results for the ionic resistance as a function of the active pore length.

8.2.3 Discussion

Novel membrane designs that combine a thin active layer with a thicker support layer have shown improved performance in the literature. In nanoporous membranes, this concept can be implemented by introducing a top layer with very small, highly selective pores. Taking advantage of the fabrication properties of porous silicon, such a structure can be produced in a single electrochemical etching step.

The addition of an active layer can indeed improve the I–V characteristics of a porous silicon membrane. However, a trade-off must be considered: while the active layer increases the membrane potential, it also increases the ionic resistance. Numerically, an optimal active-layer thickness exists, but in practice this optimum was not observed, since a membrane etched entirely at 3 mA/cm^2 performed better than any hybrid active/support configuration with a support layer etched at 3 mA/cm^2. It should be noted, however, that the fabrication time for a full 3 mA/cm^2 membrane is about 11 hours, compared with only 1.5 hours for a 3–100–a membrane.

To further enhance the maximum output power of fs-pSi membranes, the pore

Membrane Type	**Solutions ratio**	$\mathbf{E_m}$ **[mV]**	$\mathbf{I_{sc}}$ **[μA]**	$\mathbf{R \cdot A}$ **[$\Omega \cdot$ m^2]**	$\mathbf{T_+}$ **(2.14) [-]**	$\mathbf{P_{max}}$ **(2.9) [mW/m^2]**	$\boldsymbol{\eta}_{\max}$ **(2.13) [%]**
3	S1/S2	-42.54	0.1718	2.9761	0.8690	0.1536	27.24
	S1/S3	-74.80	0.3944	2.2914	0.8278	0.6190	21.49
	S2/S3	-42.80	1.4877	0.3448	0.8793	1.3343	28.77
50	S1/S2	-38.29	0.1611	2.8545	0.8321	0.1306	22.06
	S1/S3	-54.40	0.2874	2.2967	0.7385	0.3332	11.37
	S2/S3	-30.20	1.0968	0.3309	0.7672	0.7087	14.28
100	S1/S2	-31.49	0.1616	2.3710	0.7732	0.1078	14.92
	S1/S3	-48.40	0.3055	1.9107	0.7120	0.3133	8.99
	S2/S3	-24.30	0.8814	0.3320	0.7149	0.4557	9.24
3-50	S1/S2	-46.0	0.1874	2.9318	0.9070	0.18019	33.13
	S1/S3	-70.8	0.3123	2.7088	0.8102	0.46244	19.24
	S2/S3	-39.6	1.3193	0.3583	0.8502	1.10000	24.53
3-100-a	S1/S2	-37.7	0.1534	2.9337	0.8266	0.12083	21.34
	S1/S3	-67.7	0.3350	2.4137	0.7964	0.47412	17.58
	S2/S3	-32.0	1.1057	0.3460	0.7835	0.74060	16.07
3-100-b	S1/S2	-39.2	0.1881	2.4927	0.8404	0.15445	23.17
	S1/S3	-72.5	0.3770	2.2995	0.8179	0.57215	20.21
	S2/S3	-35.6	1.2324	0.3449	0.8149	0.91700	19.83

Table 8.3: Experimental average results for the different step-shaped nanopore membranes. Columns 3–4 (E_{m}, I_{sc}) contain average measured quantities, while columns 5–8 ($R \cdot A$, T_+, $P_{\max}$, $\eta_{\max}$) report average values obtained by extrapolation (linear regression) or calculation.

size of the active layer could be reduced by lowering the etching current density while keeping the same electrolyte conditions used in this work. This improvement would come at the cost of lower porosity, potentially reducing the total number of pores, and significantly longer etching times.

8.3 Surface charge regulation as an improvement over the fixed-charge model for numerical analysis

In most electrochemical membrane and nanochannel models, the surface charge density σ is assumed to be a fixed value because it allows for easier numerical computation. While convenient, this approximation neglects the dependence of surface charge on local pH, ionic strength, and electrostatic potential. Oxide surfaces, porous silicon, and ion-exchange membranes all exhibit surface charge regulation, meaning that their charge state dynamically adapts according to local chemical equilibria. Including this effect in continuum models improves the description of the electric double layer (EDL), ionic selectivity, and electrochemical performance in systems such as reverse electrodialysis (RED).

As detailed in 4.1.2.3, for oxide-based surfaces, a fundamental reaction is the protonation/deprotonation of surface hydroxyl groups:

$$\mathrm{SiOH} \rightleftharpoons \mathrm{SiO^-} + \mathrm{H^+}. \tag{8.1}$$

The mass-action law defines the equilibrium constant

$$K_a = \frac{a_{\mathrm{SiO^-}}\, a_{\mathrm{H^+}}}{a_{\mathrm{SiOH}}}, \tag{8.2}$$

where a_i denotes activities of surface species. To simplify the notation and introduce the model in COMSOL, we define the fractional surface coverage $\theta_i = N_i/N_{\mathrm{Total}}$, where N_{Total} is the total site density, the fraction of deprotonated sites is derived by combining eq. (4.24),(4.22) and (4.23)

$$\theta_{\mathrm{SiO^-}} = \frac{1}{1 + a_{\mathrm{H^+}}/K_a}. \tag{8.3}$$

The resulting surface charge density follows directly from Faraday's law:

$$\sigma_s = -F\, N_{\mathrm{Total}}\, \theta_{\mathrm{SiO^-}}, \tag{8.4}$$

where F is Faraday's constant. In contrast to the fixed-charge model, where $\sigma = \sigma_0$ is constant, the regulated model introduces a dynamic boundary condition,

$$\sigma = \sigma(c_{\mathrm{H^+}}, \varphi), \tag{8.5}$$

which depends on the local proton concentration c_{H^+} and electrostatic potential φ. The activity of protons near a charged surface may be written using a Boltzmann factor,

$$a_{H^+} = c_{H^+} \exp\left(-\frac{F\varphi}{RT}\right), \tag{8.6}$$

thus coupling the chemical state of the surface to the electrostatic solution.

8.3.1 COMSOL model for adaptive surface charge density

The numerical model used here is identical to the one presented in Section 6.2.2, except that the surface charge density is now obtained by solving the coupled equations (8.4), (8.3), and (8.2). This requires introducing a third ionic species, namely H^+, whose concentration is fixed by the pH of the system.

Because the activity a_{H^+} in Eq. (8.2) depends on the local electrostatic potential φ, and since φ itself depends on the surface charge density σ_s, an initial guess $\sigma_{s,0}$ must be supplied to ensure numerical convergence. The model then iteratively updates σ_s until a self-consistent solution is reached. The parameters required from the user for this adaptive surface charge model are summarized in Table 8.4.

Table 8.4: Typical values used for the numerical simulations.

Parameter	**Values [units] [reference]**
K_a	2.5e-5 [mol/m^3] [143]
N_{Total}	2e6 [mol/m^2] [401]
pH	6 [-]
D_{H^+}	9.31e-9 [m^2/s] [95]

8.3.2 Numerical results

We first ran the simulation with identical concentrations on both sides of the pore in order to analyse the influence of the ionic concentration and pore size on the adaptive surface charge density. Figure 8.7 shows the resulting surface charge profile along the pore axis. The surface charge density is essentially uniform inside the pore, except near the pore entrances, where the electrostatic potential rapidly drops to zero. This local variation modifies the H^+ concentration and therefore affects σ_s.

The corresponding values of the surface charge density are reported in Table 8.5. With the adaptive model, σ_s now varies with both pore radius and local ionic concentration. The simulations show that higher ionic concentrations increase the absolute value of the surface charge density, confirming the hypothesis proposed in the previous chapter. However, when the pore radius is reduced, the adaptive

model predicts a *decrease* in the absolute surface charge density, which differs from the trend previously assumed.

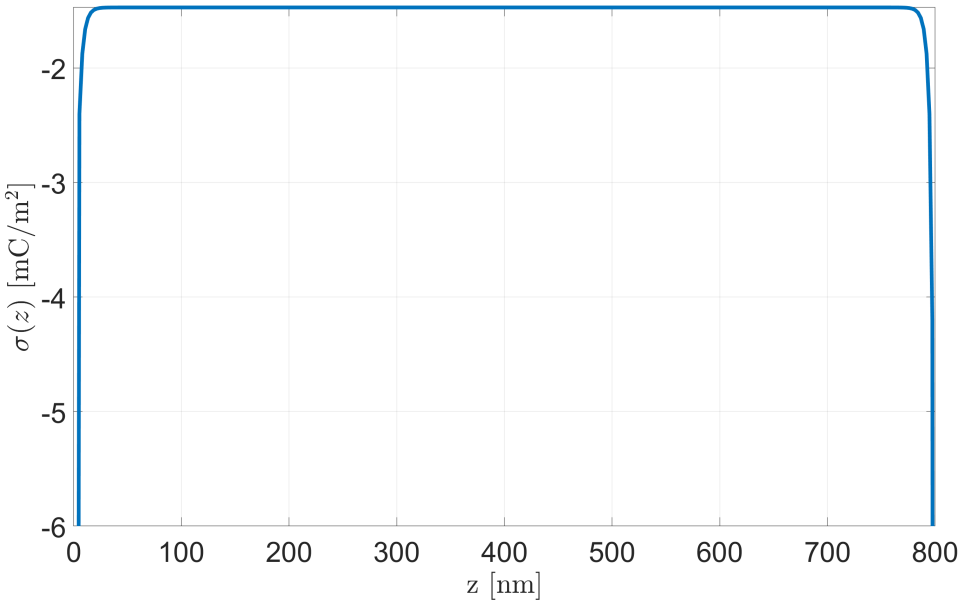


Figure 8.7: Numerical results for the surface charge density along the pore surface when no concentration gradient is present. Parameter: $r = 6$ nm and concentration S1.

Table 8.5: Numerical results for the surface charge density values for different pore size and concentration when no concentration gradient is present.

Radius [nm]	**Concentration**	**Surface charge density [mC/m^2]**
12	S1	-2.068
10	S1	-1.909
6	S1	-1.472
6	S2	-5.649
6	S3	-17.819

In a second step, we ran I–V simulations under an imposed concentration ratio. We first examined how the surface charge density varies in this configuration for two different applied potentials, as shown in Figure 8.8. Unlike the symmetric case, the surface charge density is no longer constant along the pore but changes according to the local ion concentration and the applied voltage. The concentration gradient modifies c_{H^+}, and therefore a_{H^+}, through electrostatic interactions, while the applied

potential directly alters a_{H^+} by modifying the local electrostatic potential ϕ in Eq. (8.2).

These results confirm the assumption made in the previous chapter when interpretating the experimental I–V trends in Section 7.4.2.2: the surface charge density cannot be considered constant but must instead depend on the local concentration and electric potential.

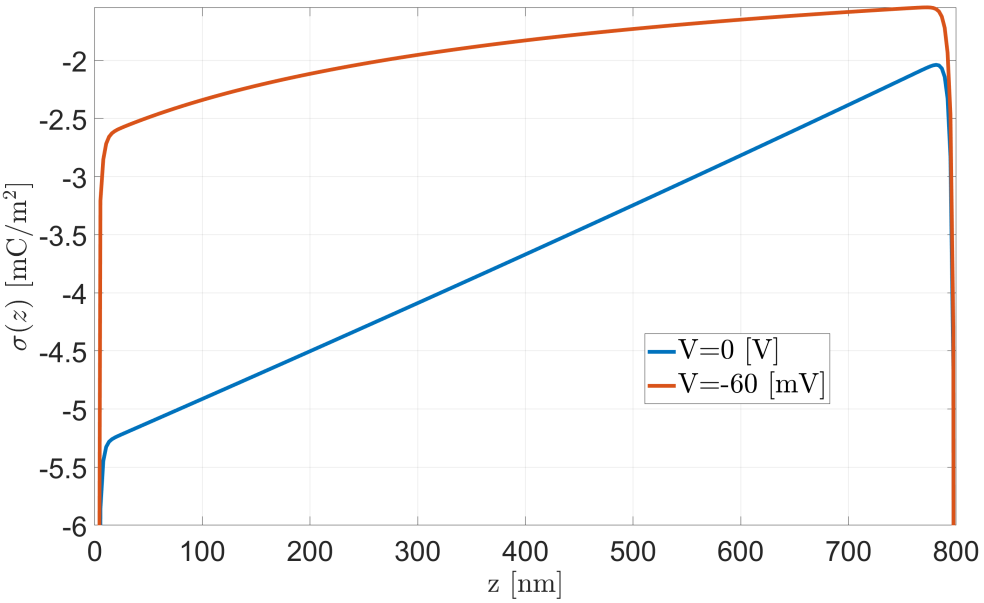


Figure 8.8: Numerical results for the surface charge density along the pore surface whit a concentration gradient under tow different applied voltage V. Parameter: $r = 6$ nm and concentration S1/S2.

Figure 8.9 shows the I–V characteristics for a nanopore with a radius of $r = 6$ nm at different concentration ratios. As can be seen, the adaptive surface charge density model affects the I–V characteristics; however, the overall tendency remains similar to that obtained with a fixed surface charge density. In particular, the model still fails to explain why the S2/S3 configuration exhibits a much lower ionic resistance than S1/S2 and S1/S3.

Table 8.6 summarizes the key metrics for different pore sizes at S1/S2 and for different concentration ratios at $r = 6$ nm. Even when accounting for pore density and comparing the relative area resistance between $r = 6$ nm, $r = 10$ nm, and $r = 12$ nm, the experimental trends cannot be reproduced. Experimentally, the ionic resistance decreases with increasing pore size, but at a much slower rate than predicted by the numerical simulations. This discrepancy suggests that the surface

charge density decreases as the pore size increases, which is opposite to the trend predicted by the current adaptive surface charge density model.

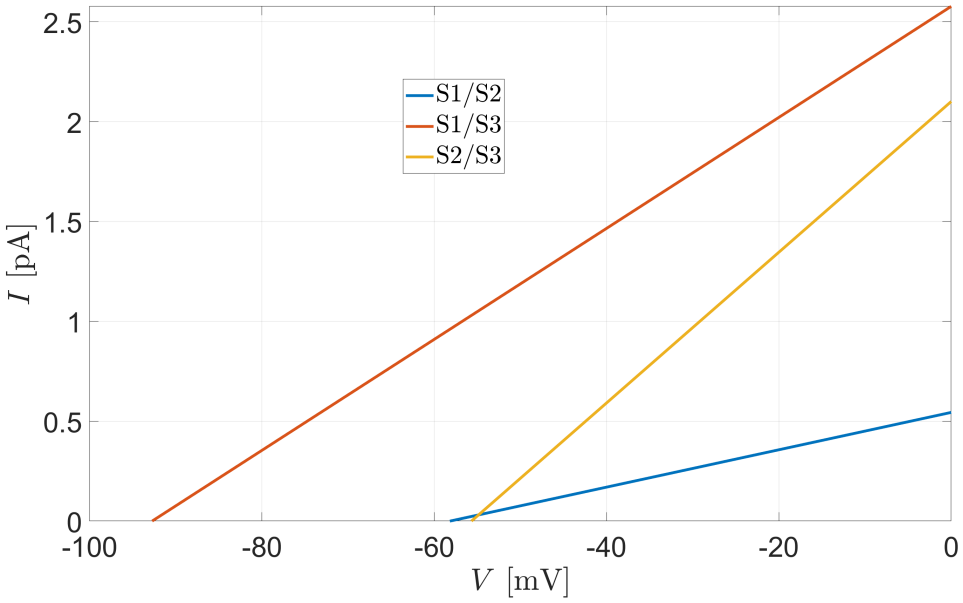


Figure 8.9: Numerical I–V characteristics of a nanopore obtained with the adaptive surface charge density regulation model under a concentration gradient. Parameters: *pore radius* $r = 6$ nm and concentration ratio S1/S2.

Table 8.6: Measured or extracted metrics for a nanopore under different concentration ratios and different pore size using the adaptive surface charge density regulation model. I_{sc} is the short-circuit current, E_m the membrane potential, R the pore resistance, $P_{\max}$ the maximum output power, and T_+ the cation transport number.

Radius [nm]	**Concentration Ratio**	I_{sc} **[pA]**	E_{m} **[mV]**	R **[GΩ]**	$P_{\max}$ **[fW]**	T_+ **[-]**
6	S1/S2	-58.16	0.544	106.92	7.91	0.999
6	S1/S3	-92.75	2.577	35.996	59.744	0.898
6	S2/S3	-55.681	2.1	26.511	29.237	0.978
10	S1/S2	-58.008	1.081	53.656	15.678	0.998
12	S1/S2	-57.740	1.346	42.885	19.435	0.996

8.3.3 Discussion

Another observation from Table 8.6 is the consistently high membrane potentials obtained for each pore size. This results from the relatively large surface charge densities to which the model converges. Experimentally, such high membrane potentials are not observed, indicating that the model overestimates the surface charge. According to Eq. (8.4), two parameters govern the magnitude of the surface charge density: the total site density N_{Total} and the mass-action equilibrium constant K_a. Although the values used here were taken from the literature, they intrinsically depend on the specific surface chemistry of the material and are therefore not necessarily directly applicable to our free-standing porous silicon membranes.

For example, reducing the equilibrium constant to $K_a = 10^{-7}\,\text{mol/m}^3$ leads to a decrease in the surface charge density and, consequently, to lower membrane potentials, as shown in Table 8.7. Similarly, decreasing N_{Total} would also reduce the surface charge density. These observations highlight the need for a dedicated study of the surface chemistry in order to determine appropriate values for these parameters. It is also possible that K_a and the site density depend on pore shape and size, which could explain the opposite trends observed experimentally and numerically for the evolution of surface charge density with pore radius.

Table 8.7: Measured or extracted metrics for a nanopore under different concentration ratios and different pore size using the adaptive surface charge density regulation model for a lower equilibirum constant $K_a = 1e-7$. I_{sc} is the short-circuit current, E_m the membrane potential, R the pore resistance, P_{max} the maximum output power, and T_+ the cation transport number.

Concentration	I_{sc} **[pA]**	E_{m} **[mV]**	R **[GΩ]**	P_{max} **[fW]**	T_+ **[-]**
S1/S2	- -49.314	0.112	441.608	1.377	0.923
S1/S3	-57.657	0.576	100.064	8.306	0.748
S2/S3	-32.610	0.453	71.993	3.693	0.780

For example, in [402], it was shown for silica nanoparticles that a surface–complexation model incorporating a curvature-dependent equilibrium constant provides much better agreement with measured zeta potentials. Their results demonstrated an increase in the absolute surface charge density as the particle size decreases, attributed to curvature-induced modifications of the hydrogen-bond network between surface silanol groups that favour deprotonation.

In our case, the pore surface is concave rather than convex, but a similar curvature-dependent mechanism may still occur. Reducing the pore radius could

shift the chemical equilibrium toward increased deprotonation because fewer stabilizing hydrogen bonds are possible within the confined geometry. This could qualitatively explain why smaller pores may exhibit a higher (more negative) intrinsic surface charge density in the experimental observations. Experimentally, an indirect indication of this trend was obtained for polycarbonate membranes through electroosmotic pumping measurements, as discussed in Section B, where decreasing pore size led to an increase in the surface charge density inferred from the measured flow rates.

However, curvature-dependent chemistry alone may not fully account for the observed discrepancies. In this work, the porous silicon membranes were intentionally thermally oxidized (1 h at 250 °C in an O_2-rich atmosphere). Under such conditions, the final oxide state is expected to depend on the porous morphology. Indeed, it has been shown that increasing porosity leads to a larger fraction of oxidized phases (SiO_x/SiO_2) relative to non-oxidized Si, which is attributed to the larger internal surface area available for oxidation in high-porosity structures [403]. Consequently, membranes fabricated at different etching current densities (and therefore different pore radius and porosity) may exhibit systematically different oxide stoichiometry and defect populations after the same oxidation treatment, thereby modifying the effective electrostatic boundary condition governing ion transport.

In addition to variations in oxide stoichiometry, the density of electrically active defects may also depend on the porous morphology and oxidation pathway. Dangling-bond defects at Si/SiO_x interfaces (commonly referred to as Pb centers) have been shown to host localized charge and to significantly modify the interfacial electrostatic potential, even when oxide thickness and overall composition remain similar [404]. By analogy, a membrane fabricated at lower etching current density (smaller pore radius, lower porosity) may retain a higher density of suboxide species or electrically active dangling bonds after thermal oxidation, owing to its different wall microstructure. Such defects could introduce an additional fixed or trapped charge contribution to the effective surface charge density inferred from electrokinetic measurements. Conversely, a higher-porosity membrane may develop a more conformal and fully oxidized surface with fewer electrically active defects, resulting in a lower effective surface charge despite its larger internal surface area.

This distinction between intrinsic chemical charge (as described by surface complexation models) and additional morphology-dependent defect or trap-related charge provides a plausible explanation for the experimentally inferred increase of the effective surface charge density with decreasing pore radius, which cannot be captured by a classical SCM formulation alone.

Thus, although the adaptive surface charge density model exhibits improved tendencies compared to the fixed-charge formulation, it still does not reproduce

the experimental trends with sufficient accuracy. The remaining discrepancy likely arises from a combination of effects that are not included in the present model. In addition to the morphology-dependent interfacial charge discussed above, the model neglects the finite size of ions. For the pore radii considered here, steric exclusion and ion–ion correlations become non-negligible and can substantially modify ion distributions and local electric fields. Incorporating finite-size effects into the Nernst–Planck–Poisson framework would therefore be expected to further improve agreement with experiments. However, such extensions significantly increase the computational complexity and simulation time, making them difficult to implement within the scope of this work.

8.4 Conclusion

In this chapter, we explored two complementary strategies aimed at advancing the central objective of this thesis: improving the electrochemical performance of free-standing porous silicon (fs-pSi) membranes for nanofluidic reverse electrodialysis (nRED) while refining the physical modelling framework used to describe their behaviour.

First, inspired by multilayer ion-exchange membrane architectures, we investigated the introduction of a thin, highly selective active layer supported by a thicker, less resistive porous layer. For porous silicon, this architecture can be realized by modulating the current density during electrochemical porosification: low current density yields small, highly selective pores, whereas higher current density generates larger pores with lower hydraulic and ionic resistance. This approach directly addresses the trade-off between permselectivity and conductance identified in previous chapters.

Numerically, the step-shaped nanopore model captured the essential physics of this hybrid configuration and revealed the existence of an optimal active-layer thickness resulting from the balance between enhanced selectivity and increased resistance. Although the simplified one-to-one pore geometry overestimates the resistance compared to a real membrane where multiple small pores branch from a larger support pore, the model provides a first-order design map for structural optimization.

Experimentally, membranes combining a 3 mA/cm^2 active layer with support layers etched at 50 mA/cm^2 or 100 mA/cm^2 confirmed that structural engineering can improve performance relative to single-porosity membranes. However, under identical operating conditions, a membrane composed entirely of the highly selective porosity still achieved the highest power output. This result highlights that, in the present fabrication regime, the gain in membrane potential provided by the active layer remains insufficient to offset the added resistance of the hybrid architecture.

The study therefore establishes both the potential and the practical limits of multilayer design for fs-pSi membranes.

In the second part of the chapter, we incorporated an adaptive surface charge regulation model into the numerical simulations in order to strengthen the coupling between chemical surface equilibria and ion transport. By solving the surface complexation equilibrium self-consistently, the surface charge density became dynamically linked to local ionic concentration and electrostatic potential. This framework successfully reproduced the experimentally observed increase in surface charge magnitude with increasing concentration, thereby validating the relevance of charge regulation effects in porous silicon membranes.

Nevertheless, discrepancies remain, particularly regarding the dependence of ionic resistance and effective surface charge on pore radius. While the adaptive model predicts an increase in surface charge with pore size, the experimental trends suggest the opposite behaviour. This divergence indicates that additional mechanisms, such as morphology-dependent interfacial charge, defect-related contributions, or confinement-induced transport effects, are not fully captured by the present surface complexation formulation.

Overall, this chapter contributes in two key ways. First, it demonstrates that the performance of porous silicon membranes can be systematically tuned through controlled structural engineering, thereby advancing their optimisation for nRED applications. Second, it highlights the limitations of current surface-charge modelling approaches and identifies the need for a unified framework that couples surface chemistry, morphology-dependent interfacial effects, and confined ion transport. These insights provide a critical bridge between fabrication, experimental benchmarking, and numerical modelling, and define the next steps toward achieving predictive design of CMOS-compatible porous silicon membranes for osmotic energy harvesting.

Chapter 9

Complementary studies and perspectives

9.1 Complementary work

In parallel with the core research developed in this dissertation, several Master theses were conducted under our supervision. These works addressed complementary scientific and technological challenges directly related to porous silicon membranes, electrokinetic transport, and reverse electrodialysis (RED). Together, they contribute to a broader understanding of surface electrostatics, system-level energy harvesting, and membrane fabrication scalability.

9.1.1 Surface charge density determination from electroosmotic flow

The first project, summarized in Appendix B, aimed at analytically determining the surface charge density of nanoporous silicon membranes from electroosmotic flow (EOF) measurements. The methodology relied on extracting the zeta potential from measured flow rates using established EOF models, and subsequently converting it into surface charge density through electrostatic relations combined with the Boltzmann distribution for proton activity.

Although no detectable electroosmotic flow was measured for the investigated nanoporous silicon membrane, the study provided important insights. A comparative experimental and numerical analysis of different membrane materials confirmed that surface charge density increases as pore size decreases, due to curvature-induced modifications of the electrical double layer. The absolute zeta potential followed the trend:

$$|\zeta_{Al_2O_3}| > |\zeta_{PI}| > |\zeta_{PC}| > |\zeta_{PE}|.$$

Additionally, electroosmotic flow was shown to exhibit a transient regime before reaching steady state. Surface modifications of polycarbonate membranes further demonstrated that reducing pore size via atomic layer deposition (ALD) can both enhance flow rate and reverse flow direction, highlighting the strong coupling between surface chemistry, pore geometry, and electrokinetic transport.

9.1.2 Paper-based reverse electrodialysis systems

The second project, summarized in Appendix C, focused on the development of pump-free, paper-based stacked RED devices for salinity-gradient energy harvesting. Because conventional RED systems require continuous external pumping, the use of paper as a capillary medium was investigated as a passive alternative for electrolyte transport.

A rapid fabrication method based on plotter-patterned hydrophobic barriers enabled the production of multilayer three-dimensional paper microfluidic devices. An analytical model describing flow in fan-shaped paper channels was established and successfully calibrated, demonstrating the possibility of generating quasi-steady capillary-driven flow.

Single-membrane RED cells achieved power densities of 4–8 μW/cm^2, while a stacked configuration reached 35.5 μW/cm^2, although performance degradation limited long-term operation. The study demonstrated that optimized microfluidic design significantly enhances paper-based RED performance and enables pump-free operation over time scales exceeding one hour.

The integration of free-standing porous silicon (fs-PSi) membranes into a paper-stacked RED configuration was also explored. Initial proof-of-concept experiments confirmed that fs-PSi membranes are compatible with paper-based microfluidics, with measurable membrane potentials obtained after a short wetting stabilization period. This result highlights the potential synergy between porous silicon membranes and passive capillary-driven systems.

9.1.3 Upscaling of free-standing porous silicon membranes

The third project, summarized in Appendix D, addressed the scalability of fs-PSi membrane fabrication. While the established anodization and electropolishing process yields high-quality membranes with good reproducibility, it produces only a single flake per run and remains time-intensive.

A lift-off strategy using patterned masking and reactive ion etching (RIE) was investigated to enable the fabrication of multiple fs-PSi membranes from a single wafer. Experiments confirmed that lift-off occurs during electropolishing, and that mask removal by RIE can successfully release the porous layer at die scale. However, full-wafer implementation proved challenging due to mechanical retention effects,

under-etching during anodization, and difficulties in protecting the fragile porous layer during mask removal.

Although not fully optimized, this approach remains a promising pathway toward wafer-scale production of fs-PSi membranes, which is essential for large-scale RED applications.

9.1.4 General perspectives

Collectively, these complementary works strengthen the present dissertation at three levels: (i) fundamental understanding of surface charge and electrokinetic transport, (ii) system-level development of pump-free salinity-gradient energy harvesting, and (iii) technological perspectives for scalable membrane fabrication.

Future research should focus on improving the electrokinetic characterization of fs-PSi membranes, optimizing their integration into multilayer RED stacks, and developing robust masking and handling strategies for wafer-scale membrane production.

9.2 Perspectives for improving the characterisation and performances of pSi as an IEM

Despite the limited performances presented Chapter 7 and 8, the performance and characterisation of porous silicon membranes as ion–exchange membranes for RED could potentially still be significantly improved. Several promising routes for enhancement can be identified:

- *Stronger anisotropic structure:* As demonstrated in this work, adding a thin active layer with small nanopores can improve membrane performance. Further reducing the pore size in this active layer would help maintain stronger membrane potentials at higher concentrations. Several approaches can be followed to push these limits.

  A first strategy is a two-step anodization process in which the active and support layers are formed in different HF-based electrolytes. In this approach, a thin active layer with very small pores is produced first in the conventional ethanol-based electrolyte, where pore size can be precisely controlled. The electrolyte is then switched to a 1-butanol–based solution for the second anodization step. As shown in [380], anodization in 1-butanol leads to larger and mechanically more stable pores without prematurely entering the electropolishing regime. This makes 1-butanol particularly suitable for producing a robust support layer beneath the selective active layer.

Additionally, the use of substrates with different doping levels could extend the range of achievable pore sizes while retaining acceptable porosity levels, thus mitigating the risk of membrane fracture. Thinner membranes may also further reduce ionic resistance, provided that mechanical stability can be preserved.

- *Controlling the surface chemistry:* Numerical simulations highlighted that surface charge density is a key parameter governing nanopore selectivity and RED performance. Improving the uniformity and magnitude of surface charge within the porous network is therefore critical. Atomic layer deposition (ALD) is a promising approach: in this work and in prior studies, ALD coatings improved electroosmotic pumping, indicating an increase in surface charge density. ALD is already well established for porous silicon [206]. Beyond modifying surface chemistry, ALD also reduces pore size and enhances the chemical stability of the porous structure in aqueous environments.

- *Fluidic integration:* Minimizing hydraulic losses and mitigating concentration polarization will be essential for practical RED operation. Paper-based microfluidics or PDMS channels with optimized geometries could help reduce the effective pumping burden. Another promising strategy is patterned surface texturing of the silicon prior to anodization [224], which induces mixing and recirculation when the feed solutions flow across the membrane surface, thereby reducing concentration polarization and enhancing overall performance.

9.3 Is pSi for nRED application worth it ?

The ultimate objective of employing porous silicon (pSi) as an ion-exchange membrane (IEM) in nanofluidic reverse electrodialysis (nRED) is to generate sufficient electrical power to supply a low-power energy harvesting interface, such as an ultra-low-power power management integrated circuit (PMIC) for IoT applications (e.g., tens of μW average power).

However, practical energy harvesting also requires continuous feeding of the electrolyte solutions to maintain the salinity gradient across the membrane. This feeding implies hydraulic pumping, which consumes energy and therefore reduces the net harvested power. The main objective of the feeding stream is to preserve the concentration difference at the membrane interface, enabling continuous operation near the ideal power output. Consequently, a rigorous optimization of the overall nRED system, including both electrical generation and hydraulic pumping losses, is required to evaluate true feasibility.

One of the major limitations in RED and nRED systems is concentration polarization (CP), which reduces the effective concentration difference Δc experienced by the membrane. The secondary role of the feed stream is therefore to induce sufficient tangential convection to mitigate the formation of thick diffusion boundary layers near the membrane surface. In large-scale RED stacks, numerous studies have investigated optimal flow direction, spacer configuration, and flow velocity in order to maximize power density and system efficiency [19, 405].

In contrast, the present work targets small-scale nRED systems intended for IoT integration. In such configurations, stacking possibilities are limited and geometric constraints restrict mixing enhancement strategies. As a result, the feed stream velocity becomes the primary hydrodynamic parameter available to control external concentration polarization.

In the following section, a simplified electro-hydrodynamic model is proposed to estimate the minimum required flow velocity and to assess whether, given the experimentally achieved membrane performance, a pSi-based nRED device can realistically operate within energetically reasonable limits.

9.3.1 Hydrodynamic feasibility model for small-scale NRED operation

To assess the feasibility of nRED for low-power IoT applications, we formulate a minimal coupled electro-hydrodynamic model based on the configuration presented in Figure 9.1. The membrane is modeled as a rectangular active area $A = wL$, where w is the channel width and L the flow length. The feed stream flows tangentially to the membrane with mean velocity U in a slit-like channel of height h. The corresponding hydraulic diameter is $d_h \approx 2h$ (for $w \gg h$). The analysis is conducted symbolically, without fixing geometric dimensions, in order to identify scaling constraints.

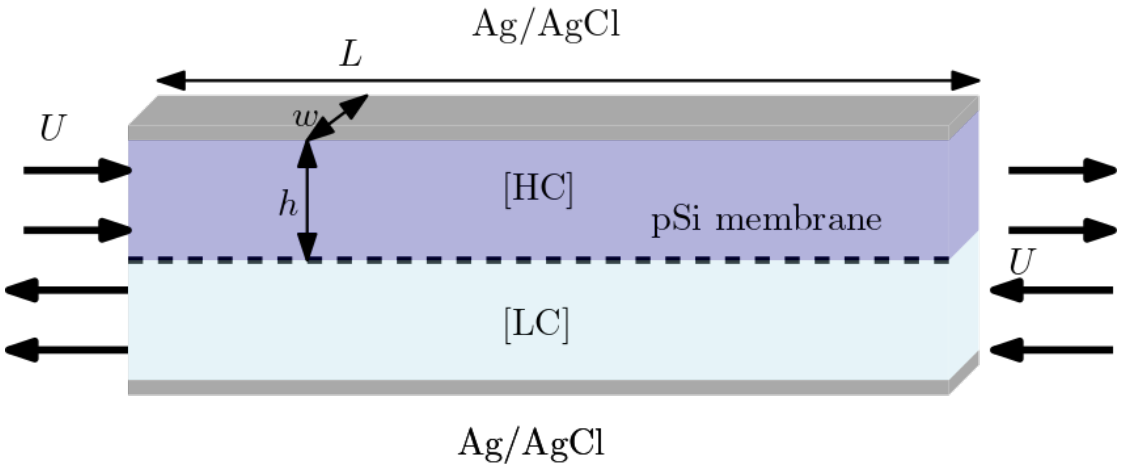


Figure 9.1: Schematic representation of the small-scale nRED configuration considered for feasibility analysis.

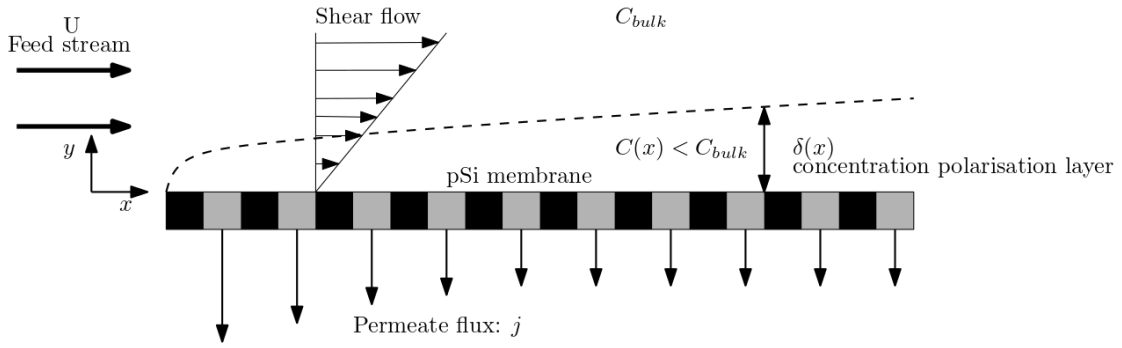


Figure 9.2: Schematic representation of the concentration boundary layer formed under tangential shear flow along a selective membrane surface.

Phenomenological situation. When an electrolyte flows tangentially along a membrane surface, a hydrodynamic boundary layer develops due to the no-slip condition at the solid interface. In parallel, a concentration boundary layer forms when ionic species are transported across the membrane. This situation is illustrated in Figure 9.2.

Similarly to the momentum boundary layer, where the velocity increases from zero at the membrane surface to the bulk value U_∞, the ionic concentration varies from the surface value c_s to the bulk concentration c_b outside the concentration boundary layer. Under steady-state current, selective ion transport through the membrane induces a concentration gradient normal to the surface, resulting in external concentration polarization (CP) [406].

The thickness of this concentration boundary layer is governed by the competition between convective transport parallel to the membrane and diffusive transport normal to the surface.

Although the classical description is often introduced in the context of dissolution phenomena [406], the governing transport equations are identical. In the present nRED configuration, diffusion does not originate from solid dissolution but from the electrochemically imposed ionic flux across the membrane, leading to the same boundary-layer structure.

Electrical performance. The membrane delivers an areal power density p_A at operating voltage V_{op}. The corresponding current density is approximated by

$$j \approx \frac{p_A}{V_{\mathrm{op}}}. \tag{9.1}$$

External concentration polarization (CP). Under tangential flow, the concentration drop across the diffusion boundary layer is described using film theory as

$$\Delta c \approx \frac{j}{zFk_m}, \tag{9.2}$$

where k_m is the mass-transfer coefficient, z the ionic valence, and F the Faraday constant. This formulation follows classical boundary-layer descriptions of concentration polarization in crossflow membrane systems [406–409].

To ensure near-bulk conditions at the membrane surface, the admissible polarization is limited to a fraction β (close to zero) of the available salinity contrast:

$$\Delta c \leq \beta \Delta c_{\mathrm{bulk}}. \tag{9.3}$$

This yields the minimum required mass-transfer coefficient

$$k_{m,\mathrm{min}} = \frac{p_A}{V_{\mathrm{op}} zF\beta\Delta c_{\mathrm{bulk}}}. \tag{9.4}$$

Hydrodynamic scaling. For laminar crossflow in a slit-like channel, the mass-transfer coefficient can be expressed using a Sherwood correlation,

$$Sh = \frac{k_m d_h}{D} \sim C\left(Re\, Sc\, \frac{d_h}{L}\right)^{1/3}, \tag{9.5}$$

where Sh is the Sherwood number, $Re = \rho U d_h/\mu$ is the Reynolds number, $Sc = \mu/(\rho D)$ is the Schmidt number, d_h is the hydraulic diameter (for $w \gg h$, $d_h \approx 2h$), L is the flow length, and C is a dimensionless constant of order unity ($C \approx 1.6$–1.9

for laminar boundary-layer conditions). This cubic-root dependence follows from the classical Lévêque boundary-layer solution for convection–diffusion problems [406, 407].

The minimum velocity required to avoid CP limitation is implicitly defined by

$$k_m(U_{\min}) = k_{m,\min}. \tag{9.6}$$

Pumping penalty. For laminar flow between parallel plates ($w \gg h$), the pressure drop along the channel is given by

$$\Delta p = \frac{12\mu L}{h^2} U, \tag{9.7}$$

where μ is the dynamic viscosity. The corresponding pumping power is

$$P_{\text{pump}} = \Delta p\, Q = \frac{12\mu L}{h^2} U \cdot (Uwh) = \frac{12\mu L w}{h} U^2. \tag{9.8}$$

This pumping power needs to be doubled to account for both feeding solutions.

Feasibility criterion. The net harvested power is therefore

$$P_{\text{net}} = p_A A - 2P_{\text{pump}}(U_{\min}), \tag{9.9}$$

with $A = wL$. Feasibility requires

$$P_{\text{net}} > 0 \quad \text{and} \quad p_A A \geq P_{\text{req}}, \tag{9.10}$$

where P_{req} denotes the target average power required by the IoT load.

9.3.2 Proposed theoretical strategy for feasibility assessment

Although no dedicated hydrodynamic experiments were conducted in the present work, the above model defines a structured pathway for future feasibility evaluation of PSi-based nRED harvesters.

1. **Electrical scaling.** Determine the achievable areal power density p_A as a function of membrane morphology and salinity gradient. From the target load requirement P_{req}, deduce the required membrane area $A_{\text{req}} = P_{\text{req}}/p_A$.

2. **CP tolerance definition.** Select an admissible polarization fraction β representing acceptable deviation from bulk concentration. This defines $k_{m,\min}$ and therefore the minimal hydrodynamic requirement.

3. **Hydrodynamic regime identification.** Using laminar mass-transfer scaling, estimate the minimum crossflow velocity $U_{\min}$ required to satisfy $k_m \geq k_{m,\min}$. This step allows identification of whether mitigation of external concentration polarization requires only mild tangential flow or comparatively strong convection.

   Because the mass-transfer coefficient $k_m(U)$ depends sensitively on the specific channel geometry (gap height, aspect ratio, entrance effects, and possible spacer-induced mixing), its precise functional form and prefactor must be determined experimentally for the chosen configuration. Therefore, the present scaling analysis provides only the governing trends, while quantitative determination of $U_{\min}$ requires experimental calibration of $k_m(U)$ for the considered set-up.

4. **Hydraulic penalty estimation.** Estimate pumping losses at $U_{\min}$ and evaluate P_{net}. If pumping exceeds harvested power, the architecture is not energetically viable.

5. **Dominant limitation analysis.** If $k_{m,\min}$ is found to be small for the achieved p_A, external concentration polarization (CP) is unlikely to be the dominant performance limitation. In that case, further improvements should primarily target intrinsic membrane properties, such as permselectivity, internal ionic resistance, and mitigation of ionic shortcut currents.

   It is also important to emphasize that increasing the tangential flow velocity U yields diminishing returns: under laminar boundary-layer conditions, the mass-transfer coefficient scales approximately as $k_m \propto U^{1/3}$, whereas the pumping power increases much more rapidly, approximately as $P_{\text{pump}} \propto U^2$. Consequently, excessive increases in flow velocity are energetically inefficient, and hydrodynamic optimization should aim at the minimum velocity required to avoid CP limitation.

This framework enables feasibility discussion without committing to a specific device geometry, while preserving physical consistency between electrical output, mass transport, and hydraulic cost.

9.3.2.1 Ultra-low-power power management integrated circuit (PMIC) for IoT: requirements

Among commercially available PMICs (e.g., e-peas company in Belgium), the most favorable option for PSi-based nRED harvesting is the device with the lowest cold-start power, namely the AEM13920 (cold start from 1.5 μW at 275 mV) [410]. This corresponds to an input current of $I_{\text{cold}} = P/V \approx 5.5$ μA. By contrast, the

AEM15820 requires 5 μW at 275 mV [411], while a thermo-oriented PMIC such as the AEM20941 requires 650 μA at 80 mV ($\approx$ 52 μW) [412], which is substantially more demanding in power terms for low-current electrochemical harvesters.

For continuous harvesting, the cold-start threshold is no longer the limiting specification. Once running, the PMIC can harvest provided that the harvester input remains within the operating range (e.g., 120 mV–4.5 V for the AEM13920) and that the average harvested power exceeds the average system demand after conversion losses [410]. In typical ultra-low-power IoT duty-cycled operation, $P_{\mathrm{avg,load}}$ can be as low as 10–100 μW, depending on sensing frequency and wireless transmission interval.

On the nRED side, the relevant constraint is therefore the areal power density: $P_{\mathrm{elec}} = p_A A$, so that sustaining an average load power $P_{\mathrm{req,avg}}$ requires

$$A_{\mathrm{cont}} = \frac{P_{\mathrm{req,avg}}}{p_A}. \tag{9.11}$$

For $p_A = 1.33\ \mathrm{mW\,m^{-2}}$ and a minimal continuous power requirement of $P_{\mathrm{req,avg}} = 10\ \mu$W, this corresponds to

$$A_{\mathrm{cont}} \approx 7.5 \times 10^{-3}\ \mathrm{m^2} \tag{9.12}$$

(about 75 cm^2), before accounting for any pumping losses.

The minimal continuous power requirement of 10 μW corresponds to an active membrane area of approximately 75 cm^2 at the present measured power density. From a purely geometrical standpoint, such an area is comparable to that of a 4-inch silicon wafer ($\sim$ 78 cm^2), suggesting that wafer-scale fabrication is, in principle, sufficient.

However, the practical limitation arises from the mechanical fragility of highly porous free-standing pSi membranes. In the current state of the art (Chapter 5), large-area free-standing porous silicon membranes above a few square centimeters are difficult to fabricate without cracking, particularly at high porosity and small thickness. Consequently, realistic scaling would likely require either supported membrane architectures or modular integration of multiple smaller membrane units connected hydraulically in parallel and electrically as needed.

Such modular strategies are more consistent with established MEMS fabrication approaches and would improve mechanical robustness while allowing scalable energy harvesting architectures.

Thus, while not fundamentally infeasible, the integration of porous silicon (pSi) membranes for nRED-based energy harvesting appears unrealistic at the current measured power densities. The principal limitation arises from the relatively low areal output power, which would require impractically large membrane areas to sustain IoT-scale continuous operation.

Improvements in intrinsic membrane properties, particularly enhanced permselectivity and reduced membrane resistance, could significantly increase the achievable power density. Since the maximum electrical power of an electrochemical generator scales inversely with its internal resistance, reducing the membrane resistance by a factor of two would, in principle, approximately double the maximum extractable power, provided that selectivity and open-circuit voltage are preserved.

Achieving increases of several orders of magnitude in power density, however, would likely require substantially higher salinity gradients. The open-circuit voltage follows a Nernst-type dependence and therefore scales with the logarithm of the concentration ratio. Consequently, increasing the concentration ratio enhances V_{OC} and may increase the theoretical maximum power.

However, increasing the absolute ionic concentrations while keeping the same concentration ratio does not modify V_{OC}. Instead, it increases the electrolyte conductivity and reduces the internal resistance of the system, thereby enhancing the short-circuit current I_{sc} and the achievable power density.

In practice, both mechanisms may contribute to performance improvement, but gains remain conditional on maintaining high membrane selectivity at elevated salinities and avoiding excessive internal shortcut currents or concentration polarization effects.

Consequently, although the present results do not exclude the feasibility of pSi-based nRED harvesting, significant optimization of membrane electrochemical performance and system-level operating conditions is still required before practical implementation can be considered.

Chapter 10

Conclusions

In this thesis, we investigated the design and fabrication of a nanoporous ion-exchange membrane based on porous silicon for energy harvesting from salinity-gradient power using a reverse electrodialysis (RED) configuration. Four key aspects have been examined:

1. The structural properties of highly doped p++ porous silicon and the development of a numerical model assuming a uniform surface charge density on the inner pore walls (Chapter 6).

2. Two fabrication routes for producing porous silicon membranes for RED, self-supported and free-standing membranes, and their structural and electrical characterization (Chapter 7).

3. Experimental characterization of the RED performance of self-supported and free-standing pSi membranes, combined with interpretation based on numerical analysis (Chapter 7).

4. Routes for performance enhancement, including (i) hybrid membranes combining an active layer and a support layer, and (ii) an adaptive surface-charge regulation model for numerical analysis (Chapter 8).

Each of these studies has produced innovations or contributions that address challenges in the fields of nanoporous reverse electrodialysis and porous silicon membrane technologies. The main contributions of this work are summarized below:

- First demonstration of nanoporous RED using porous silicon as the ion-selective material. This study establishes, to our knowledge, the first evidence of the feasibility of porous silicon as an active material for ion-selective energy harvesting.

- Understanding and optimization of porous silicon membranes for RED applications. The combination of high porosity and small pore size was found to be the most effective for maximizing power output and efficiency due to strong electrical double-layer overlap and moderate ionic resistance. A maximum power density of 1.33 mW/m^2 was obtained using a 10/1 mM KCl concentration gradient with a 90 μm thick fs-pSi membrane.

- Fabrication of robust and repeatable free-standing porous silicon membranes using a single electropolishing step. The mechanism of spontaneous lift-off of the porous layer has been investigated, and a physical explanation based on HF depletion and gas accumulation beneath the porous film is proposed.

- Fabrication of hybrid pSi membranes combining an active and a support layer using a single anodization step by controlling the current density. This approach aims to couple a highly selective porous layer with a low-resistance support layer. Experimental results show improved performance relative to membranes without an active layer.

- Analysis of the dependence of surface charge density on electrolyte concentration and pore size. Numerical and surface-complexation analyses suggest that smaller pores and higher ionic concentrations lead to larger (more negative) surface charge densities in porous silicon. This finding has important implications for other ion-transport applications involving porous silicon.

- Indirect determination of surface charge density using electroosmotic pumping. Although no measurable flow was obtained for our pSi membranes, the study demonstrated the effect of atomic layer deposition (ALD) and pore size on several track-etched membranes. ALD significantly enhanced EO pumping, evidence of increased surface charge, while smaller pores consistently exhibited higher surface charge density, supporting conclusions drawn for porous silicon.

- Integration of passive capillary pumping into paper-based microfluidics for RED. The study demonstrated controllable and nearly constant power output over approximately 30 min and showed the feasibility of integrating fs-pSi membranes with paper-based platforms.

These findings highlight the range of developments required when advancing a nanoporous membrane platform for salinity-gradient energy harvesting. The work conducted throughout this thesis spanned multiple disciplines, from silicon electrochemistry, structural and electrical characterisation, and numerical modelling of ion transport, to membrane fabrication, microfluidic integration, and electrochemical performance testing. Together, these efforts enabled the design, fabrication,

and evaluation of porous silicon membranes as ion-exchange materials for RED, leading to new understanding of their surface chemistry, transport properties, and technological potential.

The resulting set of tools, including a repeatable fabrication route for free-standing pSi membranes, numerical frameworks for analysing nanopore selectivity, and exploratory coupling with paper-based microfluidics, constitutes a versatile platform for future research. Although further optimisation is still required, particularly regarding surface charge regulation and large-scale manufacturing, the outcomes of this work demonstrate that porous silicon remains a promising candidate for next-generation nanoporous ion-exchange membranes. We hope that these contributions will support continued progress in the field and stimulate new approaches to nanoscale electrochemical energy conversion.

Comparison with polymer IEMs under identical operating conditions showed that, although the polymer membranes still exhibited slightly higher selectivity, the major advantage of nanoporous silicon lies in its significantly lower ionic resistance. As a result, the output power density of the pSi membranes was found to be nearly one order of magnitude higher than that of the polymer IEMs. However, such performance can only be achieved at very low ionic concentrations. At higher concentrations, the selectivity of pSi rapidly deteriorates, whereas polymer membranes maintain high permselectivity. This fundamentally limits the maximum achievable power density of porous silicon membranes. In addition, for energy-harvesting applications, continuous pumping would be required, which would further reduce the overall system efficiency.

The literature on AAO membranes provides useful benchmarks. In [54], a power density of 6.6 mW/m^2 was reported, much higher than the 1.33 mW/m^2 obtained here, but measured at higher salt concentrations (100/10 mM NaCl). Since AAO carries a positive surface charge and is therefore selective toward Cl^-, using NaCl enhances its output performance. Similarly, in [65], combining an active layer with a support layer enabled power densities up to 15 mW/m^2 at a 500/1 mM concentration ratio. In that work, the membranes consisted of an extremely thin active layer (1–2 μm) with very small pores (2–10 nm) supported by a high-porosity thick layer (50 μm) with much larger pores (100 nm), which explains the substantial performance improvement.

Together, these results for polymer and AAO membranes indicate that significant room for improvement remains for porous silicon. With optimized pore architecture, thinner active layers, and improved surface charge control, pSi-based nanoporous membranes could potentially achieve competitive power densities even at higher salinities.

A second aspect that requires increasing attention in the porous silicon and nanofluidic membrane community is the mechanical stability of these highly porous

layers. For energy-harvesting applications such as RED, the robustness of free-standing pSi membranes is critical, as pressure gradients, handling steps, or drying–wetting cycles can lead to deformation, fracture, or changes in ionic transport pathways. Furthermore, the propensity for crack nucleation and propagation in thick, high-porosity layers remains insufficiently understood and directly affects the long-term reliability of pSi-based ion-exchange membranes. Throughout this work, the mechanical stability challenge has motivated several design considerations, particularly regarding membrane thickness, porosity, and release strategies. Based on these insights, a number of recommendations for improved structural resilience are proposed, laying the foundation for more durable pSi membranes in future RED implementations.

Finally, the size of the membranes fabricated in this work remains too small to deliver a feasible net power output. Upscaling is required to power real devices; however, given the currently measured areal power density of 1.33 mW/m^2, the membrane area required to supply even ultra-low-power IoT electronics would be substantial. For example, commercially available power management integrated circuits (PMICs) typically require a minimum cold-start power of the order of 1.5 μW at $\sim$ 275 mV, while sustaining continuous operation generally requires tens of μW average power. Under the present performance levels, this corresponds to membrane areas on the order of $\sim$ 10 cm^2 for cold start and more than 200 cm^2 for continuous 30 μW operation, before accounting for any hydraulic pumping losses.

Because continuous salinity-gradient harvesting requires tangential feeding of the electrolyte solutions to mitigate concentration polarization and maintain the concentration gradient, pumping energy must also be supplied. The associated hydraulic losses would further reduce the net available power, making practical implementation even more challenging. Consequently, while upscaling is theoretically possible, the combination of low intrinsic power density, required membrane area, and additional pumping penalty currently renders porous silicon impractical for large-scale RED energy-harvesting applications.

Even if membrane performance were significantly improved, upscaling would remain a considerable fabrication challenge. Producing large, mechanically stable porous silicon membranes without cracks is difficult, particularly when relying on the lift-off technique, and maintaining uniform selectivity and resistance over large areas poses additional constraints.

In conclusion, we have demonstrated that porous silicon can indeed function as a nanoporous ion-exchange membrane for RED. Although the power generation remains limited, the insights gained here extend beyond energy harvesting. Applications that rely on selective transport, such as in iontronics [413], size-based filtration [261], molecular sensing, or controlled drug delivery in microfluidic systems [414], could directly benefit from this work. Moreover, porous silicon is biocompatible

and compatible with CMOS processes, providing a clear advantage for integrating such membranes directly into lab-on-chip or microsystem platforms.

Appendix A

Image processing

The image analysis used to determine the porosity and the average pore size was performed from scanning electron microscopy (SEM) images using *ImageJ*, an open-source image processing software widely employed for quantitative microstructural analysis.

ImageJ allows the extraction of several metrics from images containing features of various sizes, such as particle count, area, and equivalent diameter. To enable a quantitative analysis, the SEM images must first be calibrated by defining the scale, which converts pixel dimensions into real physical units based on the scale bar provided in the SEM image. Prior to analysis, the scale bar and any superimposed information were manually removed to avoid interference with the segmentation process.

The top-view SEM image of the porous layer was then converted into a binary (black-and-white) image using a thresholding operation. In this step, pixels corresponding to pores were assigned one value (e.g. white), while pixels corresponding to the silicon matrix were assigned the opposite value (black). This thresholding step is critical, as it directly determines the extracted pore size distribution and porosity. In practice, the selection of the threshold value is not trivial and cannot be fully automated. The apparent pore boundaries depend strongly on the SEM imaging conditions, including focus, contrast, brightness, working distance, and wall thickness. As a result, identifying where a pore ends and where the silicon wall begins inevitably requires human judgement.

Consequently, no universal thresholding routine could be applied to all images. Each SEM image was processed individually, and the threshold value was chosen manually to best represent the visually observed pore structure. This human intervention constitutes an intrinsic source of uncertainty in the analysis but remains unavoidable given the variability in image quality and pore morphology.

Once the binary image was obtained, the *Analyze Particles* routine in ImageJ was used. This tool identifies connected white regions in the binary image and

computes their geometrical properties, such as area and equivalent circular diameter. From this analysis, the total pore area fraction (porosity) and the average pore size were extracted.

A second user-defined parameter was required at this stage: the minimum particle size to be included in the analysis. Due to thresholding artefacts, very small isolated pixels or clusters may appear in the binary image. These features do not correspond to physical pores but rather originate from image noise, incomplete segmentation of pore walls, or local contrast fluctuations. To avoid overestimating the number of pores and underestimating their size, a lower cutoff for particle area was introduced.

Figure A.1(a) shows the original SEM image as acquired. Figure A.1(b) presents the same image after thresholding and conversion into a binary (inverted) image. Figures A.1(c) and (d) show the results of the particle analysis for two different minimum particle area thresholds.

The quantitative results are summarized in Table A.1. When excluding only particles smaller than 3 nm^2, a total of 2367 particles are counted, yielding an average pore size of 14.7 nm and a porosity of 37.5%. In contrast, when a more restrictive exclusion threshold of 20 nm^2 is applied, only 700 particles are counted. The corresponding average pore size increases to 26.8 nm, almost a factor of two, while the porosity decreases only slightly to 36.8%. This indicates that a large number of very small, non-physical features are included when using a low exclusion threshold, strongly biasing the average pore size while having a limited effect on the total porosity.

This analysis highlights that porosity is a more robust metric than average pore size, whereas the latter is highly sensitive to image segmentation parameters and user-defined thresholds. The reported values must therefore be interpreted with these limitations in mind.

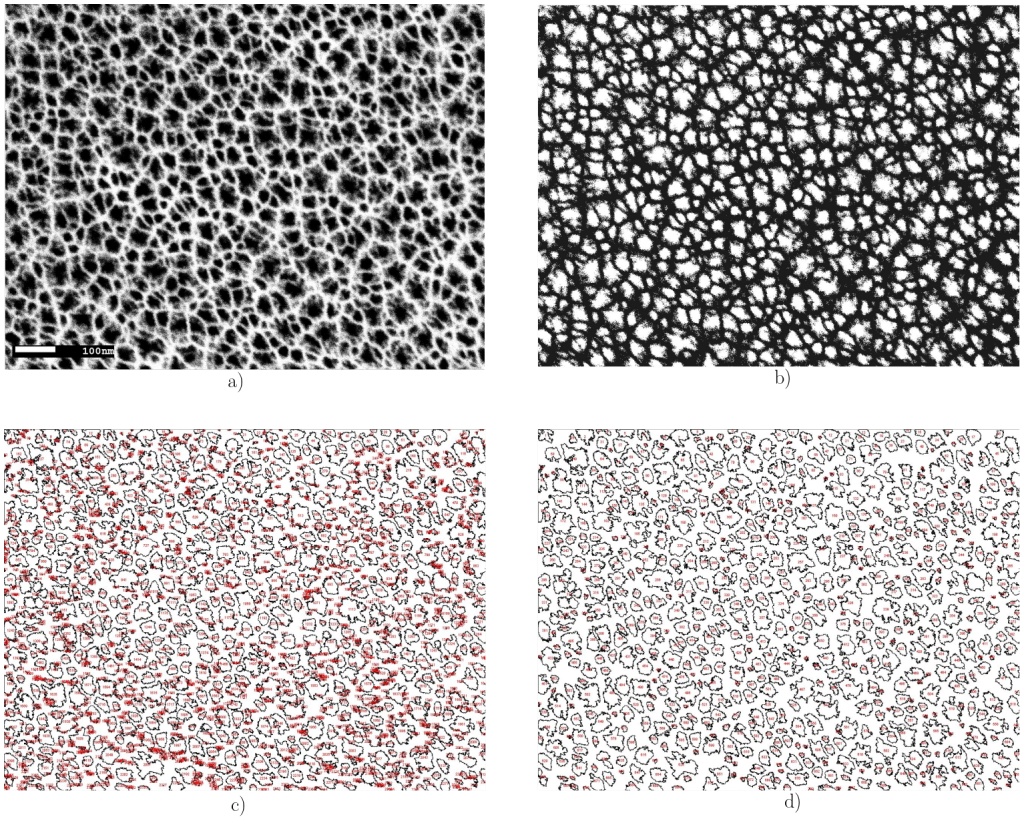


Figure A.1: Image-processing workflow used for pore size and porosity extraction from SEM images. (a) Original top-view SEM image of the porous silicon layer obtained at 100 mA/cm^2. (b) Binary image after manual thresholding and inversion, where pores are shown in white. (c,d) Results of the *Analyze Particles* routine in ImageJ for two different minimum particle-area exclusion thresholds, illustrating the strong influence of thresholding on the identified pore population.

Table A.1: Quantitative pore statistics extracted from ImageJ analysis of the SEM image shown in Figure A.1, illustrating the influence of the minimum particle-area exclusion threshold on pore count, average pore size, and porosity.

Image name	**Exclusion size [nm^2]**	**Count**	**Average area [nm^2]**	**Porosity [%]**	**Circularity [-]**	**Average pore size [nm]**
100mA-1	<20	700	562	36.8	0.255	26.8
100mA-2	<2	2367	169	37.5	0.255	14.7

Appendix B

Determination of the surface charge density of a nanoporous silicon membrane during electroosmotic pumping

This chapter presents the work carried out by master's students under our supervision during the doctoral thesis. This project was defined around a specific scientific challenge directly related to the core objectives of this dissertation.

This project, entitled *"Determination of the surface charge density of a nanoporous silicon membrane during electroosmotic pumping,"* was conducted by Laura Dubus [415]. The role of the surface charge density has been central throughout this thesis, particularly in the numerical analysis and power-generation modelling. Consequently, the possibility of experimentally determining the surface charge density of our porous silicon membranes motivated the definition of this research topic.

B.1 Abstract

The surface charge density of a porous membrane plays a crucial role in the functioning of an electroosmotic pump, as it determines the flow performance of the device. This study focuses on determining this important parameter for membranes of various materials and geometrical characteristics. The determination is achieved through a combination of experimental, analytical, and numerical methods, using the Comsol Multiphysics software.

The investigation reveals that the highest flow rate, and consequently the maximum surface charge density, is obtained with a polycarbonate membrane with a pore size of 3 μm, yielding a flow rate of 17.5 μL/min. Furthermore, the study

introduces two surface modifications applied to polycarbonate membranes. An atomic layer deposition (ALD) of alumina produces a 10% reduction in pore size, which significantly increases the electroosmotic flow rate by 30% and induces a reversal in flow direction. Additionally, depositing gold on one side of a polycarbonate membrane results in a substantial 1.85-fold increase in electroosmotic flow rate.

B.2 Electro-osmotic pumping

Electroosmosis is a phenomenon occurring when an electrolyte contained in a microchannel is subjected to an electric field. This results in the movement of the fluid, as shown in Figure B.1. Electroosmosis, first observed by Reuss in 1809, refers to the movement of a fluid through capillaries under an applied electric field. Since the development of electroosmotic pumps (EOPs) in the 1990s, a wide range of materials has been explored to enhance their performance. EOPs offer several advantages, including continuous pulse-free flow, precise control of flow rate and direction, the absence of moving parts, and compatibility with standard microfabrication techniques, making them well suited for applications such as HPLC, lab-on-chip systems, microelectronic cooling, and drug delivery.

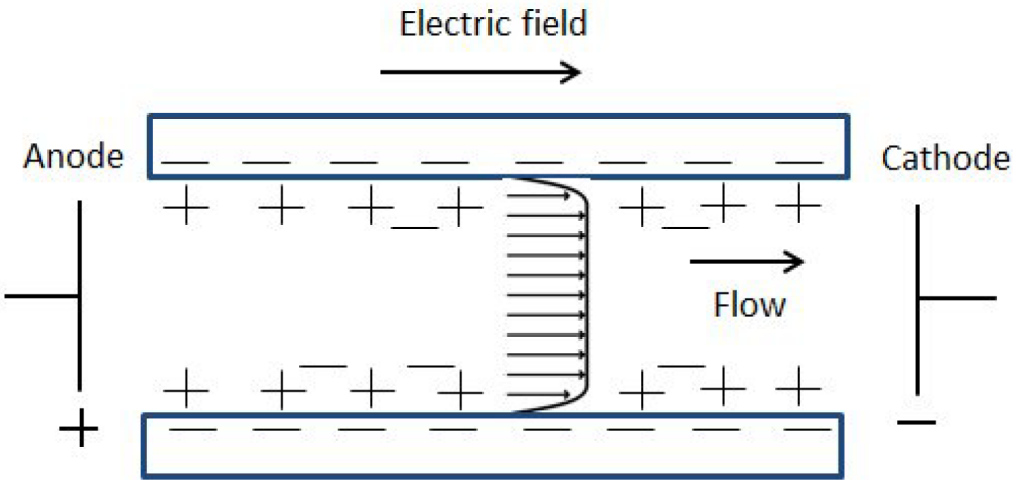


Figure B.1: Electroosmotic flow in a capillary tube. The application of an electric field along the tube induces the motion of ions in the electrical double layer, which in turn drags the surrounding fluid through viscous forces.

At the interface between a solid surface and an electrolyte, surface charges appear and an electrical double layer develops. When an electric field is applied, ions in the EDL migrate toward the electrodes and are accelerated by the field. Through

viscous interactions between these ions and the surrounding liquid molecules, the fluid is set into motion. Thus, the ionic charges located near the solid surface are responsible for driving the flow.

The profile of the electroosmotic flow in a straight microchannel is shown in the upper part of Figure B.2. In the case of a large capillary, meaning that the capillary radius is significantly greater than the Debye length, the electroosmotic flow can be approximated as uniform across most of the channel cross-section. Under these conditions, the flow profile becomes essentially plug-like. This simplification relies on two main assumptions. First, the velocity at the solid–liquid interface is zero, as imposed by the no-slip boundary condition. Second, viscous (hydrodynamic) resistance within the fluid is considered negligible. With these assumptions, the electroosmotic velocity can be expressed as:

$$u_{\mathrm{EOF}}(y) = -\frac{\varepsilon E_x}{\mu}\,\zeta, \tag{B.1}$$

where ε denotes the dielectric permittivity of the electrolyte, E_x is the externally applied electric field in the axial direction, μ is the dynamic viscosity of the fluid and ζ the zeta-potential.

In nanochannels, the electroosmotic velocity profile differs markedly from that in larger capillaries. When the channel radius becomes comparable to or smaller than the Debye length, the electrical double layers originating from opposite walls overlap. In this regime, essentially all ions within the channel, except those immobilized in the Stern layer, contribute to charge transport and fluid motion (i.e ion-selective behavior). When the channel size falls below approximately 100 nm, the electroosmotic flow velocity becomes size-dependent for a given electrolyte concentration as seen in Figure B.2. In this regime, the EOF velocity decreases as the channel diameter is reduced. The total fluid velocity in a nanochannel is given bys:

$$u(y) = -\frac{P}{2\mu}\Big(y^2 - 2hy\Big) + \frac{E_x\varepsilon}{\mu}\Big(\Psi(y) - \zeta\Big). \tag{B.2}$$

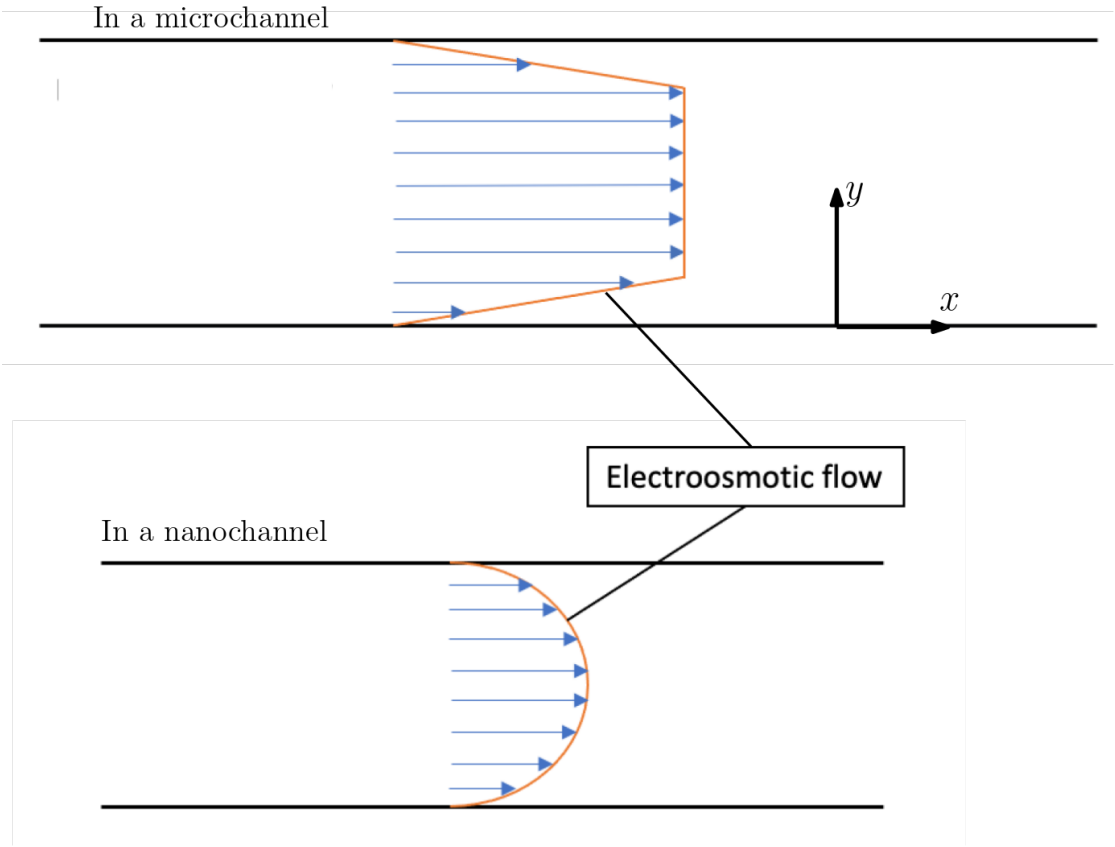


Figure B.2: Flow profile in a straight microchannel (top) and a straight nanochannel (bottom).

B.3 Existing PSi electroosmotic pumps

Various electroosmotic pumps (EOPs) based on porous silicon have been reported in the literature, spanning a wide range of geometries and operating conditions. To enable meaningful comparison between pumps operating at different voltages and possessing different active surface areas, researchers commonly normalize the flow rate by both the applied voltage and the membrane area in contact with the electrolyte. This normalized flow rate, expressed in μL/(min cm^{2}V), serves as a standardized performance metric. The values reported for several porous–silicon EOPs are summarized in Table B.1.

Inspection of the table reveals two distinct classes of porous–silicon EOPs: those employing ultrathin membranes and those based on substantially thicker porous structures. In Refs. [28] and [29], the membrane thicknesses are reported to be 15 nm and 75 nm, respectively, roughly four orders of magnitude thinner than the

membranes used in the first two EOPs listed in the table. Since electroosmotic flow is inversely proportional to membrane thickness, a reduction in thickness by a factor of 1000 has a dramatic impact on pump performance.

It should be noted, however, that the normalized maximum flow rate does not account for the electric field strength within the membrane nor for its thickness. As a consequence, a one-to-one comparison between devices with vastly different membrane geometries is not straightforward.

Table B.1: Performance of electroosmotic pumps based on porous silicon membranes, reported in the literature. The values are normalized by the applied voltage and the membrane area in contact with the electrolyte.

Article	[416]	[417]	[418]	[419]
Pore size [μm]	3	3.6	19.5×10^{-3}	2.3×10^{-3}
Effective area [cm^2]	1	0.07	36×10^{-4}	1.89×10^{-5}
Pore density [%]	45	37.8	5.7	16.7
Thickness [μm]	350	500	0.015	0.075
Applied voltage [V]	25	60	20	1
Distance electrodes [mm]	2	3	/	4
Electrolyte	10^{-3} M NaCl	DI water	0.1 M KCl	0.4 M KCl
Maximum normalized flow rate [μL/(min cm^2 V)]	128	19.8	138.9	10.72×10^3

B.4 Objectives of this master's thesis

The literature contains several studies demonstrating the feasibility of using porous silicon as a membrane material in electroosmotic pumps (EOPs). Moreover, Eqs. (B.1) and (B.2) enable the calculation of EOF in microchannels and nanochannels while accounting for various parameters, including the zeta potential. Consequently, by measuring the flow rate generated during electroosmotic pumping, it becomes possible to infer the zeta potential of a porous silicon membrane.

From the zeta potential, it is possible to infer the surface charge density using model such as the one in (4.26). If one assumes the Boltzmann distribution for c_{H^+},

$$a_{H^+} = c_{\mathrm{H}^+,0} \exp\left(\frac{F\,\zeta}{RT}\right), \tag{B.3}$$

with $c_{\mathrm{H}^+,0}$ the concentration of H^+ in the bulk, knowing the zeta potential allows to compute the surface charge density.

The ultimate goal of this work is therefore to analytically determine the surface charge density of a porous silicon membrane. This is achieved by experimentally extracting the zeta potential from electroosmotic flow measurements and subsequently converting it into a surface charge density through established analytical relations. By combining experimental observations with analytical modeling, a comprehensive understanding of the surface properties and electrostatic behavior of porous silicon membranes in electroosmotic pumps can be obtained.

B.5 Materials and methods

B.5.1 Materials

Various polymer membranes are used in this work. They differ in geometry, including pore size and thickness, as well as in material composition. The membranes employed are made of polycarbonate (PC), polyethylene (PE), or polyimide (PI). All polymer track-etched membranes used in this work were purchased from it4ip, a company specialized in ion-track membrane technology and a spin-off from UCLouvain. These membranes are produced using the track-etching technique. Aluminium oxide (AAO) membrane filters (13 mm diameter) were purchased from Sterlitech. The last type of membrane used in this work is the self-supported porous silicon (PSi) membrane, fabricated using the process detailed in Section 7.3.1. Their pore size and porosity were analysed with SEM images and image processing using imageJ. For the solution, no electrolyte is used, just dionized water at pH around 6.

B.5.2 Methods

B.5.2.1 Characterisation set-up

The experimental setup of the electroosmotic pump used in this work is shown in Fig. 3.6. To ensure that no hydrostatic pressure difference influences the measurements, the setup is positioned horizontally so that only electroosmotic flow is observed. The flow is monitored by tracking the displacement of the water meniscus in two graduated pipettes. Each pipette is connected to a reservoir filled with electrolyte, and the two reservoirs are separated by a porous membrane. The effective contact area between the membrane and the electrolyte is 29.7 mm^2.

An electric potential is applied across the system using two platinum mesh electrodes (area 1 cm^2), positioned symmetrically on each side of the membrane at a separation distance of 2.4 cm. The voltage is supplied by a Keithley 6418 source meter. Electrolyte is introduced into the device through two tubes connected to the reservoirs and controlled using a pressure-driven flow system (LineUp Flow

EZ^{TM}). To ensure leak-tight operation, the electrodes and pipettes are inserted through perforated sealing plugs.

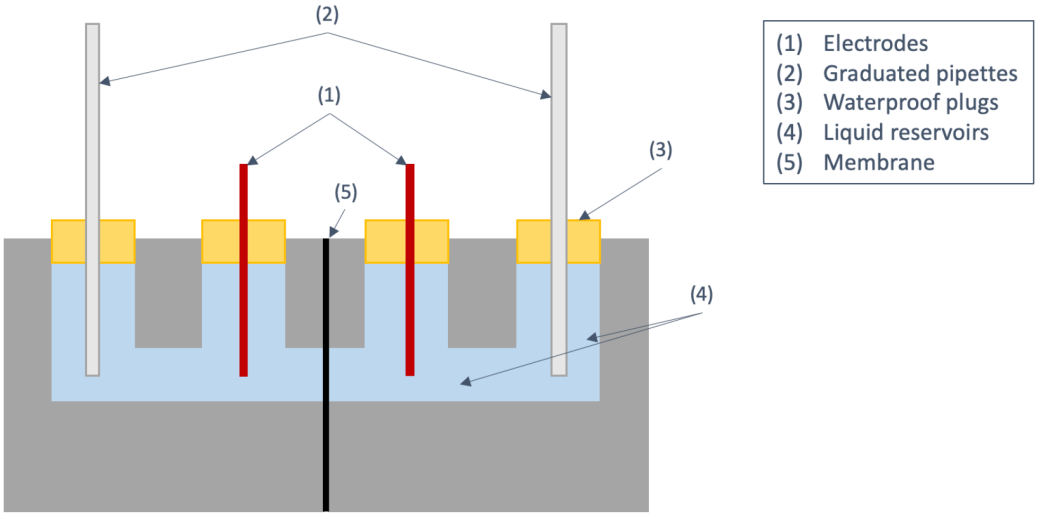


Figure B.3: Schematic of the set-up used for electroomostic pumping measurement. The applied voltage at the electrodes (1) establishes an electric field within the electrolyte reservoirs (4). Owing to the surface-charge properties of the porous membrane (5), this electric field induces electroosmotic flow through the membrane. The resulting fluid motion is detected by observing the change in liquid level within the graduated pipettes (2).

B.5.2.2 Surface modification

Atomic layer deposition (ALD) enables the formation of ultrathin film, typically a few nanometers thick, with excellent conformality and atomic-scale control. In this work, ALD is used to deposit alumina (Al_2O_3) throughout the porous membrane, coating the internal pore walls uniformly. The deposition is carried out at 100°C using a plasma-assisted process. As illustrated in Fig. B.4, one ALD cycle consists of two self-limiting half-reactions.

In the first half-cycle, a precursor (trimethylaluminum, TMA, for alumina deposition) is introduced into the reactor and chemisorbs onto the reactive surface sites until saturation. Excess precursor molecules are then removed by purging with an inert carrier gas. During the second half-cycle, a plasma pulse is applied, reactivating the surface and enabling the conversion of the adsorbed precursor into Al_2O_3. A second purge completes the cycle. By repeating these two steps, the film thickness increases in a highly controlled manner, with the final thickness

determined by the total number of ALD cycles.

The primary objective of this surface modification is to reduce the effective pore diameter of the membrane. In addition, coating the pore walls with a different material alters the zeta potential of the electrical double layer. This provides an opportunity to study how the surface charge density, and thus electrokinetic performance, changes upon modification. Two depositions were performed: one with 50 ALD cycles and another with 200 cycles of Al_2O_3. Alumina was selected because it is compatible with plasma-enhanced ALD and exhibits the highest zeta potential among the oxides available in the laboratory. All depositions were carried out using a Cambridge Fiji ALD system.

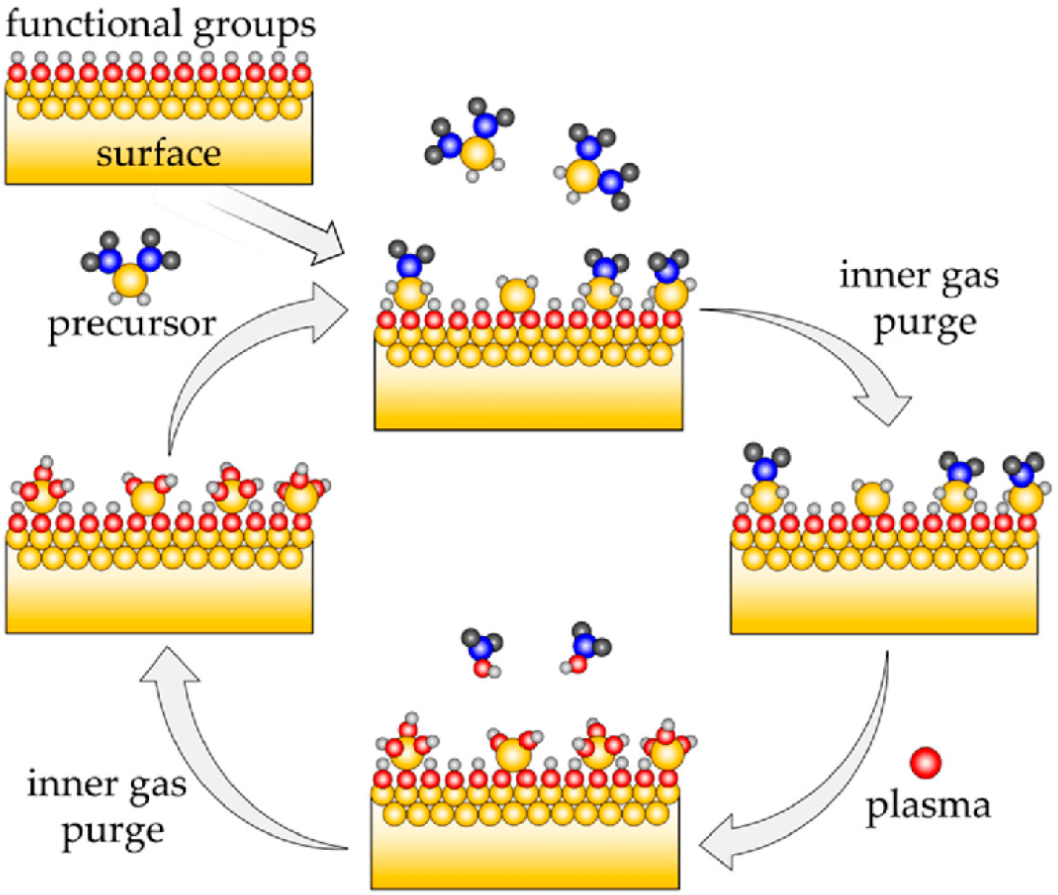


Figure B.4: Schematic representation of the plasma-enhanced atomic layer deposition process. Figure taken from [420].

The second surface modification performed in this work is a metallization of

one side of some track etched membranes. For this work, a 5 nm titanium deposit is first deposited as an adhesive layer. A second 50 nm gold deposit is then applied. This metallization is performed by evaporation of the metal by a heating element in a vacuum chamber. The objective of this surface modification is to use the metallized membrane as one of the two electrodes in the electroosmotic pump to enhance the EOF. The distance between the electrodes is thus halved and a higher electric field is normally induced with the same amount of applied tension. The deposition of the gold on the membranes is performed using the E-Gun Vacotec.

B.5.3 Analytical model determining pump flow performance

To evaluate the efficiency of an electroosmotic pump, the volume flow rate must be determined. This quantity can be obtained by integrating the electroosmotic velocity profile over the cross-section of the channel. For a single cylindrical microchannel, the velocity distribution is given by [421]:

$$u(r) = -\frac{1}{4\mu}\left(a^2 - r^2\right)\frac{dP}{dx} - \frac{\varepsilon E}{\mu}\Big(\zeta - \Psi(r)\Big), \tag{B.4}$$

where $\frac{dP}{dx}$ is the pressure gradient, a is the channel radius, r is the radial coordinate, $\Psi(r)$ is the electrical potential, and E is the applied electric field.

Integrating this velocity profile over the circular cross-section yields the total volume flow rate:

$$Q = \int_0^{2\pi}\int_0^a u(r)\, r\, dr\, d\phi = -\frac{\pi a^4}{8\mu}\frac{dP}{dx} - \frac{\pi a^2 \varepsilon \zeta E}{\mu}\, f, \tag{B.5}$$

where the function f accounts for the influence of electrical double-layer overlap and varies between zero and one. The function f, which accounts for the influence of electrical double-layer effects on the electroosmotic flow rate, can be expressed as:

$$f = \int_0^a \left(1 - \frac{\Psi(r)}{\zeta}\right)\frac{2r}{a^2}\, dr = 1 - \frac{2I_1(a)}{a\, I_0(a)}, \tag{B.6}$$

where I_0 and I_1 are the modified Bessel functions of the first kind of order 0 and 1, respectively. If the function tends to unity, that means that the velocity across the channel tends to be uniform and that the pore size is relatively larger than the Debye length. In this expression, I_0 and I_1 denote the modified Bessel functions of the first kind, of order zero and one, respectively.

For an array of cylindrical microchannels, both the porosity and the tortuosity of the membrane must be taken into account when determining the total volume

flow rate. Shuhuai Yao *et al.* derived the following expression for the volumetric flow rate Q (in m^3/s):

$$Q = \frac{\psi}{\tau}\left[-\frac{a^2 A}{8\mu L}\,\Delta P - \frac{\varepsilon\zeta E A}{\mu}\,f\right]. \tag{B.7}$$

In summary, the parameters influencing the electroosmotic flow rate in a porous medium include the porosity ψ, the tortuosity τ, the geometrical characteristics of the microchannels (cross-sectional area A, radius a, and length L), the applied pressure difference ΔP, the zeta potential ζ, the axial electric field E, and the viscosity and permittivity of the fluid, μ and ε, respectively.

Tortuosity quantifies the degree to which the channel path deviates from a straight line. It is defined as:

$$\tau = \left(\frac{L_\mathrm{e}}{L}\right)^2, \tag{B.8}$$

where L_e is the effective flow-path length and L is the physical length of the membrane. A tortuosity of one corresponds to a straight channel, allowing less hindered flow.

The porosity is defined as the ratio of the pore volume V_p to the total volume V:

$$\psi = \frac{V_p}{V}. \tag{B.9}$$

A higher porosity increases the available flow area and enhances electroosmotic transport, as a larger charged surface contributes to ion-driven flow. Thus, electroosmotic pumps perform more efficiently when fabricated from highly porous substrates.

From Equation (B.7), the maximum flow rate Q_max and the maximum pressure ΔP_max can be derived as:

$$Q_\mathrm{max} = -\frac{\psi}{\tau}\frac{\varepsilon\zeta A E}{\mu}\,f, \tag{B.10}$$

$$\Delta P_\mathrm{max} = -\frac{8\varepsilon\zeta V_\mathrm{app}}{a^2}\,f, \tag{B.11}$$

where V_app is the applied voltage.

Additionally to the analytical model, a numerical model was also implemented in COMSOL. By introducing a volume electric body force on the ions and imposing a no-slip boundary condition at the pore walls within the Nernst–Planck–Poisson framework, the electroosmotic flow rate inside a nanopore could be simulated and analysed under various operating conditions.

B.6 Experimental results

B.6.1 Variation of material and pore size

Figure B.5 presents the experimentally measured flow rates generated by the electroosmotic pump for the different membranes. The highest flow rate, -17 μL/min, is obtained with the polycarbonate membrane featuring a pore diameter of 3 μm. For a fixed pore size of 0.4 μm, the polyimide membrane outperforms both polyethylene and polycarbonate in terms of flow rate.

Another noteworthy observation is the flow rate of 9 μL/min measured for the alumina membrane with a pore size of 200 nm. In addition to being relatively high, the flow direction is opposite to that observed for the polymer membranes. For the same nominal pore diameter, the polycarbonate membrane produces a significantly smaller flow rate in absolute value, namely -3 μL/min.

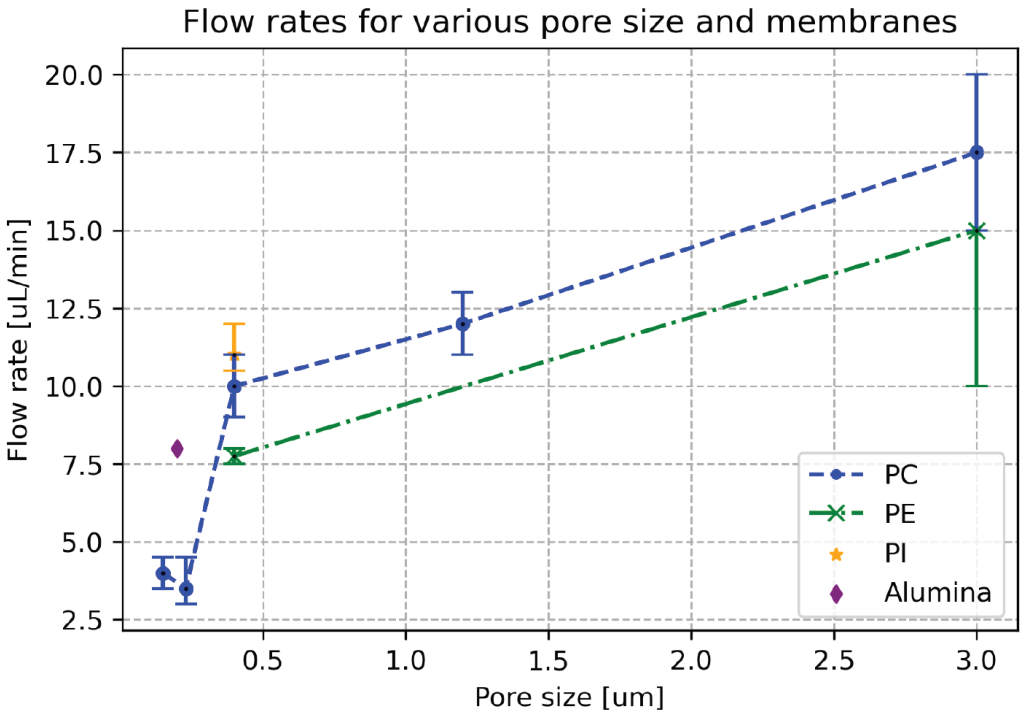


Figure B.5: Flow rate in absolute value obtained for 4 various materials (PC, PE, PI and Al_2O_3) and varying pore size (from 0.2 μm to 3 μm). Vertical bars represents the confidence interval.

The final material investigated in this study was porous silicon (PSi). The tested membrane had a pore diameter of 25 nm and a thickness of 100 µm. No

measurable electroosmotic flow was observed, even after 24 hours of continuous pumping. This outcome indicates that the combination of very small pore diameter and relatively large membrane thickness results in a hydraulic resistance too high to permit detectable electroosmotic transport. It also suggests that, under the applied experimental conditions, the zeta potential or the effective pore geometry of the PSi membrane is insufficient to generate an appreciable flow.

Although very low ionic concentrations such as deionized (DI) water are, in principle, expected to yield high zeta potentials due to reduced electrostatic screening, the extremely low conductivity of DI water severely limits the electric field that can be sustained across the membrane. As a result, even a nominally large zeta potential cannot produce a measurable electroosmotic body force. The corresponding flow rate is therefore likely far below the detection threshold of the experimental setup, manifesting as an absence of observable pumping.

B.6.2 Surface modification

Two polycarbonate membranes with pore sizes of 152 nm were modified with 50 and 200 ALD cycles of Al_2O_3. As seen in Figure B.6, the surface treatment reverses the electroosmotic flow direction, leading to positive flow rates for both membranes, in contrast to the untreated samples. The membrane coated with 200 ALD cycles shows the highest absolute flow rate, reaching 13.5 μL/min, although with a notably large variance. The membrane with 50 ALD cycles exhibits a transient regime before stabilizing after approximately 35 minutes of pumping.

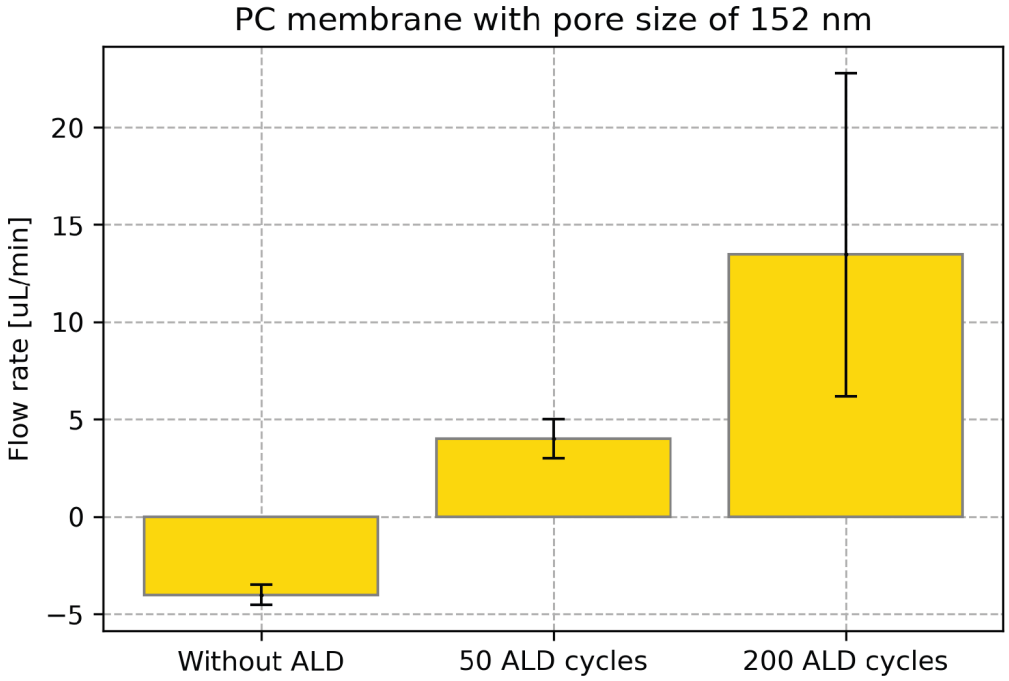


Figure B.6: Comparison of experimental flow rates obtained with the same initial membrane in 3 various conditions: without surface modification, with 50 ALD cycles of Al2O3 and with an 200 ALD cycles of the same material. Flow rates are determined after 40 minutes of pumping. Vertical bars represent the confidence interval.

B.6.3 Determination of zeta potential and surface charge density

B.6.3.1 Influence of Materials

In Table B.2, experimental results obtained from membranes with identical geometric characteristics show that electroosmotic performance depends primarily on the material's zeta potential. Among the polymers tested, polyimide yields the highest flow rate, followed by polycarbonate and polyethylene, establishing the trend $\zeta_{\mathrm{PI}} > \zeta_{\mathrm{PC}} > \zeta_{\mathrm{PE}}$ under identical operating conditions, consistent with literature [422].

A comparison between a polycarbonate membrane (233 nm pores) and an alumina membrane (200 nm pores) further highlights the strong influence of surface chemistry: the alumina membrane exhibits a flow rate more than 150% higher despite its slightly smaller pores and nearly twice the thickness (Figure B.5). In addition, the opposite flow direction indicates that the alumina zeta potential

has a larger magnitude and opposite sign compared to the polymers. The ratio of flow enhancement (2.57 for alumina vs. 1.10 for PI over PC) suggests that $|\zeta_{Al_2O_3}| > |\zeta_{PI}|$.

Analytical determination of zeta potentials and corresponding surface charge densities using the cylindrical-channel model (Eq. (B.7)) and Eq. (4.20) confirms the ranking

$$|\zeta_{Al_2O_3}| > |\zeta_{PI}| > |\zeta_{PC}| > |\zeta_{PE}|,$$

which applies equally to σ since it is proportional to ζ. These results identify alumina as the most efficient material tested for electroosmotic pump applications.

Table B.2: Zeta potentials and surface charge densities of membranes made from different materials but having comparable geometrical characteristics.

Material	**Pore size [nm]**	**Zeta potential [mV]**	**Surface charge density [C/m^2]**
PC	400	-18.21	-1.26×10^{-4}
PE	400	-14.12	-9.74×10^{-5}
PI	400	-20.03	-1.38×10^{-4}
PC	233	-12.08	-8.34×10^{-5}
Al_2O_3	200	16.73	1.15×10^{-4}

B.6.3.2 Influence of pore size

The pore size of the membrane has a significant influence on the electroosmotic velocity. As shown in Figure B.7, the experimental flow rate increases by approximately 150% when the pore diameter rises from 150 to 400 nm, but only by about 20% when increasing from 400 to 1200 nm. This behaviour agrees with numerical predictions, which indicate that the electroosmotic velocity does not increase linearly with pore size: it grows rapidly for small diameters and then approaches a plateau. Beyond this limit, further increases in flow can only be achieved by increasing the number of pores rather than their size.

Using Eq. (B.7), the zeta potentials were analytically determined from the experimental flow rates. As illustrated in Figure B.7, ζ increases sharply for small pore sizes and levels off for larger pores, mirroring the behaviour of the flow rate. Since surface charge density is proportional to the zeta potential, its magnitude decreases with increasing pore size. This has been observed in [423], where the pore size of mesoporous silica nanoparticle showed higher zeta potential due to EDL overlap. In our case, the Debye length is around 400 nm for DI water at pH 6, thus we could expect similar effect as [423].

The 233 nm PC membrane constitutes an exception. Its extracted zeta potential (-12 mV) is higher than those obtained for the 150 nm and 400 nm membranes

(−29 mV and −18 mV, respectively). Looking as the general trend in Figure B.7, all the membranes did follow the same except the 233 nm. For this reason, the flow rate associated with the 233 nm membrane is considered an outlier and is excluded from the discussion of factors influencing surface charge density.

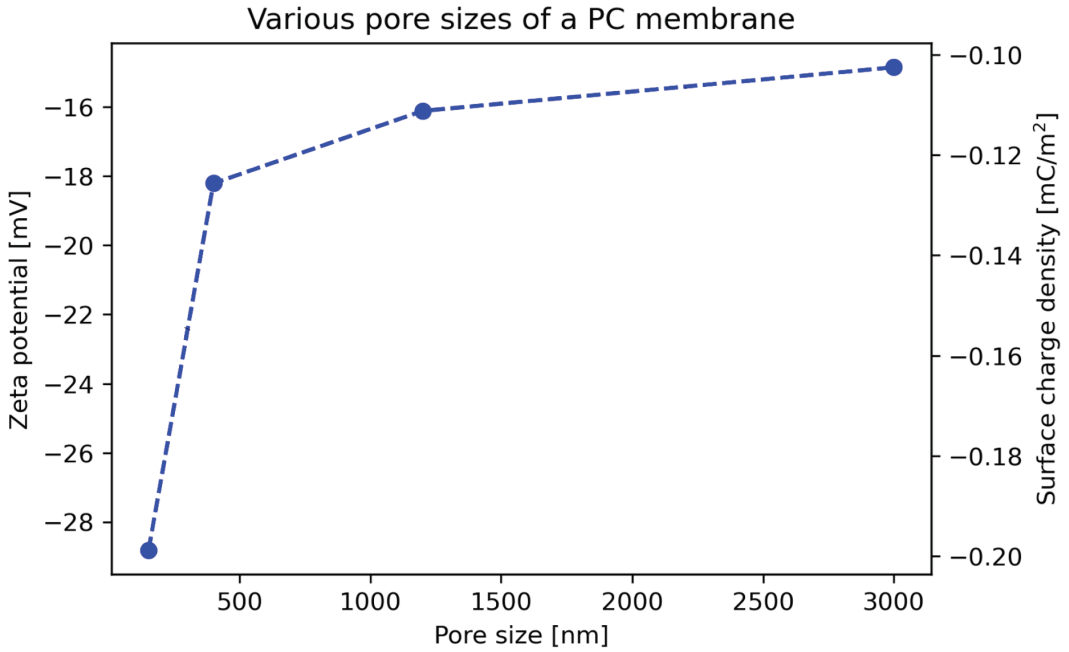


Figure B.7: Zeta potentials and corresponding surface charge density for different pore sizes of a polycarbonate membrane. The curvature of the pore influencing both parameters is shown.

B.6.3.3 Impact of ALD

Experimental results show that membranes subjected to alumina ALD exhibit a reversal of electroosmotic flow direction. This behaviour arises from the opposite sign of the alumina zeta potential compared to that of polymers: while polycarbonate carries a negative ζ potential, alumina surfaces are positively charged. Analytical determination of the zeta potentials from the measured flow rates (Table B.3) confirms this sign inversion and the corresponding change in surface charge density.

The PC membrane coated with 50 ALD cycles of alumina displays a higher ζ potential than the unmodified membrane, despite an 8.5% reduction in pore size, which would normally decrease ζ considering the same surface. This indicates that Al_2O_3 deposition substantially improves the electroosmotic performance of

polycarbonate. Literature observations support this enhancement: Zijing *et al.* [424] report that ALD of alumina on SiO_2 increases the zeta potential from approximately -10 mV to $+70$ mV after 100 cycles. These results confirm that alumina ALD markedly increases surface charge and enables flow reversal in polymer membranes.

Table B.3: Experimental flow rates, zeta potentials, and surface charge densities for polycarbonate (PC) membranes with and without alumina coatings (ALD cycles).

Membrane	**Flow rate** [μ**L/min**]	**Zeta potential** [**mV**]	**Surface charge density** [**mC/m^2**]
PC 152 nm	-4	-28.82	-0.20
PC 152 nm + 50 ALD cycles	4	34.6	0.24
PC 152 nm + 200 ALD cycles	13	121.6	0.84

B.7 Conclusion

In this master's thesis, the primary objective was to analytically determine the surface charge density of a nanoporous silicon membrane based on experimental measurements of electroosmotic flow. However, despite the dedicated setup and measurement efforts, no detectable flow could be observed for this membrane.

To better understand the parameters influencing surface charge density, the study investigated a variety of membrane materials through both experimental flow-rate measurements and numerical simulations performed using COMSOL Multiphysics. Consistent with trends reported in the literature, it was confirmed that surface charge density increases as pore size decreases, an effect attributed to curvature- induced modifications of the electrical double layer. A comparative analysis of materials further allowed ranking their surface charge densities through their zeta potentials, yielding the following order (in decreasing magnitude): $|\zeta_{Al_2O_3}| > |\zeta_{PI}| > |\zeta_{PC}| > |\zeta_{PE}|$. Additionally, experiments revealed that electroosmotic flow exhibits a time-dependent evolution: an initial transient regime is consistently observed before reaching a steady state.

Two surface modifications were also applied to polycarbonate membranes. First, one side of the membrane was metallized to reduce the electrode separation and thereby enhance the local electric field. This modification indeed increased the flow rate, although not as strongly as theoretically expected, with improvements being more pronounced at larger pore sizes. Second, atomic layer deposition (ALD) of alumina was used to decrease the pore size. This treatment resulted in both a reversal of the flow direction and an overall increase in flow rate.

Appendix C

Paper-based stacked reverse electrodialysis cells for energy generation from salinity gradient

This chapter presents the work carried out by master's students under our supervision during the doctoral thesis. This project was defined around a specific scientific challenge directly related to the core objectives of this dissertation.

This project, *"Paper-based stacked reverse electrodialysis cells for energy generation from salinity gradients,"* was carried out by Ramy Moumneh [425]. Its motivation stemmed from the intrinsic efficiency limitations of RED technology. Because salinity-gradient systems possess low energy density, refuelling of the feed solutions is continuously required, which typically involves external pumping and reduces the overall energy efficiency. Using paper as a capillary medium to passively transport electrolyte toward the membranes was therefore investigated as a potential solution.

C.1 Abstract

Microfluidic paper-based electrochemical devices (μPEDs) have recently gained attention for their ability to leverage the natural capillarity of paper, thereby eliminating the need for external pumping while enabling low-cost, point-of-care electrochemical detection. A major limitation, however, is that the electrical components of μPEDs still require external power sources, which undermines the portability advantages inherent to paper-based analytical systems. One promising solution is the integration of an onboard power source, enabling the development of fully self-powered sensors.

In this work, a paper-based stack of reverse electrodialysis (RED) cells is

investigated as a potential integrated power supply for μPEDs. A low-cost and easily implementable fabrication process is proposed, involving the creation of microfluidic channels on paper using an automated plotter equipped with a permanent marker, followed by the assembly of multilayer structures using double-sided adhesive film.

Because reverse electrodialysis requires a continuous supply of high- and low-salinity feed solutions, dedicated microfluidic channel designs were developed. An analytical microfluidic model was employed to characterize the parameters governing flow velocity within these channels and to optimize RED performance. The model accurately predicted flow behavior once the microfluidic properties of paper were appropriately calibrated.

Both single-membrane and stacked paper-based RED cells were fabricated and evaluated. Single-membrane cells produced a power density of approximately 4 μW/cm^2, with performance increasing to 8 μW/cm^2 using optimized channel geometries. A stacked RED configuration achieved a peak power density of 35.5 μW/cm^2, although its performance degraded rapidly. Importantly, the operational duration of power generation was tunable through the channel design, and generation times exceeding one hour were demonstrated.

C.2 Properties of paper

Paper is an abundant, low-cost, cellulose-based material whose hydrophilicity, porosity, and biocompatibility make it highly suitable for microfluidic applications. Its porous network of interconnected cellulose fibers provides a high surface-to-volume ratio, enabling efficient capillary-driven flow without external pumps and facilitating surface functionalization for biological assays. These characteristics confer several advantages for paper-based analytical devices (PADs), including simple and inexpensive fabrication, portability, biodegradability, ease of disposal by incineration, mechanical flexibility, and strong optical contrast for colorimetric detection.

Paper is produced from aqueous suspensions of cellulose fibers that are formed, pressed, and dried to create a fibrous, porous matrix. The resulting properties, such as pore size, porosity, density, and wicking behavior, depend strongly on the manufacturing conditions and on subsequent treatments such as refining, surface sizing, coating, and calendering. Consequently, a wide variety of paper types is available for PADs, including chromatography paper (excellent wicking), filter paper (uniform thickness and good reagent retention), bioactive paper (incorporating biomolecules), glossy paper (easily surface-modified), and nitrocellulose (high nonspecific biomolecule adsorption but intrinsically hydrophobic unless treated with surfactants).

However, the papermaking process inherently leads to local inhomogeneities and

anisotropy due to fiber flocculation and non-uniform aggregation. These structural variations, which can be qualitatively observed by holding the paper to the light, make accurate modeling of paper microstructure and properties challenging and can reduce the robustness and reproducibility of paper-based sensors.

C.3 Fabrication of paper based microfluidic

The fabrication of two-dimensional paper-based microfluidic devices is low-cost, rapid, and far simpler than conventional microfabrication on glass, silicon, or PDMS. The basic principle is to define hydrophilic and hydrophobic regions on a paper substrate so as to confine and guide liquid flow, where the patterning process sets the channel width and length, and the paper thickness defines the channel height. Existing patterning methods can be broadly divided into two-step and one-step approaches. Two-step methods first render the entire paper hydrophobic (e.g. by photolithography, plasma processing, or hydrophobic coatings) and then locally remove the hydrophobic layer to create hydrophilic channels. One-step methods, in contrast, locally deposit or define hydrophobic barriers directly, for example by cutting, screen-printing wax or polymers, inkjet printing hydrophobic inks, or drawing channel boundaries using automated plotters or permanent markers. These one-step methods are generally simpler, cheaper, and well suited for rapid prototyping, although they may offer lower resolution or pattern fidelity than cleanroom-based approaches.

Three-dimensional paper-based microfluidic devices are obtained by stacking or folding patterned two-dimensional layers. Common assembly techniques include bonding layers with double-sided adhesive tape (often with cut-out through-holes for vertical flow), using spray adhesives, folding a single patterned sheet in an origami configuration, or binding layers mechanically (bookbinding) with staples or threads. All these methods are inexpensive and do not require sophisticated equipment, enabling complex 3D fluidic architectures at very low cost.

The integration of electrical components on paper is achieved by printing conductive structures using functional inks. Screen-printing methods squeeze metallic, carbon-based, or conductive polymer inks through patterned screens, which is advantageous for low-cost mass production. Direct printing methods (digital or maskless), such as aerosol printing, inkjet printing, extrusion printing, and automated-plotter "pencil-on-paper" techniques, allow flexible, customized electrode geometries well suited for prototyping electrochemical paper-based devices. Most printed electrodes require a subsequent sintering or annealing step (thermal, electrical, photonic, or plasma) to remove solvents and promote particle coalescence, thereby ensuring sufficient electrical conductivity on temperature-sensitive substrates such as paper.

C.4 Paper based microfluidic

In paper-based microfluidics, liquid motion is governed primarily by capillary forces rather than external pumping. Surface tension γ and the equilibrium contact angle θ at the liquid–solid–air interface determine the Laplace pressure at curved menisci, which drives spontaneous imbibition in pores and fibers. When the contact angle is below 90° (wetting condition), the capillary pressure is negative and the liquid is pulled into the paper network. The dynamics of this wicking can, in simple geometries, be described by the Lucas–Washburn law, which predicts that the penetration length scales as $l \propto \sqrt{t}$, and by Jurin's law, which gives the maximum rise height in a vertical capillary from a balance between capillary and gravitational forces.

Dimensionless numbers quantify which physical effects dominate. In paper microchannels and pores, the Reynolds number is typically very low, indicating laminar, viscosity-dominated flow; the Bond number is usually $\ll 1$, showing that surface tension dominates over gravity at the pore scale; and the Capillary number compares viscous stresses to interfacial forces. At the material scale, paper acts as a porous medium: its porosity and pore-size distribution control the available void volume and hydraulic resistance, and thus set the overall wicking speed and flow capacity of paper-based microfluidic devices.

C.4.0.1 Achieving quasi stationnary flow in paper channel

In paper-based microfluidics, a constant (stationary) flow rate is usually not obtained in straight channels, since the Lucas–Washburn dynamics predict that the velocity decreases as the penetration length increases. Mendez *et al.* showed that a quasi-stationary flow can be achieved by connecting a narrow rectangular channel to a fan-shaped porous region. The fan consists of a rectangular segment followed by a circular sector of opening angle ω as shown in Figure C.1. Once the liquid front reaches the circular sector, the available dry porous volume increases continuously as the front advances radially. This progressive increase in wetted area compensates for the rise in viscous resistance that would normally slow down the flow.

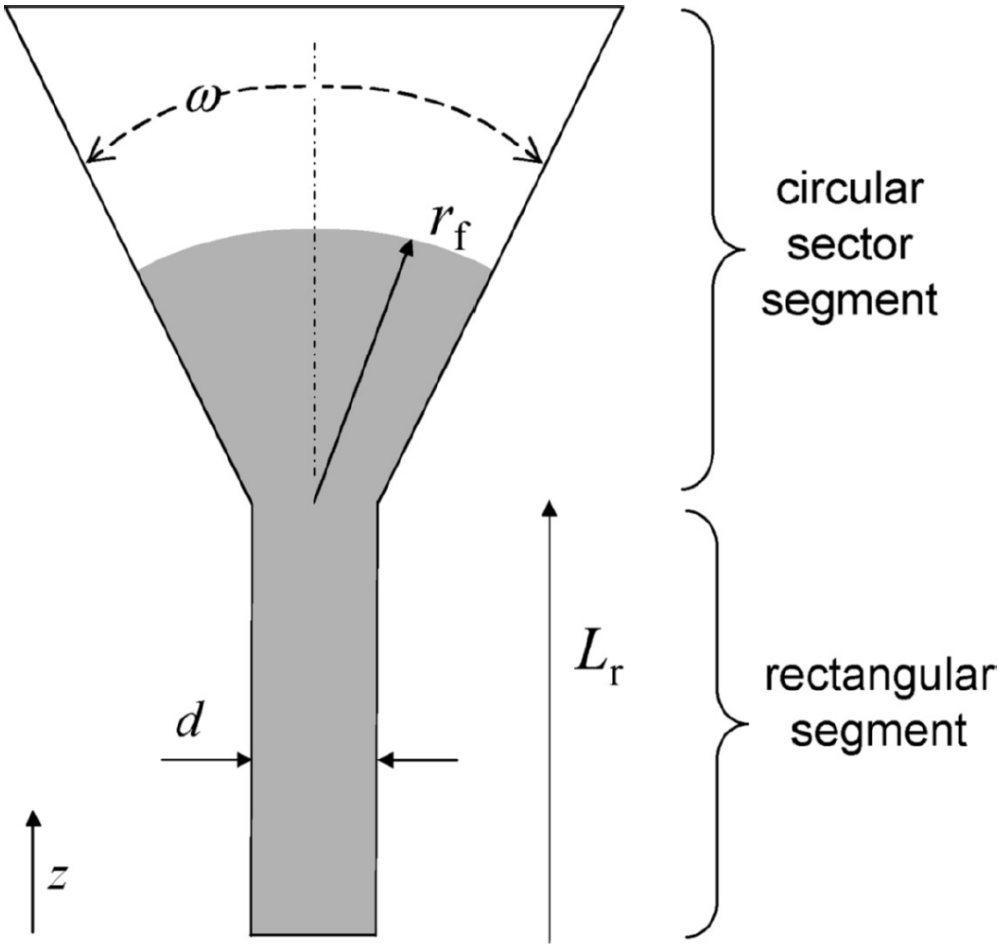


Figure C.1: Schematic of fan, A rectangular segment is appended to a circular sector segment of central angle ω.

Under appropriate geometric conditions,

$$\frac{L_r\,\omega}{d} \gg \ln\left(\frac{2r_f(t)}{d}\right),$$

with L_r the length and d the width of the rectangular section and $r_f(t)$ the radial front position in the fan, the flow rate in the rectangular channel becomes approximately constant. In this regime, the average velocity in the rectangular section is given by the Mendez model,

$$V \simeq \frac{\kappa_i P_c}{\mu L_r}, \qquad P_c = \frac{2\gamma\cos\theta}{R_c},$$

which has the same form as Darcy's law but with the penetration length replaced by the fixed rectangular length L_r. Thus, by appending a suitably designed fan-shaped region to a straight paper channel, one can sustain a nearly stationary capillary-driven flow in the region of interest.

C.5 Paper-based RED

Paper-based reverse electrodialysis (RED) exploits the intrinsic capillary action of paper to deliver high- and low-salinity solutions to an ion-exchange membrane without external pumping, overcoming one of the main efficiency limitations of conventional RED systems. Chang *et al.* [205] demonstrated a fully paper-based RED cell in which two fan-shaped microfluidic paper channels feed a Nafion cation exchange membrane, with Ag/AgCl paper electrodes completing the electrochemical circuit as shown in Figure C.2. The fan geometry ensures a quasi-stationary flow rate: as the liquid front enters the circular sector, the increasing unwetted porous volume compensates for the rise in viscous resistance, maintaining stable flow until the fan is fully saturated. This geometric control also allows tuning of the device lifetime.

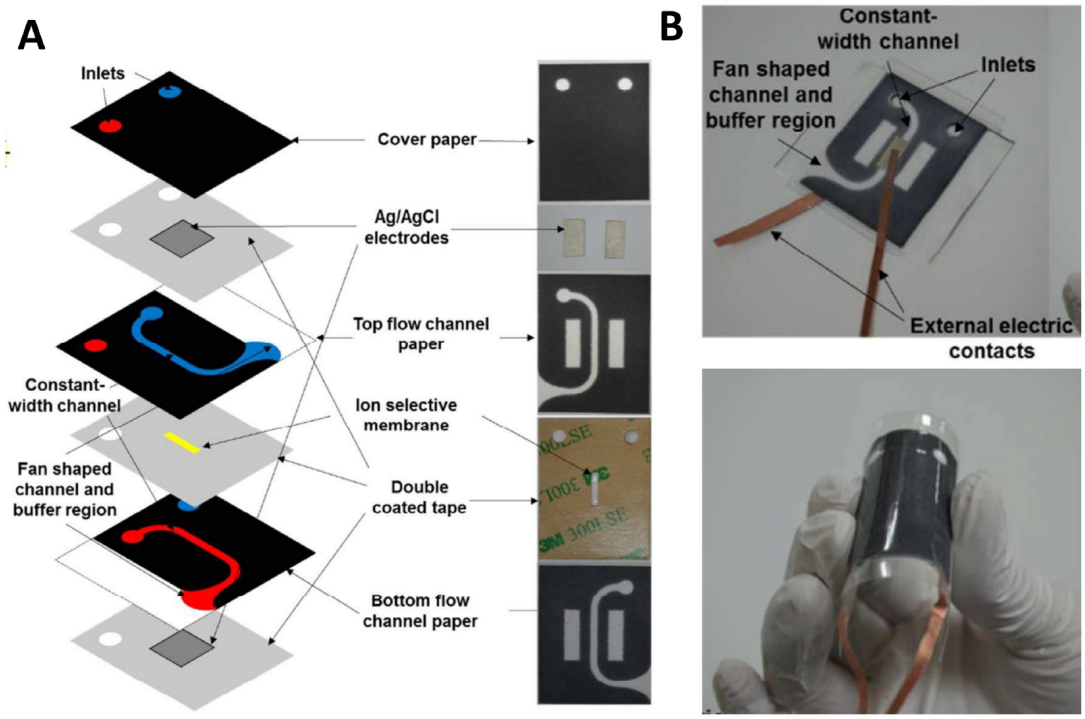


Figure C.2: **A** Exploded view of a paper-based reverse electrodialysis cell and **B** pictures of paper-based reverse electrodialysis cell assembled [205].

Experiments showed that power density follows the expected dependence on concentration ratio, with an optimum arising from the trade-off between Nernst voltage and membrane permselectivity. Larger membrane areas reduced power density, likely due to increased co-ion leakage. Higher flow velocities improved performance without incurring pumping losses, since flow is capillary driven. The paper-based RED devices produced up to 275 $\mathrm{nW/cm^2}$, remained functional when bent, and operated for more than an hour depending on the fan geometry, highlighting their suitability as low-cost, disposable power sources for point-of-care diagnostic systems.

C.6 Objectives of this master's thesis

The main objective of this thesis was to fabricate and characterize a paper-based stacked RED system in order to eliminate the need for external pumping and to further advance the current state of the art.

The first part of the work focused on understanding and developing a model and procedure to generate microfluidic flow in paper with a controlled flow rate,

which is essential for maintaining a stable output power in the RED system.

The second part consisted of fabricating the paper-based stacked RED device and measuring its power output over time. Because typical microfluidic applications operate for less than 30 minutes, this time scale defined the target operational range for the paper-based RED system studied here.

C.7 Materials and methods

For this thesis, Whatman Grade 4 qualitative filter paper was selected as the substrate for the paper-based RED cells. Its homogeneous pore distribution reduces anisotropy effects, and its relatively large pore size enables higher wicking velocities than lower-grade papers. This is essential to ensure sufficiently fast replenishment of the high- and low-salinity streams, thereby avoiding flow-rate limitations that could hinder RED performance. Because the devices developed here do not require biomolecular functionalization, more specialized substrates such as nitrocellulose were unnecessary.

Microfluidic channels were patterned using an automated plotter with a permanent marker as shown in Figure C.3. The hydrophobic resin in the ink infiltrates the paper matrix as the solvent evaporates, forming effective flow barriers. This approach is simple, rapid, inexpensive, and well suited for iterative optimization of channel geometries.

Device assembly relied on a 170 μm-thick 3M LSE double-sided adhesive, chosen for its ability to bond low-energy surfaces and its adequate mechanical robustness. Although wax-coated regions initially showed poor adhesion, a mild heating step (65 °C) successfully improved bonding without affecting flow properties. Thinner adhesives were tested but proved too fragile for reliable handling.

Ag/AgCl electrodes were fabricated by brushing conductive paste onto entire paper sheets, followed by thermal annealing at 105 °C for 60 min to evaporate the solvent and promote particle coalescence. Individual electrodes were then cut from the coated sheets and placed in contact with the channels, with external electrical connection provided by silver wires. While this simple method ensures functional electrodes for characterization, future designs could integrate more advanced printed electronic components (e.g. capacitors or LEDs) directly onto the paper substrate.

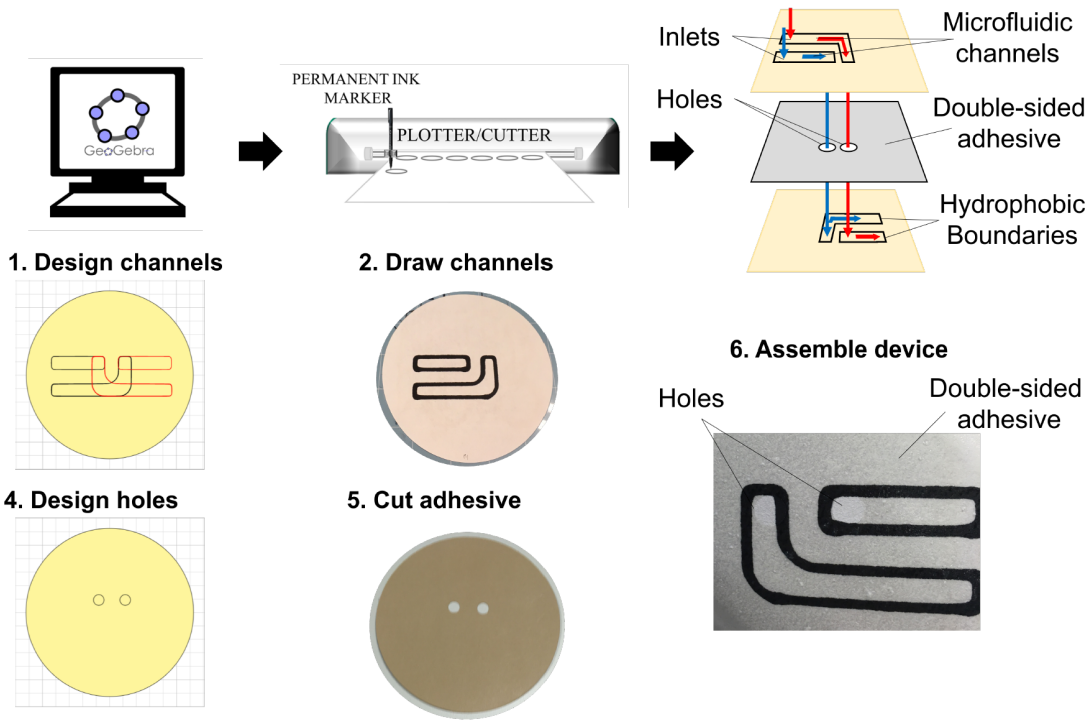


Figure C.3: Schematic view of the fabrication process for three-dimensional paper-based microfluidic devices using the automated plotter patterning method.

C.8 Experimental results

C.8.1 Fan-shaped for controlled flow rate

Figure C.4 presents a time-lapse sequence of the imbibition of a fan-shaped plotted channel, obtained by periodically switching between two reservoirs containing differently colored solutions. As observed for the fan-shaped cut channels, a regular alternation of color bands appears, confirming that a quasi-stationary flow velocity is established.

Figure C.5 shows the measured flow velocities over time in the rectangular section of the plotted fan-shaped channel. These measurements are compared with the theoretical prediction as well as with the initial velocity, defined as the velocity of the liquid front when it reaches the circular section. The theoretical curve corresponds to the HKM model, which extends the Mendez quasi-stationary flow framework to channels with hydrophobic boundaries.

From Figure C.5, it can be concluded that a quasi-stationary flow regime is

successfully achieved and that the HKM model developed in this thesis accurately predicts the experimental results. Furthermore, channels incorporating hydrophobic boundaries exhibit slower flow velocities than channels of identical dimensions without hydrophobic confinement. This reduction in velocity is fully consistent with the predictions of the HKM model.

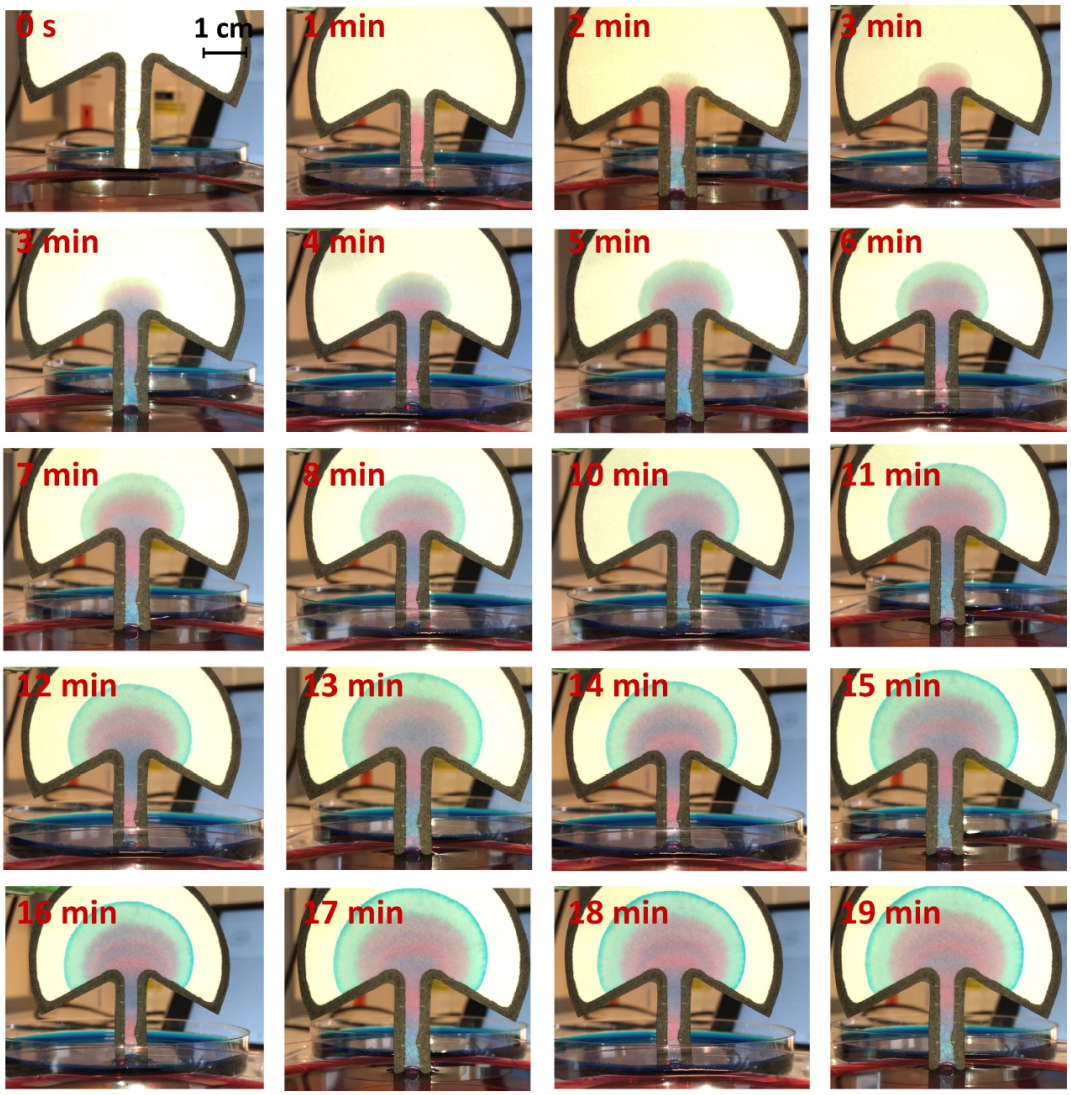


Figure C.4: Time-lapse photography of a fan plotted channel immersed periodically in a tank filled with red and blue colorant. The width and the length of the rectangular sections are 4 mm and 25 mm, respectively.

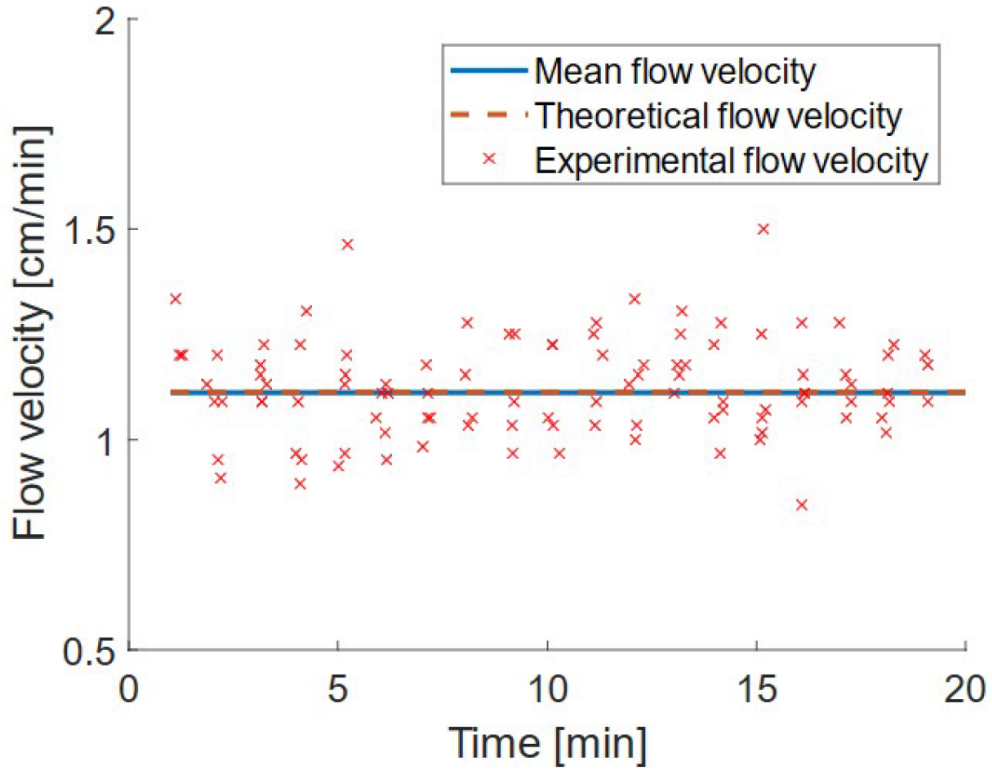


Figure C.5: Velocities of the liquid front as a function of time in a rectangular plotted paper channel terminated by a circular section, measured at 23 °C and 70% relative humidity. The rectangular section has a width of 4 mm and a length of 25 mm.

C.8.2 stacked paper-based RED devices

Figure C.7 shows the power density and the open-circuit voltage (OCV) generated over time by the stacked paper-based RED cell (Fig. C.6) connected to an external resistance of 180 Ω. The device was filled with NaCl solutions of 10^{-2} M and 1 M at $t = 0$ s. No power generation is observed during the first four minutes, indicating the time required for the solutions to reach the membrane. Once the liquids reach the membrane, the power density increases rapidly and reaches a maximum of 35.5 μW/cm^2. It then decreases progressively and stabilizes at approximately 2.5 μW/cm^2 until the flow stops. The end of the flow can be identified in Figure C.7 from the subsequent decrease in OCV. The long power-generation duration results from the large circular section at the end of the channels, which maintains a quasi-stationary flow for an extended time.

These results demonstrate that high power density (35.5 μW/cm^2) can be produced by stacked paper-based RED cells. However, the power density drops rapidly after a few minutes. Because the OCV remains stable, neither flow leakage nor membrane fracture is responsible. The decrease in power density therefore reflects an increase in internal resistance. A plausible explanation is the rapid consumption of the Ag/AgCl electrodes. Since the electrodes consist of Ag/AgCl paste brushed onto paper and only one face is in contact with the channels, the redox reaction may quickly deplete the locally available reactive material, increasing electrode resistance.

Despite this limitation, the device reached a maximal power density of 35.5 μW/cm^2 and maintained a stable power density of 2.5 μW/cm^2 for more than 100 min. The stable OCV of 285 mV indicates that sustained operation at the maximal power density would be achievable if the electrode degradation issue is resolved.

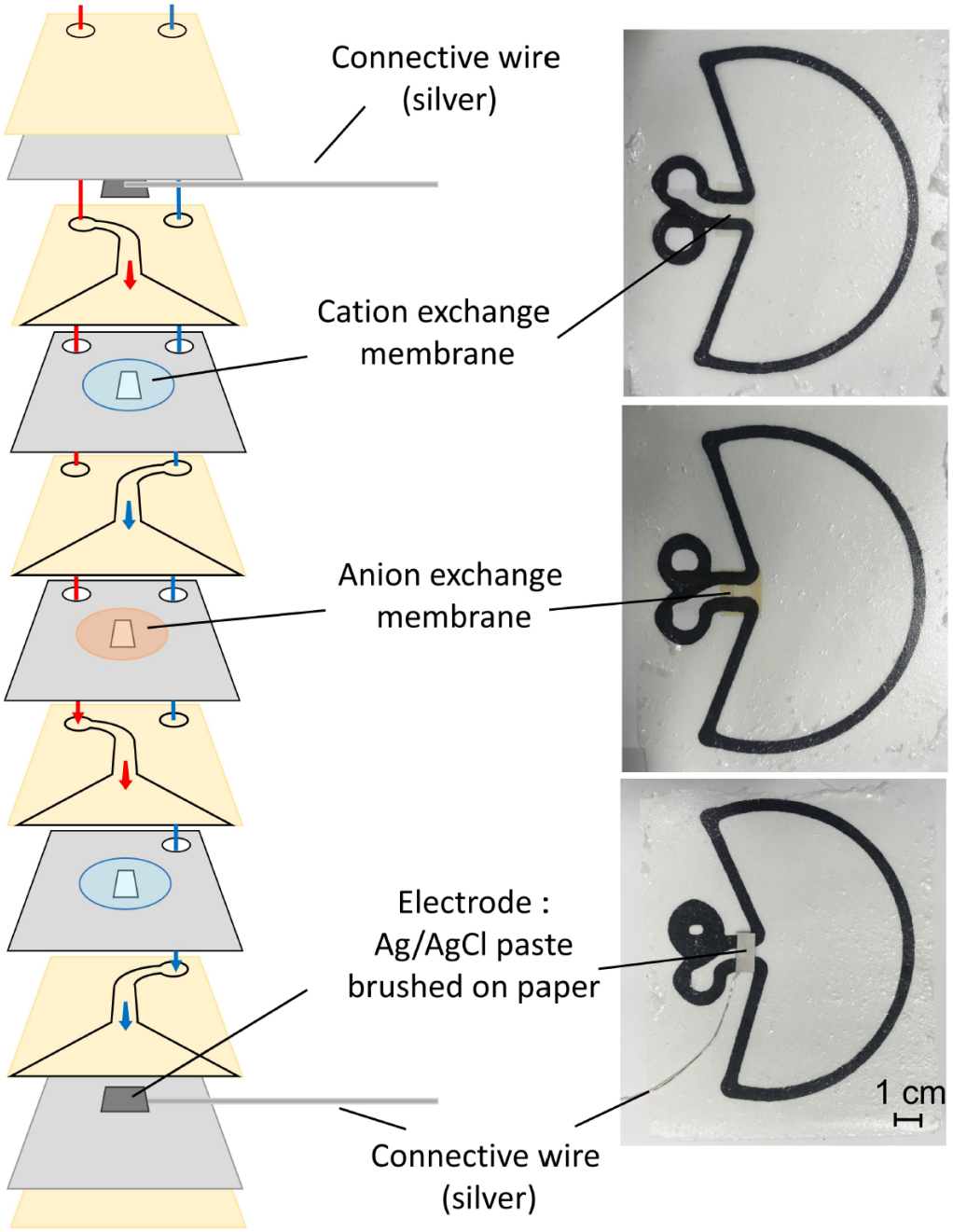


Figure C.6: Exploded diagram of a stacked paper-based reverse electrodialysis cells. The cut hole in the middle of the double-sided adhesive represent the active membrane area.

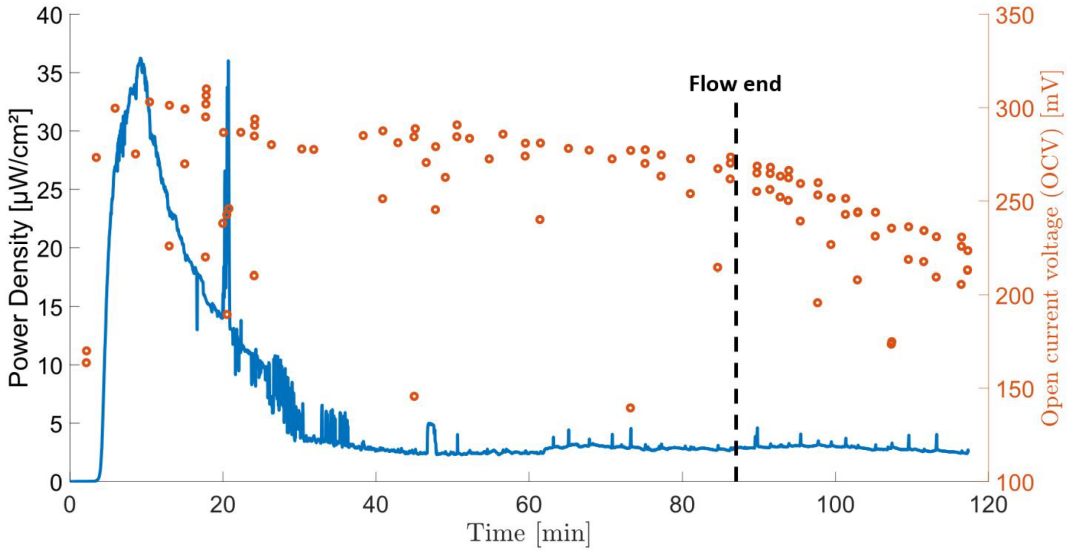


Figure C.7: **A** Exploded view of a paper-based reverse electrodialysis cell and **B** pictures of paper-based reverse electrodialysis cell assembled [205].

C.8.3 Power density depending on the flow rate

Two single-membrane paper-based RED devices were fabricated with identical geometries except for the channel length, thereby producing different quasi-stationary flow rates. As seen in Figure C.8, the shorter device, exhibiting approximately twice the flow rate of the longer one, generated a significantly higher power density ($\sim 6.6\,\mu W/cm^2$) compared to the long-channel device ($\sim 1\,\mu W/cm^2$). Since both devices showed similar open-circuit voltages ($\sim 165\,mV$), the improvement in power density is attributed to a reduction in internal resistance resulting from enhanced hydrodynamic mixing at higher flow rate.

The duration of power generation was shorter for the high-flow device because the circular expansion section at the end of the channel was filled more rapidly. Conversely, the long-channel device sustained power production for almost twice as long, consistent with its slower filling kinetics. These results confirm that higher flow rates substantially improve power density in paper-based RED systems, though the circular section dimensions must be adapted to maintain the desired operational lifetime.

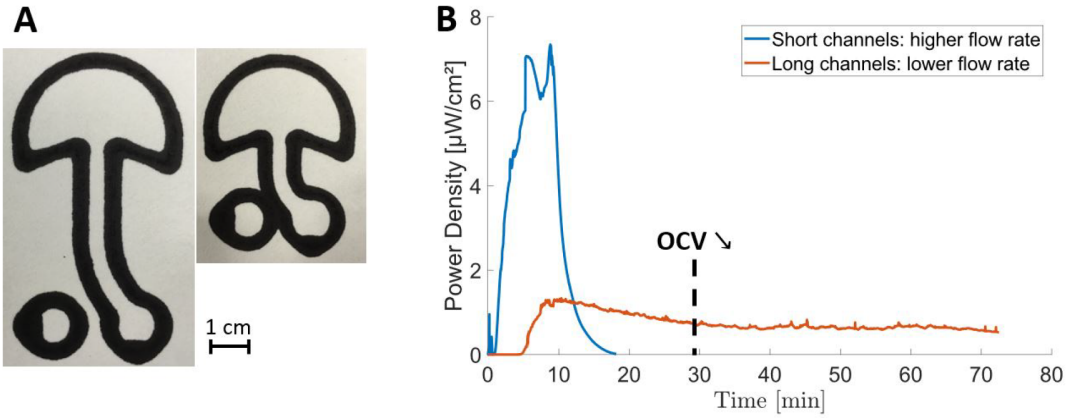


Figure C.8: **A** Picture of the long and short channel used in the reverse electrodialysis devices. **B** Power density generation over time of single-membraned reverse electrodialysis devices with cation-exchange membrane of different lengths and connected to a resistance load of 180 Ω. The long and short channels have a length of 2 and 4 cm, respectively. The high and low concentrations of the NaCl electrolyte solution were 1 and 10e-2 M. The paper-based RED devices with a lower flow rate continue to generated power after the OCV drop because the inlets were refilled by mistake.

C.9 Paper-based RED with porous silicon membranes

When the project was initially conceived, the integration of porous silicon membranes as ion-exchange membranes (IEMs) in a paper-stacked RED device was explored. At that time, only self-supported PSi membranes were available within the group, and achieving reliable liquid contact between wet paper and the fragile PSi surface proved impractical.

The development of free-standing PSi (fs-PSi) membranes made such integration considerably more feasible. A proof-of-concept paper-stacked RED device incorporating a single fs-PSi membrane was assembled, as shown in Figure C.9. The resulting I–V characteristics at different times (Figure C.10) exhibit an initial stabilization period, most likely due to slow wetting of the PSi through the paper substrate, but ultimately yield a measurable membrane potential, confirming the operational compatibility between fs-PSi and paper-based microfluidics.

Additional evidence supporting this approach is provided in [256], where open-ended porous silicon membranes mounted onto paper demonstrated efficient passive flow-through transport without external pumping. In that system, the paper acts

simultaneously as a mechanical support and a capillary pump, enabling rapid solution infiltration and producing analyte-dependent optical responses within the PSi.

These results highlight the strong synergy between porous silicon membranes and paper-based fluidic architectures. They further motivate the exploration of multi-layer paper-integrated RED stacks employing fs-PSi membranes, which may enable entirely pump-free salinity-gradient energy harvesting in future implementations.

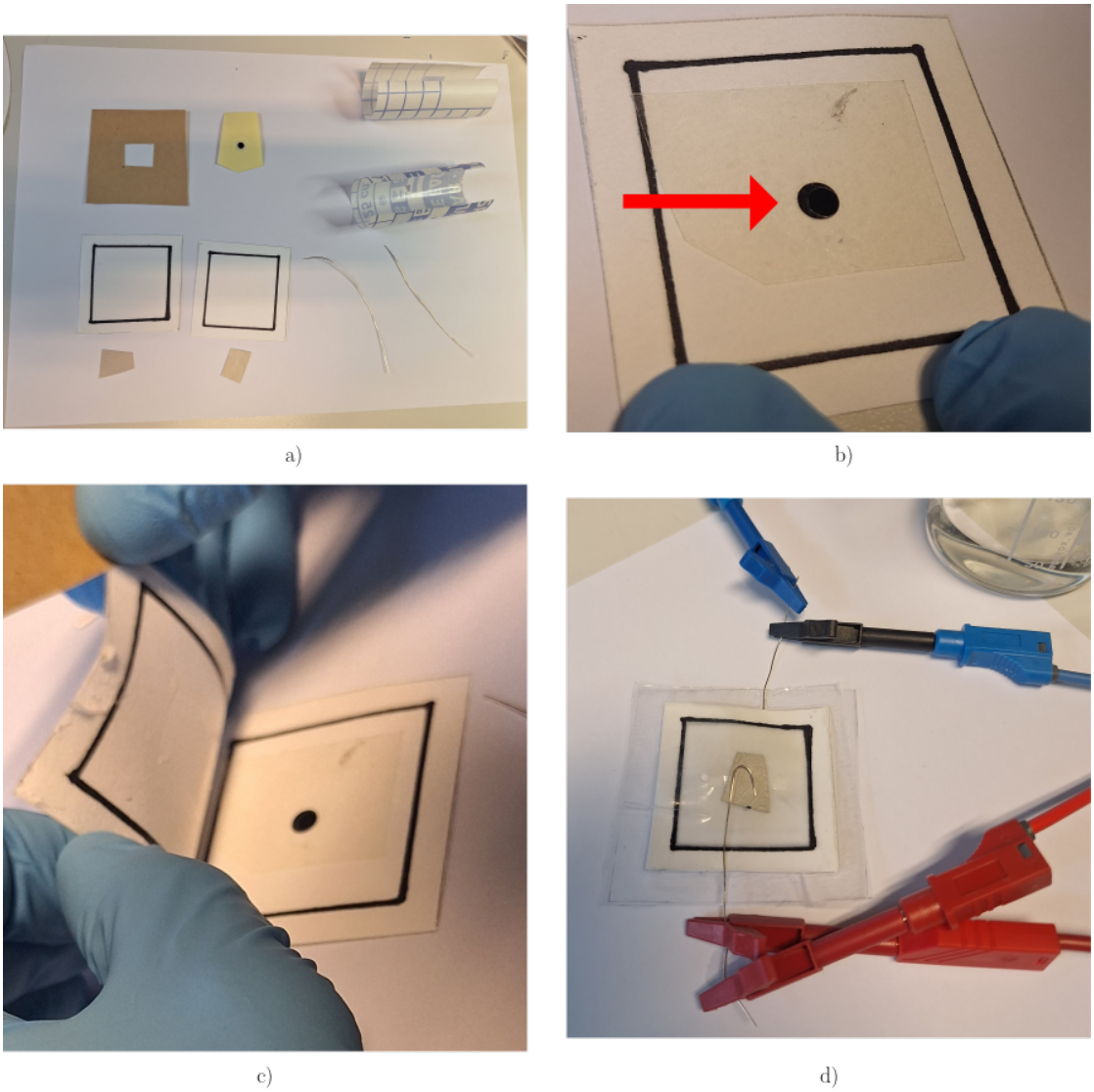


Figure C.9: Photos showing the montage of the free-standing porous silicon membrane (Red arrow) chronically from a) to d). The fs-pSi membrane (Area= 27 mm^2) is first sealed with thin double-tape then it is stacked similarly as shown in Fig. C.6.

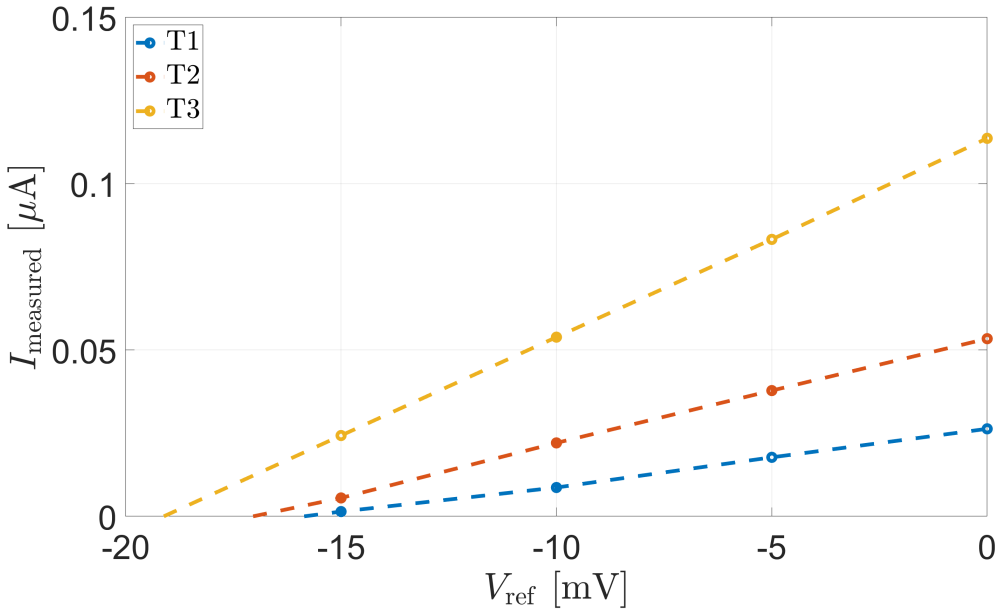


Figure C.10: I–V characteristics for the paper stacked fs-pSi (50 mA/cm^2) membrane with concentration KCl 1e-4/1e-3 M taken at different time T1<T2<T3. From T3, the I–V response was stabilized. Note that the measured voltage is made though the WE/CE directly.

C.10 Conclusion

This work focused on improving paper-based reverse electrodialysis (RED) systems for salinity-gradient energy harvesting through three main contributions:

- Microfluidic fabrication: The plotter method proved faster, more accurate, and easier to use, and enabled the fabrication of multilayer 3D paper microfluidic devices.
- Flow modelling: An analytical model describing flow in fan-shaped paper channels with hydrophobic boundaries was established. When calibrated with simple straight-channel experiments, the model accurately predicted flow velocity and confirmed the ability of fan-shaped geometries to generate quasi-steady flow.
- Paper-based RED devices: Single-membrane RED cells were fabricated and achieved power densities of 4-8 WmuW/cm^2, a tenfold improvement over

prior work, with operation exceeding 100 minutes. A stacked RED configuration reached 35.5 μW/cm^2, although device degradation limited sustained operation.

Overall, the thesis demonstrates that optimized microfluidic design and improved fabrication strategies substantially enhance the performance of paper-based RED systems.

Appendix D

Porous silicon flake fabrication from a full Si wafer for membrane use in RED applications

This chapter presents the work carried out by master's students under our supervision during the doctoral thesis. This project was defined around a specific scientific challenge directly related to the core objectives of this dissertation.

This project, *"Micro and nanofabrication techniques: Porous silicon flake fabrication from a full Si wafer for membrane use in RED applications,"* was conducted within the framework of the course LELEC2560 on micro- and nanofabrication. The aim of this project was to propose and test a process capable of upscaling the production of free-standing porous silicon membranes from a single electrochemical etching step.

D.1 Objective

The fabrication process for free-standing porous silicon membranes described in Section 7.4.1 has been thoroughly studied and is now well controlled. The success rate for producing clean fs-pSi membranes exceeds 80% provided that the selected current density yields a porous layer with porosity below 70%. However, this method produces only a single membrane (flake) per run and is highly time-consuming, particularly for membranes etched at 3 mA/cm^2, where the etch rate is very low and long processing times are required.

For this reason, it was proposed to investigate the feasibility of producing multiple free-standing porous silicon membranes from a single wafer in a single process using a lift-off technique.

D.2 Material and methods

The substrates consisted of double-side polished, heavily boron-doped (p++), "100"-oriented silicon wafers, with a resistivity of 0.9–1 mΩ·cm and a thickness in the range of 380–400 µm. The wafers were supplied by ZHONGGUI Semiconductor (Yangzhou) Co., Ltd. (China).

The initial proposed process steps for producing multiple free-standing porous silicon membranes is summarized in Figure D.1.

The procedure begins with a standard cleaning sequence in a freshly prepared piranha solution (H_2O_2:H_2SO_4, 2:5), followed by two rinsing steps in continuously flowing deionised (DI) water for 20 min each. The native oxide is subsequently removed in a 2% HF bath until the silicon surface becomes hydrophobic. A 90 nm SiO_2 layer is then grown by wet thermal oxidation at 1000 °C, after which a 500 nm polycrystalline silicon (PolySi) film is deposited at 620 °C using LPCVD.

Patterning is performed by i-line optical lithography (positive resist AZ® MIR™ 701, MicroChemicals GmbH), followed by RIE to open the PolySi layer and clear it from the rear side of the wafer. The exposed SiO_2 at the bottom of the etched features is removed in diluted HF (5% v/v). This patterned SiO_2/PolySi bilayer subsequently acts as the hard mask during the electrochemical formation of porous silicon [206].

Porosification is carried out in a custom Teflon® single-bath etch cell using a platinum coil counter-electrode, an aluminium working electrode and Keithley DC power supply (Model 2460) as current source. Etching takes place in an HF (49%):ethanol electrolyte (3:1 vol. ratio) according to a two-step sequence: (i) formation and removal of a sacrificial layer with a current density identical to the one used in the next step for 60 s; then 1 M KOH until reaction ceases); This serves as an efficient cleaning step, providing clean and reproducible surfaces [383] as discussed in 5.1.1. (ii) etching using the etch stop technique (10 seconds current on, 2 seconds current off) of the porous layer at 50 mA/cm^2 for 107 cycles (iii) lift-off by imposing an electropolishing current of 444 mA/cm^2 for 10 seconds.

Once the flake are recovered from the wafer, they are thermally oxidised in a Heraeus furnace under a 1.5 L min^{-1} O_2 / 1.2 L min^{-1} N_2 atmosphere at 250 C for 30 min. This mild oxidation step stabilises the porous matrix.

The fabricated free-standing membranes are produced either as 4 mm^2 squares or as circular membranes of 3.14 mm^2 (same mask as before). Final membrane thicknesses range from 65 to 100 μm depending on membrane size, wafer position, and batch variations. Thinner structures were avoided due to their tendency to deform or crack during subsequent processing.

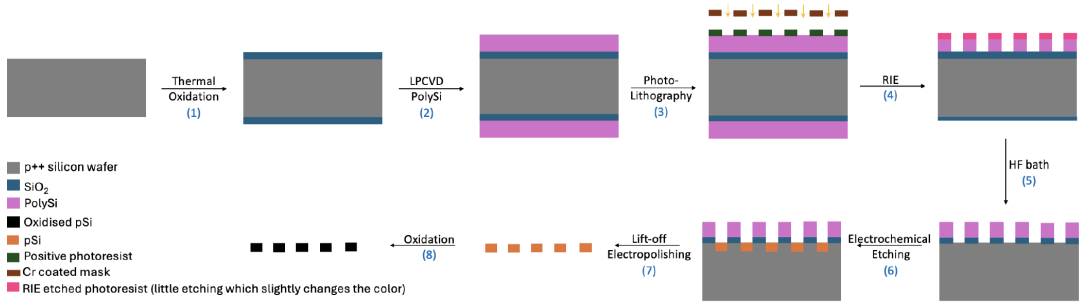


Figure D.1: Schematic illustration of the manufacturing process of fs-PSi membranes. Starting from a cleaned 3-in diameter highly doped silicon wafer, the process goes through the following steps: (1) thermal oxidation, (2) deposition of a polysilicon layer (PolySi) using Low Pressure Chemical Vapour Deposition (LPCVD); (3-4-5) positive photolithography on the frontside and opening of the PolySi and SiO2 layers using Reactive Ion Etching (RIE) and diluted HF respectively; (6) formation of the porous silicon layer by electrochemical etching; (7) lift-off electropolishing; and finally (8) low temperature thermal oxidation

D.3 Results

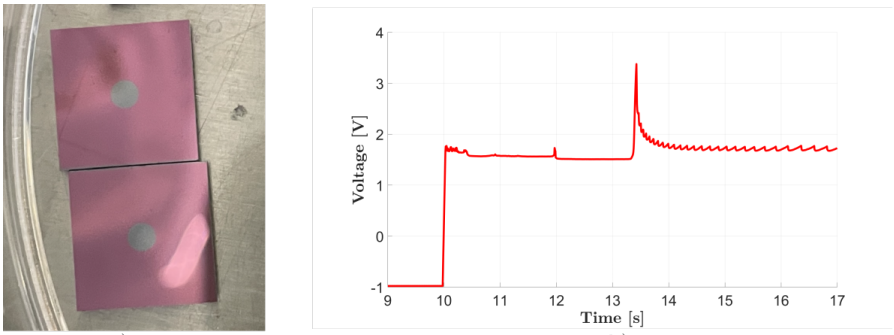
D.3.1 Single masked die membrane study

Previously, the porous region was defined solely by the O-ring pressing on the silicon substrate. As a result, the porous layer was noticeably thinner toward the edges, i.e. near the boundary imposed by the O-ring. The lift-off process was therefore characterised under this specific configuration.

Since the situation changes when a lithographic mask is used, we first examined the implications of the mask on the lift-off mechanism. A wafer patterned with the SiO_2/polysilicon mask was diced into individual dies, as shown in Fig. D.2(a), after which anodisation was performed followed by the lift-off step.

The lift-off time for a square area of 4 mm^2 is shown in Fig. D.2(b). Similarly to the lift-off performed without any mask, we observed the appearance of a sharp voltage peak after a certain time, which suggests that the HF had been depleted and that significant gas production caused a rapid increase in the system impedance. For porous layers processed without masking, such a peak usually indicates that the lift-off of the porous layer has occurred.

However, after removing the die from the cell and rinsing away the HF, no visible separation of the porous layer was observed. This phenomenon was systematically observed for the other samples as well.



a) b)

Figure D.2: (a) Individual dies used to study the impact of a masking layer on the fabrication of free-standing porous silicon (fs-pSi) membranes by lift-off of the porous layer. Radius of the exposed Silicon is 1 mm. (b) Measured voltage during the electropolishing step, showing the appearance of a characteristic peak associated with the lift-off mechanism.

In order to verify whether the porous layer was still attached to the substrate, cross-section images were taken. During the cutting of the die in half, the porous layer detached from the substrate. This observation suggests two possibilities: either the porous layer was already fully detached and only held in place mechanically, or it remained attached locally, most likely near the edges,such that the mechanical stress from cutting released it. The latter explanation would be consistent with what was previously observed for porous layers fabricated without a mask (see Fig. 7.21).

As shown in Fig. D.3, cross sections of the remaining substrate reveal clear traces of the porous layer. Near the mask edge, due to under etch, the top layer of the mask remains hanging. This layer, approximately 600 nm is the thcikness of the polysilicon layer of the mask. The polysilicon itself is not etched during anodisation nor by HF, but the underlying SiO_2 is attacked by HF during the process, resulting in lateral etching beneath the polysilicon. In addition, the anodisation of the silicon substrate produces further underetching due to the redistribution of current lines under the mask, a phenomenon commonly reported in such processes [224]. The depth of this anodisation-induced underetching is typically of the same order as the thickness of the porous layer.

From these observations, we conclude that the porous layer was indeed lifted off from the silicon substrate, but remained imprisoned under the polysilicon mask. A proper electropolishing step occurred, forming a cavity beneath the porous layer. This interpretation is further supported by the presence of two distinct etching planes visible under the mask as seen in Figure D.3: the first one directly under the polysilicon corresponding to HF etching of the SiO_2/Si during anodisation, and the second plane corresponding the sudden increase in current density during

electropolishing of the substrate.

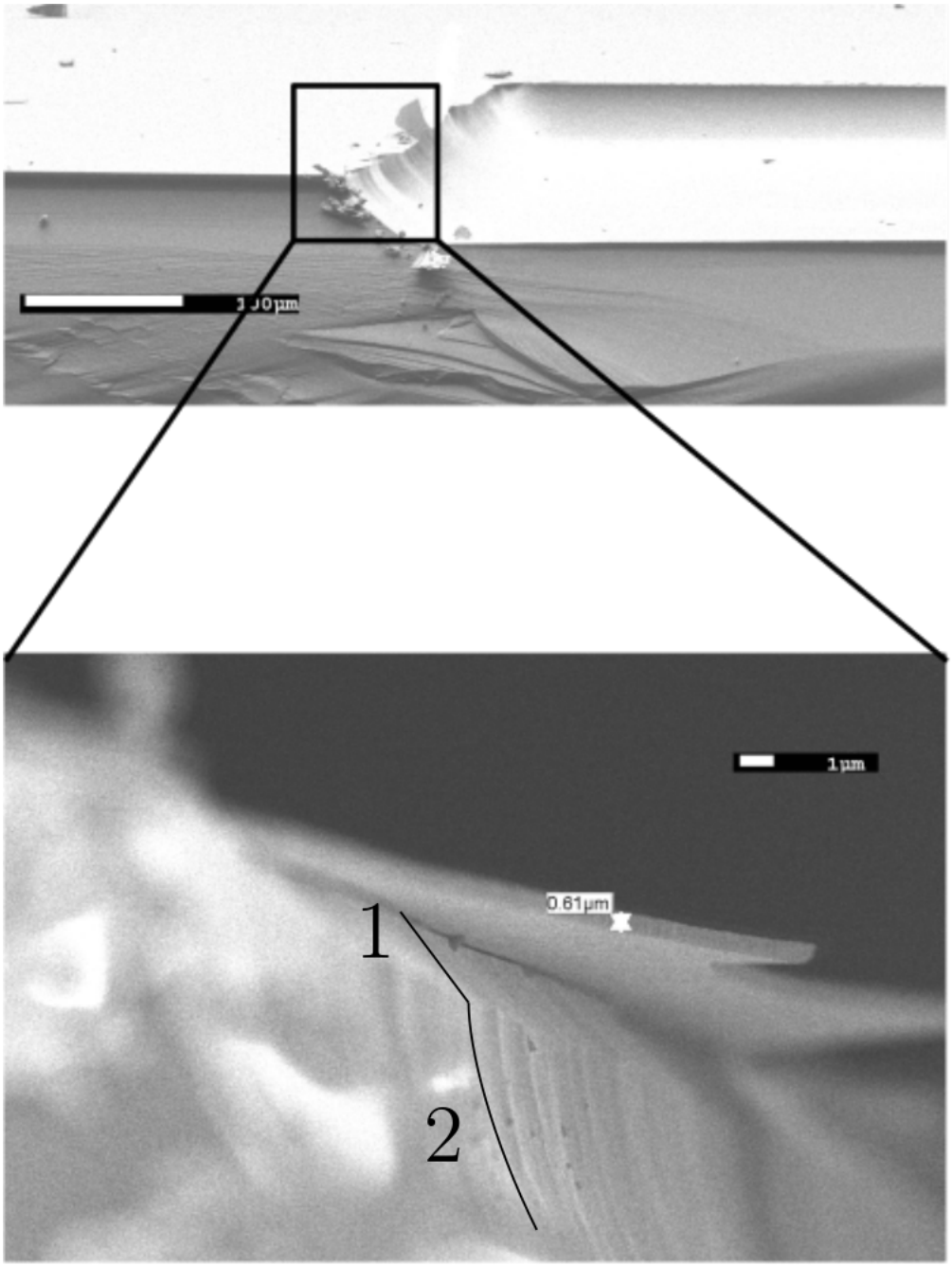


Figure D.3: Cross-section SEM images of a substrate with a masked die. Top: the porous silicon layer has been detached from the substrate after lift-off. Bottom: zoom-in near the mask edge showing two distinct under-etching fronts: one corresponding to HF etching beneath the SiO_2/polysilicon mask, and the other originating from the electropolishing step.

Because of the presence of the polysilicon layer, the porous membrane could not be released during the electropolishing step. One possible way to recover the flake is to remove the polysilicon by etching. A simple test was performed in which a die was placed in the RIE chamber for 15 seconds, while the porous silicon layer was protected manually using a photoresist coating. As expected, the etching of the polysilicon released the fs-pSi layer, as shown in Fig. D.4.

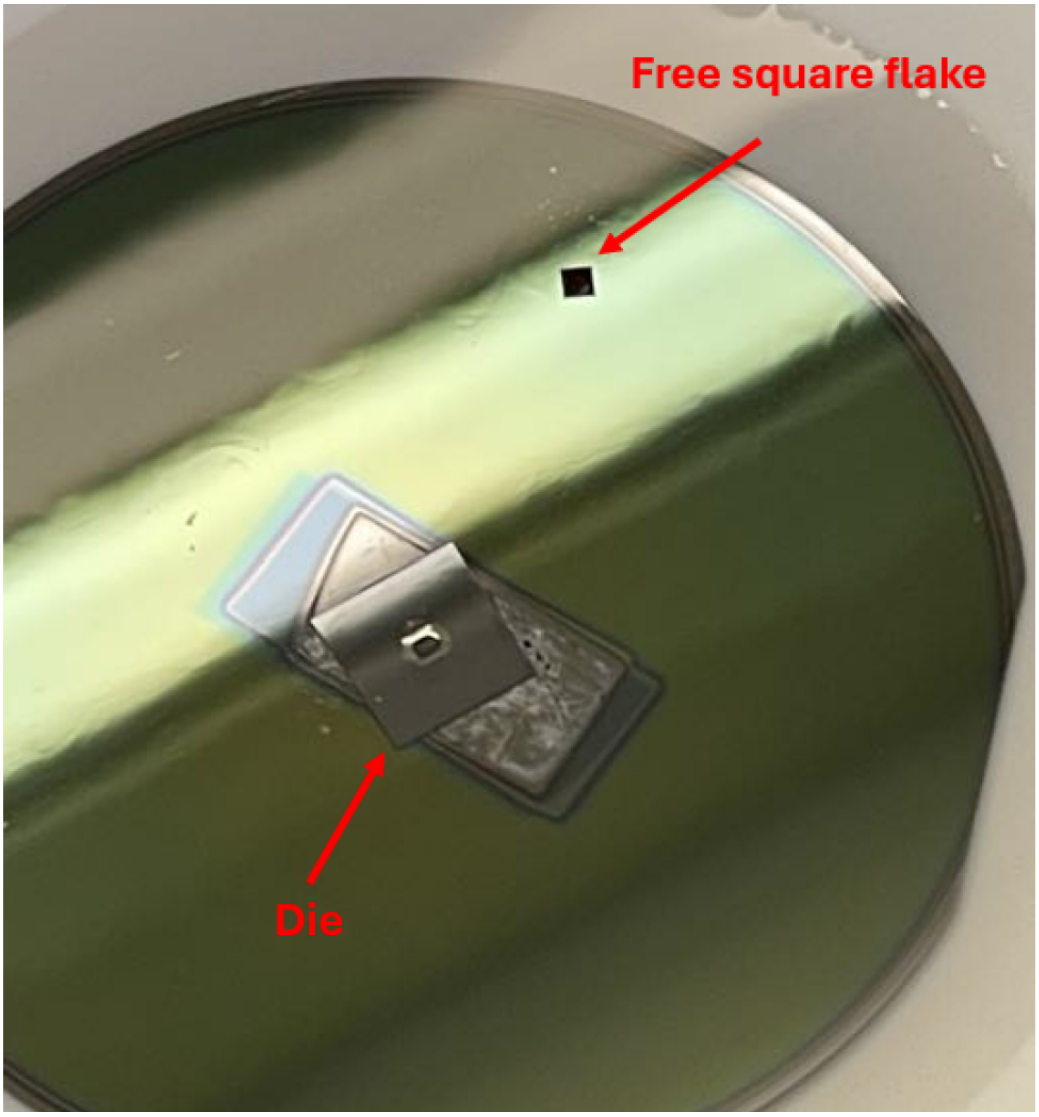
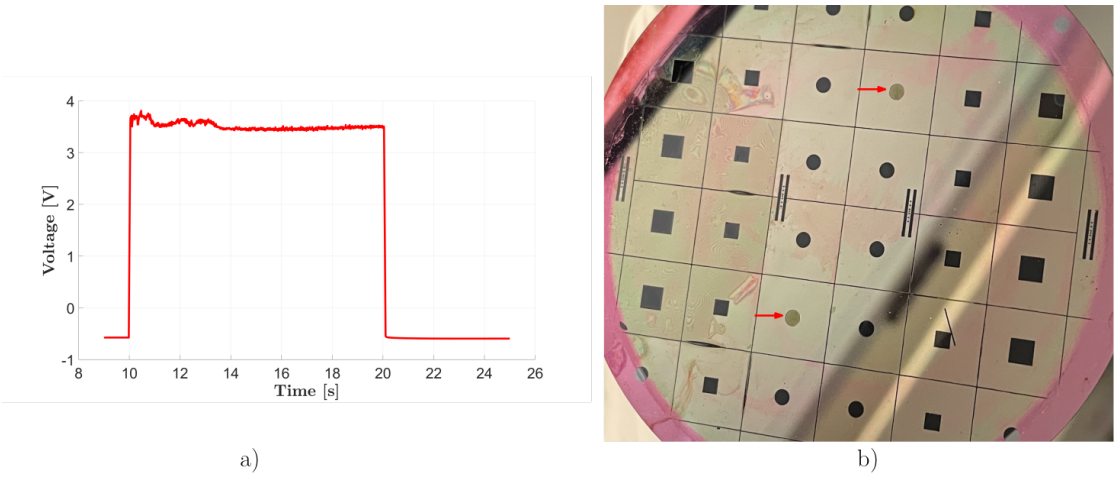


Figure D.4: Photo of a die just after the RIE plasma etch. Due to the removal of the polysilicon layer, the fs-pSi has been released. The square fs-pSi membrane is $2{\times}2$ mm^2.

D.3.2 Full masked wafer

The next step was to test the production of fs-pSi membranes from a full wafer. After completing the anodization, an electropolishing current density of 444 mA/cm^2 was applied for 10 s. The measured voltage did not exhibit the sharp peak typically associated with lift-off, as seen in Fig. D.5. This can be explained by two factors. First, the current density is not uniform across the entire wafer: it decreases toward the edges, meaning that the conditions required for electropolishing are not met for dies located near the periphery, and no lift-off occurs there. Second, for dies that do experience lift-off, the moment at which it happens likely varies depending on their position on the wafer. Because of these two effects, no sudden change in impedance is produced, and the measured voltage only fluctuates slightly.

A photograph of the wafer taken immediately after processing (Fig. D.5b) shows that several circular flakes were missing, indicating that the polysilicon mask does not completely confine or retain the porous layer for these particular regions.



a) b)

Figure D.5: a) Measured voltage during the electropolishing step for lift-off of the porous layer on a full wafer. An applied current density of 444 mA/cm^2 was used over an exposed area of 2.29 cm^2 for 10 s. b) Photograph of the wafer after the electropolishing step. Two circular flakes are missing (indicated by red arrows).

A new added step added step after step (7) in Figure D.1 is performed. To remove the remaining parts of the wafer, we followed a procedure analogous to that used for the individual dies by first protecting the pSi regions with a negative photoresist, enabling selective etching of the unprotected silicon. Since a full wafer was processed, the resist was not applied manually but deposited using standard lithography steps:

- The wafer was first immersed in acetone to remove any residual resist from the first mask, as this region must be etched later.
- A layer of AZ5510 negative photoresist was then deposited by spin coating at 3000 rpm at 90° C for 60 s.
- The wafer was exposed using front-side alignment to ensure proper registration with the previous mask. Proximity-contact exposure was used to avoid damaging the fragile pSi layer. An exposure dose of 120 mJ/cm^2 was applied.
- A reversal bake at 110° C for 90 s was performed, followed by a 60 s development step.

Due to a technical issue during mask alignment, the resist pattern was not correctly transferred. As a consequence, most flakes detached during development because of chemical interaction with the developer, and these fragments were subsequently ejected during the rinsing spin. For this reason, the RIE etching step on the full wafer was not pursued, as the patterned regions no longer corresponded to the intended areas.

D.4 Perspectives and conclusion

In this project, the feasibility of producing fs-pSi membranes using a patterned mask on a silicon substrate was explored. Experiments on individual dies showed that the porous layer does lift off during the electropolishing step, but in most cases the mask on top mechanically retained the porous layer. Removal of the mask by RIE plasma etching was sufficient to release the porous silicon flake, confirming that the lift-off had indeed occurred.

Although the approach was not successful at the full-wafer scale in the present work, the results indicate that this RIE-based strategy could be applied to an entire wafer provided that appropriate precautions are taken. In particular, applying a negative photoresist to protect the porous layer before RIE can be problematic: spin coating may detach loosely held flakes, and accurate alignment is required to prevent undesired reactions between the developer and the pSi surface.

The method therefore remains a promising route for upscaling fs-pSi membrane fabrication from a single wafer, but the choice of masking strategy is critical. The mask must act as a hard mask during anodization while ideally not retaining the porous flake after lift-off. Because under-etching is unavoidable during anodization, flakes will inevitably remain partially attached, and the hard mask must eventually be removed. This adds complexity, as the fragile porous layer must be sufficiently protected throughout the mask-removal steps.

If a robust masking and protection strategy is developed, a final challenge remains regarding the reliable retrieval and handling of the released fs-pSi membranes. This aspect should be addressed in future work.

Bibliography

[1] *That 'Internet of Things' Thing - RFID Journal*. URL: https://archive.ph/20120910115905/http://www.rfidjournal.com/article/view/4986 (visited on 03/17/2025).

[2] *IoT connections worldwide 2022-2033 | Statista*. URL: https://www.statista.com/statistics/1183457/iot-connected-devices-worldwide/ (visited on 03/17/2025).

[3] Nga Dang, Elaheh Bozorgzadeh, and Nalini Venkatasubramanian. "Energy Harvesting for Sustainable Smart Spaces". In: *Advances in Computers*. Vol. 87. Elsevier, Jan. 2012, pp. 203–251. ISBN: 9780123965288. DOI: 10.1016/B978-0-12-396528-8.00006-7. URL: https://www.sciencedirect.com/science/article/pii/B9780123965288000067.

[4] Vibhav Kumar Sachan, Syed Akhtar, and M T Beg. *Energy-efficient Communication Methods in Wireless Sensor Networks: A Critical Review*. Tech. rep. 17. 2012, pp. 975–8887. URL: https://pdfs.semanticscholar.org/5ef3/80ad9861abdb3cd3f9731910a39704ce2734.pdf.

[5] Cesare Alippi et al. "An adaptive sampling algorithm for effective energy management in wireless sensor networks with energy-hungry sensors". In: *IEEE Transactions on Instrumentation and Measurement* 59.2 (2010), pp. 335–344. ISSN: 00189456. DOI: 10.1109/TIM.2009.2023818. URL: http://citeseerx.ist.psu.edu/viewdoc/download?doi=10.1.1.158.5918%7B%5C&%7Drep=rep1%7B%5C&%7Dtype=pdf.

[6] K. Najafi et al. "Microsystems for energy harvesting". In: *2011 16th International Solid-State Sensors, Actuators and Microsystems Conference*. IEEE, June 2011, pp. 1845–1850. ISBN: 978-1-4577-0157-3. DOI: 10.1109/TRANSDUCERS.2011.5969888. URL: http://ieeexplore.ieee.org/document/5969888/.

[7] Zhong Lin Wang. "Self-powered nanotech". In: *Scientific American* 298.1 (Jan. 2008), pp. 82–87. ISSN: 00368733. DOI: 10.1038/scientificamerican0108-82. URL: http://www.nature.com/doifinder/10.1038/scientificamerican0108-82.

[8] *Energy demand from AI – Energy and AI – Analysis - IEA*. URL: https://www.iea.org/reports/energy-and-ai/energy-demand-from-ai (visited on 12/12/2025).

[9] Zhiyi Wu, Tinghai Cheng, and Zhong Lin Wang. "Self-Powered Sensors and Systems Based on Nanogenerators". In: *Sensors 2020, Vol. 20, Page 2925* 20.10 (May 2020), p. 2925. ISSN: 14248220. DOI: 10.3390/s20102925. URL: https://www.mdpi.com/1424-8220/20/10/2925/htm%20https://www.mdpi.com/1424-8220/20/10/2925.

[10] Avinash Alagumalai et al. "Self-powered sensing systems with learning capability". In: *Joule* 6.7 (July 2022), pp. 1475–1500. ISSN: 25424351. DOI: 10.1016/j.joule.2022.06.001. URL: https://doi.org/10.1126/scirobotics.aat0429.

[11] Jan Kokert, Leonhard M. Reindl, and Stefan J. Rupitsch. "Behavioral Modeling of DC/DC Converters in Self-Powered Sensor Systems with Modelica". In: *Sensors 2021, Vol. 21, Page 4599* 21.13 (July 2021), p. 4599. ISSN: 14248220. DOI: 10.3390/s21134599. URL: https://www.mdpi.com/1424-8220/21/13/4599/htm%20https://www.mdpi.com/1424-8220/21/13/4599.

[12] M. Jirgl, Z. Bradac, and P. Fiedler. "Testing the E-PEAS Energy Management circuit for Embedded Systems". In: *IFAC-PapersOnLine* 51.6 (Jan. 2018), pp. 432–437. ISSN: 24058963. DOI: 10.1016/j.ifacol.2018.07.115. URL: https://doi.org/10.1049/iet-map.2016.1040.

[13] Ramato Ashu Tufa et al. *Progress and prospects in reverse electrodialysis for salinity gradient energy conversion and storage*. Sept. 2018. DOI: 10.1016/j.apenergy.2018.04.111. URL: https://www.sciencedirect.com/science/article/pii/S0306261918306792.

[14] Robert M. Rosenberg Irving M. Klotz. *Methods, Chemical Thermodynamics: Basic Concepts and*. Wiley, 2007. DOI: 10.1002/9780470285237. URL: https://onlinelibrary.wiley.com/doi/book/10.1002/9780470285237.

[15] Byeong Dong Kang et al. "Numerical study on energy harvesting from concentration gradient by reverse electrodialysis in anodic alumina nanopores". In: *Energy* 86 (June 2015), pp. 525–538. ISSN: 03605442. DOI: 10.1016/j.energy.2015.04.056. URL: https://www.sciencedirect.com/science/article/pii/S0360544215005113.

[16] Ngai Yin Yip et al. "Salinity gradients for sustainable energy: Primer, progress, and prospects". In: *Environmental Science and Technology* 50.22 (Oct. 2016), pp. 12072–12094. ISSN: 15205851. DOI: 10.1021/ACS.EST.6B03448/ASSET/IMAGES/LARGE/ES-2016-03448C_0008.JPEG. URL: /doi/pdf/10.1021/acs.est.6b03448.

[17] Jan W. Post et al. "Salinity-gradient power: Evaluation of pressure-retarded osmosis and reverse electrodialysis". In: *Journal of Membrane Science* 288.1-2 (Feb. 2007), pp. 218–230. ISSN: 0376-7388. DOI: 10.1016/J.MEMSCI.2006.11.018. URL: https://www.sciencedirect.com/science/article/pii/S0376738806007575.

[18] H Strathmann. *Ion-exchange membrane separation processes*. Elsevier, 2004, p. 348. ISBN: 9780080509402.

[19] Ramato Ashu Tufa et al. "Progress and prospects in reverse electrodialysis for salinity gradient energy conversion and storage". In: *Applied Energy* 225 (Sept. 2018), pp. 290–331. ISSN: 03062619. DOI: 10.1016/J.APENERGY.2018.04.111.

[20] Soumya Pandit et al. "Blue energy meets green energy in microbial reverse electrodialysis cells: Recent advancements and prospective". In: *Sustainable Energy Technologies and Assessments* 57 (June 2023), p. 103260. ISSN: 2213-1388. DOI: 10.1016/J.SETA.2023.103260. URL: https://www.sciencedirect.com/science/article/pii/S2213138823002539.

[21] Younggy Kim and Bruce E Logan. "Microbial reverse electrodialysis cells for synergistically enhanced power production". In: *Environmental Science and Technology* 45.13 (July 2011), pp. 5834–5839. ISSN: 0013936X. DOI: 10.1021/es200979b. URL: https://pubs.acs.org/doi/10.1021/es200979b.

[22] Fabio La Mantia et al. "Batteries for Efficient Energy Extraction from a Water Salinity Difference". In: *Nano Letters* 11.4 (Apr. 2011), pp. 1810–1813. ISSN: 1530-6984. DOI: 10.1021/nl200500s. URL: https://pubs.acs.org/doi/10.1021/nl200500s.

[23] D Brogioli et al. "Capacitive mixing for the extraction of energy from salinity differences: Survey of experimental results and electrochemical models". In: *Journal of Colloid and Interface Science* 407 (Oct. 2013), pp. 457–466. ISSN: 00219797. DOI: 10.1016/j.jcis.2013.06.050. URL: https://www.sciencedirect.com/science/article/pii/S0021979713006048%7B%5C#%7Df0075.

[24] Mark Olsson, Gerald L Wick, and John D Isaacs. "Salinity gradient power: Utilizing vapor pressure differences". In: *Science* 206.4417 (Oct. 1979), pp. 452–454. ISSN: 00368075. DOI: 10.1126/science.206.4417.452. URL: http://www.ncbi.nlm.nih.gov/pubmed/17809370%20http://www.sciencemag.org/cgi/doi/10.1126/science.206.4417.452.

[25] R. E. Pattle. "Production of electric power by mixing fresh and salt water in the hydroelectric pile [19]". In: *Nature* 174.4431 (1954), p. 660. ISSN: 00280836. DOI: 10.1038/174660A0;KWRD=SCIENCE. URL: https://www.nature.com/articles/174660a0.

[26] J. C. Fair and J. F. Osterle. "Reverse Electrodialysis in Charged Capillary Membranes". In: *The Journal of Chemical Physics* 54.8 (Apr. 1971), pp. 3307–3316. ISSN: 0021-9606. DOI: 10.1063/1.1675344. URL: /aip/jcp/article/54/8/3307/214320/Reverse-Electrodialysis-in-Charged-Capillary.

[27] John N. Weinstein and Frank B. Leitz. "Electric Power from Differences in Salinity: The Dialytic Battery". In: *Science* 191.4227 (Feb. 1976), pp. 557–559. ISSN: 00368075. DOI: 10.1126/SCIENCE.191.4227.557. URL: /doi/pdf/10.1126/science.191.4227.557.

[28] Bert H. Clampitt and Fred E. Kiviat. "Energy Recovery from Saline Water by Means of Electrochemical Cells". In: *Science* 194.4266 (Nov. 1976), pp. 719–720. ISSN: 00368075. DOI: 10.1126/SCIENCE.194.4266.719. URL: /doi/pdf/10.1126/science.194.4266.719.

[29] Gerald L. Wick. "Power from salinity gradients". In: *Energy* 3.1 (Feb. 1978), pp. 95–100. ISSN: 0360-5442. DOI: 10.1016/0360-5442(78)90059-2. URL: https://www.sciencedirect.com/science/article/abs/pii/0360544278900592.

[30] R. Audinos. "Electrodialyse inverse. Etude de l'energie electrique obtenue a partir de deux solutions de salinites differentes". In: *Journal of Power Sources* 10.3 (Jan. 1983), pp. 203–217. ISSN: 0378-7753. DOI: 10.1016/0378-7753(83)80077-9. URL: https://www.sciencedirect.com/science/article/abs/pii/0378775383800779.

[31] Ohya. "Dialytic battery convertible free energy of mixing of sea water and river water". In: *Organized by Korean Inst of Chemical Engineers,* (1983), pp. 451–456.

[32] L. Fiksdal S. Ratkje, T. Holt. "Effect of biofilm formation on salinity power plant output on a laboratory scale". In: *AIChE Symp. Ser* (1986), pp. 39–44.

[33] Joseph Jagur-Grodzinskr and Rlry Kramer. "Novel Process for Direct Conversion of Free Energy of Mixing into Electric Power". In: *Industrial and Engineering Chemistry Process Design and Development* 25.2 (1986), pp. 443–449. ISSN: 01964305. DOI: 10.1021/I200033A016/ASSET/I200033A016.FP.PNG_V03. URL: /doi/pdf/10.1021/i200033a016.

[34] Andrea Achilli and Amy E. Childress. "Pressure retarded osmosis: From the vision of Sidney Loeb to the first prototype installation — Review". In: *Desalination* 261.3 (Oct. 2010), pp. 205–211. ISSN: 0011-9164. DOI: 10.1016/J.DESAL.2010.06.017. URL: https://www.sciencedirect.com/science/article/pii/S0011916410004091.

[35] Piotr Dlugolecki et al. "Current status of ion exchange membranes for power generation from salinity gradients". In: *Journal of Membrane Science* 319.1-2 (July 2008), pp. 214–222. ISSN: 0376-7388. DOI: 10.1016/J.MEMSCI.2008.03.037. URL: https://www.sciencedirect.com/science/article/pii/S0376738808002548.

[36] J. Veerman et al. "Reverse electrodialysis: Comparison of six commercial membrane pairs on the thermodynamic efficiency and power density". In: *Journal of Membrane Science* 343.1-2 (Nov. 2009), pp. 7–15. ISSN: 0376-7388. DOI: 10.1016/J.MEMSCI.2009.05.047. URL: https://www.sciencedirect.com/science/article/pii/S0376738809004165.

[37] Jan W. Post, Hubertus V.M. Hamelers, and Cees J.N. Buisman. "Energy recovery from controlled mixing salt and fresh water with a reverse electrodialysis system". In: *Environmental Science and Technology* 42.15 (Aug. 2008), pp. 5785–5790. ISSN: 0013936X. DOI: 10.1021/ES8004317/ASSET/IMAGES/LARGE/ES-2008-004317_0005.JPEG. URL: /doi/pdf/10.1021/es8004317.

[38] J. Veerman et al. "Reducing power losses caused by ionic shortcut currents in reverse electrodialysis stacks by a validated model". In: *Journal of Membrane Science* 310.1-2 (Mar. 2008), pp. 418–430. ISSN: 0376-7388. DOI: 10.1016/J.MEMSCI.2007.11.032. URL: https://www.sciencedirect.com/science/article/pii/S0376738807008174.

[39] Piotr Dlugolecki et al. "Practical potential of reverse electrodialysis as process for sustainable energy generation". In: *Environmental Science and Technology* 43.17 (Sept. 2009), pp. 6888–6894. ISSN: 0013936X. DOI: 10.1021/ES9009635/ASSET/IMAGES/LARGE/ES-2009-009635_0004.JPEG. URL: /doi/pdf/10.1021/es9009635.

[40] M. Turek and B. Bandura. "Renewable energy by reverse electrodialysis". In: *Desalination* 205.1-3 (Feb. 2007), pp. 67–74. ISSN: 0011-9164. DOI: 10.1016/J.DESAL.2006.04.041. URL: https://www.sciencedirect.com/science/article/pii/S0011916406013622.

[41] E. Brauns. "Salinity gradient power by reverse electrodialysis: effect of model parameters on electrical power output". In: *Desalination* 237.1-3 (Feb. 2009), pp. 378–391. ISSN: 0011-9164. DOI: 10.1016/J.DESAL.2008.10.003. URL: https://www.sciencedirect.com/science/article/pii/S0011916408006991.

[42] J. Veerman et al. "Reverse electrodialysis: Performance of a stack with 50 cells on the mixing of sea and river water". In: *Journal of Membrane Science* 327.1-2 (Feb. 2009), pp. 136–144. ISSN: 0376-7388. DOI: 10.1016/J.MEMSCI.2008.11.015. URL: https://www.sciencedirect.com/science/article/pii/S0376738808009794.

[43] M. Turek, B. Bandura, and P. Dydo. "Power production from coal-mine brine utilizing reversed electrodialysis". In: *Desalination* 221.1-3 (Mar. 2008), pp. 462–466. ISSN: 0011-9164. DOI: 10.1016/J.DESAL.2007.01.106. URL: https://www.sciencedirect.com/science/article/pii/S0011916407007291.

[44] E. Brauns. "Towards a worldwide sustainable and simultaneous large-scale production of renewable energy and potable water through salinity gradient power by combining reversed electrodialysis and solar power?" In: *Desalination* 219.1-3 (Jan. 2008), pp. 312–323. ISSN: 0011-9164. DOI: 10.1016/J.DESAL.2007.04.056. URL: https://www.sciencedirect.com/science/article/pii/S0011916407005851.

[45] Enver Guler et al. "Tailor-made anion-exchange membranes for salinity gradient power generation using reverse electrodialysis". In: *ChemSusChem* 5.11 (Nov. 2012), pp. 2262–2270. ISSN: 18645631. DOI: 10.1002/cssc.201200298. URL: http://doi.wiley.com/10.1002/cssc.201200298.

[46] Doo Hee Cho et al. "Effect of cationic groups in poly(arylene ether sulfone) membranes on reverse electrodialysis performance". In: *Chemical Communications* 53.15 (Feb. 2017), pp. 2323–2326. ISSN: 1364548X. DOI: 10.1039/c6cc08440k. URL: http://xlink.rsc.org/?DOI=C6CC08440K.

[47] Jin Gi Hong and Yongsheng Chen. "Nanocomposite reverse electrodialysis (RED) ion-exchange membranes for salinity gradient power generation". In: *Journal of Membrane Science* 460 (June 2014), pp. 139–147. ISSN: 18733123. DOI: 10.1016/j.memsci.2014.02.027. URL: https://www.sciencedirect.com/science/article/pii/S0376738814001501.

[48] Seoyoon Lee, Mun Sik Shin, and Jin Soo Park. "Anion-conducting Pore-filling Membranes with Optimization of Transport Number and Resistance for Reverse Electrodialysis". In: *Chemistry Letters* 43.5 (May 2014), pp. 621–623. ISSN: 0366-7022. DOI: 10.1246/CL.131221. URL: https://dx.doi.org/10.1246/cl.131221.

[49] Ju Young Lee et al. "Morphologically Aligned Cation-Exchange Membranes by a Pulsed Electric Field for Reverse Electrodialysis". In: *Environmental Science and Technology* 49.14 (July 2015), pp. 8872–8877. ISSN: 15205851. DOI: 10.1021/ACS.EST.5B01151/ASSET/IMAGES/LARGE/ES-2015-01151X_0006.JPEG. URL: /doi/pdf/10.1021/acs.est.5b01151.

[50] Weipeng Chen et al. "Polymer-based membranes for promoting osmotic energy conversion". In: *Giant* 10 (June 2022), p. 100094. ISSN: 2666-5425. DOI: 10.1016/J.GIANT.2022.100094. URL: https://www.sciencedirect.com/science/article/pii/S2666542522000054?via%7B%5C%%7D3Dihub.

[51] Alessandro Siria et al. "Giant osmotic energy conversion measured in a single transmembrane boron nitride nanotube". In: *Nature* 494.7438 (Feb. 2013), pp. 455–458. ISSN: 00280836. DOI: 10.1038/NATURE11876;SUBJMETA=119,639,766;KWRD=CONDENSED-MATTER+PHYSICS. URL: https://www.nature.com/articles/nature11876.

[52] Wei Guo et al. "Energy harvesting with single-ion-selective nanopores: A concentration-gradient-driven nanofluidic power source". In: *Advanced Functional Materials* 20.8 (Apr. 2010), pp. 1339–1344. ISSN: 1616301X. DOI: 10.1002/ADFM.200902312;WGROUP:STRING:PUBLICATION. URL: /doi/pdf/10.1002/adfm.200902312%20https://onlinelibrary.wiley.com/doi/abs/10.1002/adfm.200902312%20https://advanced.onlinelibrary.wiley.com/doi/10.1002/adfm.200902312.

[53] Dong Kwon Kim et al. "Power generation from concentration gradient by reverse electrodialysis in ion-selective nanochannels". In: *Microfluidics and Nanofluidics* 9.6 (Dec. 2010), pp. 1215–1224. ISSN: 16134982. DOI: 10.1007/S10404-010-0641-0/TABLES/3. URL: https://link.springer.com/article/10.1007/s10404-010-0641-0.

[54] Juwan Kim, Sung Jin Kim, and Dong Kwon Kim. "Energy harvesting from salinity gradient by reverse electrodialysis with anodic alumina nanopores". In: *Energy* 51 (Mar. 2013), pp. 413–421. ISSN: 0360-5442. DOI: 10.1016/J.ENERGY.2013.01.019. URL: https://www.sciencedirect.com/science/article/abs/pii/S0360544213000388.

[55] Zhen Zhang et al. "Engineered Asymmetric Heterogeneous Membrane: A Concentration-Gradient-Driven Energy Harvesting Device". In: *Journal of the American Chemical Society* 137.46 (Nov. 2015), pp. 14765–14772. ISSN: 15205126. DOI: 10.1021/JACS.5B09918/SUPPL_FILE/JA5B09918_SI_001.PDF. URL: /doi/pdf/10.1021/jacs.5b09918.

[56] Tsung Chen Tsai, Chia Wei Liu, and Ruey Jen Yang. "Power Generation by Reverse Electrodialysis in a Microfluidic Device with a Nafion Ion-Selective Membrane". In: *Micromachines 2016, Vol. 7, Page 205* 7.11 (Nov. 2016), p. 205. ISSN: 2072-666X. DOI: 10.3390/MI7110205. URL: https://www.mdpi.com/2072-666X/7/11/205/htm%20https://www.mdpi.com/2072-666X/7/11/205.

[57] Xin Tong et al. "Nanofluidic Membranes to Address the Challenges of Salinity Gradient Power Harvesting". In: *ACS Nano* 15.4 (Apr. 2021), pp. 5838–5860. ISSN: 1936086X. DOI: 10.1021/ACSNANO.0C09513/SUPPL_FILE/NN0C09513_SI_001.PDF. URL: /doi/pdf/10.1021/acsnano.0c09513.

[58] Van Phung Mai, Wei Hao Huang, and Ruey Jen Yang. "Enhancing Ion Transport through Nanopores in Membranes for Salinity Gradient Power Generation". In: *ACS ES and T Engineering* 1.12 (Dec. 2021), pp. 1725–1752. ISSN: 26900645. DOI: 10.1021/ACSESTENGG.1C00309/ASSET/IMAGES/MEDIUM/EE1C00309_0018.GIF. URL: /doi/pdf/10.1021/acsestengg.1c00309.

[59] Li Wang et al. "Nanopore-Based Power Generation from Salinity Gradient: Why It Is Not Viable". In: *ACS Nano* 15.3 (Mar. 2021), pp. 4093–4107. ISSN: 1936086X. DOI: 10.1021/ACSNANO.0C08628/ASSET/IMAGES/MEDIUM/NN0C08628_M046.GIF. URL: /doi/pdf/10.1021/acsnano.0c08628.

[60] Zhangxin Wang, Li Wang, and Menachem Elimelech. "Viability of Harvesting Salinity Gradient (Blue) Energy by Nanopore-Based Osmotic Power Generation". In: *Engineering* 9 (Feb. 2022), pp. 51–60. ISSN: 2095-8099. DOI: 10.1016/J.ENG.2021.02.016. URL: https://www.sciencedirect.com/science/article/pii/S2095809921001697?via%7B%5C%%7D3Dihub.

[61] Michal Macha et al. "2D materials as an emerging platform for nanopore-based power generation". In: *Nature Reviews Materials* 4.9 (Sept. 2019), pp. 588–605. ISSN: 20588437. DOI: 10.1038/S41578-019-0126-Z;SUBJMETA=1013,1018,299,301,357,639,925;KWRD=POROUS+MATERIALS,TWO-DIMENSIONAL+MATERIALS. URL: https://www.nature.com/articles/s41578-019-0126-z.

[62] Suzanne Lee, Susan Ayers, and Des Holden. "Risk perception and choice of place of birth in women with high risk pregnancies: A qualitative study". In: *Midwifery* 38 (July 2016), pp. 49–54. ISSN: 0266-6138. DOI: 10.1016/J.MIDW.2016.03.008. URL: https://www.sciencedirect.com/science/article/abs/pii/S0266613816300122.

[63] Khadija Yazda et al. "High Osmotic Power Generation via Nanopore Arrays in Hybrid Hexagonal Boron Nitride/Silicon Nitride Membranes". In: *Cite This: Nano Lett* 21 (2021), pp. 4152–4159. DOI: 10.1021/acs.nanolett.0c04704. URL: https://doi.org/10.1021/acs.nanolett.0c04704.

[64] Jianjian Su et al. "Anomalous Pore-Density Dependence in Nanofluidic Osmotic Power Generation". In: *Chinese Journal of Chemistry* 36.5 (May 2018), pp. 417–420. ISSN: 16147065. DOI: 10.1002/CJOC.201800067;REQUESTEDJOURNAL:JOURNAL:16147065;CTYPE:STRING:JOURNAL. URL:

/doi/pdf/10.1002/cjoc.201800067%20https://onlinelibrary.wiley.com/doi/abs/10.1002/cjoc.201800067%20https://onlinelibrary.wiley.com/doi/10.1002/cjoc.201800067.

[65] Yunhyun Lee, Hyun Jung Kim, and Dong Kwon Kim. "Power Generation from Concentration Gradient by Reverse Electrodialysis in Anisotropic Nanoporous Anodic Aluminum Oxide Membranes". In: *Energies 2020, Vol. 13, Page 904* 13.4 (Feb. 2020), p. 904. ISSN: 1996-1073. DOI: 10.3390/EN13040904. URL: https://www.mdpi.com/1996-1073/13/4/904/htm%20https://www.mdpi.com/1996-1073/13/4/904.

[66] Shuhui Ma et al. "Confined amphipathic ionic-liquid regulated anodic aluminum oxide membranes with adjustable ion selectivity for improved osmotic energy conversion". In: *Journal of Colloid and Interface Science* 653 (Jan. 2024), pp. 1217–1224. ISSN: 0021-9797. DOI: 10.1016/J.JCIS.2023.09.181. URL: https://www.sciencedirect.com/science/article/pii/S0021979723018957.

[67] Liuxuan Cao et al. "Towards understanding the nanofluidic reverse electrodialysis system: well matched charge selectivity and ionic composition". In: *Energy & Environmental Science* 4.6 (June 2011), pp. 2259–2266. ISSN: 1754-5706. DOI: 10.1039/C1EE01088C. URL: https://pubs.rsc.org/en/content/articlehtml/2011/ee/c1ee01088c%20https://pubs.rsc.org/en/content/articlelanding/2011/ee/c1ee01088c.

[68] Jyh Ping Hsu et al. "Power generation from a pH-regulated nanochannel through reverse electrodialysis: Effects of nanochannel shape and nonuniform H+ distribution". In: *Electrochimica Acta* 294 (Jan. 2019), pp. 84–92. ISSN: 0013-4686. DOI: 10.1016/J.ELECTACTA.2018.10.074. URL: https://www.sciencedirect.com/science/article/pii/S0013468618323132?via%7B%5C%%7D3Dihub.

[69] Javier Cervera et al. "Asymmetric nanopore rectification for ion pumping, electrical power generation, and information processing applications". In: *Electrochimica Acta* 56.12 (Apr. 2011), pp. 4504–4511. ISSN: 0013-4686. DOI: 10.1016/J.ELECTACTA.2011.02.056. URL: https://www.sciencedirect.com/science/article/pii/S0013468611002714?via%7B%5C%%7D3Dihub.

[70] Shan Zhou et al. "Interfacial Super-Assembly of Ordered Mesoporous Carbon-Silica/AAO Hybrid Membrane with Enhanced Permselectivity for Temperature- and pH-Sensitive Smart Ion Transport". In: *Angewandte Chemie - International Edition* 60.50 (Dec. 2021), pp. 26167–26176. ISSN: 15213773. DOI: 10.1002/ANIE.202110731.

[71] Huijie Wang et al. "In Situ Synthesized HOF Ion Rectification Membrane with Ultrahigh Permselectivity for Nanofluidic Osmotic Energy Harvesting". In: *Advanced Functional Materials* (Jan. 2024). ISSN: 16163028. DOI: 10.1002/ADFM.202412477.

[72] Mengyuan Chen et al. "In Situ Growth of Imine-Bridged Anion-Selective COF/AAO Membrane for Ion Current Rectification and Nanofluidic Osmotic Energy Conversion". In: *Advanced Functional Materials* 33.36 (Sept. 2023). ISSN: 16163028. DOI: 10.1002/ADFM.202302427.

[73] Chin An Ku et al. "Advances in the Fabrication of Nanoporous Anodic Aluminum Oxide and Its Applications to Sensors: A Review". In: *Nanomaterials* 13.21 (Nov. 2023). ISSN: 20794991. DOI: 10.3390/NANO13212853,. URL: https://pubmed.ncbi.nlm.nih.gov/37947698/%20https://pubmed.ncbi.nlm.nih.gov/37947698/?utm%7B%5C_%7Dsource=chatgpt.com.

[74] Gibson P. Scisco et al. "Single step bonding of thick anodized aluminum oxide templates to silicon wafers for enhanced system-on-a-chip performance". In: *Journal of Power Sources* 474 (Oct. 2020), p. 228643. ISSN: 0378-7753. DOI: 10.1016/J.JPOWSOUR.2020.228643. URL: https://www.sciencedirect.com/science/article/abs/pii/S0378775320309472.

[75] Thelese R.B. Foong, Alan Sellinger, and Xiao Hu. "Origin of the Bottlenecks in Preparing Anodized Aluminum Oxide (AAO) Templates on ITO Glass". In: *ACS Nano* 2.11 (Nov. 2008), pp. 2250–2256. ISSN: 19360851. DOI: 10.1021/NN800435N. URL: https://pubs.acs.org/doi/abs/10.1021/nn800435n.

[76] Bumjin Jang et al. "Silicon-supported aluminum oxide membranes with ultrahigh aspect ratio nanopores". In: *RSC Advances* 5.114 (Nov. 2015), pp. 94283–94289. ISSN: 2046-2069. DOI: 10.1039/C5RA20170E. URL: https://pubs.rsc.org/en/content/articlehtml/2015/ra/c5ra20170e%20https://pubs.rsc.org/en/content/articlelanding/2015/ra/c5ra20170e.

[77] Hatice Ulku Osmanbeyoglu, Tae Bong Hur, and Hong Koo Kim. "Thin alumina nanoporous membranes for similar size biomolecule separation". In: *Journal of Membrane Science* 343.1-2 (Nov. 2009), pp. 1–6. ISSN: 0376-7388. DOI: 10.1016/J.MEMSCI.2009.07.027. URL: https://www.sciencedirect.com/science/article/pii/S0376738809005493%7B%5C#%7Dfig1.

[78] Chanyoung Jeong et al. "Control of the Nanopore Architecture of Anodic Alumina via Stepwise Anodization with Voltage Modulation and Pore Widening". In: *Nanomaterials* 13.2 (Jan. 2023), p. 342. ISSN: 20794991.

DOI: 10.3390/NANO13020342. URL: https://pmc.ncbi.nlm.nih.gov/articles/PMC9863362/.

[79] Roselien Vercauteren et al. "Porous silicon membranes and their applications: Recent advances". In: *Sensors and Actuators A: Physical* 318 (Feb. 2021), p. 112486. ISSN: 0924-4247. DOI: 10.1016/J.SNA.2020.112486. URL: https://www.sciencedirect.com/science/article/pii/S092442472031801X?via%7B%5C%%7D3Dihub.

[80] Michael J. Sailor. *Porous Silicon in Practice: Preparation, Characterization and Applications*. Wiley-VCH, 2012, p. 249. ISBN: 9783527313785. DOI: 10.1002/9783527641901. URL: https://www.wiley.com/en-be/Porous+Silicon+in+Practice:+Preparation,+Characterization+and+Applications-p-9783527313785.

[81] Allen J. Bard and Larry R. Faulkner. *ELECTROCHEMICAL METHODS Fundamentals and Applications*. 2nd. Wiley, 2001.

[82] Karen E. Thomas-Alyea John Newman. *Electrochemical systems*. 3rd. Wiley-Interscience, 2004.

[83] D. J. G. Ives, G. J. Janz, and C. V. King. "Reference Electrodes: Theory and Practice". In: *Journal of The Electrochemical Society* 108.11 (1961), p. 246C. ISSN: 00134651. DOI: 10.1149/1.2427957/PDF.

[84] Arthur Kenneth Covington. "Ion selective electrode method". In: *Ion Selective Electrode Method* 2 (Jan. 1979), pp. 1–129. DOI: 10.1201/9781351073875/ION-SELECTIVE-ELECTRODE-METHOD-COVINGTON/RIGHTS-AND-PERMISSIONS. URL: https://www.taylorfrancis.com/books/mono/10.1201/9781351073875/ion-selective-electrode-method-covington.

[85] Michele Tedesco et al. "Performance of the first reverse electrodialysis pilot plant for power production from saline waters and concentrated brines". In: *Journal of Membrane Science* 500 (Feb. 2016), pp. 33–45. ISSN: 18733123. DOI: 10.1016/j.memsci.2015.10.057. URL: https://www.sciencedirect.com/science/article/pii/S0376738815302878.

[86] Nur Hidayati Othman, Nalan Kabay, and Enver Guler. "Principles of reverse electrodialysis and development of integrated-based system for power generation and water treatment: a review". In: *Reviews in Chemical Engineering* 38.8 (Nov. 2022), pp. 921–958. ISSN: 01678299. DOI: 10.1515/REVCE-2020-0070/MACHINEREADABLECITATION/RIS. URL: https://www.degruyterbrill.com/document/doi/10.1515/revce-2020-0070/html?srsltid=AfmBOorSAIHxDr3PKYD22tC7ojcFv6G8AtPhtDdc-wivar58Ye%7B%5C_%7Dfsuur.

[87] Ksenia Solonchenko, Anna Kirichenko, and Ksenia Kirichenko. "Stability of Ion Exchange Membranes in Electrodialysis". In: *Membranes* 13.1 (Jan. 2022), p. 52. ISSN: 20770375. DOI: 10.3390/MEMBRANES13010052. URL: https://pmc.ncbi.nlm.nih.gov/articles/PMC9866250/.

[88] Piotr Długołecki et al. "On the resistances of membrane, diffusion boundary layer and double layer in ion exchange membrane transport". In: *Journal of Membrane Science* 349.1-2 (Mar. 2010), pp. 369–379. ISSN: 03767388. DOI: 10.1016/j.memsci.2009.11.069. URL: https://www.sciencedirect.com/science/article/pii/S0376738809008849.

[89] Victor V. Nikonenko and Anton E. Kozmai. "Electrical equivalent circuit of an ion-exchange membrane system". In: *Electrochimica Acta* 56.3 (Jan. 2011), pp. 1262–1269. ISSN: 00134686. DOI: 10.1016/j.electacta.2010.10.094. URL: https://www.sciencedirect.com/science/article/pii/S0013468610015057.

[90] Insoo Choi et al. "Experimental Investigation of Operating Parameters in Power Generation by Lab-Scale Reverse Electro-Dialysis (RED)". In: *Bulletin of the Korean Chemical Society* 37.7 (July 2016), pp. 1010–1019. ISSN: 1229-5949. DOI: 10.1002/BKCS.10810. URL: /doi/pdf/10.1002/bkcs.10810%20https://onlinelibrary.wiley.com/doi/abs/10.1002/bkcs.10810%20https://onlinelibrary.wiley.com/doi/10.1002/bkcs.10810.

[91] Diego Pintossi et al. "Electrochemical impedance spectroscopy of a reverse electrodialysis stack: A new approach to monitoring fouling and cleaning". In: *Journal of Power Sources* 444 (Dec. 2019), p. 227302. ISSN: 0378-7753. DOI: 10.1016/J.JPOWSOUR.2019.227302. URL: https://www.sciencedirect.com/science/article/pii/S0378775319312959.

[92] Yunjin Lee et al. "Membranes, Synthetic, Applications". In: *Proceedings - Pacific Conference on Computer Graphics and Applications* (Jan. 2003), pp. 279–344. ISSN: 15504085. DOI: 10.1016/B0-12-227410-5/00419-1. URL: https://www.sciencedirect.com/science/article/abs/pii/B0122274105004191.

[93] Y. Tanaka. "Chapter 4 Theory of Teorell, Meyer and Sievers (TMS Theory)". In: *Membrane Science and Technology* 12 (Jan. 2007), pp. 59–66. ISSN: 0927-5193. DOI: 10.1016/S0927-5193(07)12004-0. URL: https://www.sciencedirect.com/science/article/abs/pii/S0927519307120040.

[94] Wenyao Zhang et al. "An extended Teorell-Meyer-Sievers theory for membrane potential under non-isothermal conditions". In: *Journal of Membrane Science* 643 (Mar. 2022), p. 120073. ISSN: 0376-7388. DOI: 10.1016/J.

MEMSCI.2021.120073. URL: https://www.sciencedirect.com/science/article/pii/S0376738821010139.

[95] *Table of Diffusion Coefficients*. URL: https://www.aqion.de/site/diffusion-coefficients (visited on 11/11/2025).

[96] Peter G. Bruce, Martin T. Hardgrave, and Colin A. Vincent. "The determination of transference numbers in solid polymer electrolytes using the Hittorf method". In: *Solid State Ionics* 53-56.PART 2 (July 1992), pp. 1087–1094. ISSN: 0167-2738. DOI: 10.1016/0167-2738(92)90295-Z. URL: https://www.sciencedirect.com/science/article/abs/pii/0167273892902952.

[97] Kayo Santana Barros et al. "Investigation of ion-exchange membranes by means of chronopotentiometry: A comprehensive review on this highly informative and multipurpose technique". In: *Advances in Colloid and Interface Science* 293 (July 2021). ISSN: 00018686. DOI: 10.1016/j.cis.2021.102439. URL: https://pubmed.ncbi.nlm.nih.gov/34058435/.

[98] Isaak Rubinstein. "Electro-Diffusion of Ions". In: *Electro-Diffusion of Ions* (Jan. 1990). DOI: 10.1137/1.9781611970814.

[99] Alexandra Höltzel and Ulrich Tallarek. *Ionic conductance of nanopores in microscale analysis systems: Where microfluidics meets nanofluidics*. July 2007. DOI: 10.1002/jssc.200600427. URL: http://www.ncbi.nlm.nih.gov/pubmed/17623420%20http://doi.wiley.com/10.1002/jssc.200600427.

[100] Ying Mei and Chuyang Y. Tang. "Recent developments and future perspectives of reverse electrodialysis technology: A review". In: *Desalination* 425 (Jan. 2018), pp. 156–174. ISSN: 0011-9164. DOI: 10.1016/J.DESAL.2017.10.021. URL: https://www.sciencedirect.com/science/article/pii/S001191641731977X?via%7B%5C%%7D3Dihub.

[101] Taha Furkan Gül et al. "Review on reverse electrodialysis process-a pioneering technology for energy generation by salinity gradient". In: *Frontiers in Membrane Science and Technology* 3 (Aug. 2024), p. 1414721. ISSN: 2813-1010. DOI: 10.3389/FRMST.2024.1414721.

[102] Muhammad A. Shehzad et al. "A Review of Nanostructured Ion-Exchange Membranes". In: *Advanced Materials Technologies* 6.10 (Oct. 2021), p. 2001171. ISSN: 2365-709X. DOI: 10.1002/ADMT.202001171. URL: /doi/pdf/10.1002/admt.202001171%20https://onlinelibrary.wiley.com/doi/abs/10.1002/admt.202001171%20https://advanced.onlinelibrary.wiley.com/doi/10.1002/admt.202001171.

[103] B. Zaltzman and I. Rubinstein. "Electro-osmotic slip and electroconvective instability". In: *Journal of Fluid Mechanics* 579 (May 2007), pp. 173–226. ISSN: 1469-7645. DOI: 10.1017/S0022112007004880. URL: https://www.cambridge.org/core/journals/journal-of-fluid-mechanics/article/abs/electroosmotic-slip-and-electroconvective-instability/7946A81E29012E0379D08239AF109933.

[104] A. Campione et al. "Electrodialysis for water desalination: A critical assessment of recent developments on process fundamentals, models and applications". In: *Desalination* 434 (May 2018), pp. 121–160. ISSN: 0011-9164. DOI: 10.1016/J.DESAL.2017.12.044. URL: https://www.sciencedirect.com/science/article/pii/S0011916417321604?via%7B%5C%%7D3Dihub.

[105] Muhammad Nidzhom Zainol Abidin, Mohamed Mahmoud Nasef, and Joost Veerman. "Towards the development of new generation of ion exchange membranes for reverse electrodialysis: A review". In: *Desalination* 537 (Sept. 2022), p. 115854. ISSN: 0011-9164. DOI: 10.1016/J.DESAL.2022.115854. URL: https://www.sciencedirect.com/science/article/abs/pii/S0011916422003095?via%7B%5C%%7D3Dihub.

[106] Alaaeldin A.E. Elozeiri et al. "Water content of ion-exchange membranes: Measurement technique and influence on the ion mobility". In: *Journal of Membrane Science* 698 (Apr. 2024), p. 122538. ISSN: 0376-7388. DOI: 10.1016/J.MEMSCI.2024.122538. URL: https://www.sciencedirect.com/science/article/pii/S0376738824001327.

[107] David Kitto and Jovan Kamcev. "The need for ion-exchange membranes with high charge densities". In: *Journal of Membrane Science* 677 (July 2023), p. 121608. ISSN: 0376-7388. DOI: 10.1016/J.MEMSCI.2023.121608. URL: https://www.sciencedirect.com/science/article/pii/S0376738823002648.

[108] Ahmet H. Avci et al. "Sulfonated polyethersulfone based cation exchange membranes for reverse electrodialysis under high salinity gradients". In: *Journal of Membrane Science* 595 (Feb. 2020), p. 117585. ISSN: 0376-7388. DOI: 10.1016/J.MEMSCI.2019.117585. URL: https://www.sciencedirect.com/science/article/pii/S0376738819314528.

[109] Enver Güler et al. "Performance-determining membrane properties in reverse electrodialysis". In: *Journal of Membrane Science* 446 (Nov. 2013), pp. 266–276. ISSN: 03767388. DOI: 10.1016/j.memsci.2013.06.045. URL: https://www.sciencedirect.com/science/article/pii/S0376738813005383.

[110] Jin Gi Hong and Tae Won Park. "Electrochemical characterizations and reverse electrodialysis performance of hybrid anion exchange membranes for salinity gradient energy". In: *Journal of Electroanalytical Chemistry* 817

(May 2018), pp. 134–140. ISSN: 1572-6657. DOI: 10.1016/J.JELECHEM.2018.04.005. URL: https://www.sciencedirect.com/science/article/pii/S1572665718302510?via%7B%5C%%7D3Dihub.

[111] Ramin Banan Sadeghian et al. "Miniaturized concentration cells for small-scale energy harvesting based on reverse electrodialysis". In: *Applied Physics Letters* 99.17 (Oct. 2011), p. 173702. ISSN: 00036951. DOI: 10.1063/1.3656279. URL: https://www.scopus.com/record/display.uri?eid=2-s2.0-80555145092%7B%5C&%7Dorigin=inward.

[112] E. Yu Safronova et al. "New cation-exchange membranes based on cross-linked sulfonated polystyrene and polyethylene for power generation systems". In: *Journal of Membrane Science* 515 (Oct. 2016), pp. 196–203. ISSN: 0376-7388. DOI: 10.1016/J.MEMSCI.2016.05.006. URL: https://www.sciencedirect.com/science/article/abs/pii/S0376738816303234?via%7B%5C%%7D3Dihub.

[113] Sylwin Pawlowski et al. "Improved fluid mixing and power density in reverse electrodialysis stacks with chevron-profiled membranes". In: *Journal of Membrane Science* 531 (June 2017), pp. 111–121. ISSN: 0376-7388. DOI: 10.1016/J.MEMSCI.2017.03.003. URL: https://www.sciencedirect.com/science/article/pii/S0376738816322918?via%7B%5C%%7D3Dihub.

[114] Fujiang Dong et al. "Cross-linked poly(vinyl alcohol)/sulfosuccinic acid (PVA/SSA) as cation exchange membranes for reverse electrodialysis". In: *Separation and Purification Technology* 267 (July 2021), p. 118629. ISSN: 1383-5866. DOI: 10.1016/J.SEPPUR.2021.118629. URL: https://www.sciencedirect.com/science/article/pii/S1383586621003415?via%7B%5C%%7D3Dihub.

[115] Jin Gi Hong, Shira Glabman, and Yongsheng Chen. "Effect of inorganic filler size on electrochemical performance of nanocomposite cation exchange membranes for salinity gradient power generation". In: *Journal of Membrane Science* 482 (May 2015), pp. 33–41. ISSN: 0376-7388. DOI: 10.1016/J.MEMSCI.2015.02.018. URL: https://www.sciencedirect.com/science/article/pii/S0376738815001313?via%7B%5C%%7D3Dihub.

[116] Heru Susanto et al. "Effects of fly ash loading on the characteristics of PVC-based cation exchange membranes for reverse electrodialysis". In: *International Journal of Technology* 11.3 (July 2020), pp. 544–553. ISSN: 20872100. DOI: 10.14716/IJTECH.V11I3.3773. URL: https://ijtech.eng.ui.ac.id/article/view/3773.

[117] Rahul Singh and Daejoong Kim. "High-Temperature Proton Conduction in Covalent Organic Frameworks Interconnected with Nanochannels for Reverse Electrodialysis". In: *ACS Applied Materials & Interfaces* 13.28 (July 2021), pp. 33437–33448. ISSN: 19448252. DOI: 10.1021/ACSAMI.1C06285. URL: /doi/pdf/10.1021/acsami.1c06285?ref=article%7B%5C_%7DopenPDF.

[118] Jin Gi Hong, Tae Won Park, and Yatin Dhadake. "Property evaluation of custom-made ion exchange membranes for electrochemical performance in reverse electrodialysis application". In: *Journal of Electroanalytical Chemistry* 850 (Oct. 2019), p. 113437. ISSN: 1572-6657. DOI: 10.1016/J.JELECHEM.2019.113437. URL: https://www.sciencedirect.com/science/article/pii/S1572665719307052?via%7B%5C%%7D3Dihub.

[119] Jin Gi Hong and Yongsheng Chen. "Evaluation of electrochemical properties and reverse electrodialysis performance for porous cation exchange membranes with sulfate-functionalized iron oxide". In: *Journal of Membrane Science* 473 (Jan. 2015), pp. 210–217. ISSN: 0376-7388. DOI: 10.1016/J.MEMSCI.2014.09.012. URL: https://www.sciencedirect.com/science/article/pii/S0376738814007054?via%7B%5C%%7D3Dihub.

[120] Syed Abdullah Shah et al. "Modified single-wall carbon nanotube for reducing fouling in perfluorinated membrane-based reverse electrodialysis". In: *International Journal of Hydrogen Energy* 45.55 (Nov. 2020), pp. 30703–30719. ISSN: 0360-3199. DOI: 10.1016/J.IJHYDENE.2020.08.111. URL: https://www.sciencedirect.com/science/article/pii/S0360319920331153?via%7B%5C%%7D3Dihub.

[121] Xin Tong, Bopeng Zhang, and Yongsheng Chen. "Fouling resistant nanocomposite cation exchange membrane with enhanced power generation for reverse electrodialysis". In: *Journal of Membrane Science* 516 (Oct. 2016), pp. 162–171. ISSN: 0376-7388. DOI: 10.1016/J.MEMSCI.2016.05.060. URL: https://www.sciencedirect.com/science/article/pii/S037673881630518X?via%7B%5C%%7D3Dihub.

[122] Han Ki Kim et al. "High power density of reverse electrodialysis with pore-filling ion exchange membranes and a high-open-area spacer". In: *Journal of Materials Chemistry A* 3.31 (July 2015), pp. 16302–16306. ISSN: 20507496. DOI: 10.1039/c5ta03571f. URL: http://xlink.rsc.org/?DOI=C5TA03571F.

[123] Mi Soon Lee et al. "Thin Pore-Filled Ion Exchange Membranes for High Power Density in Reverse Electrodialysis: Effects of Structure on Resistance, Stability, and Ion Selectivity". In: *ChemistrySelect* 2.5 (Feb. 2017), pp. 1974–1978. ISSN: 23656549. DOI: 10.1002/SLCT.201700167;WEBSITE:WEBSITE:CHEMISTRY-EUROPE;ISSUE:ISSUE:DOI. URL: /doi/pdf/10.1002/slct.

201700167%20https://onlinelibrary.wiley.com/doi/abs/10.1002/slct.201700167%20https://chemistry-europe.onlinelibrary.wiley.com/doi/10.1002/slct.201700167.

[124] Seung Cheol Yang et al. "R2R Fabrication of Pore-Filling Cation-Exchange Membranes via One-Time Impregnation and Their Application in Reverse Electrodialysis". In: *ACS Sustainable Chemistry & Engineering* 7.14 (July 2019), pp. 12200–12213. ISSN: 21680485. DOI: 10.1021/ACSSUSCHEMENG.9B01450. URL: /doi/pdf/10.1021/acssuschemeng.9b01450?ref=article%7B%5C_%7DopenPDF.

[125] Hanki Kim et al. "Correlations between properties of pore-filling ion exchange membranes and performance of a reverse electrodialysis stack for high power density". In: *Membranes* 11.8 (Aug. 2021), p. 609. ISSN: 20770375. DOI: 10.3390/MEMBRANES11080609/S1. URL: https://www.mdpi.com/2077-0375/11/8/609/htm%20https://www.mdpi.com/2077-0375/11/8/609.

[126] Seung Cheol Yang et al. "Green fabrication of pore-filling anion exchange membranes using R2R processing". In: *Journal of Membrane Science* 584 (Aug. 2019), pp. 181–190. ISSN: 0376-7388. DOI: 10.1016/J.MEMSCI.2019.04.075. URL: https://www.sciencedirect.com/science/article/pii/S037673881930506X.

[127] Daniel V. Golubenko, Bart Van der Bruggen, and Andrey B. Yaroslavtsev. "Novel anion exchange membrane with low ionic resistance based on chloromethylated/quaternized-grafted polystyrene for energy efficient electromembrane processes". In: *Journal of Applied Polymer Science* 137.19 (May 2020), p. 48656. ISSN: 10974628. DOI: 10.1002/APP.48656;WGROUP:STRING:PUBLICATION. URL: /doi/pdf/10.1002/app.48656%20https://onlinelibrary.wiley.com/doi/abs/10.1002/app.48656%20https://onlinelibrary.wiley.com/doi/10.1002/app.48656.

[128] D. V. Golubenko, B. Van der Bruggen, and A. B. Yaroslavtsev. "Ion exchange membranes based on radiation-induced grafted functionalized polystyrene for high-performance reverse electrodialysis". In: *Journal of Power Sources* 511 (Nov. 2021), p. 230460. ISSN: 0378-7753. DOI: 10.1016/J.JPOWSOUR.2021.230460. URL: https://www.sciencedirect.com/science/article/pii/S0378775321009642?via%7B%5C%%7D3Dihub.

[129] Rachida Bance-Soualhi et al. "Radiation-grafted anion-exchange membranes for reverse electrodialysis: a comparison of N,N,N,N -tetramethylhexane-1,6-diamine crosslinking (amination stage) and divinylbenzene crosslinking (grafting stage)". In: *Journal of Materials Chemistry A* 9.38 (Oct. 2021), pp. 22025–22038. ISSN: 2050-7496. DOI: 10.1039/D1TA05166K. URL: https://pubs.rsc.org/en/content/articlehtml/2021/ta/d1ta05166k%

20https://pubs.rsc.org/en/content/articlelanding/2021/ta/d1ta05166k.

[130] Su Hong Kwak et al. "Densely charged polyelectrolyte-stuffed nanochannel arrays for power generation from salinity gradient". In: *Scientific Reports* 6 (May 2016), p. 26416. ISSN: 20452322. DOI: 10.1038/srep26416. URL: https://www.scopus.com/record/display.uri?eid=2-s2.0-84971016753%7B%5C&%7Dorigin=inward.

[131] Jiyeon Choi et al. "Fabrication of an Anion-Exchange Membrane by Pore-Filling Using Catechol–1,4-Diazabicyclo-[2,2,2]octane Coating and Its Application to Reverse Electrodialysis". In: *Langmuir* 34.37 (Sept. 2018), pp. 10837–10846. ISSN: 15205827. DOI: 10.1021/ACS.LANGMUIR.8B01666. URL: /doi/pdf/10.1021/acs.langmuir.8b01666?ref=article%7B%5C_%7DopenPDF.

[132] Enver Güler et al. "Monovalent-ion-selective membranes for reverse electrodialysis". In: *Journal of Membrane Science* 455 (Apr. 2014), pp. 254–270. ISSN: 0376-7388. DOI: 10.1016/J.MEMSCI.2013.12.054. URL: https://www.sciencedirect.com/science/article/pii/S037673881301017X?via%7B%5C%%7D3Dihub.

[133] Seung Cheol Yang et al. "Fabrication of photocured anion-exchange membranes using water-soluble siloxane resins as cross-linking agents and their application in reverse electrodialysis". In: *Journal of Membrane Science* 573 (Mar. 2019), pp. 544–553. ISSN: 0376-7388. DOI: 10.1016/J.MEMSCI.2018.12.034. URL: https://www.sciencedirect.com/science/article/pii/S0376738818321525.

[134] Richard A. Layton and Thomas M. Adams. *Introductory MEMS: Fabrication and Applications, 2010*. Springer, Jan. 2010. URL: https://scholar.rose-hulman.edu/mechanical%7B%5C_%7Dengineering%7B%5C_%7Dfac/629.

[135] H. Helmholtz. "Ueber einige Gesetze der Vertheilung elektrischer Ströme in körperlichen Leitern mit Anwendung auf die thierisch-elektrischen Versuche". In: *Annalen der Physik* 165.6 (Jan. 1853), pp. 211–233. ISSN: 1521-3889. DOI: 10.1002/ANDP.18531650603. URL: /doi/pdf/10.1002/andp.18531650603%20https://onlinelibrary.wiley.com/doi/abs/10.1002/andp.18531650603%20https://onlinelibrary.wiley.com/doi/10.1002/andp.18531650603.

[136] M. Gouy. "Sur la constitution de la charge électrique à la surface d'un électrolyte". In: *Journal de Physique Théorique et Appliquée* 9.1 (1910), pp. 457–468. ISSN: 0368-3893. DOI: 10.1051/JPHYSTAP:019100090045700. URL: http://dx.doi.org/10.1051/jphystap:019100090045700.

[137] David Leonard Chapman. "LI. A contribution to the theory of electrocapillarity". In: *The London, Edinburgh, and Dublin Philosophical Magazine and Journal of Science* 25.148 (Apr. 1913), pp. 475–481. ISSN: 1941-5982. DOI: 10.1080/14786440408634187. URL: https://www.tandfonline.com/doi/abs/10.1080/14786440408634187.

[138] Otto Stern. "ZUR THEORIE DER ELEKTROLYTISCHEN DOPPELSCHICHT". In: *Zeitschrift für Elektrochemie und angewandte physikalische Chemie* 30.21-22 (Nov. 1924), pp. 508–516. ISSN: 0005-9021. DOI: 10.1002/BBPC.192400182. URL: /doi/pdf/10.1002/bbpc.192400182%20https://onlinelibrary.wiley.com/doi/abs/10.1002/bbpc.192400182%20https://onlinelibrary.wiley.com/doi/10.1002/bbpc.192400182.

[139] Jérémie Janssens. "Etude du micro-pompage électro-osmotique de membranes polymères micro-poreuses". MasterThesis. UCL University of Louvain-la-Neuve, 2012.

[140] Johannes Lützenkirchen. "The Constant Capacitance Model and Variable Ionic Strength: An Evaluation of Possible Applications and Applicability". In: *Journal of Colloid and Interface Science* 217.1 (Sept. 1999), pp. 8–18. ISSN: 0021-9797. DOI: 10.1006/JCIS.1999.6348. URL: https://www.sciencedirect.com/science/article/abs/pii/S0021979799963488.

[141] T. Hiemstra and W. H. Van Riemsdijk. "A Surface Structural Approach to Ion Adsorption: The Charge Distribution (CD) Model". In: *Journal of Colloid and Interface Science* 179.2 (May 1996), pp. 488–508. ISSN: 0021-9797. DOI: 10.1006/JCIS.1996.0242. URL: https://www.sciencedirect.com/science/article/abs/pii/S0021979796902428.

[142] P. Leroy and A. Revil. "A triple-layer model of the surface electrochemical properties of clay minerals". In: *Journal of Colloid and Interface Science* 270.2 (Feb. 2004), pp. 371–380. ISSN: 0021-9797. DOI: 10.1016/J.JCIS.2003.08.007. URL: https://www.sciencedirect.com/science/article/abs/pii/S0021979703008117.

[143] Ezat Keshavarzi and Fatemeh Dehghan Safiabad. "Surface Charge Regulation on the Concave Wall of a Spherical Silica Pore, Impact of the EDL Overlap, Potential Drop in the Stern Region, and Deviation from the Electroneutrality Principle". In: *Journal of Physical Chemistry C* 128.22 (June 2024), pp. 9256–9269. ISSN: 19327455. DOI: 10.1021/ACS.JPCC.4C00410/ASSET/IMAGES/LARGE/JP4C00410_0013.JPEG. URL: /doi/pdf/10.1021/acs.jpcc.4c00410?ref=article%7B%5C_%7DopenPDF.

[144] Thiago Colla, Lucas Nunes Lopes, and Alexandre P. Dos Santos. "Ionic size effects on the Poisson-Boltzmann theory". In: *Journal of Chemical Physics* 147.1 (July 2017). ISSN: 00219606. DOI: 10.1063/1.4990737/594473. arXiv: 1708.08584. URL: /aip/jcp/article/147/1/014104/594473/Ionic-size-effects-on-the-Poisson-Boltzmann-theory.

[145] Giacomo Bruno et al. "Unexpected behaviors in molecular transport through size-controlled nanochannels down to the ultra-nanoscale". In: *Nature Communications* 9.1 (Dec. 2018), p. 1682. ISSN: 20411723. DOI: 10.1038/S41467-018-04133-8. URL: https://pmc.ncbi.nlm.nih.gov/articles/PMC5923292/.

[146] Alexander H. Boschitsch and Pavel V. Danilov. "Formulation of a New and Simple Non-Uniform Size-Modified Poisson-Boltzmann Description". In: *Journal of Computational Chemistry* 33.11 (Apr. 2012), p. 1152. ISSN: 01928651. DOI: 10.1002/JCC.22946. URL: https://pmc.ncbi.nlm.nih.gov/articles/PMC3306476/.

[147] Sayantan Mondal and Biman Bagchi. "How different are the dynamics of nanoconfined water?" In: *The Journal of chemical physics* 152.22 (June 2020), p. 224707. ISSN: 10897690. DOI: 10.1063/5.0010613/1062028. URL: /aip/jcp/article/152/22/224707/1062028/How-different-are-the-dynamics-of-nanoconfined.

[148] Felipe Mourão Coelho and Luís Fernando Mercier Franco. "The Interplay between Dynamics and Structure on the Dielectric Tensor of Nanoconfined Water: Surface Charge and Salinity Effect". In: *Journal of Physical Chemistry B* 128.47 (Nov. 2024), p. 11759. ISSN: 15205207. DOI: 10.1021/ACS.JPCB.4C05803/SUPPL_FILE/JP4C05803_SI_001.PDF. URL: https://pmc.ncbi.nlm.nih.gov/articles/PMC11613631/.

[149] Jinbo Peng et al. "Water-solid interfaces probed by high-resolution atomic force microscopy". In: *Surface Science Reports* 77.1 (Mar. 2022), p. 100549. ISSN: 0167-5729. DOI: 10.1016/J.SURFREP.2021.100549. URL: https://www.sciencedirect.com/science/article/pii/S0167572921000340.

[150] J. Israelachvili et al. "Recent advances in the surface forces apparatus (SFA) technique". In: *Reports on Progress in Physics* 73.3 (Jan. 2010), p. 036601. ISSN: 0034-4885. DOI: 10.1088/0034-4885/73/3/036601. URL: https://iopscience.iop.org/article/10.1088/0034-4885/73/3/036601%20https://iopscience.iop.org/article/10.1088/0034-4885/73/3/036601/meta.

[151] L. Fumagalli et al. “Anomalously low dielectric constant of confined water”. In: *Science* 360.6395 (June 2018), pp. 1339–1342. ISSN: 10959203. DOI: 10.1126/SCIENCE.AAT4191/SUPPL_FILE/AAT4191_FUMAGALLI_SM.PDF. URL: /doi/pdf/10.1126/science.aat4191.

[152] T. Dufils et al. “Origin of dielectric polarization suppression in confined water from first principles”. In: *Chemical Science* 15.2 (Jan. 2024), pp. 516–527. ISSN: 20416539. DOI: 10.1039/D3SC04740G. URL: https://pubs.rsc.org/en/content/articlehtml/2024/sc/d3sc04740g%20https://pubs.rsc.org/en/content/articlelanding/2024/sc/d3sc04740g.

[153] Jon Zubeltzu et al. “Redefining the dielectric response of nanoconfined liquids: insights from water”. In: (Mar. 2025). arXiv: 2412.01347v1. URL: http://arxiv.org/abs/2412.01347.

[154] Jean François Olivieri, James T. Hynes, and Damien Laage. “Confined water’s dielectric constant reduction is due to the surrounding low dielectric media and not to interfacial molecular ordering”. In: *Journal of Physical Chemistry Letters* 12.17 (May 2021), pp. 4319–4326. ISSN: 19487185. DOI: 10.1021/ACS.JPCLETT.1C00447/SUPPL_FILE/JZ1C00447_SI_001.PDF. URL: https://pubs.acs.org/doi/abs/10.1021/acs.jpclett.1c00447.

[155] Ben Corry, Serdar Kuyucak, and Shin Ho Chung. “Dielectric Self-Energy in Poisson-Boltzmann and Poisson-Nernst-Planck Models of Ion Channels”. In: *Biophysical Journal* 84.6 (June 2003), pp. 3594–3606. ISSN: 0006-3495. DOI: 10.1016/S0006-3495(03)75091-7. URL: https://www.sciencedirect.com/science/article/pii/S0006349503750917?utm%7B%5C_%7Dsource=chatgpt.com.

[156] Itamar Borukhov, David Andelman, and Henri Orland. “Steric Effects in Electrolytes: A Modified Poisson-Boltzmann Equation”. In: *Physical Review Letters* 79.3 (July 1997), p. 435. ISSN: 10797114. DOI: 10.1103/PhysRevLett.79.435. arXiv: 9803258 [cond-mat]. URL: https://journals.aps.org/prl/abstract/10.1103/PhysRevLett.79.435.

[157] P. M. Biesheuvel and M. Z. Bazant. “Nonlinear dynamics of capacitive charging and desalination by porous electrodes”. In: *Physical Review E* 81.3 (Mar. 2010), p. 031502. ISSN: 15393755. DOI: 10.1103/PhysRevE.81.031502. URL: https://journals.aps.org/pre/abstract/10.1103/PhysRevE.81.031502.

[158] Alexander Schlaich, Ernst W. Knapp, and Roland R. Netz. “Water Dielectric Effects in Planar Confinement”. In: *Physical Review Letters* 117.4 (July 2016), p. 048001. ISSN: 10797114. DOI: 10.1103/PHYSREVLETT.117.048001/FIGURES/5/THUMBNAIL. URL: https://journals.aps.org/prl/abstract/10.1103/PhysRevLett.117.048001.

[159] *Electrophoresis of solid particles at large Peclet numbers | Request PDF*. URL: https://www.researchgate.net/publication/11179249%7B%5C_%7DElectrophoresis%7B%5C_%7Dof%7B%5C_%7Dsolid%7B%5C_%7Dparticles%7B%5C_%7Dat%7B%5C_%7Dlarge%7B%5C_%7DPeclet%7B%5C_%7Dnumbers (visited on 10/02/2025).

[160] Martin Z. Bazant, Katsuyo Thornton, and Armand Ajdari. "Diffuse-charge dynamics in electrochemical systems". In: *Physical Review E* 70.2 (Aug. 2004), p. 021506. ISSN: 1063651X. DOI: 10.1103/PhysRevE.70.021506. arXiv: 0401118 [cond-mat]. URL: https://journals.aps.org/pre/abstract/10.1103/PhysRevE.70.021506.

[161] Reto B. Schoch, Jongyoon Han, and Philippe Renaud. "Transport phenomena in nanofluidics". In: *Reviews of Modern Physics* 80.3 (July 2008), pp. 839–883. ISSN: 00346861. DOI: 10.1103/REVMODPHYS.80.839/FIGURES/33/THUMBNAIL. URL: https://journals.aps.org/rmp/abstract/10.1103/RevModPhys.80.839.

[162] Sébastien Balme et al. "Ionic transport through sub-10 nm diameter hydrophobic high-aspect ratio nanopores: experiment, theory and simulation". In: *Scientific Reports* 5 (June 2015). DOI: 10.1038/srep10135. arXiv: 1506.03568v1. URL: http://arxiv.org/abs/1506.03568%20http://dx.doi.org/10.1038/srep10135.

[163] Celso Molina et al. "Streaming potential and surface charge density of microporous membranes with pore diameter in the range of thickness". In: *Journal of Membrane Science* 163.2 (Nov. 1999), pp. 239–255. ISSN: 0376-7388. DOI: 10.1016/S0376-7388(99)00162-3. URL: https://www.sciencedirect.com/science/article/abs/pii/S0376738899001623.

[164] Yulia V. Samukhina, Natalia E. Rusakova, and Peter A. Polyakov. "Dependence of surface charge density on curvature of surface of conductive body with complicated shape". In: *Journal of Electrostatics* 125 (Sept. 2023), p. 103844. ISSN: 0304-3886. DOI: 10.1016/J.ELSTAT.2023.103844. URL: https://www.sciencedirect.com/science/article/pii/S0304388623000530.

[165] H. Gokberk Ozcelik and Murat Barisik. "Electric charge of nanopatterned silica surfaces". In: *Physical Chemistry Chemical Physics* 21.14 (Apr. 2019), pp. 7576–7587. ISSN: 1463-9084. DOI: 10.1039/C9CP00706G. URL: https://pubs.rsc.org/en/content/articlehtml/2019/cp/c9cp00706g%20https://pubs.rsc.org/en/content/articlelanding/2019/cp/c9cp00706g.

[166] B. Oyku Alan, Murat Barisik, and H. Gokberk Ozcelik. "Roughness Effects on the Surface Charge Properties of Silica Nanoparticles". In: *Journal of Physical Chemistry C* 124.13 (Apr. 2020), pp. 7274–7286. ISSN: 19327455. DOI: 10.1021/ACS.JPCC.0C00120/ASSET/IMAGES/LARGE/JP0C00120_0007.JPEG. URL: /doi/pdf/10.1021/acs.jpcc.0c00120?ref=article%7B%5C_%7DopenPDF.

[167] Murat Barisik et al. "Size dependent surface charge properties of silica nanoparticles". In: *Journal of Physical Chemistry C* 118.4 (Jan. 2014), pp. 1836–1842. ISSN: 19327447. DOI: 10.1021/JP410536N/ASSET/IMAGES/LARGE/JP-2013-10536N_0010.JPEG. URL: /doi/pdf/10.1021/jp410536n?ref=article%7B%5C_%7DopenPDF.

[168] Li Hsien Yeh, Mingkan Zhang, and Shizhi Qian. "Ion transport in a pH-regulated nanopore". In: *Analytical Chemistry* 85.15 (Aug. 2013), pp. 7527–7534. ISSN: 00032700. DOI: 10.1021/AC401536G/SUPPL_FILE/AC401536G_SI_001.PDF. URL: /doi/pdf/10.1021/ac401536g?ref=article%7B%5C_%7DopenPDF.

[169] Tumcan Sen and Murat Barisik. "Size dependent surface charge properties of silica nano-channels: double layer overlap and inlet/outlet effects". In: *Physical Chemistry Chemical Physics* 20.24 (June 2018), pp. 16719–16728. ISSN: 1463-9084. DOI: 10.1039/C8CP01906A. URL: https://pubs.rsc.org/en/content/articlehtml/2018/cp/c8cp01906a%20https://pubs.rsc.org/en/content/articlelanding/2018/cp/c8cp01906a.

[170] Selcuk Atalay et al. "Surface charge of a nanoparticle interacting with a flat substrate". In: *Journal of Physical Chemistry C* 118.20 (May 2014), pp. 10927–10935. ISSN: 19327455. DOI: 10.1021/JP5023554/ASSET/IMAGES/LARGE/JP-2014-023554_0007.JPEG. URL: /doi/pdf/10.1021/jp5023554?ref=article%7B%5C_%7DopenPDF.

[171] Yu Ma et al. "pH-Regulated Ionic Conductance in a Nanochannel with Overlapped Electric Double Layers". In: *Analytical Chemistry* 87.8 (Apr. 2015), pp. 4508–4514. ISSN: 15206882. DOI: 10.1021/ACS.ANALCHEM.5B00536. URL: https://pubs.acs.org/doi/abs/10.1021/acs.analchem.5b00536.

[172] Kaushik K. Rangharajan and Shaurya Prakash. "Surface charge regulation mediates anomalous ion transport in silica nanochannels". In: *Analyst* 150.13 (June 2025), pp. 2837–2844. ISSN: 13645528. DOI: 10.1039/D5AN00198F. URL: https://pubs.rsc.org/en/content/articlehtml/2025/an/d5an00198f%20https://pubs.rsc.org/en/content/articlelanding/2025/an/d5an00198f.

[173] Jamie W. Gittins et al. "Understanding Electrolyte Ion Size Effects on the Performance of Conducting Metal–Organic Framework Supercapacitors". In: *Journal of the American Chemical Society* 146.18 (May 2024), pp. 12473–12484. ISSN: 15205126. DOI: 10.1021/JACS.4C00508. URL: /doi/pdf/10.1021/jacs.4c00508?ref=article%7B%5C_%7DopenPDF.

[174] Christian M. Schott et al. "How to Assess and Predict Electrical Double Layer Properties. Implications for Electrocatalysis". In: *Chemical Reviews* 124.22 (Nov. 2024), pp. 12391–12462. ISSN: 15206890. DOI: 10.1021/ACS.CHEMREV.3C00806. URL: /doi/pdf/10.1021/acs.chemrev.3c00806?ref=article%7B%5C_%7DopenPDF.

[175] P. Apel. "Track etching technique in membrane technology". In: *Radiation Measurements* 34.1-6 (June 2001), pp. 559–566. ISSN: 1350-4487. DOI: 10.1016/S1350-4487(01)00228-1. URL: https://www.sciencedirect.com/science/article/pii/S1350448701002281.

[176] Zhiyuan Zeng et al. "Fabrication of Graphene Nanomesh by Using an Anodic Aluminum Oxide Membrane as a Template". In: *Advanced Materials* 24.30 (Aug. 2012), pp. 4138–4142. ISSN: 1521-4095. DOI: 10.1002/ADMA.201104281. URL: /doi/pdf/10.1002/adma.201104281%20https://onlinelibrary.wiley.com/doi/abs/10.1002/adma.201104281%20https://advanced.onlinelibrary.wiley.com/doi/10.1002/adma.201104281.

[177] Rini John et al. "New emerging review on advances in block copolymer based water purification membranes". In: *Journal of Molecular Structure* 1231 (May 2021), p. 129926. ISSN: 0022-2860. DOI: 10.1016/J.MOLSTRUC.2021.129926. URL: https://www.sciencedirect.com/science/article/abs/pii/S0022286021000570.

[178] Yao Zhang et al. "Asymmetric Nanoporous Alumina Membranes for Nanofluidic Osmotic Energy Conversion". In: *Chemistry - An Asian Journal* 18.23 (Dec. 2023). ISSN: 1861471X. DOI: 10.1002/asia.202300876. URL: https://www.scopus.com/pages/publications/85175972206?origin=resultslist.

[179] Khoiruddin et al. "Surface modification of ion-exchange membranes: Methods, characteristics, and performance". In: *Journal of Applied Polymer Science* 134.48 (Dec. 2017), p. 45540. ISSN: 1097-4628. DOI: 10.1002/APP.45540. URL: /doi/pdf/10.1002/app.45540%20https://onlinelibrary.wiley.com/doi/abs/10.1002/app.45540%20https://onlinelibrary.wiley.com/doi/10.1002/app.45540.

[180] Adetunji Alabi et al. "Review of nanomaterials-assisted ion exchange membranes for electromembrane desalination". In: *npj Clean Water* 1.1 (Dec. 2018), pp. 1–22. ISSN: 20597037. DOI: 10.1038/S41545-018-0009-7; SUBJMETA. URL: https://www.nature.com/articles/s41545-018-0009-7.

[181] Francis Kotoka, Ivan Merino-Garcia, and Svetlozar Velizarov. "Surface Modifications of Anion Exchange Membranes for an Improved Reverse Electrodialysis Process Performance: A Review". In: *Membranes 2020, Vol. 10, Page 160* 10.8 (July 2020), p. 160. ISSN: 2077-0375. DOI: 10.3390/MEMBRANES10080160. URL: https://www.mdpi.com/2077-0375/10/8/160/htm%20https://www.mdpi.com/2077-0375/10/8/160.

[182] Prashant Kumar et al. "Surface modification of inter-polymer cation exchange membrane by controlled loading of polyaniline/metal particles for improved electrodialytic performance during mono-/bi-valent ions separation". In: *Journal of Membrane Science* 711 (Nov. 2024), p. 123168. ISSN: 0376-7388. DOI: 10.1016/J.MEMSCI.2024.123168. URL: https://www.sciencedirect.com/science/article/pii/S0376738824007622.

[183] Outi Toikkanen et al. "Al2O3 coating grown on Nafion membranes by atomic layer deposition". In: *Journal of Membrane Science* 495 (Dec. 2015), pp. 101–109. ISSN: 0376-7388. DOI: 10.1016/J.MEMSCI.2015.08.021. URL: https://www.sciencedirect.com/science/article/pii/S0376738815301162.

[184] Eyal Merary Wormser, Oded Nir, and Eran Edri. "Low-resistance monovalent-selective cation exchange membranes prepared using molecular layer deposition for energy-efficient ion separations". In: *RSC Advances* 11.4 (Jan. 2021), pp. 2427–2436. ISSN: 2046-2069. DOI: 10.1039/D0RA08725D. URL: https://www.sciencedirect.com/org/science/article/pii/S2046206921002849.

[185] Sen Xiong et al. "Atomic layer deposition for membrane modification, functionalization and preparation: A review". In: *Journal of Membrane Science* 658 (Sept. 2022), p. 120740. ISSN: 0376-7388. DOI: 10.1016/J.MEMSCI.2022.120740. URL: https://www.sciencedirect.com/science/article/pii/S0376738822004859.

[186] Renqiang Cao et al. "Composite modification of anion exchange membrane by in-situ layer-by-layer assembly to improve antifouling performance". In: *Journal of Membrane Science* 690 (Jan. 2024), p. 122211. ISSN: 0376-7388. DOI: 10.1016/J.MEMSCI.2023.122211. URL: https://www.sciencedirect.com/science/article/pii/S0376738823008670.

[187] Somayyeh Rakhshani et al. “Synthesis and Characterization of a Composite Anion Exchange Membrane for Water Electrolyzers (AEMWE)”. In: *Membranes 2023, Vol. 13, Page 109* 13.1 (Jan. 2023), p. 109. ISSN: 2077-0375. DOI: 10.3390/MEMBRANES13010109. URL: https://www.mdpi.com/2077-0375/13/1/109/htm%20https://www.mdpi.com/2077-0375/13/1/109.

[188] Martyna Charyton et al. “Composite anion exchange membranes fabricated by coating and UV crosslinking of low-cost precursors tested in a redox flow battery”. In: *Polymers* 13.15 (Aug. 2021), p. 2396. ISSN: 20734360. DOI: 10.3390/POLYM13152396/S1. URL: https://www.mdpi.com/2073-4360/13/15/2396/htm%20https://www.mdpi.com/2073-4360/13/15/2396.

[189] Po Yen Chuang and Jyh Ping Hsu. “Influence of shape and charged conditions of nanopores on their ionic current rectification, electroosmotic flow, and selectivity”. In: *Colloids and Surfaces A: Physicochemical and Engineering Aspects* 658 (Feb. 2023), p. 130696. ISSN: 0927-7757. DOI: 10.1016/J.COLSURFA.2022.130696. URL: https://www.sciencedirect.com/science/article/pii/S0927775722024517.

[190] Pavel Yu Apel et al. “Accurate characterization of single track-etched, conical nanopores”. In: *Physical Chemistry Chemical Physics* 16.29 (July 2014), pp. 15214–15223. ISSN: 1463-9084. DOI: 10.1039/C4CP01686F. URL: https://pubs.rsc.org/en/content/articlehtml/2014/cp/c4cp01686f%20https://pubs.rsc.org/en/content/articlelanding/2014/cp/c4cp01686f.

[191] Tianji Ma et al. “Track-Etched Nanopore/Membrane: From Fundamental to Applications”. In: *Small Methods* 4.9 (Sept. 2020), p. 2000366. ISSN: 2366-9608. DOI: 10.1002/SMTD.202000366. URL: /doi/pdf/10.1002/smtd.202000366%20https://onlinelibrary.wiley.com/doi/abs/10.1002/smtd.202000366%20https://onlinelibrary.wiley.com/doi/10.1002/smtd.202000366.

[192] Hung Chun Yeh, Chih Chang Chang, and Ruey Jen Yang. “Reverse electrodialysis in conical-shaped nanopores: Salinity gradient-driven power generation”. In: *RSC Advances* 4.6 (2014), pp. 2705–2714. ISSN: 20462069. DOI: 10.1039/c3ra45392h. URL: http://xlink.rsc.org/?DOI=C3RA45392H.

[193] Kilsung Kwon et al. “Energy harvesting system using reverse electrodialysis with nanoporous polycarbonate track-etch membranes”. In: *International Journal of Energy Research* 38.4 (Mar. 2014), pp. 530–537. ISSN: 1099-114X. DOI: 10.1002/ER.3111. URL: /doi/pdf/10.1002/er.3111%20https://onlinelibrary.wiley.com/doi/abs/10.1002/er.3111%20https://onlinelibrary.wiley.com/doi/10.1002/er.3111.

[194] Qing Yun Wu et al. "Salinity-Gradient Power Generation with Ionized Wood Membranes". In: *Advanced Energy Materials* 10.1 (Jan. 2020), p. 1902590. ISSN: 16146840. DOI: 10.1002/AENM.201902590;JOURNAL:JOURNAL:16146840;REQUESTEDJOURNAL:JOURNAL:16146840;WGROUP:STRING:PUBLICATION. URL: /doi/pdf/10.1002/aenm.201902590%20https://onlinelibrary.wiley.com/doi/abs/10.1002/aenm.201902590%20https://advanced.onlinelibrary.wiley.com/doi/10.1002/aenm.201902590.

[195] Zaifu Lin et al. "Biomimetic Salinity Power Generation Based on Silk Fibroin Ion-Exchange Membranes". In: *ACS Nano* 15.3 (Mar. 2021), pp. 5649–5660. ISSN: 1936086X. DOI: 10.1021/ACSNANO.1C00820. URL: /doi/pdf/10.1021/acsnano.1c00820?ref=article%7B%5C_%7DopenPDF.

[196] Qijun Zheng et al. "Two-sided asymmetric nanofluidic membrane for enhanced ion transport and osmotic energy harvesting". In: *Chemical Science* 16.24 (May 2025), pp. 11138–11150. ISSN: 20416539. DOI: 10.1039/d5sc01237f. URL: https://www.scopus.com/pages/publications/105005854814?origin=resultslist.

[197] Sifan Chen et al. "Imparting Ion Selectivity to Covalent Organic Framework Membranes Using de Novo Assembly for Blue Energy Harvesting". In: *Journal of the American Chemical Society* 143.25 (June 2021), pp. 9415–9422. ISSN: 15205126. DOI: 10.1021/JACS.1C02090. URL: /doi/pdf/10.1021/jacs.1c02090?ref=article%7B%5C_%7DopenPDF.

[198] Cheng Chen et al. "Bio-inspired Nanocomposite Membranes for Osmotic Energy Harvesting". In: *Joule* 4.1 (Jan. 2020), pp. 247–261. ISSN: 2542-4351. DOI: 10.1016/J.JOULE.2019.11.010. URL: https://www.sciencedirect.com/science/article/pii/S254243511930577X?via%7B%5C%%7D3Dihub.

[199] Jinzhao Ji et al. "Osmotic Power Generation with Positively and Negatively Charged 2D Nanofluidic Membrane Pairs". In: *Advanced Functional Materials* 27.2 (Jan. 2017), p. 1603623. ISSN: 16163028. DOI: 10.1002/ADFM.201603623;REQUESTEDJOURNAL:JOURNAL:16163028;WGROUP:STRING:PUBLICATION. URL: /doi/pdf/10.1002/adfm.201603623%20https://onlinelibrary.wiley.com/doi/abs/10.1002/adfm.201603623%20https://advanced.onlinelibrary.wiley.com/doi/10.1002/adfm.201603623.

[200] Hao Wang et al. "Blue Energy Conversion from Holey-Graphene-like Membranes with a High Density of Subnanometer Pores". In: *Nano Letters* 20.12 (Dec. 2020), pp. 8634–8639. ISSN: 15306992. DOI: 10.1021/ACS.NANOLETT.0C03342. URL: /doi/pdf/10.1021/acs.nanolett.0c03342?ref=article%7B%5C_%7DopenPDF.

[201] Eunpyo Choi et al. "Tunable reverse electrodialysis microplatform with geometrically controlled self-assembled nanoparticle network". In: *Lab on a Chip* 15.1 (Dec. 2014), pp. 168–178. ISSN: 1473-0189. DOI: 10.1039/C4LC01031K. URL: https://pubs.rsc.org/en/content/articlehtml/2015/lc/c4lc01031k%20https://pubs.rsc.org/en/content/articlelanding/2015/lc/c4lc01031k.

[202] Wei Ouyang et al. "Nanofluidic crystal: a facile, high-efficiency and high-power-density scaling up scheme for energy harvesting based on nanofluidic reverse electrodialysis". In: *Nanotechnology* 24.34 (July 2013), p. 345401. ISSN: 0957-4484. DOI: 10.1088/0957-4484/24/34/345401. URL: https://iopscience.iop.org/article/10.1088/0957-4484/24/34/345401%20https://iopscience.iop.org/article/10.1088/0957-4484/24/34/345401/meta.

[203] Khanh Nhien Vu et al. "Harnessing the Intrinsic Ionic Rectification Properties of Blind-Hole Nanoporous Anodic Alumina for Osmotic Energy Generation". In: *Advanced Functional Materials* 34.29 (July 2024), p. 2400697. ISSN: 16163028. DOI: 10.1002/ADFM.202400697;REQUESTEDJOURNAL:JOURNAL:16163028;WGROUP:STRING:PUBLICATION. URL: /doi/pdf/10.1002/adfm.202400697%20https://onlinelibrary.wiley.com/doi/abs/10.1002/adfm.202400697%20https://advanced.onlinelibrary.wiley.com/doi/10.1002/adfm.202400697.

[204] Sang Woo Lee, Hyun Jung Kim, and Dong Kwon Kim. "Power generation from concentration gradient by reverse electrodialysis in dense silica membranes for microfluidic and nanofluidic systems". In: *Energies* 9.1 (2016). ISSN: 19961073. DOI: 10.3390/EN9010049.

[205] Hyung Kwan Chang, Eunpyo Choi, and Jungyul Park. "Paper-based energy harvesting from salinity gradients". In: *Lab on a Chip* 16.4 (Feb. 2016), pp. 700–708. ISSN: 1473-0189. DOI: 10.1039/C5LC01232E. URL: https://pubs.rsc.org/en/content/articlehtml/2016/lc/c5lc01232e%20https://pubs.rsc.org/en/content/articlelanding/2016/lc/c5lc01232e.

[206] Roselien Vercauteren. "Porous silicon flow-through membrane : application to the optical detection of bacteria from their lysate". PhD thesis. UCLouvain, 2022. URL: https://dial.uclouvain.be/pr/boreal/object/boreal:271063.

[207] G. Barillaro and L. M. Strambini. "An integrated CMOS sensing chip for NO2 detection". In: *Sensors and Actuators B: Chemical* 134.2 (Sept. 2008), pp. 585–590. ISSN: 0925-4005. DOI: 10.1016/J.SNB.2008.05.

044. URL: https://www.sciencedirect.com/science/article/pii/S0925400508004012.

[208] G. Barillaro et al. "Validation of the compatibility between a porous silicon-based gas sensor technology and standard microelectronic process". In: *IEEE Sensors Journal* 10.4 (2010), pp. 893–899. ISSN: 1530437X. DOI: 10.1109/JSEN.2009.2034861. URL: https://www.scopus.com/pages/publications/77949397975.

[209] Marie Capelle et al. "Porous Silicon/Silicon Hybrid Substrate Applied to the Monolithic Integration of Common-Mode and Bandpass RF Filters". In: *IEEE Transactions on Electron Devices* 62.12 (Dec. 2015), pp. 4169–4173. ISSN: 00189383. DOI: 10.1109/TED.2015.2483840. URL: https://www.scopus.com/pages/publications/84959478249.

[210] Marie Capelle et al. "Monolithic integration of low-pass filters with ESD protections on p+ silicon/porous silicon substrates". In: *Solid-State Electronics* 116 (Feb. 2016), pp. 12–14. ISSN: 0038-1101. DOI: 10.1016/J.SSE.2015.11.026. URL: https://www.sciencedirect.com/science/article/pii/S0038110115003457.

[211] Gilles Scheen et al. "Post-process porous silicon for 5G applications". In: *Solid-State Electronics* 168 (June 2020), p. 107719. ISSN: 0038-1101. DOI: 10.1016/J.SSE.2019.107719. URL: https://www.sciencedirect.com/science/article/pii/S0038110119307221.

[212] Gilles Scheen et al. "Homogeneous Backside Porosification of Standard Silicon Wafers for Post-Fab Process Integration of Porous Silicon". In: *Journal of The Electrochemical Society* (July 2025). ISSN: 0013-4651. DOI: 10.1149/1945-7111/ADF66E.

[213] Romain Tuyaerts et al. "Post-fab porous silicon in silicon-on-insulator substrates for improved radio frequencies performances". In: *Materials Science in Semiconductor Processing* 201 (Jan. 2026), p. 110098. ISSN: 1369-8001. DOI: 10.1016/J.MSSP.2025.110098. URL: https://www.sciencedirect.com/science/article/pii/S1369800125008364?utm%7B%5C_%7Dsource=chatgpt.com.

[214] Leigh Canham, ed. *Handbook of Porous Silicon: Second Edition*. Vol. 1-2. Springer International Publishing, July 2018. ISBN: 9783319713816. DOI: 10.1007/978-3-319-71381-6/COVER.

[215] Kurt W. Kolasinski. "Electron transfer during metal-assisted and stain etching of silicon". In: *Semiconductor Science and Technology* 31.1 (Oct. 2015), p. 014002. ISSN: 0268-1242. DOI: 10.1088/0268-1242/31/1/014002. URL: https://iopscience.iop.org/article/10.1088/0268-1242/31/

1/014002%20https://iopscience.iop.org/article/10.1088/0268-1242/31/1/014002/meta.

[216] Gilles Scheen. *Metal electrode integration and Palladium nanoparticule functionalization on a miniaturized macroporous silicon chemiresistor*. 2015. URL: http://hdl.handle.net/2078.1/165078.

[217] Jonathan Rasson. *Stable porous silicon-based optical sensing platform towards detection of bacterial lysis*. Louvain-la-Neuve, 2018. URL: https://dial.uclouvain.be/pr/boreal/fr/object/boreal%7B%5C%%7D3A198385.

[218] "Recommendations for the characterization of porous solids (Technical Report)". In: *Pure and Applied Chemistry* 66.8 (1994), pp. 1739–1758. ISSN: 13653075. DOI: 10.1351/PAC199466081739.

[219] X. G. Zhang. "Morphology and Formation Mechanisms of Porous Silicon". In: *Journal of The Electrochemical Society* 151.1 (Dec. 2003), p. C69. ISSN: 1945-7111. DOI: 10.1149/1.1632477. URL: https://iopscience.iop.org/article/10.1149/1.1632477%20https://iopscience.iop.org/article/10.1149/1.1632477/meta.

[220] Pushpendra Kumar et al. "Effect of HF Concentration on Physical and Electronic Properties of Electrochemically Formed Nanoporous Silicon". In: *Journal of Nanomaterials* 2009.1 (Jan. 2009), p. 728957. ISSN: 1687-4129. DOI: 10.1155/2009/728957. URL: /doi/pdf/10.1155/2009/728957%20https://onlinelibrary.wiley.com/doi/abs/10.1155/2009/728957%20https://onlinelibrary.wiley.com/doi/10.1155/2009/728957.

[221] *Parameter Dependence of Pore Formation in Silicon within a Model of Local Current Bursts - Carstensen - 2000 - physica status solidi (a) - Wiley Online Library*. URL: https://onlinelibrary.wiley.com/doi/abs/10.1002/1521-396X%7B%5C%%7D28200011%7B%5C%%7D29182%7B%5C%%7D3A1%7B%5C%%7D3C63%7B%5C%%7D3A%7B%5C%%7D3AAID-PSSA63%7B%5C%%7D3E3.0.CO%7B%5C%%7D3B2-E (visited on 11/03/2025).

[222] R. Massami Sassaki et al. "Structure imaging by atomic force microscopy and transmission electron microscopy of different light emitting species of porous silicon". In: *Journal of Vacuum Science & Technology B: Microelectronics and Nanometer Structures Processing, Measurement, and Phenomena* 14.4 (July 1996), pp. 2432–2437. ISSN: 1071-1023. DOI: 10.1116/1.588874. URL: /avs/jvb/article/14/4/2432/1072835/Structure-imaging-by-atomic-force-microscopy-and.

[223] S. F. Chuang, S. D. Collins, and R. L. Smith. "Porous silicon microstructure as studied by transmission electron microscopy". In: *Applied Physics Letters* 55.15 (Oct. 1989), pp. 1540–1542. ISSN: 0003-6951. DOI: 10.1063/1.102239. URL: /aip/apl/article/55/15/1540/55887/Porous-silicon-microstructure-as-studied-by.

[224] *Porous Silicon: From Formation to Application: Formation and Properties, Volume One*. CRC Press, Apr. 2016. DOI: 10.1201/B19342/POROUS-SILICON-FORMATION-APPLICATION-FORMATION-PROPERTIES-VOLUME-ONE-GHENADII-KOROTCENKOV.

[225] O. Bisi, Stefano Ossicini, and L. Pavesi. "Porous silicon: a quantum sponge structure for silicon based optoelectronics". In: *Surface Science Reports* 38.1-3 (Apr. 2000), pp. 1–126. ISSN: 0167-5729. DOI: 10.1016/S0167-5729(99)00012-6. URL: https://www.sciencedirect.com/science/article/pii/S0167572999000126.

[226] J. Zheng, M. Christophersen, and P. L. Bergstrom. "Thick macroporous membranes made of p-type silicon". In: *physica status solidi (a)* 202.8 (June 2005), pp. 1402–1406. ISSN: 1862-6319. DOI: 10.1002/PSSA.200461113. URL: /doi/pdf/10.1002/pssa.200461113%20https://onlinelibrary.wiley.com/doi/abs/10.1002/pssa.200461113%20https://onlinelibrary.wiley.com/doi/10.1002/pssa.200461113.

[227] B. Bardet et al. "Integration of low-loss inductors on thin porous silicon membranes". In: *Microelectronic Engineering* 194 (July 2018), pp. 96–99. ISSN: 0167-9317. DOI: 10.1016/J.MEE.2018.03.020. URL: https://www.sciencedirect.com/science/article/pii/S0167931718301321.

[228] Roselien Vercauteren et al. "Porous Silicon Biosensor for the Detection of Bacteria through Their Lysate". In: *Biosensors 2021, Vol. 11, Page 27* 11.2 (Jan. 2021), p. 27. ISSN: 2079-6374. DOI: 10.3390/BIOS11020027. URL: https://www.mdpi.com/2079-6374/11/2/27%20https://www.mdpi.com/2079-6374/11/2/27.

[229] Thierry Leïchlé and David Bourrier. "Integration of lateral porous silicon membranes into planar microfluidics". In: *Lab on a Chip* 15.3 (Jan. 2015), pp. 833–838. ISSN: 1473-0189. DOI: 10.1039/C4LC01094A. URL: https://pubs.rsc.org/en/content/articlehtml/2015/lc/c4lc01094a%20https://pubs.rsc.org/en/content/articlelanding/2015/lc/c4lc01094a.

[230] B. Graczykowski et al. "Thermal conductivity and air-mediated losses in periodic porous silicon membranes at high temperatures". In: *Nature Communications* 8.1 (Dec. 2017), pp. 1–9. ISSN: 20411723. DOI: 10.1038/

S41467-017-00115-4;SUBJMETA. URL: https://www.nature.com/articles/s41467-017-00115-4.

[231] Barrett J. Nehilla et al. "Endothelial vacuolization induced by highly permeable silicon membranes". In: *Acta Biomaterialia* 10.11 (Nov. 2014), pp. 4670–4677. ISSN: 18787568. DOI: 10.1016/j.actbio.2014.07.022. URL: https://pubmed.ncbi.nlm.nih.gov/25072618/.

[232] Steven R. Gillmer et al. "Predicting the failure of ultrathin porous membranes in bulge tests". In: *Thin Solid Films* 631 (June 2017), pp. 152–160. ISSN: 0040-6090. DOI: 10.1016/J.TSF.2017.04.004. URL: https://www.sciencedirect.com/science/article/pii/S0040609017302596.

[233] Frieder Lucklum, Alexander Schwaiger, and Bernhard Jakoby. "Development and investigation of thermal devices on fully porous silicon substrates". In: *IEEE Sensors Journal* 14.4 (Apr. 2014), pp. 992–997. ISSN: 1530437X. DOI: 10.1109/JSEN.2013.2293541. URL: https://ieeexplore.ieee.org/document/6678191.

[234] V. A. Yuzova, F. F. Merkushev, and O. V. Semenova. "A monolithic silicon-based membrane–electrode assembly for micro fuel cells". In: *Technical Physics Letters 2017 43:8* 43.8 (Sept. 2017), pp. 764–766. ISSN: 1090-6533. DOI: 10.1134/S1063785017080272. URL: https://link.springer.com/article/10.1134/S1063785017080272.

[235] Vera A. Yuzova, Fedor F. Merkushev, and Eugene A. Lyaykom. "Formation of cross-cutting structures with different porosity on thick silicon wafers". In: *Modern Electronic Materials* 3.2 (June 2017), pp. 72–75. ISSN: 2452-1779. DOI: 10.1016/J.MOEM.2017.09.003. URL: https://www.sciencedirect.com/science/article/pii/S2452177917300592.

[236] Alessandro Chiadò et al. "Immobilization of Oligonucleotides on Metal-Dielectric Nanostructures for miRNA Detection". In: *Analytical Chemistry* 88.19 (Oct. 2016), pp. 9554–9563. ISSN: 15206882. DOI: 10.1021/ACS.ANALCHEM.6B02186. URL: https://pubs.acs.org/doi/abs/10.1021/acs.analchem.6b02186.

[237] N. E. Preobrazhenskiy et al. "Anodes for Li-ion batteries based on p-Si with self-organized macropores". In: *Semiconductors 2017 51:1* 51.1 (Feb. 2017), pp. 78–87. ISSN: 1090-6479. DOI: 10.1134/S1063782617010195. URL: https://link.springer.com/article/10.1134/S1063782617010195.

[238] Hailong Ning et al. "Transfer-Printing of Tunable Porous Silicon Microcavities with Embedded Emitters". In: *ACS Photonics* 1.11 (Nov. 2014), pp. 1144–1150. ISSN: 23304022. DOI: 10.1021/PH500230J. URL: https://pubs.acs.org/doi/abs/10.1021/ph500230j.

[239] Penglun Zheng et al. "Microstructure Engineered Silicon Alloy Anodes for Lithium-Ion Batteries: Advances and Challenges". In: *Batteries and Supercaps* 6.1 (Jan. 2023), e202200481. ISSN: 25666223. DOI: 10.1002/BATT.202200481;SUBPAGE:STRING:ABSTRACT;WEBSITE:WEBSITE:CHEMISTRY-EUROPE;REQUESTEDJOURNAL:JOURNAL:25666223;WGROUP:STRING:PUBLICATION. URL: /doi/pdf/10.1002/batt.202200481%20https://onlinelibrary.wiley.com/doi/abs/10.1002/batt.202200481%20https://chemistry-europe.onlinelibrary.wiley.com/doi/10.1002/batt.202200481.

[240] Romain Mentek et al. "Photovoltaic effect with high open circuit voltage observed in electrochemically prepared nanocrystalline silicon membranes". In: *Materials Science and Engineering: B* 190 (Dec. 2014), pp. 33–40. ISSN: 0921-5107. DOI: 10.1016/J.MSEB.2014.09.005. URL: https://www.sciencedirect.com/science/article/pii/S0921510714001937.

[241] G. V. Li et al. "Negative Electrodes for Lithium-Ion Batteries Obtained by Photoanodization of Solar-Grade Silicon". In: *Technical Physics 2019 64:5* 64.5 (June 2019), pp. 660–665. ISSN: 1090-6525. DOI: 10.1134/S1063784219050141. URL: https://link.springer.com/article/10.1134/S1063784219050141.

[242] M. Balucani et al. "Porous silicon solar cells". In: *IEEE-NANO 2015 - 15th International Conference on Nanotechnology*. Institute of Electrical and Electronics Engineers Inc., 2015, pp. 724–727. ISBN: 9781467381550. DOI: 10.1109/NANO.2015.7388710. URL: https://ieeexplore.ieee.org/document/7388710.

[243] L. G. Cencha et al. "Optical performance of hybrid porous silicon-porous alumina multilayers". In: *Journal of Applied Physics* 123.18 (May 2018). ISSN: 10897550. DOI: 10.1063/1.5027073/154903. URL: /aip/jap/article/123/18/183101/154903/Optical-performance-of-hybrid-porous-silicon.

[244] Chiara Novara et al. "Surface-enhanced Raman spectroscopy on porous silicon membranes decorated with Ag nanoparticles integrated in elastomeric microfluidic chips". In: *RSC Advances* 6.26 (Feb. 2016), pp. 21865–21870. ISSN: 2046-2069. DOI: 10.1039/C5RA26746C. URL: https://pubs.rsc.org/en/content/articlehtml/2016/ra/c5ra26746c%20https://pubs.rsc.org/en/content/articlelanding/2016/ra/c5ra26746c.

[245] Chiara Novara et al. "SERS-active metal-dielectric nanostructures integrated in microfluidic devices for label-free quantitative detection of miRNA". In: *Faraday Discussions* 205.0 (Nov. 2017), pp. 271–289. ISSN: 1364-5498. DOI: 10.1039/C7FD00140A. URL: https://pubs.rsc.org/en/content/

articlehtml/2017/fd/c7fd00140a%20https://pubs.rsc.org/en/content/articlelanding/2017/fd/c7fd00140a.

[246] David Martín-Sánchez, Salvador Ponce-Alcántara, and Jaime García-Rupérez. "Sensitivity Comparison of a Self-Standing Porous Silicon Membrane under Flow-Through and Flow-Over Conditions". In: *IEEE Sensors Journal* 19.9 (May 2019), pp. 3276–3281. ISSN: 1530437X. DOI: 10.1109/JSEN.2019.2893885. URL: https://ieeexplore.ieee.org/document/8620315.

[247] I S Kryukova et al. "Enhancement of the photoluminescence of semiconductor nanocrystals in transfer-printed microcavities based on freestanding porous silicon photonic crystals". In: *Journal of Physics: Conference Series* 1439.1 (Jan. 2020), p. 12018. ISSN: 1742-6596. DOI: 10.1088/1742-6596/1439/1/012018. URL: https://iopscience.iop.org/article/10.1088/1742-6596/1439/1/012018%20https://iopscience.iop.org/article/10.1088/1742-6596/1439/1/012018/meta.

[248] Nekane Reta et al. "Porous silicon membrane-modified electrodes for label-free voltammetric detection of MS2 bacteriophage". In: *Biosensors and Bioelectronics* 80 (2016), pp. 47–53. ISSN: 0956-5663. DOI: 10.1016/J.BIOS.2016.01.038. URL: https://www.sciencedirect.com/science/article/pii/S0956566316300379.

[249] F Morales-Morales et al. "Luminescent Si quantum dots in flexible and semitransparent membranes for photon down converting material". In: *Optical Materials* 90 (2019), pp. 220–226. ISSN: 0925-3467. DOI: 10.1016/J.OPTMAT.2019.02.043. URL: https://www.sciencedirect.com/science/article/pii/S092534671930151X.

[250] I. Tzu Chen et al. "Stability Limit of Water by Metastable Vapor-Liquid Equilibrium with Nanoporous Silicon Membranes". In: *Journal of Physical Chemistry B* 120.23 (June 2016), pp. 5209–5222. ISSN: 15205207. DOI: 10.1021/ACS.JPCB.6B01618/ASSET/IMAGES/MEDIUM/JP-2016-01618H_0010.GIF. URL: https://pubs.acs.org/doi/abs/10.1021/acs.jpcb.6b01618.

[251] María R Jimenéz-Vivanco et al. "Porous Si-SiO2 based UV Microcavities". In: *Scientific Reports 2020 10:1* 10.1 (2020), pp. 1–21. ISSN: 2045-2322. DOI: 10.1038/s41598-020-59001-7. URL: https://www.nature.com/articles/s41598-020-59001-7.

[252] María R. Jimenéz-Vivanco et al. "Porous Si-SiO2 UV Microcavities to Modulate the Responsivity of a Broadband Photodetector". In: *Nanomaterials 2020, Vol. 10, Page 222* 10.2 (Jan. 2020), p. 222. ISSN: 2079-4991. DOI: 10.3390/NANO10020222. URL: https://www.mdpi.com/2079-4991/10/2/222/htm%20https://www.mdpi.com/2079-4991/10/2/222.

[253] Principia Dardano et al. "Optically monitored drug delivery patch based on porous silicon and polymer microneedles". In: *Biomedical optics express* 7.5 (May 2016), p. 1645. ISSN: 2156-7085. DOI: 10.1364/BOE.7.001645. URL: https://pubmed.ncbi.nlm.nih.gov/27231611/.

[254] Yi Pei et al. "Vertical Integration of Cell-Laden Hydrogels with Bioinspired Photonic Crystal Membranes". In: *Advanced Materials Interfaces* 5.23 (Dec. 2018), p. 1801233. ISSN: 21967350. DOI: 10.1002/ADMI.201801233;WGROUP:STRING:PUBLICATION. URL: /doi/pdf/10.1002/admi.201801233%20https://onlinelibrary.wiley.com/doi/abs/10.1002/admi.201801233%20https://advanced.onlinelibrary.wiley.com/doi/10.1002/admi.201801233.

[255] Clémentine Gevers et al. "Freestanding Porous Silicon Membranes for Sensing Enabled by Flow-Through Decoration of Gold Nanoparticles". In: *ACS Applied Nano Materials* (Oct. 2025). ISSN: 2574-0970. DOI: 10.1021/ACSANM.5C03632. URL: /doi/pdf/10.1021/acsanm.5c03632?ref=article%7B%5C_%7DopenPDF.

[256] Huijin An et al. "Porous Silicon on Paper: A Platform for Quantitative Rapid Diagnostic Tests". In: *ACS Applied Materials & Interfaces* 17.4 (Jan. 2025), pp. 6024–6030. ISSN: 19448252. DOI: 10.1021/ACSAMI.4C18940. URL: /doi/pdf/10.1021/acsami.4c18940?ref=article%7B%5C_%7DopenPDF.

[257] Samuel De La Luz-Merino, Ma Estela Calixto, and Antonio Méndez-Blas. "Nanostructured CuInSe2 by electrodeposition with the assistance of porous silicon templates". In: *Materials Chemistry and Physics* 163 (2015), pp. 362–368. ISSN: 0254-0584. DOI: 10.1016/J.MATCHEMPHYS.2015.07.051. URL: https://www.sciencedirect.com/science/article/pii/S0254058415302443.

[258] Yiliang Zhao et al. "Comparative Kinetic Analysis of Closed-Ended and Open-Ended Porous Sensors". In: *Nanoscale Research Letters 2016 11:1* 11.1 (Sept. 2016), pp. 1–9. ISSN: 1556-276X. DOI: 10.1186/S11671-016-1614-3. URL: https://link.springer.com/article/10.1186/s11671-016-1614-3.

[259] Raoudha Haddad et al. "High performance miniature glucose/O2 fuel cell based on porous silicon anion exchange membrane". In: *Electrochemistry Communications* 54 (2015), pp. 10–13. ISSN: 1388-2481. DOI: 10.1016/J.ELECOM.2015.02.010. URL: https://www.sciencedirect.com/science/article/pii/S1388248115000454.

[260] Zonglin Wu et al. "A passive vapor-feed direct methanol fuel cell based on a composite pervaporation membrane". In: *2013 Transducers and Eurosensors XXVII: The 17th International Conference on Solid-State Sensors, Actuators*

and Microsystems, TRANSDUCERS and EUROSENSORS 2013 (2013), pp. 2815–2818. DOI: 10.1109/TRANSDUCERS.2013.6627391. URL: https://ieeexplore.ieee.org/document/6627391.

[261] Norhafizah Burham et al. "Electrochemically etched nanoporous silicon membrane for separation of biological molecules in mixture". In: *Journal of Micromechanics and Microengineering* 27.7 (July 2017), p. 075021. ISSN: 13616439. DOI: 10.1088/1361-6439/aa73c8. URL: http://stacks.iop.org/0960-1317/27/i=7/a=075021?key=crossref.40d839da171d631ec3d7fb21835a1bc1.

[262] Norhafizah Burham et al. "Self-Adjusting Electrochemical Etching Technique for Producing Nanoporous Silicon Membrane". In: *New Research on Silicon - Structure, Properties, Technology* (May 2017). DOI: 10.5772/67719. URL: https://www.intechopen.com/chapters/54430%20undefined/chapters/54430.

[263] Mei Wang, Litian Liu, and Xiaohong Wang. "A novel proton exchange membrane based on sulfo functionalized porous silicon for monolithic integrated micro direct methanol fuel cells". In: *Sensors and Actuators B: Chemical* 253 (Dec. 2017), pp. 621–629. ISSN: 0925-4005. DOI: 10.1016/J.SNB.2017.06.173. URL: https://www.sciencedirect.com/science/article/pii/S0925400517311929.

[264] Mei Wang, Litian Liu, and Xiaohong Wang. "Effects of grafting parameters on the properties of proton exchange membranes based on sulfo-functionalized porous silicon for micro direct methanol fuel cells". In: *Journal of Polymer Engineering* 39.7 (Aug. 2019), pp. 620–627. ISSN: 03346447. DOI: 10.1515/POLYENG-2019-0134/XML. URL: https://www.degruyterbrill.com/document/doi/10.1515/polyeng-2019-0134/html?srsltid=AfmBOopW65hr7L1UXnXGZj6hpBuEPfZMzD-fW6iaU1ubnja%7B%5C_%7Des3GxOeH.

[265] Frieder Lucklum, Alexander Schwaiger, and Bernhard Jakoby. "Highly insulating, fully porous silicon substrates for high temperature micro-hotplates". In: *Sensors and Actuators A: Physical* 213 (2014), pp. 35–42. ISSN: 0924-4247. DOI: 10.1016/J.SNA.2014.04.004. URL: https://www.sciencedirect.com/science/article/pii/S0924424714001691.

[266] V. V. Bolotov et al. "Formation of Multilayer Structures with Integrated Membranes Based on Porous Silicon". In: *Semiconductors 2020 54:5* 54.5 (May 2020), pp. 609–613. ISSN: 1090-6479. DOI: 10.1134/S1063782620050024. URL: https://link.springer.com/article/10.1134/S1063782620050024.

[267] Tristan Pichonat and Bernard Gauthier-Manuel. "A new process for the manufacturing of reproducible mesoporous silicon membranes". In: *Journal of Membrane Science* 280.1-2 (Sept. 2006), pp. 494–500. ISSN: 0376-7388. DOI:

10.1016/J.MEMSCI.2006.02.010. URL: https://www.sciencedirect.com/science/article/pii/S0376738806001281.

[268] Yiliang Zhao et al. "Flow-Through Porous Silicon Membranes for Real-Time Label-Free Biosensing". In: *Analytical Chemistry* 88.22 (Nov. 2016), pp. 10940–10948. ISSN: 15206882. DOI: 10.1021/ACS.ANALCHEM.6B02521. URL: https://pubs.acs.org/doi/abs/10.1021/acs.analchem.6b02521.

[269] Hongyun So et al. "All-in-One Nanowire-Decorated Multifunctional Membrane for Rapid Cell Lysis and Direct DNA Isolation". In: *ACS Applied Materials and Interfaces* 6.23 (Dec. 2014), pp. 20693–20699. ISSN: 19448252. DOI: 10.1021/AM506153Y. URL: /doi/pdf/10.1021/am506153y?ref=article%7B%5C_%7DopenPDF.

[270] Hongyun So et al. "Hierarchical Silicon Nanospikes Membrane for Rapid and High-Throughput Mechanical Cell Lysis". In: *ACS Applied Materials and Interfaces* 6.10 (May 2014), pp. 6993–6997. ISSN: 19448252. DOI: 10.1021/AM501221B. URL: /doi/pdf/10.1021/am501221b?ref=article%7B%5C_%7DopenPDF.

[271] Zaoxi Yu et al. "Optimally catalyzed porous-silicon electrode of self-breathing micro fuel cells". In: *Microsystem Technologies 2016 23:8* 23.8 (Aug. 2016), pp. 3257–3262. ISSN: 1432-1858. DOI: 10.1007/S00542-016-3122-X. URL: https://link.springer.com/article/10.1007/s00542-016-3122-x.

[272] Abdoullatif Baraket et al. "Long duration stabilization of porous silicon membranes in physiological media: Application for implantable reactors". In: *Materials Science and Engineering: C* 108 (Mar. 2020), p. 110359. ISSN: 0928-4931. DOI: 10.1016/J.MSEC.2019.110359. URL: https://www.sciencedirect.com/science/article/pii/S0928493118338852.

[273] Gyoko Nagayama et al. "Effects of nano/microstructures on performance of Si-based microfuel cells". In: *Applied Thermal Engineering* 72.2 (Nov. 2014), pp. 298–303. ISSN: 1359-4311. DOI: 10.1016/J.APPLTHERMALENG.2014.07.006. URL: https://www.sciencedirect.com/science/article/pii/S1359431114005547.

[274] M. A. Parashchenko et al. "Electroosmotic pump based on asymmetric silicon microchannel membranes". In: *Optoelectronics, Instrumentation and Data Processing 2014 50:3* 50.3 (July 2014), pp. 315–322. ISSN: 1934-7944. DOI: 10.3103/S8756699014030170. URL: https://link.springer.com/article/10.3103/S8756699014030170.

[275] M. A. Parashchenko, N. S. Filippov, and V. V. Kirienko. "Microfluidic electric generator based on a silicon microchannel membrane". In: *Optoelectronics, Instrumentation and Data Processing 2015 51:1* 51.1 (Apr. 2015), pp. 94–102. ISSN: 1934-7944. DOI: 10.3103/S875669901501015X. URL: https://link.springer.com/article/10.3103/S875669901501015X.

[276] V. V. Starkov et al. "Composite electrodes for current sources based on graphene-like films in porous silicon". In: *Protection of Metals and Physical Chemistry of Surfaces 2017 53:1* 53.1 (Mar. 2017), pp. 85–87. ISSN: 2070-206X. DOI: 10.1134/S2070205116060198. URL: https://link.springer.com/article/10.1134/S2070205116060198.

[277] V. V. Bolotov et al. "The formation of membranes based on oxidized two-layer porous silicon". In: *AIP Conference Proceedings* 2141.1 (Aug. 2019). ISSN: 15517616. DOI: 10.1063/1.5122136/889350. URL: /aip/acp/article/2141/1/040017/889350/The-formation-of-membranes-based-on-oxidized-two.

[278] Khalid Hasan Tantawi et al. "Porous silicon membrane for investigation of transmembrane proteins". In: *Superlattices and Microstructures* 58 (June 2013), pp. 72–80. ISSN: 0749-6036. DOI: 10.1016/J.SPMI.2013.02.014. URL: https://www.sciencedirect.com/science/article/pii/S0749603613000530.

[279] Muhammad Shuja Khan and John Dalton Williams. "Fabrication of Solid State Nanopore in Thin Silicon Membrane Using Low Cost Multistep Chemical Etching". In: *Materials 2015, Vol. 8, Pages 7389-7400* 8.11 (Nov. 2015), pp. 7389–7400. ISSN: 1996-1944. DOI: 10.3390/MA8115390. URL: https://www.mdpi.com/1996-1944/8/11/5390/htm%20https://www.mdpi.com/1996-1944/8/11/5390.

[280] Muhammad S. Khan et al. "Electrochemical impedance spectroscopy for black lipid membranes fused with channel protein supported on solid-state nanopore". In: *European Biophysics Journal 2016 45:8* 45.8 (Aug. 2016), pp. 843–852. ISSN: 1432-1017. DOI: 10.1007/S00249-016-1156-8. URL: https://link.springer.com/article/10.1007/s00249-016-1156-8.

[281] Muhammad Shuja Khan et al. "Electrophysiology of Epithelial Sodium Channel (ENaC) Embedded in Supported Lipid Bilayer Using a Single Nanopore Chip". In: *Langmuir* 33.47 (Nov. 2017), pp. 13680–13688. ISSN: 15205827. DOI: 10.1021/ACS.LANGMUIR.7B02404. URL: https://pubs.acs.org/doi/abs/10.1021/acs.langmuir.7b02404.

[282] Torsten Schmidt et al. "Nanopore arrays in a silicon membrane for parallel single-molecule detection: fabrication". In: *Nanotechnology* 26.31 (July 2015), p. 314001. ISSN: 0957-4484. DOI: 10.1088/0957-4484/26/31/314001. URL: https://iopscience.iop.org/article/10.1088/0957-4484/26/31/314001%20https://iopscience.iop.org/article/10.1088/0957-4484/26/31/314001/meta.

[283] Miao Zhang et al. "Nanopore arrays in a silicon membrane for parallel single-molecule detection: DNA translocation". In: *Nanotechnology* 26.31 (Aug. 2015). ISSN: 1361-6528. DOI: 10.1088/0957-4484/26/31/314002. URL: https://pubmed.ncbi.nlm.nih.gov/26180050/.

[284] I. T. Chen and A. D. Stroock. "A tree-on-a-chip: design and analysis of MEMS-based superheated loop heat pipes exploiting nanoporous silicon membranes". In: *Journal of Physics: Conference Series* 557.1 (Nov. 2014), p. 012067. ISSN: 1742-6596. DOI: 10.1088/1742-6596/557/1/012067. URL: https://iopscience.iop.org/article/10.1088/1742-6596/557/1/012067%20https://iopscience.iop.org/article/10.1088/1742-6596/557/1/012067/meta.

[285] Chii Rong Yang et al. "Performance evaluation of μDMFCs based on porous-silicon electrodes and methanol modification". In: *Energy* 192 (Feb. 2020), p. 116666. ISSN: 0360-5442. DOI: 10.1016/J.ENERGY.2019.116666. URL: https://www.sciencedirect.com/science/article/pii/S0360544219323618.

[286] Daiki Ogura et al. "Miniature fuel cell with monolithically fabricated Si electrodes-Alloy catalyst formation". In: *Journal of Physics: Conference Series* 476.1 (2013). ISSN: 17426596. DOI: 10.1088/1742-6596/476/1/012066.

[287] Masahiro Kobayashi, Takahiro Suzuki, and Masanori Hayase. "A miniature fuel cell with monolithically fabricated Si electrodes - Reduction of residual porous Si on catalyst layer". In: *Journal of Power Sources* 267 (Dec. 2014), pp. 622–628. ISSN: 03787753. DOI: 10.1016/J.JPOWSOUR.2014.05.108.

[288] N. Sabaté et al. "New approach for batch microfabrication of silicon-based micro fuel cells". In: *Microsystem Technologies 2013 20:2* 20.2 (Mar. 2013), pp. 341–348. ISSN: 1432-1858. DOI: 10.1007/S00542-013-1781-4. URL: https://link.springer.com/article/10.1007/s00542-013-1781-4.

[289] Yingning He and Thierry Leïchlé. "Fabrication of lateral porous silicon membranes for planar microfluidics by means of ion implantation". In: *Sensors and Actuators B: Chemical* 239 (Feb. 2017), pp. 628–634. ISSN: 0925-4005. DOI: 10.1016/J.SNB.2016.08.035. URL: https://www.sciencedirect.com/science/article/pii/S0925400516312679.

[290] Douglas Silva de Vasconcellos et al. "Process for integrating multiple porous silicon membranes with variable characteristics into planar microfluidics". In: *Sensors and Actuators A: Physical* 377 (Oct. 2024), p. 115715. ISSN: 0924-4247. DOI: 10.1016/J.SNA.2024.115715. URL: https://www.sciencedirect.com/science/article/abs/pii/S092442472400709X.

[291] Harutoshi Hagino et al. "Thermal and Electrical Conductivities of Porous Si Membranes". In: *International Journal of Thermophysics 2014 36:10* 36.10 (June 2014), pp. 2548–2564. ISSN: 1572-9567. DOI: 10.1007/S10765-014-1643-Z. URL: https://link.springer.com/article/10.1007/s10765-014-1643-z.

[292] Yahya Hosseini et al. "A Silicon-Based Porous Thin Membrane as a Cancer Cell Transmigration Assay". In: *Journal of Microelectromechanical Systems* 26.2 (Apr. 2017), pp. 308–316. ISSN: 10577157. DOI: 10.1109/JMEMS.2016.2618774. URL: https://ieeexplore.ieee.org/document/7845638.

[293] Bhuvanendran Nair Gourikutty Sajay, Chiam Su Yin, and Qasem Ramadan. "Optimization of micro-fabricated porous membranes for intestinal epithelial cell culture and in vitro modeling of the human intestinal barrier". In: *Journal of Micromechanics and Microengineering* 27.12 (Nov. 2017), p. 124004. ISSN: 0960-1317. DOI: 10.1088/1361-6439/AA96BD. URL: https://iopscience.iop.org/article/10.1088/1361-6439/aa96bd%20https://iopscience.iop.org/article/10.1088/1361-6439/aa96bd/meta.

[294] Andrew Stephens et al. "Mass-producible microporous silicon membranes for specific leukocyte subset isolation, immunophenotyping, and personalized immunomodulatory drug screening in vitro". In: *Lab on a Chip* 19.18 (Sept. 2019), pp. 3065–3076. ISSN: 1473-0189. DOI: 10.1039/C9LC00315K. URL: https://pubs.rsc.org/en/content/articlehtml/2019/lc/c9lc00315k%20https://pubs.rsc.org/en/content/articlelanding/2019/lc/c9lc00315k.

[295] Marianna Sledzinska et al. "Thermal conductivity in disordered porous nanomembranes". In: *Nanotechnology* 30.26 (Apr. 2019), p. 265401. ISSN: 0957-4484. DOI: 10.1088/1361-6528/AB0ECD. URL: https://iopscience.iop.org/article/10.1088/1361-6528/ab0ecd%20https://iopscience.iop.org/article/10.1088/1361-6528/ab0ecd/meta.

[296] Maxime Verdier et al. "Thermal conductivity of phononic membranes with aligned and staggered lattices of holes at room and low temperatures". In: *Physical Review B* 95.20 (May 2017), p. 205438. ISSN: 24699969. DOI: 10.1103/PhysRevB.95.205438. URL: https://journals.aps.org/prb/abstract/10.1103/PhysRevB.95.205438.

[297] Maxime Verdier, David Lacroix, and Konstantinos Termentzidis. "Heat transport in phononic-like membranes: Modeling and comparison with modulated nano-wires". In: *International Journal of Heat and Mass Transfer* 114 (Nov. 2017), pp. 550–558. ISSN: 0017-9310. DOI: 10.1016/J.IJHEATMASSTRANSFER.2017.06.067. URL: https://www.sciencedirect.com/science/article/pii/S0017931017317477.

[298] Tandra Ghoshal, Justin D. Holmes, and Michael A. Morris. "Development of Ordered, Porous (Sub-25 nm Dimensions) Surface Membrane Structures Using a Block Copolymer Approach". In: *Scientific Reports 2018 8:1* 8.1 (May 2018), pp. 1–11. ISSN: 2045-2322. DOI: 10.1038/s41598-018-25446-0. URL: https://www.nature.com/articles/s41598-018-25446-0.

[299] Stefanie Greil et al. "Gas Transport Selectivity of Ultrathin, Nanoporous, Inorganic Membranes Made from Block Copolymer Templates". In: *Chemistry of Materials* 29.21 (Nov. 2017), pp. 9572–9578. ISSN: 15205002. DOI: 10.1021/ACS.CHEMMATER.7B04174. URL: https://pubs.acs.org/doi/abs/10.1021/acs.chemmater.7b04174.

[300] Chengzhu Qi et al. "Highly porous silicon membranes fabricated from silicon nitride/silicon stacks". In: *Small* 10.14 (July 2014), pp. 2946–2953. ISSN: 16136829. DOI: 10.1002/SMLL.201303447;PAGE:STRING:ARTICLE/CHAPTER. URL: /doi/pdf/10.1002/smll.201303447%20https://onlinelibrary.wiley.com/doi/abs/10.1002/smll.201303447%20https://onlinelibrary.wiley.com/doi/10.1002/smll.201303447.

[301] Carolin Drieschner et al. "Fish-gut-on-chip: development of a microfluidic bioreactor to study the role of the fish intestine in vitro". In: *Lab on a Chip* 19.19 (Sept. 2019), pp. 3268–3276. ISSN: 1473-0189. DOI: 10.1039/C9LC00415G. URL: https://pubs.rsc.org/en/content/articlehtml/2019/lc/c9lc00415g%20https://pubs.rsc.org/en/content/articlelanding/2019/lc/c9lc00415g.

[302] Chun Zhou et al. "Enhanced Reduction of Thermal Conductivity in Amorphous Silicon Nitride-Containing Phononic Crystals Fabricated Using Directed Self-Assembly of Block Copolymers". In: *ACS Nano* 14.6 (June 2020), pp. 6980–6989. ISSN: 1936086X. DOI: 10.1021/ACSNANO.0C01463. URL: https://pubs.acs.org/doi/abs/10.1021/acsnano.0c01463.

[303] Masniza Sairi et al. "Electrochemical Characterisation of Nanoscale Liquid|Liquid Interfaces Located at Focused Ion Beam-Milled Silicon Nitride Membranes". In: *ChemElectroChem* 2.1 (Jan. 2015), pp. 98–105. ISSN: 21960216. DOI: 10.1002/CELC.201402252;CTYPE:STRING:JOURNAL. URL: /doi/pdf/10.1002/celc.201402252%20https://onlinelibrary.wiley.

com/doi/abs/10.1002/celc.201402252%20https://chemistry-europe.onlinelibrary.wiley.com/doi/abs/10.1002/celc.201402252.

[304] Yazan Bdour, Juan Gomez-Cruz, and Carlos Escobedo. "Structural Stability of Optofluidic Nanostructures in Flow-Through Operation". In: *Micromachines 2020, Vol. 11, Page 373* 11.4 (Apr. 2020), p. 373. ISSN: 2072-666X. DOI: 10.3390/MI11040373. URL: https://www.mdpi.com/2072-666X/11/4/373/htm%20https://www.mdpi.com/2072-666X/11/4/373.

[305] Gregory R. Madejski et al. "Monolithic Fabrication of NPN/SiNx Dual Membrane Cavity for Nanopore-Based DNA Sensing". In: *Advanced Materials Interfaces* 6.14 (July 2019), p. 1900684. ISSN: 2196-7350. DOI: 10.1002/ADMI.201900684. URL: /doi/pdf/10.1002/admi.201900684%20https://onlinelibrary.wiley.com/doi/abs/10.1002/admi.201900684%20https://advanced.onlinelibrary.wiley.com/doi/10.1002/admi.201900684.

[306] J. P.S. DesOrmeaux et al. "Nanoporous silicon nitride membranes fabricated from porous nanocrystalline silicon templates". In: *Nanoscale* 6.18 (Aug. 2014), pp. 10798–10805. ISSN: 2040-3372. DOI: 10.1039/C4NR03070B. URL: https://pubs.rsc.org/en/content/articlehtml/2014/nr/c4nr03070b%20https://pubs.rsc.org/en/content/articlelanding/2014/nr/c4nr03070b.

[307] R. Maboudian. "Micro Devices: Stiction and Adhesion". In: *Encyclopedia of Materials: Science and Technology* (2001), pp. 5591–5593. DOI: 10.1016/B0-08-043152-6/00977-3.

[308] Takashi Sumigawa et al. "Fracture toughness of silicon in nanometer-scale singular stress field". In: *Engineering Fracture Mechanics* 150 (Dec. 2015), pp. 161–167. ISSN: 0013-7944. DOI: 10.1016/J.ENGFRACMECH.2015.05.054. URL: https://www.sciencedirect.com/science/article/pii/S0013794415002519.

[309] Gennady Y. Gor et al. "Elastic response of mesoporous silicon to capillary pressures in the pores". In: *Applied Physics Letters* 106.26 (June 2015). ISSN: 00036951. DOI: 10.1063/1.4923240/27328. arXiv: 1507.06482. URL: /aip/apl/article/106/26/261901/27328/Elastic-response-of-mesoporous-silicon-to.

[310] A. Grosman, J. Puibasset, and E. Rolley. "Adsorption-induced strain of a nanoscale silicon honeycomb". In: *Europhysics Letters* 109.5 (Mar. 2015), p. 56002. ISSN: 0295-5075. DOI: 10.1209/0295-5075/109/56002. URL: https://iopscience.iop.org/article/10.1209/0295-5075/109/56002%20https://iopscience.iop.org/article/10.1209/0295-5075/109/56002/meta.

[311] E. Rolley, N. Garroum, and A. Grosman. "Using capillary forces to determine the elastic properties of mesoporous materials". In: *Physical Review B* 95.6 (Feb. 2017), p. 064106. ISSN: 24699969. DOI: 10.1103/PhysRevB.95.064106. URL: https://journals.aps.org/prb/abstract/10.1103/PhysRevB.95.064106.

[312] Xiaoyue Gong et al. "FEM simulation on elastic parameters of porous silicon with different pore shapes". In: *International Journal of Solids and Structures* 190 (2020), pp. 238–243. ISSN: 0020-7683. DOI: 10.1016/J.IJSOLSTR.2019.11.001. URL: https://www.sciencedirect.com/science/article/pii/S0020768319304627.

[313] Ch Populaire et al. "On mechanical properties of nanostructured mesoporous silicon". In: *Applied Physics Letters* 83.7 (Aug. 2003), pp. 1370–1372. ISSN: 0003-6951. DOI: 10.1063/1.1603336. URL: /aip/apl/article/83/7/1370/511261/On-mechanical-properties-of-nanostructured-meso.

[314] R. S. Dariani and M. Nazari. "Comparison of stress, strain, and elastic properties for porous silicon layers supported by substrate and corresponding membranes". In: *Journal of Molecular Structure* 1119 (Sept. 2016), pp. 308–313. ISSN: 0022-2860. DOI: 10.1016/J.MOLSTRUC.2016.04.061. URL: https://www.sciencedirect.com/science/article/pii/S0022286016303945.

[315] Romain Guider, Cristina Traversa, and Paolo Bettotti. "Mechanical stress relief in porous silicon free standing membranes". In: *Optical Materials Express* 5.10 (Oct. 2015), p. 2128. ISSN: 21593930. DOI: 10.1364/OME.5.002128.

[316] Norhafizah Burham, Azrul Azlan Hamzah, and Burhanudin Yeop Majlis. "Mechanical characteristics of porous silicon membrane for filtration in artificial kidney". In: *IEEE International Conference on Semiconductor Electronics, Proceedings, ICSE* (Oct. 2014), pp. 119–122. DOI: 10.1109/SMELEC.2014.6920810. URL: https://ieeexplore.ieee.org/document/6920810.

[317] Muhammad Fahmi Bin Jaafar, Rhonira Latif, and Burhanuddin Yeop Majlis. "Simulation on mechanical properties of porous nanocrystalline silicon membrane for artificial kidney". In: *Proceedings of the 2017 IEEE Regional Symposium on Micro and Nanoelectronics, RSM 2017* (Oct. 2017), pp. 26–29. DOI: 10.1109/RSM.2017.8069135. URL: https://ieeexplore.ieee.org/document/8069135.

[318] S. H.C. Anderson et al. "Dissolution of different forms of partially porous silicon wafers under simulated physiological conditions". In: *Physica Status Solidi (A) Applied Research* 197.2 (May 2003), pp. 331–335. ISSN: 00318965.

DOI: 10.1002/PSSA.200306519;ISSUE:ISSUE:DOI. URL: /doi/pdf/10.1002/pssa.200306519%20https://onlinelibrary.wiley.com/doi/abs/10.1002/pssa.200306519%20https://onlinelibrary.wiley.com/doi/10.1002/pssa.200306519.

[319] Feng Wang, Timothy J. Barnes, and Clive A. Prestidge. "Controlling and Predicting the Dissolution Kinetics of Thermally Oxidised Mesoporous Silicon Particles: Towards Improved Drug Delivery". In: *Pharmaceutics* 11.12 (Dec. 2019), p. 634. ISSN: 19994923. DOI: 10.3390/pharmaceutics11120634. URL: https://pmc.ncbi.nlm.nih.gov/articles/PMC6955814/.

[320] Mouna Hecini et al. "Study of formation, stabilization and properties of porous silicon and porous silica". In: *Journal of Physics and Chemistry of Solids* 74.9 (Sept. 2013), pp. 1227–1234. ISSN: 0022-3697. DOI: 10.1016/J.JPCS.2013.03.021. URL: https://www.sciencedirect.com/science/article/pii/S0022369713001285.

[321] M. P. Stewart et al. *Three methods for stabilization and functionalization of porous silicon surfaces via hydrosilylation and electrografting reactions*. 2000. DOI: 10.1002/1521-396X(200011)182:1<109::AID-PSSA109>3.0.CO;2-#. URL: https://onlinelibrary.wiley.com/doi/abs/10.1002/1521-396X%7B%5C%%7D28200011%7B%5C%%7D29182%7B%5C%%7D3A1%7B%5C%%7D3C109%7B%5C%%7D3A%7B%5C%%7D3AAID-PSSA109%7B%5C%%7D3E3.0.CO%7B%5C%%7D3B2-%7B%5C%%7D23 (visited on 11/04/2025).

[322] Jonathan Rasson and Laurent A. Francis. "Improved Stability of Porous Silicon in Aqueous Media via Atomic Layer Deposition of Oxides". In: *Journal of Physical Chemistry C* 122.1 (Jan. 2017), pp. 331–338. ISSN: 19327455. DOI: 10.1021/ACS.JPCC.7B08569. URL: https://pubs.acs.org/doi/abs/10.1021/acs.jpcc.7b08569.

[323] J. Salonen et al. "Stabilization of porous silicon surface by thermal decomposition of acetylene". In: *Applied Surface Science* 225.1-4 (Mar. 2004), pp. 389–394. ISSN: 0169-4332. DOI: 10.1016/J.APSUSC.2003.10.028. URL: https://www.sciencedirect.com/science/article/pii/S0169433203012121.

[324] Wing Yin Tong et al. "Towards a subcutaneous optical biosensor based on thermally hydrocarbonised porous silicon". In: *Biomaterials* 74 (Jan. 2016), pp. 217–230. ISSN: 0142-9612. DOI: 10.1016/J.BIOMATERIALS.2015.09.045. URL: https://www.sciencedirect.com/science/article/pii/S0142961215007966.

[325] Yazad D. Irani et al. "Oral Mucosal Epithelial Cells Grown on Porous Silicon Membrane for Transfer to the Rat Eye". In: *Scientific Reports 2017 7:1* 7.1 (Aug. 2017), pp. 1–11. ISSN: 2045-2322. DOI: 10.1038/s41598-017-10793-1. URL: https://www.nature.com/articles/s41598-017-10793-1.

[326] Yingning He et al. “Lateral porous silicon membranes with tunable pore size for on-chip separation”. In: *Proceedings of the IEEE International Conference on Micro Electro Mechanical Systems (MEMS)* 2016-Febru (Feb. 2016), pp. 497–500. ISSN: 10846999. DOI: 10.1109/MEMSYS.2016.7421670.

[327] Yingning He et al. “Lateral porous silicon membranes with size and charge selectivity”. In: *2017 IEEE 12th International Conference on Nano/Micro Engineered and Molecular Systems, NEMS 2017* (Aug. 2017), pp. 770–773. DOI: 10.1109/NEMS.2017.8017132. URL: https://ieeexplore.ieee.org/document/8017132.

[328] Kayli Hill et al. “Second Generation Nanoporous Silicon Nitride Membranes for High Toxin Clearance and Small Format Hemodialysis”. In: *Advanced healthcare materials* 9.4 (Feb. 2020). ISSN: 2192-2659. DOI: 10.1002/ADHM.201900750. URL: https://pubmed.ncbi.nlm.nih.gov/31943849/.

[329] Jan W. Kuhlmann, Ingo P. Mey, and Claudia Steinem. “Modulating the Lateral Tension of Solvent-Free Pore-Spanning Membranes”. In: *Langmuir* 30.27 (July 2014), pp. 8186–8192. ISSN: 15205827. DOI: 10.1021/LA5019086. URL: https://pubs.acs.org/doi/abs/10.1021/la5019086.

[330] Martin Gleisner et al. “Driving a planar model system into the 3rd dimension: Generation and control of curved pore-spanning membrane arrays”. In: *Soft Matter* 10.33 (Sept. 2014), pp. 6228–6236. ISSN: 17446848. DOI: 10.1039/C4SM00702F.

[331] Ilja Kusters, Antoine M. Van Oijen, and Arnold J.M. Driessen. “Membrane-on-a-chip: Microstructured silicon/silicon-dioxide chips for high-throughput screening of membrane transport and viral membrane fusion”. In: *ACS Nano* 8.4 (Apr. 2014), pp. 3380–3392. ISSN: 1936086X. DOI: 10.1021/NN405884A/SUPPL_FILE/NN405884A_SI_003.AVI. URL: https://pubs.acs.org/doi/abs/10.1021/nn405884a.

[332] Lando L.G. Schwenen et al. “Resolving single membrane fusion events on planar pore-spanning membranes”. In: *Scientific Reports 2015 5:1* 5.1 (July 2015), pp. 1–15. ISSN: 2045-2322. DOI: 10.1038/srep12006. URL: https://www.nature.com/articles/srep12006.

[333] Jan W. Kuhlmann et al. “SNARE-Mediated Single-Vesicle Fusion Events with Supported and Freestanding Lipid Membranes”. In: *Biophysical Journal* 112.11 (June 2017), pp. 2348–2356. ISSN: 0006-3495. DOI: 10.1016/J.BPJ.2017.04.032. URL: https://www.sciencedirect.com/science/article/pii/S0006349517304484.

[334] Jeremias Sibold et al. "Phase separation in pore-spanning membranes induced by differences in surface adhesion". In: *Physical Chemistry Chemical Physics* 22.17 (May 2020), pp. 9308–9315. ISSN: 1463-9084. DOI: 10.1039/D0CP00335B. URL: https://pubs.rsc.org/en/content/articlehtml/2020/cp/d0cp00335b%20https://pubs.rsc.org/en/content/articlelanding/2020/cp/d0cp00335b.

[335] Yanping Sun et al. "Lipid membranes supported by planar porous substrates". In: *Chemistry and Physics of Lipids* 228 (May 2020), p. 104893. ISSN: 0009-3084. DOI: 10.1016/J.CHEMPHYSLIP.2020.104893. URL: https://www.sciencedirect.com/science/article/pii/S0009308420300244.

[336] María del Rayo Jiménez Vivanco et al. "Time-Resolved Spectroscopy of Ethanol Evaporation on Free-Standing Porous Silicon Photonic Microcavities". In: *Materials 2018, Vol. 11, Page 894* 11.6 (May 2018), p. 894. ISSN: 1996-1944. DOI: 10.3390/MA11060894. URL: https://www.mdpi.com/1996-1944/11/6/894/htm%20https://www.mdpi.com/1996-1944/11/6/894.

[337] Hyeok Gi Kim and Ki Won Lee. "Electrostatic gas sensor with a porous silicon diaphragm". In: *Sensors and Actuators B: Chemical* 219 (Nov. 2015), pp. 10–16. ISSN: 0925-4005. DOI: 10.1016/J.SNB.2015.04.118. URL: https://www.sciencedirect.com/science/article/pii/S092540051500595X.

[338] Yingning He et al. "Lateral Porous Silicon Interferometric Transducer for Sensing Applications". In: *Proceedings of IEEE Sensors* 2018-Octob (Dec. 2018). ISSN: 21689229. DOI: 10.1109/ICSENS.2018.8589773. URL: https://ieeexplore.ieee.org/abstract/document/8589773.

[339] Gaël Gautier and Sebastien Kouassi. "Integration of porous silicon in microfuel cells: A review". In: *International Journal of Energy Research* 39.1 (Jan. 2015), pp. 1–25. ISSN: 1099114X. DOI: 10.1002/ER.3206;WGROUP:STRING:PUBLICATION. URL: /doi/pdf/10.1002/er.3206%20https://onlinelibrary.wiley.com/doi/abs/10.1002/er.3206%20https://onlinelibrary.wiley.com/doi/10.1002/er.3206.

[340] G. V. Li et al. "Microstructured silicon anodes for lithium-ion batteries". In: *Russian Journal of Electrochemistry 2015 51:10* 51.10 (Oct. 2015), pp. 899–907. ISSN: 1608-3342. DOI: 10.1134/S1023193515100080. URL: https://link.springer.com/article/10.1134/S1023193515100080.

[341] M. Ge et al. "Review of porous silicon preparation and its application for lithium-ion battery anodes". In: *Nanotechnology* 24.42 (Sept. 2013), p. 422001. ISSN: 0957-4484. DOI: 10.1088/0957-4484/24/42/422001. URL: https://iopscience.iop.org/article/10.1088/0957-4484/24/42/422001%20https://iopscience.iop.org/article/10.1088/0957-4484/24/42/422001/meta.

[342] Erwann Luais et al. “Improved cycling performances of binder-free macroporous silicon Li-ion negative electrodes using room temperature ionic liquid electrolyte”. In: *Journal of Solid State Electrochemistry 2019 23:3* 23.3 (Jan. 2019), pp. 937–941. ISSN: 1433-0768. DOI: 10.1007/S10008-019-04197-6. URL: https://link.springer.com/article/10.1007/s10008-019-04197-6.

[343] Jay D. Sircar et al. “High heat flux evaporation from nanoporous silicon membranes”. In: *Proceedings of the 16th InterSociety Conference on Thermal and Thermomechanical Phenomena in Electronic Systems, ITherm 2017* (July 2017), pp. 505–513. DOI: 10.1109/ITHERM.2017.7992516.

[344] Sung Jin Park et al. “All-optical modulation in Mid-Wavelength Infrared using porous Si membranes”. In: *Scientific Reports 2016 6:1* 6.1 (July 2016), pp. 1–8. ISSN: 2045-2322. DOI: 10.1038/srep30211. URL: https://www.nature.com/articles/srep30211.

[345] Priyanka Bhadra et al. “Selective transportation of charged ZnO nanoparticles and microorganism dialysis through silicon nanoporous membranes”. In: *Journal of Membrane Science* 503 (Apr. 2016), pp. 16–24. ISSN: 0376-7388. DOI: 10.1016/J.MEMSCI.2015.12.058. URL: https://www.sciencedirect.com/science/article/pii/S0376738815304063.

[346] Tushar H. Punde et al. “A biologically inspired lung-on-a-chip device for the study of protein-induced lung inflammation”. In: *Integrative biology : quantitative biosciences from nano to macro* 7.2 (Feb. 2015), pp. 162–169. ISSN: 1757-9708. DOI: 10.1039/C4IB00239C. URL: https://pubmed.ncbi.nlm.nih.gov/25486073/.

[347] Wen Hao Wu et al. “A capillary-endothelium-mimetic microfluidic chip for the study of immune responses”. In: *Sensors and Actuators B: Chemical* 209 (Mar. 2015), pp. 470–477. ISSN: 0925-4005. DOI: 10.1016/J.SNB.2014.11.123. URL: https://www.sciencedirect.com/science/article/pii/S0925400514015184.

[348] Marcus A.C. Williams et al. “Fabrication of a novel porous silicon biomembrane for applications in organ-on-chip technology”. In: *Biomedical Microdevices 2025 27:3* 27.3 (June 2025), pp. 32–. ISSN: 1572-8781. DOI: 10.1007/S10544-025-00760-3. URL: https://link.springer.com/article/10.1007/s10544-025-00760-3.

[349] Neeraj Kumar et al. “Investigation of non-specific signals in nanoporous flow-through and flow-over based sensors”. In: *Analyst* 139.6 (Feb. 2014), pp. 1345–1349. ISSN: 1364-5528. DOI: 10.1039/C3AN01996A. URL: https://pubs.rsc.org/en/content/articlehtml/2014/an/c3an01996a%20https://pubs.rsc.org/en/content/articlelanding/2014/an/c3an01996a.

[350] Yongbae Lee and Kiwon Lee. "Sensing of dissolved-gas concentration in water using a rugate-structured porous silicon membrane". In: *Sensors and Actuators B: Chemical* 202 (Oct. 2014), pp. 417–425. ISSN: 0925-4005. DOI: 10.1016/J.SNB.2014.05.108. URL: https://www.sciencedirect.com/science/article/pii/S0925400514006479.

[351] David Martin-Sanchez, Todora Angelova, and Jaime Garcia-Ruperez. "Simultaneous Refractive Index Sensing Using an Array of Suspended Porous Silicon Membranes". In: *IEEE Sensors Journal* 20.15 (Aug. 2020), pp. 8497–8504. ISSN: 15581748. DOI: 10.1109/JSEN.2020.2983218. URL: https://ieeexplore.ieee.org/document/9046829.

[352] Noel Prashant Ratchagar et al. "Sensor for Continuous and Real-Time Monitoring of Biomolecule Permeation Through Ultrathin Silicon Nanoporous Membranes". In: *IEEE Sensors Journal* 19.12 (June 2019), pp. 4419–4427. ISSN: 15581748. DOI: 10.1109/JSEN.2019.2900285. URL: https://ieeexplore.ieee.org/document/8644003.

[353] Nekane Reta et al. "Label-Free Bacterial Toxin Detection in Water Supplies Using Porous Silicon Nanochannel Sensors". In: *ACS Sensors* 4.6 (June 2019), pp. 1515–1523. ISSN: 23793694. DOI: 10.1021/ACSSENSORS.8B01670. URL: https://pubs.acs.org/doi/abs/10.1021/acssensors.8b01670.

[354] Sang Woo Seo, Hojjat Rostami Azmand, and Amarachukwu N. Enemuo. "Hollow Core Waveguide Sensor Array Based on a Macroporous Silicon Membrane Structure". In: *Journal of Lightwave Technology* 37.9 (May 2019), pp. 2036–2041. ISSN: 15582213. DOI: 10.1109/JLT.2019.2897427. URL: https://ieeexplore.ieee.org/document/8633890.

[355] Hirohito Yamazaki et al. "Optical detection of DNA translocation through silicon nanopore by ultraviolet light". In: *Applied Physics A 2013 115:1* 115.1 (Sept. 2013), pp. 53–56. ISSN: 1432-0630. DOI: 10.1007/S00339-013-7956-0. URL: https://link.springer.com/article/10.1007/s00339-013-7956-0.

[356] Hirohito Yamazaki et al. "Optical observation of DNA translocation through Al2O3 sputtered silicon nanopores in porous membrane". In: *Applied Physics A 2016 122:3* 122.3 (Feb. 2016), pp. 1–6. ISSN: 1432-0630. DOI: 10.1007/S00339-016-9764-9. URL: https://link.springer.com/article/10.1007/s00339-016-9764-9.

[357] Hirohito Yamazaki, Keiko Esashika, and Toshiharu Saiki. "A 150 nm ultraviolet excitation volume on a porous silicon membrane for direct optical observation of DNA coil relaxation during capture into nanopores". In: *Nano Futures* 1.1 (Apr. 2017), p. 011001. ISSN: 2399-1984. DOI: 10.1088/2399-1984/

AA655D. URL: https://iopscience.iop.org/article/10.1088/2399-1984/aa655d%20https://iopscience.iop.org/article/10.1088/2399-1984/aa655d/meta.

[358] Neng Yu and Jianmin Wu. "Rapid and reagentless detection of thrombin in clinic samples via microfluidic aptasensors with multiple target-binding sites". In: *Biosensors and Bioelectronics* 146 (Dec. 2019), p. 111726. ISSN: 0956-5663. DOI: 10.1016/J.BIOS.2019.111726. URL: https://www.sciencedirect.com/science/article/pii/S095656631930805X.

[359] Yiliang Zhao et al. "Resonant photonic structures in porous silicon for biosensing". In: *https://doi.org/10.1117/12.2256893* 10081 (Feb. 2017), pp. 26–35. ISSN: 16057422. DOI: 10.1117/12.2256893. URL: https://www.spiedigitallibrary.org/conference-proceedings-of-spie/10081/100810D/Resonant-photonic-structures-in-porous-silicon-for-biosensing/10.1117/12.2256893.full%20https://www.spiedigitallibrary.org/conference-proceedings-of-spie/10081/100810D/Resonant-.

[360] Wouter J.C. Vijselaar et al. "A Stand-Alone Si-Based Porous Photoelectrochemical Cell". In: *Advanced Energy Materials* 9.19 (May 2019), p. 1803548. ISSN: 16146840. DOI: 10.1002/AENM.201803548;WGROUP:STRING:PUBLICATION. URL: /doi/pdf/10.1002/aenm.201803548%20https://onlinelibrary.wiley.com/doi/abs/10.1002/aenm.201803548%20https://advanced.onlinelibrary.wiley.com/doi/10.1002/aenm.201803548.

[361] Kuan-Lun Chu et al. "Miniature fuel cell with monolithically fabricated Si electrodes – Uniformity of Catalyst Layer Thickness -". In: *Journal of Physics: Conference Series* 557.1 (Nov. 2014), p. 012108. ISSN: 1742-6596. DOI: 10.1088/1742-6596/557/1/012108. URL: https://iopscience.iop.org/article/10.1088/1742-6596/557/1/012108%20https://iopscience.iop.org/article/10.1088/1742-6596/557/1/012108/meta.

[362] Aude Roland et al. "In-depth study of annealed porous silicon: Understand the morphological properties effect on negative LiB electrode performance". In: *Electrochimica Acta* 323 (Nov. 2019), p. 134758. ISSN: 0013-4686. DOI: 10.1016/J.ELECTACTA.2019.134758. URL: https://www.sciencedirect.com/science/article/pii/S0013468619316299.

[363] C. Yaddaden et al. "Study and Characterization of the Porous Silicon Membrane Anode for LITHIUM-Ion Batteries". In: *Silicon 2022 14:18* 14.18 (May 2022), pp. 12213–12221. ISSN: 1876-9918. DOI: 10.1007/S12633-022-01885-3. URL: https://link.springer.com/article/10.1007/s12633-022-01885-3.

[364] Byeong Dong Kang et al. "Numerical study on energy harvesting from concentration gradient by reverse electrodialysis in anodic alumina nanopores". In: *Energy* 86 (June 2015), pp. 525–538. ISSN: 0360-5442. DOI: 10.1016/J.ENERGY.2015.04.056. URL: https://www.sciencedirect.com/science/article/abs/pii/S0360544215005113.

[365] Hirofumi Daiguji et al. "Electrochemomechanical energy conversion in nanofluidic channels". In: *Nano Letters* 4.12 (2004), pp. 2315–2321. ISSN: 15306984. DOI: 10.1021/nl0489945. URL: https://pubs.acs.org/doi/10.1021/nl0489945.

[366] Shizhi Qian, Aihua Wang, and Juan K. Afonien. "Electrophoretic motion of a spherical particle in a converging–diverging nanotube". In: *Journal of Colloid and Interface Science* 303.2 (Nov. 2006), pp. 579–592. ISSN: 0021-9797. DOI: 10.1016/J.JCIS.2006.08.003. URL: https://www.sciencedirect.com/science/article/abs/pii/S0021979706007041.

[367] David A. Boy, Frédéric Gibou, and Sumita Pennathur. "Simulation tools for lab on a chip research: Advantages, challenges, and thoughts for the future". In: *Lab on a Chip* 8.9 (2008), pp. 1424–1431. ISSN: 14730189. DOI: 10.1039/B812596C.

[368] Reiyu Chein and Bogan Chung. "Numerical Study on Ionic Transport through Micro- Nanochannel Systems". In: *International Journal of Electrochemical Science* 7.12 (Dec. 2012), pp. 12159–12180. ISSN: 1452-3981. DOI: 10.1016/S1452-3981(23)16534-5. URL: https://www.sciencedirect.com/science/article/pii/S1452398123165345.

[369] M. A. Butler and D. S. Ginley. "Prediction of Flatband Potentials at Semiconductor-Electrolyte Interfaces from Atomic Electronegativities". In: *Journal of the Electrochemical Society* 125.2 (Feb. 1978), pp. 228–232. ISSN: 19457111. DOI: 10.1149/1.2131419. URL: http://jes.ecsdl.org/cgi/doi/10.1149/1.2131419.

[370] Roe Hoan Yoon, Talat Salman, and Gabrielle Donnay. "Predicting points of zero charge of oxides and hydroxides". In: *Journal of Colloid And Interface Science* 70.3 (July 1979), pp. 483–493. ISSN: 00219797. DOI: 10.1016/0021-9797(79)90056-0. URL: https://www.sciencedirect.com/science/article/abs/pii/0021979779900560.

[371] Chenhang Sun and John C. Berg. *A review of the different techniques for solid surface acid-base characterization*. Sept. 2003. DOI: 10.1016/S0001-8686(03)00066-6. URL: https://www.sciencedirect.com/science/article/pii/S0001868603000666.

[372] Murat Barisik et al. "Size dependent surface charge properties of silica nanoparticles". In: *Journal of Physical Chemistry C* 118.4 (2014), pp. 1836–1842. ISSN: 19327447. DOI: 10.1021/jp410536n. URL: www.comsol.com.

[373] J. Sonnefeld. "Surface charge density on spherical silica particles in aqueous alkali chloride solutions - Part 2. Evaluation of the surface charge density constants". In: *Colloid & Polymer Science* 273.10 (Oct. 1995), pp. 932–938. ISSN: 0303402X. DOI: 10.1007/BF00660370. URL: http://link.springer.com/10.1007/BF00660370.

[374] David Wooten et al. "Surface Charging of n-type Gd 2 O 3 and HfO 2 thin Films". In: *MRS Proceedings* 1111 (Feb. 2008), pp. 1111–D07–16. ISSN: 0272-9172. DOI: 10.1557/proc-1111-d07-16. URL: https://www.cambridge.org/core/product/identifier/S1946427400022430/type/journal%7B%5C_%7Darticle.

[375] Justin W. Ntalikwa. "Determination of surface charge density of α-alumina by Acid - base titration". In: *Bulletin of the Chemical Society of Ethiopia* 21.1 (Apr. 2007). ISSN: 1011-3924. DOI: 10.4314/bcse.v21i1.61391. URL: http://www.ajol.info/index.php/bcse/article/view/61391.

[376] R. Herino et al. "Porosity and Pore Size Distributions of Porous Silicon Layers". In: *Journal of The Electrochemical Society* 134.8 (Aug. 1987), p. 1994. ISSN: 1945-7111. DOI: 10.1149/1.2100805. URL: https://iopscience.iop.org/article/10.1149/1.2100805%20https://iopscience.iop.org/article/10.1149/1.2100805/meta.

[377] *Stable porous silicon membranes for biosensing.* URL: https://thesis.dial.uclouvain.be/entities/masterthesis/c99ed8c2-b4d2-4a07-b4af-b6ba3e94effa (visited on 10/14/2025).

[378] Abdelazim M. Mebed, Alaa M. Abd-Elnaiem, and Wim De Malsche. "Influence of Anodizing Parameters on the Electrochemical Characteristics and Morphology of Highly Doped P-type Porous Silicon". In: *Silicon* 13.3 (Mar. 2021), pp. 819–829. ISSN: 18769918. DOI: 10.1007/S12633-020-00490-6/METRICS. URL: https://link.springer.com/article/10.1007/s12633-020-00490-6.

[379] Atefeh Ghaderi et al. "Nanoscale morphology, optical dynamics and gas sensor of porous silicon". In: *Scientific Reports* 14.1 (Dec. 2024), p. 3677. ISSN: 20452322. DOI: 10.1038/S41598-024-54336-X. URL: https://pmc.ncbi.nlm.nih.gov/articles/PMC10866982/.

[380] Tomoko Urata et al. “Pore formation in p-type silicon in solutions containing different types of alcohol”. In: *Nanoscale Research Letters* 7.1 (2012), p. 329. ISSN: 1556276X. DOI: 10.1186/1556-276X-7-329. URL: https://pmc.ncbi.nlm.nih.gov/articles/PMC3724496/.

[381] Shailesh N. Sharma, R. K. Sharma, and S. T. Lakshmikumar. “Role of an electrolyte and substrate on the stability of porous silicon”. In: *Physica E: Low-dimensional Systems and Nanostructures* 28.3 (Aug. 2005), pp. 264–272. ISSN: 1386-9477. DOI: 10.1016/J.PHYSE.2005.03.020. URL: https://www.sciencedirect.com/science/article/pii/S1386947705001177.

[382] Xiaoge Gregory Zhang. “Electrochemistry of Silicon and Its Oxide”. In: *Electrochemistry of Silicon and Its Oxide* (2004). DOI: 10.1007/B100331.

[383] Michael J.. Sailor. *Porous silicon in practice : preparation, characterization and applications*. Wiley-VCH, 2012, p. 249. ISBN: 9783527641901.

[384] Woo Lee et al. “Ionic Current Rectification of Porous Anodic Aluminum Oxide (AAO) with a Barrier Oxide Layer”. In: *ACS Nano* 14.10 (Oct. 2020), pp. 13727–13738. ISSN: 1936086X. DOI: 10.1021/ACSNANO.0C05954. URL: https://pubs.acs.org/doi/abs/10.1021/acsnano.0c05954.

[385] Filipe Henrique, Paweł J. Zuk, and Ankur Gupta. “A network model to predict ionic transport in porous materials”. In: *Proceedings of the National Academy of Sciences of the United States of America* 121.22 (May 2024), e2401656121. ISSN: 10916490. DOI: 10.1073/PNAS.2401656121/SUPPL_FILE/PNAS.2401656121.SM03.MP4. URL: /doi/pdf/10.1073/pnas.2401656121?download=true.

[386] Tumcan Sen and Murat Barisik. “Internal surface electric charge characterization of mesoporous silica”. In: *Scientific Reports* 9.1 (Dec. 2019), pp. 1–9. ISSN: 20452322. DOI: 10.1038/S41598-018-36487-W;TECHMETA=118,119;SUBJMETA=357,542,638,639,925;KWRD=NANOSCALE+MATERIALS,SURFACE+CHEMISTRY. URL: https://www.nature.com/articles/s41598-018-36487-w.

[387] Marios Sophocleous and John K. Atkinson. “A review of screen-printed silver/silver chloride (Ag/AgCl) reference electrodes potentially suitable for environmental potentiometric sensors”. In: *Sensors and Actuators A: Physical* 267 (Nov. 2017), pp. 106–120. ISSN: 0924-4247. DOI: 10.1016/J.SNA.2017.10.013. URL: https://www.sciencedirect.com/science/article/pii/S0924424717313638.

[388] J. Riistama and J. Lekkala. "Electrochemical noise properties of different electrode materials in different electrolytes". In: *IFMBE Proceedings* 13 (2007), pp. 149–154. ISSN: 16800737. DOI: 10.1007/978-3-540-70994-7_26. URL: https://link.springer.com/chapter/10.1007/978-3-540-70994-7%7B%5C_%7D26.

[389] Wen Zhang et al. "Design and Testing of Nanovolt-Level Low-Noise Ag-AgCl Electrodes for Expendable Current Profilers". In: *Electronics 2025, Vol. 14, Page 2402* 14.12 (June 2025), p. 2402. ISSN: 2079-9292. DOI: 10.3390/ELECTRONICS14122402. URL: https://www.mdpi.com/2079-9292/14/12/2402/htm%20https://www.mdpi.com/2079-9292/14/12/2402.

[390] Walter J. Hamer and Y. Yung chi. "Osmotic Coefficients and Mean Activity Coefficients of Uni-univalent Electrolytes in Water at 25°C". In: *Journal of Physical and Chemical Reference Data* 1.4 (1972), pp. 1047–1100. ISSN: 15297845. DOI: 10.1063/1.3253108.

[391] S. Billat et al. "Influence of etch stops on the microstructure of porous silicon layers". In: *Thin Solid Films* 297.1-2 (Apr. 1997), pp. 22–25. ISSN: 0040-6090. DOI: 10.1016/S0040-6090(96)09421-7. URL: https://www.sciencedirect.com/science/article/abs/pii/S0040609096094217.

[392] O. Belmont et al. "About the origin and the mechanisms involved in the cracking of highly porous silicon layers under capillary stresses". In: *Thin Solid Films* 276.1-2 (Apr. 1996), pp. 219–222. ISSN: 0040-6090. DOI: 10.1016/0040-6090(95)08057-0. URL: https://www.sciencedirect.com/science/article/abs/pii/0040609095080570.

[393] O. Belmont, D. Bellet, and Y. Bréchet. "Study of the cracking of highly porous p+ type silicon during drying". In: *Journal of Applied Physics* 79.10 (May 1996), pp. 7586–7591. ISSN: 0021-8979. DOI: 10.1063/1.362415. URL: /aip/jap/article/79/10/7586/491859/Study-of-the-cracking-of-highly-porous-p-type.

[394] X. Yang et al. "Porous Silicon Fabrication and Surface Cracking Behavior Research Based on Anodic Electrochemical Etching". In: *Fuel Cells* 21.1 (Feb. 2021), pp. 52–57. ISSN: 16156854. DOI: 10.1002/FUCE.202000048.

[395] C. S. Solanki et al. "New Approach for the Formation and Separation of a Thin Porous Silicon Layer". In: *physica status solidi (a)* 182.1 (Nov. 2000), pp. 97–101. ISSN: 1521-396X. DOI: 10.1002/1521-396X(200011)182:1<97::AID-PSSA97>3.0.CO;2-L. URL: /doi/pdf/10.1002/1521-396X%7B%5C%%7D28200011%7B%5C%%7D29182%7B%5C%%7D3A1%7B%5C%%7D3C97%7B%5C%%7D3A%7B%5C%%7D3AAID-PSSA97%7B%5C%%7D3E3.0.CO%7B%5C%%7D3B2-L%20https://onlinelibrary.wiley.com/doi/abs/10.

1002/1521-396X%7B%5C%7D28200011%7B%5C%7D29182%7B%5C%7D3A1%7B%5C%7D3C97%7B%5C%7D3A%7B%5C%7D3AAID-PSSA97%7B%5C%7D3E3.0.CO%7B%5C%7D3B2-L%20https://onlinelibrary.wiley.com/doi/10.1002/1521-396X(200011.

[396] G. Mauckner et al. "Quantum confinement effects in absorption and emission of freestanding porous silicon". In: *Solid State Communications* 91.9 (Sept. 1994), pp. 717–720. ISSN: 0038-1098. DOI: 10.1016/0038-1098(94)00443-9. URL: https://www.sciencedirect.com/science/article/abs/pii/0038109894004439.

[397] M. Ghulinyan et al. "Free-standing porous silicon single and multiple optical cavities". In: *Journal of Applied Physics* 93.12 (June 2003), pp. 9724–9729. ISSN: 00218979. DOI: 10.1063/1.1578170.

[398] C. S. Solanki et al. "Self-Standing Porous Silicon Films by One-Step Anodizing". In: *Journal of The Electrochemical Society* 151.5 (Mar. 2004), p. C307. ISSN: 00134651. DOI: 10.1149/1.1688797/XML. URL: https://iopscience.iop.org/article/10.1149/1.1688797%20https://iopscience.iop.org/article/10.1149/1.1688797/meta.

[399] D. N. Goryachev, L. V. Belyakov, and O. M. Sreseli. "Free-standing luminescent layers of porous silicon". In: *Semiconductors* 44.12 (Dec. 2010), pp. 1588–1591. ISSN: 10637826. DOI: 10.1134/S1063782610120092/METRICS. URL: https://link.springer.com/article/10.1134/S1063782610120092.

[400] Md Mushfequr Rahman. "Membranes for Osmotic Power Generation by Reverse Electrodialysis". In: *Membranes 2023, Vol. 13, Page 164* 13.2 (Jan. 2023), p. 164. ISSN: 2077-0375. DOI: 10.3390/MEMBRANES13020164. URL: https://www.mdpi.com/2077-0375/13/2/164%20https://www.mdpi.com/2077-0375/13/2/164.

[401] L. T. Zhuravlev. "The surface chemistry of amorphous silica. Zhuravlev model". In: *Colloids and Surfaces A: Physicochemical and Engineering Aspects* 173.1-3 (Nov. 2000), pp. 1–38. ISSN: 0927-7757. DOI: 10.1016/S0927-7757(00)00556-2. URL: https://www.sciencedirect.com/science/article/abs/pii/S0927775700005562.

[402] Ya Rong Shi et al. "Experimental Determination of Particle Size-Dependent Surface Charge Density for Silica Nanospheres". In: *The Journal of Physical Chemistry C* 122.41 (Oct. 2018), pp. 23764–23771. ISSN: 19327455. DOI: 10.1021/ACS.JPCC.8B07566. URL: https://pubs.acs.org/doi/abs/10.1021/acs.jpcc.8b07566.

[403] Aleksandr S. Lenshin et al. "Features of the Composition and Photoluminescent Properties of Porous Silicon Depending on Its Porosity Index". In: *Coatings 2023, Vol. 13, Page 385* 13.2 (Feb. 2023), p. 385. ISSN: 20796412. DOI: 10.3390/coatings13020385. URL: https://www.mdpi.com/2079-6412/13/2/385/htm%20https://www.mdpi.com/2079-6412/13/2/385.

[404] P. Ragonese et al. "Effect of Interfacial SiOx Defects on the Functional Properties of Si-Transition Metal Oxide Photoanodes for Water Splitting". In: *ACS Applied Materials & Interfaces* 15.40 (Oct. 2023), pp. 46933–46940. ISSN: 19448252. DOI: 10.1021/acsami.3c09555. URL: /doi/pdf/10.1021/acsami.3c09555?ref=article%7B%5C_%7DopenPDF.

[405] Jordi Moreno et al. "Upscaling Reverse Electrodialysis". In: *Environmental Science & Technology* 52.18 (Sept. 2018), pp. 10856–10863. ISSN: 15205851. DOI: 10.1021/acs.est.8b01886. URL: /doi/pdf/10.1021/acs.est.8b01886?ref=article%7B%5C_%7DopenPDF.

[406] R Shankar Subramanian. *Convective Mass Transfer*. Tech. rep.

[407] A. S. Kim. "Permeate flux inflection due to concentration polarization in crossflow membrane filtration: A novel analytic approach". In: *The European Physical Journal E 2008 24:4* 24.4 (Jan. 2008), pp. 331–341. ISSN: 1292895X. DOI: 10.1140/epje/i2007-10244-x. URL: https://link.springer.com/article/10.1140/epje/i2007-10244-x.

[408] Alexandre Giacobbo et al. "Concentration Polarization in Ultrafiltration/-Nanofiltration for the Recovery of Polyphenols from Winery Wastewaters". In: *Membranes 2018, Vol. 8, Page 46* 8.3 (July 2018), p. 46. ISSN: 20770375. DOI: 10.3390/membranes8030046. URL: https://www.mdpi.com/2077-0375/8/3/46/htm%20https://www.mdpi.com/2077-0375/8/3/46.

[409] Zhou Yu et al. "Computational Fluid Dynamics Modeling of Hollow Membrane Filtration for Concentration Polarization". In: *Water 2021, Vol. 13, Page 3605* 13.24 (Dec. 2021), p. 3605. ISSN: 20734441. DOI: 10.3390/w13243605. URL: https://www.mdpi.com/2073-4441/13/24/3605/htm%20https://www.mdpi.com/2073-4441/13/24/3605.

[410] *AEM13920 Dual-source Energy Harvesting PMIC | e-peas*. URL: https://e-peas.com/product/aem13920/ (visited on 02/19/2026).

[411] *AEM15820 Energy harvesting IC: discover our AEM product family*. URL: https://e-peas.com/product/aem15820/ (visited on 02/19/2026).

[412] *AEM20941 Energy harvesting IC: discover our AEM product family*. URL: https://e-peas.com/product/aem20941/ (visited on 02/19/2026).

[413] Honggu Chun and Taek Dong Chung. "Iontronics". In: *Annual Review of Analytical Chemistry* 8.1 (July 2015), pp. 441–462. ISSN: 1936-1327. DOI: 10.1146/annurev-anchem-071114-040202. URL: http://www.annualreviews.org/doi/10.1146/annurev-anchem-071114-040202.

[414] Tommy Tarvainen et al. "Drug release from a porous ion-exchange membrane in vitro". In: *Biomaterials* 20.22 (Nov. 1999), pp. 2177–2183. ISSN: 0142-9612. DOI: 10.1016/S0142-9612(99)00122-2. URL: https://www.sciencedirect.com/science/article/abs/pii/S0142961299001222.

[415] Dubus Laura. "Determination of the surface charge density of a nanoporous silicon membrane during electroosmotic pumping". Master's thesis. UCLouvain, 2023. URL: https://thesis.dial.uclouvain.be/entities/masterthesis/0316d4d1-f2b3-43a3-8d62-2aefe9e173e9.

[416] Shuhuai Yao et al. "Electroosmotic pumps fabricated from porous silicon membranes". In: *Journal of Microelectromechanical Systems* 15.3 (June 2006), pp. 717–728. ISSN: 10577157. DOI: 10.1109/JMEMS.2006.876796. URL: https://ieeexplore.ieee.org/document/1638499.

[417] J. Z. Wallner et al. "Macro porous silicon as pump media for electroosmotic pumps". In: *Physica Status Solidi (A) Applications and Materials Science* 204.5 (May 2007), pp. 1327–1331. ISSN: 18626300. DOI: 10.1002/PSSA.200674326;REQUESTEDJOURNAL:JOURNAL:18626319;CTYPE:STRING:JOURNAL. URL: /doi/pdf/10.1002/pssa.200674326%20https://onlinelibrary.wiley.com/doi/abs/10.1002/pssa.200674326%20https://onlinelibrary.wiley.com/doi/10.1002/pssa.200674326.

[418] Jessica L. Snyder et al. "High-performance, low-voltage electroosmotic pumps with molecularly thin silicon nanomembranes". In: *Proceedings of the National Academy of Sciences of the United States of America* 110.46 (Nov. 2013), pp. 18425–18430. ISSN: 00278424. DOI: 10.1073/PNAS.1308109110/-/DCSUPPLEMENTAL. URL: https://pmc.ncbi.nlm.nih.gov/articles/PMC3831982/.

[419] Qian Yang et al. "Low-voltage efficient electroosmotic pumps with ultrathin silica nanoporous membrane". In: *Electrophoresis* 40.16 (Aug. 2019), pp. 2149–2156. ISSN: 15222683. DOI: 10.1002/ELPS.201800533;JOURNAL:JOURNAL:15222683;CSUBTYPE:STRING:SPECIAL;PAGE:STRING:ARTICLE/CHAPTER. URL: /doi/pdf/10.1002/elps.201800533%20https://onlinelibrary.wiley.com/doi/abs/10.1002/elps.201800533%20https://analyticalsciencejournals.onlinelibrary.wiley.com/doi/10.1002/elps.201800533.

[420] Martin Becker and Marek Sierka. "Atomistic Simulations of Plasma-Enhanced Atomic Layer Deposition". In: *Materials 2019, Vol. 12, Page 2605* 12.16 (Aug. 2019), p. 2605. ISSN: 1996-1944. DOI: 10.3390/MA12162605. URL: https://www.mdpi.com/1996-1944/12/16/2605/htm%20https://www.mdpi.com/1996-1944/12/16/2605.

[421] Hervé Rigneault et al. "Etude théorique et expérimentale de pompes électro-osmotiques et de leur utilisation dans une boucle de refroidissement de l'électronique de puissance". PhD thesis. Université de Limoges, Oct. 2008, p. 255. DOI: 10.34894/VQ1DJA. URL: https://theses.hal.science/tel-00335282%20https://theses.hal.science/tel-00335282/document.

[422] Zdeňka Kolská et al. "Electrokinetic Potential and Other Surface Properties of Polymer Foils and Their Modifications". In: *Polymer Science* (Jan. 2013). DOI: 10.5772/46144. URL: https://www.intechopen.com/chapters/42101%20undefined/chapters/42101.

[423] Fetiye Esin Yakin, Murat Barisik, and Tumcan Sen. "Pore Size and Porosity Dependent Zeta Potentials of Mesoporous Silica Nanoparticles". In: *The Journal of Physical Chemistry C* 124.36 (Sept. 2020), pp. 19579–19587. ISSN: 19327455. DOI: 10.1021/ACS.JPCC.0C04602. URL: https://pubs.acs.org/doi/abs/10.1021/acs.jpcc.0c04602.

[424] Zijing Xia et al. "Surface Zeta Potential of ALD-Grown Metal-Oxide Films". In: *Langmuir* 37.39 (Oct. 2021), pp. 11618–11624. ISSN: 15205827. DOI: 10.1021/ACS.LANGMUIR.1C02028. URL: https://pubs.acs.org/doi/abs/10.1021/acs.langmuir.1c02028.

[425] Moumneh Ramy. "Paper-based stacked reverse electrodialysis cells for energy generation from salinity gradient". PhD thesis. UCLouvain, 2022. URL: https://thesis.dial.uclouvain.be/entities/masterthesis/a474334f-4675-4fa8-8aec-a30fd879087b.

UNIVERSITÉ CATHOLIQUE DE LOUVAIN
École polytechnique de Louvain
Rue Archimède, 1 bte L6.11.01, 1348 Louvain-la-Neuve, Belgique | **www.uclouvain.be/epl**